

ABSTRACT

ALLEN, ELIZABETH LEIGH. Water Quality Signatures of Switchgrass (*Panicum virgatum*) Intercropped in Managed Forests and Mixed Land Use in the Southeastern United States. (Under the Direction of Dr. François Birgand and Dr. George Chescheir).

Recent advances in *in situ* water quality data collection methods have created an incredible amount of high frequency quantitative and qualitative data. Synthesis of methods and guidelines outlining how to extract reliable concentrations and meaningful interpretations of patterns and the ‘drivers’ responsible remains a work in progress. There is dire need to identify robust indicators of hydrochemical and biogeochemical signatures and to evaluate which indicators or combination of indicators strengthen our ability to detect and quantify effects of changes in controlling processes, such as those induced by a land use change.

In the first chapter, the hydrology and water quality effects of site preparation activities associated with intercropping switchgrass as a dedicated energy crop in managed Loblolly pine forests were evaluated for upland watersheds in Mississippi. Cumulative indicators of water quality were robust enough to detect effects in total suspended solids (TSS) and dissolved organic carbon (DOC) export patterns that were synchronous with management operations.

The second chapter proposed numerical solutions to calibrate portable UV-vis spectrometers for DOC, in a ‘worst case scenario’ in which optics had the tendency to become extremely fouled in a forested watershed of the NC coastal plain. Results detail methods to calibrate these sensors in these cases and show that it is important to recognize that the relationship between the ‘color matrix’ of the water and DOC concentration may change following a single large event.

The third chapter tests the ability of a suite of hydrochemical indicators to describe the interplay between hydrological and biogeochemical processes in a North Carolina lower coastal

plain, mixed land use watershed. Statistical concentration indicators, flux duration curves, and double mass curve approaches were evaluated alongside the event hysteresis (C-Q) indicators widely adopted in the literature. The latter is the main indicator from which most hydrological and biogeochemical processes are generally inferred. Each indicator explored had its own strength, but the indicator that provided the most information about nutrient export patterns and controlling biogeochemical processes was the double mass curve approach, which examined cumulative water quality load as a function of cumulative flow. The C-Q indicators were also useful but strengthened when combined with the context provided by the double mass curves.

Water Quality Signatures of Switchgrass (*Panicum virgatum*) Intercropped in Managed Forests
and Mixed Land Use in the Southeastern United States

by
Elizabeth Leigh Allen

A dissertation submitted to the Graduate Faculty of
North Carolina State University
in partial fulfillment of the
requirements for the degree of
Doctor of Philosophy

Biological and Agricultural Engineering

Raleigh, North Carolina
2021

APPROVED BY:

Dr. François Birgand
Committee Co-Chair

Dr. George Chescheir
Committee Co-Chair

Dr. R. Wayne Skaggs

Dr. Christopher Osburn

BIOGRAPHY

Elizabeth “Beth” Allen grew up in eastern North Carolina and attended Nash County schools during grades K-12. In high school, she applied to East Carolina University to continue her education and received a letter inviting her to join the first class of the new Systems Engineering program. After two years in the Systems Engineering program at ECU, she decided that she would like the opportunity to explore other types of engineering and applied to North Carolina State University. There, she studied Materials Science and Engineering for one semester, then transferred to the Department of Biological and Agricultural Engineering with an interest in studying engineering solutions to address environmental issues. She graduated from the department with a Bachelor of Science in Biological Engineering with a concentration in Environmental Engineering in 2009.

In the semester following graduation, she entered the doctoral program in Biological and Agricultural Engineering at North Carolina State University, where she was offered an exciting opportunity to study hydrology and water quality as part of a large, multi-disciplinary, collaborative research project funded by the US Department of Energy, Weyerhaeuser Company, and Catchlight Energy, LLC under the direction of Dr. François Birgand. Beth spent one semester of her program studying at Cemagref (now INRAE) in Antony, France under the direction of Dr. Vazken Andréassian as a recipient of the Chateaubriand Fellowship.

Outside of education, Beth was surrounded by music her entire life and her passion for music played a huge role in shaping her as a person. Her parents are both musicians and her grandmother was a gifted pianist and piano teacher. She studied piano and dance for nearly 10

years followed by learning to play other instruments including the drums. Music has intricately woven pieces of her life together and she believes the relationship between music and mathematics has highly influenced her path in education. In the most challenging times, her love for music has provided a creative outlet that connected her with many of the important people she considers family.

ACKNOWLEDGEMENTS

Reflecting on the many kind and special people who helped me achieve this goal over the years is quite overwhelming and difficult to put into words. If you were any part of this journey, I appreciate you. Thank you to my advisor, committee, NCSU faculty/staff, Cemagref faculty/staff, project collaborators, fellow students, family, and friends for the incredible amount of support and encouragement you provided in this endeavor!

TABLE OF CONTENTS

LIST OF TABLES	x
LIST OF FIGURES	xiv
General Introduction	1
References	4
Chapter 1: Hydrology and water quality impacts associated with site preparation for intercropped Loblolly pine (<i>Pinus taeda</i>) and switchgrass (<i>Panicum virgatum</i>) in upland forested watersheds in Mississippi, USA	6
1.1 Abstract.....	6
1.2 Introduction.....	7
1.3 Methods.....	11
1.3.1 Sites and Treatment Description	11
1.3.2 Site Preparation and Treatment Establishment Operations	13
1.3.3 Data Collection	15
Discharge Data	15
Weather Data	17
Water Quality Data	17
1.3.4 Data Analysis	18
Hydrology	18
Water Quality Calculations and Analyses	23
1.4 Results and Discussion.....	25
1.4.1 Hydrology	25
Overview of Hydrology	25
Paired relationships.....	30
Flashiness	33
1.4.2 Water Quality.....	46

1.5 Discussion and conclusions	62
1.5.1 Hydrology	62
1.5.2 Water Quality	63
1.6 Acknowledgements	70
1.7 References.....	71
Chapter 2: Methods to improve DOC concentration time-series predictions from <i>in situ</i> UV-Vis continuous measurements in a coastal watershed	76
2.1 Abstract.....	76
2.2 Introduction.....	77
2.3 Methods.....	80
2.3.1 Site Description.....	80
2.3.2 Hydrology	82
2.3.3 Continuous water quality monitoring instrumentation and maintenance procedures..	83
Automatic cleaning of the optics	83
Manual cleaning and maintenance of the optics	84
2.3.4 Water Quality Sampling and Analysis Scheme	85
2.3.5 Absorbance Data Post-Processing	87
2.3.6 Local Calibration Methods	88
Local Calibration Statistical Method: Partial Least Squares Regression.....	88
Local Calibration of PLSR Models: Three Approaches	89
2.3.7 PLSR Model Evaluation Criteria	95
Selecting Number of PLSR Model Components	97
2.3.8 Cumulative Load as Indicator of Performance of PLSR	98
2.4 Results	99
2.4.1 Local Calibration Using Entire Time Range.....	100
2.4.2 Local Calibrations Using a Moving Window	106

Suggested number of components highly dependent upon criteria	107
Robustness of concentration prediction outside of calibration windows.....	110
Possible changes in the relationship between the color matrix and concentrations	111
2.4.3 Local Calibration to Stable Periods	119
2.5 Discussion and conclusions	129
2.6 Acknowledgements	134
2.7 References.....	135
Chapter 3: A multi-indicator approach to the characterization of water quality in a mixed land use lower coastal plain watershed	139
3.1 Abstract.....	139
3.2 Introduction.....	140
3.3 Methods.....	142
3.3.1 Site Description.....	142
3.3.2 Data acquisition and Preparation	144
Flow Data.....	144
Water Table Depth, water temperature, and rainfall.....	145
Water Quality Sampling and data	145
3.3.3 Integrative and cumulative Indicators.....	146
Cumulative Flow and Load Estimation	146
Cumulative Flux Duration Curves	147
Double Cumulative Curves/Double Mass Curves	148
3.3.4 Event Scale Dynamics: C-Q Indicators	151
Event Identification.....	151
Hysteresis and Flushing Indices.....	152
3.4 Results	154
3.4.1 Hydrology fed by intermittent subsurface flow in a very flat watershed.....	154

Land use determined contribution to flow	159
3.4.2 Water Quality	161
High resolution data for water quality and quantity	161
Annual concentration indicators reveal influence of agriculture in a context of a low land organically rich stream.....	162
Cumulative Flux Duration Indicators show sluggish hydrological reactivity during high flows, and during low flows, quenching mechanisms for water and nitrate export, while sustained release of reduced C and N	165
Double Cumulative Loading Curves give the big picture of the drivers of the nutrient and material exports.....	171
Nitrogen Double Cumulative Loading Curves	179
Water table near the surface is associated with relatively low chloride export	183
Double mass hydronium curve reveals significant flow contribution from forested area during phase 4	184
Phase 1 drivers: subsurface flow associated with high water table following hurricanes and isolated storms	185
Phase 2: Intense drainage season starts with high nitrate and phosphate exports	194
Surface drainage as a likely key driver for processes during phase 3	196
Significance of water from forested areas and release of water trapped behind beaver dams as key drivers to phase 4.....	197
Flow from and fertilization on agricultural fields during the growing season as key drivers of phase 5	198
Event Hysteresis indicators provide valuable information given a hydrochemical context.....	200
A relatively small number of events exhibiting unusual patterns.....	204
Event hysteresis indices provide further evidence of very active denitrification and sediment diagenetic processes	209
Shortcomings of the HI and FI indices analyzed out of context.....	212
3.5 Discussion and conclusions	213
3.6 Acknowledgements	217

3.7 References.....	218
General Conclusion.....	222
APPENDIX A: 60-Day Moving Window Calibration Residuals.....	227
A.1 Prediction outside of 60-day calibration windows for models with 1-20 components	227
A.2 Trends surrounding hinge-point when $ncomp_{nse65}$ components are selected.....	233
APPENDIX B: 30-Day Moving Window Analysis.....	237
B.1 Effect of full concentration range vs. smaller concentration range on prediction trends.....	237
APPENDIX C: A1 Single Water Quality Parameter Flow and Flux Duration Curves.....	252
APPENDIX D: A1 Hysteresis Plots.....	256
APPENDIX E: A1 Event Selection for Hysteresis Analysis.....	333
APPENDIX F: A1 Hysteresis Index vs. Flushing Index Plots for Original Event Data	356

LIST OF TABLES

Table 1.1.	Site characteristics and land cover treatments of Mississippi watersheds.	13
Table 1.2.	Synopsis of major management operations that took place in each of the treatment watersheds (BF1-4).	14
Table 1.3.	Selected indicators of hydrologic alteration to analyze flashiness of watersheds during	23
Table 1.4.	Tipping bucket rain gauge station rainfall totals (P_C) from 3 stations corresponding to approximate watershed location, cumulative discharge (Q_C) and runoff coefficient (RC) for the 3-year period spanning March 20, 2010 – March 20, 2013.	26
Table 1.5.	Tipping bucket rain gauge station rainfall totals (P_C) from 3 stations corresponding to approximate watershed location, annual cumulative discharge (Q_C) and runoff coefficient (RC) for each hydrological year.	26
Table 1.6.	R-B index for all study watersheds for each year. Relative flashiness rankings are included. A value of 5 indicates the most flashy while 1 represents the least flashy of the watersheds.	42
Table 1.7.	Select IHA flashiness indicators for watersheds BF1 (YP), BF2 (IC/Th), BF3 (SG), BF4 (IC/Rp) and BFREF (MP) for 3 study years. The first value listed in each column is the calculated flashiness indicator value and the second value is the flashiness ranking among watersheds for that parameter in each year. 5 indicates the most flashy while 1 represents the least flashy of the watersheds.	44
Table 1.8.	Annual cumulative water quality loads for the second pre-treatment year (year 2) and establishment year (year 3).	46
Table 1.9.	Annual sediment yields exported from relatively smaller watersheds across a range of literature involving paired watershed studies evaluating water quality effects of land use change and forestry management practices.	65
Table 2.1.	PLSR calibration results for models consisting of 1-20 components built using the total time range of observed DOC concentrations and absorption spectra.	100
Table 2.2.	60-day moving window calibration cross-validation results for 1-20 component models (per each calibration window) with number of components selected based on 4 selection methods: 1) Minimum root mean square error of prediction (RMSEP) 2) minimum number of components necessary to produce an “acceptable” Nash Sutcliffe Efficiency ($NSE \geq 0.65$) 3) automatic selection using the “one-sigma” method found in the R <i>pls</i> package 4) automatic selection using the “permutation” method found in the R <i>pls</i> package.	

	Number of components selected based on method for each window calibration model are in <i>Italics</i> while corresponding NSE values produced by models with the selected number of components are listed to the right in each selection method column.....	109
Table 2.3.	Stable period calibration cross-validation results for 1-20 component models (per each calibration) with number of components selected based on 4 selection methods: 1) Minimum root mean square error of prediction (RMSEP) 2) minimum number of components necessary to produce an “acceptable” Nash Sutcliffe Efficiency ($NSE \geq 0.65$) 3) automatic selection using the “one-sigma” method found in the R <i>pls</i> package 4) automatic selection using the “permutation” method found in the R <i>pls</i> package. The three columns of results under each selection method category are the number of components selected, NSE and mean noise (%) values.	123
Table 2.4.	Cumulative DOC loads calculated from predicted time series using models with <i>ncomp_{rmsep}</i> and <i>ncomp_{nse65}</i> numbers of components for both stable period calibrations and the full range calibration.....	128
Table 3.1.	Summary data for double cumulative loading curve phases and intermittent low flow occurring during the months of July and August prior to Phase 1 for July 1998 – June 1999 at A1. Flow-weighted average concentration (FWAC) ratio is equal to the phase FWAC divided by the Annual FWAC. FWAC values for major phases 3, 4, and 5 are provided in italics below subphases 3a, 4a and 5a respectively.	176
Table 3.2.	Summary of double mass curves shape and Flow Weighted Average Concentration (FWAC) for each 5 phases identified and the 10 parameters.	181
Table 3.3.	Flushing vs dilution patterns observed for 8 parameters. The text in bold is to highlight the majority of flushing vs. dilution effects. The number of patterns per phase appears as flushing/dilution.	208
Table B.1.	30-day moving window calibration cross-validation results for 1-20 component models (per each calibration window) with number of components selected based on 2 selection methods: 1) Minimum root mean square error of prediction (RMSEP) 2) minimum number of components necessary to produce an “acceptable” Nash Sutcliffe Efficiency ($NSE \geq 0.65$). Number of components selected based on method for each window calibration model are in <i>Italics</i> while corresponding NSE values produced by models with the selected number of components are listed to the right in each selection method column. * refers to the situation in which the number of components selected to evaluate model results are those corresponding to the $NSE \geq 0.65$ criterion because the number of components producing the minimum RMSEP did not produce an acceptable model.....	238

Table E.1.	Summary of hysteresis index and flushing index value interpretations relating to C-Q dynamics.	333
Table E.2.	Minimum interval (int) at which there were matching Q_{int} values on the rising and falling limb for each event initially analyzed. HI_{int} values were calculated at 1% intervals. Single-peak events that occurred as parts of a multi-peak event listed following the “Multi” event with which they were associated and indicated by superscript letters A, B & C (i.e. Event 11 Multi was composed of single-peak events 11 & 12).....	334
Table E.3.	Event hysteresis results for PO4-P. An x in the Final Analysis column indicates the event was included in final HI and FI results presented in Chapter 3. Single-peak events that occurred as parts of a multi-peak event are listed following the “Multi” event with which they were associated and indicated by superscript letters A, B & C (e.g., Event 11 Multi was composed of single-peak events 11 & 12).	336
Table E.4.	Event hysteresis results for TP. An x in the Final Analysis column indicates the event was included in final HI and FI results presented in Chapter 3. Single-peak events that occurred as parts of a multi-peak event are listed following the “Multi” event with which they were associated and indicated by superscript letters A, B & C (e.g., Event 11 Multi was composed of single-peak events 11 & 12).	338
Table E.5.	Event hysteresis results for NO3-N. An x in the Final Analysis column indicates the event was included in final HI and FI results presented in Chapter 3. Single-peak events that occurred as parts of a multi-peak event are listed following the “Multi” event with which they were associated and indicated by superscript letters A, B & C (e.g., Event 11 Multi was composed of single-peak events 11 & 12).	340
Table E.6.	Event hysteresis results for NH4-N. An x in the Final Analysis column indicates the event was included in final HI and FI results presented in Chapter 3. Single-peak events that occurred as parts of a multi-peak event are listed following the “Multi” event with which they were associated and indicated by superscript letters A, B & C (e.g., Event 11 Multi was composed of single-peak events 11 & 12).	342
Table E.7.	Event hysteresis results for ON. An x in the Final Analysis column indicates the event was included in final HI and FI results presented in Chapter 3. Single-peak events that occurred as parts of a multi-peak event are listed following the “Multi” event with which they were associated and indicated by superscript letters A, B & C (e.g., Event 11 Multi was composed of single-peak events 11 & 12).	344
Table E.8.	Event hysteresis results for DOC. An x in the Final Analysis column indicates the event was included in final HI and FI results presented in	

Chapter 3. Single-peak events that occurred as parts of a multi-peak event are listed following the “Multi” event with which they were associated and indicated by superscript letters A, B & C (e.g., Event 11 Multi was composed of single-peak events 11 & 12). 346

Table E.9. Event hysteresis results for TSS. An x in the Final Analysis column indicates the event was included in final HI and FI results presented in Chapter 3. Single-peak events that occurred as parts of a multi-peak event are listed following the “Multi” event with which they were associated and indicated by superscript letters A, B & C (e.g., Event 11 Multi was composed of single-peak events 11 & 12). 348

Table E.10. Event hysteresis results for pH. An x in the Final Analysis column indicates the event was included in final HI and FI results presented in Chapter 3. Single-peak events that occurred as parts of a multi-peak event are listed following the “Multi” event with which they were associated and indicated by superscript letters A, B & C (e.g., Event 11 Multi was composed of single-peak events 11 & 12). 350

Table E.11. Event hysteresis results for Cl. Single-peak events that occurred as parts of a multi-peak event are listed following the “Multi” event with which they were associated and indicated by superscript letters A, B & C (e.g. Event 11 Multi was composed of single-peak events 11 & 12). 352

Table E.12. Event hysteresis results for DIC. Single-peak events that occurred as parts of a multi-peak event are listed following the “Multi” event with which they were associated and indicated by superscript letters A, B & C (e.g. Event 11 Multi was composed of single-peak events 11 & 12). 354

LIST OF FIGURES

Figure 1.1.	Aerial view highlighting proximity of five watersheds monitored in Calhoun County, Mississippi.....	12
Figure 1.2.	Cumulative discharge (Q_C) plotted as a function of cumulative rainfall (P_C) for the entire 3-year monitoring period for watersheds BF1 (YP), BF2 (IC/Th), BF3 (SG), BF4 (IC/Rp) and BFREF (MP).....	28
Figure 1.3.	Cumulative discharge and rainfall as a function of time in (a) both pre-treatment years (years 1 & 2) and (b) second pre-treatment year (year 2) and treatment year (year 3) which were most similar in rainfall totals.	29
Figure 1.4.	Logarithmic daily flow volumes of watersheds as a function of logarithmic daily flow volumes in the young pine control watershed, BF1 for both pre-treatment years and the establishment year. Linear regressions were performed for flows to the right of the vertical grey line and above the horizontal grey line which were visually determined as cutoff points for lower flows that would not affect annual cumulative volume substantially.....	32
Figure 1.5.	Flow duration curves in (a) pre-treatment year 1, (b) pre-treatment year 2 and (c) treatment (year 3) for watersheds BF1 (YP), BF2 (IC/Th), BF3 (SG), BF4 (IC/Rp) and BFREF (MP).....	34
Figure 1.6.	Double probability graphs where volume of water is as expressed as a percentage of total annual volume (V_x) occurring in x percentage of the time in (a) pre-treatment year 1, (b) pre-treatment year 2 and (c) treatment (year 3) for watersheds BF1 (YP), BF2 (IC/Th), BF3 (SG), BF4 (IC/Rp) and BFREF (MP).....	38
Figure 1.7.	Cumulative TSS load, L_C , and hydrograph plotted for each treatment watershed BF1 (YP), BF2 (IC/Th), BF3 (SG), and BF4 (IC/Rp). Points and vertical grey lines correspond to the cumulative load corresponding with the time each composite sample was collected. Upward tick marks below the hydrograph represent each time the ISCO sampler was triggered to take a water sample. Black vertical lines indicate the time that each treatment (labeled) began to take place.....	48
Figure 1.8.	Cumulative TSS, TP and DOC flux as a function of cumulative flow volume for the entire water quality monitoring period in BF1 (YP), BF2 (IC/Th), BF3 (SG), BF4 (IC/Rp) and BFREF (MP). Points represent the time at which a composite sample was collected. Vertical lines correspond to the treatments in legend.....	52
Figure 1.9.	Daily cumulative TSS flux of watershed (a) BF2 (IC/Th), (b) BF3 (SG), and (c) BF4 (IC/Rp) as a function of daily cumulative TSS flux of the young pine control watershed, BF1 (YP).....	55

Figure 1.10.	Daily cumulative DOC flux of watershed (a) BF2 (<i>IC/Th</i>), (b) BF3 (<i>SG</i>), and (c) BF4 (<i>IC/Rp</i>) as a function of daily cumulative DOC flux of the young pine control watershed, BF1 (<i>YP</i>).....	59
Figure 2.1.	Aerial view of D1 among three others in a paired watershed design study located in Carteret County, NC.....	81
Figure 2.2.	Comparison of DOC concentrations calculated by the s::can global calibration and discrete sample DOC concentrations measured in the lab. Original s::can concentration data was used to determine which data were reliable for local calibration purposes. Examples of unreliable data corresponding with measurements of air are observed as sudden decreases in the s::can DOC (Original) time series occurring in the interval between servicing periods. Gray polygons represent days in which the spectrometer was serviced, correlating with a large decrease in s::can DOC concentration due to optics cleaning. The s::can DOC (Cleaned) time series represents the subset of data left available for local calibration after unreliable data were removed.....	90
Figure 2.3.	Windows 1-4 of a 60-day moving calibration window with a chronological 7-day shift in beginning window date for each window.....	92
Figure 2.4.	Evaluation criteria RMSEP, NSE and Mean Noise (%) plotted as a function of the number of components included in the PLSR model calibrated using the entire date range of data available. The vertical black line corresponds to the number of components included in the model associated with the measured DOC concentrations as a function of predicted DOC concentrations (top right). This line is meant to more easily illustrate how a 7-component model performs comparatively to other number of component selections and where visually a plateau begins to form in the RMSEP and NSE curves.....	102
Figure 2.5.	Comparison of the 15-minute DOC concentration time series for the February events predicted by a 5-component, 9-component, and 12-component PLSR model calibrated using the entire date range of concentrations. The grey area indicates a field maintenance day when the spectrometer optics were cleaned.	104
Figure 2.6.	Measured DOC concentrations subset by calibration window. Bottom and top lines of boxes represent the 25th and 75th quartile values respectively while whisker notches represent the subset minimum and maximum concentrations.	107
Figure 2.7.	Residuals plotted as a percent difference from observed concentrations for the model selected for each calibration window built with the number of components producing the absolute minimum RMSEP. Top and bottom box notches represent the 25 th and 75 th quartile, the middle black line	

	represents the median, and whisker notches represent the minimum and maximum values in the data range.....	110
Figure 2.8.	Measured vs. predicted concentrations for calibration Windows (a) 5, (b) 6, (c) 7, (d) 8, (e) 9, and (f) 10 showing the progression in general over-prediction to under-prediction of concentrations. Triangles represent all samples that preceded the calibration window and squares represent all samples that fell after the calibration window. Circles indicate “clusters” of over-predicted samples.	113
Figure 2.9.	Three periods of time in which the data was split for calibration of periods indicative of a similar water color-concentration relationship based on 60-day and 30-day moving window analyses. Period A ranges from December 20, 2012 – February 7, 2013. Period B ranges from February 7, 2013 – February 14, 2013 and signifies the 7-day shift between 60-day and 30-day calibration Windows 8 & 9. Period C ranges from February 14, 2013 – May 20, 2013. Filled circles indicate DOC measured samples that were included in the dataset used to calibrate a plsr model and hollow circles indicate samples remaining that were evaluated for prediction trends. The calibrations are shown as follow: (A) Calibration AB (B) Calibration C (C) Calibration A (D) Calibration BC.....	120
Figure 2.10.	Side by side comparison of measured DOC concentrations as a function of predicted DOC concentrations produced from a model with $ncomp_{nse65}$ number of components (left) and $ncomp_{rmsep}$ number of components (right) for stable period (a) Calibration AB (b) Calibration C (c) Calibration A (d) Calibration BC.	124
Figure 3.1.	Location, land use and flow direction in the 1,531 ha subcatchment upstream of station A1 and location of the raingauge and water table wells (after Birgand, 2000).	144
Figure 3.2.	Cumulative discharge as a function of cumulative rainfall from July 1998 – June 1999 in A1 subcatchment. Gridlines indicate the beginning of a new month and the x- and y- axes represent beginning of July 1998. Gray shaded area indicates active late-fall to winter flow period spanning December 13, 1998 – April 23, 1999.	156
Figure 3.3.	Time series data for the hydrological year July 1998 – June 1999 for the A1 subcatchment including a) 10-min interval discharge rates and rainfall total pulses and cumulative discharge and precipitation as a percentage of annual totals, b) water table depth recorded in F6 and P2 plots representative of forested and agricultural water table depth dynamics respectively and c) temperature recorded at 3 and 20 cm depths below the water surface at A1.....	158

Figure 3.4.	Hydrograph and chemographs of NO ₃ -N, NH ₄ -N, ON, TP, PO ₄ -P, DOC and DIC during summer events at the outlet of the A1 watershed in 1998 (events 9, 10, and 11) and 1999 (events 30, 31; after Birgand, 2000).....	161
Figure 3.5.	Boxplot representation of concentration data statistics representing concentrations associated with flow rates greater than 5 L/s (n = 26240). This subset of data corresponds to the 50% of the year that comprised 98.9% of the annual total discharge. Whiskers represent minimum and maximum concentration values. Bottoms and tops of gray boxes indicate 25 th and 75 th quartile values and the intermediate black line represents the median concentration value. Red triangles indicate means.	164
Figure 3.6.	Flux duration curves for nitrate, ammonium, organic nitrogen, DOC, DIC, phosphate, TP, TSS and flow for the 1998-99 hydrological year at the A1 watershed station.....	167
Figure 3.7.	Cumulative nitrate load export as a function of cumulative discharge for July 1998 – June 1999 at the A1 subcatchment outlet.	172
Figure 3.8.	Cumulative chloride load export as a function of cumulative discharge for July 1998 – June 1999 at the A1 subcatchment outlet.....	183
Figure 3.9.	Cumulative hydronium load export as a function of cumulative discharge for July 1998 – June 1999 at the A1 subcatchment outlet.....	185
Figure 3.10.	Cumulative ammonium load export as a function of cumulative discharge for July 1998 – June 1999 at the A1 subcatchment outlet.....	187
Figure 3.11.	Cumulative organic nitrogen load export as a function of cumulative discharge for July 1998 – June 1999 at the A1 subcatchment outlet.....	188
Figure 3.12.	Cumulative dissolved organic carbon load export as a function of cumulative discharge for July 1998 – June 1999 at the A1 subcatchment outlet.....	189
Figure 3.13.	Cumulative total suspended solids load export as a function of cumulative discharge for July 1998 – June 1999 at the A1 subcatchment outlet.....	190
Figure 3.14.	Cumulative phosphate load export as a function of cumulative discharge for July 1998 – June 1999 at the A1 subcatchment outlet.....	191
Figure 3.15.	Cumulative total phosphorus load export as a function of cumulative discharge for July 1998 – June 1999 at the A1 subcatchment outlet.....	192
Figure 3.16.	Cumulative dissolved inorganic carbon load export as a function of cumulative discharge for July 1998 – June 1999 at the A1 subcatchment outlet.	194

Figure 3.17.	Examples of hydrographs and chemographs showing A) dilution effect (FI<0) and the chemograph lagging (clockwise, HI>0) after the flow peak (event 25, NO ₃ -N), B) concentration effect (FI>0) and the chemograph lagging (anticlockwise, HI<0) after the flow peak (event 10, NO ₃ -N), C) dilution effect (FI<0) and the chemograph leading (anticlockwise, HI<0) before the flow peak (event 36, NO ₃ -N) and D) concentration effect (FI>0) and the chemograph leading (clockwise, HI>0) before the flow peak (event 58, NH ₄ -N).	201
Figure 3.18.	Hysteresis index plotted as a function of flushing index values for nitrate (NO ₃ -N), ammonium (NH ₄ -N), organic nitrogen (ON), and dissolved organic carbon (DOC). The color and symbol correspond with the identified double mass curve phase in which the event occurred. Sizes of points are scaled to reflect percent annual flow contributed by the event. Labels indicate event number and a letter “M” indicates a multi-peak event treated as a singular event.	206
Figure 3.19.	Hysteresis index plotted as a function of flushing index values for phosphate (PO ₄ -P), total phosphorus (TP), total suspended solids (TSS), and pH. The color and symbol correspond with the identified double mass curve phase in which the event occurred. Sizes of points are scaled to reflect percent annual flow contributed by the event. Labels indicate event number and a letter “M” indicates a multi-peak event treated as a singular event.	207
Figure A.1.	Residuals plotted as a percent difference from observed concentrations for PLSR models composed of 1-20 components for each 60-day calibration window. Top and bottom box notches represent the 25th and 75th quartile, the middle black line represents the median, and whisker notches represent the minimum and maximum values in the data range.	228
Figure A.2.	Residuals plotted as a percent difference from observed concentrations for the PLSR model selected for each calibration window built with the number of components producing the absolute minimum RMSEP (<i>ncomp_{rmsep}</i>).....	228
Figure A.3.	Measured discrete sample DOC concentrations as a function of predicted DOC concentrations resulting from a (a) 1-component, (b) 5-component, (c) 10-component and (d) 20-component model calibrated for Window 1 of the 60-day moving window sequence (12/20/12 – 2/18/13). The circle indicates a cluster of samples that become isolated with larger residuals when additional components are included in the PLSR model.	230
Figure A.4.	Measured discrete sample DOC concentrations as a function of predicted DOC concentrations resulting from a 1-component, 5-component, 10-component and 20-component model calibrated for Window 9 of the 60-day moving window sequence (2/14/13 – 4/15/13).....	232

Figure A.5.	Measured vs. predicted concentrations for model calibrations built with the minimum number of components needed to produce an NSE value of 0.65 or greater for Windows (a) 5, (b) 6, (c) 7, (d) 8, (e) 9, and (f) 10 showing the progression in general over-prediction to under-prediction of concentrations. Triangles represent all samples that preceded the calibration window and the squares represent all samples that fell after the calibration window.	234
Figure B.1.	Measured vs. predicted concentrations for model calibrations built $ncomp_{rmsep}$ for Windows (a) 1, (b) 3, (c) 8, (d) 9, (e) 10, (f) 11, (g) 12, (h) 13, (i) 14 and (j) 18 showing the progression in general over-prediction to under-prediction of concentrations. Triangles represent all samples that preceded the calibration window and the squares represent all samples that fell after the calibration window.	240
Figure B.2.	Side by side comparison of measured DOC concentrations as a function of predicted DOC concentrations produced from a model with $ncomp_{nse65}$ number of components (left) and $ncomp_{rmsep}$ number of components (right) for 30-day calibration analysis for Windows (a) 11, (b) 12, (c) 13 & (d) 14. The $ncomp_{rmsep}$ number of components produced an unacceptable model for the Window 11 calibration, therefore only the results from a calibration model with $ncomp_{nse65}$ number of components is shown here.	245
Figure B.3.	Side by side comparison of measured DOC concentrations as a function of predicted DOC concentrations produced from a model with $ncomp_{nse65}$ number of components (left) and $ncomp_{rmsep}$ number of components (right) for 30-day calibration Windows (a) 1, (b) 2 & (c) 3.	249
Figure C.1.	Flow and flux duration curves for phosphate (PO ₄ -P).	252
Figure C.2.	Flow and flux duration curves for total phosphorus (TP).	252
Figure C.3.	Flow and flux duration curves for nitrate (NO ₃ -N).	253
Figure C.4.	Flow and flux duration curves for ammonium (NH ₄ -N).	253
Figure C.5.	Flow and flux duration curves for organic nitrogen (ON).	254
Figure C.6.	Flow and flux duration curves for total suspended solids (TSS).	254
Figure C.7.	Flow and flux duration curves for dissolved organic carbon (DOC).	255
Figure C.8.	Flow and flux duration curves for dissolved inorganic carbon (DIC).	255
Figure D.1.	Event 8 hydrographs, chemographs, and hysteresis loops for nitrogen and phosphorous species.	257
Figure D.2.	Event 8 hydrographs, chemographs, and hysteresis loops for carbon species, suspended solids, chloride and pH.	258

Figure D.3.	Event 9 hydrographs, chemographs, and hysteresis loops for nitrogen and phosphorous species.....	259
Figure D.4.	Event 9 hydrographs, chemographs, and hysteresis loops for carbon species, suspended solids, chloride and pH.....	260
Figure D.5.	Event 10 hydrographs, chemographs, and hysteresis loops for nitrogen and phosphorous species.....	261
Figure D.6.	Event 10 hydrographs, chemographs, and hysteresis loops for carbon species, suspended solids, chloride, and pH.....	262
Figure D.7.	Event 11 Multi (Events 11 & 12) hydrographs, chemographs, and hysteresis loops for nitrogen and phosphorous species.	263
Figure D.8.	Event 11 Multi (Events 11 & 12) hydrographs, chemographs, and hysteresis loops for carbon species, suspended solids, chloride, and pH.	264
Figure D.9.	Event 11 hydrographs, chemographs, and hysteresis loops for nitrogen and phosphorous species.....	265
Figure D.10.	Event 11 hydrographs, chemographs, and hysteresis loops for carbon species, suspended solids, chloride, and pH.....	266
Figure D.11.	Event 16 hydrographs, chemographs, and hysteresis loops for nitrogen and phosphorous species.....	267
Figure D.12.	Event 16 hydrographs, chemographs, and hysteresis loops for carbon species, suspended solids, chloride, and pH.....	268
Figure D.13.	Event 23 Multi (Events 23 & 24) hydrographs, chemographs, and hysteresis loops for nitrogen and phosphorous species	269
Figure D.14.	Event 23 Multi (Events 23 & 24) hydrographs, chemographs, and hysteresis loops for carbon species, suspended solids, chloride, and pH.	270
Figure D.15.	Event 23 hydrographs, chemographs, and hysteresis loops for nitrogen and phosphorous species.....	271
Figure D.16.	Event 23 hydrographs, chemographs, and hysteresis loops for carbon species, suspended solids, chloride, and pH.....	272
Figure D.17.	Event 24 hydrographs, chemographs, and hysteresis loops for nitrogen and phosphorous species.....	273
Figure D.18.	Event 24 hydrographs, chemographs, and hysteresis loops for carbon species, suspended solids, chloride, and pH.....	274

Figure D.19.	Event 25 hydrographs, chemographs, and hysteresis loops for nitrogen and phosphorous species.....	275
Figure D.20.	Event 25 hydrographs, chemographs, and hysteresis loops for carbon species, suspended solids, chloride, and pH.....	276
Figure D.21.	Event 26 hydrographs, chemographs, and hysteresis loops for nitrogen and phosphorous species.....	277
Figure D.22.	Event 26 hydrographs, chemographs, and hysteresis loops for carbon species, suspended solids, chloride, and pH.....	278
Figure D.23.	Event 27 hydrographs, chemographs, and hysteresis loops for nitrogen and phosphorous species.....	279
Figure D.24.	Event 27 hydrographs, chemographs, and hysteresis loops for carbon species, suspended solids, chloride, and pH.....	280
Figure D.25.	Event 28 Multi (Events 28 & 29) hydrographs, chemographs, and hysteresis loops for nitrogen and phosphorous species.	281
Figure D.26.	Event 28 Multi (Events 28 & 29) hydrographs, chemographs, and hysteresis loops for carbon species, suspended solids, chloride, and pH.	282
Figure D.27.	Event 28 hydrographs, chemographs, and hysteresis loops for nitrogen and phosphorous species.....	283
Figure D.28.	Event 28 hydrographs, chemographs, and hysteresis loops for carbon species, suspended solids, chloride, and pH.....	284
Figure D.29.	Event 29 hydrographs, chemographs, and hysteresis loops for nitrogen and phosphorous species.....	285
Figure D.30.	Event 29 hydrographs, chemographs, and hysteresis loops for carbon species, suspended solids, chloride, and pH.....	286
Figure D.31.	Event 30 hydrographs, chemographs, and hysteresis loops for nitrogen and phosphorous species.....	287
Figure D.32.	Event 30 hydrographs, chemographs, and hysteresis loops for carbon species, suspended solids, chloride, and pH.....	288
Figure D.33.	Event 31 hydrographs, chemographs, and hysteresis loops for nitrogen and phosphorous species.....	289
Figure D.34.	Event 31 hydrographs, chemographs, and hysteresis loops for carbon species, suspended solids, chloride, and pH.....	290

Figure D.35.	Event 32 Multi (Events 32, 33 & 34) hydrographs, chemographs, and hysteresis loops for nitrogen and phosphorous species.	291
Figure D.36.	Event 32 Multi (Events 32, 33 & 34) hydrographs, chemographs, and hysteresis loops for carbon species, suspended solids, chloride, and pH.	292
Figure D.37.	Event 32 hydrographs, chemographs, and hysteresis loops for nitrogen and phosphorous species.....	293
Figure D.38.	Event 32 hydrographs, chemographs, and hysteresis loops for carbon species, suspended solids, chloride, and pH.....	294
Figure D.39.	Event 35 hydrographs, chemographs, and hysteresis loops for nitrogen and phosphorous species.....	295
Figure D.40.	Event 35 hydrographs, chemographs, and hysteresis loops for carbon species, suspended solids, chloride, and pH.....	296
Figure D.41.	Event 36 hydrographs, chemographs, and hysteresis loops for nitrogen and phosphorous species.....	297
Figure D.42.	Event 36 hydrographs, chemographs, and hysteresis loops for carbon species, suspended solids, chloride, and pH.....	298
Figure D.43.	Event 37 hydrographs, chemographs, and hysteresis loops for nitrogen and phosphorous species.....	299
Figure D.44.	Event 37 hydrographs, chemographs, and hysteresis loops for carbon species, suspended solids, chloride, and pH.....	300
Figure D.45.	Event 41 hydrographs, chemographs, and hysteresis loops for nitrogen and phosphorous species.....	301
Figure D.46.	Event 41 hydrographs, chemographs, and hysteresis loops for carbon species, suspended solids, chloride, and pH.....	302
Figure D.47.	Event 44 hydrographs, chemographs, and hysteresis loops for nitrogen and phosphorous species.....	303
Figure D.48.	Event 44 hydrographs, chemographs, and hysteresis loops for carbon species, suspended solids, chloride, and pH.....	304
Figure D.49.	Event 48 hydrographs, chemographs, and hysteresis loops for nitrogen and phosphorous species.....	305
Figure D.50.	Event 48 hydrographs, chemographs, and hysteresis loops for carbon species, suspended solids, chloride, and pH.....	306

Figure D.51.	Event 49 Multi (Events 49 & 50) hydrographs, chemographs, and hysteresis loops for nitrogen and phosphorous species.	307
Figure D.52.	Event 49 Multi (Events 49 & 50) hydrographs, chemographs, and hysteresis loops for carbon species, suspended solids, chloride, and pH.	308
Figure D.53.	Event 50 hydrographs, chemographs, and hysteresis loops for nitrogen and phosphorous species.....	309
Figure D.54.	Event 50 hydrographs, chemographs, and hysteresis loops for carbon species, suspended solids, chloride, and pH.....	310
Figure D.55.	Event 52 hydrographs, chemographs, and hysteresis loops for nitrogen and phosphorous species.....	311
Figure D.56.	Event 52 hydrographs, chemographs, and hysteresis loops for carbon species, suspended solids, chloride, and pH.....	312
Figure D.57.	Event 53 hydrographs, chemographs, and hysteresis loops for nitrogen and phosphorous species.....	313
Figure D.58.	Event 53 hydrographs, chemographs, and hysteresis loops for carbon species, suspended solids, chloride, and pH.....	314
Figure D.59.	Event 54 hydrographs, chemographs, and hysteresis loops for nitrogen and phosphorous species.....	315
Figure D.60.	Event 54 hydrographs, chemographs, and hysteresis loops for carbon species, suspended solids, chloride, and pH.....	316
Figure D.61.	Event 58 hydrographs, chemographs, and hysteresis loops for nitrogen and phosphorous species.....	317
Figure D.62.	Event 58 hydrographs, chemographs, and hysteresis loops for carbon species, suspended solids, chloride, and pH.....	318
Figure D.63.	Event 59 Multi (Events 59 & 60) hydrographs, chemographs, and hysteresis loops for nitrogen and phosphorous species.	319
Figure D.64.	Event 59 Multi (Events 59 & 60) hydrographs, chemographs, and hysteresis loops for carbon species, suspended solids, chloride, and pH.	320
Figure D.65.	Event 59 hydrographs, chemographs, and hysteresis loops for nitrogen and phosphorous species.....	321
Figure D.66.	Event 59 hydrographs, chemographs, and hysteresis loops for carbon species, suspended solids, chloride, and pH.....	322

Figure D.67.	Event 60 hydrographs, chemographs, and hysteresis loops for nitrogen and phosphorous species.....	323
Figure D.68.	Event 60 hydrographs, chemographs, and hysteresis loops for carbon species, suspended solids, chloride, and pH.....	324
Figure D.69.	Event 61 Multi (Events 61 & 62) hydrographs, chemographs, and hysteresis loops for nitrogen and phosphorous species.	325
Figure D.70.	Event 61 (Events 61 & 62) hydrographs, chemographs, and hysteresis loops for carbon species, suspended solids, chloride, and pH.....	326
Figure D.71.	Event 61 hydrographs, chemographs, and hysteresis loops for nitrogen and phosphorous species.....	327
Figure D.72.	Event 61 hydrographs, chemographs, and hysteresis loops for carbon species, suspended solids, chloride, and pH.....	328
Figure D.73.	Event 62 hydrographs, chemographs, and hysteresis loops for nitrogen and phosphorous species.....	329
Figure D.74.	Event 62 hydrographs, chemographs, and hysteresis loops for carbon species, suspended solids, chloride, and pH.....	330
Figure D.75.	Event 63 hydrographs, chemographs, and hysteresis loops for nitrogen and phosphorous species.....	331
Figure D.76.	Event 63 hydrographs, chemographs, and hysteresis loops for carbon species, suspended solids, chloride, and pH.....	332
Figure F.1.	Hysteresis index plotted as a function of flushing index for phosphate (PO ₄ -P) including all rainfall triggered events originally available for analysis.....	357
Figure F.2.	Hysteresis index plotted as a function of flushing index for total phosphorus (TP) including all rainfall triggered events originally available for analysis.	358
Figure F.3.	Hysteresis index plotted as a function of flushing index for nitrate (NO ₃ -N) including all rainfall triggered events originally available for analysis.....	359
Figure F.4.	Hysteresis index plotted as a function of flushing index for ammonium (NH ₄ -N) including all rainfall triggered events originally available for analysis.....	360
Figure F.5.	Hysteresis index plotted as a function of flushing index for organic nitrogen (ON) including all rainfall triggered events originally available for analysis. ...	361

Figure F.6.	Hysteresis index plotted as a function of flushing index for dissolve organic carbon (DOC) including all rainfall triggered events originally available for analysis.....	362
Figure F.7.	Hysteresis index plotted as a function of flushing index for dissolved inorganic carbon (DIC) including all rainfall triggered events originally available for analysis.....	363
Figure F.8.	Hysteresis index plotted as a function of flushing index for total suspended solids (TSS) including all rainfall triggered events originally available for analysis.....	364
Figure F.9.	Hysteresis index plotted as a function of flushing index for chloride (Cl) including all rainfall triggered events originally available for analysis.....	365
Figure F.10.	Hysteresis index plotted as a function of flushing index for pH including all rainfall triggered events originally available for analysis.....	366

General Introduction

Advances in water quality monitoring since the late 2000s have increased accessibility to the dynamic details enveloped in high-resolution datasets and provided measurement frequencies of water quality that have long been accessible in the field of hydrology. The use of *in situ* sensors has led to improvements in our ability to characterize the hydrochemical signatures of watersheds and reduce uncertainty in the estimation of nutrient and sediment loads exported to streams (Lin, 2017; Birgand et al. 2010; Burns et al., 2019; Ruhala & Zarnetske, 2017; Rode et al., 2016; Vaughan et al., 2018; Heathwaite & Bierozza, 2020). The possibility to obtain nearly seamless water quality and hydrology time series data provides the opportunity to capture quickly changing short-term dynamics, such as those associated with storm events, diurnal patterns, and more immediate impacts of a land use change (Lloyd et al., 2016; Kincaid et al., 2020; Pellerin et al., 2012). It also can potentially create a fuller picture of longer-term loading patterns that may evolve more steadily through time. Because water quality monitoring at high frequencies can now be carried out for longer durations of time, a setting is created where short- and long-term trends can be observed simultaneously and where each may provide context for the other. These improvements hold potential for us to better understand sources and pathways of nutrients and sediment observed in streams and how they may be influenced by short- and long-term changes in environmental and anthropogenic factors. Continued research that couples reliable, high frequency hydrology and water quality data across multiple temporal and spatial scales in a wide variety of settings will aid in further development of hydro-biogeochemical models and allow for better informed management decisions needed to effectively protect water resources (Burns et al., 2019; Pellerin et al 2016; Rode et al., 2016; Li et al., 2020).

The development of methods necessary to collect, prepare and analyze high-resolution datasets is crucial to quantify and characterize effects that land use, including implementation of BMPs, Best or Beneficial Management Practices, may have on hydrology and water quality (Pellerin et al., 2016; Rode et al., 2016). Detecting trends in nearly continuous hydrological data is already challenging due to the inherent noise carried by the hydrological signal, and the addition of high frequency concentration data has added complexity to the process, making the task even more difficult. Questions that still require research across a wide variety of land uses and sites are which conclusions can be drawn from specific indicators and which combinations can strengthen our ability to detect patterns in hydrology and water quality, and why? Addressing these questions first requires strategies of monitoring and data preparation that produce reliable high-resolution time series data that accurately represent stream hydrochemistry. The studies presented in this dissertation contribute to this body of work by developing and evaluating the robustness of methods and indicators associated with preparing and analyzing reliable high frequency datasets to detect patterns and change in the hydrochemical signature of watersheds. Research goals included quantifying and characterizing trends to detect effects of land use change and mixed land use on hydrology and water quality at the watershed scale in three study sites located in the southeast region of the United States.

The first chapter uses a suite of hydrological and water quality indicators to detect and quantify the impact of switchgrass interplanting in upland watersheds of the Southeastern US. Water quality was not analyzed on a continuous basis, but composite samples collected on a weekly basis were used to compute loads instead.

The second chapter addresses the difficulties that may arise from the use of newly available continuous water quality sensors to extract reliable concentrations. The original aim of the use of these sensors was to also detect the water quality impact of switchgrass interplanting in lowland watersheds, but the technical difficulties to extract concentrations turned the original aim into a methodological work to define better guidelines to measure concentrations using UV-vis *in situ* spectrophotometers.

The third chapter revisits a 20-year old near continuous water quantity and water quality dataset to test a suite of hydrochemical indicators' ability to best describe the interplay between hydrological and biogeochemical processes at play in the watershed. Mixed land use consisting of agriculture and managed forests, the presence of organic soils and highly organic sediments, and water table driven flow absent of deep groundwater contributions and minimal surface runoff provided a unique combination of site characteristics for which the interaction of flow and water quality concentration dynamics could be observed. The indicators tested included statistical indicators of concentration, integrative duration indicators of flow and water quality, double mass curve indicators, and indicators of the concentration-discharge (C-Q) relationships that become apparent during hydrological events.

References

- Birgand, F., Faucheux, C., Gruau, G., Augéard, B., Moatar, F., & Bordenave, P. (2010). Uncertainties in assessing annual nitrate loads and concentration indicators: Part 1. impact of sampling frequency and load estimation algorithms. *Transactions of the ASABE*, *53*(2), 437-446.
- Burns, D. A., Pellerin, B. A., Miller, M. P., Capel, P. D., Tesoriero, A. J., & Duncan, J. M. (2019). Monitoring the riverine pulse: Applying high-frequency nitrate data to advance integrative understanding of biogeochemical and hydrological processes. *Wiley Interdisciplinary Reviews: Water*, *6*(4), e1348.
- Heathwaite, A. L., & Bierozza, M. (2021). Fingerprinting hydrological and biogeochemical drivers of freshwater quality. *Hydrological Processes*, *35*(1), e13973. doi:<https://doi.org/10.1002/hyp.13973>
- Kincaid, D. W., Seybold, E. C., Adair, E. C., Bowden, W. B., Perdrial, J. N., Vaughan, M. C., & Schroth, A. W. (2020). Land use and season influence Event-Scale nitrate and soluble reactive phosphorus exports and export stoichiometry from headwater catchments. *Water Resources Research*, *56*(10), e2020WR027361.
- Li, L., Sullivan, P. L., Benettin, P., Cirpka, O. A., Bishop, K., Brantley, S. L., . . . Seibert, J. (2021). Toward catchment hydro-biogeochemical theories. *Wiley Interdisciplinary Reviews: Water*, *8*(1), e1495.
- Lin, C., (2017). *Characterization of the Solute Dynamics Signature of an Agricultural Coastal Plain Stream, North Carolina, USA*. (Doctoral dissertation, North Carolina State University, Raleigh, NC, USA). Retrieved from <https://repository.lib.ncsu.edu/handle/1840.20/34568>
- Lloyd, C., Freer, J. E., Johnes, P. J., & Collins, A. L. (2016). Using hysteresis analysis of high-resolution water quality monitoring data, including uncertainty, to infer controls on nutrient and sediment transfer in catchments. *Science of the Total Environment*, *543*, 388-404.
- Pellerin, B. A., Saraceno, J. F., Shanley, J. B., Sebestyen, S. D., Aiken, G. R., Wollheim, W. M., & Bergamaschi, B. A. (2012). Taking the pulse of snowmelt: In situ sensors reveal seasonal, event and diurnal patterns of nitrate and dissolved organic matter variability in an upland forest stream. *Biogeochemistry*, *108*(1), 183-198.
- Pellerin, B. A., Stauffer, B. A., Young, D. A., Sullivan, D. J., Bricker, S. B., Walbridge, M. R., . . . Shaw, D. M. (2016). Emerging tools for continuous nutrient monitoring networks: Sensors advancing science and water resources protection. *JAWRA Journal of the American Water Resources Association*, *52*(4), 993-1008.
- Rode, M., Wade, A. J., Cohen, M. J., Hensley, R. T., Bowes, M. J., Kirchner, J. W., . . . Jomaa, S. (2016). Sensors in the Stream: The High-Frequency Wave of the Present. *Environmental Science & Technology*, *50*(19), 10297-10307. doi: 10.1021/acs.est.6b02155

Ruhala, S. S., & Zarnetske, J. P. (2017). Using in-situ optical sensors to study dissolved organic carbon dynamics of streams and watersheds: A review. *Science of the Total Environment*, 575, 713-723.

Vaughan, M. C., Bowden, W. B., Shanley, J. B., Vermilyea, A., Wemple, B., & Schroth, A. W. (2018). Using in situ UV-Visible spectrophotometer sensors to quantify riverine phosphorus partitioning and concentration at a high frequency. *Limnology and Oceanography: Methods*, 16(12), 840-855.

Chapter 1: Hydrology and water quality impacts associated with site preparation for intercropped Loblolly pine (*Pinus taeda*) and switchgrass (*Panicum virgatum*) in upland forested watersheds in Mississippi, USA

1.1 Abstract

Incorporation of bioenergy crops in existing agricultural systems has been proposed as a solution to meet growing demands for alternative energy. Environmental impacts associated with conversion of land to these types of multifunctional systems must be identified. Managed loblolly pine forests located in the Southeastern region of the United States provide a setting in which perennial grasses, such as switchgrass, may be operationally introduced in the space that exists between the rows of young trees. Few studies have focused on the potential short-term hydrological and water quality effects of the initial site preparation and establishment periods. In this study, we used a suite of indicators to evaluate the impacts of site preparation for intercropped switchgrass (*Panicum virgatum*) in managed Loblolly pine (*Pinus taeda*) forests on hydrology and water quality. Five, small upland watersheds (10.9 – 15.2 ha) located in Calhoun County, Mississippi were monitored as part of a paired watershed experiment. No obvious impact of site preparation on hydrology was made evident by flashiness indicators. A combination of plotting methods allowed for the detection of site preparation effects on total suspended solids (TSS) and dissolved organic carbon (DOC) export but impacts on total phosphorus (TP) were unclear. Increases in TSS and DOC loading patterns were short lived and appeared to return to baseline rather quickly. TSS annual loads (285 – 1636 kg ha⁻¹) in the upland watersheds were relatively comparable to values reported among the literature associated with a variety of studies evaluating effects of land use changes and forestry practices on sediment yields.

1.2 Introduction

Determining a land management practice strategy is crucial to implementing and maintaining an environmentally sustainable agricultural system, especially one that involves a land use conversion. As food crop production and marginal agricultural lands are increasingly transformed to incorporate biomass crops to meet the population's growing energy demands, land management practice plans must be evaluated and adapted accordingly to protect our natural resources, especially the healthy functioning of our water bodies (Acharya and Blanco-Canqui, 2018; Gopalakrishnan et al. 2009; Guo et al. 2018; Heidari et al. 2019; King et al. 2013; Li and Zipp, 2019). Potential short-term hydrology and water quality effects of land use alterations associated with biomass cultivation, particularly those affiliated with site preparation, must be assessed as an initial contribution to understanding the overall environmental impacts of transforming traditional agricultural systems to biomass cultivation systems (Heidari et al., 2019).

Mandated production of biofuels by multiple countries including the United States, those of the European Union, China, India, and Brazil among others implies dedication of large tracks of land to biomass production (Caldwell et al., 2018; Englund et al., 2020; Gopalakrishnan et al., 2009; Jin et al. 2019; Longato et al. 2019). A solution to avoid conversion of agricultural lands already dedicated to food production is to cultivate energy crops on marginal lands, lands that have less than desirable characteristics for successful production of food crops valuable to the local economy (Archaya and Blanco-Canqui, 2018). Managed forests, where trees are cultivated in rows, leave sizable land areas in between that have traditionally not been managed for harvesting purposes, although the potential exists. Managed forests present a landscape in which

intercropping of bioenergy crops can be operationally introduced. Perennial grasses, such as switchgrass, capable of producing high biomass yields with relatively low maintenance requirements have been proposed as a viable species that can be planted in the otherwise unutilized space between rows of young trees in forested settings (Albaugh et al., 2012; Blazier et al. 2009; Blazier et al. 2012; Susaeta et al., 2012). This relatively novel cultivation system, and even further, the conversion of forested land to grass monoculture, are valid and likely scenarios in which environmental consequences must be explored (Cacho et al., 2018; Cacho et al., 2019; Tian et al., 2015).

Few studies have focused on the potential implications on hydrology and water quality of converting land to incorporate dedicated non-grain energy crops such as perennial warm season grasses and short-term woody crops, especially on the initial site preparation and establishment periods, which can be the most expensive and unpredictable of the entire process (Archaya and Blanco-Canqui, 2018; King et al. 2013). If bioenergy grasses fail to establish within the first year following planting, they lose economic value as feedstocks thus making it important to determine the most optimum implementation procedures. Proper selection of site preparation treatments involving clearing woody debris and soil preparation for seed planting as well as selection and timing of chemical treatments such as fertilizer and herbicide applications is critical for ensuring a combination of successful crop growth and minimal environmental impacts. Field studies are still needed among a variety of sites, climates and potential bioenergy crop vegetative species and scenarios, especially at the watershed scale, to contribute to model parameterizations and improvements in current management practices (Griffiths et al., 2019).

Stream responses to classic forestry management practices such as thinning and harvesting have been widely discussed and have demonstrated that nutrient and sediment exports to surface waters typically exhibit increases within the first few years following treatment before returning to baseline levels (Aust and Blinn, 2004; Beltran et al. 2010; Boggs et al. 2016). Bare soil exposure and soil compaction are issues of concern following these operations, creating a highly sensitive time in which rainfall infiltration may be reduced, resulting in increased surface runoff and the landscape left vulnerable to erosion and elevated sediment concentrations at watershed outlets (Cacho et al., 2018). Soil nutrient pools are subject to effects relating to site preparation activities that alter controlling factors. Soil disturbance can cause changes in soil structure altering mineralization processes. Removal of vegetation can reduce nutrient uptake and change the quality/quantity of litter inputs available in the soil. Additional inputs of herbicides and fertilizers may alter the distribution of nutrient forms and increase leachable inorganic forms of nitrogen and phosphorus. These changes may be observed in streamflow through nutrient transport by leaching, subsurface flow, and overland flow (Griffiths et al., 2017).

Southeastern managed forests in the United States have a potential to produce a large portion of biomass feedstocks due to favorable climatic and environmental conditions, with Loblolly pine being one of the most prevalent species grown (Cacho et al., 2018; Griffiths et al., 2017; Susaeta et al., 2012). In this study, we focus on evaluating the hydrology and water quality effects of site preparation for switchgrass intercropping in southeastern U.S. managed Loblolly pine stands through an experimental paired watershed field study. This design is a widely used classical approach that has been applied to detect and monitor impacts of land cover change (Andréassian, 2004; Brown et al. 2005). In the application of this experimental design, hydrological and

nutrient/sediment export relationships are established between treatment and control watersheds to account for inherent heterogeneity existing *among* watersheds and to examine changes in the relationship through time that may be indicative of treatment effects. The design reduces the effect that temporal variability in climate may pose between pre- and post-treatment periods by assuming that control and treatment watersheds are subject to similar climatological factors. Alternatively, responses to treatment can be examined *within* each watershed by characterizing the existing pre- and post-treatment hydrological and nutrient/sediment export behavior and comparing the two. Both concepts were applied in this study to draw conclusions.

Our hypotheses are that, because of additional soil preparation activities and increased trafficability, establishing switchgrass will increase runoff and soil erosion. A reduction in vegetative cover and compacted soil conditions before and during planting are factors expected to lower infiltration capacity of the soils, causing higher proportions of surface runoff and increased mobilization of exposed bare ground soil particles. We expect there may be an increase in the volume of water exported from treatment watersheds due to a reduction in vegetation and therefore a decrease in evapotranspiration. We further hypothesize that herbicide and fertilizer applications will increase nutrient export to surrounding water bodies, especially during the first storm events following these procedures. We hypothesize that some of the impacts may be instantaneous and exist for a short duration with conditions returning to similar pre-establishment states while others may gradually become detectable and linger in time. Until Weyerhaeuser, Chevron, and NC State University partnered together, there had been no studies of the hydrological effects of switchgrass at the watershed level, and particularly no study on the

hydrology and water quality impacts of practices involved during the short yet sensitive period of switchgrass soil preparation and switchgrass establishment.

1.3 Methods

1.3.1 Sites and Treatment Description

The experimental site is located in Calhoun County, Mississippi (33°45' N, 89°17' W). Five small watersheds similar in size (10.9 – 15.2 ha) were monitored during the period March 2010 – March 2013. This 3-year period was composed of two years in which treatment watersheds were under similar land cover and management (pre-treatment), and approximately one year in which biomass treatments involving site preparation and seeding establishment were implemented.

Figure 1.1 provides an aerial view of the spatial proximity of the watersheds. BF1 & BF2 and BF3 & BF4 are adjacent watershed pairs located 4.5 km apart and 6.4 km and 2.8 km northwest of BFREF respectively.

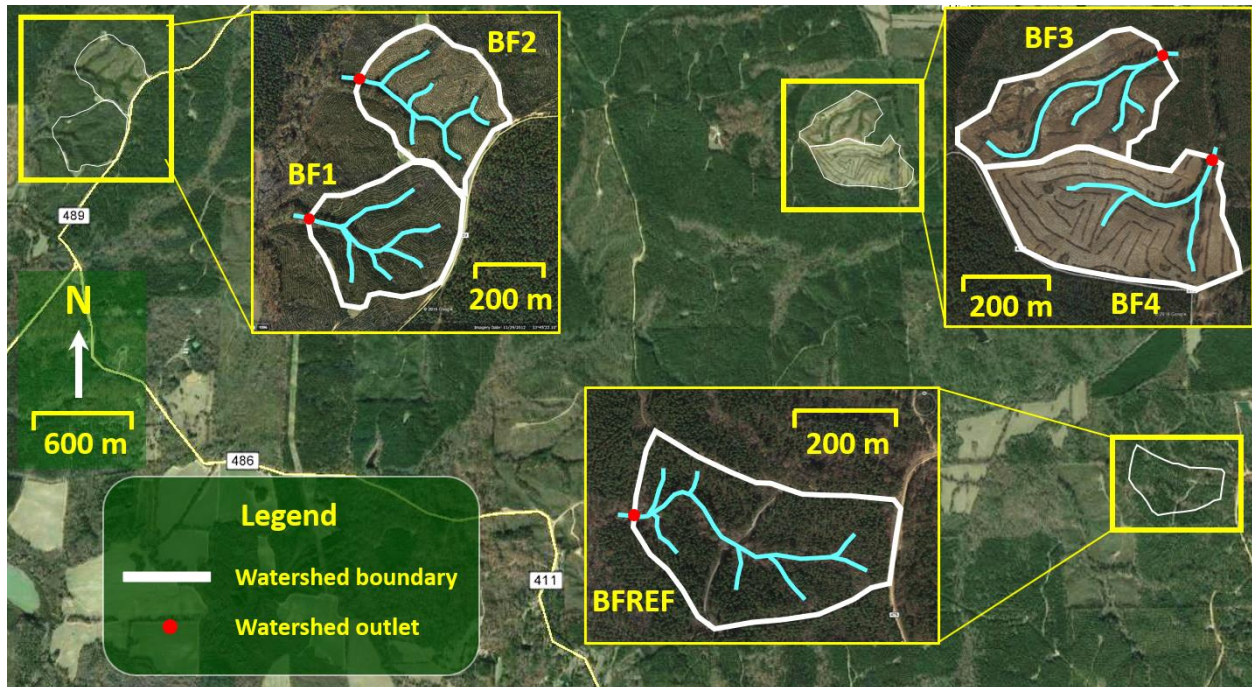


Figure 1.1. Aerial view highlighting proximity of five watersheds monitored in Calhoun County, Mississippi.

A brief description of each watershed including land cover treatment can be found in Table 1.1. Watersheds BF1-4 were biomass treatment watersheds similar in land cover and management leading up to treatment. At the beginning of the 2-year pre-treatment period in which monitoring took place (March 20, 2010 – March 20, 2012), the watersheds were occupied by 3-4-year-old pine stands with a stand density of 1077 tree ha⁻¹. BF1, planted in 2007, was a ‘standard’ young pine (*YP*) plantation that remained under typical management operations during the establishment period (March 20, 2012-2013), designating it as the *control* watershed for the paired watershed experimental design. Site preparation for biomass treatments began in March 2012, first with BF2. The 5-year-old pine stand was thinned (*Th*) and intercropped (*IC*) with switchgrass between rows of trees. Pine stands in BF3 and BF4, planted in 2006, were completely removed and BF3 was replanted in switchgrass (*SG*) monoculture while BF4 was

replanted (*Rp*) with pine trees in preparation for intercropped switchgrass planting later in 2013. BFREF was considered a *reference* watershed in this study, representative of a mature pine (*MP*) stand under conventional management.

Table 1.1. Site characteristics and land cover treatments of Mississippi watersheds.

Watershed	Land Cover Treatment Description	Area (ha)	Average Slope (%)	Soil Type
BF1	Pine (<i>YP</i>)	14.1	11.7	Silt loam
BF2	Thinned Pine with Intercropped Switchgrass (<i>IC/Th</i>)	12.8	10.9	Silt loam
BF3	Switchgrass (<i>SG</i>)	10.9	7.7	Sandy loam
BF4	Replanted Pine in Preparation for Intercropped Switchgrass (<i>IC/Rp</i>)	15.2	7.9	Sandy loam
BFREF	Mid-Rotation Pine (<i>MP</i>)	12.6	15.7	Silt loam

1.3.2 Site Preparation and Treatment Establishment Operations

Site preparation and treatment establishment involved various management operations across each watershed (Table 1.2). Pine tree thinning in BF2 was carried out by a trackhoe mounted shredder on slopes less than 12%. Stand density and tree spacing were reduced to 247 tree ha⁻¹ and a 6.1 x 6.1 m spacing respectively. Following thinning procedures, remaining stumps between rows were sheared by a D8 Bulldozer equipped with a V-blade on the front. Shearing in BF2 concurred with the beginning of treatment in BF3 in which shearing took place to remove all trees in preparation for switchgrass planting of the entire field. Following removal, tree residues were piled into windrows 61 m apart by a D8 Bulldozer with a mounted rake. Following shearing in BF2 and BF3, a post-emergent herbicide (Glyphosate 2% at 169 L ha⁻¹ +

0.25% surfactant) was applied. These operations concluded preparation for switchgrass planting which began to take place on May 22, 2012 in BF2 and BF3. Switchgrass seeding procedures were carried out by first disking the top 0.3 cm of the soil with a tractor, followed by broadcast seeding using a spin spreader mounted on the front of a four-wheeler. Seeds were covered with soil clods resulting from disking by a chain-connected steel bar attached to the back of the four-wheeler. A release herbicide was applied to remove competing hardwoods and understory growing in BF1, BF2 and BF4 in mid-September 2012.

Table 1.2. Synopsis of major management operations that took place in each of the treatment watersheds (BF1-4).

Year	Month/Day	BF1 (YP)	BF2 (IC/Th)	BF3 (SG)	BF4 (IC/Rp)
2006				Pine planting	Pine planting
2007		Pine planting	Pine planting		
2012	3/20 – 3/28		Thinning		
	3/20 – 3/28		Shearing	Shearing	
	4/21 – 4/22		Herbicide	Herbicide	
	5/22		SG planting	SG planting	
	9/10 – 9/11	Herbicide	Herbicide		Herbicide
	10/15 – 10/18				Shearing
	11/29 – 11/30				Offset rip
2013	1/24				Pine planting

While switchgrass had already been planted between rows in the thinned pine plantation (BF2) and the switchgrass monoculture watershed (BF3), BF4 still remained in young pine cover. In preparation for pine and switchgrass planting, shearing and piling were performed in mid-October with same practices applied in BF2 and BF3. Additionally, soil was loosened along proposed tree planting beds by employing a D8 tractor to run an offset rip with mounted blades

that cut to a depth of 61 cm. Pine seedlings were planted in late January 2013 with a density of 1077 trees ha⁻¹ and spacing of 6.1 m x 1.5 m.

The first operation that took place associated with site preparation in the watersheds occurred on March 20th, 2012 in BF2 and BF3, therefore March 20th was selected as the beginning date defining hydrological years for data analysis. Any data collected following this date in 2012 would be associated with a land cover change. It is important to note that the first treatment for BF4 did not occur until later in the establishment year in September 2012 and consisted of an herbicide application to remove competing hardwoods and understory followed by shearing of the 6-year-old pine stand. Therefore a 6-month lag in tree removal operations occurring at BF4 was considered when detecting and comparing possible treatment effects with those of BF2 and BF3.

1.3.3 Data Collection

Discharge Data

Each watershed outlet was fitted with a trapezoidal wooden flume such that flow could be calculated using a wetted cross section area of known dimensions. An ISCO flow meter (750 Area Velocity Flow Module, Teledyne ISCO, Lincoln, NE, USA) was installed at the outlet of the flumes to measure stage and velocity data continuously at a 2-minute time interval. Data was downloaded during biweekly field servicing of the watershed stations. Stations were additionally equipped with a pressure transducer and water level recorder (U20 HOB0 Water Level Data Logger, Onset, Cape Cod, MA, USA) as a redundant water level measurement system.

The 2-minute measurement interval was selected to best characterize the overall discharge dynamics, particularly to more fully represent sudden, large fluctuations and best capture storm events majorly contributing to flow in these small, reactive watersheds. A multi-step procedure was developed to pre-process stage and velocity data. This data correction procedure included removal of outliers, smoothing of internal instrument noise and natural small fluctuations in discharge, correcting for instrument measurement drift, and filling in periods of missing data by either using backup water level data when available or established rating curves. Most of the streamline stage and velocity data were produced using AQUARIUS software (AQUARIUS, Aquatic Informatics, Vancouver, British Columbia, Canada) and R Statistical Software.

Following this “streamlining” of the data, adjustments were applied to account for the relationships between instrument and manual measurements. Streamlined velocity data were adjusted by a factor relating sensor velocity to the cross-sectional average velocity in the flumes. Manual gauging was performed according to the velocity area method (ISO 748) with a Marsh-McBirney® portable flow meter and measurements were taken where the acoustic velocity measurements were made, i.e., at about 10 cm in front of the ISCO sensor. Because of a hydraulic drop downstream of the instrument near the end of the flume, the stage recorded at the instrument (i.e., above the instrument) was lower than the water level corresponding with sensor velocity measurements. To calculate the wetted cross-sectional area 10 cm upstream the instrument, streamlined stage data were adjusted. For this, several experiments were conducted to dam up and suddenly release water in the flume. During these, the hydraulic drops were measured for several stage values. Once stage and the cross-sectional average velocity were corrected and adjusted, termed index stage and index velocity respectively, discharge was

calculated. To fill in remaining gaps in the flow data, values from established stage-discharge rating curves were applied.

Weather Data

Weather data were recorded every 15 minutes at a station (HOBO U30 Cellular Data Logger, Onset, Cape Cod, MA, USA) located between BF3 and BF4. Precipitation, atmospheric pressure, solar radiation, wind speed, gust speed, wind direction, temperature, and relative humidity were parameters measured. Tipping bucket rain gauges and manual rain gauges were installed to provide backup rainfall data and location specific rainfall data, as these watersheds were not all adjacent. Tipping bucket rainfall data were calibrated to reflect rainfall levels measured at a nearby manual rain gauge for every servicing interval. Three sets of rainfall data were determined, one corresponding with the location of BF1 and BF2, the second corresponding with the location of BF3 and BF4, and the third corresponding with the location of BFREF.

Water Quality Data

Flow proportional composite sampling was employed to obtain water quality data. Automatic samplers (ISCO 6712) were programmed to collect a sample each time a threshold volume of water passed through the flume. Each of these samples was routed to a single 5 L bottle, mixing with the previous ones, and a “composite” sample was collected from the field at every servicing interval. The concentration obtained theoretically serves as a good estimate of the flow-weighted concentration and can be used to calculate the load corresponding with the total volume of discharge that occurred over the sampling time associated with the sample. The threshold value

to trigger sampling was modified throughout the monitoring period according to flow conditions and among sites to sample frequently enough to optimally represent storm event export. Larger portions of annual loads are expected to be associated with event discharge, therefore sampling these events often enough is important in estimating annual water quality loads. If a composite sample was not taken due to instrument error or low flow conditions, a grab sample was taken to account for the sampling period if there was enough flow to do so.

The composite bottles were fit with an acidifying system that dispensed 2 mL of 95-98% concentrated sulfuric acid for every 0.5 L of sample volume collected to maintain pH below 2 to preserve the sample from degradation over the approximate two weeks in between servicing intervals. The composite sample collected every two weeks was analyzed for concentrations of nitrate (NO_3^- -N), ammonium (NH_4^+ -N), total Kjeldahl nitrogen (TKN), total suspended solids (TSS), total phosphorous (TP), and dissolved organic carbon (DOC) that were reported in mg L^{-1} . Unfortunately, nitrogen species results are not included in this chapter because lab values were considered unreliable. Therefore, we only focus on sediment, phosphorous and carbon species in the results section. Water quality monitoring began in January 2011 and continued until March 2013.

1.3.4 Data Analysis

Hydrology

Flow Data Subsets

Pre-treatment year hydrograph, cumulative discharge, and cumulative discharge as a function of cumulative precipitation plots demonstrated that a majority of flow was event driven in the

treatment watersheds as reviewed in the results. Therefore, for some analyses (discussed below) triage of the data was performed to focus more on times of the hydrological year in which the watersheds were reactive. Flow data were subset to reduce the effect of lower flow rates and place emphasis on those corresponding with events. Two-minute interval flow rate values were sorted from highest to lowest in each hydrological year in each watershed, and cumulative volume was calculated in the order of the sorted flow rates. Each cumulative flow value was then evaluated as a percentage of the total annual volume, with the highest volume percentages corresponding with the highest flow rates. A threshold percentage of the total annual volume, 98%, was selected to represent the majority of flow rates pertaining to events, eliminating low flow values contributing only a small portion (2%) of water to the total annual volume. Flow data that were subset using this method are referred to as $Q_{98\%}$ in the results section of this paper, otherwise it can be assumed that all 2-minute data including low flow rates were included in a particular analysis discussed.

Paired Daily Flow Relationships

A comparison of 2-minute interval flow rates for the switchgrass watersheds as a function of the young pine control watershed made little sense, and a daily time-step was selected to eliminate the effects of noise and slight differences in timing of rainfall. The previously explained method of subsetting data was applied in the same manner except to daily flow rates rather than 2-minute flow rates. Once data were subset, relationships between the logarithmic daily flow volumes of the treatment watersheds and the young pine control watershed (BF1) were established for each of the two pre-treatment years and the post-treatment year by plotting and determining treatment daily flow rates as a linear function of control daily flow rates. Although subsetting data to

sorted flow rates contributing to 98% of the cumulative volume eliminated much of the lower flow rates that did not seem to fall within the range of data forming an observable relationship in some years/watersheds, there were still low flow values that needed to be excluded to determine a relationship for a fair comparison among years. In this case, threshold values were visually set to further remove low flow rates appearing to diverge from a relatively linear relationship between higher flow rates. These low flow rates typically exhibited higher variability in values for a small range of variability of values in the comparative watershed. The underlying hypothesis of this method is that changes in the relationships between the pre-treatment and establishment years could be indicative of a treatment effect. Slope values and R^2 values were compared among years to determine if treatments changed the switchgrass watershed flow regimes from pre-treatment conditions.

Flashiness

Flashiness is the “frequency and rapidity of short-term changes in streamflow, especially during runoff events” as defined by Baker et al. (2004), although various definitions and interpretations of the meaning of flashiness exist among the literature. Methods to measure relative ‘flashiness’ have been established including the Richard-Baker Index (Baker et al., 2004), flow-duration curves (Searcy, 1959), double probability curve and $V_{x\%}$ (Moatar and Meybeck, 2007) and indicators of hydrologic alterations (IHA parameters) (Richter et al., 1996). These methods were applied and compared to evaluate relative differences in the hydrological response to rainfall among the watersheds in the pre-treatment and establishment periods. We hypothesized that the watersheds with lower slopes and sandier soils (BF1, BF2, BFREF) would be relatively less flashy than those with siltier soils and higher average slopes (BF3, BF4) in the pre-treatment

years. Following site preparation operations, we hypothesized there would be an increase in soil compaction and a decrease in infiltration that would increase flashiness for treatment watersheds BF2-4. Reduction in vegetative cover would also increase surface runoff and therefore increase flashiness in the treatment watersheds with rain events, especially in BF3 and BF4 where all trees were removed.

Flow duration curves were compared among watersheds in all three hydrological years to evaluate if differences in the distribution of flow rates differed between the pre-treatment and establishment years. Steep curves in the slope towards the high end of the curve (lower percentage of the time) indicate higher variability in flow due to runoff and flatter slopes toward the low end of the curve (higher percentages of the time) indicate higher storage capacity of the watersheds. Double probability curves were additionally plotted to determine the portion of the total cumulative water volume ($V_{x\%}$) that occurred in a percentage (x) of the total time (Moatar and Meybeck, 2007). These curves were examined in each of the three years to determine if any changes in flow patterns could be detected, such as the proportion of annual flow volume contributed by the highest flows associated with storm events. The highest flow volumes occurring in small percentages of the time (i.e., $V_{1\%}$, $V_{2\%}$) were interpreted as representing the most variable or flashy watersheds while lower flow volumes at these percentages were interpreted as watersheds exhibiting greater contributions of “baseflow” or groundwater throughout the year. $V_{2\%}$ was considered a low enough percentage of the time to differentiate contributions of event flows to annual volumes among the reactive treatment watersheds and served as an indicator of flashiness.

Baker et al. (2004) created the Richards-Baker (R-B) index to indicate flashiness using average daily flow rates. Streams with higher R-B index values are considered flashier, however size of a watershed can play a role in comparing relative flashiness values. In this study, the sizes of the watersheds are all similar however, and the R-B index was compared directly as a relative indicator. The R-B Index values were calculated on the 2-minute interval data in this case and subset to $Q_{98\%}$.

Indicators of Hydrologic Alteration (IHA) are a set of parameters that have been applied to calculate relative level of flashiness among watersheds. Specific IHA parameters used to calculate flashiness in this study are listed in Table 1.3. The data were subset to exclude lower flow rates, $Q_{98\%}$, before calculating the high pulse counts, high pulse durations, and rise/fall rate parameters, as these discharge values are not indicative of flashiness and relate more to groundwater contribution rather than response to rainfall. The number of flow reversals was calculated for a 10-minute moving interval and for flow rates equal to or greater than 10 L s^{-1} as an objective way to reduce small oscillations due to noise associated with high-frequency measurements, 2 minutes in this case. The flashiness indices among watersheds were ranked from 1 to 5, with 5 representing the flashiest watershed and 1 representing the least flashy. Most flashy would be considered the highest value of the flashiness indicator values for all indicators except high pulse duration. A shorter duration is considered the flashiest in the literature.

Table 1.3. Selected indicators of hydrologic alteration to analyze flashiness of watersheds during pre-treatment and establishment years.

IHA Parameter	Description
High pulse count	Number of occurrences for which flow remains above a defined high pulse (i.e., 75 th , 85 th and 95 th percentile) lasting at least 6 minutes
High pulse duration	Mean duration of high pulses within each year lasting at least 6 minutes (min)
Rise/Fall rate	Mean of all positive/negative differences between consecutive flow values ($L\ s^{-1}\ min^{-1}$)
Number of flow reversals	Number of negative and positive changes

Water Quality Calculations and Analyses

The concept of flow-proportional composite sampling is that the concentration of the sample collected at each field servicing closely approximates the flow-weighted concentration for the volume occurring over the duration of the sampling period. The load (L_i) for each sampling period (i) between servicing intervals was calculated as the product of the composite sample concentration (C_i) and the volume of discharge (V_i) that occurred over the period for each water quality parameter of interest multiplied by uc as a unit conversion factor (Equation 1.1). These values were summed to determine the cumulative load (L_C) for the time period of interest in this study. The annual total cumulative loads were calculated for one pre-treatment year (March 2011 – March 2012) and one establishment year (March 2012 – March 2013) and compared among treatments.

$$L_C = \sum_i L_i = \sum_i uc * V_i C_i \quad 1.1$$

The double mass curve plotting method allows for visualization of the relationship between two variables through time by plotting cumulative quantities (Searcy, 1960). Theoretically, a linear function represents a relationship that remains proportional between the two cumulative quantities and the slope of the curve is the ratio at which the two occur. Two types of double-mass curves were employed to detect treatment effects in the nutrient and sediment export behaviors exhibited by the watersheds. The first of these types examined cumulative water quality load as a function of cumulative flow volume *within* each watershed. The second type evaluated the relationship *between* control and treatment watershed cumulative water quality loads.

In each watershed, cumulative load was plotted as a function of cumulative discharge to examine changes in proportionality, particularly following management activities. Trends in the shape and slope of the curve indicate a phase of similar proportionality between mass exported and volume of water reaching the watershed outlet. Points of transition between trends, “breakpoints”, indicated by a change in slope, would indicate that availability of the nutrient/sediment changed. Shifts in availability could relate to changes resulting from land management practices that in turn, affect biogeochemical mechanisms controlling transportable quantities or an increase or decrease in the hydrological connectivity to nutrient/sediment sources.

Even though synchrony between breakpoints and land management operations occurrence were considered strong evidence of a short-term treatment effect in this study, another plotting technique was used to further distinguish if the breakpoints were not simply due to some other

hydrological factor than the volume of water leaving the system, such as rainfall intensity. The paired watershed approach was used to compare cumulative loading in the treatment watersheds (BF2-4) to that of the young pine control (BF1). If there was a breakpoint in this double cumulative curve corresponding to times of management practices, this further suggested that there was an effect on water quality loading due to treatment. Not every station was serviced nor had a sample collected on the same day and time, therefore the cumulative loads were linearized to a daily time step such that daily cumulative load values could be directly compared among the watersheds. Data was available in the first pre-treatment year beginning in January (2011), thus these plots include these data in the results to add to the overall analysis.

1.4 Results and Discussion

Hydrology results are presented for two pre-treatment years referred to as Year 1 and Year 2 and for one establishment year (Year 3) including and following treatment related to management operations. Water quality data was limited to comparison of one full pre-treatment year, Year 2, and Year 3 due to the shorter monitoring period for data collected. Plots of water quality data, however, include a small portion of water quality data collected and analyzed in January and February of Year 1.

1.4.1 Hydrology

Overview of Hydrology

Over the three-year period, all five watersheds received similar amounts of rainfall, with a 5% maximum difference in total precipitation for three-year totals (Table 1.4.). However, differences are evident in the water yields: very similar runoff coefficients of 24% to 26% of the

total rainfall flowed at the group of three BF3 (*SG*), BF4 (*IC/Rp*) and BFREF (*MP*) stations, while only 19% and 14% of the total rainfall flowed at the BF1 (*YP*) and BF2 (*IC/Th*) stations. The group of three watersheds are all located in the eastern part of the region over sandy loam soils. The low water yield for BF1 and BF2 is rather surprising as the average watershed slope is a lot higher than those of BF3 and BF4, and the soils are siltier and expected to allow lower infiltration.

Table 1.4. Tipping bucket rain gauge station rainfall totals (P_C) from 3 stations corresponding to approximate watershed location, cumulative discharge (Q_C) and runoff coefficient (RC) for the 3-year period spanning March 20, 2010 – March 20, 2013.

Watershed	3 Year Total		
	P_C (mm)	Q_C (mm)	RC
BF1 (<i>YP</i>)	3803	705	0.19
BF2 (<i>IC/Rp</i>)		525	0.14
BF3 (<i>SG</i>)	3991	938	0.24
BF4 (<i>IC/Rp</i>)		989	0.25
BFREF (<i>MP</i>)	3825	997	0.26

Table 1.5. Tipping bucket rain gauge station rainfall totals (P_C) from 3 stations corresponding to approximate watershed location, annual cumulative discharge (Q_C) and runoff coefficient (RC) for each hydrological year.

Watershed	Year 1			Year2			Year 3		
	P_C (mm)	Q_C (mm)	RC	P_C (mm)	Q_C (mm)	RC	P_C (mm)	Q_C (mm)	RC
BF1 (<i>YP</i>)	1029	158	0.15	1393	288	0.21	1381	259	0.19
BF2 (<i>IC/Th</i>)		106	0.10		237	0.17		182	0.13
BF3 (<i>SG</i>)	1128	214	0.19	1446	330	0.23	1417	394	0.28
BF4 (<i>IC/Rp</i>)		236	0.21		363	0.25		390	0.28
BFREF (<i>MP</i>)	1112	317	0.28	1316	310	0.24	1397	370	0.27

Annual cumulative flow volumes (Table 1.5.) in watersheds BF1-4 were mainly contributed to by flow occurring during approximately 4-5 months of the year (December – April) in both pre-treatment years. Discharge followed seasonal patterns that can be described as ‘S’ shape curves on Figure 1.2: discharge increases almost linearly with rainfall in the winter and yields very little water with rainfall (flat parts of the curves) in summer (Figure 1.2 & Figure 1.3). The reference stand BFREF seems to deviate quite a bit from this general pattern. A plausible explanation for sustained summer flows at BFREF is the likely addition of some groundwater from adjacent watersheds. The mostly flat sloped section in the curves produced in the months of May – November in years 1 and 2 are shortened for watersheds BF3 and BF4 in year 3. These watersheds begin producing larger amounts of discharge beginning in September 2012 versus December with no obvious difference in rainfall pattern between years 2 and 3 (Figure 1.3).

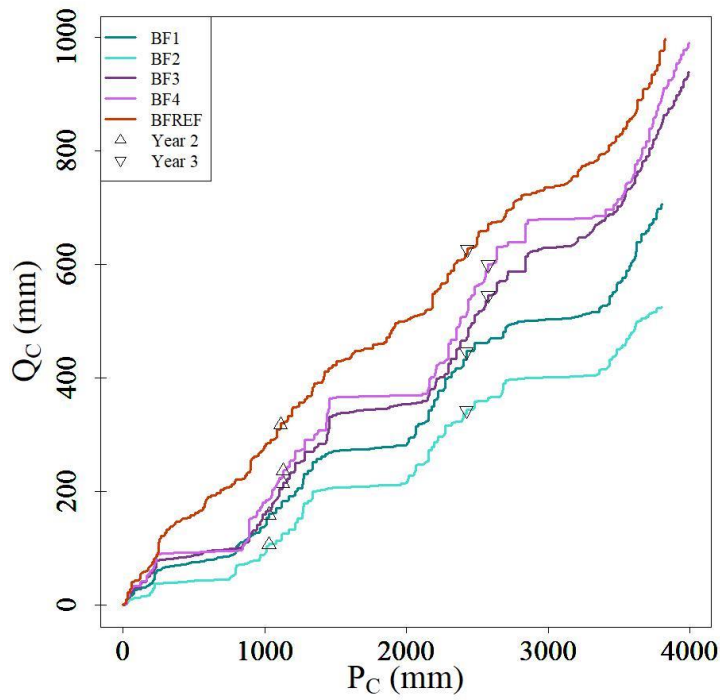


Figure 1.2. Cumulative discharge (Q_C) plotted as a function of cumulative rainfall (P_C) for the entire 3-year monitoring period for watersheds BF1 (*YP*), BF2 (*IC/Th*), BF3 (*SG*), BF4 (*IC/Rp*) and BFREF (*MP*).

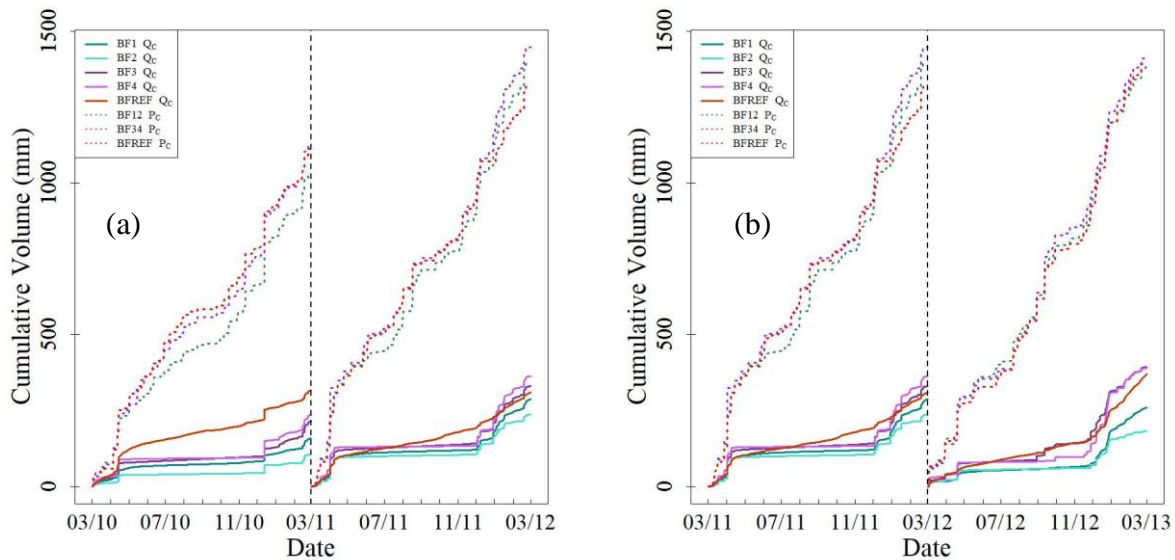


Figure 1.3. Cumulative discharge and rainfall as a function of time in (a) both pre-treatment years (years 1 & 2) and (b) second pre-treatment year (year 2) and treatment year (year 3) which were most similar in rainfall totals.

These results suggest several things. The vast differences in runoff coefficients suggest that BF1 (*YP*) and BF2 (*IC/Th*) are yielding abnormally low flow volumes, compared to the three others, although geographical factors (e.g., slope, soil type) are not conducive to this pattern.

Subsurface flow by-pass near the stations was surmised and observed early on during station installation and trenches were dug to intercept it about 15 m upstream the stations. It is very likely that some of this piping still existed despite the efforts to limit it. This would explain why flow volumes at BF1 and BF2 are so different, despite being adjacent. This unfortunate reality obviously has some effect on the ability to detect treatment effects, as clearly the low annual flow volumes generated at BF1 and BF2 cannot be attributed to a treatment effect, nor can the quantitative differences in total flow volume accumulated between BF1 and BF2 watersheds and BF3 (*SG*) and BF4 (*IC/Rp*) watersheds in Year 3. Treatment effects may thus be better detected

through sudden changes of the hydrological signature, as some of the longer-term effects may be masked by this experimental artifact.

Paired relationships

The logarithmic daily flows for each watershed plotted as a function of those of the control (Figure 1.4) show that the linear regression established in all watersheds was strongest in the second pre-treatment year, as indicated by higher R^2 values. This is most likely because a wider range of flow values was observed due to increases in rainfall. The strongest correlation between BF1 (*YP*) and BF2 (*IC/Th*) in year 2 among watersheds was most likely due to spatial proximity of the watersheds. Similarity in land cover in BF1 and BF2 in year 3, both watersheds still consisting fully or partially of pine trees, could be why the relationship was still somewhat strong even though BF2 underwent treatment, but also could be due to the fact that some of the flow observed at BF3 and BF4 may have by-passed BF1. This would be generally true for low flow periods, but not as much for high flow values. The correlations weaken in year 3 to R^2 values lower than those of years 1 and 2 in each watershed. There seems to be a larger amount of higher daily flows in BF3 and BF4 in year 3 occurring across a range of daily flows in BF1, demonstrated by a larger dispersion of points around the regression when compared with years 1 and 2. Notably, the largest difference in slope of the regressions between years 2 and 3 occurs in BF3 and there is a decrease in slope for BF3 (*SG*) and BF4 (*IC/Rp*). This could be indicative of a new distribution of flow rates where a higher number of greater daily flow values exist in treatment watersheds when corresponding flows in BF1 remain similar, thus dragging the slope downward. In particular, this is most likely due to the months in which BF3 and BF4 begin flowing in September rather than December in year 3, while the response to rainfall remains

similar in BF1 and BF2. Overall, change in the relationships observed in years 2 and 3 suggests that during the establishment year, new patterns of flow may have existed at BF3 and BF4, corresponding to the early flow generation in September of year 3.

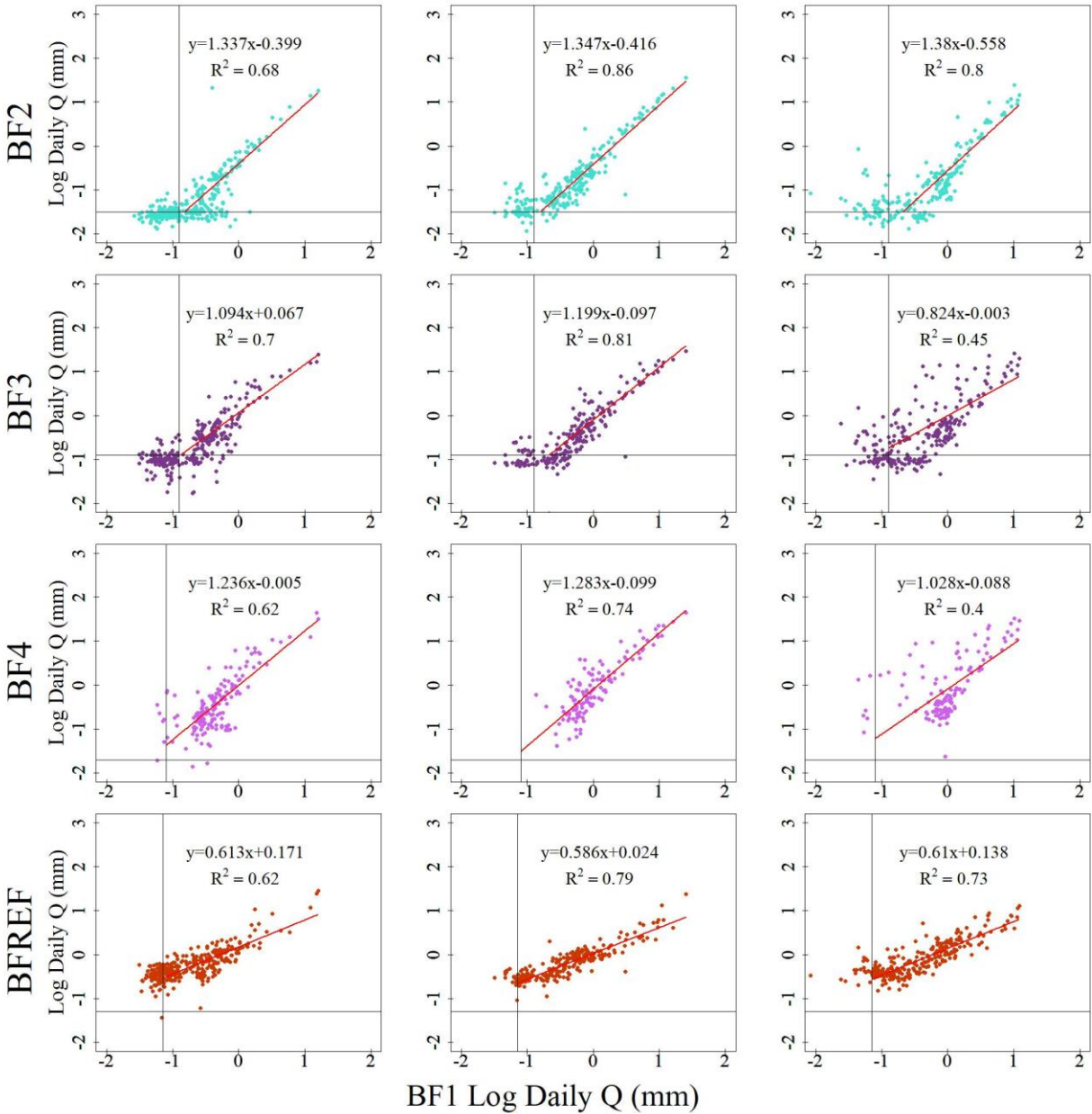
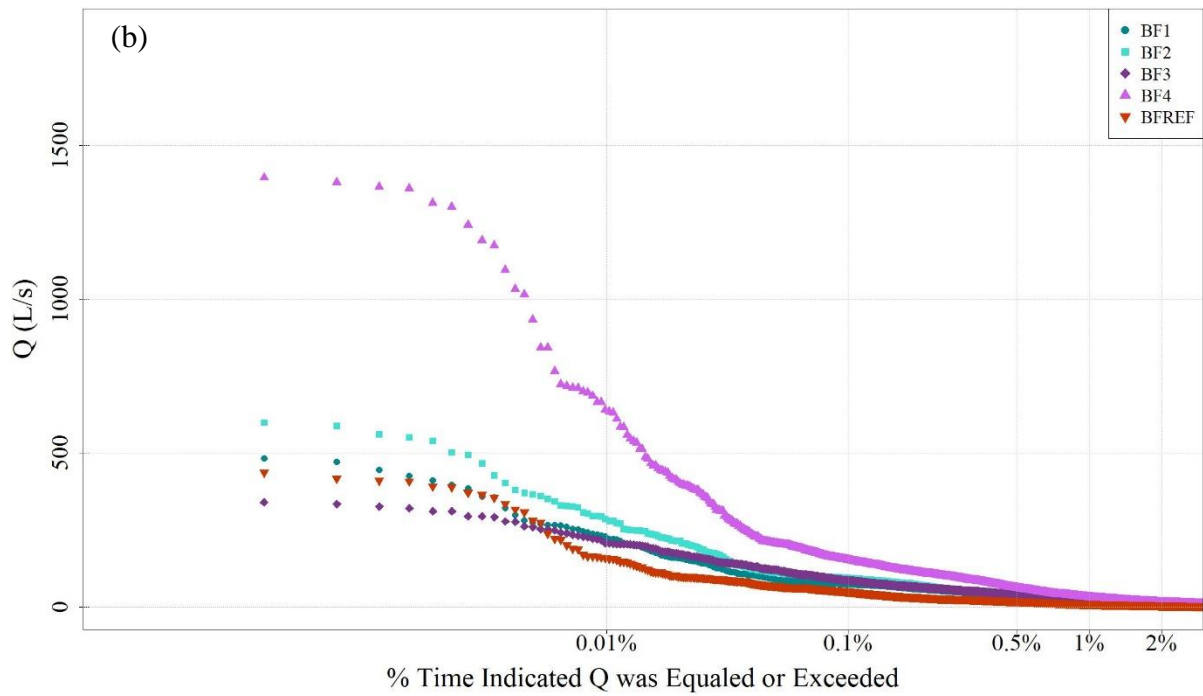
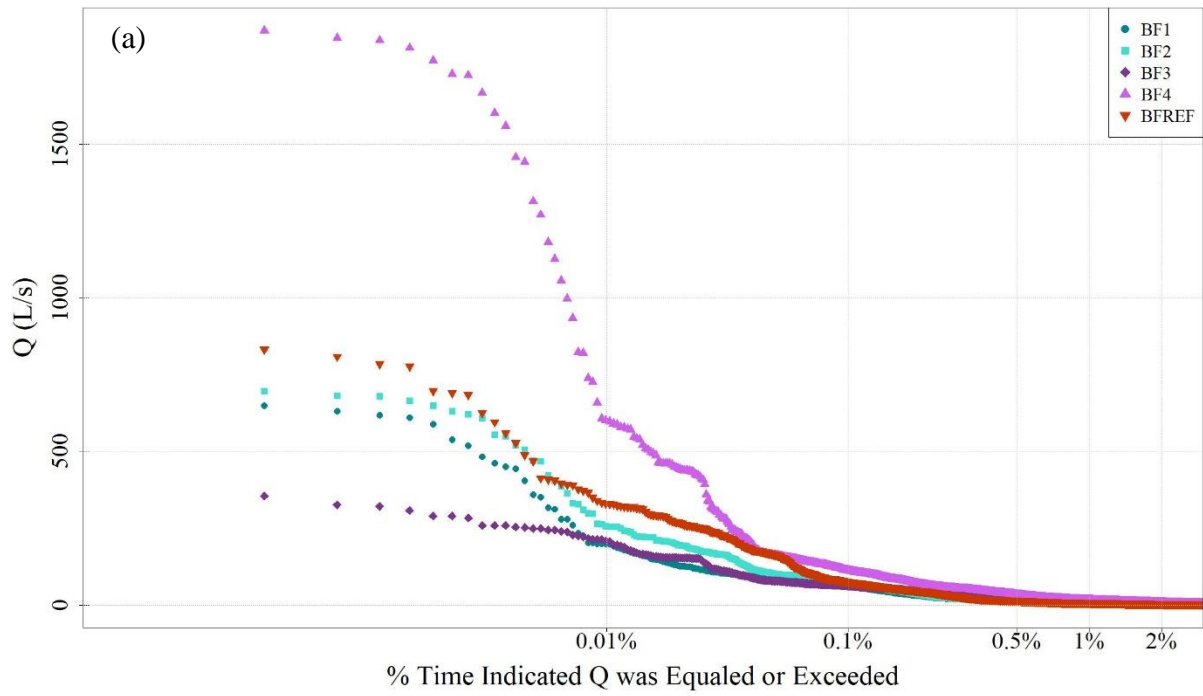


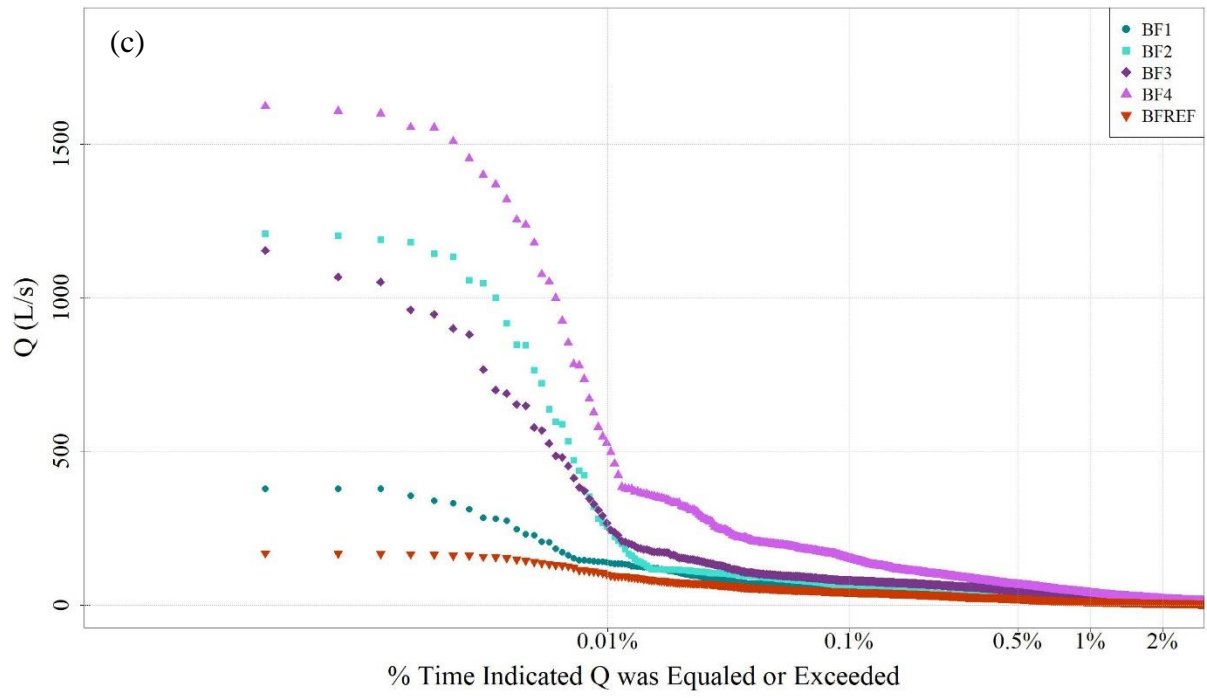
Figure 1.4. Logarithmic daily flow volumes of watersheds as a function of logarithmic daily flow volumes in the young pine control watershed, BF1 for both pre-treatment years and the establishment year. Linear regressions were performed for flows to the right of the vertical grey line and above the horizontal grey line which were visually determined as cutoff points for lower flows that would not affect annual cumulative volume substantially.

Flashiness

The flow duration curves (Figure 1.5) confirm the behavior observed in the watershed hydrographs, which were characterized by short duration events, low inter-event flow in the active winter and early spring, and even smaller flows (sometimes no flow) sustained in spring, summer and fall. The distribution of higher/peak flow rates corresponding with storm events was mostly captured in flow rates equaled or exceeded in 2% of the year. Flow rates equaled or exceeded in 5% of the year for all watersheds in all years were less than 10 L s^{-1} . In every year, BF4 (*IC/Rp*) flow rates equaled or exceeded in 2% or less of the time are the highest among all watersheds. However, the gap between flow rates during those events exhibiting the highest peak flow rates begins to narrow among treatment watersheds in year 3. In this year, BF3 (*SG*) transitions from having the lowest pre-treatment peak flows among the watersheds to the third highest behind BF2 (*IC/Th*) in the treatment year. This suggests that during extreme events in year 3, treatment watersheds acted more similarly to BF4 indicated by heightened peak flow rates in comparison with pre-treatment years. This also makes evident that BF4 (*IC/Rp*) is relatively flashier than the other watersheds because in a small percentage of the time, corresponding with events, the magnitudes of flow rates rise much higher than those of the other watersheds.

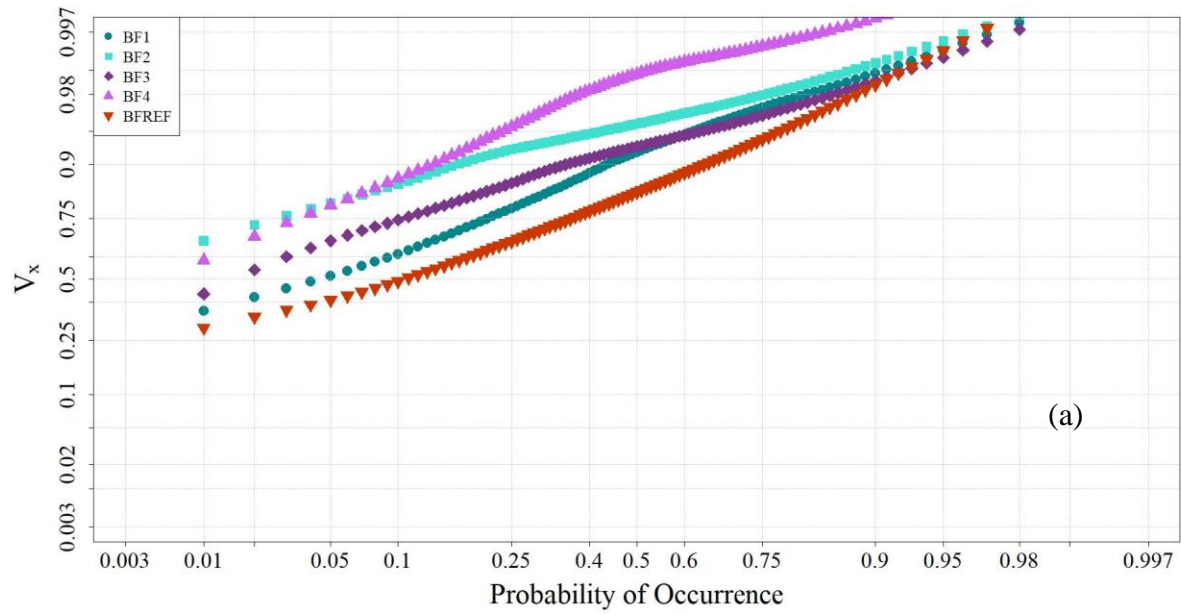
Figure 1.5. Flow duration curves in (a) pre-treatment year 1, (b) pre-treatment year 2 and (c) treatment (year 3) for watersheds BF1 (*YP*), BF2 (*IC/Th*), BF3 (*SG*), BF4 (*IC/Rp*) and BFREF (*MP*).



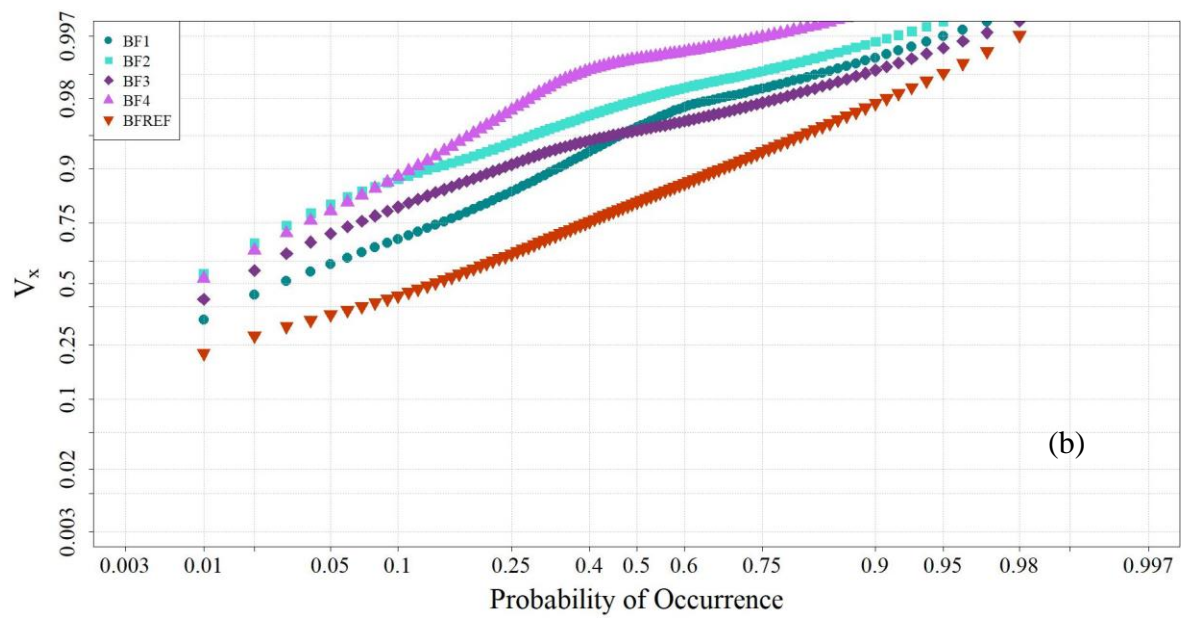


Another indicator of flashiness was performed by plotting water volume as a percentage of the total cumulative discharge ($V_x\%$) that occurred during a percentage x of the total time. Results for each hydrological year are presented in Figure 1.6 where the data is plotted as a normal distribution to more clearly define smaller percentages of the time corresponding with event discharge.

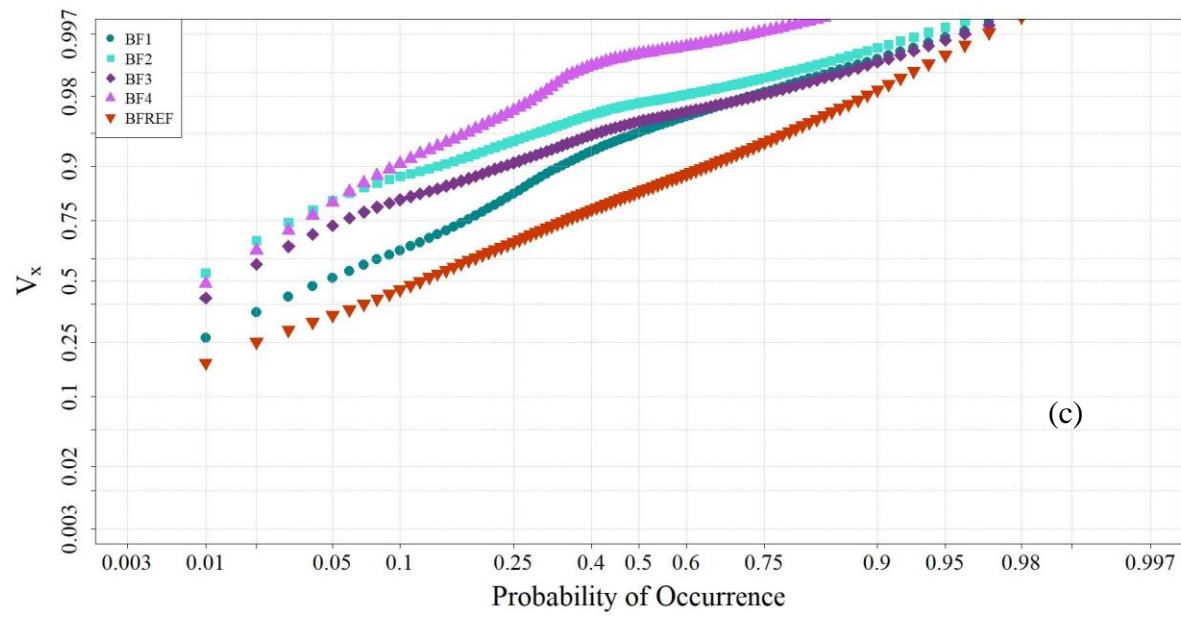
Figure 1.6. Double probability graphs where volume of water is as expressed as a percentage of total annual volume (V_x) occurring in x percentage of the time in (a) pre-treatment year 1, (b) pre-treatment year 2 and (c) treatment (year 3) for watersheds BF1 (*YP*), BF2 (*IC/Th*), BF3 (*SG*), BF4 (*IC/Rp*) and BFREF (*MP*).



(a)



(b)



(c)

With this method, the definition of relatively higher flashiness would pertain to a larger portion of the cumulative volume occurring in a smaller percentage of the time. This means that flows in other portions of the time do not contribute as greatly to the total annual discharge, which would indicate higher responsiveness of the watershed to rainfall events. It is obvious that these small watersheds produce a majority of total discharge in a small percentage of time, sometimes up to 50% in only 1% of the entire year as observed for BF2 (*IC/Th*) and BF4 (*IC/Rp*). $V_{2\%}$ is considered a relative measure of flashiness. In Figure 1.6 (a) and (b), pre-treatment years 1 and 2 respectively, BF2 and BF4 would be considered relatively flashier than watersheds BF1 and BF3, and all of the watersheds would be considered flashier than the reference watershed. This remains the case in the establishment year Figure 1.6 (c), however the differences in $V_{2\%}$ between the control watershed BF1 (*YP*) and treated watersheds increase, which agrees with the trends observed in the low ends of the flow duration curves. This could possibly indicate a shift in hydrologic behavior and response to events, more specifically the watersheds becoming relatively flashier following treatment. However, the suspiciously low flow volumes at BF2, should they be due to piping or flow by-passing the measurement station, would inflate the $V_{2\%}$ value of that station, regardless of treatment effect. The larger contribution of low flow to the total flow volume at BF3 (*SG*) does mechanically lower its $V_{2\%}$ value. This indicator can thus be somewhat ubiquitous and does not seem to provide, used by itself, a clear indicator of trends in flashiness.

Other indicators of “flashiness”, pertaining to the frequency, quickness, and magnitude of streamflow responses to rainfall, the R-B Index and certain IHA parameters used are provided in Table 1.6 and Table 1.7 respectively. High pulse counts and pulse mean durations were

calculated for the 75%, 85%, and 95% quantiles, with high pulses counting as a pulse that lasted equal to or longer than 6 minutes. Flow rise and fall rates were calculated for the 2-minute interval and flow reversals were calculated only for flow rates greater than or equal to 10 L s⁻¹ for a 10-minute moving window. The reason for subsetting the data in this manner for flow reversal calculation is because with high resolution data, some noise still exists and each small oscillation in flow rate would be counted as a reversal which would not clearly represent response to rainfall.

Table 1.6. R-B index for all study watersheds for each year. Relative flashiness rankings are included. A value of 5 indicates the most flashy while 1 represents the least flashy of the watersheds.

Watershed	Year 1		Year 2		Year 3	
	<i>R-B Index</i>	<i>Rank</i>	<i>R-B Index</i>	<i>Rank</i>	<i>R-B Index</i>	<i>Rank</i>
BF1 (<i>YP</i>)	0.016	2	0.013	1	0.0083	1
BF2 (<i>IC/Th</i>)	0.026	5	0.019	4	0.025	5
BF3 (<i>SG</i>)	0.014	1	0.016	3	0.020	4
BF4 (<i>IC/Rp</i>)	0.025	4	0.021	5	0.019	3
BFREF (<i>MP</i>)	0.017	3	0.014	2	0.011	2

A larger value in all flashiness indicators presented would indicate a flashier system, except the mean duration values, according to the literature. The various flashiness indicators seem to follow no clear pattern when ranking flashiness from most to least among watersheds in each year. The R-B Index values most closely followed the concept of the ranking of flashiness among watersheds that were discussed using the flow duration curves and double probability plotting method. BF2 and BF4 displayed a relatively higher level of flashiness in years 1 and 2 than the other watersheds. In year 3, the flashiness ranking slightly changed according to the R-

B Index values. BF2 became most flashy and BF3 became the second most flashy among treatment watersheds instead of third. The control watershed BF1 remained the least flashy in all 3 years suggesting that treatment possibly could have produced changes in the flashiness of these watersheds.

Table 1.7. Select IHA flashiness indicators for watersheds BF1 (*YP*), BF2 (*IC/Th*), BF3 (*SG*), BF4 (*IC/Rp*) and BFREF (*MP*) for 3 study years. The first value listed in each column is the calculated flashiness indicator value and the second value is the flashiness ranking among watersheds for that parameter in each year. 5 indicates the most flashy while 1 represents the least flashy of the watersheds.

Watershed	High Pulses												Avg Rise Rate (L/s/min)	Avg Fall Rate (L/s/min)	N Flow Rev			
	75% Quantile				85% Quantile				95% Quantile									
	N	Mean Dur (min)			N	Mean Dur (min)			N	Mean Dur (min)								
	Year 1																	
BF1	120	4	874	3	61	3	1030	2	37	4	565	4	1.22	2	-0.51	2	57	2
BF2	78	2	1062	2	62	4	800	4	21	3	788	2	1.73	4	-0.65	4	35	1
BF3	96	3	858	4	58	2	852	3	17	2	969	1	0.58	1	-0.25	1	93	4
BF4	33	1	1495	1	25	1	1184	1	15	1	657	3	1.35	3	-0.57	3	157	5
BFREF	142	5	811	5	156	5	442	5	71	5	323	5	2.26	5	-0.84	5	65	3
	Year 2																	
BF1	61	4	1374	3	36	3	1398	1	19	3	882	1	0.57	1	-0.21	1	215	4
BF2	38	2	1774	1	34	2	1189	2	17	1,2	792	2	0.88	4	-0.30	4	157	2
BF3	42	3	1570	2	39	4	1014	3	21	4	626	3	0.62	2	-0.23	2	217	5
BF4	28	1	1327	4	22	1	1013	4	17	1,2	436	4	1.42	5	-0.44	5	181	3
BFREF	376	5	313	5	296	5	237	5	56	5	424	5	0.84	3	-0.29	3	127	1
	Year 3																	
BF1	49	2	1941	1	36	2,3	1585	1	19	1	1000	1	0.23	1	-0.14	1	243	4
BF2	181	4	359	5	42	4	953	3	21	2	637	2	0.67	4	-0.39	5	197	2
BF3	138	3	530	4	36	2,3	1226	2	29	3,4	506	3	0.66	3	-0.33	3,4	235	3
BF4	24	1	1604	2	29	1	796	4	29	3,4	264	5	0.91	5	-0.33	3,4	313	5
BFREF	196	5	590	3	103	5	677	5	46	5	502	4	0.30	2	-0.15	2	170	1

The number of high pulses in years 1 and 2 produce the total opposite in flashiness interpretation. In many cases, these values would suggest that BF1 (*YP*), BF3 (*SG*), and BFREF (*MP*) are most flashy and that BF2 (*IC/Th*) and BF4 (*IC/Rp*) are the least flashy among the watersheds, and the rankings change depending upon which quantile one decides to calculate the number of high pulses from. There seems to be no obvious pattern or change in flashiness according to these indicators from year to year. There is no obvious pattern when assessing number of flow reversals either as well as the other IHA parameters.

The flow rate distributions in these watersheds vary in the pre-treatment periods and perhaps some of the flashiness indicators calculated, such as the IHA parameters, are masked by the difference in flow distributions. The high pulse counts and durations can be influenced by this. Watersheds with a greater portion of baseflow during the year will contribute more low flow rates to the subset of data assessed, causing the flow rate quantiles to be smaller, therefore picking up on smaller oscillations in flow versus watersheds where most flow rates occur in the high range and correspond with events.

This short discussion and contradicting trends suggest that in the watersheds studied, the flashiness tools used are either ill-suited, and/or that the changes in flashiness are not clearly apparent. This result, although somewhat disappointing, may suggest that flashiness indicators used in these small watersheds underlying very similar settings and climate, are not discriminatory enough.

1.4.2 Water Quality

Despite the lack of definite trend in the hydrological data, flow generation during the establishment period may have occurred at an earlier time, possibly due to treatment effects on BF3 and BF4. Should this be true, the dynamics of nutrient and sediment loads should magnify this effect. The overall nutrient and sediment exports over the 5-year period of study is reported by Carter (2016). This study reports the short-term water quality changes that can be attributed to treatment effects, as most of the treatment activities were performed during the establishment year. The annual cumulative water quality loadings for the second pre-treatment year and establishment year are listed in Table 1.8.

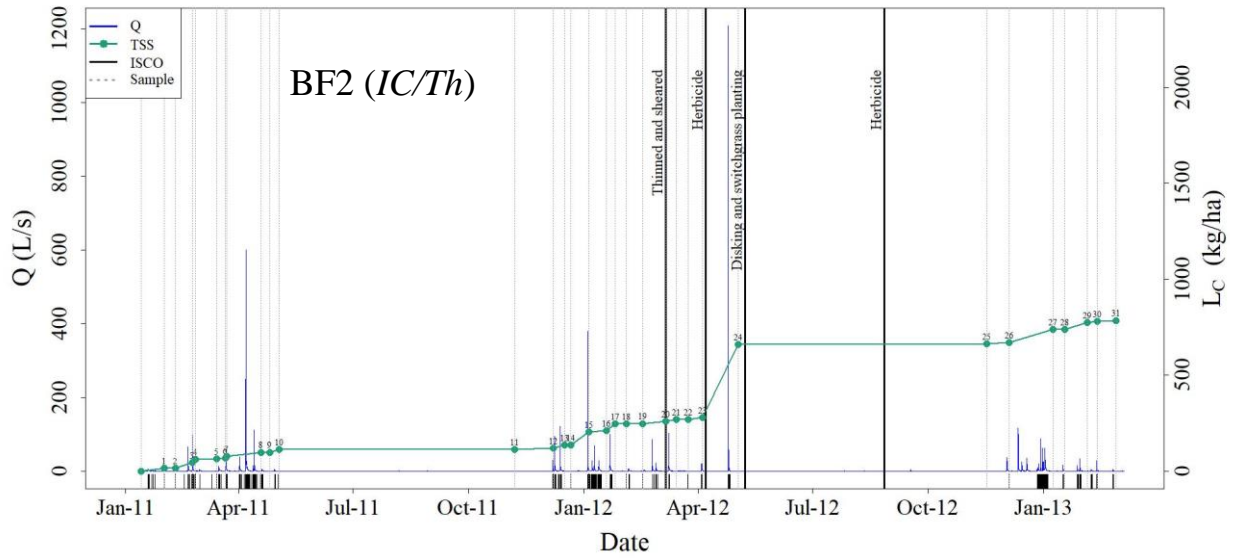
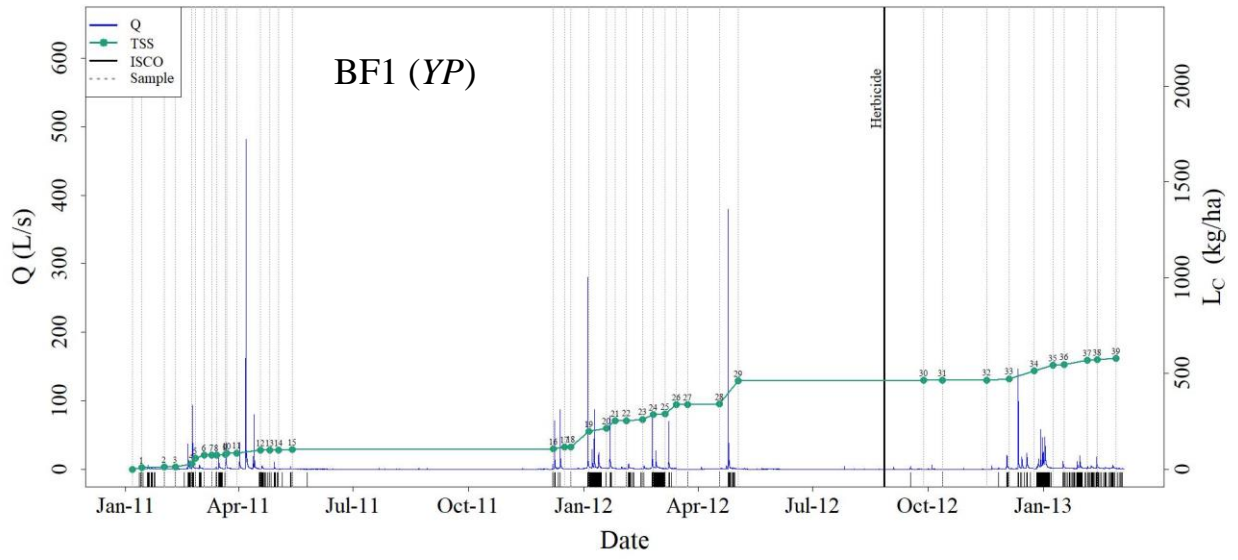
Table 1.8. Annual cumulative water quality loads for the second pre-treatment year (year 2) and establishment year (year 3).

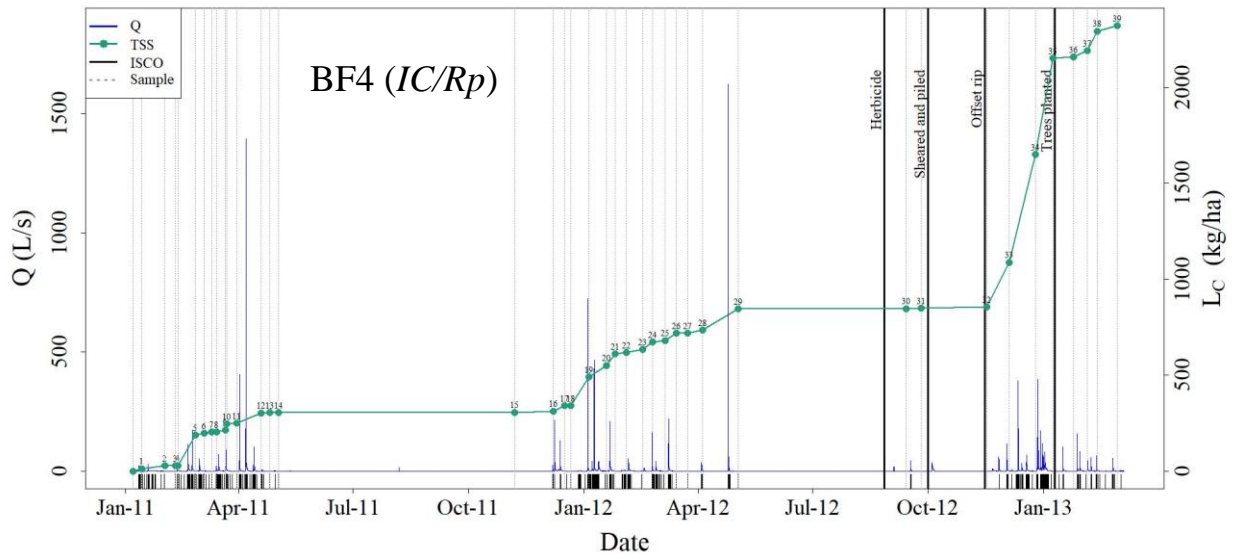
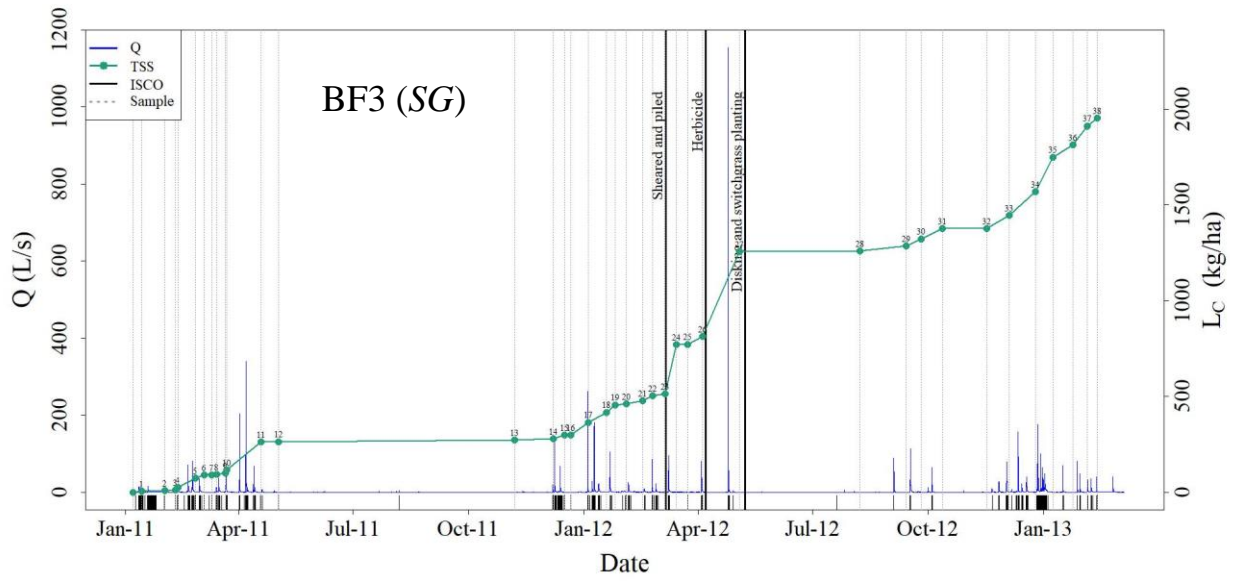
Watershed	TSS (kg/ha/yr)		TP (kg/ha/yr)		DOC (kg/ha/yr)	
	Pre-	Est	Pre-	Est	Pre-	Est
BF1 (<i>YP</i>)	220	285	0.71	0.65	27.6	20.8
BF2 (<i>IC/Th</i>)	197	526	0.29	0.34	23.7	21.4
BF3 (<i>SG</i>)	451	1412	2.03	1.72	49.3	63.3
BF4 (<i>IC/Rp</i>)	485	1636	0.89	1.51	44.0	58.4
BFREF (<i>MP</i>)	645	469	0.26	0.81	18.2	29.2

As expected, nutrient and sediment load increases occurred following events, as cumulative loading plotted with the hydrograph demonstrates. Sudden increases in loads seem to also sometimes occur when management practices occurred. An example of this can be seen where the TSS cumulative loading curve and hydrograph are plotted for watersheds BF2-4 in Figure

1.7. A majority of the TSS load was exported directly following management practices applied for treatment implementation.

Figure 1.7. Cumulative TSS load, L_C , and hydrograph plotted for each treatment watershed BF1 (*YP*), BF2 (*IC/Th*), BF3 (*SG*), and BF4 (*IC/Rp*). Points and vertical grey lines correspond to the cumulative load corresponding with the time each composite sample was collected. Upward tick marks below the hydrograph represent each time the ISCO sampler was triggered to take a water sample. Black vertical lines indicate the time that each treatment (labeled) began to take place.





The large increases in sediment yield appear to correspond with times of treatment, but also with high flow events. Therefore, the increase could be due to a larger fluctuation in water being exported from the system. The large event occurring in May of 2012 produced an obvious substantial increase in sediment load in BF2 (*IC/Th*) and BF3 (*SG*) which also followed treatments in these watersheds. However, we did not observe such a substantial increase in BF4 with the same event. The most intense increases in sediment load occurred in December and January of the establishment year for this watershed, which also corresponded with flow that began following treatments that occurred later than those in BF2 and BF3.

To normalize the effect of flow on sediment and nutrient loads, we further plotted cumulative loading as a function of cumulative discharge volume. Synchrony between sudden breaks in the curves and treatment activities were taken as strong evidence of a treatment effect as observed in the TSS plots (Figure 1.8). Breakpoints, where the slope trend of the double cumulative curve sharply increases, are observed following treatments in BF2-4 for sediment loading. This indicates an increase in supply of the amount of sediment that could be exported to the streams, mainly following tree shearing and herbicide application. Following the sharp increase, the slope, or average flow weighted concentration, tends to return to the trend occurring before treatments rather quickly in BF2 and BF3. The increase is not quite as sharp in BF4, but treatments in this watershed did not occur until later in the dry period during fall months, thus the sediment increase was observed when the watershed started flowing consistently again. In BF2 and BF3, the treatments occurred near the end of the flow period for the watersheds, and therefore possibly had time to re-stabilize in the dry months following switchgrass planting.

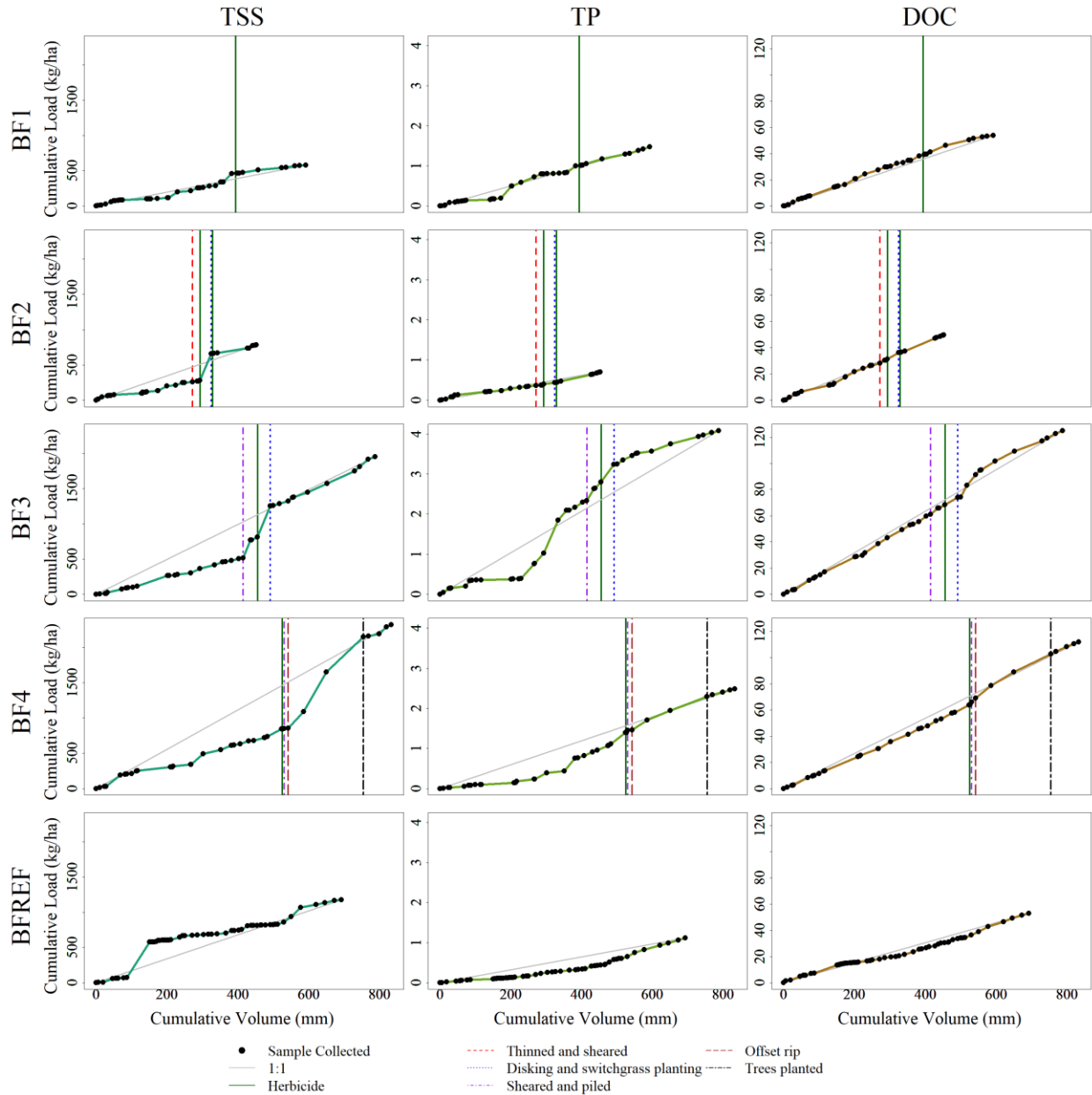


Figure 1.8. Cumulative TSS, TP and DOC flux as a function of cumulative flow volume for the entire water quality monitoring period in BF1 (*YP*), BF2 (*IC/Th*), BF3 (*SG*), BF4 (*IC/Rp*) and BFREF (*MP*). Points represent the time at which a composite sample was collected. Vertical lines correspond to the treatments in legend.

The timing of the responses of the export of TP with the treatment is not as obvious as that of TSS (Figure 1.8). No similar ‘jump’ following treatments can be observed for BF1 and BF2. A

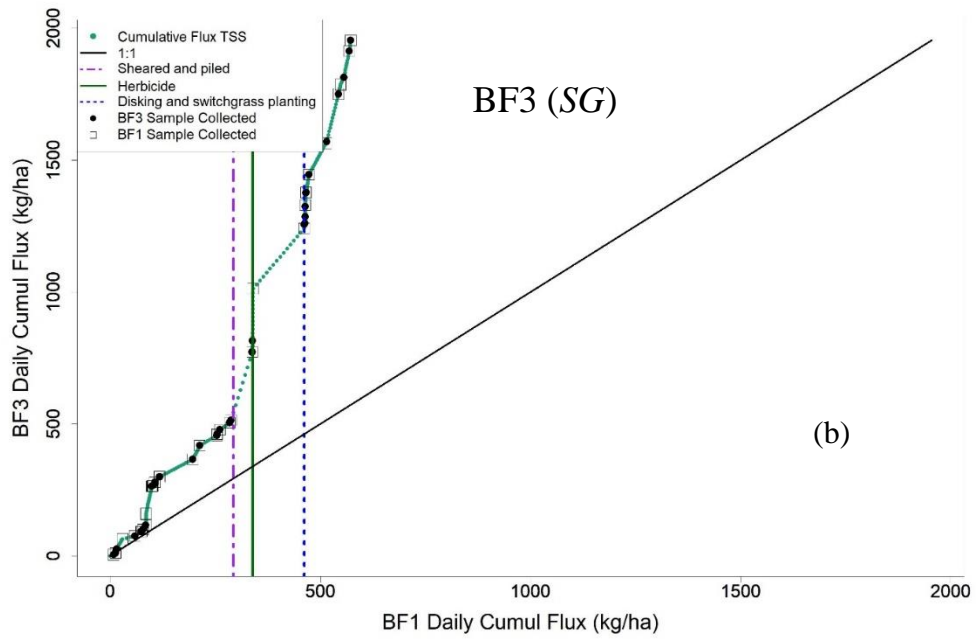
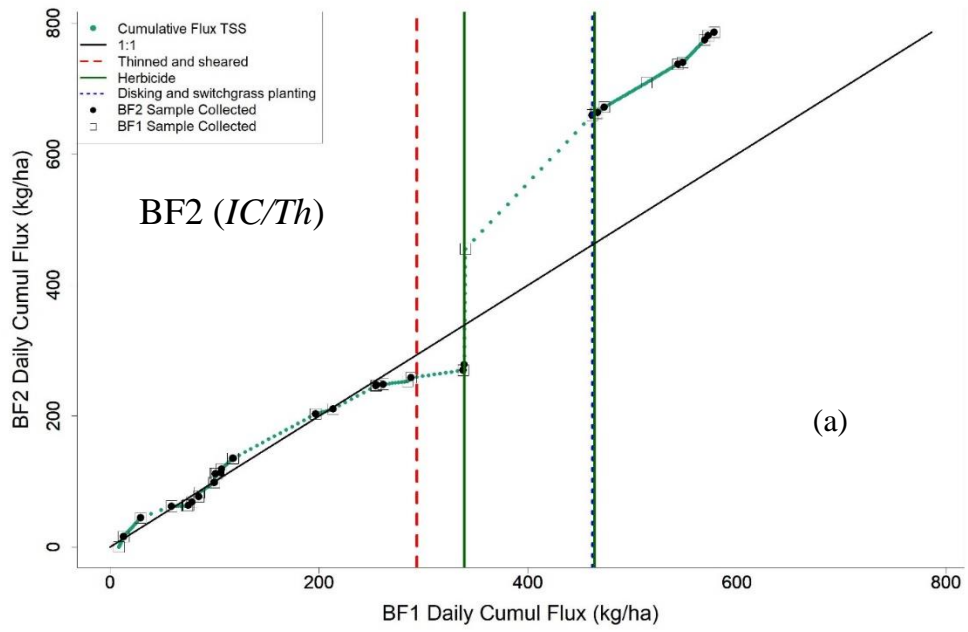
jump does occur for BF3 after treatment, but another one does occur before then unrelated to treatment. There are two apparent sudden jumps for TP export for BF4, but one occurs before treatment and may thus be unrelated. It is not clear why the TP exports do not follow those of TSS as expected. This suggests that there were other sources of phosphorus unbound to particles in the watersheds of study.

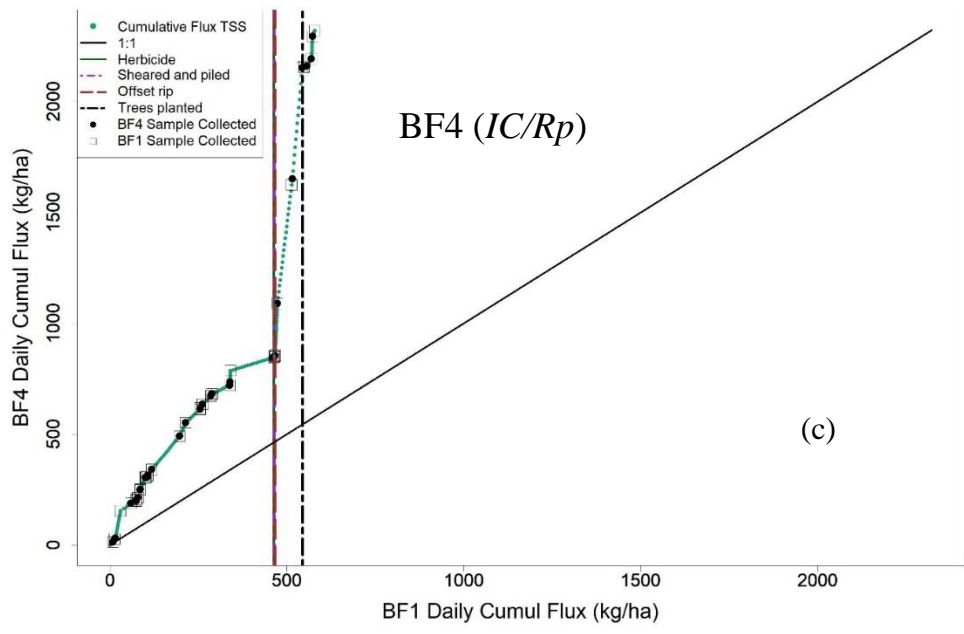
Cumulative DOC as a function of cumulative discharge (Figure 1.8) did not show substantial breakpoints or changes in trends for BF1 (*YP*) and BF2 (*IC/Th*). For these two watersheds, DOC seemed to be a non-reactive water quality constituent to hydrology and to have a constant supply indicated by the curve keeping a rather consistent linear shape throughout the entire monitoring period. However, there was an increase occurring after treatments in BF3 (*SG*) and BF4 (*IC/Rp*), although not as distinct of an increase as found with TSS loading curves. These increases only occurred after treatment and may be related to soil disking, which has the potential to increase organic matter breakdown and thus release DOC to water.

The previous analysis detects potential changes in the nutrient export pattern as a function of the water export pattern. This analysis implies, however, that the increase in the nutrient export pattern does not correspond to a concurrent change in the water export patterns. In other words, between consecutive points, the surface and subsurface runoff patterns stay the same, but during large events fed by large and/or intense rainfall events, the flow export pattern may change. In this case, the observed changes in load export pattern may result from a change in the water export processes, rather than a treatment effect.

Such large events are expected to occur in all watersheds at the same time. To alleviate the effects of potential flow changes and further detect the treatment effects, we propose to use a double mass curve approach using BF1 watershed as a reference. With such method, large increases in loads associated with cumulative flow corresponding to large events are expected to increase proportionally from treatment to reference watersheds. Deviation from this proportionality that would occur in synchrony with treatment would be a further indication of treatment effects. For this, daily cumulative loading values for the treatment watersheds were plotted as a function of the daily cumulative loading values of the control watershed. In Figure 1.9, substantial increases in TSS loading can be observed corresponding with times that particular management practices took place in all of the switchgrass watersheds. This is an indication that there was a treatment effect on TSS that occurred that was not observed in BF1.

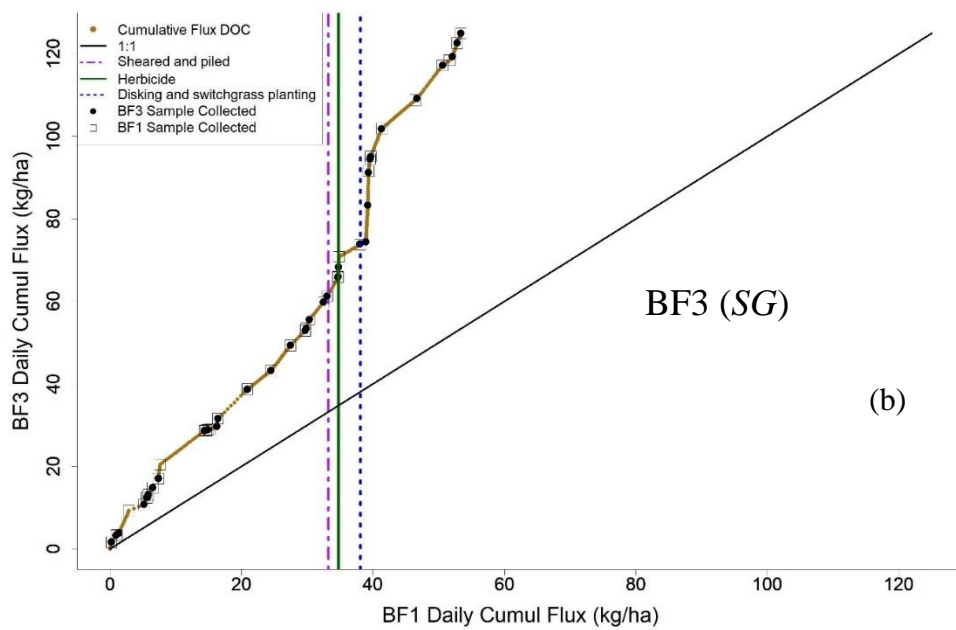
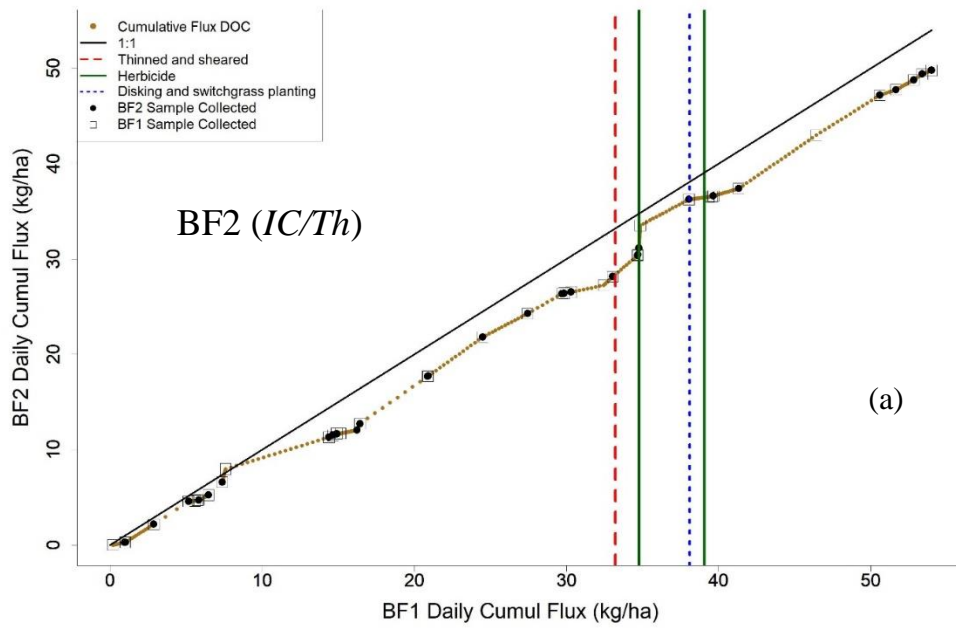
Figure 1.9. Daily cumulative TSS flux of watershed (a) BF2 (*IC/Th*), (b) BF3 (*SG*), and (c) BF4 (*IC/Rp*) as a function of daily cumulative TSS flux of the young pine control watershed, BF1 (*YP*).

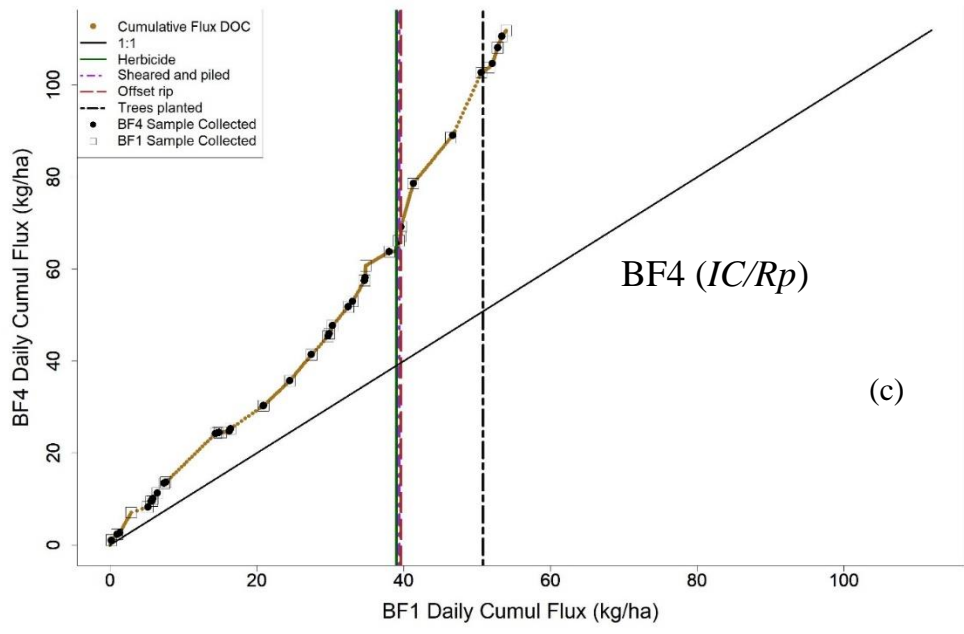




Daily cumulative fluxes of BF3 (*SG*) and BF4 (*IC/Rp*) plotted as a function of the daily cumulative flux of BF1 corresponded with previous observations that DOC loading seems to be reactive to the shearing treatments, in particular disking in BF3, and BF2 DOC release did not seem reactive to treatments (Figure 1.10). These watersheds already exhibited a release of DOC at a higher daily rate than the control, but the inflection in the curves after disking seemed to be likely due to treatment.

Figure 1.10. Daily cumulative DOC flux of watershed (a) BF2 (*IC/Th*), (b) BF3 (*SG*), and (c) BF4 (*IC/Rp*) as a function of daily cumulative DOC flux of the young pine control watershed, BF1 (*YP*).





1.5 Discussion and conclusions

An increase in land affected by novel biomass production scenarios is expected in forthcoming years due to the growing demand for alternative energy sources. Assessing the short-term environmental impacts of land management practices associated with establishing these biomass cultivation systems is considered just as important as understanding the long-term effects because hydrology and water quality effects can be observed almost immediately, as observed in the results of this study.

Potential harmful effects correlating to establishment of switchgrass cultivation systems include equipment traffic compacting soils, reducing infiltration, and increasing runoff and sediment erodibility and leaching of phosphorus and nitrogen in streamwaters due to fertilization practices. Removal of trees can also reduce evapotranspiration occurring on the site which could additionally produce higher amounts of discharge. When the soil is disturbed and vegetation changed, via removal or addition of a carbon source, there is also the potential to alter biogeochemical processes occurring in the soils which could potentially affect streamwater chemistry observed.

1.5.1 Hydrology

The volume of water being exported from a watershed and the way in which it is transported varies from year to year in response to changes in climate. Therefore, it can be a challenging task to distinguish treatment effects from the natural variability in hydrology from year to year in addition to growing vegetation in a typically managed forest. We observed differences in the

water export patterns among watersheds, but these seemed to be related more closely to the inherent differences in hydrological signature between the watersheds rather than treatment.

The proximity of the watersheds led to the observation that BF1 (*YP*) and BF2 (*IC/Th*) appeared to be more hydrologically similar than BF3 (*SG*) and BF4 (*IC/Rp*) and vice versa in the amount of discharge produced throughout the year. The watersheds only flowed an average of 4-5 months and responded to rainfall similarly during each pre-treatment year. The ranking of total annual discharge remained similar throughout all 3 years.

Using the paired logarithmic daily flows technique, the flow values became more dispersed and the correlations in the relationship between daily flows decreased in the establishment year in each watershed. There was stronger evidence for a potential treatment effect in BF3 and BF4 than in BF2, however this may also be masked by the difference in location of these watersheds. Analysis tended to portray that these flow differences seemed to correspond with timing of treatments and type of treatments. Perhaps the differences in flow observed in these watersheds were larger because trees were completely removed rather than thinned like in BF2, meaning there was more equipment traffic that could have increased soil compaction and much less vegetation to intercept and transpire water causing increased runoff.

1.5.2 Water Quality

A land cover change has the potential to affect biogeochemical processes controlling quantities of nutrient pools and sediment available for transport in the landscape as well as the potential to alter the hydrological signature of the watershed, which in turn can affect how nutrients/sediment are transported through the landscape to the stream. If changes in water quality are detected, it is

difficult to distinguish if the change is due to a treatment effect on controlling mechanisms of the nutrient/sediment supply to be transported or simply due to variability in the quantity of water exported. This can be highly variable due to climate since a majority of annual water quality loads are contributed by storm events, which is especially true due to the intermittent and pulsing nature of flow in the small upland watersheds studied in this research. A combination of plotting methods including a paired watershed approach was performed in this study in an attempt to separate the influence of variability in fluctuations of flow from what could potentially be treatment effects. A clear impact on TSS and DOC fluxes following treatments was observed using these methods.

There was a large increase in flux immediately following treatments in watersheds BF2 (*IC/Th*), BF3 (*SG*), and BF4 (*IC/Rp*) which could be observed in all 3 plotting methods. It is true that a large event occurred in May 2012 immediately following treatments in BF2 and BF3, which could have attributed to the large flux, but plotting the cumulative loading as a function of cumulative volume and as a function of the young pine reference cumulative loading further supported that this increase was not solely due to the quantity of flow associated with this storm.

There was a clear indicator of treatment effect when comparing a large increase in export of sediment in relation to treatment timing among the switchgrass treatment watersheds. The peak flow rate of the major event in May 2012 was the greatest of the two years evaluated and almost 3 times that of the largest peak flow rate in 2011. Thinning and removal of trees occurred in months prior to the May 2012 event. Treatment did not occur until September 2012 in BF4, and in comparison, the flux increase associated with the May 2012 event did not contribute a

substantial quantity to the annual load, nor was the peak flow rate for this event 3 times that of the largest event in 2011. However, a large increase in TSS flux was observed in months following removal of trees in BF4, whereas this was not as large of a contribution to annual load in watersheds BF2 and BF3.

Following thinning and removal of trees in the watersheds, bare soil was exposed and further disturbed from disking in preparation for switchgrass planting, therefore providing larger amounts of loose sediment to be eroded with event runoff. Event runoff could also have been intensified due to compacted soils from equipment traffic and reduced infiltration as well as decreased evapotranspiration with a decrease in vegetation cover. It does appear that large fluxes of TSS were localized to the time immediately following treatments and that loading rates appeared to return to trends close to those observed in the pre-treatment year by the end of the establishment year. We compared the values of annual sediment loads in this study to others evaluating effects of forestry practices/land use changes across a wide range of landscapes and found that our values fell among the range of values found among the literature (Table 1.9).

Table 1.9. Annual sediment yields exported from relatively smaller watersheds across a range of literature involving paired watershed studies evaluating water quality effects of land use change and forestry management practices.

Catchment	Location	Land use	Area (ha)	Sediment yield (kg/ha/yr)	Reference
GR1	Alabama, USA	Young pine	11.6	394 - 681	Bennett et al.
GR2	Alabama, USA	Thinned intercropped young pine	26.7	497 - 1435	Bennett et al.

Table 1.9. (continued)

GR3	Alabama, USA	Newly established pine with switchgrass intercropping	25.9	252 - 1899	Bennett et al.
GR4	Alabama, USA	Switchgrass establishment	16.5	96 - 814	Bennett et al.
GRREF	Alabama, USA	Mature managed forest	8.0	109 - 389	Bennett et al.
WEPP simulations	Alabama, USA	Grassland to conventional corn	-	1,300 - 45,000	Bennett et al.
BF1	Mississippi, USA	Young managed pine (Control)	14.1	220 – 285	This article
BF2	Mississippi, USA	Thinned young pine intercropped with switchgrass	12.8	197 – 526	This article
BF3	Mississippi, USA	Switchgrass establishment	10.9	451 – 1412	This article
BF4	Mississippi, USA	Pine and switchgrass intercrop planting	15.2	485 – 1636	This article
BFREF	Mississippi, USA	Mature managed pine (Control)	12.6	469-645	This article
Mørdre	Norway	Agriculture, croplands	680	1450 – 3000	Øygarden et al. (2003)
Skuterud	Norway	Agriculture, croplands	450	1000 - 2500	Øygarden et al. (2003)
Moulinet	France	Agriculture, grass- and croplands	453	254	Lefrançois et al. (2007)
Violette	France	Agriculture, grass- and croplands	225	360	Lefrançois et al. (2007)
Jubilee	England	Agriculture, croplands	31	1310	Walling et al. (2002)
Belmont	England	Agriculture, croplands	150	819	Walling et al. (2002)
Lower Smisby	England	Agriculture, croplands	260	803	Walling et al. (2002)
New Cliftonthorpe	England	Agriculture, croplands	96	640	Walling et al. (2002)
Stanley Cars	England	Mixed pastures and urban	455	936	Goodwin et al. (2003)
Literature review	England	Upland low impact	<10 km ²	1090	Walling et al. (2008)

Table 1.9. (continued)

Literature review	England	Upland Agriculture	<10 km ²	270	Walling et al. (2008)
Literature review	England	Lowland low impact	<10 km ²	70	Walling et al. (2008)
Literature review	England	Lowland Agriculture	<10 km ²	510	Walling et al. (2008)
Literature review	England	Lowland urban	<10 km ²	100	Walling et al. (2008)
Clem	Victoria, Aus.	Planted pine	46	744	Hopmans et al. (2007)
Ella	Victoria, Aus.	Eucalyptus native forest	113	57	Hopmans et al. (2007)
San Salvador	Spain	Natural forest	9.2	12,000	Garcia-Ruiz et al. (2008)
Literature review	Western USA	Forested watersheds before fire	-	78 - 1100	Moody et al. (2009)
Literature review	Western USA	Forested watersheds after fire	-	8200	Moody et al. (2009)
Clem	Victoria, Aus.	Planted pine after fire	46	18,000 - 4,500*	Smith et al. (2011)
Ella	Victoria, Aus.	Eucalyptus native forest after fire	113	110 - 20*	Smith et al. (2011)
Betsy	Victoria, Aus.	Eucalyptus native forest after fire	44	680 - 250*	Smith et al. (2011)
Mangaotama	New Zealand	Indigenous forest	268	970 ± 390	Hughes et al. (2012)
Whakakai	New Zealand	Mixed pine and pasture	311	600 ± 220	Hughes et al. (2012)
El Salado	Spain	Mixed forest and agriculture	670	1800	Durán et al. (2012)
Flynn Creek	Oregon, USA	Natural mature red alder and douglas fir (Control)	219	550 - 3130	Hatten et al.(2018)
Needle Branch (Lower Gage)	Oregon, USA	Douglas fir and red alder with management	94	310 - 1020	Hatten et al.(2018)
Deer Creek	Oregon, USA	Douglas fir and red alder with no recent management (Control)	315	690 - 1270	Hatten et al.(2018)

Table 1.9. (continued)

Duke Forest 1, Duke Forest 2, General Electric, Hill Demonstration Forest, Montgomery, Orange County	North Carolina, USA	Six catchments with dominantly forest cover with management	17 - 343	22 - 123	Boggs et al. (2018)
Hill Demonstration Forest (HF1)	North Carolina, USA	Forest with clearcut	12	74.2 + (23.9) – 94.4 (14.8)	Boggs et al. (2016)
Hill Demonstration Forest (HFW1)	North Carolina, USA	Forest with partial clearcut	29	82.5 + (29.1) – 59.8 (13.9)	Boggs et al. (2016)
Umstead Research Forest (UF1)	North Carolina, USA	Forest with clearcut	19	93.4 (27.4) – 84.5(25.9)	Boggs et al. (2016)
C1	Queensland, Australia	Natural brigalow woodland	16.8	81	Elledge and Thornton (2016)
C2	Queensland, Australia	Cropland	11.7	525	Elledge and Thornton (2016)
C3	Queensland, Australia	Pasture	12.7	119	Elledge and Thornton (2016)
Watershed 1	Idaho, USA	Forest 50% clearcut, burned and replanted	140	24.93-115.5	Karwan et al. (2007)
Watershed 2	Idaho, USA	Forest 50% partial cut	177	17.98-147.31	Karwan et al. (2007)
Watershed 3	Idaho, USA	Forest (control)	227	11.38-77.25	Karwan et al. (2007)
SW3, SW5, SW8	Texas, USA	Pine plantation controls	2.62-2.87	0.13 – 539.46	McBroom et al. (2008)
SW2,SW4, SW9	Texas, USA	Pine plantations with conventional site prep	2.63-2.79	0.06-329.78	McBroom et al. (2008)
SW1, SW6, SW7, LW1, LW2, LW3, LW4	Texas, USA	Pine plantations with intensive site prep	2.24-135.12	0.13-1088.88	McBroom et al. (2008)
Forest a	Brazil	Forest	832	30.4	Riskin et al. (2017)

Table 1.9. (continued)

Forest b	Brazil	Forest	1312	5.12	Riskin et al. (2017)
Forest c	Brazil	Forest	513	9.22	Riskin et al. (2017)
Soy a	Brazil	Pasture converted to soybean	356	50.5	Riskin et al. (2017)
Soy b	Brazil	Pasture converted to soybean	198	110	Riskin et al. (2017)
Soy c	Brazil	Pasture converted to soybean	206	57.5	Riskin et al. (2017)
Soy d	Brazil	Pasture converted to soybean	411	50.5	Riskin et al. (2017)

*Higher numbers first corresponding to first year after fire, last number 2 to 3 years later

DOC export increased after treatment for BF3 (*SG*) and BF4 (*IC/Rp*), although no such changes were detected for BF1 (*YP*) and BF2 (*IC/Th*). It is possible that soil disturbance leading to increased mineralization was the cause for the increased export of DOC for BF3 and BF4. Long-term effects beyond the establishment period may be more important to evaluate for how DOC flux is affected by switchgrass intercropping. TP did not seem to be reactive to treatment timings in any of the watersheds even though sediment yields increased.

The largest differences in export trends could be detected using our methods and corresponded with treatments, however most of these sudden changes were quick lived with nutrient and sediment loading returning to patterns like those observed before treatment rather quickly. For this reason, special attention should be given in the future to refining BMPs to address the potential immediate impacts associated with site preparation and establishment for these types of biomass cultivation system. The establishment period of the switchgrass was thus accompanied by a notable relative effect on water quality, i.e., TSS and DOC. The overall absolute effect as

quantified by comparing the TSS export from these upland watersheds to other exports reported in the literature was relatively mild and export values were much smaller than those reported by wildfires.

1.6 Acknowledgements

Logistical and financial support for this work was provided by Weyerhaeuser NR Company and Catchlight Energy, LLC, a Chevron and Weyerhaeuser Joint Venture. Additional research funds were provided by the U.S. DOE (Award No. DE-EE0004395: Optimization of southeastern forest biomass crop production: A watershed-scale evaluation of the sustainability and productivity of dedicated energy crop and woody biomass operations).

1.7 References

- Acharya, B. S., & Blanco-Canqui, H. (2018). Lignocellulosic-based bioenergy and water quality parameters: A review. *Global Change Biology Bioenergy*, *10*(8), 504-533. doi:10.1111/gcbb.12508
- Albaugh, J. M., Sucre, E. B., Leggett, Z. H., Domec, J., & King, J. S. (2012). Evaluation of intercropped switchgrass establishment under a range of experimental site preparation treatments in a forested setting on the lower coastal plain of North Carolina, U.S.A. *Biomass & Bioenergy*, *46*, 673-682. doi:https://doi.org/10.1016/j.biombioe.2012.06.029
- Andréassian, V. (2004). Waters and forests: From historical controversy to scientific debate. *Journal of Hydrology*, *291*(1-2), 1-27. doi:10.1016/j.jhydrol.2003.12.015
- Aust, W. M., & Blinn, C. R. (2004). Forestry best management practices for timber harvesting and site preparation in the eastern united states: An overview of water quality and productivity research during the past 20 years (1982–2002). *Water, Air and Soil Pollution: Focus*, *4*(1), 5-36.
- Baker, D. B., Richards, R. P., Loftus, T. T., & Kramer, J. W. (2004). A new flashiness index: Characteristics and applications to midwestern rivers and streams. *Journal of the American Water Resources Association*, *40*(2), 503-522. doi:10.1111/j.1752-1688.2004.tb01046.x
- Beltran, B. J., Amatya, D. M., Youssef, M., Jones, M., Callahan, T. J., Skaggs, R. W., & Nettles, J. E. (2010). Impacts of fertilization on water quality of a drained pine plantation: A worst case scenario. *Journal of Environmental Quality*, *39*(1), 293-303. doi:10.2134/jeq2008.0506
- Bennett, E. M. (2013). Hydrology and Water Quality Impacts of Site Preparation for Loblolly Pine (*Pinus taeda*) and Switchgrass (*Panicum virgatum*) Intercropping in Upland Forested Watersheds in Alabama. M.S. Thesis. North Carolina State University, Raleigh, NC.
- Blazier, M. (2009). Switchgrass and trees. *Louisiana Agriculture*.
- Blazier, M. A., Clason, T. R., Vance, E. D., Leggett, Z., & Sucre, E. B. (2012). Loblolly pine age and density affects switchgrass growth and soil carbon in an agroforestry system. *Forest Science*, *58*(5), 485-496. doi:10.5849/forsci.11-052
- Boggs, J. L., Sun, G., & McNulty, S. G. (2018). The effects of stream crossings on total suspended sediment in north carolina piedmont forests. *Journal of Forestry*, *116*(1), 13-24.
- Boggs, J., Sun, G., Jones, D., & McNulty, S. G. (2013). Effect of soils on water quantity and quality in piedmont forested headwater watersheds of north carolina. *Journal of the American Water Resources Association*, *49*(1), 132-150. doi:10.1111/jawr.12001

- Boggs, J., Sun, G., & McNulty, S. (2016). Effects of timber harvest on water quantity and quality in small watersheds in the piedmont of north carolina. *Journal of Forestry*, 114(1), 27-40. doi:10.5849/jof.14-102
- Brown, A. E., Zhang, L., McMahon, T. A., Western, A. W., & Vertessy, R. A. (2005). A review of paired catchment studies for determining changes in water yield resulting from alterations in vegetation. *Journal of Hydrology*, 310, 28-61.
- Cacho, J. F., Youssef, M. A., Chescheir, G. M., Skaggs, R. W., Appelboom, T. W., Leggett, Z. H., . . . Arellano, C. (2018). Effects of forest-based bioenergy feedstock production on shallow groundwater quality of a drained forest soil. *Science of the Total Environment*, 631-632, 13-22. doi:10.1016/j.scitotenv.2018.03.020
- Cacho, J. F., Youssef, M. A., Shi, W., Chescheir, G. M., Skaggs, R. W., Tian, S., . . . Arellano, C. (2019). Impacts on soil nitrogen availability of converting managed pine plantation into switchgrass monoculture for bioenergy. *Science of the Total Environment*, 654, 1326-1336. doi:10.1016/j.scitotenv.2018.11.133
- Cacho, J. F., Youssef, M. A., Shi, W., Chescheir, G. M., Skaggs, R. W., Tian, S., . . . Arellano, C. (2018). Impacts of forest-based bioenergy feedstock production on soil nitrogen cycling. *Forest Ecology and Management*, 419, 227-239. doi:10.1016/j.foreco.2018.04.002
- Caldwell, P. V., Jackson, C. R., Miniati, C. F., Younger, S. E., Vining, J. A., McDonnell, J. J., & Aubrey, D. P. (2018). Woody bioenergy crop selection can have large effects on water yield: A southeastern united states case study. *Biomass & Bioenergy*, 117, 180-189. doi:10.1016/j.biombioe.2018.07.021
- Carter, T. M. (2016). Impacts of Established Loblolly Pine (*Pinus taeda*) and Switchgrass (*Panicum virgatum*) Intercropping in Forested Watersheds on Hydrology and Water Quality. M.S. Thesis. North Carolina State University, Raleigh, NC.
- Durán, Z.V.H., Francia Martinez, J. R., Garcia Tejero, I., Rodriguez Pleguezuelo, C. R., Martinez Raya, A., & Cuadros Tavera, S. (2012). Runoff and sediment yield from a small watershed in southeastern Spain (Lanjarón): Implications for water quality. *Hydrological Sciences Journal-Journal Des Sciences Hydrologiques*, 57(8), 1610-1625. doi:10.1080/02626667.2012.726994
- Elledge, A., & Thornton, C. (2017). Effect of changing land use from virgin brigalow (*Acacia harpophylla*) woodland to a crop or pasture system on sediment, nitrogen and phosphorus in runoff over 25 years in subtropical Australia. *Agriculture, Ecosystems & Environment*, 239, 119-131. doi:https://doi.org/10.1016/j.agee.2016.12.031
- Englund, O., Dimitriou, I., Dale, V. H., Kline, K. L., Mola-Yudego, B., Murphy, F., . . . Mishra, S. K. (2020). Multifunctional perennial production systems for bioenergy: Performance and progress. *WIREs Energy and Environment*, 9(5), e375. doi:https://doi-org.prox.lib.ncsu.edu/10.1002/wene.375

- García-Ruiz, J. M., Regüés, D., Alvera, B., Lana-Renault, N., Serrano-Muela, P., Nadal-Romero, E., . . . Arnáez, J. (2008). Flood generation and sediment transport in experimental catchments affected by land use changes in the central Pyrenees. *Journal of Hydrology*, 356(1-2), 245-260.
- Goodwin, T. H., Young, A. R., Holmes, M. G., Old, G. H., Hewitt, N., Leeks, G. J., . . . Smith, B. P. (2003). The temporal and spatial variability of sediment transport and yields within the Bradford Beck catchment, West Yorkshire. *Science of the Total Environment*, 314, 475-494.
- Gopalakrishnan, G., Negri, M. C., Wang, M., Wu, M., Snyder, S. W., & Lafreniere, L. (2009). Biofuels, land, and water: A systems approach to sustainability. *Environmental Science & Technology*, 43(15), 6094-6100. doi:10.1021/es900801u
- Griffiths, N. A., Jackson, C. R., Bitew, M. M., Fortner, A. M., Fouts, K. L., McCracken, K., & Phillips, J. R. (2017). Water quality effects of short-rotation pine management for bioenergy feedstocks in the southeastern united states. *Forest Ecology and Management*, 400, 181-198. doi:10.1016/j.foreco.2017.06.011
- Guo, T., Cijin, R., Chaubey, I., Gitau, M., Arnold, J. G., Srinivasan, R., . . . Engel, B. A. (2018). Evaluation of bioenergy crop growth and the impacts of bioenergy crops on streamflow, tile drain flow and nutrient losses in an extensively tile-drained watershed using SWAT. *Science of the Total Environment*, 613, 724-735. doi:10.1016/j.scitotenv.2017.08.148
- Hatten, J. A., Segura, C., Bladon, K. D., Hale, V. C., Ice, G. G., & Stednick, J. D. (2018). Effects of contemporary forest harvesting on suspended sediment in the Oregon coast range: Alsea watershed study revisited. *Forest Ecology and Management*, 408, 238-248.
- Heidari, A., Mayer, A., & Watkins, D., Jr. (2019). Hydrologic impacts and trade-offs associated with forest-based bioenergy development practices in a snow-dominated watershed, Wisconsin, USA. *Journal of Hydrology*, 574, 421-429. doi:10.1016/j.jhydrol.2019.04.067
- Hopmans, P., & Bren, L. J. (2007). Long-term changes in water quality and solute exports in headwater streams of intensively managed radiata pine and natural eucalypt forest catchments in south-eastern Australia. *Forest Ecology and Management*, 253(1-3), 244-261.
- Hughes, A. O., Quinn, J. M., & McKergow, L. A. (2012). Land use influences on suspended sediment yields and event sediment dynamics within two headwater catchments, Waikato, New Zealand. *New Zealand Journal of Marine and Freshwater Research*, 46(3), 315-333.
- Jin, E., Mendis, G. P., & Sutherland, J. W. (2019). Integrated sustainability assessment for a bioenergy system: A system dynamics model of switchgrass for cellulosic ethanol production in the US midwest. *Journal of Cleaner Production*, 234, 503-520. doi:10.1016/j.jclepro.2019.06.205
- Karwan, D. L., Gravelle, J. A., & Hubbart, J. A. (2007). Effects of timber harvest on suspended sediment loads in Mica Creek, Idaho. *Forest Science*, 53(2), 181-188.

- King, J. S., Ceulemans, R., Albaugh, J. M., Dillen, S. Y., Domec, J., Fichot, R., . . . Zenone, T. (2013). The challenge of lignocellulosic bioenergy in a water-limited world. *Bioscience*, 63(2), 102-117. doi:10.1525/bio.2013.63.2.6
- Lefrançois, J., Grimaldi, C., Gascuel-Oudou, C., & Gilliet, N. (2007). Suspended sediment and discharge relationships to identify bank degradation as a main sediment source on small agricultural catchments. *Hydrological Processes: An International Journal*, 21(21), 2923-2933.
- Li, X., & Zipp, K. Y. (2019). Dynamics and uncertainty in land use conversion for perennial energy crop production: Exploring effects of payments for ecosystem services policies. *Agricultural and Resource Economics Review*, 48(2), 328-358. doi:10.1017/age.2019.3
- Longato, D., Gaglio, M., Boschetti, M., & Gissi, E. (2019). Bioenergy and ecosystem services trade-offs and synergies in marginal agricultural lands: A remote-sensing-based assessment method. *Journal of Cleaner Production*, 237, UNSP 117672. doi:10.1016/j.jclepro.2019.117672
- McBroom, M. W., Beasley, R. S., Chang, M., & Ice, G. G. (2008). Storm runoff and sediment losses from forest clearcutting and stand re-establishment with best management practices in East Texas, USA. *Hydrological Processes: An International Journal*, 22(10), 1509-1522.
- Moatar, F., & Meybeck, M. (2007). Riverine fluxes of pollutants: Towards predictions of uncertainties by flux duration indicators. *Comptes Rendus Geoscience*, 339(6), 367-382. doi:10.1016/j.crte.2007.05.001
- Moody, J. A., & Martin, D. A. (2009). Synthesis of sediment yields after wildland fire in different rainfall regimes in the western united states. *International Journal of Wildland Fire*, 18(1), 96-115.
- Øygarden, L., Deelstra, J., Eggestad, H. O., & Vandsemb, S. M. (2003). Sediment transport in agricultural catchments-the need for methods to trace sediment sources. *IAHS Publication*, , 79-87.
- Richter, B. D., Baumgartner, J. V., Powell, J., & Braun, D. P. (1996). A method for assessing hydrologic alteration within ecosystems. *Conservation Biology*, 10(4), 1163-1174.
- Riskin, S. H., Neill, C., Jankowski, K., Krusche, A. V., McHorney, R., Elsenbeer, H., . . . Porder, S. (2017). Solute and sediment export from Amazon forest and soybean headwater streams. *Ecological Applications*, 27(1), 193-207.
- Searcy, J. K. (1959). *Flow-duration curves*. US Government Printing Office.
- Searcy, J. K., & Hardison, C. H. (1960). *Double-mass curves* US Government Printing Office.

- Smith, H. G., Sheridan, G. J., Lane, P. N., & Bren, L. J. (2011). Wildfire and salvage harvesting effects on runoff generation and sediment exports from radiata pine and eucalypt forest catchments, south-eastern Australia. *Forest Ecology and Management*, 261(3), 570-581.
- Susaeta, A., Lal, P., Alavalapati, J., Mercer, E., & Carter, D. (2012). Economics of intercropping loblolly pine and switchgrass for bioenergy markets in the southeastern united states. *Agroforestry Systems*, 86(2), 287-298.
- Walling, D. E., Russell, M. A., Hodgkinson, R. A., & Zhang, Y. (2002). Establishing sediment budgets for two small lowland agricultural catchments in the UK. *Catena*, 47(4), 323-353.
- Walling, D., Webb, B., & Shanahan, J. (2007). Investigations into the use of critical sediment yields for assessing and managing fine sediment inputs into aquatic ecosystems. *Natural England Research Reports*, (007).

Chapter 2: Methods to improve DOC concentration time-series predictions from *in situ* UV-Vis continuous measurements in a coastal watershed

2.1 Abstract

UV-vis spectrometers have become more widely accessible to monitor water quality *in situ* on a nearly continuous basis in the last decade. The sensors provide the ability to predict concentration time series based on the user's ability to accurately calibrate raw absorption spectra to discrete sample concentrations measured in the lab. However, these sensors are very susceptible to optics fouling, which may render their use problematic or sometimes apparently impossible. Development and testing of robust calibration methods to predict DOC concentrations from continuous absorbance measurements in a context of severe fouling is necessary. Due to the highly complex compositional nature of chromophoric dissolved organic matter (CDOM) and the dynamic nature of processes that regulate CDOM in streams, one calibration may not be sufficient to reflect the relationship between absorbance properties of CDOM and DOC concentration if it changes. Partial least squares regression (PLSR) is a statistical method that has been used to successfully relate measurements spanning the entire absorption spectrum to concentrations of several water quality parameters including DOC. In this study, 5 months of nearly continuous (15-min) absorption spectra were 'locally' calibrated in an artificially drained watershed in the coastal plain region of North Carolina. Partial Least Squares Regression was performed using a 60-day moving calibration window. Trends in over-prediction and under-prediction of lab measurements falling outside of calibration windows hinged around the largest storm event observed during the study. Additional calibrations were performed to represent 'stable' periods by grouping moving windows that produced similar

prediction trends. Prediction accuracy and reduction in noise were compared among ‘stable’ calibrations and one calibration including all 5 months of data.

2.2 Introduction

Optical properties of water samples have been used as index data to predict concentrations of a variety of water quality parameters of interest (Etheridge et al., 2013; Wolf et al., 2013; reviewed by Lepot et al., 2016). In particular, the availability of UV-Vis spectrometers capable of measuring optical properties *in situ* and at a high frequency are part of a ‘sensor revolution’ in water quality monitoring and research (Burns et al., 2019; Rode et al., 2016). These optical sensors can generate, for the first time, water *quality* information at the same frequency as that of water *quantity*, or flow. This opens the possibility to capture in stream concentration variations associated with biogeochemical processes (Heathwaite & Bierozza, 2020; Pellerin et al., 2012) and hydrological events (Lloyd et al., 2016; Kincaid et al., 2020; Blaen et al., 2017), on a long-term basis, which was not previously possible. Benefits of these sensors include much lower uncertainties on nutrient loads at the watershed scale, and much greater insight on hydrological and biogeochemical processes at the watershed scale (e.g., Vaughan et al., 2018).

However, the benefits of sensors such as spectrometers to provide water quality concentration data relies heavily on the robustness of the instrument’s calibration to predict concentration. A “global” calibration is often provided by the instrument manufacturer to calculate concentrations of water quality parameters using the raw absorption spectra. All optical instrument makers provide a ‘global calibration’ for nitrate, and some also provide for Dissolved Organic Carbon (DOC), and turbidity (spectro::lyser from s::can®). These global calibrations assume that a

similar relationship between absorption and concentration exists *across sites* with varying water color matrices and that this relationship remains relatively *stable through time*.

Instrument makers and recent research suggest to establish local calibrations between the raw absorption spectra and concentrations measured in the lab of actual samples. Such ‘local’ calibrations are more likely to better capture the relationship between a site’s characteristic water color matrix and absorption spectra in relation to concentrations of water quality parameters. Several local calibration methods have been recently tested and reviewed (Etheridge et al., 2013; Wolf et al., 2013; Lepot et al., 2016). Among them, the Partial Least Square (PLS) regression method has been shown to work rather satisfactorily in marshes, stream, sewers and wastewater treatment plants (e.g., Etheridge et al., 2014; Vaughan et al., 2017; Lepot et al., 2016; Addy et al., 2018).

To establish a local calibration using PLS, all applicable absorption spectra and corresponding lab concentrations from the entire monitoring period are typically used to build a PLS model to predict time series data. This implies that the model produced is robust enough to capture any temporal changes in the relationship between color and concentration and/or that this relationship remains fairly stable throughout the entire monitoring/calibrating period. In particular, the correspondence of Dissolved Organic Carbon (DOC) concentration to absorption spectra is not well understood. CDOM, chromophoric or colored dissolved organic matter, is the portion of dissolved organic matter that absorbs light and its absorbance properties have been related to DOC concentrations applying various techniques in previous studies (Saraceno et al., 2009; Fichot & Benner, 2011). CDOM is highly heterogeneous and compositionally complex, making

its absorbance properties as a whole less understood and easily defined. Overall, CDOM participates in what is sometimes referred to as the ‘color matrix’ of water. Much of its sources back to the organically rich soil horizons in watersheds, which may differ depending upon soil moisture content and saturation, themselves varying with storms and seasons. Along flowpaths, CDOM can further undergo processes that can alter the color matrix of water and its proportion to DOC. Land use alteration could also play a role in drastically shifting the water color matrix of a system with short-term and long-term effects. Generally, the color matrix of water must remain relatively stable through time and space for CDOM to be a good predictor of DOC concentration, and/or the local calibration model be good enough to take into account possible changes in the color matrix for spectrophotometers to reliably measure DOC in watersheds.

Another very important consideration is whether or not the local calibration method can correct for chemical and biological fouling that might occur on the optics. This problem has been recognized as the ‘Achille’s heel’ of optical instruments. Most manufacturers provide solutions to minimize fouling, often in the form of automatic brushes or scrapers that intermittently wipe the optics. Despite these, in many cases, fouling does affect the data (Etheridge et al., 2013).

In this study, we use a 6-month flow season dataset of 15-minute interval absorption spectra measurements and discrete sample DOC concentrations from a flat, artificially drained, and managed forest watershed of the coastal plain of North Carolina. This dataset exhibited some extreme fouling of the optics, despite efforts to minimize it. Additionally, it is thought that in these flat systems, the hydrologic mobilization of DOC and color matrix of the water might change drastically depending on whether or not the water table reaches the organically rich

horizon of the soil. The objectives of this study are thus to use a difficult absorbance dataset to evaluate the ability of, and define guidelines and the conditions for which PLSR may provide acceptable local calibrations to measure DOC.

2.3 Methods

2.3.1 Site Description

The watershed monitored (~25 ha; referred to as D1 hereafter) is located in the Coastal Plain region of North Carolina in Carteret County (34 48' N, 76 42' W). The topography is substantially flat (<0.02% slope) and the Deloss soil series type is present, composed mostly of fine sandy loam with 7-35% clay content. Flat topography and poorly drained soils at this site contribute to a long history of studies evaluating the hydrologic and water quality effects of various silviculture and water management practices, particularly controlled drainage, on artificially drained pine forests using a paired watershed experimental design.

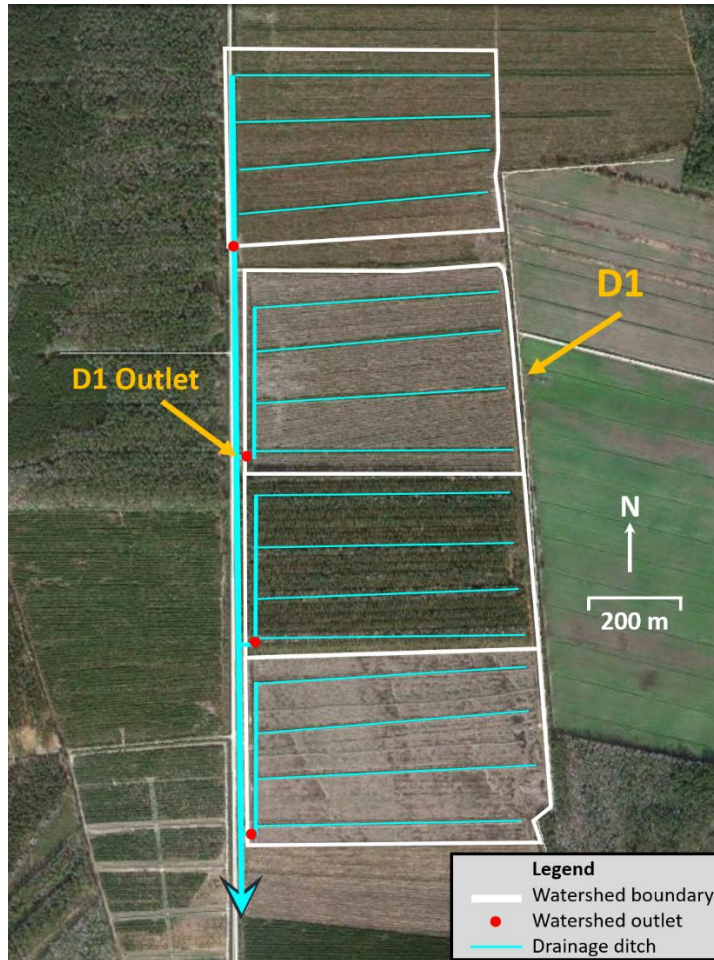


Figure 2.1. Aerial view of D1 among three others in a paired watershed design study located in Carteret County, NC.

The land use on the watershed was pine newly intercropped with switchgrass (*Panicum virgatum*) and the site was instrumented to determine environmental implications of biofuel feedstock production in southeastern US forests. The watershed is artificially drained by 4 parallel canals spaced 100m apart that each drain to a main perpendicular canal in which water flows to a main outlet (Figure 2.1). Trees planted in 1974 were harvested (clear-cut) from D1 in 2009 and the site was sheared and bedded in preparation for planting of pine seedlings in January of 2010 at a density of 1080 trees ha⁻¹. In December 2010, rows between pine beds were sheared

in preparation for switchgrass planting which occurred first in August 2011 and again in April 2012 because the August planting had a low survival rate. D1 was fertilized with Aborite in early April 2012. Water quality and hydrology data were monitored from October 2012 – November 2013 at the outlet of D1 when the watershed was considered to be in the switchgrass establishment phase.

2.3.2 Hydrology

Stages upstream and downstream a 120° V-notch weir at the D1 outlet were measured every 12 minutes using In-Situ® 500 pressure transducers and logged by a Campbell Scientific® CR200 logger. Flow rate were calculated from the 120° V-notch weir equation using the upstream stages for when the weir was unsubmerged. Due to the low slope of the landscape, during large rain events, the weir could become submerged and submergence equations were applied to calculate flow rate using both up- and downstream stages.

Water table stages midway between the drainage ditches were measured hourly by the same In-Situ 500® pressure transducers placed in PVC wells (~3 m deep). One was placed about ¼ of the length of the plot perpendicular to the main collector canal and the other well was located ¾ the length of the plot away from the main canal. Measurements were taken once every hour. A HOBO tipping bucket rain gauge collected rainfall data. The 12-minute flow dataset and rainfall dataset were linearly interpolated to 15-minute time steps to reflect the time step of the continuous water quality measurements.

2.3.3 Continuous water quality monitoring instrumentation and maintenance procedures

Automatic cleaning of the optics

Light absorbance of water was measured at wavelengths ranging from 220 – 732.5 nm at 2.5 nm increments by a UV-Vis spectrophotometer (s::can spectro::lyser™) installed at the outlet of D1. The probe was not equipped with cleaning brushes as these were not offered by s::can at this time. The compressed air bursts designed to provide antifouling by the s::can spectrometer did not work as they provided oxidized conditions in the presence of reduced radicals and enhanced chemical fouling on the optics (Etheridge et al., 2013). Aware of this problem from a precedent project, the anti-fouling system developed by Etheridge et al. (2013) was used. The objective of the anti-fouling system was to remove the probe from constant submergence, and instead, pump sample water to the spectrometer only just before measurement times, leave water there just enough time for the measurements to take place, and purge the water back to the stream afterwards to reduce the amount of time the optics were exposed to potential chemical and biological fouling. This system had been shown to reduce fouling to acceptable levels in a nearby tidal marsh (Etheridge et al., 2013). The spectrometer was installed adjacent to the outlet of D1 and stored in a PVC casing to ensure sunlight did not interfere with absorbance measurements. An overflow sleeve was placed around the probe at the 5 mm measurement path and water from the ditch was delivered to the spectrometer every 15 minutes via the solar-powered system. The pumping intake was placed directly upstream of the weir at a level slightly lower than the bottom of the V-notch weir.

An Arduino Uno® microcontroller was programmed to control the series of pumping and optics cleaning processes of the antifouling system. The 12V signal originally designed to send a burst

of compressed air to the optics before each measurement was used to trigger the sequence of pumping/purging of the antifouling system every 15 minutes just before each of the scan measurements. Upon this signal, water was pumped to an overflow sleeve for a short period of time to pre-rinse the intake tubing and overflow sleeve with at least 5 times the sleeve volume, flushing out pre-existing water remaining from the previous sampling cycle. The probe took an absorbance measurement several seconds after pumping had stopped and once completed, a valve was opened below the sleeve to drain the water out. The optics were rinsed for a duration of 3-5 seconds with tap water delivered by a windshield wiper pump from a 38-L tank refilled at every field visit. The polarity of the peristaltic pump was then reversed to purge remaining water left in the sleeve and tubing from the system. Fifteen-minute data was collected when possible, depending upon if there was enough water in the canal for sample collection and if the sample delivery system and spectrometer were functioning properly.

Manual cleaning and maintenance of the optics

The anti-fouling system and spectrometers were serviced approximately every 14 days as this was the duration of time that 15-minute measurements could be acquired before the spectrometer's data logging memory became full and tanks supplying water for rinsing of the optics were emptied. Data was downloaded and an initial absorbance measurement was taken in the field to determine severity of fouling. Spectrometer optics were cleaned thoroughly with 2% HCl solution using a Q-tip to remove biological and chemical fouling as best as possible.

Fouling was typically severe, and the saturated Q-tip was left on the lenses 5-10 minutes at a time for deeper cleaning. Deionized water was used to rinse the lenses after cleaning with acid and lenses were then dried carefully with a Chem-wipe. A measurement was taken while the

lenses were dry to obtain a clean “air” fingerprint (absorption spectrum). If absorption was low at 220 nm, $\sim 10 \text{ m}^{-1}$ or less, and the fingerprint resembled that of the clean air fingerprint after lenses were cleaned during the previous field visit, the lenses were considered clean and logging was begun again.

2.3.4 Water Quality Sampling and Analysis Scheme

A 24-bottle Sigma Automated Water Sampler was placed at the outlet of the watershed with the intake installed adjacent to and at the same depth as the spectrometer system intake for comparable water sampling. Discrete samples were taken approximately every 12 hours and sampling times were scheduled to correspond closely (within seconds) to times that water was pumped to the spectrometer for calibration purposes. The 1 L sample bottles were not pre-acidified because this would have altered DOM absorption/fluorescence properties of the samples that were of interest and additionally such that samples would be comparable to those measured by the probe (more details below). Samples were collected and placed on ice upon each field visit and stored at 4°C until filtered for analysis and sent to the lab (following day).

The raw absorption spectra, also referred to as fingerprints, were downloaded during each field visit. The data were typically plotted, or “visualized”, in the ana::pro software while in the field to ensure the sampling system was functioning properly. In order to visualize the data, the raw absorption spectra data file (*.fp file) was provided as an input to a proprietary global freshwater calibration provided by scan Measuring Systems. This particular calibration predicted concentrations of DOC, TOC, NO_3^- -N in addition to turbidity for each fingerprint in the time series, and these concentrations were plotted and output to a parameter (*.par) file. These plots

allowed for initial visualization of concentration dynamics in addition to the degree of optics fouling during the monitoring period.

Upon returning from the field, the globally calibrated chemographs in addition to rainfall data were used to determine which discrete samples would be analyzed in the lab and contribute to the local calibration. The goal of sample selection was to capture concentration dynamics as fully as possible without oversampling when concentrations were relatively stable. Therefore, samples collected preceding, during and following storm events were analyzed more frequently than those occurring during “baseflow” conditions to capture rapidly responding and greater magnitude changes in concentrations. This ensured that a fuller range of sample concentrations and absorption spectra would be available for local calibration while keeping lab analyses cost as minimal as possible. About 12 ml of selected samples were filtered using Millipore Sterivex-GP 0.22 μm filters, acidified with H_2SO_4 and analyzed for DOC using a Shimadzu TOC/TON analyzer and Standard Method 5310 B (Greenberg et al., 2005).

A degradation study was performed to ensure that DOC concentrations remained stable when samples were left in the field un-acidified for up to two weeks. Two grab samples (1 L each) were collected each field visit, one was left in the automatic sampler and one was placed on ice with the collected discrete samples. Upon returning from the field, the fresh sample was stored, filtered and analyzed along with the selected discrete samples and the same procedure was followed when the approximately two-week-old sample was collected the next field visit. A paired T-test was performed between the fresh and old sample concentrations to detect if there was a significant change over the two-week period and results demonstrated there was not.

2.3.5 Absorbance Data Post-Processing

The absorption data were post-processed to remove poor quality measurements corresponding with times in which there was insufficient water pumped to the spectrometer resulting in measurement of air. These measurements in addition to gaps occurring in the continuous dataset were related to electrical equipment failures, freezing temperatures, wildlife interference and when the water level in the drainage canal was lower than the sampling intake. In order to prepare the absorption data to be locally calibrated, DOC concentration data predicted by the global freshwater calibration was imported into AQUARIUS Time-Series software (AQUARIUS, Aquatic Informatics™, Vancouver, British Columbia, Canada) to determine which data could be considered reliable. Concentrations that spiked from continuous chemograph trends in DOC that did not concur with rainfall and discrete sample concentration trends were visually removed from the dataset using the adjustable trim correction tool. The exported original and corrected time series data were then used to categorize corresponding fingerprint data as ‘reliable’, ‘unreliable’ or ‘missing’ using R statistical software (R Core Team, 2020). During the 13-month monitoring period, nearly 5 months of continuous data covering most of the flow season were considered reliable. There was no flow in the drainage canal for a large portion of the monitoring period and equipment failures also occurred. For these reasons, the dataset was narrowed to only approximately 5 months of continuous absorbance data for local calibration purposes in this study, with dates ranging from December 20, 2012 – May 20, 2013.

2.3.6 Local Calibration Methods

Local Calibration Statistical Method: Partial Least Squares Regression

Rather than locally calibrating the spectrometer using s::can Measuring Systems' software, per the manufacturer's recommendation, raw absorption spectra were calibrated to the water color matrix using Partial Least Squares Regression (PLSR). PLSR provided the most accurate predictions of water quality parameter concentrations from absorption data logged by s::can spectrometers in an Eastern North Carolina tidal stream when compared with other commonly used statistical models to correlate absorbance measurements to DOC concentrations (Etheridge et al., 2014).

PLSR is a statistical technique often used in chemometrics where multicollinearity is addressed among a set of independent predictor variables. A set of latent variables, termed components, are determined to explain the covariance between a set of independent, yet possibly auto-correlated, predictor variables and a dependent variable or set of variables. PLSR model components require all independent variable responses of a measurement to predict a dependent variable response rather than determining which independent variables best predict dependent variable responses and employing those variables for prediction. In this particular study, this means that the model is built by a number of components, each of which describe the entire absorption spectrum distinctly, and collectively build a model to predict concentration. PLSR is particularly applicable when fewer observations exist than independent variables, correlating spectral data measured at nearly 200 wavelengths to a relatively small pool of sample concentrations. Detailed steps of the modeling process are provided herein. In short, PLSR modeling consists in identifying, over a given period of time, reliable measured absorbance

spectra for which there is a laboratory concentration value. The next step is to choose the number of components that will provide the best calibration without overfitting the data. The last step consists in validating the calibration.

Local Calibration of PLSR Models: Three Approaches

To explain why several approaches were tested in the first place with this dataset, it is important to realize that despite our anti-fouling system, the fouling of the optics was severe. This was indicated by the steady rise of DOC concentrations predicted by the global freshwater calibration over the approximate 2-week duration between field visits and the immediate drop following servicing and cleaning of the optics (Figure 2.2). Predicted concentrations rose higher than double the maximum sample concentration observed for the entire sampling period during each of the 2-week monitoring intervals according to this calibration. Sometimes values toward the end of the monitoring intervals became elevated to greater than 40 mg/L. It thus became unclear whether the PLSR method used in the past (Etheridge et al., 2014) would be able to yield usable data.

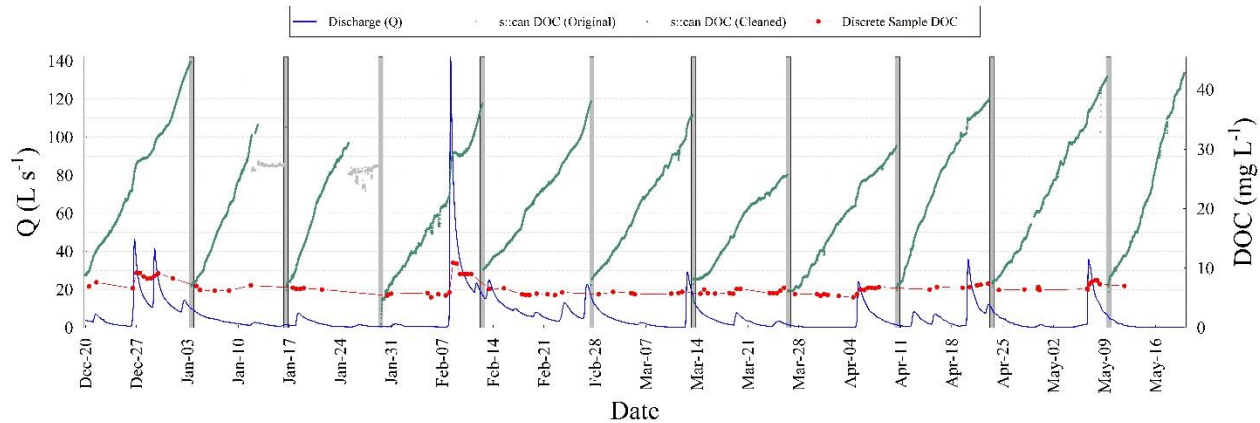


Figure 2.2. Comparison of DOC concentrations calculated by the s::can global calibration and discrete sample DOC concentrations measured in the lab. Original s::can concentration data was used to determine which data were reliable for local calibration purposes. Examples of unreliable data corresponding with measurements of air are observed as sudden decreases in the s::can DOC (Original) time series occurring in the interval between servicing periods. Gray polygons represent days in which the spectrometer was serviced, correlating with a large decrease in s::can DOC concentration due to optics cleaning. The s::can DOC (Cleaned) time series represents the subset of data left available for local calibration after unreliable data were removed.

Initial calibration trials suggested that in addition to numerically correcting for fouling, it would be valuable to assess whether or not, and under what conditions the PLSR approach would concurrently be able to consider expected seasonal or shorter variations in the relationship between water color matrix and concentrations. Three approaches varying the time range of input spectral and concentration values used for calibration were applied to evaluate the capabilities of PLSR to calibrate the 5-month dataset.

Full Time Range Local Calibration

An initial calibration was performed similar to that proposed by Etheridge et al. (2013) to predict tidal water quality data from spectral measurements recorded by s::can spectrophotometers. The extreme fouling of the spectrophotometer lenses over the two-week periods between cleanings

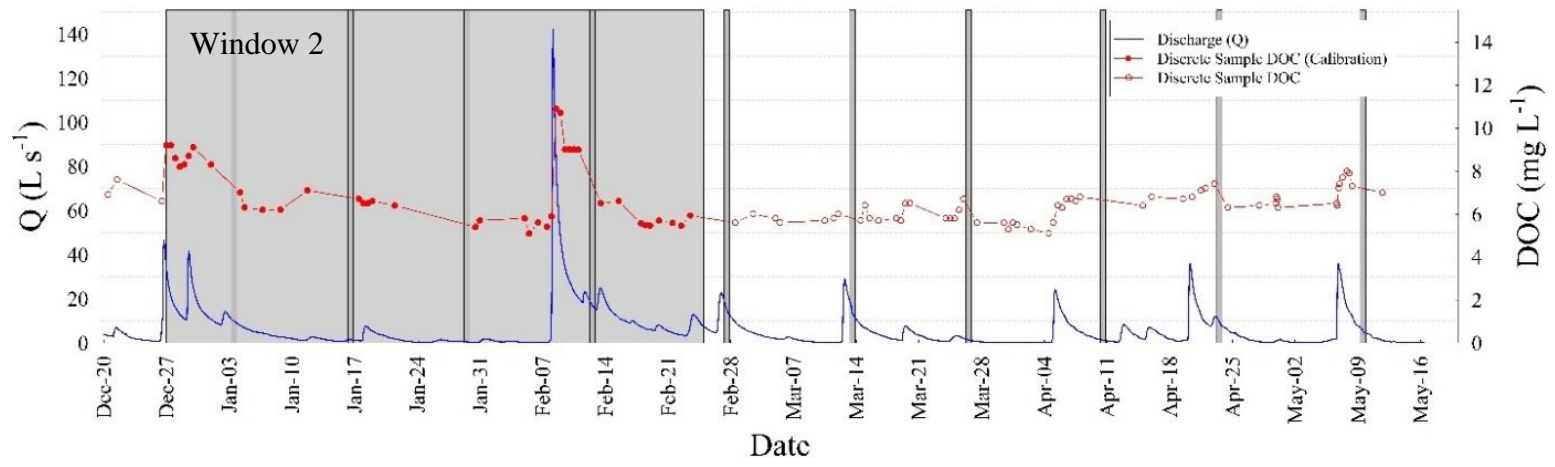
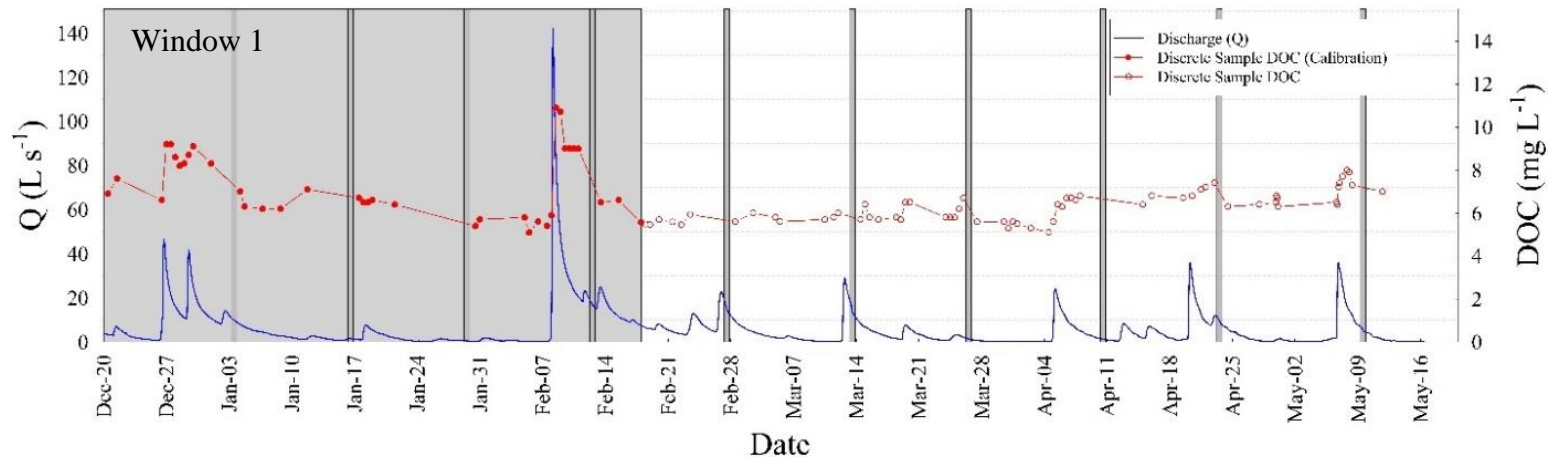
caused concern that a calibration that could reliably predict DOC concentration may not be possible for this site. A PLSR model was calibrated using all available streamlined raw absorption spectra measurements and corresponding lab DOC concentrations occurring during the entire 5-month period.

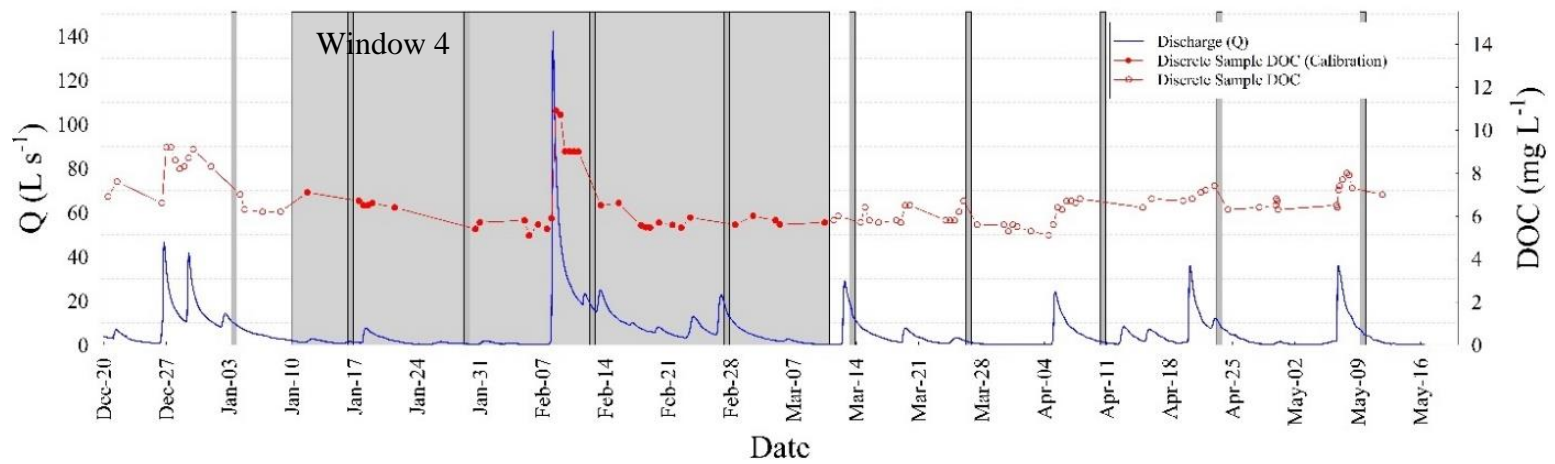
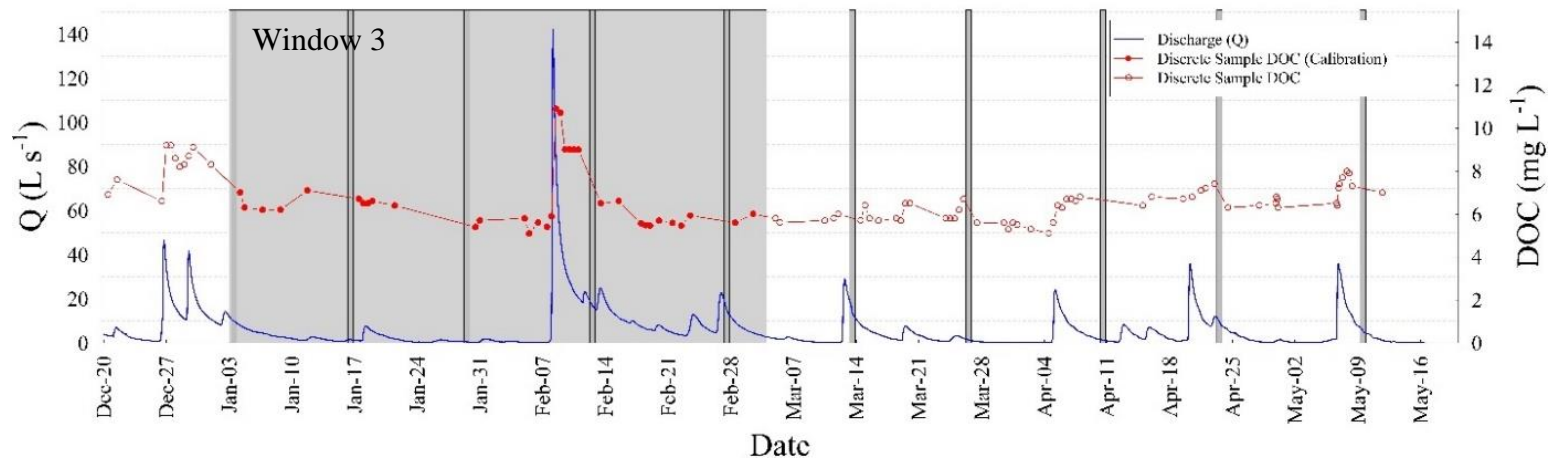
Moving Window Local Calibration

Our second modeling exercise consisted in narrowing the data into small moving time period windows on which local PLSR calibrations could be performed. This moving window calibration approach was applied to explore if there were any obvious shifts in prediction trends (under- or over-predicting) due to potential temporal variation in the water color matrix and DOC concentration relationship. A moving window of 60 days was used as a calibration period in which only observations occurring within the 60 days were used to calibrate a PLSR model. The number of observations varied among calibrations depending upon the number of available concentration data points. The 60-day calibrated model was then used to predict the entire 5-month time period.

Calibration results were plotted for each moving window period as measured versus predicted concentration values. Validation concentrations, all concentrations falling outside of the calibration window, were plotted in addition to calibration concentrations. This provided the ability to observe trends in how the model calibrated to the 60-day time period predicted concentrations falling outside of it. As many 60-day calibrations were performed as possible by shifting the window forward in 7-day intervals until the full 60-day window no longer fell within the 5-month period (Figure 2.3).

Figure 2.3. Windows 1-4 of a 60-day moving calibration window with a chronological 7-day shift in beginning window date for each window.





Stable Period Local Calibration

The third modeling approach was built upon the results of the moving window local calibration. The moving period approach revealed systematic patterns of under- and over-prediction before and after, respectively, concentration and flow peaks in February (details in results), where the water table reached the surface and stayed in the organic horizon for several days. The two periods before and after the peaks appeared to yield rather stable responses to PLSR modeling, hence the name given here. The stable period calibrations were then evaluated to determine if similar trends could be observed when the same plotting method was used as was for the moving window approach. Predicted concentrations were plotted versus observed concentrations for all available data falling outside of the calibration period and analyzed for trends. These calibrations were used to assess whether the PLSR method would perform better during periods where it was reasonable for the relationship between concentrations and the color matrix to be considered relatively stable.

2.3.7 PLSR Model Evaluation Criteria

PLSR modeling was performed using the `pls` package (Mevik et al., 2011) in R Statistical Software (R Core Team, 2020). A 10-fold cross-validation was performed where the dataset was broken into 10 random segments, each with 90% of the data randomly selected for training and the remaining 10% of data used to validate the model and calculate the root mean square error of prediction (Equation 2.1). Cross-validation RMSEP results were evaluated for models consisting of 1 component and up to 20 components (when possible) to select the number of components to build the final models for each modeling objective. The Nash-Sutcliffe coefficient of efficiency (NSE) was also calculated to evaluate prediction performance (Equation 2.2).

$$RMSEP = \sqrt{\frac{\sum_{i=1}^n (O_i - P_i)^2}{n}} \quad 2.1$$

$$NSE = 1 - \frac{\sum_{i=1}^n (O_i - P_i)^2}{\sum_{i=1}^n (O_i - \bar{O})^2} \quad 2.2$$

The RMSEP and NSE are ill suited to assess model overfitting. Overfitting can be identified on the predicted concentration time series as ‘noise’ where concentrations ‘jump’ up and down from one data point to the next. To assess the ‘noise’, hence potential overfitting, we introduce a third performance indicator that determines the average of normalized adjacent concentration differences in the predicted time series as a percentage (Equation 2.3). We determined this value for differences between concentrations occurring at the 15-, 30-, 45-, 60- and 75-minute increments (lag = 1,2,3,4,5 respectively) to ensure there were no obvious patterns prevailing at certain time increments due to an inherent pattern in measurements made by the spectrometer. This was performed by comparing rankings of the mean noise values for PLSR models with 1-20 components for the full time range local calibration. No change in rankings of mean noise values among the models was observed among the five increments. The 60-minute increment results are provided in this chapter.

$$Mean\ Noise\ (\%) = \frac{1}{n - lag} \sum_{i=1}^{n-lag} \frac{P_{i+lag} - P_i}{P_i} \quad 2.3$$

n = total number of PLSR predicted continuous time series concentration values
 lag = integer multiple of the time interval between consecutive concentration values

P_i = PLSR predicted continuous time series concentration i

P_{i+lag} = PLSR predicted continuous time series concentration $i + lag$

Selecting Number of PLSR Model Components

Selecting an appropriate number of components to build a PLSR model is an important part of the modeling process that can be somewhat subjective to the modeler's specific goals. The `pls` package does provide an objective system to automatically select the number of components if the user so chooses (Mevik et al., 2011). Two methods of selecting the number of components are available and are referred to as the "one sigma" and "permutation" methods. The one-sigma method selects the smallest number of components still capable of producing an RMSEP less than one standard error from the absolute minimum RMSEP. This number of components will be referred to as $ncomp_{sigma}$. The permutation method removes components one by one, using the absolute minimum RMSEP number of components as an initial starting point, and evaluates if model performance significantly decreases based on $\alpha = 0.01$. The number of components selected by this method will be referred to as $ncomp_{perm}$. Our experience shows that these two methods do not necessarily yield the same number of components (see below). It is therefore important to provide guidance on how to choose an acceptable number of components.

Previous studies report using the number of components producing the absolute minimum RMSEP (e.g., Etheridge et al., 2014; Messer et al., 2019), or the number of components corresponding to the near absolute minimum RMSEP, when improvement of RMSEP with each additional component remained relatively small (Vaughan et al., 2017; Addy et al., 2018). We chose by default the number of components that produced the absolute minimum RMSEP for evaluating the results of the moving window calibrations. Overfitting of the data, or the noise indicator, was not as much of a concern because our goal with this approach was to determine trends in predicted sample concentrations falling outside of the calibration window, not

producing the optimum time series curve. However, we did require that the calibrated model at least be considered valid by the NSE indicator. In the case that the model with the number of components corresponding with the absolute RMSEP did not yield an acceptable NSE value, we added components until the NSE reached a value of 0.65 or greater. The number of components corresponding to the absolute minimum RMSEP for any model will be referred to as $ncomp_{rmsep}$ and the number of components corresponding to the minimum number of components necessary to result in an NSE value of at least acceptable, 0.65, will be referred to as $ncomp_{nse65}$. We did compare the $ncomp_{rmsep}$ and $ncomp_{nse65}$ values in most calibration scenarios in addition to the automated selection numbers of components to examine prediction sensitivity to number of components.

In some cases, a higher NSE value than 0.65 is preferred and the modeler may choose to add more components to accomplish prediction of a chemograph that does not display drastic over- or under-prediction, particularly during events. The addition of components to improve overall fit however may still come at the cost of overfitting and increasing the level of noise in the time series. This is further discussed in the results section of this paper.

2.3.8 Cumulative Load as Indicator of Performance of PLSR

Cumulative dissolved organic carbon loads were calculated on continuous predicted time series data for the stable period scenarios and calibration over the five months for comparison purposes. Prior to cumulative load calculation, minor gaps in the time series were filled using the last constant predicted concentration at the beginning of the gap. These gaps contributed little to the cumulative load calculation as they occurred during times of low flow. Cumulative

load (L) was estimated as the sum of the predicted time-series instantaneous loads calculated at the 15-minute interval, where the i^{th} predicted DOC concentration (C_i) was multiplied by the i^{th} flow volume (V_i), calculated as the flow rate (Q_i) multiplied by the time interval occurring between measurements, t , equal to 15 minutes in this case. N is the number of absorption measurements/predicted concentrations in the time series and K is applied as an adjustment factor to account for units and the watershed area such that L is reported in units of (kg ha^{-1}).

$$V_i = Q_i t \quad 2.4$$

$$L \approx K \sum_{i=1}^{i=N-1} C_i V_i \quad 2.5$$

2.4 Results

The three calibration approaches were applied to the 99-observation streamlined dataset composed of DOC lab concentrations corresponding with good quality absorption measurements from December 20, 2012 to May 20, 2013. Lab concentrations ranged from 5.1 mg/L to 10.9 mg/L with an average of 6.7 mg/L. There was a total of 25 rain events that occurred during the 5-month period with the maximum flow rate (142 L s^{-1}) occurring at the peak of an event in early February. Maximum DOC concentrations were observed during a delayed concentration effect coinciding with this storm ($n=6$, 9 - 10.9 mg/L) and two consecutive storms occurring in December ($n=8$, 8.2 - 9.2 mg/L). DOC concentration effects coincided with a majority of events and were present in the chemograph produced by discrete sample concentration and somewhat in the chemograph predicted by the global calibration provided with the scan instrument however these effects were dampened by the degree of fouling on the lenses.

2.4.1 Local Calibration Using Entire Time Range

A PLSR model was constructed using all available fingerprint data with corresponding sample concentrations from the full 5-month dataset. Results evaluating models composed of 1-20 components indicated that a model with 12 components produced the absolute minimum RMSEP ($ncomp_{rmsep} = 12$) and that a model with 5 components was considered acceptable according to the Nash-Sutcliffe Efficiency indicator ($ncomp_{nse65} = 5$). A 12-component model produced a very high NSE value (NSE = 0.97) at the cost of an increase in average noise from 1.4% to 5.7% when compared to the 5-component model (Table 2.1 and Figure 2.4).

Table 2.1. PLSR calibration results for models consisting of 1-20 components built using the total time range of observed DOC concentrations and absorption spectra.

Components	RMSEP	NSE	Mean Noise (%)
1	1.086	0.209	0.22
2	0.990	0.364	1.81
3	0.948	0.442	0.72
4	0.874	0.573	0.84
5 ^d	0.787	0.666	1.42
6	0.663	0.760	2.78
7	0.517	0.877	3.51
8 ^c	0.468	0.906	3.97
9 ^b	0.455	0.927	4.05
10	0.431	0.946	4.53
11	0.428	0.968	5.94
12 ^a	0.416	0.974	5.67
13	0.418	0.980	5.72
14	0.421	0.985	6.22
15	0.418	0.988	6.34
16	0.432	0.990	6.45
17	0.428	0.992	6.62

Table 2.1. (continued)

18	0.437	0.994	6.67
19	0.446	0.995	6.70
20	0.461	0.996	6.83

^a Absolute minimum RMSEP number of model components, $ncomp_{rmsep}$

^b One-sigma method selected number of model components, $ncomp_{sigma}$

^c Permutation method selected number of model components, $ncomp_{perm}$

^d $NSE \geq 0.65$ least number of model components, $ncomp_{nse65}$

The automated selection methods used in the pls package yielded number of component selections fell between those of the NSE and minimum RMSEP indicators. The one-sigma method selected 9 components and the permutation method suggested an 8-component model. Both models performed at NSE values greater than 0.9 which would be considered “very good” according to standards provided by the evaluation scheme outlined by Ritter & Muñoz-Carpena (2013). Noise values in the modeled time series data predicted by the model with the number of components chosen by the auto-selection methods were more than doubled when compared with that produced by the 5-component “acceptable” model.

Full Time Range Calibration

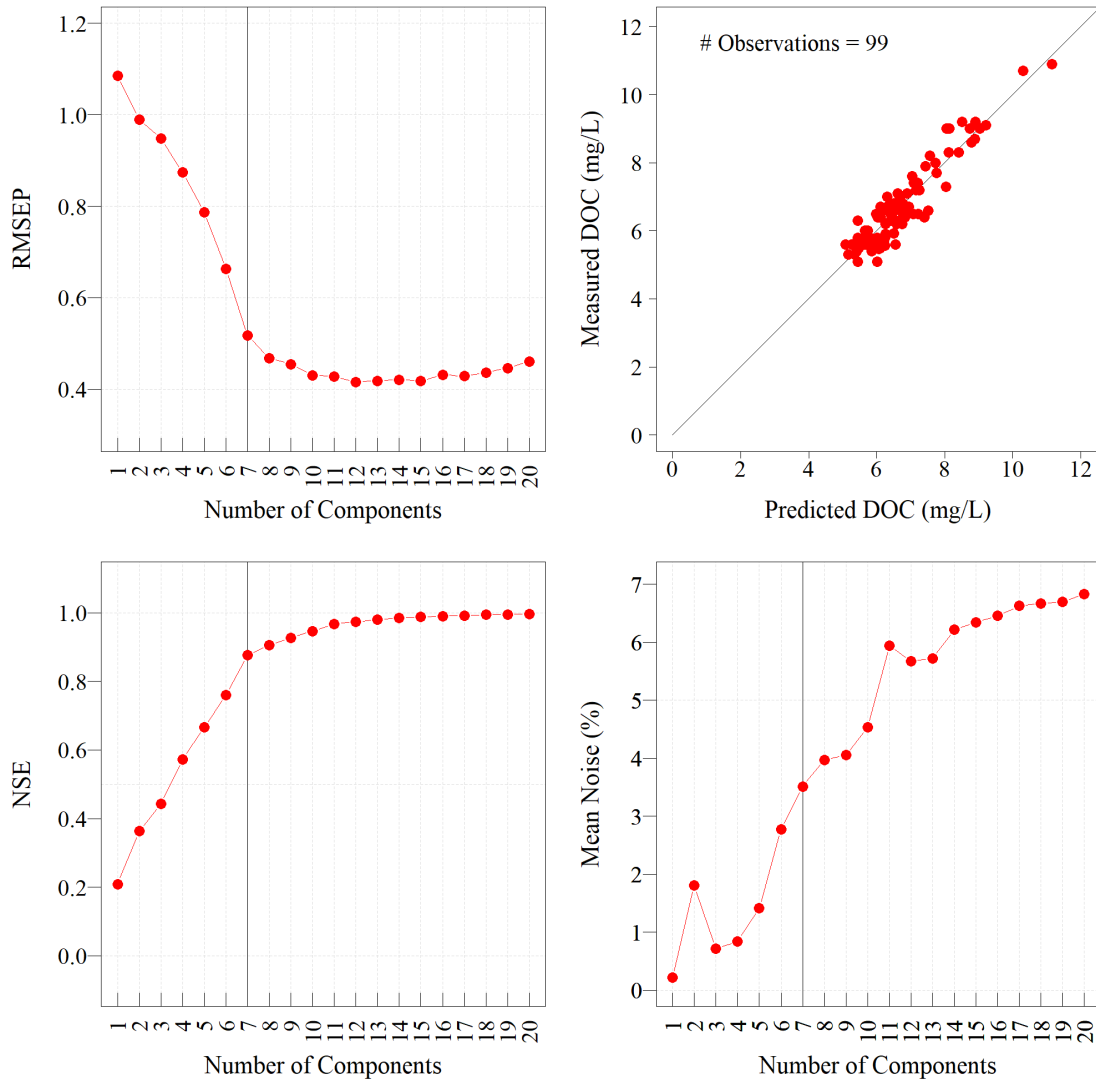


Figure 2.4. Evaluation criteria RMSEP, NSE and Mean Noise (%) plotted as a function of the number of components included in the PLSR model calibrated using the entire date range of data available. The vertical black line corresponds to the number of components included in the model associated with the measured DOC concentrations as a function of predicted DOC concentrations (top right). This line is meant to more easily illustrate how a 7-component model performs comparatively to other number of component selections and where visually a plateau begins to form in the RMSEP and NSE curves.

These results show that finding the correct number of components is not straightforward. Plotting results as a function of the number of components was instructive to provide guidelines to select the optimum number of components (Figure 2.4). Until the 7th component, RMSEP and NSE values rapidly decreased and increased, respectively, after which the curves more or less plateaued. Figure 2.4 thus hints that there might be a hinge point (7 components) beyond which the RMSEP and NSE values improve much less significantly. One could argue to take this hinge point as the optimum number of components as this diminishes the risk of overfitting with goodness of fit indicators close to their optimum. The permutation auto-selection number of components fell at 8 components, and the one-sigma method yielded 9 components, all of which much lower than the absolute minimum yielding 12 components. There was no such break in the noise level trends other than a sharp increase in the noise level with the addition of the 11th component (Figure 2.4).

Plotting each of the evaluation criteria curves in this manner could aid the modeler in selecting the number of components that best meets modeling needs. For other PLSR models, these curves may look different and may present more local troughs and peaks like that seen in the mean noise curve, although overall plateau shapes are expected in RMSEP and NSE curves. This gives a set of criteria for component selection. Another criterion is the resulting predicted chemograph.

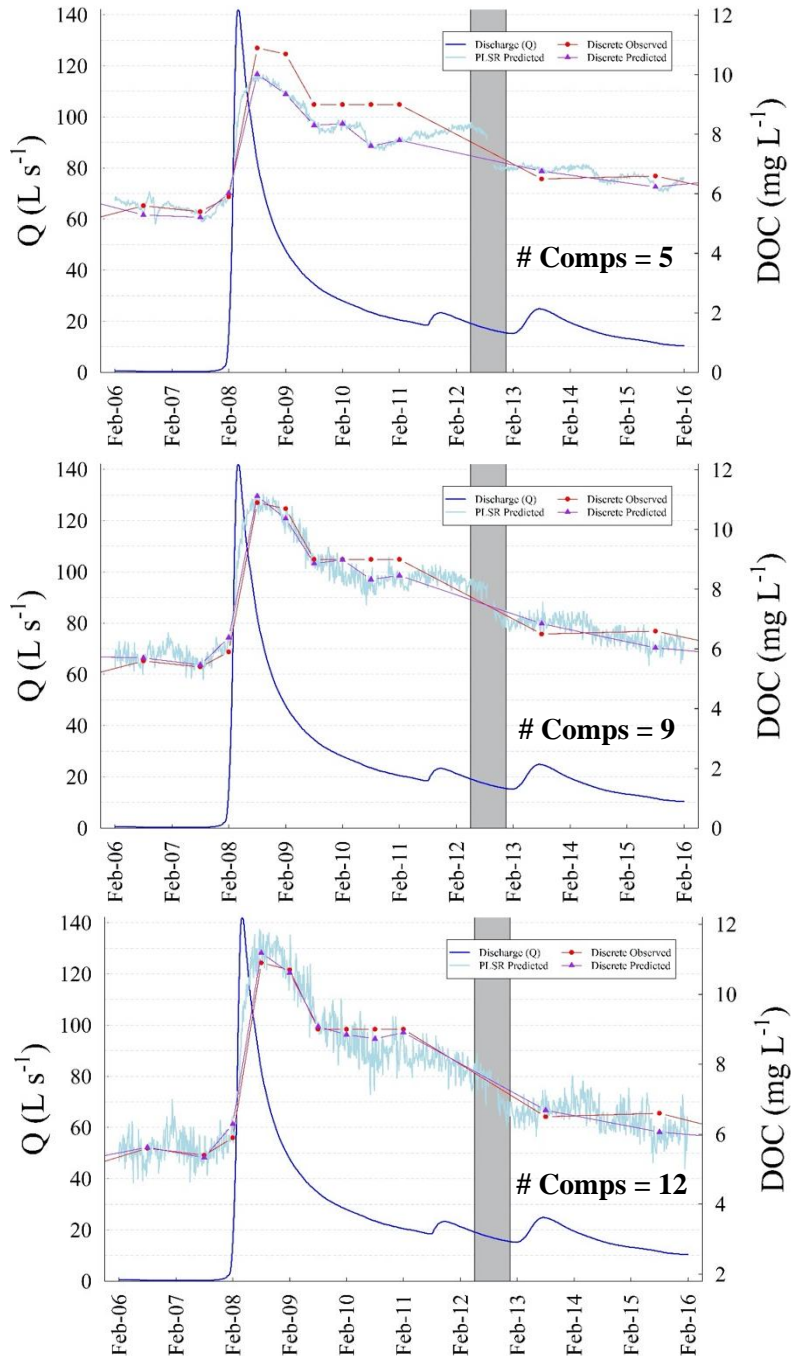


Figure 2.5. Comparison of the 15-minute DOC concentration time series for the February events predicted by a 5-component, 9-component, and 12-component PLSR model calibrated using the entire date range of concentrations. The grey area indicates a field maintenance day when the spectrometer optics were cleaned.

Figure 2.5 illustrates the consequences of compromising smoothness of the predicted time series curve in exchange for noise and prediction accuracy (NSE) for 5, 9, and 12 component model predictions. The model with the lowest number of components deemed acceptable according to the $NSE \geq 0.65$ criterion yielded the smoothest chemograph, but at the cost of prediction accuracy by underestimating the concentration peak corresponding with the largest event that occurred in the month of February. The 9 and 12 component models better predicted the lab measured DOC, particularly those associated with the Feb 8-9 event, but at the cost of noisy and probably less realistic chemographs. In these cases, this suggests that the PLSR models with 9 and 12 components are overfitting the data to some extent, but on average better capture the chemograph hinted by the lab data.

All 5, 9, and 12 component models dramatically correct for fouling that occurred on the optics at this period (Figure 2.5). However, the transition between before and after the optics were cleaned (indicated by gray area), is the smoothest in the time series predicted by the 12-component model. The transition appears more abrupt in the 5-component model predicted time series and becomes slightly more seamless with the 9-component model predicted time series. More components seem to correlate to more fouling compensation. From these observations, we hypothesized that one or a combination of the following could be the reason for noisiness in the predicted concentration time series overall: 1) the relationship throughout the 5 months between water color matrix and concentration was inconsistent; 2) the model was built using periods of time in which the optics ranged from clean to extremely fouled and was therefore trying to accommodate for both extremes which occurred in approximately 2-week cycles. In both

scenarios, similar water DOC concentrations could be paired with vastly different absorption fingerprints.

2.4.2 Local Calibrations Using a Moving Window

The moving window exercise aimed at assessing the robustness of the PLSR approach to predict concentrations outside of the calibration windows, detect times when the color matrix to concentration relationship remained relatively stable, and detect whether, and detect the instances when, this relationship would change. Fourteen PLSR models were established using fingerprints and lab data available within the fourteen 60-day windows moved by 7-day increments.

Number of observations varied from 33-51 samples in the fourteen 60-day moving window calibration periods (Figure 2.6). The maximum measured DOC concentrations corresponding with the relatively large February storm were included in the first 8 calibrations, which concentrations all ranged from about 5 to 11 mg C/L. Windows 1 and 2 display greater 75th quartile values because of concentration effects that coincided with the two consecutive December storms (Figure 2.6). The range of concentrations between the 25th and 75th quartiles for Windows 3-14 remained between 5-7 mg C/L, however the maximum values for Windows 9-14 were reduced to at most 8 mg C/L.

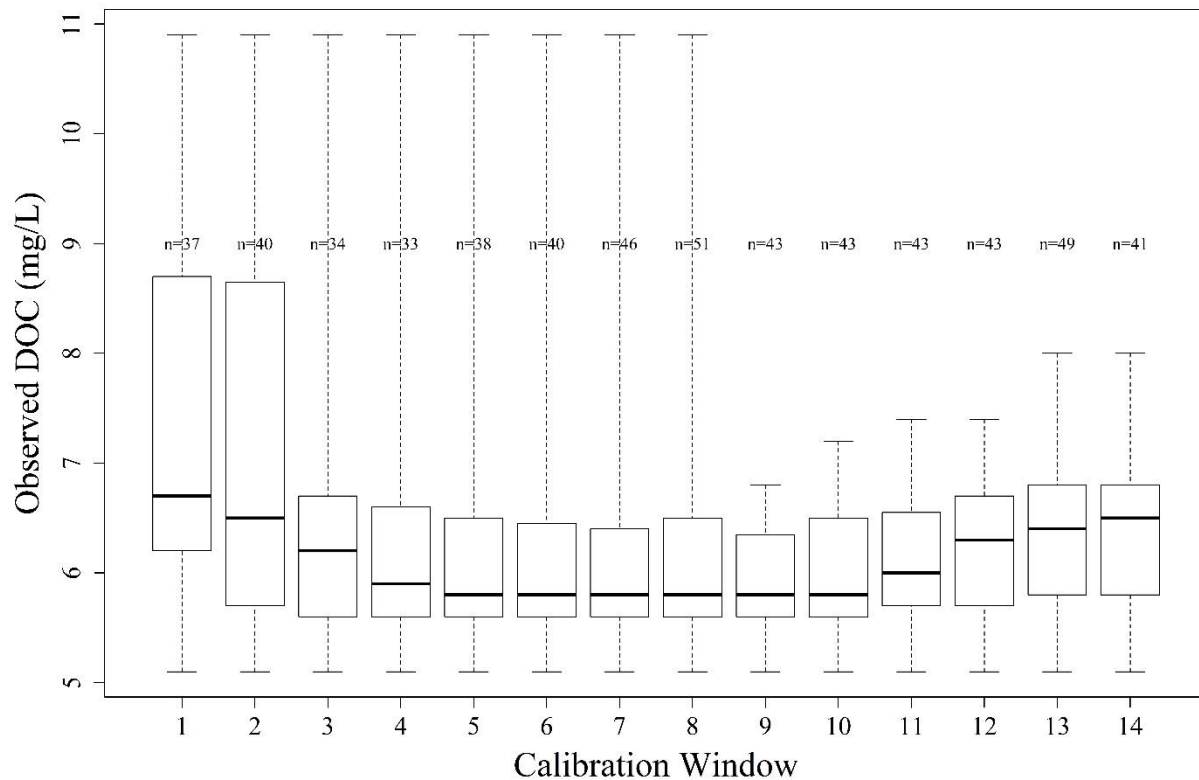


Figure 2.6. Measured DOC concentrations subset by calibration window. Bottom and top lines of boxes represent the 25th and 75th quartile values respectively while whisker notches represent the subset minimum and maximum concentrations.

Suggested number of components highly dependent upon criteria

The $NSE \geq 0.65$ ($ncomp_{nse65}$) and one-sigma criteria suggested relatively few and consistent 3-6, and 4-7 components, with 3 and 4 components for most windows, respectively. The permutation method suggested a lot more variable number of components (0 to 7). The number of components that produced the absolute minimum RMSEP value during cross-validation of each window model ranged widely, from 5 to 20 (Table 2.2). The absolute value is located somewhere along the plateaued area of the RMSEP vs. components curve and a very small change in RMSEP may correspond to large changes in the number of components.

Typically, the automatic selection of components fell somewhere within the range of $ncomp_{nse65}$ and $ncomp_{rmsep}$ numbers for Windows 1-8, while these values fell mostly at or below the $ncomp_{nse65}$ value for Windows 9-14 with the exception of the $ncomp_{sigma}$ values for Windows 13 & 14. The permutation method consistently suggested models performing at values of NSE falling below 0.65 for Windows 9-14. This demonstrates that while choosing a lower number of components may not cause significant degradation in the value of RMSEP, there may be a tradeoff for the model's ability to accurately predict concentrations. For this reason, a combination of evaluation criteria with requirements defined to meet the specific goals of the modeling study is necessary for the selection of the number of components to build an optimum model, and the auto selection function in R should be used with caution.

Table 2.2. 60-day moving window calibration cross-validation results for 1-20 component models (per each calibration window) with number of components selected based on 4 selection methods: 1) Minimum root mean square error of prediction (RMSEP) 2) minimum number of components necessary to produce an “acceptable” Nash Sutcliffe Efficiency ($NSE \geq 0.65$) 3) automatic selection using the “one-sigma” method found in the R *pls* package 4) automatic selection using the “permutation” method found in the R *pls* package. Number of components selected based on method for each window calibration model are in Italics while corresponding NSE values produced by models with the selected number of components are listed to the right in each selection method column.

Window	Date Range (M/D/Y)	Minimum RMSEP		NSE ≥ 0.65		One-Sigma		Permutation	
1	12/20/12 – 2/18/13	8	0.97	3	0.86	4	0.89	3	0.86
2	12/27/12 – 2/25/13	9	0.98	3	0.70	7	0.97	7	0.97
3	1/3/13 – 3/4/13	8	0.98	3	0.70	7	0.97	6	0.93
4	1/10/13 – 3/11/13	<i>11</i>	1.0	3	0.73	6	0.94	5	0.87
5	1/17/13 – 3/18/13	5	0.90	3	0.77	5	0.90	5	0.90
6	1/24/13 – 3/25/13	8	0.98	3	0.83	6	0.92	5	0.87
7	1/31/13 – 4/1/13	8	0.96	3	0.79	6	0.88	6	0.88
8	2/7/13 – 4/8/13	7	0.94	5	0.69	7	0.94	7	0.94
9	2/14/13 – 4/15/13	<i>20</i>	1.0	6	0.75	4	0.38	0	-
10	2/21/13 – 4/22/13	<i>18</i>	1.0	6	0.72	6	0.72	3	0.40
11	2/28/13 – 4/29/13	7	0.85	4	0.66	4	0.66	1	0.35
12	3/7/13 – 5/6/13	6	0.78	4	0.70	4	0.70	3	0.50
13	3/14/13 – 5/13/13	<i>17</i>	1.0	3	0.67	4	0.77	1	0.56
14	3/21/13 – 5/20/13	5	0.79	2	0.66	4	0.79	1	0.55

Robustness of concentration prediction outside of calibration windows

The first approach to assess the robustness of the PLSR model to predict concentrations, particularly those outside of the calibration windows (the ones inside each window are well predicted as acceptable NSE show) was to plot all of the residuals of the models expressed as a percentage difference with all observed data (within and outside the calibration window). We were able to show that the number of components chosen for the models did not affect the trend observed (Appendix A), and we chose the $ncomp_{rmsep}$ for the number of components. Results show that a majority of concentrations were over-predicted using Windows 1-7 calibrations and a majority of concentrations were under-predicted in using calibrations from Windows 8 to 13 (Figure 2.7).

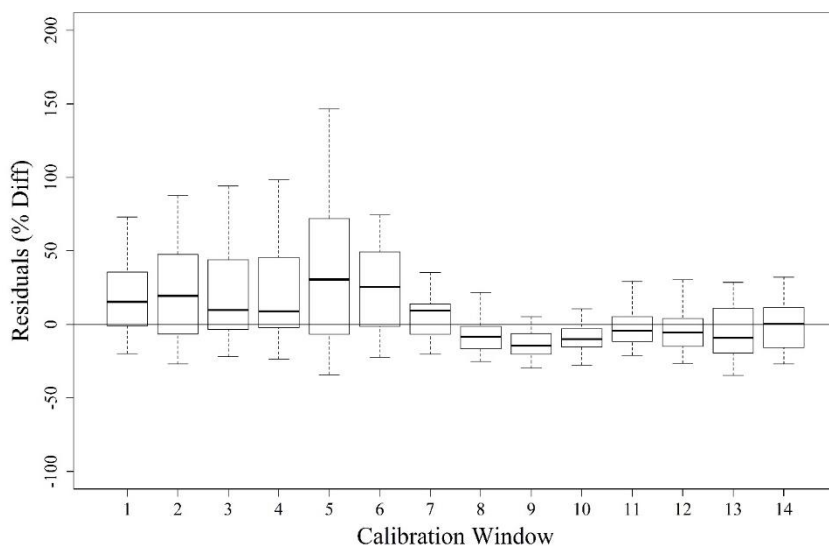


Figure 2.7. Residuals plotted as a percent difference from observed concentrations for the model selected for each calibration window built with the number of components producing the absolute minimum RMSEP. Top and bottom box notches represent the 25th and 75th quartile, the middle black line represents the median, and whisker notches represent the minimum and maximum values in the data range.

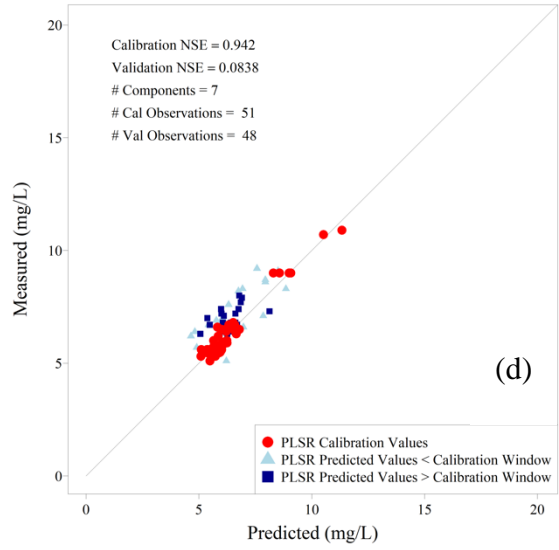
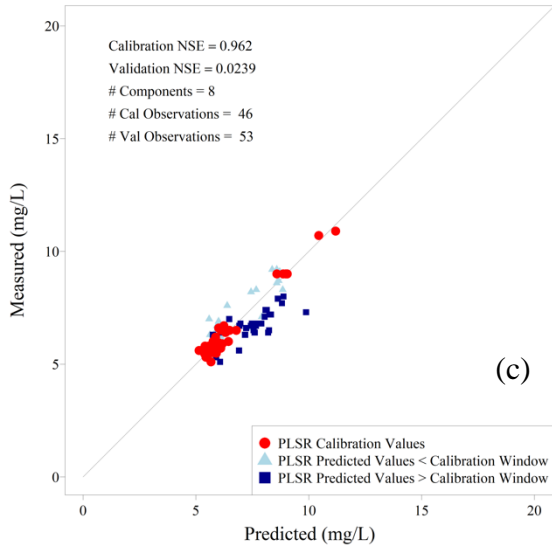
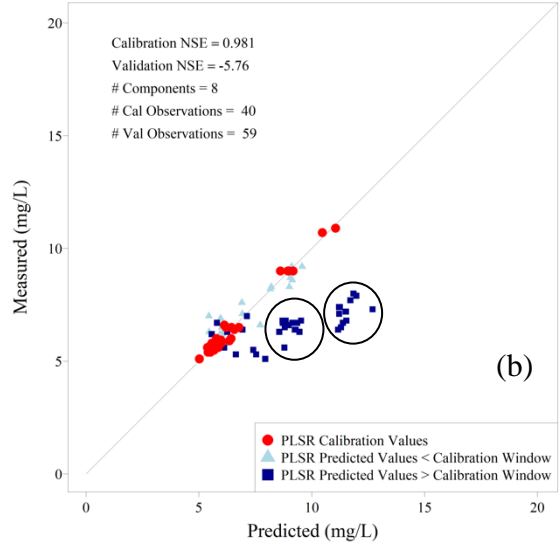
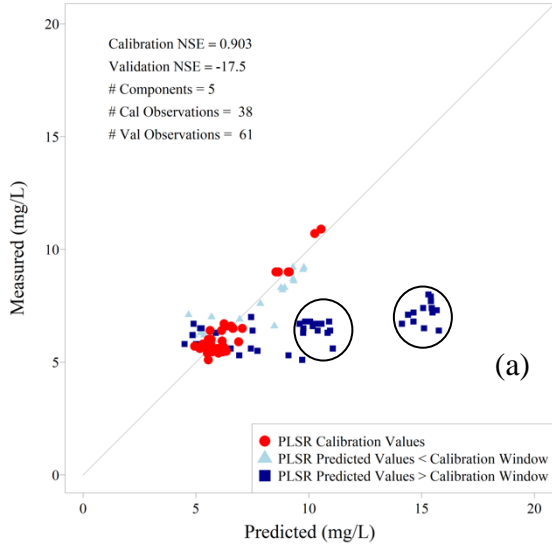
The results of the overestimations and underestimations observed in Figure 2.7 yielded NSE values that were much lower when considering prediction concentrations of the validation data for models incorporating the $ncomp_{rmsep}$ number of components. NSE values ranged from approximately -17.5 – 0.6 with Window 11 calibration predicting validation concentrations with the greatest NSE value and Window 5 the lowest. Using a subset of concentration data to extrapolate outside the calibration windows did not produce satisfactory results as a rule, and therefore is not recommended. There might be mathematical reasons as the concentrations predicted may be out of the calibration data, and/or this might be due to a drastic change in the relationship between the color matrix of the water and the concentration values.

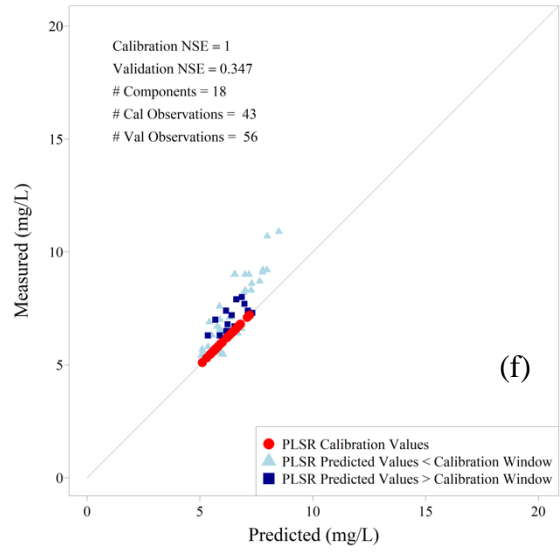
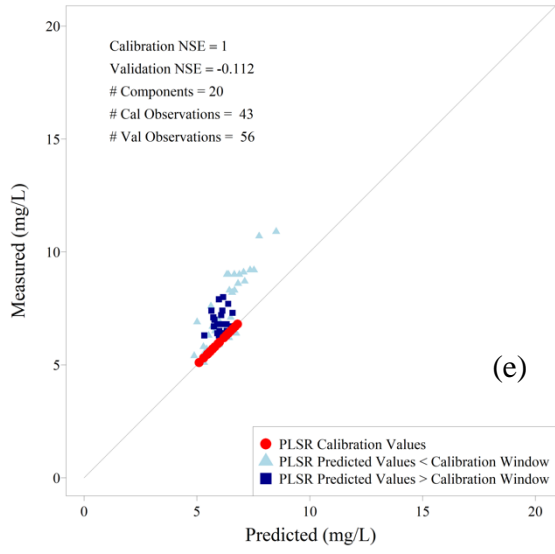
Possible changes in the relationship between the color matrix and concentrations

Figure 2.8 illustrates the relationships between predicted vs. observed concentrations and highlights whether the predicted points correspond to within, before, and after the calibration windows. Not surprisingly, the points within the calibration window match well with the observed data (red dots). Although only 6 of the 14 possible relationships are plotted in Figure 2.8, an interesting trend appeared. The majority of sample concentrations falling after the calibration window were over-predicted in the first 6 moving windows (dark blue squares in Windows 5 and 6 in Figure 2.8). Two ‘clusters’ of points appear in Windows 5 & 6 with large overestimations (circled in Figure 2.8). Both sets of values fell towards the end of the two weeks right before cleaning of the optics took place, possibly corresponding to very significant fouling. Calibration windows 1 to 6 all have the largest concentration ranges (Figure 2.6), so the over prediction cannot be associated with extrapolation outside the calibration range values. The overpredictions of sample concentrations falling after the calibration window may be associated

with differing degrees of fouling on the spectrophotometer lenses and/or with varying color-concentration relationship. The analyses herein may help further conclude.

Figure 2.8. Measured vs. predicted concentrations for calibration Windows (a) 5, (b) 6, (c) 7, (d) 8, (e) 9, and (f) 10 showing the progression in general over-prediction to under-prediction of concentrations. Triangles represent all samples that preceded the calibration window and squares represent all samples that fell after the calibration window. Circles indicate “clusters” of over-predicted samples.





The transition from Window 6 to 7 displayed a shift from over-prediction of a majority of the concentrations to more of a balance between over- and under-prediction of concentrations as well as more consistent magnitudes of under- and over-prediction when compared with Windows 5 and 6 (Figure 2.8). The majority of discrete samples falling after the Window 7 date range were over-predicted and the majority of concentrations falling after the Window 8 date range were under-predicted indicating a potential transitional point. An under-prediction trend in validation concentrations falling before and after the calibration window could be observed most drastically in the change from Window 8 to 9 and this trend continued until Window 13. Since over- and under-prediction trends were not as obvious for Windows 7 and 8, these calibrations seemed to capture enough data on either side of a pivotal point such that over-/under- prediction trends were not as distinct. The number of components did not affect these shifts between over- to underestimations described above as when the number of components chosen were lowered using $ncomp_{nse65}$ as the criterion for selection (Appendix A), the observations held.

Several hypotheses were brought forth. The trends observed could be due to either H1) a temporal shift in the water color matrix/concentration relationship caused by a quickly onset change in controlling biogeochemical/hydrological transport processes after this relatively large event occurred, H2) that the concentration range and distribution provided for model calibration may have affected observed prediction trends, or that H3) over- and under-prediction could have been affected by where they fell within the two weeks between servicing and the degree of fouling of the spectrometer optics.

The second hypothesis is supported by several observations. First, the sudden underestimation of concentrations from Windows 9 and up (Figure 2.8), for which the range of concentrations was reduced to concentrations ranging only from approximately 5-7 mg/L, may suggest that the PLSR models did not do a good job of extrapolating concentrations beyond the calibration concentration range values. This is not unheard of for regressions. Second, the majority of low-mid range concentrations were over-predicted using calibrations obtained for Windows 5 and 6, and this may be viewed as a consequence of the few mid-range concentrations included in the calibration datasets, skewing the overall predictions to biased over-predictions.

The third hypothesis is supported by the appearance of clusters of over-predicted concentrations (Figure 2.8 (a) & (b)) corresponding to measurements that occurred towards the end of the two weeks right before cleaning of the optics took place, presumably when the fouling was maximal. If this hypothesis were true, then these clusters of points would have been visible for all calibration windows. However, these clusters do not clearly appear for calibration windows 7 and 8, for which these samples were not part of the calibration datasets. Although there is no doubt that fouling was incorporated in the PLSR models, Hypothesis 3 is the one that is the most difficult to verify.

The first hypothesis is first supported by the shifts observed between over- and underpredictions, and second by the fact that for Windows 7 and 8 for which there were no obvious prediction biases. There were a relatively similar number of samples before and after the February event in the calibration datasets, giving a chance for those PLSR models to represent the starkly different absorbance signatures before and after the February event. A third supporting factor is that

during the February pivotal event, the water table reached the top 30 cm more organic soil horizon, which gave a chance for the biogeochemical processes in the soil to be stimulated by wetting and drying cycles, which could have changed the nature of DOC exported (e.g., Beare et al., 2009; Boroken and Matzner, 2009; Miller et al., 2005; Palmer et al., 2016; Xiang et al., 2008).

While the third hypothesis is unsupported, there are no obvious reasons to discard the first and second hypotheses. In fact, if flooding of the organic horizon during the February event changed the color matrix to concentration relationship, it was also accompanied with the highest DOC concentrations, making the switch in the concentration range of the calibration dataset and the change in the color matrix, confounding factors. This observation would likely apply to all watersheds. An additional analysis using 30-d moving calibration windows confirmed the pivotal role of the February event observations made using the 60d moving calibration windows (Appendix B), although the number of components influenced more the over- and underpredictions observed, probably due to a lower number of samples available for calibration.

To summarize, calibration concentration range and sample concentration distribution, seasonal variability of the color matrix of the water, and the degree of fouling all potentially affected, and possibly to a variable but unknown degree, the ability of PLSR to accurately predict DOC concentrations. To further test these hypotheses, we sought to identify whether splitting the data into periods ‘stable periods’ around the ‘hinge’ February event period occurring from Window 8 to Window 9 would generate more robust PLSR models within and outside the calibration windows.

2.4.3 Local Calibration to Stable Periods

The data was separated in two ways surrounding the February event, which included four total periods to be modeled. The data leading up to the event was referred to as Period A (December 20, 2012 – February 7, 2013), a 7-day period including the peak of the event where a shift in the 60-day and 30-day moving window analysis showed a change in prediction trends was referred to as Period B (February 7, 2013 – February 14, 2013), and data following the event window was referred to as Period C (February 14, 2013 – May 20, 2013).

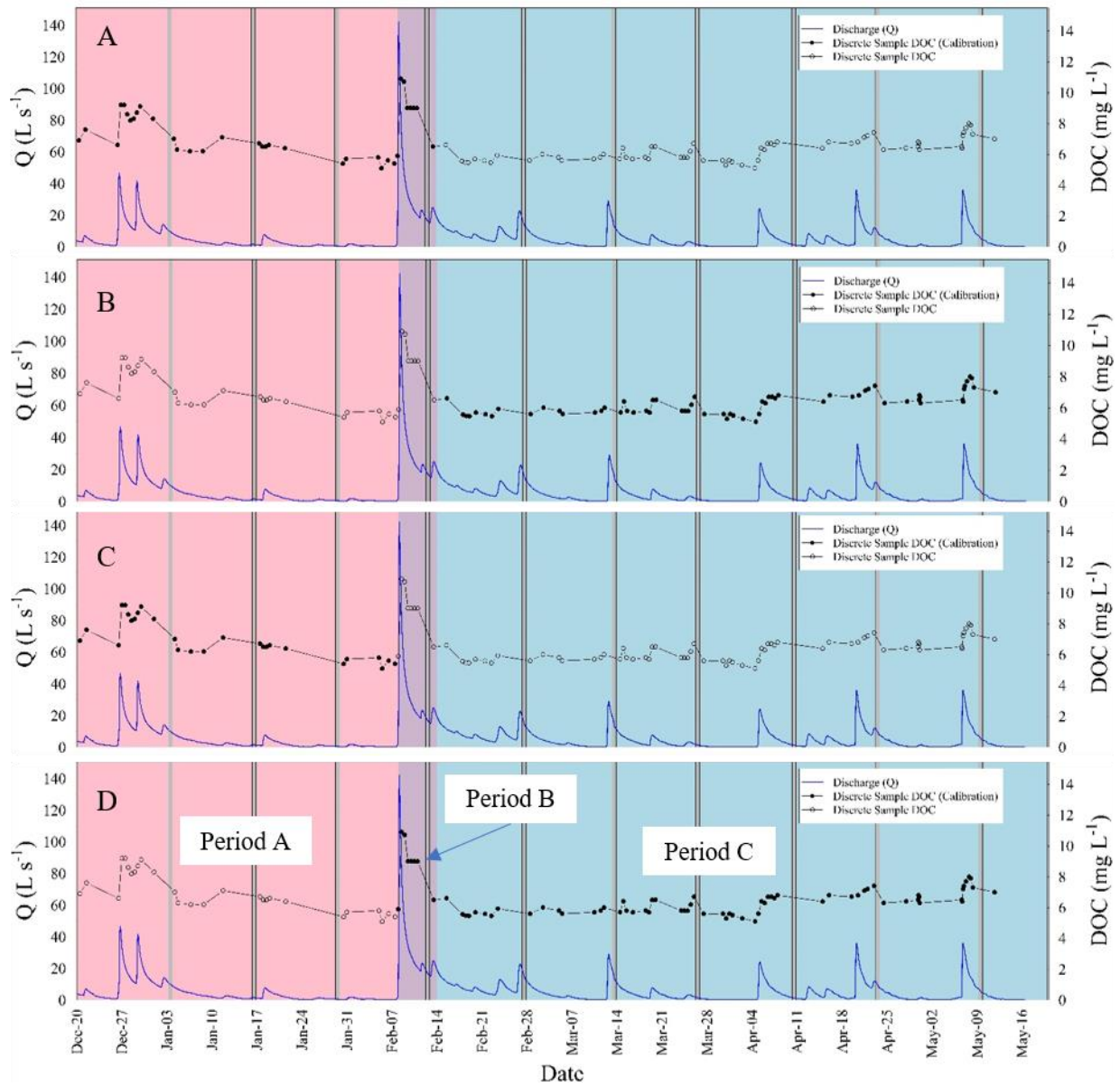


Figure 2.9. Three periods of time in which the data was split for calibration of periods indicative of a similar water color-concentration relationship based on 60-day and 30-day moving window analyses. Period A ranges from December 20, 2012 – February 7, 2013. Period B ranges from February 7, 2013 – February 14, 2013 and signifies the 7-day shift between 60-day and 30-day calibration Windows 8 & 9. Period C ranges from February 14, 2013 – May 20, 2013. Filled circles indicate DOC measured samples that were included in the dataset used to calibrate a pls model and hollow circles indicate samples remaining that were evaluated for prediction trends. The calibrations are shown as follow: (A) Calibration AB (B) Calibration C (C) Calibration A (D) Calibration BC.

The first method of modeling the data involved calibrating a model to samples occurring in both Periods A & B and calibrating a model to samples in Period C and then using each to predict remaining samples (Figure 2.9). These calibrations are referred to as Calibration AB and Calibration C. The second method calibrated a model to samples falling in Period A and calibrated a model to samples falling in both Periods B & C and the models were validated on samples in the remainder of the entire dataset (Figure 2.9). These calibrations are referred to as Calibration A and Calibration BC.

Results for each calibration period are shown in Table 2.3. Figure 2.10 illustrates the goodness of fit for calibration (red dots) and validation values (outside of calibration window; blue dots) for the AB, C, A and BC calibrations using on the left column $ncomp = ncomp_{nse65}$, and on the right column $ncomp = ncomp_{rmsep}$. Calibrations AB and A demonstrated a majority of samples following the calibration window being over-predicted, which aligned with the trends seen in the 60-day and 30-day moving window analyses. Calibration A, however, under-predicted the highest concentrations during the February event, which could be in part due to a reduction in the calibration concentration range when compared with Calibration AB. The cluster of samples associated with smaller events that occurred towards the end of two service intervals in April and May that were observed in the moving window analyses were still present when predicted using models created from Calibrations AB & A. The cluster of over-predicted samples was present for both models including the $ncomp_{rmsep}$ and $ncomp_{nse65}$ number of components for Calibration A. With (Calibration AB) or without (Calibration A) the maximum DOC concentrations of the February event, a majority of samples were over-predicted for the validation periods. This seems to lower the importance of the higher concentrations in the calibration range towards estimation,

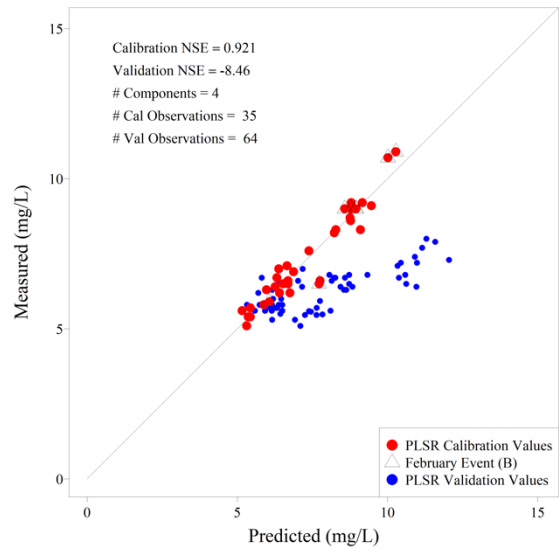
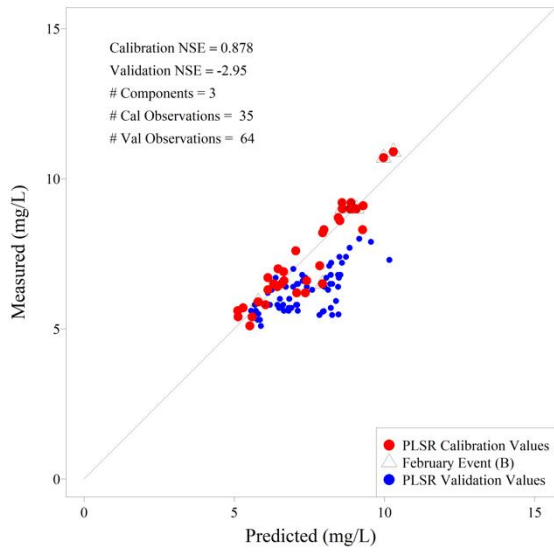
and rather give more weight to the hypothesis of a shift in water color-concentration relationship before and after the February event.

Table 2.3. Stable period calibration cross-validation results for 1-20 component models (per each calibration) with number of components selected based on 4 selection methods: 1) Minimum root mean square error of prediction (RMSEP) 2) minimum number of components necessary to produce an “acceptable” Nash Sutcliffe Efficiency ($NSE \geq 0.65$) 3) automatic selection using the “one-sigma” method found in the R *pls* package 4) automatic selection using the “permutation” method found in the R *pls* package. The three columns of results under each selection method category are the number of components selected, NSE and mean noise (%) values.

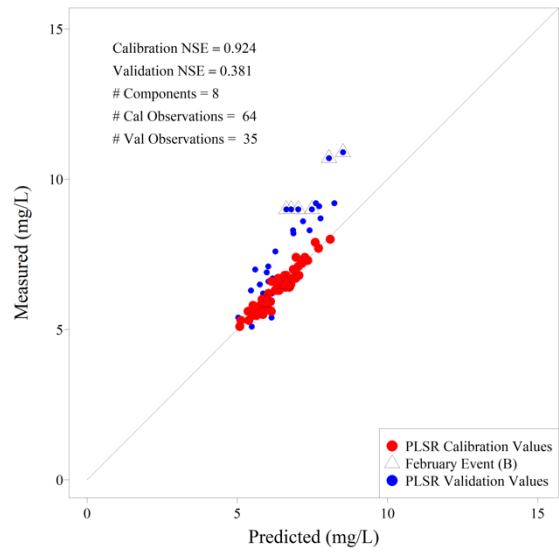
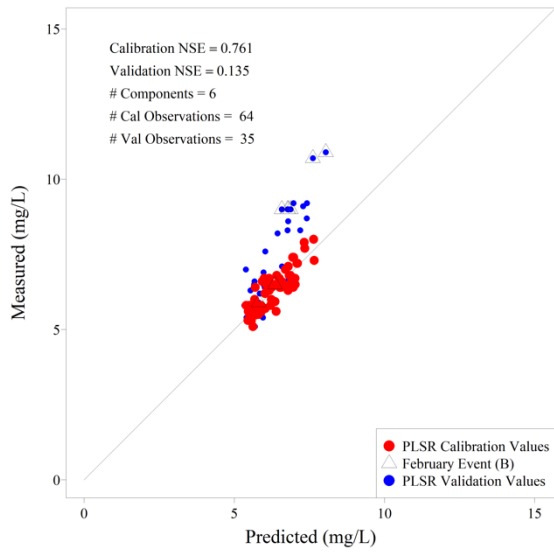
Calibration	Date Range (M/D/Y)	Minimum RMSEP			NSE ≥ 0.65			One-Sigma			Permutation		
AB	12/20/12 – 2/14/13	4	0.92	0.87	3	0.88	0.56	4	0.92	0.87	3	0.88	0.56
C	2/14/13 – 5/20/13	8	0.92	3.96	6	0.76	2.20	8	0.92	3.96	8	0.92	3.96
A	12/20/12 – 2/7/13	4	0.90	1.15	3	0.82	1.32	4	0.90	1.15	3	0.82	1.32
BC	2/7/13 – 5/20/13	19	1.0	6.63	6	0.81	2.47	7	0.89	3.81	7	0.89	3.81

Figure 2.10. Side by side comparison of measured DOC concentrations as a function of predicted DOC concentrations produced from a model with $ncomp_{nse65}$ number of components (left) and $ncomp_{rmsep}$ number of components (right) for stable period (a) Calibration AB (b) Calibration C (c) Calibration A (d) Calibration BC.

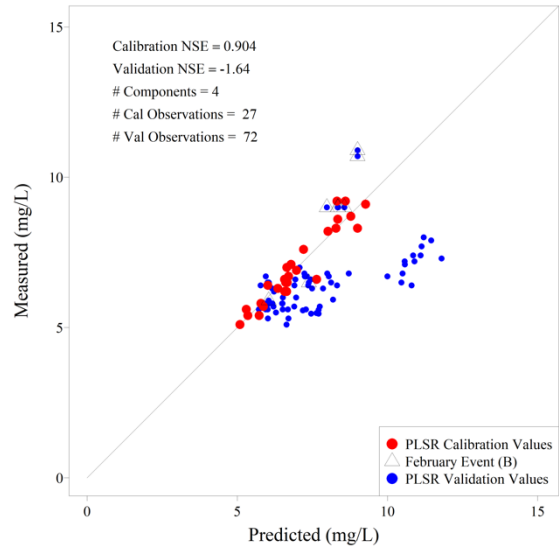
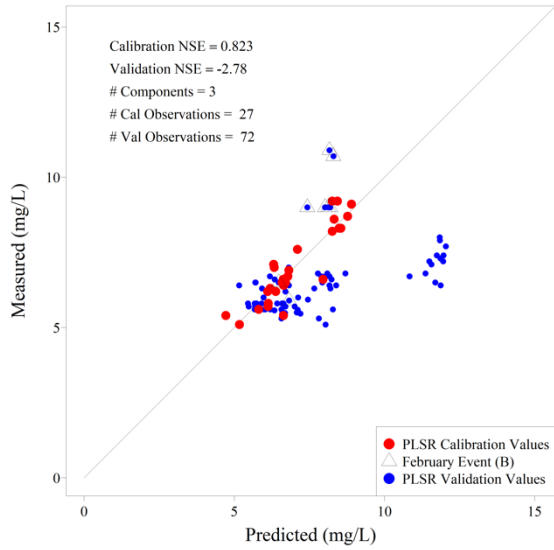
(a) Calibration AB



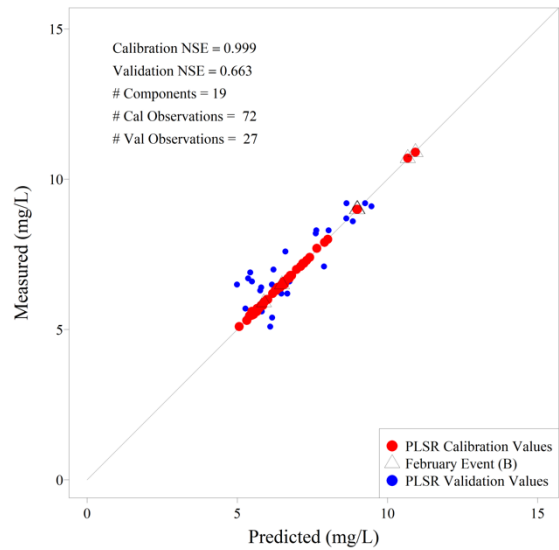
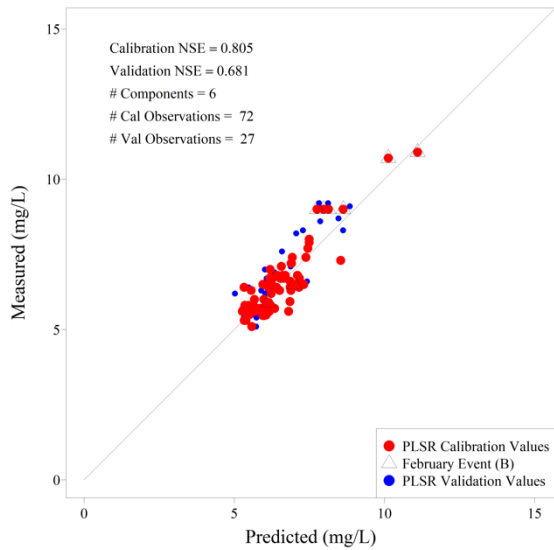
(b) Calibration C



(c) Calibration A



(d) Calibration BC



A majority of samples were under-predicted using Calibration C when the February event was not included, and the magnitude of under-prediction seemed to increase with increasing measured DOC concentration. Calibration BC, which had the February event samples included, did not demonstrate such a clear under-prediction trend nor the increase in the magnitude of under-prediction with increasing measured concentration. This could have been due to a fuller concentration range available because the February event was included. It could also suggest, and this is a more likely hypothesis, that the two high February event samples of period B had a color matrix signature close to that of the preceding period, and that the PLSR model was able to characterize decently well the color matrix signature of the periods before and after the February event. This latter hypothesis is strengthened by the fact that the calibration AB did not predict well (overestimation) concentrations for period C, suggesting that there was, conversely, no color matrix signature in the period AB able to predict that prevalent in period C.

These hypotheses are further reinforced as the PLSR model for calibrating the BC period did require the largest number of components to reach the absolute RMSEP, indicating there was possibly a wider range of types of relationships to model (February event and post- event samples). Comparatively Calibrations AB and A required only 3-4 components according to all evaluation criteria methods and the inclusion of the February event did not seem to affect number of components needed, hence the suggestion that the color matrix signature of the February event samples were similar to that of the period A.

The amounts of noise associated with Calibrations A and AB were less than 1% whereas average noise was at least 2% or more depending on the number of components selected for Calibrations

B and BC. These were not really an improvement in the reduction of noise compared to the total range calibration including the entire available sample set, but a lower number of components could be selected to model the data included in Calibrations A and AB as a separate entity, reducing noise below any total range models selected by the 4 evaluation criteria methods. Calibrations involving the latter part of the dataset required more components indicating that perhaps this data could be split further. We found that in the end, cumulative totals of DOC differed by less than 2% between the sums of the stable period predictions and the total range predictions for the models with the $ncomp_{rmsep}$ and $ncomp_{nse65}$ numbers of components (Table 2.4).

Table 2.4. Cumulative DOC loads calculated from predicted time series using models with $ncomp_{rmsep}$ and $ncomp_{nse65}$ numbers of components for both stable period calibrations and the full range calibration.

Component Selection Method	Cumulative DOC Load (kg ha⁻¹)		
	AB + C	A+BC	Full Range
<i>ncomp_{rmsep}</i>	22.74	22.83	22.41
<i>ncomp_{nse65}</i>	22.71	22.32	22.28

This stable period analysis thus reinforces the likely occurrence of a change in the color matrix signature following the rise of the water table to the ground surface in February. This is a major finding as it implies that DOC concentrations predicted using UV-vis spectrometers rely on a relative stability of the color matrix to concentration relationship. This also suggests that local calibrations using PLSR must therefore either create different calibrations corresponding to periods where the color matrix signature is thought to be constant, and/or create PLSR models

that can incorporate the changes in the color matrix, at the cost of a higher number of components and possibly more noise in the concentration time series produced.

2.5 Discussion and conclusions

There has been increasing awareness that DOC concentrations in watershed streamwater is highly variable with time (Rode et al., 2016; Vaughan et al., 2019; Ruhala & Zarnetske, 2017). DOC loads from watersheds, particularly coastal watersheds, provide key information linking DOM transport to coastal waters influencing estuarine food webs and nutrient availability (Harrison et al., 2005). UV-vis *in situ* spectrometers open a great opportunity to better quantify the DOC loads in small watersheds where the reactivity of the concentrations is expected to be high and follow the sometimes flashy hydrological behavior of these watersheds.

Chromophoric dissolved organic matter (CDOM) is the portion of dissolved organic matter that reacts with light by absorbance. UV-vis spectrometers take advantage of this property to establish a relationship between the CDOM absorbance and the concentration of all DOC, i.e., the light reactive and unreactive part of DOC. However, DOC encompasses hundreds of different molecules which composition is expected to change over time depending on the soil leaching processes at play and how these processes may vary temporally and spatially in watersheds, particularly following rain driven flow events (Hood et al., 2006; Jaffe et al., 2008; Boyer et al., 1997; Fellman et al., 2009). The proportion of light reactive/unreactive organic molecules and the makeshift of the light reactive portion may thus vary with time.

Measuring DOC concentrations in stream water using UV-vis spectrophotometers involves the ability to obtain a robust enough method that can account for the changing nature of DOC over time. Additionally, fouling of the optics on these instruments is highly problematic, particularly in coastal watersheds where the redox conditions are often reduced, leaving significant concentrations of reduced iron and manganese in the water to precipitate on the optics. In many cases, the concentrations calculated by the algorithms on board the instrument are unable to correct for fouling, rendering these instruments seemingly unusable.

This manuscript thus intended to derive the conditions for which chemometrics techniques could be used to correct for fouling and obtain best results in a coastal forested watershed. Admittedly, the 5+ months of data did not allow us to explore all difficulties that researchers might encounter to obtain reliable DOC data under these conditions. This manuscript explored the conditions for use of the Partial Least Squares Regression, a technique widely used to calculate concentrations from UV-vis spectrometers. This effort started with initial difficulties in predicting DOC concentrations in the studied coastal watershed using the PLSR method, particularly because of the extreme fouling observed on the optics, despite all the efforts to minimize it. In the end, we took advantage of the initial difficulties to derive additional rules that had not been published until then.

The initial difficulties caused by extreme fouling of the optics were made evident when attempting to locally calibrate all available spectral fingerprint data to discrete sample lab measured DOC concentrations using PLSR. Selecting the number of components to build the PLSR model was expected to be a somewhat subjective process, but objectively we attempted to

model the data using the number of components based upon previously suggested methods (i.e., number of components relating to minimum RMSEP). From these preliminary results, we quickly learned there was a trade-off between improvement in prediction of sample concentrations and increased time-series noise/over-fitting of the data relating to the number of components selected. This finding led us to investigate if the noise observed could be reduced by splitting the data into smaller, more localized calibrations. A sliding 60-day window approach was tested to build locally calibrated models chronologically through the time-series. If prediction patterns were present in data falling outside of the windows, this implied that the model using the full time range could be attempting to account for periods in which the relationship between spectral data and concentrations were different, thus producing noise.

The moving window calibration unveiled two distinct patterns in predictions around a hinge-point aligned with a relatively large storm event in February. This suggested that a change in the absorption spectra-concentration relationship was associated with this particular storm and was indicative of an increasing water table reaching DOM pools in shallower soil layers. The hinge-point event prompted us to split the data into two local calibrations representative of the theoretically 'stable' periods exhibiting similar moving window prediction patterns to determine if model goodness-of-fit could be improved and noise in the predicted time series reduced.

Breaking the data into separate calibrations in this manner allowed for a reduction in the number of components used, particularly for the period of time falling before and surrounding the February event. The reduction in number of components allowed for acceptable model NSE and a reduction in noise. In the moving window and stable period calibration analyses, we found that

sometimes the addition of one component to the model could isolate certain groups of samples and predict these values more poorly than others. This observation made evident the importance of the component selection process and that additional components may emphasize optical properties in some isolated groups of samples, particularly those falling toward the end of the period between optics cleanings.

This study was only performed on a 5-month period in a location where fouling of the optics was considered extreme. A PLSR model using all data available could be produced and depending upon the number of components, could be considered acceptable according to the NSE criterion. Improvement in NSE came at the price of an increase in time series noise and predicted concentrations of discrete samples possibly falling on troughs and peaks of the noisy predicted time series. This was most likely due to a change in water color-concentration relationship that occurred when the water table reached the top 30 cm of the soil during a February event, but some variation could have been the model trying to compensate for a range in the degree of fouling on the optics, or a combination of both of these. Overall, the shape of the predicted time series using the full time range followed discrete sample chemographs and the drift due to fouling was mostly corrected for. If the data is modeled in this way, this may call for post-processing of the predicted time series where the noise is smoothed by a moving average.

In the end, we believe that the results from this study contribute a number of findings to the growing body of work that involves the development of methods to process/handle high-resolution datasets measured by in-situ optical sensors. The first is that a dataset that appears unusable due to extreme fouling of the optics can still be calibrated using PLSR to produce

usable predicted time-series data where fouling is somewhat/mostly compensated for. However, we do recognize that in the attempt to compensate for variation in the degree of fouling, adding components to a calibration model may appear to increase prediction accuracy, while truly overfitting the data and placing too much emphasis on correcting parts of the time series that are particularly fouled. Second, this leads to the confirmation that there may be a trade-off in model prediction accuracy and noise when determining the appropriate number of components used to build the PLSR calibration due to extreme fouling and steady changes in the water color matrix. We suspect more local calibrations determined by the moving window calibration technique will improve model performance while reducing noise due to better capturing the changing nature of the water color matrix and by reducing the number of components necessary to produce an acceptable model. Although our data suggest marginal improvements in prediction accuracy when using two “stable” period calibrations over one full time range calibration, we were able to reduce the number of components necessary for an acceptable prediction resulting in reduced predicted noise in one of the stable period calibrations.

Finally, one model calibration performed on even a short range of data, such as the 5-month period in this study, may not perform optimally when all data is included because of an evolving relationship between CDOM and DOC concentration. This finding shows that the calibration methods explored in this study provide an additional bonus to modeling reliable high-resolution time-series data, as detecting these types of temporal variation is expected to contribute to understanding drivers of stream DOC concentrations in the future. This method should be tested among a wide variety of environments and on larger datasets and time scales as it releases the constraint of yearly and seasonal scales and rather detects the window of change as it occurs.

This could potentially be useful particularly in detecting effects of a land use change for example. This calibration technique could potentially improve otherwise unusable data in other environments conducive to extreme optics fouling, but longer periods of data and a variety of concentration ranges are needed to test this hypothesis.

2.6 Acknowledgements

Logistical and financial support for this work was provided by Weyerhaeuser NR Company and Catchlight Energy, LLC, a Chevron and Weyerhaeuser Joint Venture. Additional research funds were provided by the U.S. DOE (Award No. DE-EE0004395: Optimization of southeastern forest biomass crop production: A watershed-scale evaluation of the sustainability and productivity of dedicated energy crop and woody biomass operations).

2.7 References

- Addy, K., Gold, A. J., Loffredo, J. A., Schroth, A. W., Inamdar, S. P., Bowden, W. B., . . . Birgand, F. (2018). Stream response to an extreme drought-induced defoliation event. *Biogeochemistry*, *140*(2), 199-215.
- Beare, M. H., Gregorich, E. G., & St-Georges, P. (2009). Compaction effects on CO₂ and N₂O production during drying and rewetting of soil. *Soil Biology and Biochemistry*, *41*(3), 611-621.
- Blaen, P. J., Khamis, K., Lloyd, C., Comer-Warner, S., Ciocca, F., Thomas, R. M., . . . Krause, S. (2017). High-frequency monitoring of catchment nutrient exports reveals highly variable storm event responses and dynamic source zone activation. *Journal of Geophysical Research: Biogeosciences*, *122*(9), 2265-2281. doi:<https://doi.org/10.1002/2017JG003904>
- Borken, W., & Matzner, E. (2009). Reappraisal of drying and wetting effects on C and N mineralization and fluxes in soils. *Global change biology*, *15*(4), 808-824.
- Boyer, E. W., Hornberger, G. M., Bencala, K. E., & McKnight, D. M. (1997). Response characteristics of DOC flushing in an alpine catchment. *Hydrological Processes*, *11*(12), 1635-1647.
- Burns, D. A., Pellerin, B. A., Miller, M. P., Capel, P. D., Tesoriero, A. J., & Duncan, J. M. (2019). Monitoring the riverine pulse: Applying high-frequency nitrate data to advance integrative understanding of biogeochemical and hydrological processes. *Wiley Interdisciplinary Reviews: Water*, *6*(4), e1348.
- Etheridge, J. R., Birgand, F., Burchell, M. R.,II, & Smith, B. T. (2013). Addressing the fouling of in situ ultraviolet-visual spectrometers used to continuously monitor water quality in brackish tidal marsh waters. *Journal of Environmental Quality*, *42*(6), 1896-1901. doi:10.2134/jeq2013.02.0049
- Etheridge, J. R., Birgand, F., Osborne, J. A., Osburn, C. L., Burchell, M. R.,II, & Irving, J. (2014). Using in situ ultraviolet-visual spectroscopy to measure nitrogen, carbon, phosphorus, and suspended solids concentrations at a high frequency in a brackish tidal marsh. *Limnology and Oceanography-Methods*, *12*, 10-22. doi:10.4319/lom.2014.12.10
- Fellman, J. B., Hood, E., Edwards, R. T., & D'Amore, D. V. (2009). Changes in the concentration, biodegradability, and fluorescent properties of dissolved organic matter during stormflows in coastal temperate watersheds. *Journal of Geophysical Research: Biogeosciences*, *114* doi:<https://doi.org/10.1029/2008JG000790>
- Fichot, C. G., & Benner, R. (2011). A novel method to estimate DOC concentrations from CDOM absorption coefficients in coastal waters. *Geophysical Research Letters*, *38*(3)

- Harrison, J. A., Caraco, N., & Seitzinger, S. P. (2005). Global patterns and sources of dissolved organic matter export to the coastal zone: Results from a spatially explicit, global model. *Global Biogeochemical Cycles*, 19(4) doi:<https://doi.org/10.1029/2005GB002480>
- Heathwaite, A. L., & Bierozza, M. (2021). Fingerprinting hydrological and biogeochemical drivers of freshwater quality. *Hydrological Processes*, 35(1), e13973. doi:<https://doi.org/10.1002/hyp.13973>
- Hood, E., Gooseff, M. N., & Johnson, S. L. (2006). Changes in the character of stream water dissolved organic carbon during flushing in three small watersheds, Oregon. *Journal of Geophysical Research: Biogeosciences*, 111(G1)
- Jaffé, R., McKnight, D., Maie, N., Cory, R., McDowell, W. H., & Campbell, J. L. (2008). Spatial and temporal variations in DOM composition in ecosystems: The importance of long-term monitoring of optical properties. *Journal of Geophysical Research: Biogeosciences*, 113(G4)
- Kaiser, K., & Kalbitz, K. (2012). Cycling downwards – dissolved organic matter in soils. *Soil Biology and Biochemistry*, 52, 29-32. doi:<https://doi.org/10.1016/j.soilbio.2012.04.002>
- Kincaid, D. W., Seybold, E. C., Adair, E. C., Bowden, W. B., Perdrial, J. N., Vaughan, M. C., & Schroth, A. W. (2020). Land use and season influence Event-Scale nitrate and soluble reactive phosphorus exports and export stoichiometry from headwater catchments. *Water Resources Research*, 56(10), e2020WR027361.
- Lepot, M., Torres, A., Hofer, T., Caradot, N., Gruber, G., Aubin, J., & Bertrand-Krajewski, J. (2016). Calibration of UV/vis spectrophotometers: A review and comparison of different methods to estimate TSS and total and dissolved COD concentrations in sewers, WWTPs and rivers. *Water Research*, 101, 519-534. doi:<https://doi.org/10.1016/j.watres.2016.05.070>
- Lloyd, C., Freer, J. E., Johnes, P. J., & Collins, A. L. (2016). Using hysteresis analysis of high-resolution water quality monitoring data, including uncertainty, to infer controls on nutrient and sediment transfer in catchments. *Science of the Total Environment*, 543, 388-404.
- Messer, T. L., Birgand, F., & Burchell, M. R. (2019). Diel fluctuations of high level nitrate and dissolved organic carbon concentrations in constructed wetland mesocosms. *Ecological Engineering*, 133, 76-87. doi:[10.1016/j.ecoleng.2019.04.027](https://doi.org/10.1016/j.ecoleng.2019.04.027)
- Mevik, B., Wehrens, R., & Liland, K. H. (2011). Pls: Partial least squares and principal component regression. *R Package Version*, 2(3)
- Miller, A. E., Schimel, J. P., Meixner, T., Sickman, J. O., & Melack, J. M. (2005). Episodic rewetting enhances carbon and nitrogen release from chaparral soils. *Soil Biology and Biochemistry*, 37(12), 2195-2204.

- Palmer, K., Köpp, J., Gebauer, G., & Horn, M. A. (2016). Drying-rewetting and flooding impact denitrifier activity rather than community structure in a moderately acidic fen. *Frontiers in microbiology*, 7, 727.
- Pellerin, B. A., Saraceno, J. F., Shanley, J. B., Sebestyen, S. D., Aiken, G. R., Wollheim, W. M., & Bergamaschi, B. A. (2012). Taking the pulse of snowmelt: In situ sensors reveal seasonal, event and diurnal patterns of nitrate and dissolved organic matter variability in an upland forest stream. *Biogeochemistry*, 108(1), 183-198.
- Ritter, A., & Munoz-Carpena, R. (2013). Performance evaluation of hydrological models: Statistical significance for reducing subjectivity in goodness-of-fit assessments. *Journal of Hydrology*, 480, 33-45.
- Rode, M., Wade, A. J., Cohen, M. J., Hensley, R. T., Bowes, M. J., Kirchner, J. W., . . . Jomaa, S. (2016). Sensors in the Stream: The High-Frequency Wave of the Present. *Environmental Science & Technology*, 50(19), 10297-10307. doi: 10.1021/acs.est.6b02155
- Ruhala, S. S., & Zarnetske, J. P. (2017). Using in-situ optical sensors to study dissolved organic carbon dynamics of streams and watersheds: A review. *Science of the Total Environment*, 575, 713-723.
- Saraceno, J. F., Pellerin, B. A., Downing, B. D., Boss, E., Bachand, P. A., & Bergamaschi, B. A. (2009). High-frequency in situ optical measurements during a storm event: Assessing relationships between dissolved organic matter, sediment concentrations, and hydrologic processes. *Journal of Geophysical Research: Biogeosciences*, 114(G4)
- Team, R. C. (2013). R: A language and environment for statistical computing.
- Vaughan, M. C. H., Bowden, W. B., Shanley, J. B., Vermilyea, A., Sleeper, R., Gold, A. J., . . . Schroth, A. W. (2017). High-frequency dissolved organic carbon and nitrate measurements reveal differences in storm hysteresis and loading in relation to land cover and seasonality. *Water Resources Research*, 53(7), 5345-5363. doi:https://doi.org/10.1002/2017WR020491
- Vaughan, M. C., Bowden, W. B., Shanley, J. B., Vermilyea, A., & Schroth, A. W. (2019). Shining light on the storm: In-stream optics reveal hysteresis of dissolved organic matter character. *Biogeochemistry*, 143(3), 275-291.
- Vaughan, M. C., Bowden, W. B., Shanley, J. B., Vermilyea, A., Wemple, B., & Schroth, A. W. (2018). Using in situ UV-Visible spectrophotometer sensors to quantify riverine phosphorus partitioning and concentration at a high frequency. *Limnology and Oceanography: Methods*, 16(12), 840-855.
- Wolf, C., Gaida, D., Stuhlsatz, A., Ludwig, T., McLoone, S., & Bongards, M. (2013). Predicting organic acid concentration from UV/vis spectrometry measurements – a comparison of machine learning techniques. *Transactions of the Institute of Measurement and Control*, 35(1), 5-15. doi:10.1177/0142331211403797

Xiang, S. R., Doyle, A., Holden, P. A., & Schimel, J. P. (2008). Drying and rewetting effects on C and N mineralization and microbial activity in surface and subsurface California grassland soils. *Soil Biology and Biochemistry*, 40(9), 2281-2289.

Chapter 3: A multi-indicator approach to the characterization of water quality in a mixed land use lower coastal plain watershed

3.1 Abstract

Now that high-resolution water quality data are becoming more and more available at the watershed scale, it becomes important to develop and evaluate indicators to quantify and describe the hydrochemical signatures of watersheds. Within the last decade, the hysteresis indices have been widely adopted as the main indicator to describe the dynamic relationship between concentration and flow, or C-Q dynamics, at the event scale. This one indicator has been used to infer underlying controlling hydrological and biogeochemical processes at play. However, there is no reason why this indicator should be the only one used to extract information from high frequency water quality data. In this study, we re-examine a high temporal resolution, multiparameter water quality dataset obtained in the 1990s to apply a suite of indicators, including the hysteresis indices, to characterize the hydrochemical signature of a small (15 km²) lower coastal plain, mixed land use, artificially drained watershed located in North Carolina. Annual concentration statistics, flux duration curves, hysteresis and flushing indices, and double mass curves were used to analyze carbon, phosphorus, nitrogen, suspended solids, and pH time series data. The most information about export patterns and associated controlling processes were embedded in the double mass curves. The method identified homogeneous phases somewhat linked to seasons. Identified phases provided context for which the C-Q event indicators provided valuable added information, such as evidence for the effects of drainage hydraulics and in-stream denitrification on patterns in nitrate export, otherwise unseen in the double mass curves. We believe it was the combination of indicators, rather than one sole indicator, that strengthened our ability to detect the occurrence of and explanations for nutrient and material export patterns in the watershed.

3.2 Introduction

In the past 50 years, the field of hydrology and water quality has made progress in leaps, particularly in the wake of breakthroughs in monitoring equipment. Water level loggers widely used since the 1970s have revolutionized watershed hydrology, providing the needed high frequency (e.g., hourly or better) information across spatial scales to measure flow and water table depths. This has helped quantify the variability and the pulsed nature of streamflow and allowed many tools and models to be built and tested to better manage water. In the meantime, water quality has been assessed through infrequent, mostly monthly, sampling, i.e., using nearly three orders of magnitude less information. The widespread availability of automatic water samplers did generate a leap in watershed water quality science in the late 1980s, by providing great insight on water quality dynamics, but on short term periods however, and for a limited number of streams and rivers. Not surprisingly, our understanding of and our tools to manage water quality have lagged behind those of quantitative hydrology.

Starting in the late 2000s, *in situ* high frequency water quality sensors have provided the technological breakthroughs needed for water quality by providing data at frequencies on par with those used to calculate flow and measure water table depths, and over long-term periods. Many of these new sensors measure the optical properties (e.g., absorbance and fluorescence) of water, from which concentrations can be derived. Clearly, availability of continuous water quality sensors has dramatically reduced the uncertainty on load calculations associated with infrequent sampling (e.g., Lin, 2017; Birgand et al., 2010). The next research question becomes ‘what can these high frequency data tell us about the hydrochemical and biogeochemical signatures of watersheds?’.

Recently, Heathwaite and Bierozza (2020) introduced their article by stating that “insights regarding the stream hydrochemical regime and the interplay between hydrological and biogeochemical processes are encapsulated in the concentration-discharge (c-q) relationship and can be interrogated for high and low flows with the aid of high-frequency measurements”. Indeed, following the widespread availability of high frequency water quality data (mostly nitrate) over the last 15 years, dozens of articles have focused on characterizing, quantifying, and classifying the C-Q relationships from which they have tried to extract information on the “interplay between hydrological and biogeochemical processes” (reviewed by Burns et al., 2019).

The concentration-discharge relationship studies result from the observation that during hydrological events, hydrographs and chemographs often have recognizable patterns. As hydrographs are most of the time characterized by a rapid rise, a peak, and a slower fall, chemographs also tend to show a rapid rise (or fall), a peak (or trough), and a slower fall (or rise) more or less in synchrony with the hydrograph, although several local concentration peaks and troughs may occur during a single event. Much attention has been paid on the number of concentration peaks (or troughs) and whether they precede, are synced, or lag the flow peak, as it is hypothesized that this provides information on the nutrient sources and fates in watersheds. Indicators to quantify the hysteresis patterns formed during events on $c = f(q)$ plots have been nicely put together (e.g., Llyod et al., 2016), have been the focus of the last decade, and are now widely used (reviewed by Burns et al., 2019).

There is no doubt that the indicators of C-Q hysteresis have provided insights on the hydrochemical signature and on the interplay between hydrological and biogeochemical processes. However, Burns et al. (2019) in their review also note that “hysteresis patterns alone often yield ambiguous interpretations of runoff sources and processes”. In other words, C-Q hysteresis indices cannot be the *alpha* and *omega* of the interpretation of high frequency water quality data. We hypothesize that using a suite of complementary indicators may open a chance to bring a fuller picture and possibly reduce ambiguity noted by Burns et al. (2019). In particular, indicators that integrate and cumulate flow and concentration over time are, by definition, less subject to variability within or among events and may provide a context within which interpretation of the C-Q hysteresis indicators may be improved.

In this article, we propose to revisit a high frequency multiparameter water quality dataset obtained in the 1990s, and derive indicators of C-Q hysteresis, as well as of cumulative flow and loads. The dataset includes high-frequency equivalent concentrations on nitrogen, phosphorus, carbon, pH, and suspended solids in a mixed land use lower coastal plain watershed of North Carolina. We hypothesize that this may provide a fuller picture of the hydrochemical signature and the interplay of the hydrological and biogeochemical processes, as well as help identify the unique contribution that each indicator may provide on the overall picture.

3.3 Methods

3.3.1 Site Description

Flow and water quality data were obtained as part of a larger project that aimed at measuring the hydrology and water quality of a 10,000 ha watershed of the lower coastal plain near Plymouth,

North Carolina. Data for this article come from the station named ‘A1’, draining a subcatchment of this larger watershed. Agriculture accounted for 25% of the subcatchment land use (379 ha) and managed forest accounted for the remaining 75% (1,153 ha). Cape Fear loam covered a dominant portion of the subcatchment, but a sizable area of highly organic Pungo soil was present. The subcatchment was and still is artificially drained by a series of parallel open ditches approximately 1 m deep and spaced 80 – 100 m apart that drain to main collector canals (Figure 3.1). The details of management practices carried out in the A1 subcatchment were not fully disclosed, but it was generally known that the main crops grown in the agricultural plots were corn, wheat and soybean and that wheat was fertilized in February and corn was fertilized in the months of May and June. Details regarding fertilization in the managed forests were limited to fertilization rates being much lower than in agricultural fields (Chescheir et al. 2003). Data monitoring took place for a 14-month period between June 1998 and July 1999.

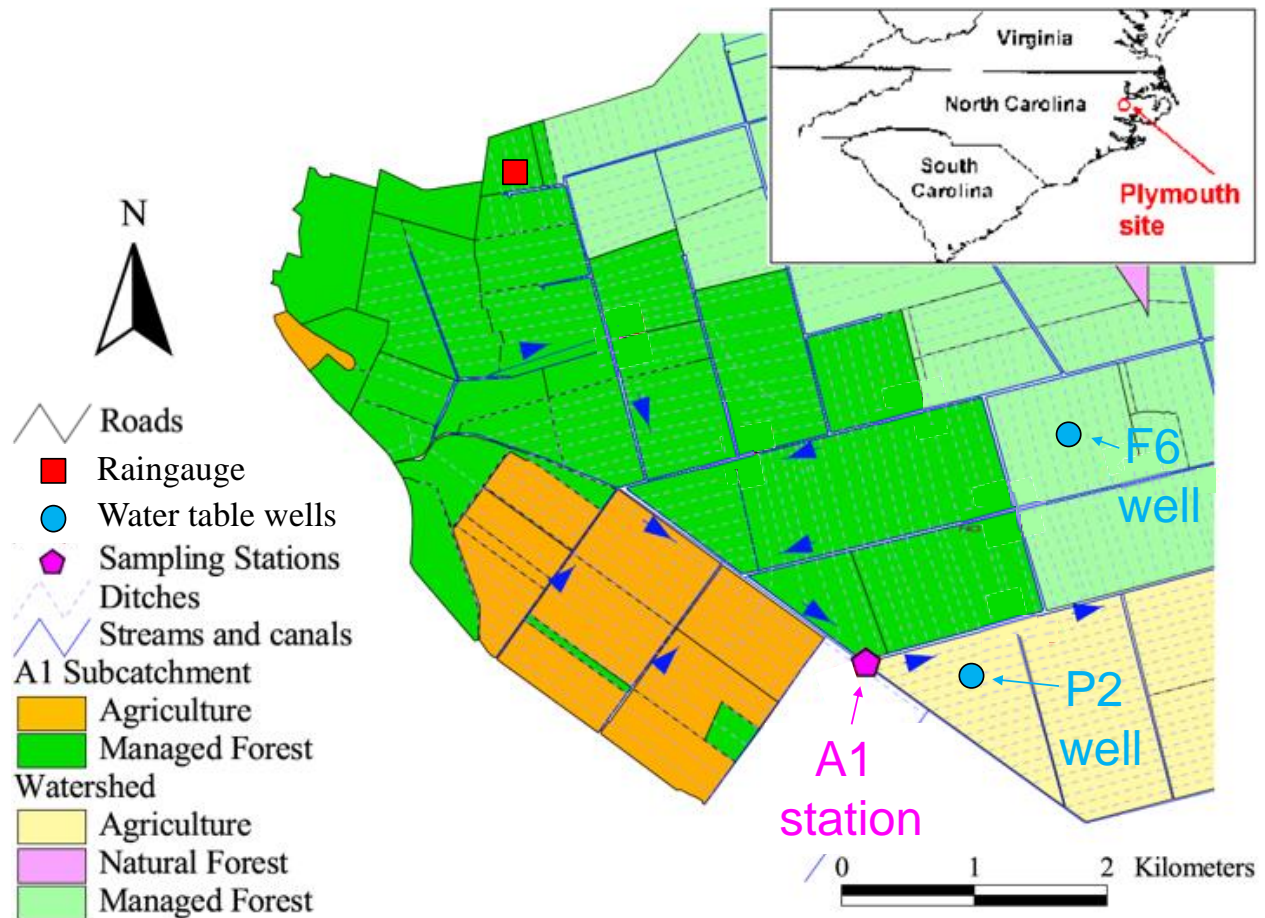


Figure 3.1. Location, land use and flow direction in the 1,531 ha subcatchment upstream of station A1 and location of the raingauge and water table wells (after Birgand, 2000).

3.3.2 Data acquisition and Preparation

Flow Data

Flow was funneled into wooden trapezoidal flumes where both stage and water velocities were recorded. Flow rates were calculated by multiplying the stage derived wetted cross section area by the section-averaged or mean velocity of water through the wetted section (ISO 15769, 2010). The wetted cross section area was calculated from the measured stage and the known dimensions of the trapezoidal shape of the flumes. The continuous mean velocity values were calculated

using the sensor velocity as ‘index data’ combined with a velocity rating curve obtained using manual flow measurements (details in Birgand, 2000 and in Birgand et al., 2013). Stage and velocity were measured and recorded every 10 min using continuous Doppler flow meters (STARFLOW, Unidata™ Australia).

Water Table Depth, water temperature, and rainfall

Water table depth was obtained using custom made pressure transducers from wells located in blocks “F6” and “P2” within the vicinity of the subcatchment. These data were assumed to be representative of forested (F6) and agricultural (P2) water table depth behavior across the subcatchment (Figure 3.1). Water temperature, 3 and 20 cm above the sediment, were measured at the A1 station using custom-made thermocouples and the data were stored onto a BlueEarth® data logger. Rainfall was measured using a tipping bucket rain gauge calibrated using cumulative rainfall manually collected on a weekly basis (Figure 3.1).

Water Quality Sampling and data

At the time the study was performed, continuous sensors capable of measuring nutrient concentrations at a high-resolution time scale (10-15 min) on-site were not widely used if available at all. Instead, water quality data were obtained from water automatically sampled at strategic times along the hydrographs, collected on a weekly basis, and kept at 4°C until analysis in the lab (details in Birgand, 2000). Caution was taken in the hotter summer months and samples remained in the field no longer than 4 days for risk of chemical transformations. Birgand (2000) showed in a sample degradation study that concentrations were not significantly altered while left in the field in this watershed.

Samples were analyzed for nitrate-nitrogen (NO₃-N), ammonium-nitrogen (NH₄-N), total Kjeldahl nitrogen (TKN), phosphate-phosphorus (PO₄-P), total phosphorus (TP), total dissolved carbon (TDC), dissolved inorganic carbon (DIC), total suspended solids (TSS), chloride (Cl), and pH. Organic nitrogen (ON) was calculated from the difference between TKN and ammonium and DOC concentrations were calculated as the difference between TDC and DIC. Analysis of pH was performed to provide information on the source of water, with higher values being expected in water draining from agricultural land due to liming practices and lower values occurring naturally in drainage water from the forests due to the acidic nature of the soils at the site. Samples analyzed for nitrate, ammonium, phosphate, dissolved carbon, and pH were filtered through a 45- μ m filter and all water quality analyses were carried out according to Standard Methods (APHA, 1995). Detailed lab analyses protocols can be found in further detail in Birgand (2000). Continuous time series data were constructed by linear interpolation of consecutive discrete sample concentrations to closely approximate the actual chemographs at a 10-minute increment. Water quality data could not be recovered for the period between December 13, 1998 6:30 PM – December 17, 1998 11:00 AM, thus all water quality related results (i.e., annual flow-weighted average concentration, annual load etc.) exclude this period of time. The original 14-month dataset was shortened to one hydrological year, from July 1, 1998 to June 30, 1999, for all results and analyses.

3.3.3 Integrative and cumulative Indicators

Cumulative Flow and Load Estimation

Cumulative flow volume (Cumul Q) and cumulative load (Cumul L) estimates were calculated for each time i in the time series data consisting of n measurement times using the equations

below. Consecutive instantaneous flow rates (Q) were averaged to approximate flow volume occurring over each 10-minute time interval (t) and flow volumes were summed (Eq. 3.1). Instantaneous flux was calculated as the product of flow rates (Q) and constituent concentrations (C). Consecutive fluxes were averaged to approximate the load occurring over each time-interval (t) and loads were summed (Eq. 3.2). Variables k and kl are unit conversion factors. All concentrations (C) were reported in units of mg/L, but in order to calculate a mass load associated with pH time series data, concentration values were expressed as H₃O⁺ in mol/L.

$$Cumul Q_{i+1} = k \sum_{i=1}^n \frac{Q_i + Q_{i+1}}{2} t \quad 3.1$$

$$Cumul L_{i+1} = kl \sum_{i=1}^n \frac{Q_i C_i + Q_{i+1} C_{i+1}}{2} t \quad 3.2$$

Cumulative Flux Duration Curves

Historically, flow-duration curves have been defined as a cumulative frequency curve that show the percent of time specified discharges were equaled or exceeded during a given period (Searcy, 1959). Moatar and Meybeck (2007) have proposed to expand the concept to cumulative fluxes of water and nutrients/material. They proposed two cumulative flux duration indicators, which they called W_{k(%)} and M_{k(%)}. These correspond to the percentage of the water volume and material load, respectively, discharged in k% of the time corresponding to the highest flows and the highest loads, respectively. For this, instantaneous flow rates and fluxes for each water quality parameter were ranked in decreasing order and cumulated to obtain sorted cumulative

flow volume and loads. Each value was given a probability of occurrence to obtain the $k\%$ values. We proposed an additional cumulative duration indicator which we call $M_{W_{k(\%)}}$, corresponding to the percentage of the material load discharged in $k\%$ of the time corresponding to the *highest flows* (and not loads this time). It was expected that in the majority of cases, the $M_{k(\%)}$ and $M_{W_{k(\%)}}$ curves should be very similar as flow rates carry the most weight in the nutrient and material fluxes. However, noticeable differences between the two curves for a given parameter would suggest that much of the load would occur on one or several events, not corresponding to the highest flows. To our knowledge, the overall shape and the meaning behind the $W_{k(\%)}$, $M_{k(\%)}$, and $M_{W_{k(\%)}}$ curves have not been described or discussed before.

Double Cumulative Curves/Double Mass Curves

A convenient tool to visualize the relationship between two variables through time is the double-mass curve (Searcy and Hardison, 1960). These curves have traditionally been used for checking consistency of a hydrological or meteorological record, with breaks in the cumulative flow volumes vs. cumulative rainfall suggesting actual changes in the rainfall-discharge relationship, and/or instrumentation error (Dubreuil, 1974). These types of curves have also been applied to identify effects of land use change on discharge in the paired-watershed context (e.g., Yao et al., 2012; Buttle and Metcalfe, 2000), and to detect inter-annual changes in discharge and sediment export in rivers (e.g., Pirnia et al., 2019; Yao et al. 2012; Gao et al. 2011; Searcy and Hardison, 1960).

More recently, double mass curves have proven useful in understanding the response of pollutant loading to consecutive events in bioretention cells at the seasonal scale (Brown et al., 2013), and

in examining the fate of applied pig slurry nitrogen at the experimental field scale (Peu et al., 2007, Liu et al., 2020). To our knowledge, double mass curves have not been widely adapted as a main method to identify intra-annual temporal variations in nutrient export at the watershed scale using high-resolution continuous time series data, at least certainly not as much as the C-Q relationship indicators.

As an integrative indicator, the effects of individual storms are purposely not emphasized. Rather, it is the trend over multiple storms, and/or the presence of breakpoints that are emphasized and for which it is hypothesized that they carry information on hydrological and biogeochemical processes. Two double cumulative curves were examined in this study: (1) cumulative flow volume as a function of cumulative precipitation and (2) cumulative load as a function of cumulative flow volume. This method provides the possibility to observe patterns and points of transition in the relationship between two variables without confinement to calendar-based temporal scales such as the seasonal and monthly scales and was expected to somewhat capture longer-term event scale patterns. Plots were constructed using cumulative data calculated at each 10-minute time interval for the full year of data.

First, cumulative flow volume was plotted as a function of cumulative rainfall to explore potential patterns in the subcatchment water balance. Subsurface drainage was expected to comprise the dominant portion of flow volume at the A1 outlet because there were no deep groundwater contributions and comparatively small contributions from surface runoff due to the flat nature of the catchment (0.01%). The slope of the curve between two points is equivalent to the runoff coefficient for a particular period and thus trends in the curve offer insight about the

response of subcatchment flow to precipitation. Smaller/flatter sloped periods in the curve would indicate that subcatchment flow was relatively less responsive to precipitation (smaller runoff coefficient) in comparison to steeper sloped periods that would suggest a greater response in flow volume to similar rainfall amounts (higher runoff coefficient). General trends were visually determined and discussed considering a simple water balance between rainfall and evapotranspiration as they relate to water table depth controlling subsurface drainage as the nearly sole input of flow at the A1 subcatchment outlet.

Second, cumulative nutrient and material loads were plotted as a function of cumulative flow to detect export patterns throughout the monitoring year. The local tangent of the double cumulative loading curve represents the instantaneous concentration while the slope of the curve between two points represents the flow-weighted average concentration for that time period. Admittedly, it was the breakpoints and the striking linear and asymptotic patterns that the nitrate double mass curve exhibited for the A1 watershed, that prompted the systematic use of this indicator for all parameters. All curves were visually examined and dissected into loading “Phases” mainly classified as linear and asymptotic in shape, although longer-lasting asymptotic phases were often divided into smaller linear portions to better estimate a flow-weighted average concentration representative of each part. Points of transition marked the beginning of new phases and typically were visualized as a shift to a longer-term curve shape and/or slope. These points of transition are sometimes referred to as “breakpoints” in the discussion.

The annual flow-weighted average concentration served as a comparative measure for loading phases as it represented the unlikely scenario in which the same loading rate was maintained

throughout the duration of the study, regardless of changes in flow rate or volume. This scenario would suggest that there was an unlimited amount of nutrient/material available for mobilization and that the mass exported was instead limited by hydrological controlling mechanisms, which too would not have changed. Relatively linear phases in the curves were interpreted with this concept in mind. Asymptotic phases were interpreted as an exhaustion or decreased availability of the source over time (e.g., because the source has been depleted by biogeochemical controlling processes), or by the decrease in the hydrological connectivity and carrying capacity to and from the source, or some combination of both. Increases or decreases in loading phase flow-weighted average concentrations suggested an increase or decrease in source availability from one phase to the next and could be compared with the annual flow-weighted average concentration. Event concentration dynamics were expected to drive the shape of the double cumulative loading curves, thus loading phases were expected to somewhat relate to groupings of similar event dynamics.

3.3.4 Event Scale Dynamics: C-Q Indicators

Event Identification

Events were visually defined in the hydrograph by a sharp rise in water level followed by a slower decrease and were often easily identified. Typically, during very low flow conditions, a significant increase in velocity and stage guided event identification. For the purposes of results and discussion in this study in particular, smaller events with peak flow rates < 10 L/s were omitted and events were numbered according to their original identification number found in Birgand (2000).

Hysteresis and Flushing Indices

The hysteresis index (HI) method established by Lloyd et al. (2016) and flushing index (FI) proposed by Vaughan et al. (2017) served as quantitative measures to describe event-scale C-Q relationships and dynamics in this study. In short, HI absolute values gave an indication of the ‘thickness’ of the hysteresis pattern between the rising and falling limb of the hydrograph, and its sign gave an indication of the direction of how the hysteresis was formed during an event, i.e., positive values indicated clockwise hysteresis and negative values indicated anticlockwise hysteresis. A positive (or negative) value for FI indicated whether concentrations generally increased (or decreased) with increasing flow during an event, while its absolute values indicated by how much concentrations were increased or diluted during an event. For each water quality parameter, a plot of HI indices versus FI values was established, each point corresponding to an event. These plots provided information of interplay between hydrological and biogeochemical process at the event-scale and were compared to those of the double cumulative loading curve analysis.

The hysteresis index (HI) was calculated for each rainfall triggered event and for multi-peak events if the dynamic examined in the chemograph responded mostly to one peak. For each set of event flow and concentration data, flow rates (Q_i) and concentrations (C_i) at timestep i were normalized to the difference between minimum and maximum event values by Equations 3.3 and 3.4 respectively.

$$Q_{i,norm} = \frac{Q_i - Q_{min}}{Q_{max} - Q_{min}} \quad 3.3$$

$$C_{i,norm} = \frac{C_i - C_{min}}{C_{max} - C_{min}} \quad 3.4$$

Q_{min} and Q_{max} are the minimum and maximum flow rates occurring during the event and C_{min} and C_{max} are minimum and maximum concentrations.

The hysteresis loop was then divided into sections corresponding with normalized flow rates at 1% increments (i.e., $Q_{int} = Q_{1\%}, Q_{2\%}, Q_{3\%} \dots Q_{97\%}, Q_{98\%}, Q_{99\%}$). Hysteresis index (HI_{int}) at each 1% interval (int) was calculated as the difference in concentration values occurring on the event rising ($C_{int,RL}$) and falling limb ($C_{int,FL}$) corresponding with the normalized flow rates $Q_{int,RL}$ and $Q_{int,FL}$ respectively (Eq. 3.5). Linear interpolation was performed between values to calculate all Q_{int} and C_{int} values.

$$HI_{int} = C_{int,RL} - C_{int,FL} \quad 3.5$$

The final event HI value was calculated as the average of all HI_{int} values calculated from available pairs of rising and falling limb concentrations. HI values ranged from -1 to 1 with a negative value representing anti-clockwise hysteresis and a positive value representing clockwise hysteresis. The distribution of HI_{int} values were examined in addition to the mean HI value to interpret hysteresis loops, especially those that crossed (i.e., Figure-of-8 and complex loop shapes). In general, higher absolute HI values indicated stronger hysteresis and corresponded with wider loops.

The event flushing index was calculated as the difference between the normalized concentrations corresponding with peak flow rate and the beginning of the event. The FI value ranged from -1 to 1 with positive values indicating an increase in concentration on the rising limb of the event and negative values indicating a decrease. We generally refer to positive and negative FI values as concentration and dilution effects respectively in the results, but chemograph C-Q dynamics were thoroughly inspected to confirm the agreeability of the value with what was observed. In theory, a positive FI value would be interpreted as a concentration effect and the sign of the hysteresis index value would correspond with the timing of the effect in relation to peak discharge. A positive HI value would relate to a rapid concentration effect on the rising limb and a negative value would reflect a concentration effect that occurred on the falling limb of the event. The opposite interpretation of timing holds for a negative “diluting” FI value. Anti-clockwise hysteresis would indicate rapid dilution on the rising limb and clockwise hysteresis would indicate a delayed dilution effect on the falling limb. The results could not always be as simply interpreted, and C-Q dynamics were cross-checked with HI and FI value combinations.

3.4 Results

3.4.1 Hydrology fed by intermittent subsurface flow in a very flat watershed

Annual rainfall was about 20% lower than the preceding 50-year average of 1299 mm for Plymouth, NC. Hydrology in this very flat watershed (0.01% slope) is thought to be entirely dominated by open-ditch subsurface drainage leading to a very low runoff coefficient. Indeed, approximately 12% of the 1024 mm of rainfall that fell in the subcatchment left as streamflow between July 1998 and June 1999. The seasonal pattern observed was somewhat typical, consisting of an active flow period spanning late fall, winter, and early spring (December 13,

1998 – April 23, 1999) illustrated by the overall steep linear portion of the logistic S-curve in Figure 3.2, in which cumulative streamflow increased relatively linearly with cumulative rainfall. Approximately 80% of the annual discharge was produced during this period accounting for only one third of the year and during which 41% of the annual precipitation occurred. In contrast, the preceding summer and fall months (July – mid December 1998), accounted for only 10% of the total discharge in response to nearly the same amount of rainfall in almost half of the year. The remaining 10% of total discharge occurred in the months of May and June 1999 during isolated events, similar to the summer and fall months.

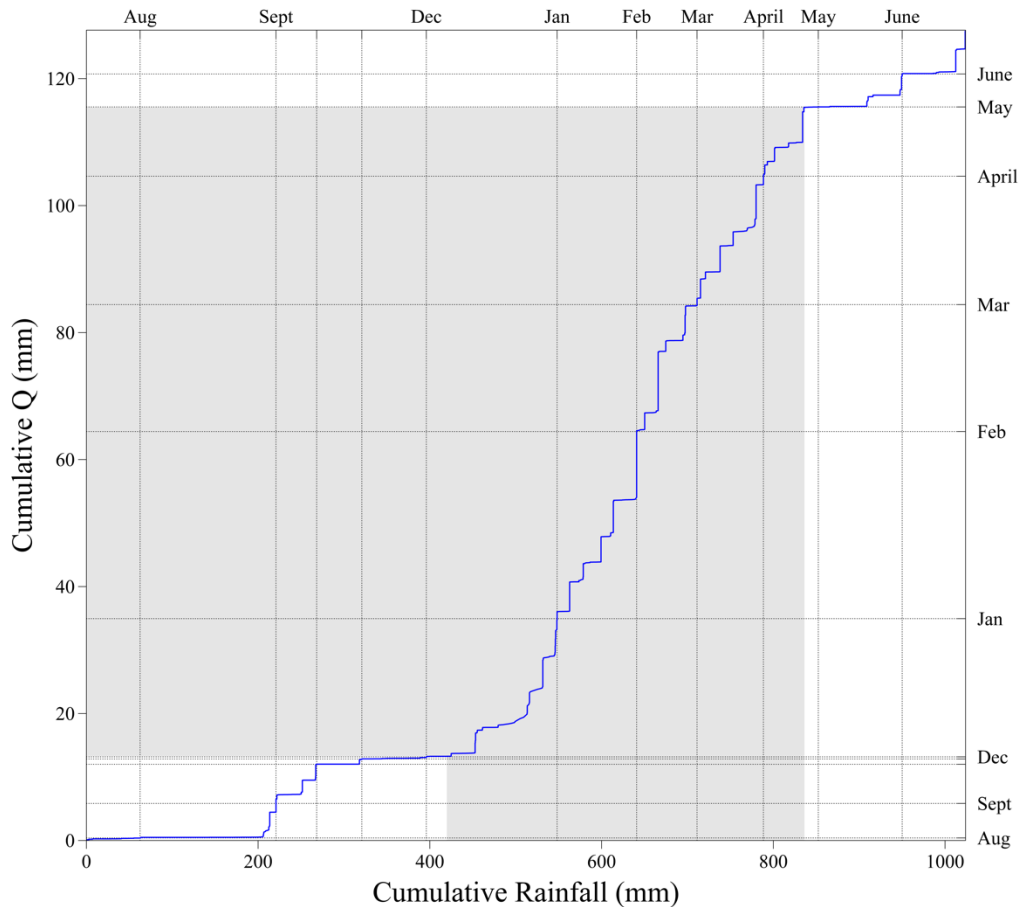


Figure 3.2. Cumulative discharge as a function of cumulative rainfall from July 1998 – June 1999 in A1 subcatchment. Gridlines indicate the beginning of a new month and the x- and y-axes represent beginning of July 1998. Gray shaded area indicates active late-fall to winter flow period spanning December 13, 1998 – April 23, 1999.

Due to the flatness of this site (slope around 0.01%), rainfall mostly infiltrated the soil and contributed to subsurface flow and/or soil storage rather than being transported as surface runoff. Possible exceptions could occur when the water table depth was nearly at the surface and/or rainfall intensity was high enough to exceed infiltration capacity of the soil. These events were rare at best and did not contribute significantly to annual discharge in 1998-99 (Birgand, 2000). Flow rates 5 L s^{-1} and below only accounted for about 1% of annual discharge although they

accounted for 50% of the time corresponding to the summer, spring, and late fall months. As a result, in this coastal plain watershed, the concept of baseflow did not really apply, as the vast majority of flow (99%) was directly consecutive to rainfall events that fell in the subcatchment.

Evapotranspiration in these coastal plain forested-dominated watersheds has been measured to correspond to about 70% of rainfall (Chescheir et al., 2003) and to lower the water table at 1.6 – 2 m depths. The forested portion of the watershed was actively managed with risers and weirs set at around 60 cm below the surface. The consequence of this was that no flow would occur unless the water level in the collector ditches was above the bottom of the weirs. The combination of these threshold requirements and lack of surface runoff and groundwater contributions to discharge meant that rainfall in late summer did not always result in a flow increase. This was clearly observed in the flatter portions of the curve in Figure 3.2 where the first 200 mm of rainfall in July 1998 were hardly accompanied with any flow. During these portions of time, greater amounts of rainfall were necessary to raise the water table depth enough to generate flow.

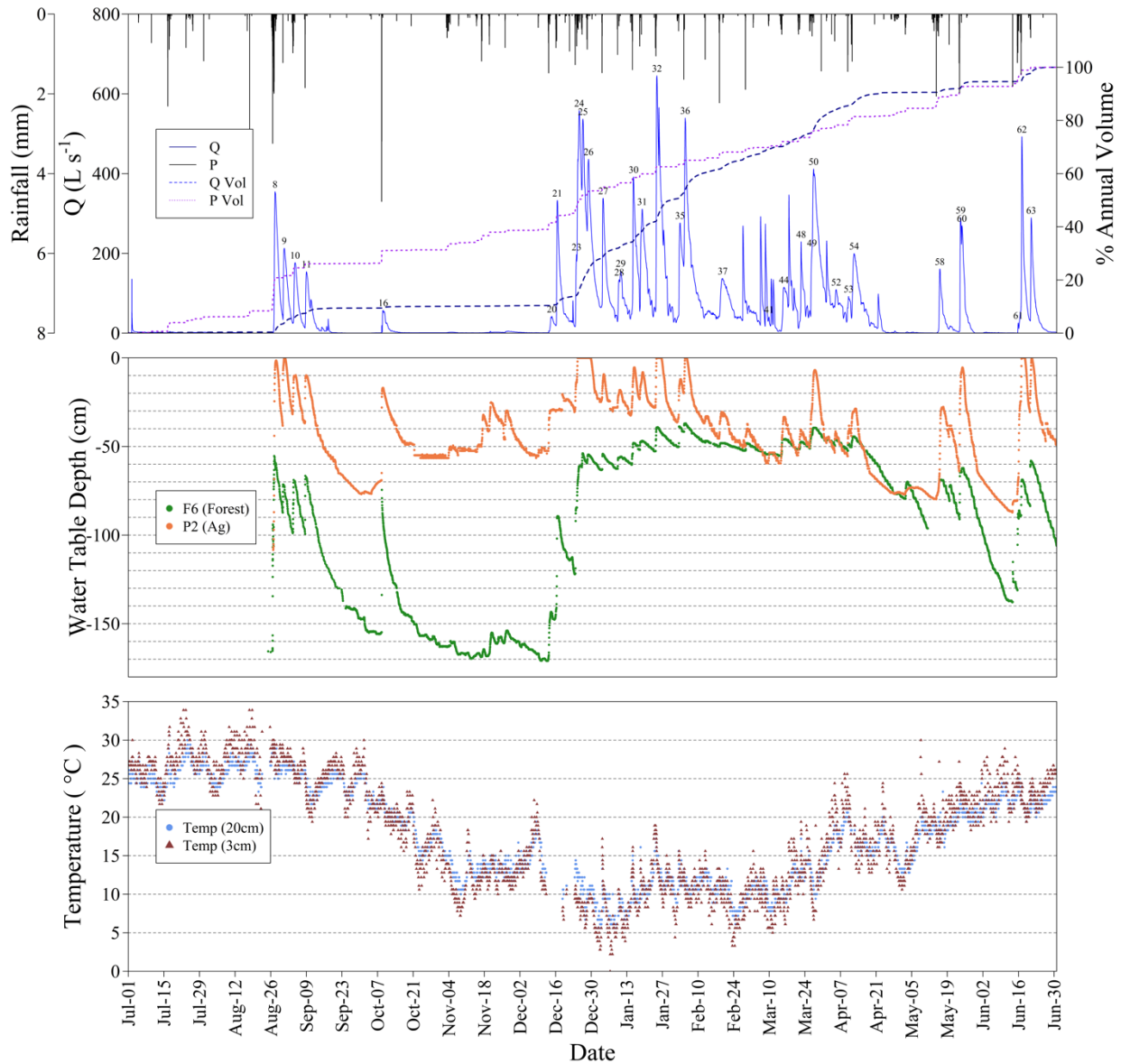


Figure 3.3. Time series data for the hydrological year July 1998 – June 1999 for the A1 subcatchment including a) 10-min interval discharge rates and rainfall total pulses and cumulative discharge and precipitation as a percentage of annual totals, b) water table depth recorded in F6 and P2 plots representative of forested and agricultural water table depth dynamics respectively and c) temperature recorded at 3 and 20 cm depths below the water surface at A1.

A total of 55 hydrological events were recorded, characterized by a rapid rise followed by a slower fall of the hydrograph during the year, but only 39 events were in response to precipitation (Figure 3.3) while release of accumulated water by opening breaches in beaver

dams resulted in 15 of the events. The overall flow volumes occurred in three main phases: late summer 1998, December to April 1999, and sporadic spring 1999 events. The first phase in late summer 1998 corresponded to the hurricane season, which included hurricanes Bonnie (event 8) and Earl (event 10) and contributed approximately 9% of annual discharge (Figure 3.2). Flow essentially stopped from late September until late December 1998, when the second phase, i.e., the active winter period started and included 36 events (events 20-54), 23 were rain triggered events, one which was simultaneously triggered by a beaver dam breach opening (event 48), and 13 events resulted solely from breach openings in beaver dams located roughly 800 m upstream of the monitoring station. The third phase was characterized by three events which occurred in the months of May and June 1999 each, when flow conditions returned to what was observed in July through mid-December with little to no flow in the canal between events. Peak flow rates of the rainfall triggered events ranged from 25.8 L/s to 645.4 L/s and averaged 262.5 L/s or 17.1 L/s/km², with the highest peak flow rate occurring during event 32 at the end of January. Times of rise (*sensu* Dingman, 2002) averaged approximately 13 hours and all but 3 events reached peak discharge in less than a day, testimony of the relative ‘sluggishness’ of the hydrology in this watershed.

Land use determined contribution to flow

The water table was expected to exhibit contrasting behavior among fields due to land cover, drainage protocol, and soil profiles. Overall, the forested area was expected to lose more water due to ET from deep-rooted pine, especially in hotter months, lowering the water table at greater depths than in the ag fields; the consequence being that more rainfall would be required to

produce flow from these areas than the agricultural fields. This was likely exacerbated as the weir levels in the forest fields were set higher than in the ag ones.

The F6 (forested) water table depth remained below that of P2 (ag) for most of the year with the largest difference in depths during the hot summer months (Figure 3.3). In the ag field, the water table reached the soil surface during 9 events (8, 9, 24-26, 32, 36, 62, and 63) and rarely fell below -60 cm, which thus appears to have been the effective drain depth in this field. In the forested field, water table reached the minimum -60 cm threshold for flow to occur briefly during hurricane Bonnie (event 8) and not until the latter part of December 1998, where it stayed above that depth most of the time until late April 1999. This suggests that the contribution of the forested areas to flow was likely not very significant until late December 1998, and after April 1999.

Overall, variation in water table depth as a response to rainfall was typically of greater magnitude in P2 compared to F6 during the active flow period. This was likely due to the smaller drainable porosity in the ag compared to the forested fields, which caused the water table to rise and to fall faster. Because of the tree root network, the drainable porosity and the hydraulic conductivities in forested fields tend to be much higher than those in ag soils (e.g., Chescheir et al., 2003). Water table dynamics varied temporally and spatially during the year, and therefore, flow at the A1 outlet at any given time was some combination of contributing portions of water from the ag and/or forested fields.

3.4.2 Water Quality

High resolution data for water quality and quantity

Because of the strategic times of sampling along the hydrographs, it was assumed that the chemographs derived from interpolation between consecutive concentration data points closely resembled the actual ones that would have been measured with *in situ* sensors had they been available (Figure 3.4). High resolution 10-min concentration data were thus calculated to match the resolution of the flow data and were the time-series from which loads and other indicators were calculated.

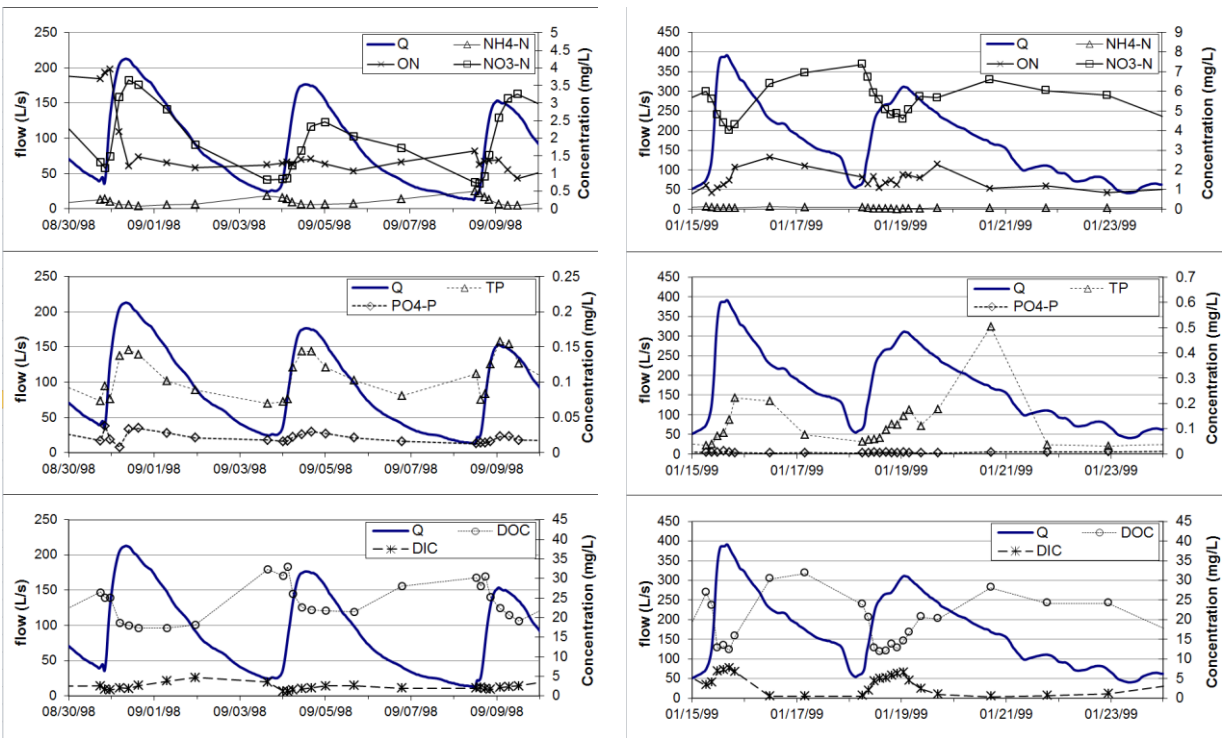


Figure 3.4. Hydrograph and chemographs of NO₃-N, NH₄-N, ON, TP, PO₄-P, DOC and DIC during summer events at the outlet of the A1 watershed in 1998 (events 9, 10, and 11) and 1999 (events 30, 31; after Birgand, 2000).

Results show (Figure 3.4) that in summer, NO₃-N, TP, PO₄-P, and TSS (not shown) exhibited a clear ‘concentration’ or ‘flushing’ effect, while ON, NH₄-N, DOC and DIC showed a clear ‘dilution’ effect. In winter 1999, concentration effects were clear for TP and DIC, dilution effects were apparent for NO₃-N and DOC, but the effects were less obvious for NH₄-N, ON, and PO₄-P.

Annual concentration indicators reveal influence of agriculture in a context of a low land organically rich stream

Annual concentration indicators reported in this section correspond to the times when flow $Q > 5$ L/s, and that accounted for 98% of the annual discharge. For $Q < 5$ L/s that accounted for ~50% of the year, some constituent concentrations, particularly TSS, DOC, ammonium, phosphate, and organic nitrogen reached very high values. These were deemed not representative of the export pattern and excluded in the calculation of annual concentration indicators.

Total nitrogen concentrations were dominated by nitrate concentrations (Figure 3.5). Nitrate displayed the widest range of concentration values throughout the year of all components contributing to total nitrogen. The mean nitrate concentration was $4.75 \text{ mg N/L} \pm 4.51 \text{ mg N/L}$, with 25th and 75th quartiles at 1.60 and 6.38 mg N/L, respectively. Nitrate concentrations reached up to 20 mg N/L and higher in some isolated events in May and June 1999. These values are more than one order of magnitude higher than the ones observed in forested lands in this area, suggesting that nitrate likely originated from the ag fields upstream of A1. The ammonium ($0.21 \text{ mg N/L} \pm 0.44 \text{ mg N/L}$, with 50% of the values between 0.04 and 0.16 mg N/L) and organic

nitrogen ($1.59 \text{ mg N/L} \pm 0.84 \text{ mg N/L}$) concentrations were higher than usually observed in upland watersheds.

DOC exhibited a very large range of concentrations with a mean of 25.3 mg C/L ($\text{SD} = 13.24 \text{ mg/L}$). Highest DOC concentrations ($> 80 \text{ mg C/L}$) were measured during lower flows fed by the very high DOC concentrations ($> 100 \text{ mg C/L}$) in the porewater of the $> 30 \text{ cm}$ thick ‘muck sediment’ of the drainage canals (Birgand, 2000). The mean DIC concentration, rarely measured and reported in stream monitoring, was equal to 2.61 mg C/L with a standard deviation of 2.77 mg C/L with half of the values falling between 0.50 to 4.04 mg C/L and a peak that reached 23.3 mg C/L .

The level of reduced nitrogen (ON and ammonium) and carbon concentrations suggests the presence of reduced conditions common in this “blackwater country” where organic and high organic mineral soils, allochthonous (leaves, needles) and autochthonous (algae, macrophytes) sources contribute to high levels of organic content in the canal sediment and drainage water (Birgand, 2000).

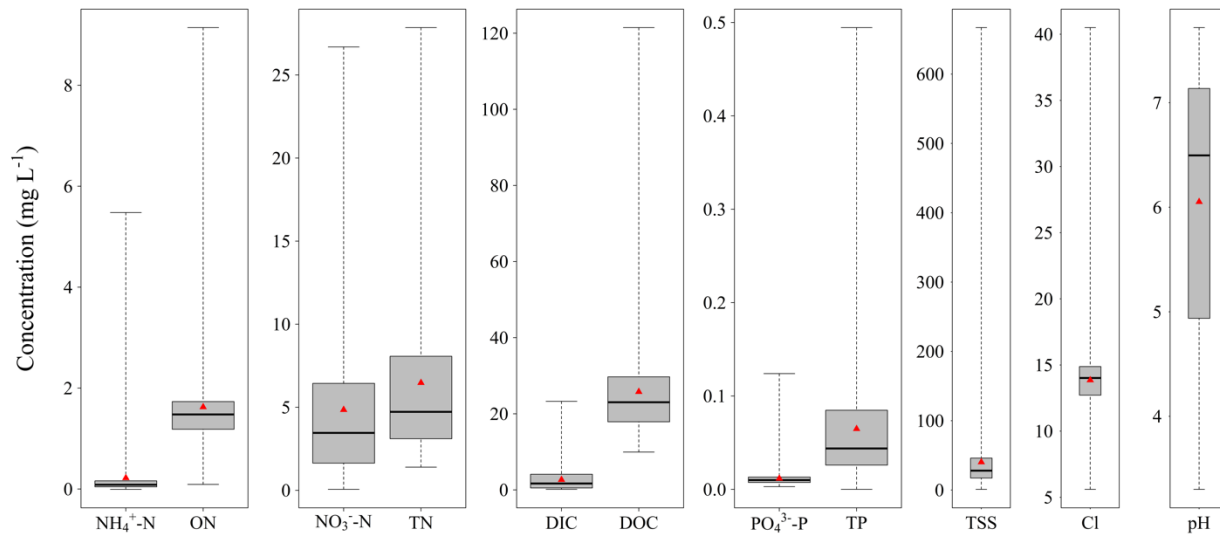


Figure 3.5. Boxplot representation of concentration data statistics representing concentrations associated with flow rates greater than 5 L/s ($n = 26240$). This subset of data corresponds to the 50% of the year that comprised 98.9% of the annual total discharge. Whiskers represent minimum and maximum concentration values. Bottoms and tops of gray boxes indicate 25th and 75th quartile values and the intermediate black line represents the median concentration value. Red triangles indicate means.

A majority of phosphate concentrations fell below 0.013 mg P/L (75th quartile) and never rose above 0.12 mg P/L. Total phosphorus concentration values ranged between 0.03 (25th quartile) to 0.08 mg P/L (75th quartile) with a mean and standard deviation of 0.06 mg P/L and 0.05 mg P/L respectively. These values were somewhat lower than those typically found in agricultural watersheds, likely due to the subsurface dominated hydrology which minimizes surface runoff and thus entrainment of particles to which P may attach (Mellander et al., 2012).

A majority of TSS concentration values fell within the range of 16.55 mg/L to 45.6 mg/L with a mean of 39.45 mg/L (SD = 47.49 mg/L). Concentrations could reach values greater than 200 mg/L at times, however the highest concentrations of TSS (> 600 mg/L) did not correspond with

the highest flow rates. These values are relatively small corresponding to the low significance of surface runoff and flatness of the watershed.

Mean pH was 5.93 (SD = 1.42) and the 25th and 75th quartile values were 4.86 and 7.12, respectively. This is a remarkable range of pH values compared to other studies, which was observed due to varying water sources and soils contributing flow to the drainage canal as lower values (pH ~ 5.5) were thought to represent water flowing from the forested area and higher values representative of ag water which pH was increased due to liming of the fields. The mean chloride concentration was 13.57 mg/L (SD = 3.05 mg/L), and half of values were between 12.54 mg/L to 14.87 mg/L.

Cumulative Flux Duration Indicators show sluggish hydrological reactivity during high flows, and during low flows, quenching mechanisms for water and nitrate export, while sustained release of reduced C and N

The curves illustrated in Figure 3.6 first confirm that the vast majority of the flow volume (nearly 99%) occurred in 50% of the time, or in other words, 50% of the time, there was no significant flow (see also Figure 3.2). The relative importance of the highest flows was thus expected to be proportionally large compared to perennial streams since all flow was ‘packed’ in 50% of the time but contrary to this expectation, in 1% of the time, about 10% of the total annual flow volume occurred, or $W_{1\%} \approx 10\%$. This value is on par with those for much larger watersheds (more than 100 times larger in size) where artificial drainage also plays an important role such as for the Grand River at Painesville, OH, or the Cuyahoga River at Independence, OH (Moatar and Meybeck, 2007). For comparison purposes, the upland watersheds monitored for

the intercropped forested watersheds (Chapter 1) were $25\% < W_{1\%} < 55\%$. This confirms that this coastal plain watershed had a much lower hydrological reactivity than expected for its size and this needs to be put in relation with the flatness of the area and the near absence of surface runoff.

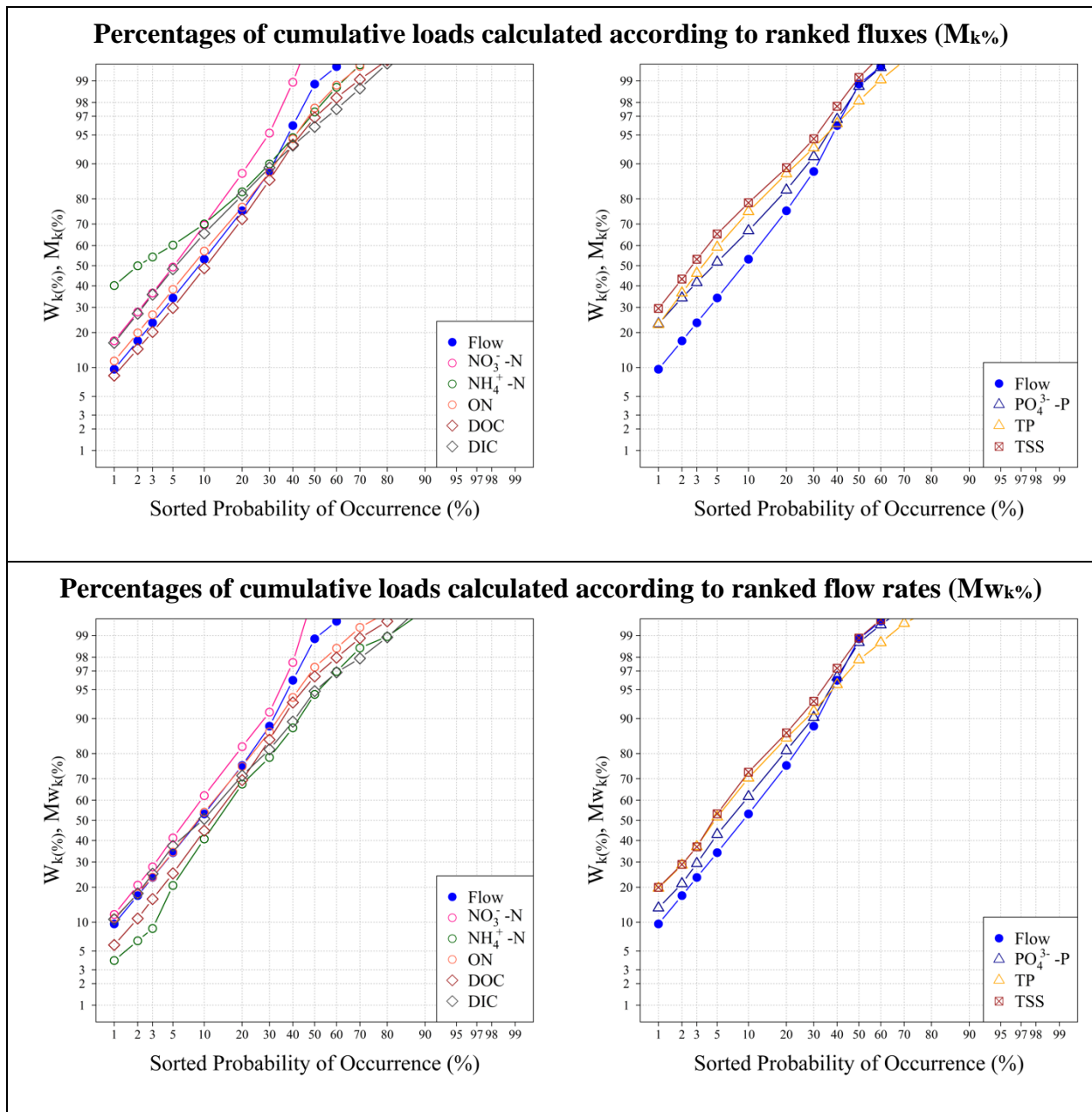


Figure 3.6. Flux duration curves for nitrate, ammonium, organic nitrogen, DOC, DIC, phosphate, TP, TSS and flow for the 1998-99 hydrological year at the A1 watershed station.

The volume duration curve was generally linear, i.e., it followed a log normal pattern, as cumulative volume accounting for about 90% of the total volume corresponding to 30% of the time, i.e., until $W_{30} \approx 90\%$ (Figure 3.6). Above W_{30} , from 90 to 99% of the cumulative flow

volume, the slope of the curve increased, testimony of the absence of deep groundwater fed baseflow and the abrupt quenching of flow during the hot E.T. dominated periods of the year. For the other cumulative flux parameters and as a recall, the difference between the $M_{k\%}$ and $Mw_{k\%}$ indicators is that $M_{k\%}$ curves are established by ranking fluxes in decreasing order, while the $Mw_{k\%}$ curves are established for the fluxes corresponding to ranked flow rates in decreasing order. We propose an analytical grid to interpret these curves. First, for the low percentage of time of occurrence, the difference between the $M_{k\%}$ and $Mw_{k\%}$ indicators gives an indication of the relative importance of the highest loads that do not necessarily correspond to highest flow rates. The interest for the $M_{k\%}$ curves ends there. Second, within the $Mw_{k\%}$ curves, we propose to observe whether the $Mw_{k\%}$ curves were always above or always below the $W_{k\%}$ curve, generally parallel to the $W_{k\%}$ one, or whether and where the $Mw_{k\%}$ curves ‘crossed’ the $W_{k\%}$ curve. With this analytical grid in mind, we believe these duration curves provide the following information.

For all parameters and for the low percentages of cumulated probability of occurrence ($k < 20\%$), all $M_{k\%}$ values were higher than the $Mw_{k\%}$ ones. This suggests that the highest flow values did not necessarily carry the highest loads in this watershed. For example, in 2% of the time, 30% of the cumulative load occurred ($M_{2\%} = 30\%$), while only 20% ($Mw_{2\%} = 20\%$) of the nitrate load occurred carried by the highest flows. This suggests that some events had a disproportionately high nitrate concentration. Most parameters exhibited $Mw_{k\%}$ values 10 percentage points lower than $M_{k\%}$ and for $k < 10\%$, with the notable exception of ammonium.

The $M_{1\%}$ and $M_{2\%}$ for $\text{NH}_4\text{-N}$ were 40% and 50%, respectively, and much higher than the $M_{w_{1\%}}$ and $M_{w_{2\%}}$ at 4% and 6%, and $W_{1\%}$ and $W_{2\%}$ at 10 and 19%. This suggested that the overall export of ammonium was dominated by very rare events, for which the flows were not among the highest, although concentrations had to be very high, and that had a preponderant impact on the annual ammonium export pattern.

The $M_{w_{k\%}}$ for nitrate, ON, and DOC were generally parallel to the volume duration curve until 30% of probability of occurrence, suggesting that the export frequency patterns of these constituents were consistent with those of water 30% of the time corresponding to the highest flows (ON curve superimposed with that of the $W_{k\%}$ curve). The nitrate cumulative load duration curve also followed the same upward pattern as that of the volume above $M_{w_{30\%}}$, suggesting that the export of nitrate during low flows corresponding to the warmest periods of the year was also quenched by a nitrate removing process.

The DOC and ammonium $M_{w_{k\%}}$ curves were always below that of the volume duration curve, suggesting that the export of DOC and ammonium during events was less than proportional to flow, or in other words that there was an overall dilution of the concentrations during flow events. This observation was confirmed by the C-Q analysis for DOC but infirmed for ammonium for the rare events that exported nearly 50% of the total loads.

The $M_{w_{k\%}}$ curves for nitrate, TSS, and phosphate were always above the $W_{k\%}$ curve, suggesting an overall 'concentration' effect during events. We shall see that this is sometimes in

contradiction with the observations, e.g., Figure 3.4, and the C-Q analysis, suggesting that the cumulative flux duration curves interpretation may be a bit ambiguous at times.

The $M_{W_k\%}$ curves for DIC, and TP cross the $W_{k\%}$ curve for the cumulative probability of occurrence of 7% and 37%, respectively. This suggests that during the highest flow rates, DIC showed a concentration effect (e.g., Figure 3.4), but that the pattern was not as obvious for the remainder of the time. For TP, the $M_{W_k\%}$ curve above the $W_{k\%}$ curve for 90% of the flow volume suggests that TP concentrations must have increased during flow events, most of the time.

The $M_{W_k\%}$ curves appear to have an inflection beyond the cumulative probability of occurrence of 50% for ON, DIC, DOC, and ammonium, suggesting a phenomenon inverse to that of the flow quenching mentioned before. During the 5% of the flow volume corresponding to the lowest flows, from 6% (ON) to 12% (DOC) of the annual loads were exported. This suggests that the sediment diagenetic processes were disproportionately active then and released these parameters into the very shallow water column at these times.

The cumulative flux duration curves thus provided an overview of the export patterns in the watershed at the annual scale, showing low hydrological reactivity, emphasizing the role of the highest flows but also revealing that during low flows, quenching mechanisms for water and nitrate exports, and conversely release mechanisms for ON, ammonium, DIC and DOC, most likely associated with sediment diagenetic processes.

Double Cumulative Loading Curves give the big picture of the drivers of the nutrient and material exports

The duration curves gave an overall pattern of the cumulated fluxes as a function of decreasing sorted flow rates expressed as probabilities of occurrence. The sequence of the export patterns was thus not part of the analysis. The sequence of flow events was at the core of the double cumulative loading curves analysis. However, cumulative loads were expressed, not as a function of time, but as a function of cumulative flow volume. This emphasized in the export, patterns of continuity, breaks or discontinuity, limitations or increases of the sources for the constituent export for a given entrainment volume, all of which are indicators of the hydro-biogeochemical functioning of the watershed. Instead of confining analysis of loading patterns to the daily, monthly, or seasonal time scales, the method allowed for the detection of general changes in export behavior as they occurred throughout the year due to a variety of potential factors.

Initially following visual inspection of the nitrate double mass curve, it appeared that all curves exhibited similar linear or asymptotic patterns. Overall, we decided that many of the patterns observed for exports of all parameters occurred roughly within 5 distinct phases separated by breakpoints clearly observable on the nitrate double mass curve (Figure 3.7). Breakpoints occurred as a transition between asymptotic and linear shapes and between phases.

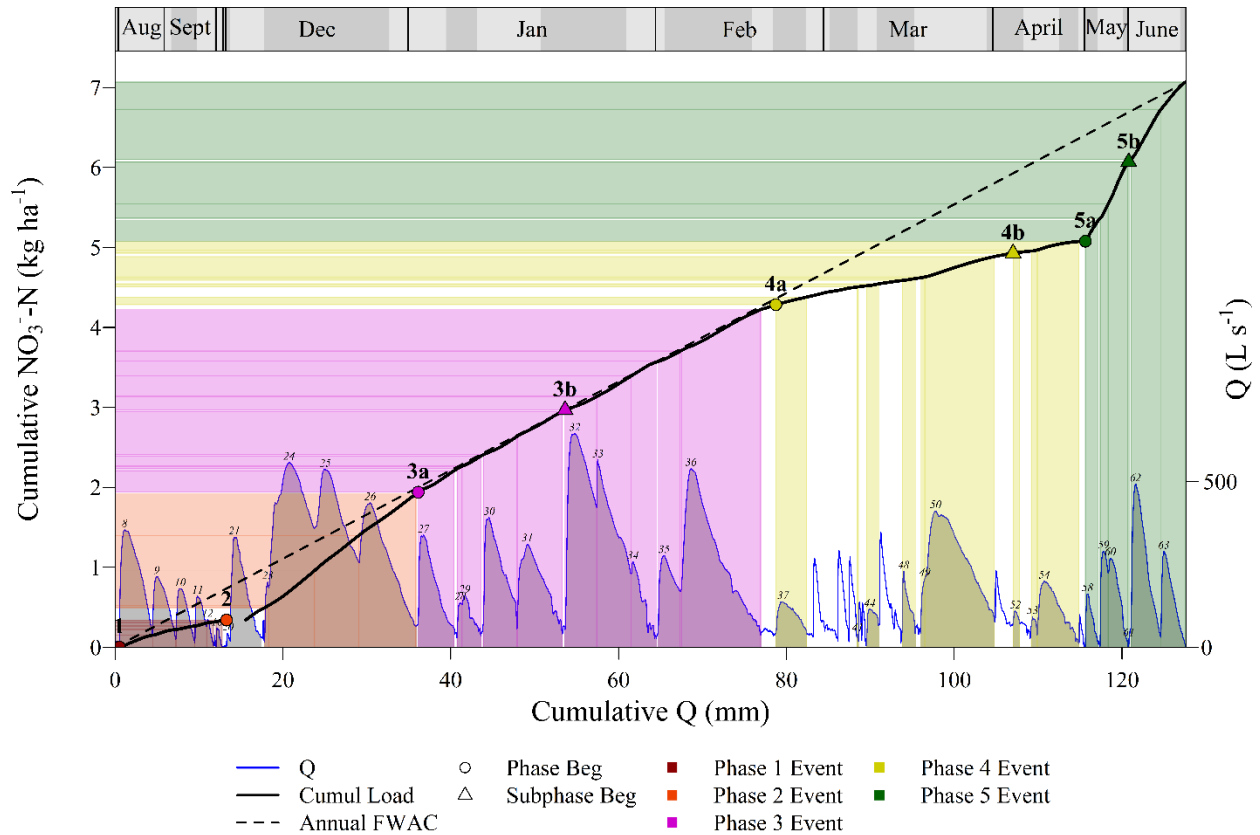


Figure 3.7. Cumulative nitrate load export as a function of cumulative discharge for July 1998 – June 1999 at the A1 subcatchment outlet.

On all double mass curve plots (e.g., Figure 3.7), the cumulative flow volume is represented on the X-axis, the cumulative load in kg ha^{-1} is on the primary Y-axis, and the instantaneous flow rates are on the secondary Y-axis. Within this scheme, the hydrological events (number label above peaks) are recognizable with rapid rising and slower falling limbs but appear contiguous. This is because any low flow periods that might have occurred between events accounted for very little flow and are thus ‘compressed’ along the X-axis and hardly visible. Time is not linear in this representation but is indicated as a timeline at the top of the plots, where months are

divided by vertical lines and shading represents alternating weeks. The months of July, October and November 1998 are hardly visible because very little flow occurred then.

The five phases are color-coded. Mostly during phase 4, some events do not have the area under the hydrographs colored because they correspond to man-triggered events (controlled drainage and beaver dam removal). “Phase Beg” points mark the beginning of each of the 5 major phases detected in the curves and “Subphase Beg” points mark the beginning of the secondary subphases within major phases 3-5. The slope of the dotted line (connecting the first and last points of the cumulative load) represents the annual Flow Weighted Average Concentration (FWAC).

Within each phase, the double mass curves were typically asymptotic or linear in shape, offering information about leaching availability and hydrological connectivity to nutrient pools. We propose that an asymptotic shaped curve represented a period in which a higher loading rate existed initially but gradually decreased during a linear increase of the volume of total water leached through the soil. A good example of an asymptotic shape is provided during phase 1 of the nitrate double mass curve. We hypothesize that this shape is indicative of an apparent “exhaustion” of the nutrient/sediment source available to be leached rather than the volume of water with the ability to mobilize it. The reason for the apparent exhaustion might be because there was a finite stock (e.g., in the soil) at the onset of export. This explanation relates well to the “first flush” concept in which large portions of nutrient accumulated during dry periods are thought to be released as a result of new rainfall followed by a gradual depletion in response to additional rainfall. Another reason for the apparent exhaustion is that the stock in the soil may

be diminished because of plant uptake, or biogeochemical processes such as denitrification, in the soil, but also in the hydraulic network. Alternatively, we hypothesize that linear shaped phases indicate times for which loading rates/fluxes were relatively consistent in response to discharge. This shape would indicate that discharge was the limiting factor controlling the amount of nutrient exported to the outlet because nutrient availability remained relatively constant regardless of additional water input to the system. We hypothesized that a gradual increase in slope indicated that the nutrient supply available for leaching increased. This was hypothesized to be associated with increased hydrological connectivity to sources previously untapped and/or to shifts in biogeochemical controlling factors causing an increase in production of available nutrients to be mobilized. We hypothesize that a breakpoint followed by a decrease in slope signified that hydrological connectivity to a nutrient pool decreased and/or biogeochemical (and human) factors changed causing a reduction (an increase) in the pool of available nutrient to be mobilized.

For each phase, the total discharge and the percentage of the annual discharge were calculated. Within each phase and for each parameter, calculated indicators included the FWAC, the cumulative load, the percentage of the cumulative load, and the FWAC ratio, the latter calculated as the phase FWAC divided by the Annual FWAC (Table 3.1.). For phases 3, 4, and 5, double mass curves of parameters other than nitrate exhibited some breakpoints, so these phases were divided into 'a' and 'b' subphases.

For ease of pinpointing breakpoints among the 10-minute time series data in addition to evaluating the relationship between double cumulative loading patterns and event-scale

dynamics, breakpoints were visually selected and defined as the beginning time of the nearest next event. For this reason, some breakpoints appeared a little before or after obvious points of transition in the curves based on the C-Q dynamics of the previous or following event. This method allowed assignment of each event to a loading phase for analysis of HI and FI values. Ultimately, breakpoints in the double cumulative loading curves among constituents typically fell within similar times throughout the year and long-term major phases for some species could be divided into sub-phases for others.

Table 3.1. Summary data for double cumulative loading curve phases and intermittent low flow occurring during the months of July and August prior to Phase 1 for July 1998 – June 1999 at A1. Flow-weighted average concentration (FWAC) ratio is equal to the phase FWAC divided by the Annual FWAC. FWAC values for major phases 3, 4, and 5 are provided in italics below subphases 3a, 4a and 5a respectively.

		Double Cumulative Loading Curve Phases									
Parameter	Variable	Jul/Aug	1	2⁺	3a	3b	4a	4b	5a	5b	Annual⁺
Q	Total Discharge (mm)	0.51	12.76	20.58	17.51	25.11	28.27	8.62	5.16	6.84	125.36
	% Annual Discharge	0.41	10.18	16.41	13.97	20.03	22.55	6.88	4.11	5.46	
NO ₃ ⁻ -N	FWAC (mg L ⁻¹)	0.79	2.65	7.77	5.87	5.25	2.27	1.75	19.20	14.64	5.64
					<i>5.50</i>		<i>2.15</i>		<i>16.60</i>		
	Load (kg ha ⁻¹)	0.004	0.34	1.60	1.03	1.32	0.64	0.15	0.99	1.00	7.07
	% Annual Load	0.06	4.77	22.60	14.54	18.64	9.08	2.13	14.00	14.17	
	FWAC Ratio	0.14	0.47	1.38	1.04	0.93	0.40	0.31	3.40	2.60	
NH ₄ ⁺ -N	FWAC (mg L ⁻¹)	2.07	0.14	0.055	0.075	0.049	0.045	0.20	1.93	0.22	0.17
					<i>0.059</i>		<i>0.082</i>		<i>0.96</i>		
	Load (kg ha ⁻¹)	0.011	0.018	0.011	0.013	0.012	0.013	0.018	0.10	0.015	0.21
	% Annual Load	5.04	8.52	5.37	6.24	5.82	6.02	8.34	47.47	7.19	
	FWAC Ratio	12.36	0.84	0.33	0.45	0.29	0.27	1.21	11.54	1.32	
ON	FWAC (mg L ⁻¹)	7.42	1.87	1.62	1.77	1.59	1.18	1.41	2.83	1.36	1.60
					<i>1.66</i>		<i>1.23</i>		<i>1.99</i>		
	Load (kg ha ⁻¹)	0.04	0.24	0.33	0.31	0.40	0.33	0.12	0.15	0.09	2.01
	% Annual Load	1.89	11.89	16.62	15.40	19.80	16.52	6.02	7.25	4.61	
	FWAC Ratio	4.63	1.17	1.01	1.10	0.99	0.73	0.88	1.76	0.84	

Table 3.1. (continued)

PO ₄ ³⁻ -P	FWAC (mg L ⁻¹)	0.020	0.029	0.016	0.006	0.010	0.009	0.008	0.028	0.026	0.013
					<i>0.008</i>		<i>0.009</i>		<i>0.027</i>		
	Load (kg ha ⁻¹)	0.0001	0.0037	0.0032	0.0011	0.0024	0.0025	0.0006	0.0014	0.0018	0.017
	% Annual Load	0.59	22.07	19.16	6.37	14.24	14.76	3.84	8.49	10.49	
	FWAC Ratio	1.45	2.17	1.17	0.46	0.71	0.65	0.56	2.06	1.92	
TP	FWAC (mg L ⁻¹)	0.27	0.12	0.12	0.13	0.075	0.028	0.043	0.15	0.10	0.087
					<i>0.10</i>		<i>0.03</i>		<i>0.12</i>		
	Load (kg ha ⁻¹)	0.001	0.016	0.025	0.022	0.019	0.008	0.004	0.008	0.007	0.11
	% Annual Load	1.28	14.27	22.95	20.38	17.34	7.17	3.40	7.13	6.09	
	FWAC Ratio	3.14	1.40	1.40	1.46	0.87	0.32	0.49	1.73	1.12	
TSS	FWAC (mg L ⁻¹)	64.77	17.82	70.05	137.52	65.37	20.22	32.21	56.62	37.22	57.02
					<i>95.01</i>		<i>23.02</i>		<i>45.56</i>		
	Load (kg ha ⁻¹)	0.33	2.27	14.41	24.08	16.42	5.72	2.78	2.92	2.55	71.47
	% Annual Load	0.46	3.18	20.17	33.69	22.97	8.00	3.89	4.08	3.56	
	FWAC Ratio	1.14	0.31	1.23	2.41	1.15	0.35	0.56	0.99	0.65	
DOC	FWAC (mg L ⁻¹)	119.33	22.76	16.25	21.41	24.62	27.97	28.38	15.91	15.73	23.16
					<i>23.30</i>		<i>28.06</i>		<i>15.81</i>		
	Load (kg ha ⁻¹)	0.61	2.90	3.34	3.75	6.18	7.91	2.45	0.82	1.08	29.04
	% Annual Load	2.10	10.00	11.52	12.91	21.29	27.23	8.43	2.82	3.71	
	FWAC Ratio	5.15	0.98	0.70	0.92	1.06	1.21	1.23	0.69	0.68	
DIC	FWAC (mg L ⁻¹)	5.07	4.61	2.46	3.20	1.22	0.85	1.03	5.36	4.04	2.29
					<i>2.03</i>		<i>0.89</i>		<i>4.61</i>		
	Load (kg ha ⁻¹)	0.026	0.59	0.51	0.56	0.31	0.24	0.089	0.28	0.28	2.87
	% Annual Load	0.90	20.52	17.65	19.53	10.67	8.36	3.09	9.63	9.64	
	FWAC Ratio	2.22	2.02	1.08	1.40	0.53	0.37	0.45	2.34	1.77	

Table 3.1. (continued)

Cl ⁻	FWAC (mg L ⁻¹)	11.19	11.24	10.56	13.62	12.48	13.79	13.84	12.82	17.37	12.86
					<i>12.95</i>		<i>13.80</i>		<i>15.41</i>		
	Load (kg ha ⁻¹)	0.06	1.43	2.17	2.38	3.13	3.90	1.19	0.66	1.19	16.12
	% Annual Load	0.35	8.89	13.47	14.79	19.44	24.18	7.40	4.10	7.37	
	FWAC Ratio	0.87	0.87	0.82	1.06	0.97	1.07	1.08	1.00	1.35	
pH	FWAC (mg L ⁻¹)*	5.78	6.76	6.77	6.67	5.54	4.82	5.11	6.89	7.05	5.97
					<i>6.01</i>		<i>4.89</i>		<i>6.98</i>		

[†]Totals exclude the period occurring from December 13th - December 17th when water quality data were not available.

*Representative concentration units (mg L⁻¹)

Nitrogen Double Cumulative Loading Curves

The nitrate curve exhibited arguably the clearest definable loading patterns among all water quality parameters considered in this study (Figure 3.7). Phase 1 was asymptotic in shape following the five events resulting from hurricanes and their aftermath occurring at the end of the hottest and driest months (lowest water tables in Figure 3.2). The active flow period ranging from mid-December to the end of April was segmented into three mostly linear phases where individual event dynamics were barely visible, although concentrations did vary with flow (e.g., Figure 3.4). Phase 5 began in mid-May, marking the regeneration of flow following a dry period occurring at the end of the active flow period and was accompanied by the highest flow weighted average concentrations of the year (> 16 mg N/L). This phase was correlated with the 6 hydrological events in the months of May and June and was somewhat asymptotic especially during the 5b subphase.

Several questions arise: why did the shapes of the cumulative nitrate load curve change from asymptotic to linear after phase 1, and back to asymptotic in phase 5b, and what might have caused the breakpoints? In reality, these questions apply to all 10 parameters for which continuous data was available. It was challenging to summarize the information brought from these 10 double mass curves into a coherent ensemble. We chose to present the results phase by phase rather than parameter by parameter, although we had recourse to this approach at times. In particular, the chloride and hydronium double mass curves give important general hydrological context. Double mass curve shapes and FWAC for each phase are summarized into Table 3.2.

In addition to the asymptotic  and linear  shapes suggested above, additional shapes appeared, most often a combination of these. An upward trend  was observed in several

cases. This suggested an apparent increased carrying capacity and/or increased stock of a source.

For DIC, a logistic curve  was observable as a combination of an apparent exhaustion of the source followed by an apparent net increase in DIC source. Because the phases were defined from the nitrate cumulative curve, a general curve over a given phase sometimes appeared as a

clear succession of asymptotic phases . Upward  and downward  'boomerang' shapes also appear and corresponded to consecutive linear shapes within a phase. 'Lightning'

shapes  were also observable in response to water release from controlled drainage and

beaver dams. Finally, a 'wrench' shape  resulting from the combination of a linear and asymptotic shape was observed for ammonium in phase 4.

Table 3.2. Summary of double mass curves shape and Flow Weighted Average Concentration (FWAC) for each 5 phases identified and the 10 parameters.

	Phase 1		Phase 2		Phase 3		Phase 4		Phase 5		Annual
	Shape	FWAC	Shape	FWAC	Shape	FWAC	Shape	FWAC	Shape	FWAC	
NO ₃ ⁻ -N		2.65		7.77		5.50		2.15		16.60	5.64
NH ₄ ⁺ -N		0.14		0.06		0.06		.08		0.96	0.17
ON		1.87		1.62		1.66		1.23		1.99	1.60
PO ₄ ³⁻ -P		0.029		0.016		0.008		0.009		0.027	0.013
TP		0.12		0.12		0.10		0.03		0.12	0.087
TSS		17.82		70.05		95.01		23.02		45.56	57.02
DOC		22.76		16.25		23.30		28.06		15.81	23.16
DIC		4.61		2.46		2.03		0.89		4.61	2.29
Cl ⁻		11.24		10.56		12.95		13.80		15.41	12.86

Table 3.2. (continued)

pH		6.76		6.77		6.01		4.89		6.98	5.97
----	--	------	--	------	--	------	--	------	--	------	------

Water table near the surface is associated with relatively low chloride export

Chloride is generally considered a non-reactive parameter. It was thus expected that its export would generally be linear with that of water volume. Observations showed, compared to the annual FWAC, the FWAC for the first two phases were lower (13% and 18%, respectively; Table 3.2), similar for phase 3, and higher (6% and 16%, respectively) for phase 4 and 5.

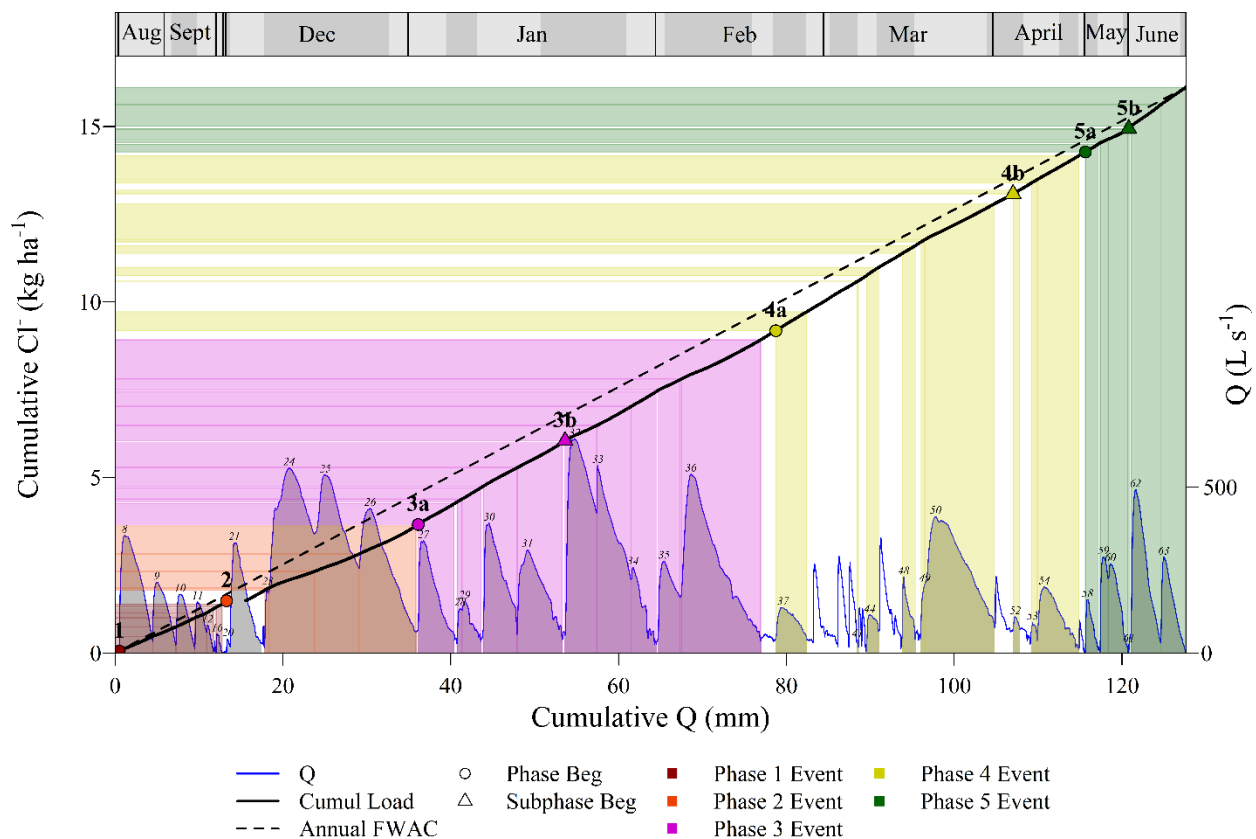


Figure 3.8. Cumulative chloride load export as a function of cumulative discharge for July 1998 – June 1999 at the A1 subcatchment outlet.

The low FWAC for phases 1 and 2, occurred while the water table was within 20 cm of the surface for a majority of the time. The upward trend clearly visible in phase 2 suggests that as

water table fell below the top 20 cm of the upper horizon, the chloride concentrations increased. This suggests that the soil drainage pattern and/or the leachable chloride stock in the upper soil horizon was lower than when the water table was below 20 cm depth. Chloride export pattern thus gives a physical indication of where the water table was located during the year.

Double mass hydronium curve reveals significant flow contribution from forested area during phase 4

The pH double mass plot reveals that 75% of the hydronium annual load occurred during phase 4, with no significant hydronium export during phases 1, 2, and 5 (Figure 3.9). During phase 4, pH was regularly around 4, signature of the very significant contribution of water from the forested areas. Until pH decreased below 5, the hydronium concentration being in log scale, the hydronium curve did not show any significant export, although pH did decrease below 6 during events 30 to 36, signifying that water from forest areas did participate to flow but not very significantly during phase 3. At most other times, pH was at or above 7, signature of contribution of agricultural limed fields to flow. Given these two contexts of the origin of water depending on land use, and on the location of the water table, it is possible to draw the big picture on the drivers of nutrient and material export in this watershed in 1998-99.

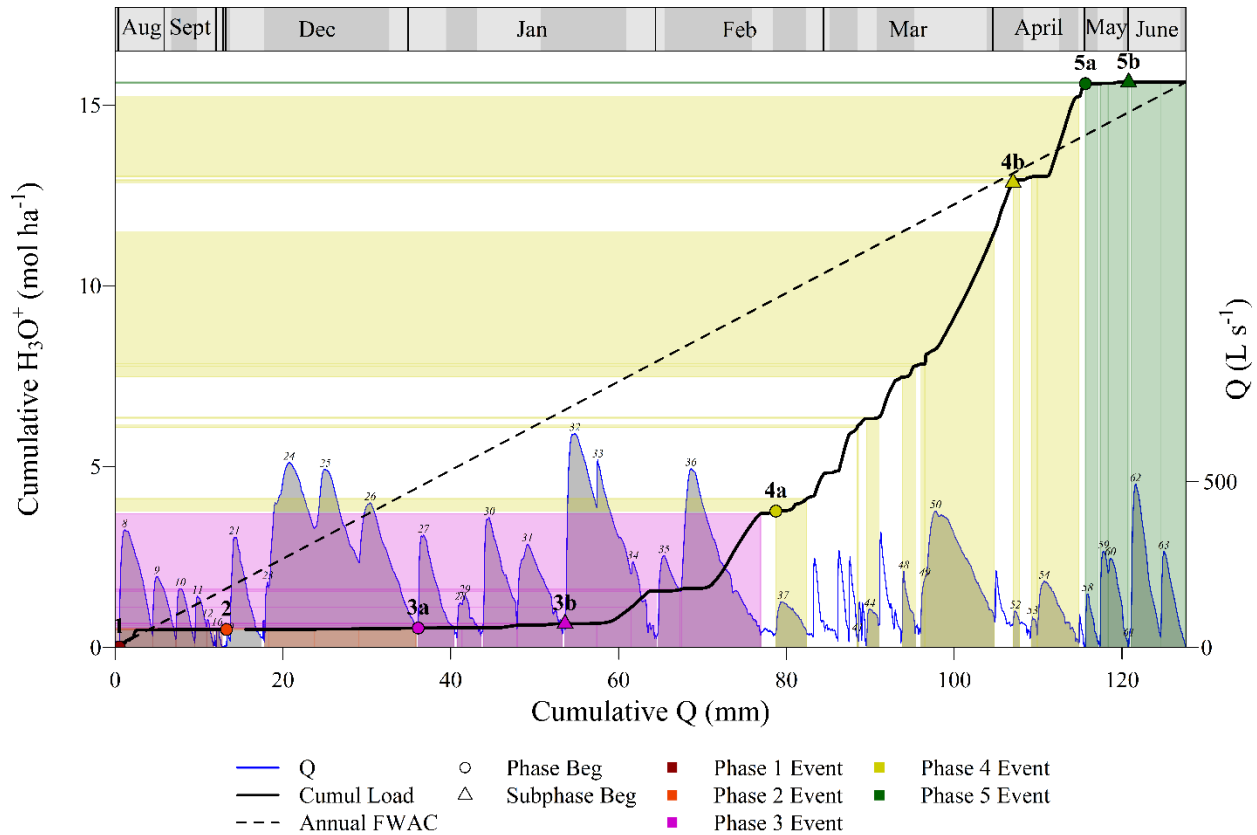


Figure 3.9. Cumulative hydronium load export as a function of cumulative discharge for July 1998 – June 1999 at the A1 subcatchment outlet.

Phase 1 drivers: subsurface flow associated with high water table following hurricanes and isolated storms

Phase 1 starts at the end of August 1998 after two months of hot and dry summer months (water temperature $>25^{\circ}C$ and 20 mm in total) when the water table fell below 1.2 m (bottom of the P2 well) and 1.5 m (bottom of the F6 well), and drainage ditches and canals were essentially dry except for few puddles left. Starting August 28, 1998, hurricane Bonnie (event 8) brought 120 mm of rainfall in less than 30 hours, for a total of 180 mm in two weeks when adding the ensuing events (30 mm for hurricane Earl, event 10). It took 60 mm of hurricane Bonnie's

rainfall for flow to start. Water table reached the surface twice during phase 1 and was within the top 20 cm of the surface a majority of the time (Figure 3.2). The flushing of ammonium, ON, and DOC that had accumulated in the puddles of the drainage canals is visible and characterized by a sharp but very short lived increase in the double mass respective curves (Figure 3.10, Figure 3.11 and Figure 3.12). The ensuing export of ammonium is characterized by an upward trend, that of ON by an upward trend followed by a linear trend, and that of DOC by a linear trend overall (Figure 3.10, Figure 3.11, Figure 3.12, and Table 3.2). We shall see that these reduced compounds are associated with dilution effects during all these events, suggesting that concentrations increased as flow decreased. We hypothesize that this is the signature of a significant contribution of reduced compounds from sediment diagenetic processes to the water column.

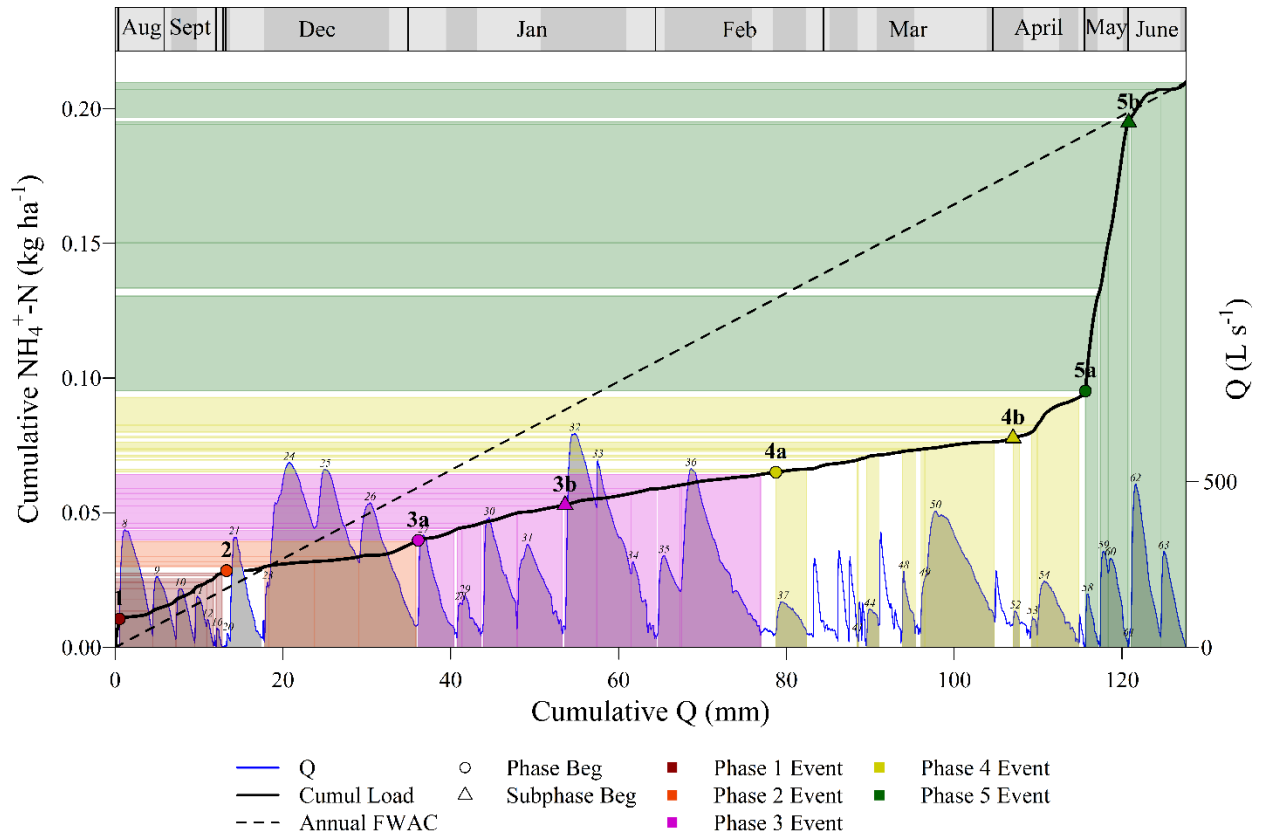


Figure 3.10. Cumulative ammonium load export as a function of cumulative discharge for July 1998 – June 1999 at the A1 subcatchment outlet.

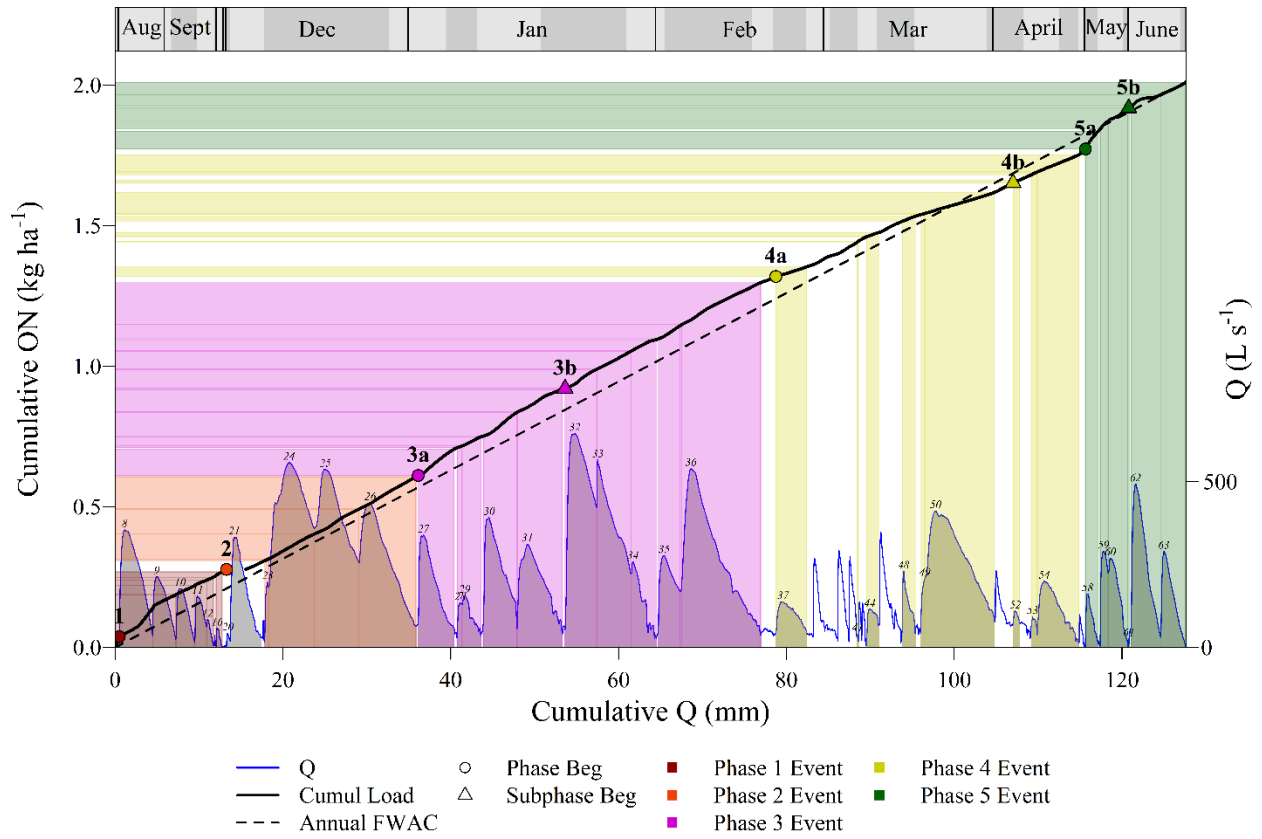


Figure 3.11. Cumulative organic nitrogen load export as a function of cumulative discharge for July 1998 – June 1999 at the A1 subcatchment outlet.

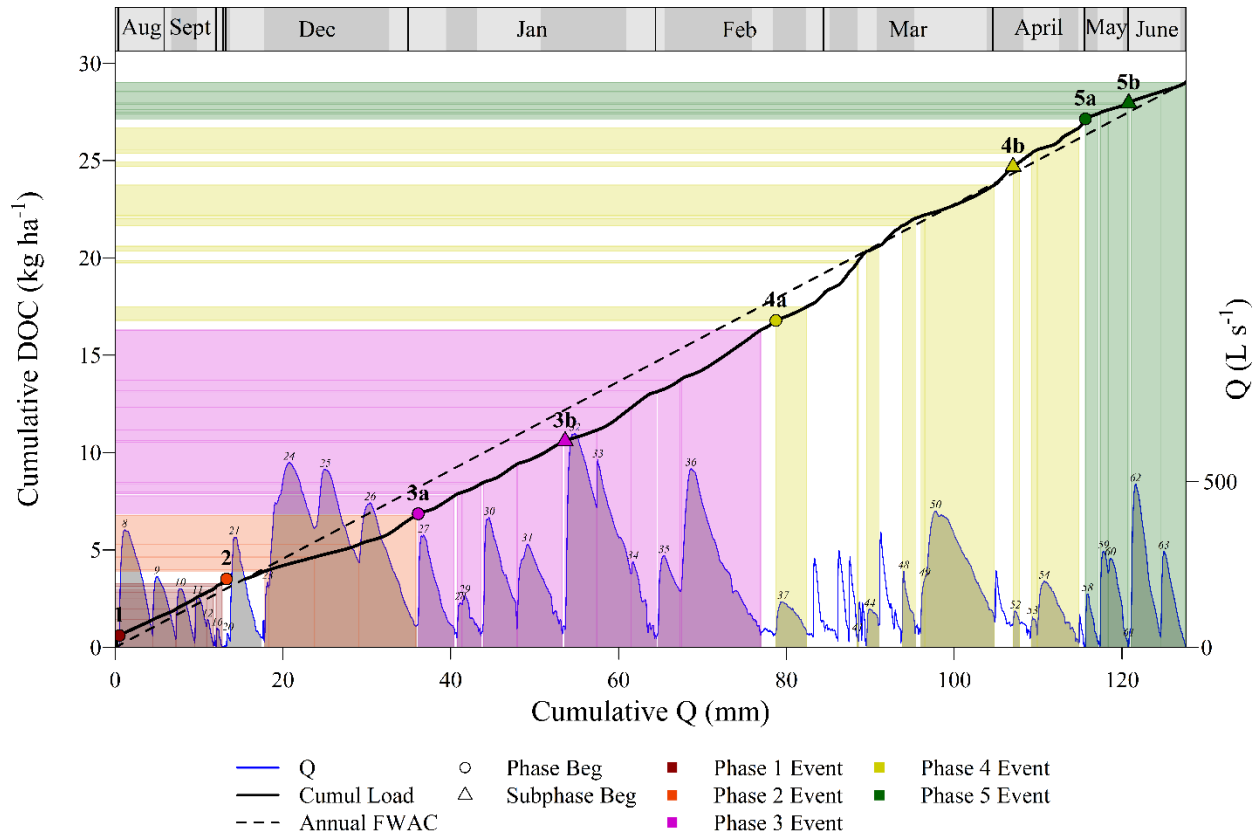


Figure 3.12. Cumulative dissolved organic carbon load export as a function of cumulative discharge for July 1998 – June 1999 at the A1 subcatchment outlet.

Contrary to what could have been surmised because of the hurricanes, the TSS load during this phase accounted for less than 5% of the annual load, showed a linear trend over the phase, and the FWAC was the lowest at 17.8 mg/L, a value three times lower than the annual FWAC of 57 mg/L, and much lower than what was measured in upland watersheds in Mississippi (Chapter 1). This is a strong indication that despite the amount and intensity of rainfall, surface runoff was not a significant contributor to flow. This can be attributed to the flatness of the watershed (for the low annual FWAC) and the presence of vegetation on the surface (crops not harvested then) which likely lowered the impact of rain drops to the ground and limited surface runoff

afterwards. Another factor was the possible filtration of particles out of the water column by the aquatic vegetation at that time.

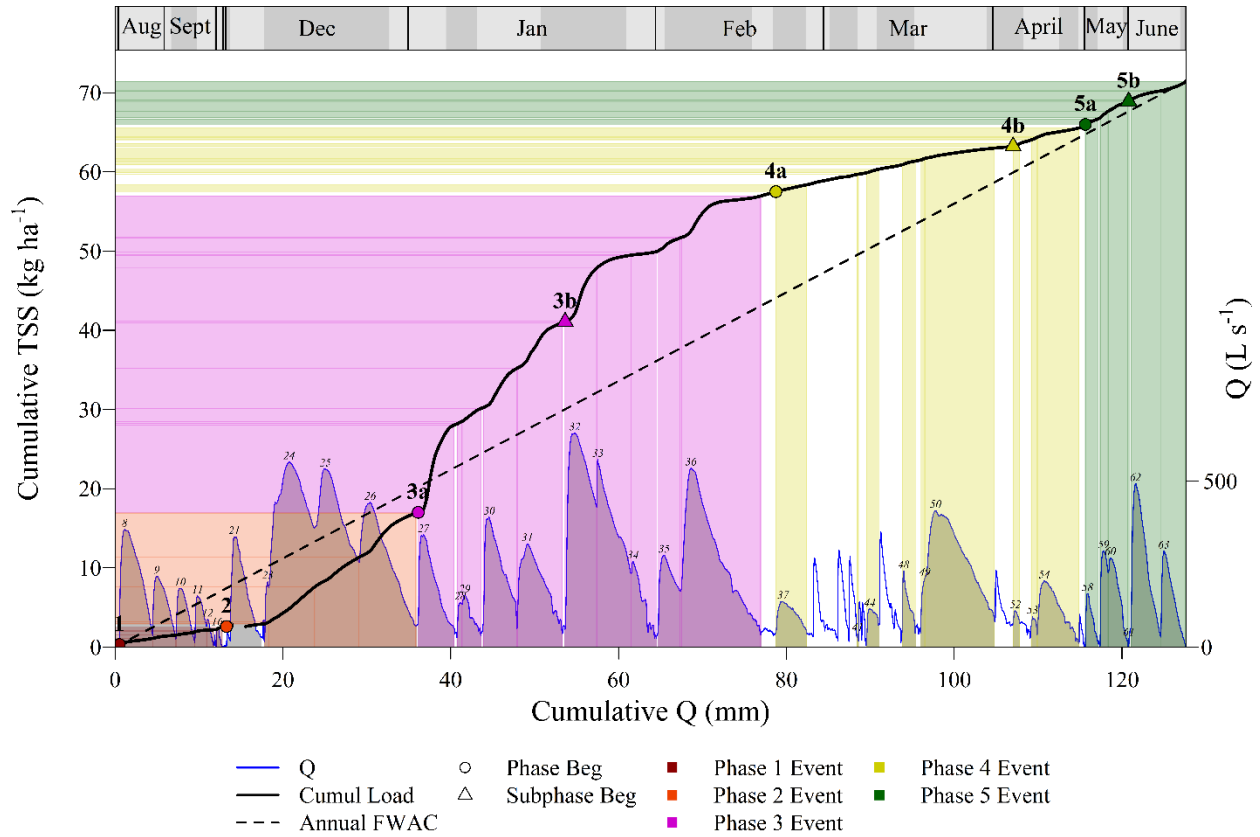


Figure 3.13. Cumulative total suspended solids load export as a function of cumulative discharge for July 1998 – June 1999 at the A1 subcatchment outlet.

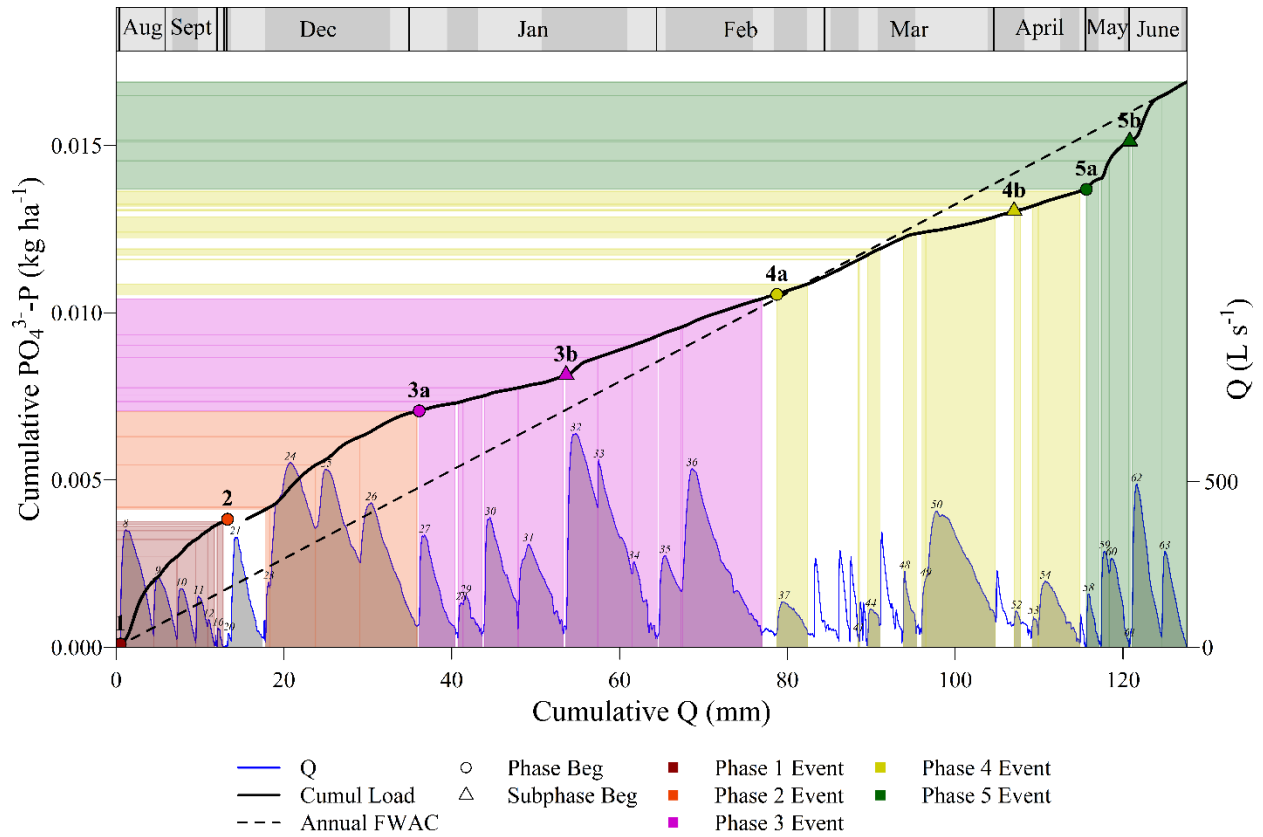


Figure 3.14. Cumulative phosphate load export as a function of cumulative discharge for July 1998 – June 1999 at the A1 subcatchment outlet.

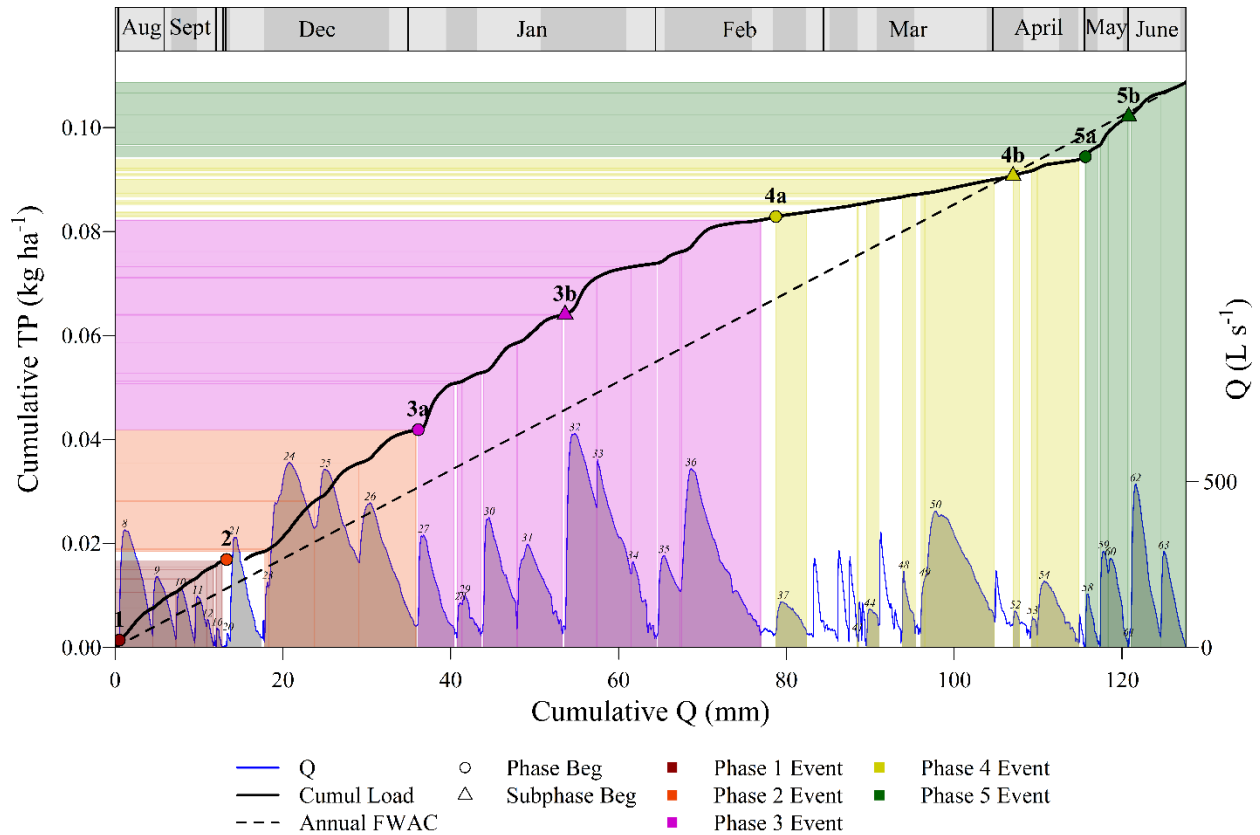


Figure 3.15. Cumulative total phosphorus load export as a function of cumulative discharge for July 1998 – June 1999 at the A1 subcatchment outlet.

The double mass curves showed a clear asymptotic shape over the phase for nitrate (Figure 3.7 and Table 3.2), phosphate (Figure 3.14 and Table 3.2), and TP (Figure 3.15 and Table 3.2). Twenty percent of the phosphate load occurred in 10% of the time, for the highest FWAC at 0.029 mg P/L. A similar phosphate export pattern occurred during the next phase, when the water table also was within the top 20 cm of the soil during long periods. The two suggest that the phosphate export in this watershed was associated/driven by very shallow subsurface flow associated with a high water table in the soil. The export of TP during phase 1 seems to be associated with the same mechanism. The asymptotic shape may be attributed to an exhaustion of the phosphate initial stock near the soil surface, to which one may add that the lowering of the

water table during events 11 to 16, likely prevented the leaching of this phosphate rich region of the soil. We propose a very similar interpretation for the asymptotic shape of the phosphate in phase 2.

The vast difference between the linear double mass nitrate curve in phase 2 compared to phase 1 suggests that nitrate export in these two phases had different drivers. The linear shape of nitrate in phase 2 suggests that the source of nitrate was apparently unlimited for the carrying capacity as the water table was near the surface. This was not true in phase 1 when an apparent ‘exhaustion’ of the nitrate source occurred. Because the physical drivers were similar as suggested by the phosphate curves, this suggests that there was a ‘nitrate quenching’ mechanism present during the hot summer days of phase 1 (water temperature $\sim 25^{\circ}\text{C}$; Figure 3.2), which were not nearly as significant in the much colder cold phase 2 (water temperature $\sim 10^{\circ}\text{C}$; Figure 3.2). Significant plant uptake from crops was unlikely at the end of the growing season. Aquatic plant uptake was possible at that time although Birgand (2000) estimated that it accounted for no more than 10% of the nitrate retention at the yearly scale. The quenching of nitrate export during phase one was thus more likely associated with processes like denitrification in the soil and in the hydraulic network.

The logistic DIC curve and the upward turn at the end of phase 1 may be attributed to the high pH values at 7.5, for which the majority of the DIC was expected to be in the bicarbonate form which prevented any form of CO_2 evasion.

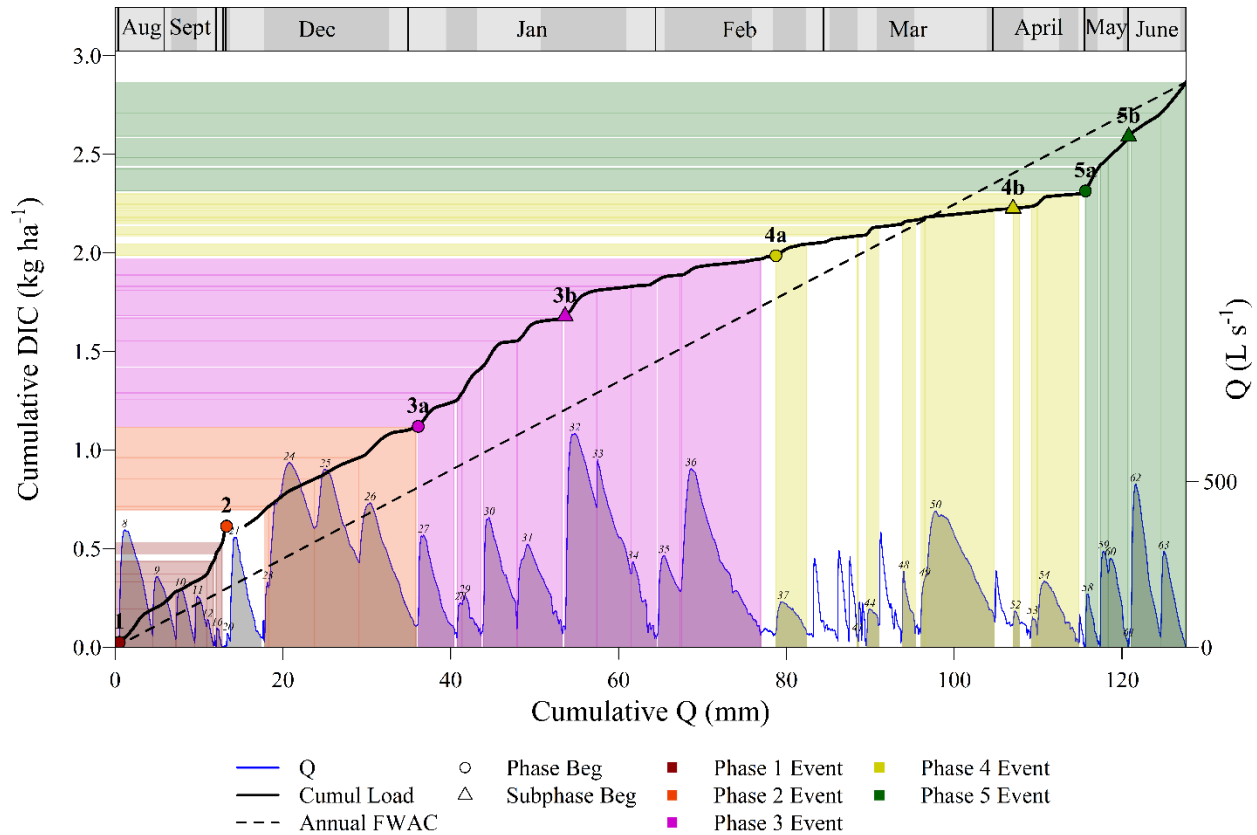


Figure 3.16. Cumulative dissolved inorganic carbon load export as a function of cumulative discharge for July 1998 – June 1999 at the A1 subcatchment outlet.

Phase 2: Intense drainage season starts with high nitrate and phosphate exports

After 2.5 months of dry weather, the intense drainage season started in late December 1998 with the week that contributed the highest to flow (16% of annual volume) and where the water table in the agricultural fields reached and stayed at the surface for the majority of that week. This resulted in relatively low chloride export and high phosphate export, the latter with an asymptotic shape (Figure 3.14 and Table 3.2), following the principles observed during phase 1. Nitrate FWAC during this phase (7.8 mg N/L) was the highest outside of the fertilization season of phase 5. The nitrate double mass curve (Figure 3.7 and Table 3.2) exhibited a linear pattern, although nitrate concentrations showed dilution patterns (see below) during events 24 to 26.

With a similarly high water table and physical driving factor as in phase 1, the difference in the export pattern between nitrate and phosphate is striking. The quenching nitrate mechanism observable during phase 1 was not significant, suggesting that nitrate retention due to denitrification did not have nearly the same impact on nitrate export. We hypothesize that nitrate concentrations were relatively homogeneous in the soil profile and that the export was not associated with the depth of the water table, as was the case for phosphate.

This phase was characterized by a higher export of TSS with FWAC of 70 mg/L, higher than the annual value of 57 mg/L. This might be associated with the lack of vegetation at this time of the year and possible instances of surface runoff when water reached the soil surface. The TP FWAC was the same as during the previous phase suggesting that most TP was associated with the same upper water table export process present during phase 1, when the overall shape of the double mass curve was a succession of asymptotic curves associated with a strong concentration effect during events (details below). The upward boomerang curves for ammonium and DOC (Figure 3.10, Figure 3.12, and Table 3.2), suggest that as flow rates decreased at the end of phase 2, the release of ammonium and DOC from the sediment became relatively significant. Had most ON export been associated with the diagenetic processes, the ON double mass curve would have followed the same shape, but it had a linear shape instead. This suggests that early during phase 2, ON export might also have been linked to particles. The export for DIC exhibited a succession of asymptotic curves associated with a 'pH concentration effect' during events.

Surface drainage as a likely key driver for processes during phase 3

To limit the residence time of the water table near the surface at the onset of the growing season, farmers in this part of the world tend to create small gullies increasing what is referred to as surface drainage. We hypothesize that the large increase in the TSS and TP export (highest TSS FWAC at 154 mg/L and TP FWAC at 0.14 mg P/L during phase 3a) was due to surface drainage. The ammonium curve exhibited an asymptotic shape, suggesting a different source of ammonium than during the previous two phases, and in accord with surface runoff. The overall rate of ON export increased compared to the previous phase, although generally remained linear. A mix of concentration and dilution effects observed suggested the dual impact of particle bound organic nitrogen and the dissolved ON associated with diagenesis in sediment. Phosphate exports were the lowest in phase 3 (FWAC at 0.008 mg P/L) and characterized by a linear pattern except at the beginning of event 32 when water table reached the surface, hence the overall ‘lightning’ shape over phase 3. Nitrate export was also linear although markedly smaller than during the previous phase and slightly above (5.9 mg N/L during phase 3a) the overall annual FWAC (5.6 mg N/L). We hypothesize that the breakpoint in the nitrate double mass curve between phases 2 and 3 can be attributed to a shift from mostly subsurface driven flow in phases 1 and 2, to a 77-23% subsurface-surface runoff in phase 3a, the ratio calculated as the ratio between the FWAC in phases 2 and 3a. Starting with event 32, the DIC double cumulative curve general trend flattened (Figure 3.16), corresponding to a lowering of pH below 6.5 with dips lower than 4.5 at the end of events 33 and 36. These generated significant hydronium loads, resulting from and indicative of significant addition of water from the forested areas during phase 3b. This tended to further ‘dilute’ the nitrate concentration during phase 3b on par with that of the annual FWAC. The ‘dilution’ by forested fields water in phase 3b was observable for

TSS, TP, ON, ammonium, and nitrate. To the contrary, phosphate and DOC exports appeared to have been stimulated by the arrival of more acidic forested waters during phase 3b. The decrease of the chloride FWAC during phase 3b suggests that the 30% increase in phosphate FWAC between phases 3a and 3b was likely due to the water table reaching the surface during events 32 and 36 (Figure 3.2). We hypothesize that the 10% increase of the DOC FWAC between phases 3a and 3b was due to the expected higher DOC concentrations from forested areas.

Significance of water from forested areas and release of water trapped behind beaver dams as key drivers to phase 4

After event 36 at the end of the first week of February 1999, water table in the agricultural field dropped down between 40 and 60 cm below the surface (Figure 3.2), not far from the effective drain depth, while the water table in the forested field was only lowered by 10 cm below its highest level. As a result, there was a drastic change in the makeshift of water at the onset of phase 4, from ag dominated to forest dominated waters, where the pH stayed mostly around 4, accounting for most of the cumulative hydronium load over the year. This resulted in an overall ‘flattening’ of all the curves similar to the one described in the previous 3b phase for TSS, TP, and nitrate. The relative increase of the chloride FWAC to 13.8 mg /L above the annual average (12.9 mg/L) is indicative of the contribution of water from the lower part of the soil profile, at least from the ag fields.

This phase was also characterized by the removal of beaver dams that created non rainfall events accounting for a third of the flow volume of this phase (Figure 3.2). These were associated with

'lightning' shape or 'inverted boomerang' double mass curves where the concentrations tended to either increase or decrease during these 'beaver dam' events. During these events, the double mass curves for phosphate, DOC, and ON (and marginally ammonium) increased, suggesting that the reduced conditions that prevailed upstream these dams were conducive to producing reducing C and N compounds, which was expected. Reversely the nitrate concentrations relatively decreased during these beaver dam events and increased during rain driven events (e.g., event 50; Figure 3.7), which suggests that beaver dams tended to provide conditions for nitrate retention. The lowest DIC FWAC of 0.9 mg C/L was measured during phase 4 resulting from the very low pH (~4), which likely favored CO₂ evasion from the water, although the contribution of higher pH waters from the ag fields resulted in a series of 'bumps'.

Flow from and fertilization on agricultural fields during the growing season as key drivers of phase 5

The level of the water table below the weir threshold in the forested field, the sudden increase in the DIC load curve (highest DIC FWAC at 5 mg C/L), and the pH at 7 and higher, all concur to suggest that the contribution of forested water was minimal or non-existent starting from the end of April into the growing season. After a nearly two-week drought in May 1999 at the end of phase 4, flow during this phase was associated with two twin-events separated by nearly two weeks that occurred in May (phase 5a) and June (phase 5b), and that brought water table to the surface. This phase was characterized by extremely high nitrate FWAC (19.2 mg N/L and 14.5 mg N/L, in phases 5a and 5b, respectively), ammonium FWAC (1.9 mg N/L in phase 5a), and the largest export of ON (FWAC at 2.8 mg N/L) during phase 5a. The sudden increase of the FWAC for nitrate, ammonium, and ON suggests a large new source of nitrogen in general. We

hypothesize that this corresponded to ammo-nitrate fertilization applied on ag fields upstream of the A1 station sometime during the dry spell in early May 1999. The small increment in the ammonium loading curve during phase 5b compared to phase 5a suggests that the ammonium added in May had been largely nitrified and/or uptaken by crops between the May and June events. The asymptotic shape of the nitrate (and ammonium curve) suggests a 'source exhaustion' pattern already observed during phase 1. The large addition of nitrogen fertilizer was designed to eventually be taken up by crops, which could explain in part the exhaustion of the nitrate source. Water temperature reached 20°C at this time of the year and could have stimulated denitrification mechanisms and aquatic plant uptake at this time of the year. In fact, Birgand (2000) found that the highest in stream nitrate retention occurred at this time of the year. The largest chloride FWAC over phase 5b reaching 17 mg/L while the water table reached the surface suggests that chlorinated products (e.g., pesticides) had likely been added onto crops between phase 5a and 5b.

The TSS FWAC at about 50 mg /L, lower than the annual FWAC suggests that surface runoff was not a significant driver during phase 5. The large TP and phosphate FWAC over this phase were likely associated with the water table reaching the soil surface, similarly to what occurred during phases 1 and 2, although it is unclear whether fertilization had anything to do with the export of P. The DOC FWAC during phase 5 were the lowest of the year at 15.8 mg C/L, close to the ones observed during phase 2 when the water table in the field reached the surface and may be indicative of low residence time of water in the canals and ditches.

Event Hysteresis indicators provide valuable information given a hydrochemical context

The tools to quantify the C-Q hysteresis during events have been recently proposed and even more recently widely adopted by the scientific community (reviewed by Burns et al., 2019). These tools are well designed to quantify ‘textbook’ patterns (e.g., Heahwaite and Bierzo, 2020) when hydrographs and chemographs are ‘simple’ and these situations existed in our watershed as illustrated in Figure 3.17.

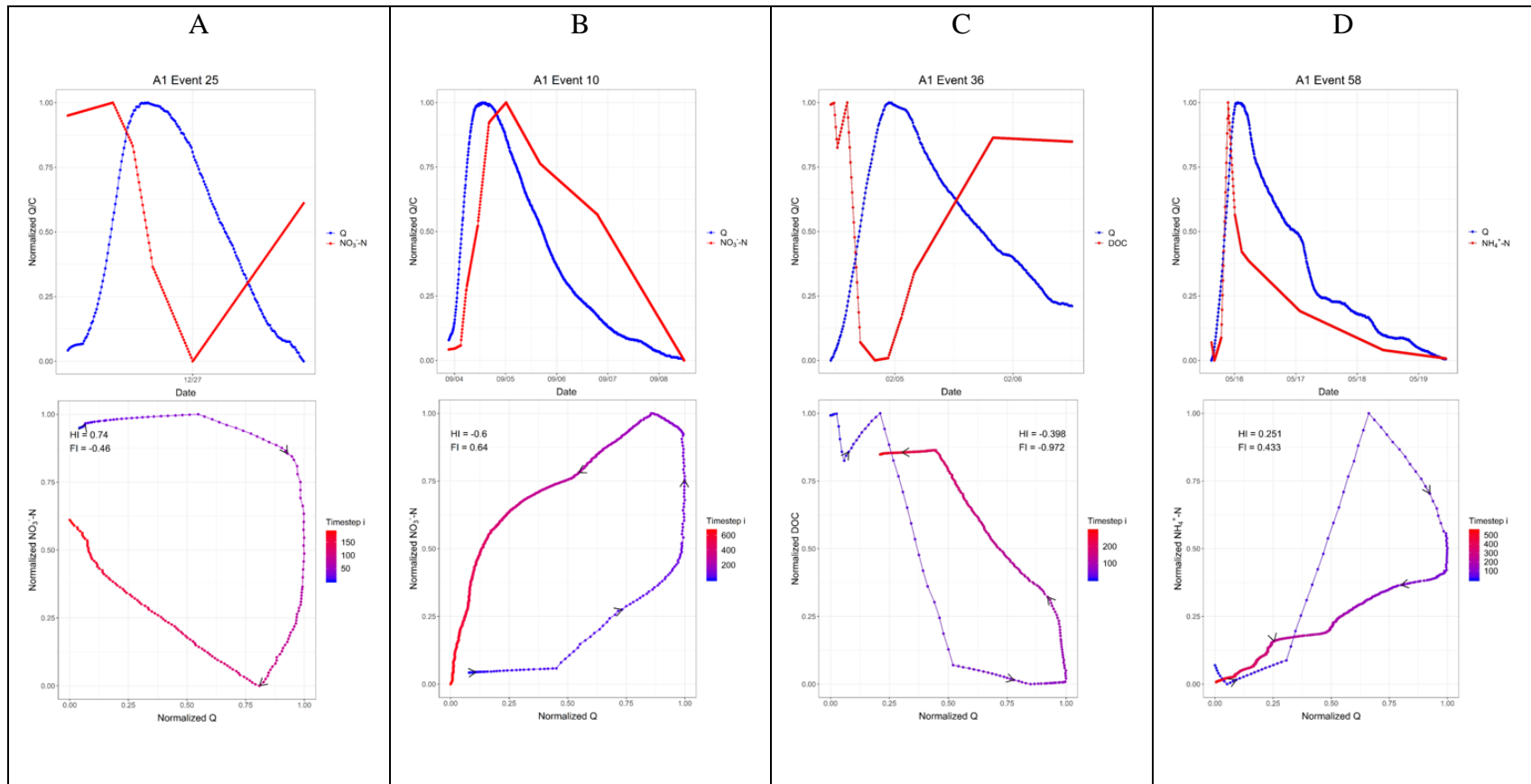


Figure 3.17. Examples of hydrographs and chemographs showing A) dilution effect ($FI < 0$) and the chemograph lagging (clockwise, $HI > 0$) after the flow peak (event 25, NO_3-N), B) concentration effect ($FI > 0$) and the chemograph lagging (anticlockwise, $HI < 0$) after the flow peak (event 10, NO_3-N), C) dilution effect ($FI < 0$) and the chemograph leading (anticlockwise, $HI < 0$) before the flow peak (event 36, NO_3-N) and D) concentration effect ($FI > 0$) and the chemograph leading (clockwise, $HI > 0$) before the flow peak (event 58, NH_4-N).

However, hysteresis patterns for some events and species did not present as easily definable loops, but this is a common problem reported in the literature (e.g., Heathwaite and Bierzoza, 2020; Burns et al., 2019; Lloyd et al., 2016). Some loops presented a Figure 8 shape or even crossed more than twice which was indicative of how quickly and frequently concentrations could fluctuate during any given event. Concentrations could change in response to a rise in flow and never reverse on the falling limb of the hydrograph and vice versa. Multi-peak events existed as well, some due to multiple rainfall events but some due to a rainfall event followed by a release of water from a breached beaver dam. Typically, these storm peaks were treated as individual storms, but a few had dynamics resembling a single storm and were analyzed as such. Multi-peak or multi-trough concentration dynamics sometimes existed within the same event as well. Some loops were left wide open creating a partial C shape or resemblance of a hook. These sometimes depended upon the location of the start and end of an event within the hydrograph and related to the sluggish nature of drainage patterns in the subcatchment between rainfall events.

Hysteresis patterns were closely examined for each event and water quality constituent and only results that were considered to present clear enough patterns were considered reliable for hysteresis and flushing indices value discussion. Multi-peak events were sometimes given one hysteresis value if the concentration dynamics of peaks did not show unique dynamics, but sometimes were still used because separate peaks did not have sufficient matching normalized flow values on the rising and falling limbs. Additionally, the shapes of some of the hysteresis loops were jagged due to the nature in which the time series data were interpolated between field measurements. Discharge on the falling limbs of a few events were noticeably noisy which

could have been due to beaver dam interference. These irregularities could have affected magnitudes of hysteresis and flushing indices although these indices were still considered valuable for relative comparison among event dynamics when available and the sign of the hysteresis index is meant to reflect the weighted average of the flow intervals existing in the clockwise and anti-clockwise portions of the loop. In theory, calculating the sign of the HI would at least provide information regarding the dominant pattern, if one exists, within a complex loop.

The literature has suggested ways to use the HI and FI indices to interpret some of the interplay between the hydrological and biogeochemical processes. The literature (e.g., Heathwaite and Bieroza, 2020; Burns et al., 2019; Vaughan et al., 2017; Lloyd et al., 2016) states that positive values of HI (clockwise responses) associated with a concentration or flushing effect be an indication of mobilization of a readily available source of solutes or particulates (e.g., resuspension of particles from stream sediments) and/or their delivery along relatively short pathways (e.g., from the hyporheic and near stream zones; Bernhardt et al., 2017). The literature also suggests that negative values of HI (anticlockwise responses) also associated with concentration or flushing effect be an indication that the source be more distant, or of delayed mobilization, and/or of longer delivery pathways (e.g., from isolated locations in the catchment or along subsurface flow pathways; Bieroza & Heathwaite, 2015).

The FI defines a concentration change between preceding and during the storm event, and therefore reflects differences in concentrations between old, pre-event water and new storm event water. Positive values of FI (concentration or flushing effect) indicate that the event peak

is accompanied by higher concentrations or becomes enriched in concentrations of a given solute or particulate by flushing surface or shallow subsurface flow pathways near the stream for example, in the riparian zone. Negative values of FI (dilution effect) indicate that storm water dilutes higher concentrations of the pre-event water for example, derived from groundwater flows, hyporheic zone or deeper subsurface flow pathways (Heathwaite and Bieroza, 2020). The sign of the FI indicator is rather univocal, but that of HI is not. For example, positive HI value when FI is positive (flushing) suggests that the peak of concentration occurred before or ‘led’ the flow peak, and the associated processes described above apply. However, in the case of a dilution effect (FI negative), the concentration trough occurring ahead or ‘leading’ the flow peak corresponds to negative HI values (Figure 3.17). In other words, when the product $HI \times FI$ is positive, the concentration peak or trough ‘led’ the flow peak, and when the product $HI \times FI$ is negative, the concentration peak or trough ‘lagged’ behind the flow peak. For this reason, we propose to use ‘lead’ and ‘lag’ on the HI vs FI plots, in hope to ease the visualization of the relative placement of the concentration peaks/trough compared to the flow peak.

A relatively small number of events exhibiting unusual patterns

Recent articles report the computation of HI and FI of over a hundred to several hundred events (Vaughan et al., 2017; Kincaid et al., 2020; Heathwaite and Bieroza, 2020), on a selected few parameters. In these cases, it is possible to calculate population statistics on the HI and FI values for each parameter, but this comes at the cost of having each event treated ‘anonymously’, although events have been sorted per season at times (e.g., Kincaid et al., 2020). In our case, HI and FI values were extracted from only ~27 events (ranged slightly depending on parameter evaluated), but on 8 parameters (yielding over 200 HI and FI values) covering the major C, N,

and P forms, in addition to suspended material and pH. While the population statistics cannot be nearly as strong because of the small number of events, it is possible to analyze the data almost event by event, and certainly phase by phase, hence use of the hydrochemical context for analysis. HI vs FI values are plotted in Figure 3.18 and Figure 3.19 and reported in Table 3.3.

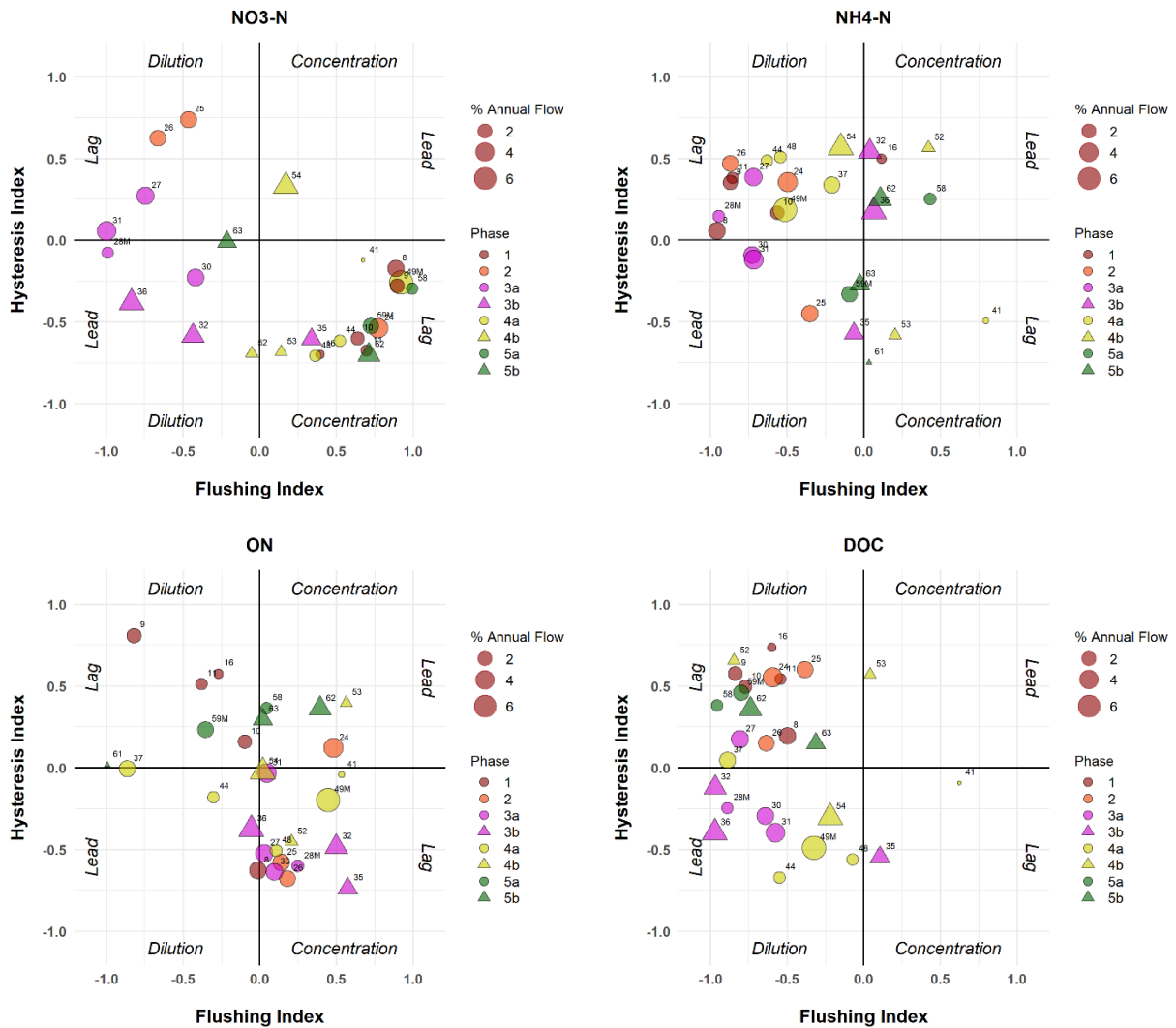


Figure 3.18. Hysteresis index plotted as a function of flushing index values for nitrate (NO₃-N), ammonium (NH₄-N), organic nitrogen (ON), and dissolved organic carbon (DOC). The color and symbol correspond with the identified double mass curve phase in which the event occurred. Sizes of points are scaled to reflect percent annual flow contributed by the event. Labels indicate event number and a letter “M” indicates a multi-peaked event treated as a singular event.

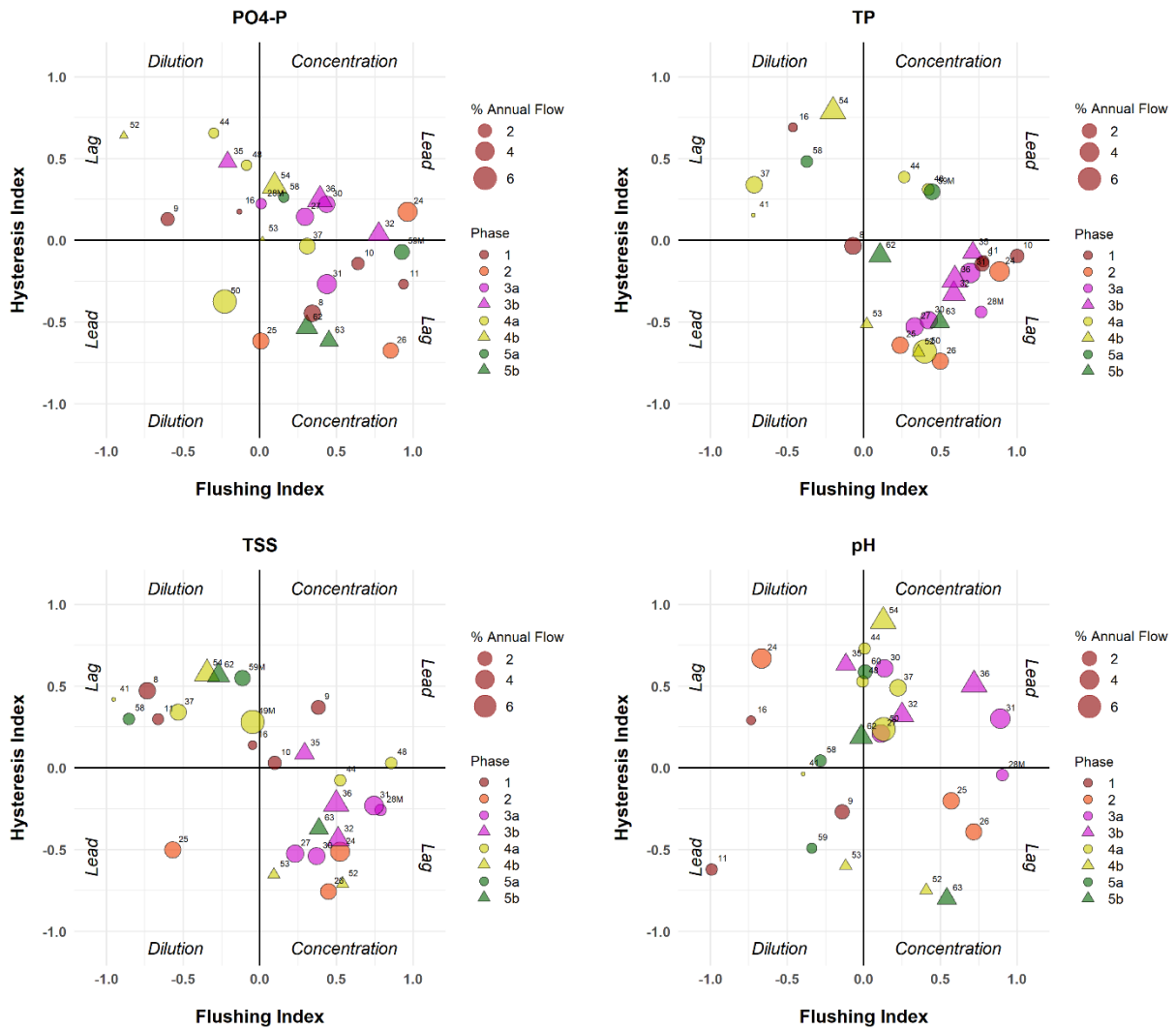


Figure 3.19. Hysteresis index plotted as a function of flushing index values for phosphate (PO₄-P), total phosphorus (TP), total suspended solids (TSS), and pH. The color and symbol correspond with the identified double mass curve phase in which the event occurred. Sizes of points are scaled to reflect percent annual flow contributed by the event. Labels indicate event number and a letter “M” indicates a multi-peak event treated as a singular event.

Overall, parameters thought to generally be associated with particulates exhibited a majority of flushing patterns (ON, Phosphate, TP, TSS; Figure 3.18, Figure 3.19, and Table 3.3; Kincaid et al., 2020). Ammonium is also usually associated with surface runoff as it adsorbs to particles and is expected to exhibit concentration patterns. In our watershed, however, dilution patterns were observed most often (Figure 3.18 and Table 3.3). Concentration effects did occur, however at the end of phase 4 and during phase 5, following expectations. Similarly, DOC export pattern in most upland watersheds usually exhibits concentration patterns (e.g., Vaughan et al., 2017) as the increase in concentrations is thought to correspond to the carbon rich near stream and riparian zone leached first during events. To the contrary in our watershed, DOC most often exhibited a dilution pattern (Figure 3.18 and Table 3.3). Finally, in most agriculture impacted watersheds, nitrate dynamics are reported to generally exhibit a dilution pattern (Vaughan et al., 2017; Kincaid et al., 2020; Heathwaite and Bierzoza, 2020), while in our watershed, the opposite was true (Figure 3.18 and Table 3.3).

Table 3.3. Flushing vs dilution patterns observed for 8 parameters. The text in bold is to highlight the majority of flushing vs. dilution effects. The number of patterns per phase appears as flushing/dilution.

Parameter	Overall		Phases				
	Flushing	Dilution	Phase 1	Phase 2	Phase 3	Phase 4	Phase 5
NO ₃ ⁻ -N	16	10	5/0	1/2	1/6	6/1	3/1
NH ₄ ⁺ -N	9	18	1/4	0/3	1/5	3/5	3/2
ON	18	10	0/5	3/0	5/1	6/2	3/2
PO ₄ ³⁻ -P	19	7	3/2	3/0	6/1	3/4	4/0
TP	21	6	3/2	3/0	7/0	5/3	3/1
TSS	16	11	2/3	2/1	7/0	4/4	1/3
DOC	3	24	0/5	0/3	1/6	2/6	0/4
pH	15	11	0/3	2/1	6/1	5/3	1/3

Event hysteresis indices provide further evidence of very active denitrification and sediment diagenetic processes

Taken in context, the prevalence of dilution patterns for ammonium and DOC, although astray from expectations and patterns reported in the literature, carry important information. The FI indices provide quantitative measure that, in this flat watershed where riparian zones do not exist and therefore are not a factor, it is the diagenetic processes in the very organic sediment that significantly contributed to the ammonium and DOC water column concentrations. Birgand (2000) has shown that the upward flux of ammonium and DOC from the sediment in the water column did not occur in pulses but was rather constant throughout the year. New water draining from the soil profile appeared less concentrated, hence the dilution effect quantified by the FI indices. One could also expect that the same sediment processes could have produced upward fluxes of organic nitrogen and phosphate and therefore dilution effects as well. The data show that phosphate exhibited mostly flushing effects, instead (details below).

Thirty percent (ON) and over 40% (TP, TSS) of the events showed dilution effects. Taken in context, these correspond to high ON and TP concentrations (but also DOC and ammonium) that accumulated at the end of extremely low flow periods, possibly the result of bioturbation from insects, fish, and turtles, and which were diluted by new water. These observations correspond to the ones already made using the cumulative flux duration curves where it was concluded that during these times, the sediment diagenetic processes were disproportionately active (compared to flow).

Possibly the most striking pattern was that of nitrate where most events from phases 1, 4 and 5 exhibited concentration patterns, while most of those of phase 2 and 3 exhibited dilution patterns. All events of phase 1 (hurricane driven) exhibited decreasing concentrations during the falling limbs of the hydrographs, and sharp increase of concentration during the rising limbs. This suggests that while water table was within the top 30 cm of the soil, there was a very strong nitrate ‘producing’ mechanism in the soil, very likely the result of mineralization processes that occurred before and during the wetting and drying cycles associated with the sequence of events (e.g., Beare et al., 2009; Boroken and Matzner, 2009; Miller et al., 2005; Palmer et al., 2016; Xiang et al., 2008). However, this nitrate source was accompanied by a very strong ‘quenching’ mechanism, very likely denitrification in the soil as the water table receded. The first event of phase 2 (event 24) also exhibited a very strong concentration effect in late December, but it was not followed by concentration decrease observed during phase 1. The water table during phase 2 and almost all of phase 3 events stayed at high levels, even during low flow, suggesting that the strong nitrate quenching mechanism during the colder periods was likely weaker, and in all cases was overwhelmed by the nitrate producing mechanisms.

Nitrate dilution in upland agricultural watersheds has usually been attributed to surface runoff and/or the early contribution of nitrate diluted shallow groundwater from riparian areas and hyporheic zones (e.g., Heathwaite and Bierozza, 2020; Burns et al., 2019; Lloyd et al., 2016). In this flat artificially drained watershed, there are no riparian zones. If anything, the near ditch or near canal areas tend to have lower water table than at midpoint between ditches and are therefore more aerobic where denitrification would be inhibited. Research on the near drain/ditch hydraulics (Liu et al., 2020; Paris-Anguela, 2004; Skaggs, pers. com.) suggests that

because of the steep hydraulic gradients in the near drain zone, there is a disproportionately high volume of water that leaches the soil profile near the drains. The stock of leachable nitrate in this zone is thus expected to be exhausted before the rest of the profile. We propose that the early stages of an event correspond to the leaching of water in the near ditch/drain zone, for which the leachable nitrate source was comparatively limited, and in which water had little time to reside in the soil. Water coming from further away from the drain would have had higher residence time to accumulate the leachable source of nitrate (e.g., Liu et al., 2020), yielding higher nitrate concentrations, which, in absence of a powerful nitrate removal process, would explain the nitrate concentration increase during the falling limbs of the hydrographs observed during phases 2 and 3. We propose these mechanisms to be the explanation for the dilution effect observed during events of phases 2 and 3.

The HI values, quantifying the magnitude of the hysteresis pattern but also the lag of the concentration peaks, suggest an increasing lag of the nitrate concentration peak as the events follow one another in phase 1. Birgand (2000) showed that plug flow existed in the watershed drainage canals, and this could explain an increasing lag with an increasing volume to be ‘pushed’ at the beginning of the next event. However, the increasing lag observed for nitrate during phase 1 (Figure 3.18), was not accompanied with a corresponding lag in TP (Figure 3.19). This suggests that the water ‘pushed’ by the next event became relatively diluted in nitrate, which suggests that in-stream processes did participate in the nitrate quenching mechanism, in addition to the one in the soil. In-stream nitrate quenching was expected during the hot summer months.

Less obvious, the HI values during phase 3 during a lot cooler periods, show that the dilution of nitrate did occur a lot earlier than the lag of the TP concentration effect (event 27). This could be interpreted by a source of TP located further away than the nitrate source. However, the source of TP was thought to be mostly surface runoff, which would have occurred at least as fast, if not faster than the subsurface flow diluted in nitrate. Plug flow was obviously a factor in phase 3, and the dilution of nitrate occurring earlier than the concentration of TP, suggests that water that had resided in the canals and pushed by new water had been stripped of nitrate and/or diluted by hyporheic waters. The comparison between the HI indices of TP versus those of nitrate revealed this mechanism and HI was the only indicator able to point this out. This corresponds to observations in Birgand (2000) where in stream nitrate removal was found to occur even during winter months.

Shortcomings of the HI and FI indices analyzed out of context

The case of the HI vs FI for phosphate is symptomatic of the shortcomings of restricting the hydrochemical analysis of a watershed to these indices only. About a third of the events gave negative FI values or dilution. The inspection, point by point of each of these events reveals that the negative FI values correspond to very small events where one concentration value in the chemograph yielded the algorithm to give a value opposite to the one the eye would have given. Similarly, about a third of the points in the HI vs FI plots for phosphate suggested that the concentration peak occurred before the flow peak. For all these events, the concentration peak was hardly visible at all, and the positive HI values were not indicative of a phosphate peak before the flow peak. However, during phases 1 and 2, all events showed a clear concentration pattern, which accounted for most of the phosphate export throughout the year. Analysis of the

phosphate HI vs FI plot out of context, would suggest an unrealistic pattern because each point is given the same weight, and statistics would not differentiate between this or that event. In reality, two thirds of the points in our case did not give a particular indication of the driving factors for phosphate export and source. The double mass source analysis did suggest that the phosphate source was likely the top 20 cm of the soil. It also showed that the diagenetic processes were the likely reason for the increase of the phosphate during beaver dam releases, something the HI and FI indices were unable to do.

3.5 Discussion and conclusions

The current revolution at play in hydrochemical research emanates from the widespread availability of continuous water quality sensors, which hydrologists, biogeochemists, ecohydrologists, and stream ecologists, to name a few, have all embraced (e.g., Burns et al., 2019; Bernhardt et al., 2017; Hensley et al., 2017, 2015; Rode et al., 2016; Cohen et al., 2013, 2012; Heffernan and Cohen, 2010). All have intuitively presupposed that behind the continuous hydrographs and chemographs lied locked information for which the proper keys would unveil new knowledge.

Quantitative hydrologists have derived their own keys of understanding for their need for a long time in the form of indicators such as flashiness indices (Baker et al. 2004), flow return periods, or flow duration curves (Searcy, 1959). All communities in search of qualifying and quantifying “the stream hydrochemical regime and the interplay between hydrological and biogeochemical processes” (Heathwaite and Bieroza, 2020) have embraced the hysteresis indices originally proposed by Butturini et al. (2008) and Lloyd et al. (2016). To the point that Heathwaite and

Bieroza (2020) suggested that much of “the stream hydrochemical regime and the interplay between hydrological and biogeochemical processes are encapsulated in the concentration-discharge (c-q) relationship”.

We hypothesized that the indicators of the C-Q relationships belonged to the toolbox for qualifying and quantifying the interplay between hydrological and biogeochemical processes, but that these should likely be accompanied with other indicators, particularly cumulative and integrative ones to give a broader view. For that we proposed to use annual statistics of flow, concentrations and loads, cumulative flux duration indicators, double mass curves and C-Q relationship indicators.

The annual indicators such as the runoff coefficient, average concentrations and loads gave the context of a very flat artificially drained watershed, where flow was intermittent. They also brought the information on the hydrochemical context: Hydrology was dominated by artificial drainage associated with high water table (within 1.2 m of the surface most of the time). High concentrations of reduced nitrogen (ON and ammonium) and carbon concentrations hinted on the high organic matter content of the soils and sediment, and the likely biogeochemical processes associated. The wide range of pH suggested the importance of the interplay between waters from agricultural and forested areas.

The cumulative flux duration indicators gave the relative importance of the events on flow and showed that there was not deep groundwater fed baseflow: more than 98% of the flow volume occurred in about 50% of the time. The hydrological reactivity of this watershed was found to be

small for its size, as it was similar with those of watersheds 100 times larger. The $Mw_{k\%}$ and $W_{k\%}$ values for the highest k values revealed a powerful flow quenching mechanism where evapotranspiration likely played a very important role. This was accompanied by the relatively important release of reduced compounds and material likely associated with faunal bioturbation of the sediments at low flow. These two sets of indicators thus provided the annual flow and concentration context.

To our knowledge, the double mass curve indicators as described in this article are new. The different shapes of the curves and the phases have not been reported before. The double mass curve approach allowed to go beyond the traditional division of seasonality. It is possible that that three specificities of this watershed were instrumental in the appearance of rather clear phases: its relatively small size (15 km²), the absence of baseflow, and two distinct land uses and associated concentrations and pH. The hydrochemical signature of most upland watersheds tends to be reset by the transport through and the processes occurring in the riparian or near stream zone, which overwhelm the signal from the upland areas (e.g., Vaughan et al., 2017). In our watershed, this was not a factor, and the interplay between the water table and soil processes was detectable. Threshold driven hydrology, and much lower pH, nitrogen, and phosphorus concentrations from the forested areas, powerfully changed the export patterns and the appearance of phases.

The identification of the phases and of the shapes associated are admittedly subjective, yet they provided a coherent framework to compare export processes, the likely sources of nutrients and material, and how they evolved throughout the year. This approach forced the finding of likely

reasons for the presence of breakpoints, sudden and progressive changes in the FWAC and the shapes of the curves. Access to 10 water quality parameters, in addition to continuous flow and water table data, was certainly key to draw a coherent hydrochemical signature of this watershed. We contend that it was the double mass curve analysis that provided most of the information on the interplay between hydrological and biogeochemical processes in this watershed.

The C-Q relationship analysis did provide additional information on the in-stream denitrification processes at play in winter months, and on the role of the near drain zone, to which the double mass curve analysis was blind. For the first case, this was unveiled thanks to the comparative analysis of the difference in HI indices between TP and nitrate. For the latter, it was fine hydraulic information from the literature that helped explain the observations from the HI and FI indices. The global analysis of the HI and FI indices did reveal that the patterns observed were drastically different from those reported in more upland watersheds (e.g., Heathwaite and Bierzoza, 2020; Vaughan et al., 2017; Lloyd et al., 2016) but could not reveal by itself the reasons for the difference. We also showed that the HI vs FI analysis treated all events evenly, possibly blurring the analysis and not highlighting interesting trends. The sampling technique to obtain this pseudo continuous dataset did not allow for the detection of diel patterns as others have (e.g., Bernhardt et al., 2017; Hensley et al., 2017, 2015; Cohen et al., 2013, 2012). This might have emphasized the shortcomings of the C-Q analysis.

Overall, this article suggests that the ‘key’ to unveiling the interplay between hydrological and biogeochemical processes is probably more like a key chain. Some indicators will likely unveil more processes while some will highlight others. This is somewhat disappointing as ‘a one size

fits all' would be highly recognized and praised, but it also highlights the robustness of cumulative indicators which help keep the focus on soil and in-stream hydrological processes as the main drivers of hydrochemical signature of nutrient export.

3.6 Acknowledgements

Logistical and financial support for the data set used in this work was provided by Weyerhaeuser NR Company. Additional research funds were provided by the North Carolina Water Resources Research Institute (WRRRI Project No. 50321), the USEPA 319 program (Project No. EW9024), and the USDA-NCREES/NRICGP (Project No. 98-35102-6493).

3.7 References

- Baker, D. B., Richards, R. P., Loftus, T. T., & Kramer, J. W. (2004). A new flashiness index: Characteristics and applications to midwestern rivers and streams. *Journal of the American Water Resources Association*, 40(2), 503-522. doi:10.1111/j.1752-1688.2004.tb01046.x
- Beare, M. H., Gregorich, E. G., & St-Georges, P. (2009). Compaction effects on CO₂ and N₂O production during drying and rewetting of soil. *Soil Biology and Biochemistry*, 41(3), 611-621.
- Bieroza, M. Z., & Heathwaite, A. L. (2015). Seasonal variation in phosphorus concentration–discharge hysteresis inferred from high-frequency in situ monitoring. *Journal of Hydrology*, 524, 333-347.
- Birgand, F., (2000). *Quantification and Modeling of In-Stream Processes in Agricultural canals of the lower coastal plain, North Carolina, USA*. (Doctoral dissertation, North Carolina State University, Raleigh, NC, USA). Retrieved from <http://www.lib.ncsu.edu/resolver/1840.16/5233>
- Birgand, F., Faucheux, C., Gruau, G., Augéard, B., Moatar, F., & Bordenave, P. (2010). Uncertainties in assessing annual nitrate loads and concentration indicators: Part 1. impact of sampling frequency and load estimation algorithms. *Transactions of the ASABE*, 53(2), 437-446.
- Birgand, F., Lellouche, G., & Appelboom, T. W. (2013). Measuring flow in non-ideal conditions for short-term projects: Uncertainties associated with the use of stage-discharge rating curves. *Journal of Hydrology*, 503, 186-195. doi:<https://doi.org/10.1016/j.jhydrol.2013.09.007>
- Borken, W., & Matzner, E. (2009). Reappraisal of drying and wetting effects on C and N mineralization and fluxes in soils. *Global Change Biology*, 15(4), 808-824.
- Brown, R. A., Birgand, F., & Hunt, W. F. (2013). Analysis of consecutive events for nutrient and sediment treatment in field-monitored bioretention cells. *Water, Air, & Soil Pollution*, 224(6), 1-14.
- Burns, D. A., Pellerin, B. A., Miller, M. P., Capel, P. D., Tesoriero, A. J., & Duncan, J. M. (2019). Monitoring the riverine pulse: Applying high-frequency nitrate data to advance integrative understanding of biogeochemical and hydrological processes. *Wiley Interdisciplinary Reviews: Water*, 6(4), e1348.
- Buttle, J. M., & Metcalfe, R. A. (2000). Boreal forest disturbance and streamflow response, northeastern Ontario. *Canadian Journal of Fisheries and Aquatic Sciences*, 57(S2), 5-18.
- Butturini, A., Alvarez, M., Bernal, S., Vazquez, E., & Sabater, F. (2008). Diversity and temporal sequences of forms of DOC and NO₃-discharge responses in an intermittent stream:

- Predictable or random succession? *Journal of Geophysical Research: Biogeosciences*, 113(G3)
- Chescheir, G. M., Lebo, M. E., Amatya, D. M., Hughes, J., Gilliam, J. W., Skaggs, R. W., & Herrmann, R. B. (2003). Hydrology and water quality of forested lands in eastern North Carolina. Paper presented at the 2003 ASAE Annual Meeting, 1.
- Cohen, M. J., Heffernan, J. B., Albertin, A., & Martin, J. B. (2012). Inference of riverine nitrogen processing from longitudinal and diel variation in dual nitrate isotopes. *Journal of Geophysical Research: Biogeosciences*, 117(G1)
- Cohen, M. J., Kurz, M. J., Heffernan, J. B., Martin, J. B., Douglass, R. L., Foster, C. R., & Thomas, R. G. (2013). Diel phosphorus variation and the stoichiometry of ecosystem metabolism in a large spring-fed river. *Ecological Monographs*, 83(2), 155-176.
- Dingman, S.L., 2002. *Physical Hydrology*. 2nd ed. Upper Saddle River, NJ: Prentice-Hall Inc.
- Dubreuil, P., (1974). *Initiation à l'analyse hydrologique*. Masson & Cie, Éditeurs et ORSTOM.
- Gao, P., Mu, X., Wang, F., & Li, R. (2011). Changes in streamflow and sediment discharge and the response to human activities in the middle reaches of the yellow river. *Hydrology and Earth System Sciences*, 15(1), 1-10.
- Heathwaite, A. L., & Bieroza, M. (2021). Fingerprinting hydrological and biogeochemical drivers of freshwater quality. *Hydrological Processes*, 35(1), e13973.
doi:<https://doi.org/10.1002/hyp.13973>
- Heffernan, J. B., & Cohen, M. J. (2010). Direct and indirect coupling of primary production and diel nitrate dynamics in a subtropical spring-fed river. *Limnology and Oceanography*, 55(2), 677-688.
- Hensley, R. T., McLaughlin, D. L., Cohen, M. J., & Decker, P. H. (2017). Stream phosphorus dynamics of minimally impacted coastal plain watersheds. *Hydrological Processes*, 31(8), 1636-1649. doi:<https://doi.org/10.1002/hyp.11132>
- Hensley, R. T., Cohen, M. J., & Korhnak, L. V. (2015). Hydraulic effects on nitrogen removal in a tidal spring-fed river. *Water Resources Research*, 51(3), 1443-1456.
- ISO 15769: (2010). Hydrometry – guidelines for the application of acoustic velocity meters using the Doppler and echo correlation methods.
- Kincaid, D. W., Seybold, E. C., Adair, E. C., Bowden, W. B., Perdrial, J. N., Vaughan, M. C., & Schroth, A. W. (2020). Land use and season influence Event-Scale nitrate and soluble reactive phosphorus exports and export stoichiometry from headwater catchments. *Water Resources Research*, 56(10), e2020WR027361.

- Lin, C., (2017). *Characterization of the Solute Dynamics Signature of an Agricultural Coastal Plain Stream, North Carolina, USA*. (Doctoral dissertation, North Carolina State University, Raleigh, NC, USA). Retrieved from <https://repository.lib.ncsu.edu/handle/1840.20/34568>
- Liu, W., Youssef, M. A., Birgand, F. P., Chescheir, G. M., Tian, S., & Maxwell, B. M. (2020). Processes and mechanisms controlling nitrate dynamics in an artificially drained field: Insights from high-frequency water quality measurements. *Agricultural Water Management*, 232, 106032.
- Lloyd, C., Freer, J. E., Johnes, P. J., & Collins, A. L. (2016). Using hysteresis analysis of high-resolution water quality monitoring data, including uncertainty, to infer controls on nutrient and sediment transfer in catchments. *Science of the Total Environment*, 543, 388-404.
- Mellander, P., Melland, A. R., Jordan, P., Wall, D. P., Murphy, P. N., & Shortle, G. (2012). Quantifying nutrient transfer pathways in agricultural catchments using high temporal resolution data. *Environmental Science & Policy*, 24, 44-57.
- Miller, A. E., Schimel, J. P., Meixner, T., Sickman, J. O., & Melack, J. M. (2005). Episodic rewetting enhances carbon and nitrogen release from chaparral soils. *Soil Biology and Biochemistry*, 37(12), 2195-2204.
- Moatar, F., & Meybeck, M. (2007). Riverine fluxes of pollutants: Towards predictions of uncertainties by flux duration indicators. *Comptes Rendus Geoscience*, 339(6), 367-382. doi:10.1016/j.crte.2007.05.001
- Palmer, K., Köpp, J., Gebauer, G., & Horn, M. A. (2016). Drying-rewetting and flooding impact denitrifier activity rather than community structure in a moderately acidic fen. *Frontiers in Microbiology*, 7, 727.
- Paris-Angueta, T., (2004). *Etude du transfert d'eau et de solutés dans un sol à nappe superficielle drainée artificiellement*. [Water and solute transfer in artificially drained soils.] (Ph.D. thesis, ENGREF (AgroParisTech), Paris, France). Retrieved from <https://tel.archives-ouvertes.fr/tel-00008704/document>
- Peu, P., Birgand, F., & Martinez, J. (2007). Long term fate of slurry derived nitrogen in soil: A case study with a macro-lysimeter experiment having received high loads of pig slurry (Solepur). *Bioresource Technology*, 98(17), 3228-3234. doi:<https://doi.org/10.1016/j.biortech.2006.07.019>
- Pirnia, A., Golshan, M., Darabi, H., Adamowski, J., & Rozbeh, S. (2019). Using the Mann–Kendall test and double mass curve method to explore stream flow changes in response to climate and human activities. *Journal of Water and Climate Change*, 10(4), 725-742.
- Rode, M., Wade, A. J., Cohen, M. J., Hensley, R. T., Bowes, M. J., Kirchner, J. W., . . . Jomaa, S. (2016). Sensors in the Stream: The High-Frequency Wave of the Present. *Environmental Science & Technology*, 50(19), 10297-10307. doi: 10.1021/acs.est.6b02155

- Searcy, J. K. (1959). *Flow-duration curves* US Government Printing Office.
- Searcy, J. K., & Hardison, C. H. (1960). *Double-mass curves* US Government Printing Office.
- Vaughan, M. C. H., Bowden, W. B., Shanley, J. B., Vermilyea, A., Sleeper, R., Gold, A. J., . . . Schroth, A. W. (2017). High-frequency dissolved organic carbon and nitrate measurements reveal differences in storm hysteresis and loading in relation to land cover and seasonality. *Water Resources Research*, *53*(7), 5345-5363. doi:<https://doi.org/10.1002/2017WR020491>
- Xiang, S., Doyle, A., Holden, P. A., & Schimel, J. P. (2008). Drying and rewetting effects on C and N mineralization and microbial activity in surface and subsurface California grassland soils. *Soil Biology and Biochemistry*, *40*(9), 2281-2289.
- Yao, Y., Cai, T., Wei, X., Zhang, M., & Ju, C. (2012). Effect of forest recovery on summer streamflow in small forested watersheds, northeastern china. *Hydrological Processes*, *26*(8), 1208-1214.

General Conclusion

There is dire need to investigate the robustness of indicators to quantify and identify patterns in high temporal resolution hydrology and water quality data to advance our understanding of and improve ability to characterize the effects of land use and management practices at the watershed scale. Additionally, the evaluation of these indicators relies heavily on the ability to produce reliable high temporal resolution data in the first place. Despite the increased availability and more wide-spread use of sensors to measure water quality data at frequencies on par with hydrology, we recognize that the process of collecting reliable data can be intensive and challenging to sustain, and that the use of this technology may still be limited by factors such as practicality associated with time, financial constraints, and site accessibility. Inadvertently, the sampling techniques used to monitor water quality data for each study in this dissertation differed and provided the opportunity to explore strengths and weaknesses of analyses methods and indicators associated with the collection of data produced from a range of sampling frequencies and data preparation. A unifying theme among studies was the demonstration of analyses to effectively detect changes in water quality.

In the first chapter, the challenge was to detect whether the establishment of switchgrass interplanted within young pine forests would have an effect on the hydrology and water quality. For this, we used a suite of hydrological indicators and water quality indicators. Most of the hydrology indicators quantified the ‘flashiness’ of these watersheds, including the Richard-Baker indicator, the flux duration indicator, the high pulse count, the high pulse duration, the rise and fall rates, and the number of positive and negative changes. These indicators were unable to provide obvious indication that treatments on the land had significant impact on the hydrology.

This might have been due in part to the inherent differences among watersheds prior to any treatment, but this is expected to be the case in most studies. The results suggest, rather, that the flashiness indicators chosen were sensitive to the inherent noise of the flow signal in these small watersheds. As a result, they did not appear to be robust enough to detect changes if there were any. To the contrary, the cumulative load indicators, either plotted as a function of cumulative volume, or as a function of cumulative load of the control watershed, were able to detect changes in water quality. We took the synchrony of these changes with actual site preparation activities as strong evidence that there were impacts due to the treatments.

In the second chapter, we focused our attention on the technical difficulties associated with obtaining high frequency data using UV-vis spectrophotometers in the field. It is not impossible that the situation we encountered was the worst possible with the presence of reduced radicals that had the tendency to precipitate on the optics, yielding seemingly unusable data. This forced us to strengthen our techniques to extract reliable data from absorption spectra. We have found that, outside nitrate for which there is strong absorbance around 232 nm, most other water quality parameters do not strongly absorb light at well identified wavelengths. As a result, current techniques aim at establishing a statistical relationship between the ‘color matrix’ of the water with the concentrations of concern. We found that following the rise of the water table to the soil surface, that the relationship changed in the forested, lowland artificially drained watershed. The change was sudden, but we hypothesize that in many watersheds there may be more gradual changes over time, for which the chemometric techniques used must adjust. We were able to provide guidelines on how to best produce local calibrations within the PLSR chemometrics approach.

In the third chapter, we observed that one type of indicators of the hydrochemical dynamics in watersheds, precisely two indicators of the hysteresis pattern that exists in the concentration-discharge (C-Q) relationship during events, had become very popular and proposed to be *the sole* type of indicator from which most of the interplay between the hydrological and biogeochemical processes could be extracted. These indicators are clearly derived one event at a time, and we hypothesized that they might suffer from the noisy nature of hydrological processes. For this we proposed a suite of indicators, rather than just one, as an analytical framework to characterize the hydrochemical signature in watersheds. These included concentration statistical indicators, flux duration curves, and double mass curve approaches. We found that each indicator had its own strength, but the one that gave the most information on the overall nutrient export patterns and biogeochemical processes was the double mass curve approach. The C-Q indicators were very useful, put back in context provided by the double mass curves.

Throughout this dissertation, the common pattern appeared to be that cumulative indicators provide more robust metrics than indicators derived at the event scale, although the latter are very useful, provided that they be put in context. Another important theme was that indicators in combination, whether they belonged to the same category or not, compiled and strengthened our ability to detect evidence of and draw conclusions about the processes and site characteristics controlling export of nutrients and sediment. In the upland watersheds in Mississippi, plotting cumulative load as a function of time indicated TSS export increased as an effect of site preparation activities, but the support provided by two additional cumulative indicators, cumulative load as a function of cumulative flow volume and as a function of load exported by the control watershed, provided supplemental evidence that the increase was not simply due to

one particularly large event. In the artificially drained watershed in Plymouth, North Carolina, supporting evidence of in-stream denitrification was first indicated by the water quality duration indicators and was supported by patterns observed in the double mass curves and C-Q dynamics. The methodological approach evaluating PLSR local calibration techniques provided an example of how even the process of producing reliable concentration data may provide evidence of a change of patterns in the composition or water color matrix of streams, and other indicators such as the double mass curve or hysteresis indices may aid in explaining what combination of processes may have caused it. These themes highlight the value of future research dedicated to developing and evaluating robust indicators to characterize hydrology and water quality at the watershed scale. This will lead to improvements in detection of change and patterns as they occur through time.

APPENDICES

APPENDIX A: 60-Day Moving Window Calibration Residuals

A.1 Prediction outside of 60-day calibration windows for models with 1-20 components

Our main goal was to examine if any trends in prediction of concentrations falling outside of the calibration window emerged depending upon placement of the window, therefore selection of the model with the number of components yielding the absolute minimum RMSEP value sufficed if the corresponding NSE was at least 0.65. To ensure that the number of components selected for each window model, and therefore goodness of fit, did not affect the prediction trends, a boxplot of the residuals was created. Residuals as a percentage resulting from predicted concentrations falling outside of the calibration window (validation) by models built with $ncomp_{rmsep}$ components were compared with those resulting from all possible model residuals (Figure A.1) for each window (i.e. set of residual values corresponding with validation predicted values resulting from calibration models built with 1-20 components for each window). The same general trends in the residuals could be observed for models consisting of 1-20 components and those with residuals resulting from models built with $ncomp_{rmsep}$ number of components (Figure A.2).

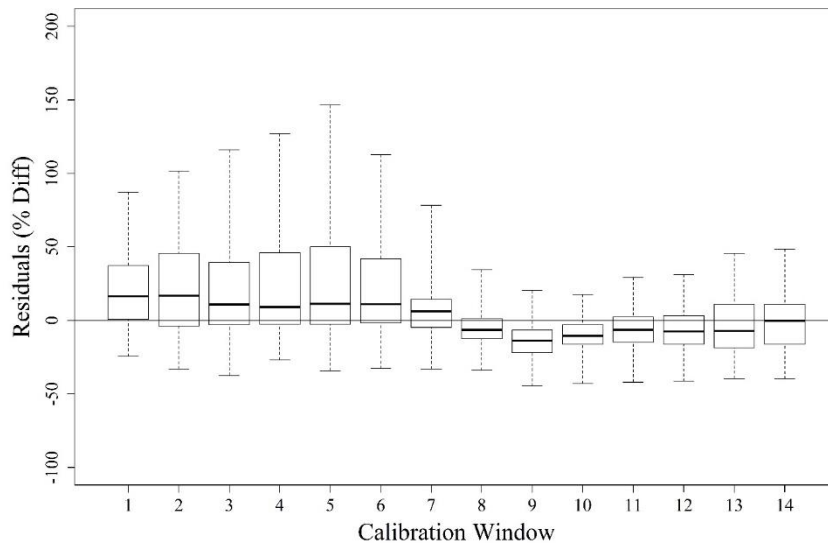


Figure A.1. Residuals plotted as a percent difference from observed concentrations for PLSR models composed of 1-20 components for each 60-day calibration window. Top and bottom box notches represent the 25th and 75th quartile, the middle black line represents the median, and whisker notches represent the minimum and maximum values in the data range.

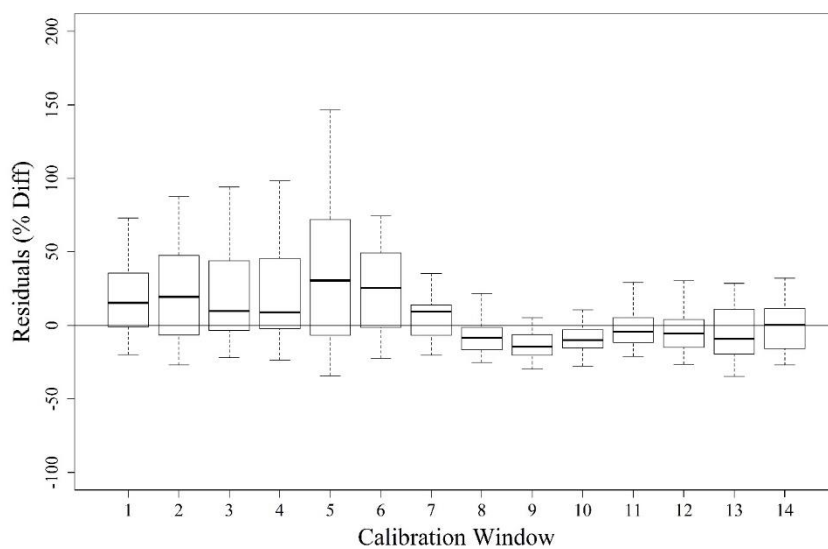


Figure A.2. Residuals plotted as a percent difference from observed concentrations for the PLSR model selected for each calibration window built with the number of components producing the absolute minimum RMSEP ($ncomp_{rmsep}$).

To further illustrate that trends in the validation data observed were not due to the number of components selected for the calibration model, the prediction data for models built with a range of number of components are presented for Windows 1 and 9. The trends in over-prediction of discrete sample concentrations falling outside of calibration Window 1 can be observed for models built with 1, 5, 10 and 20 components (Figure A.3). There are values that are under-predicted, but the over-predicted values tend to become more pronounced with additional components and greater values of NSE for the calibration dataset. This creates a flatter sloping trend associated with larger magnitude residuals per incremental change in measured value. There seems to be a cluster of samples that are the most sensitive to the addition of components, which could offer insight into variability in the water color-concentration relationship and/or where these samples fall in between service intervals.

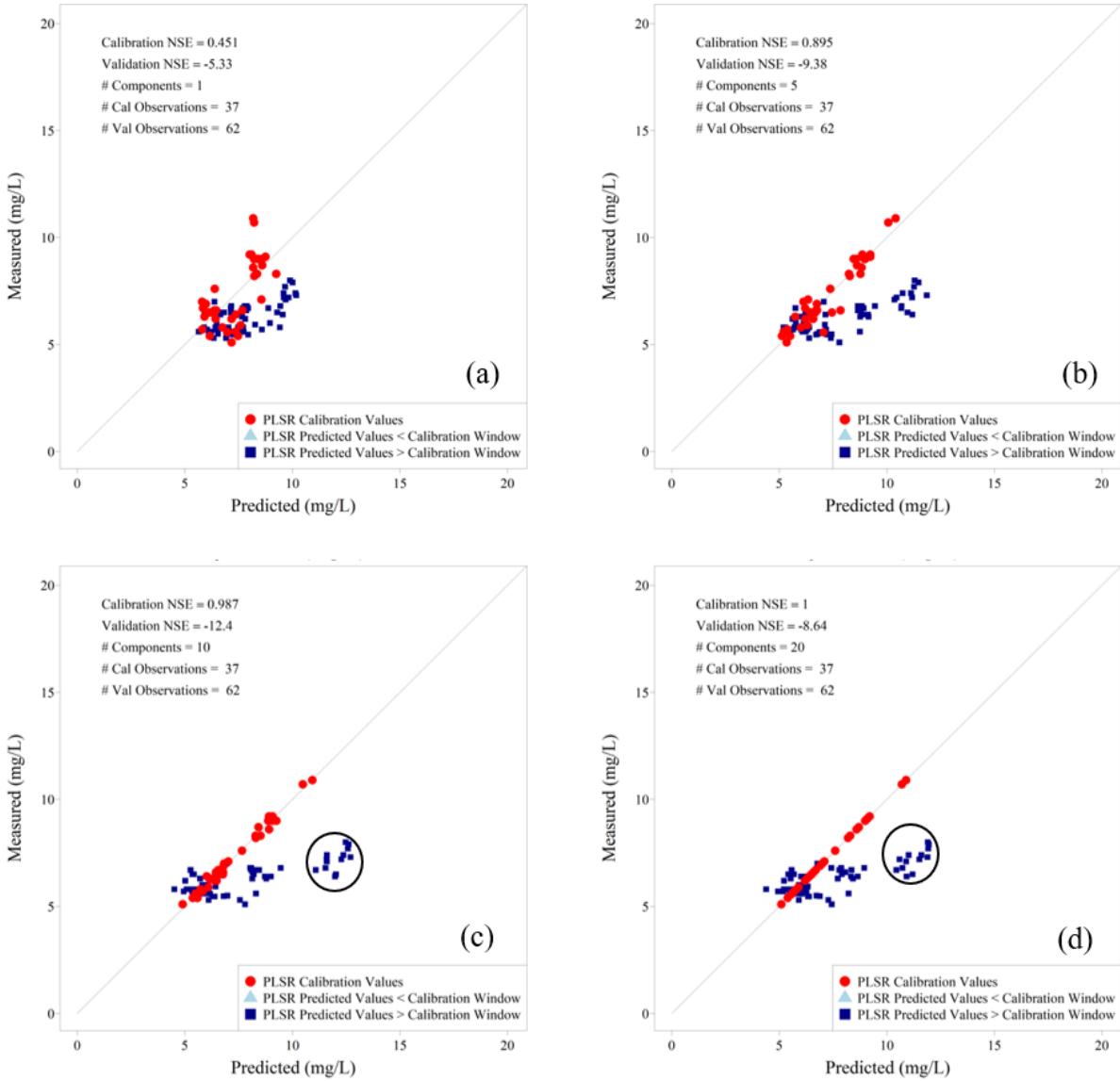


Figure A.3. Measured discrete sample DOC concentrations as a function of predicted DOC concentrations resulting from a (a) 1-component, (b) 5-component, (c) 10-component and (d) 20-component model calibrated for Window 1 of the 60-day moving window sequence (12/20/12 – 2/18/13). The circle indicates a cluster of samples that become isolated with larger residuals when additional components are included in the PLSR model.

Contrastingly, the under-prediction of discrete sample concentrations falling outside of calibration Window 9 can be observed for models built with 1, 5, 10, and 20 components in Figure A.4. The 1-component model produced a steeper sloping set of validation concentrations when compared with results from models with more components. This is the inverse of the Window 1 example, where adding components created a larger range of residuals, however the model fit was much worse than that of the 1-component Window 1 calibration. The Window 9 trend is more easily definable, but both examples demonstrate that similar inferences about over- and under-prediction trends in validation concentrations can be inferred for a 1-component model versus a 20-component model.

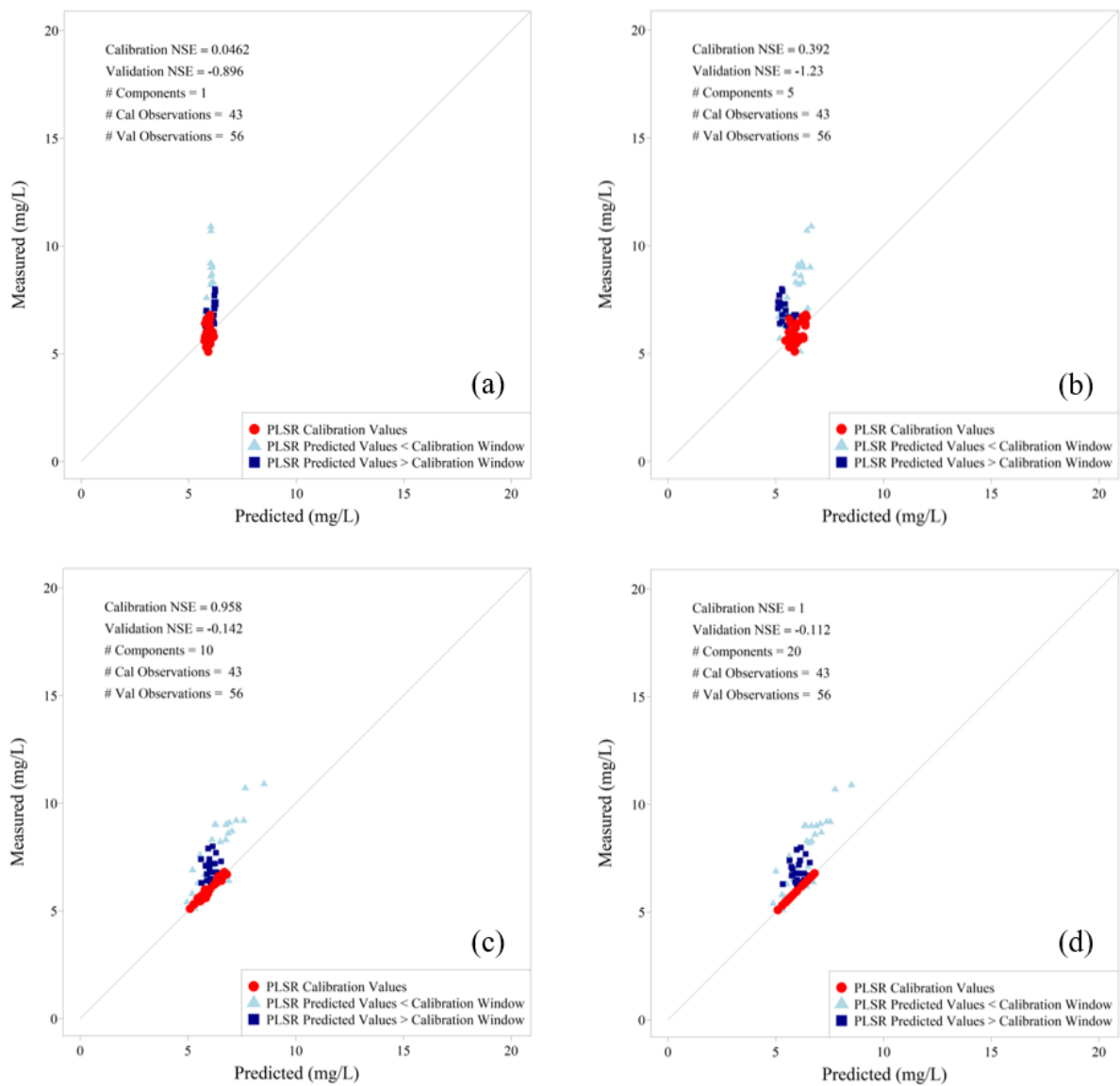
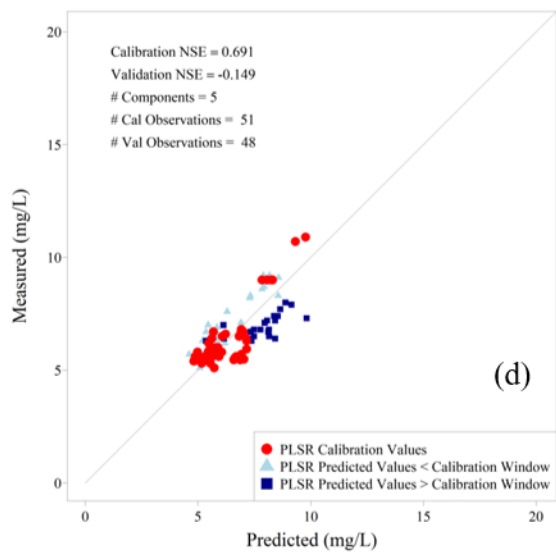
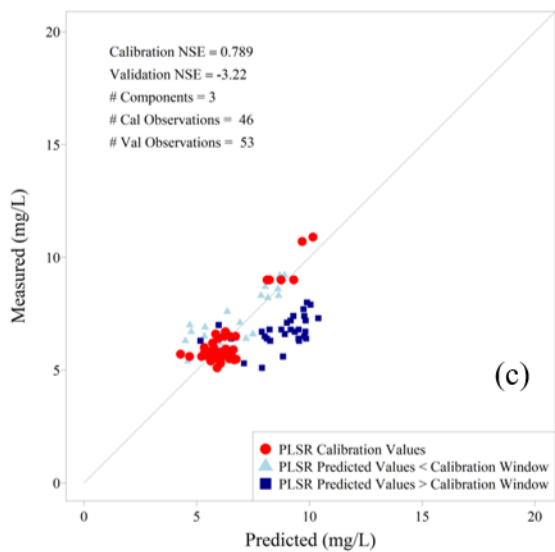
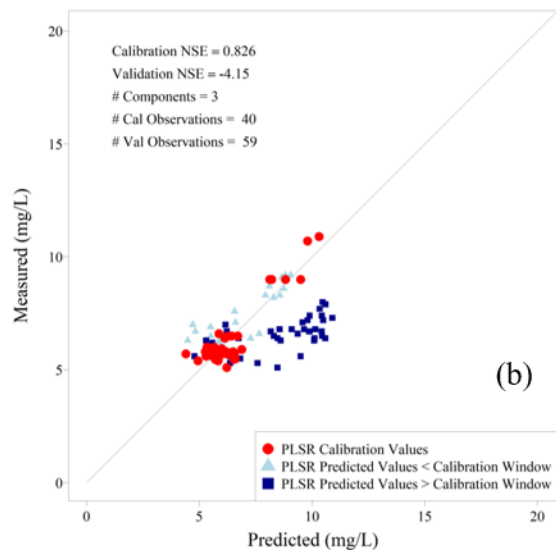
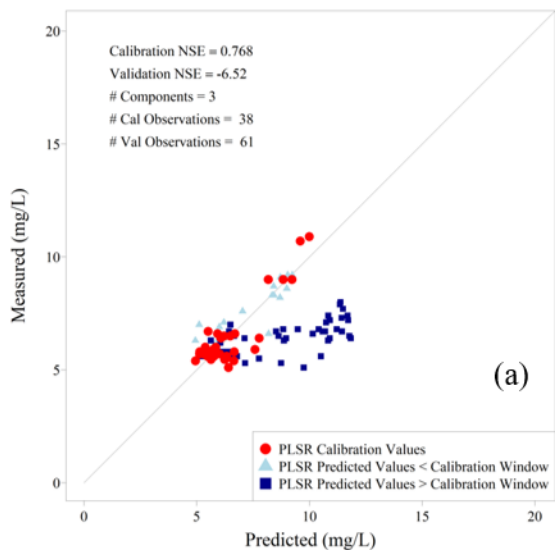


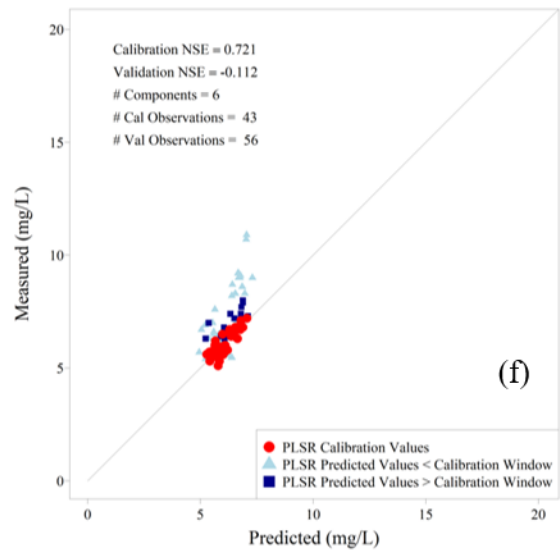
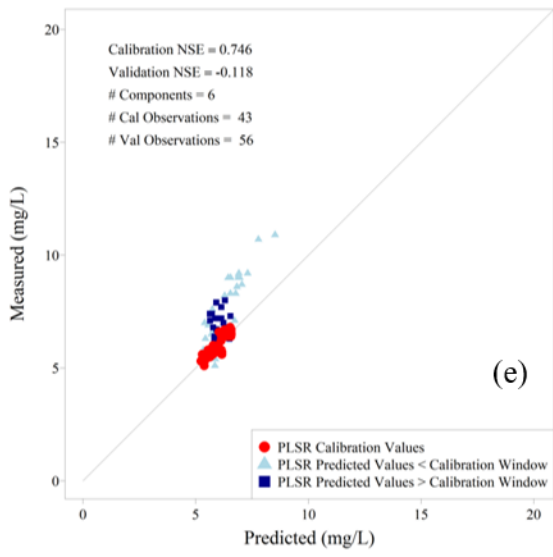
Figure A.4. Measured discrete sample DOC concentrations as a function of predicted DOC concentrations resulting from a 1-component, 5-component, 10-component and 20-component model calibrated for Window 9 of the 60-day moving window sequence (2/14/13 – 4/15/13).

A.2 Trends surrounding hinge-point when $ncomp_{nse65}$ components are selected

Even though the full range of concentrations was available for 60-day calibrations in Windows 7 and 8, a shift from over- to under-prediction occurred making it unclear if the trends observed could be explained by a particular reason. In order to verify that this less drastic shift in prediction was not affected by number of components used in the model, we compared prediction concentrations as a function of measured concentrations for the “acceptable” models using the $ncomp_{nse65}$ number of components. Figure A.5 illustrates similar trends when the $ncomp_{nse}$ number of components composed the models for Windows 5-10. Predicted values from a model composed of 5 components falling after the calibration date range in Window 8, however trended in an over-predicted manner versus under- as seen for the model using the $ncomp_{rmsep}$ (7 components). Even with this slight change in trend, overall a transitional point still seemed to fall somewhere around Window 8. Also notable was that the cluster of samples over-predicted in Windows 5 & 6 was less isolated using the lower $ncomp_{nse65}$ number of components versus the $ncomp_{rmsep}$ number of components in the model. This could be indicative of the addition of components placing emphasis on certain parts of the spectra where absorption fingerprints could have differed for calibration samples versus validation samples with similar measured concentrations. These differences could have been amplified for the “cluster” samples.

Figure A.5. Measured vs. predicted concentrations for model calibrations built with the minimum number of components needed to produce an NSE value of 0.65 or greater for Windows (a) 5, (b) 6, (c) 7, (d) 8, (e) 9, and (f) 10 showing the progression in general over-prediction to under-prediction of concentrations. Triangles represent all samples that preceded the calibration window and the squares represent all samples that fell after the calibration window.





APPENDIX B: 30-Day Moving Window Analysis

B.1 Effect of full concentration range vs. smaller concentration range on prediction trends

In order to test if the full concentration range availability for calibration explained trends in observation before and after the February storm, we narrowed the calibration window to 30 days and moved it forward 7 days at a time through the entire date range. This allowed for 3 windows at the very beginning with a smaller range of concentrations occurring before the February event that included the highest concentration values observed. The number of components selected between 1-20 to build each window calibration was selected in the same manner as the 60-day moving window calibrations where $ncomp = ncomp_{rmsep}$ for simplification of analysis purposes, although some windows had too few observations to build models with up to 20 components. The NSE values were less than 0.65 for the models built for calibration Windows 9, 10 and 11 when the $ncomp_{rmsep}$ number of components was used and therefore the $ncomp_{nse65}$ number of components was selected instead (Table B.1). This time in the series is where a transitional point seemed present in the 60-day moving window sequence.

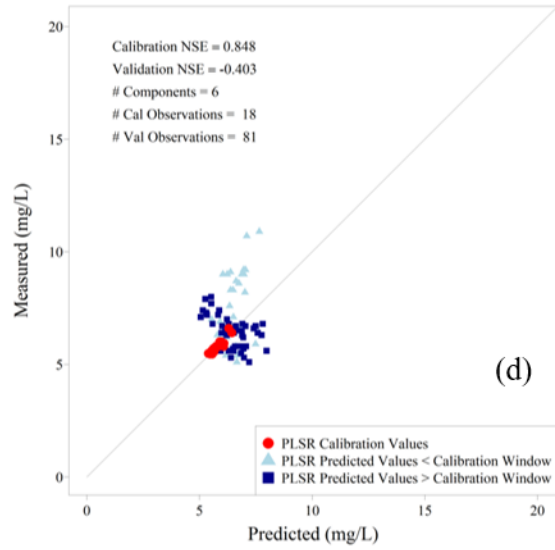
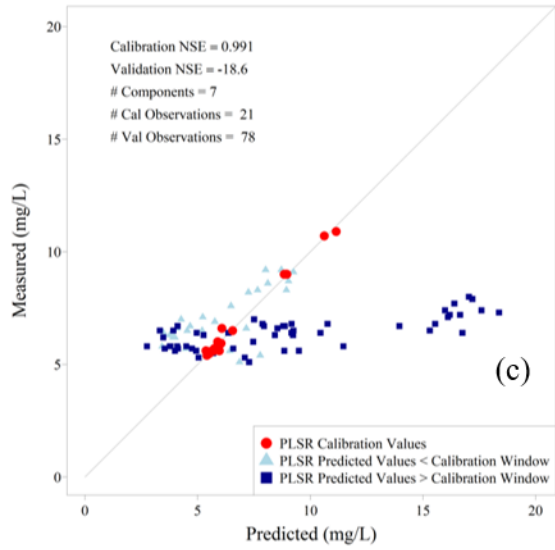
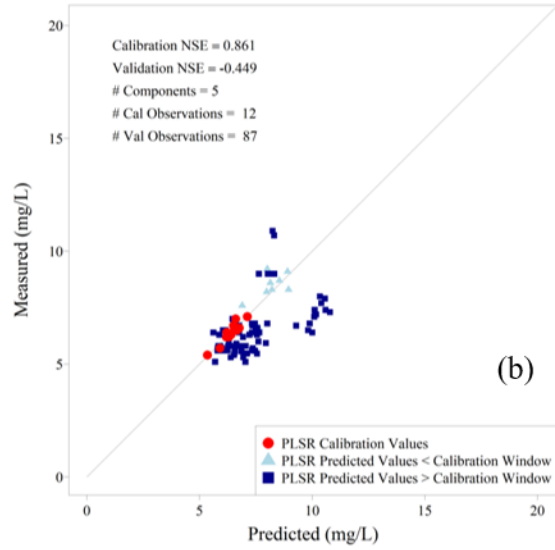
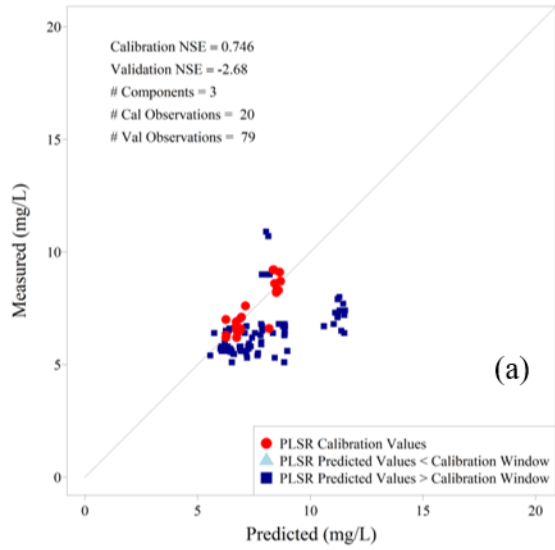
Table B.1. 30-day moving window calibration cross-validation results for 1-20 component models (per each calibration window) with number of components selected based on 2 selection methods: 1) Minimum root mean square error of prediction (RMSEP) 2) minimum number of components necessary to produce an “acceptable” Nash Sutcliffe Efficiency (NSE ≥ 0.65). Number of components selected based on method for each window calibration model are in *Italics* while corresponding NSE values produced by models with the selected number of components are listed to the right in each selection method column. * refers to the situation in which the number of components selected to evaluate model results are those corresponding to the NSE ≥ 0.65 criterion because the number of components producing the minimum RMSEP did not produce an acceptable model.

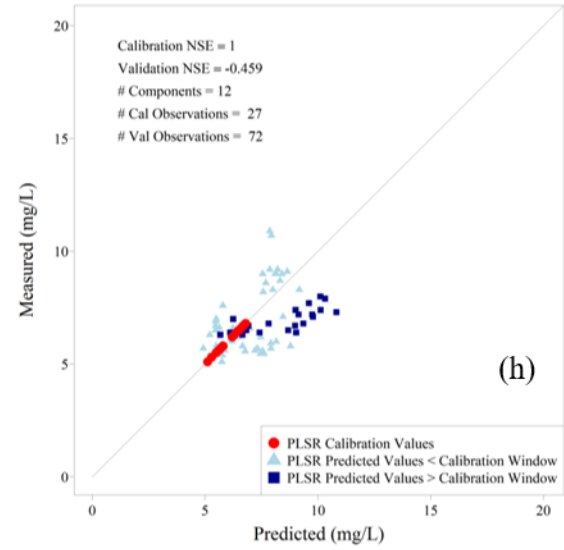
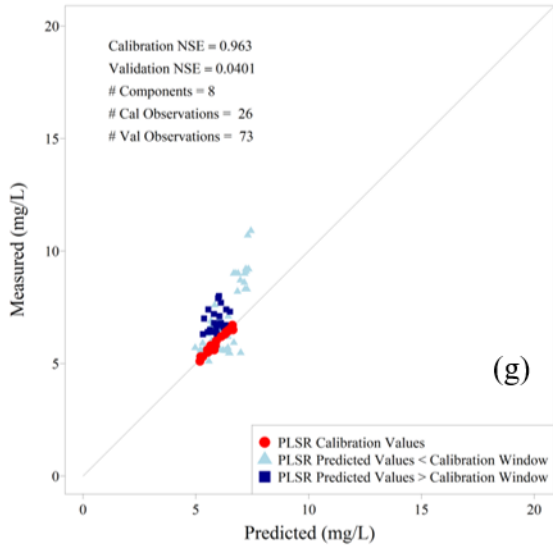
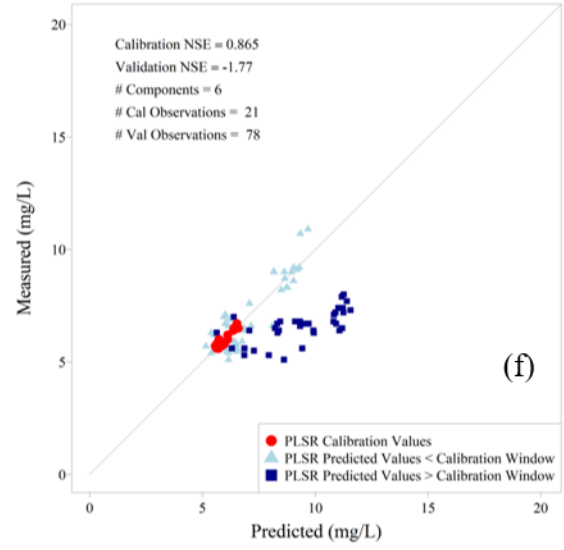
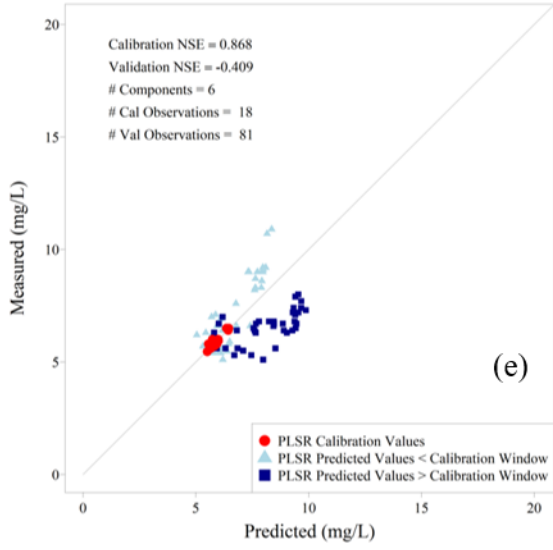
Window	Date (M/D/Y)	Minimum RMSEP		NSE≥ 0.65	
1	12/20/12 – 1/19/13	<i>3</i>	0.75	<i>2</i>	0.72
2	12/27/12 – 1/26/13	<i>4</i>	0.92	<i>2</i>	0.77
3	1/3/13 – 2/2/13	<i>5</i>	0.86	<i>3</i>	0.67
4	1/10/13 – 2/9/13	<i>4</i>	0.98	<i>3</i>	0.88
5	1/17/13 – 2/16/13	<i>6</i>	0.98	<i>2</i>	0.67
6	1/24/13 – 2/23/13	<i>5</i>	0.96	<i>3</i>	0.87
7	1/31/13 – 3/2/13	<i>5</i>	0.96	<i>3</i>	0.83
8	2/7/13 – 3/9/13	<i>7</i>	0.99	<i>3</i>	0.84
9	2/14/13 – 3/16/13	<i>1</i>	0.041	<i>*6</i>	0.85
10	2/21/13 – 3/23/13	<i>1</i>	0.023	<i>*6</i>	0.87
11	2/28/13 – 3/30/13	<i>3</i>	0.32	<i>*6</i>	0.86
12	3/7/13 – 4/6/13	<i>8</i>	0.96	<i>5</i>	0.73
13	3/14/13 – 4/13/13	<i>12</i>	1.0	<i>4</i>	0.67
14	3/21/13 – 4/20/13	<i>17</i>	1.0	<i>3</i>	0.77
15	3/28/13 – 4/27/13	<i>3</i>	0.93	<i>2</i>	0.65
16	4/4/13 – 5/4/13	<i>4</i>	0.88	<i>3</i>	0.85
17	4/11/13 – 5/11/13	<i>4</i>	0.78	<i>3</i>	0.66
18	4/18/13 – 5/18/13	<i>4</i>	0.76	<i>4</i>	0.76

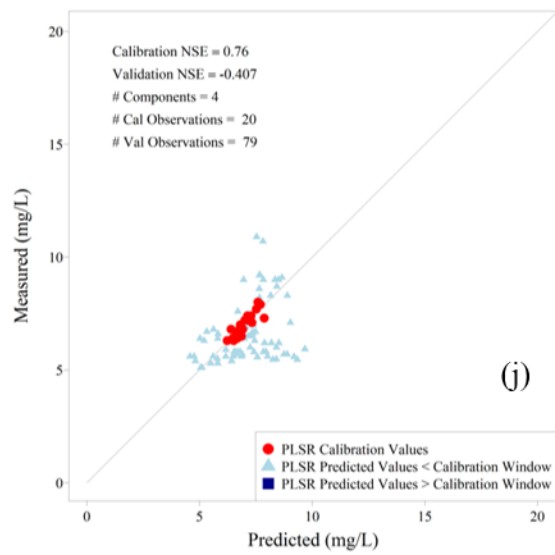
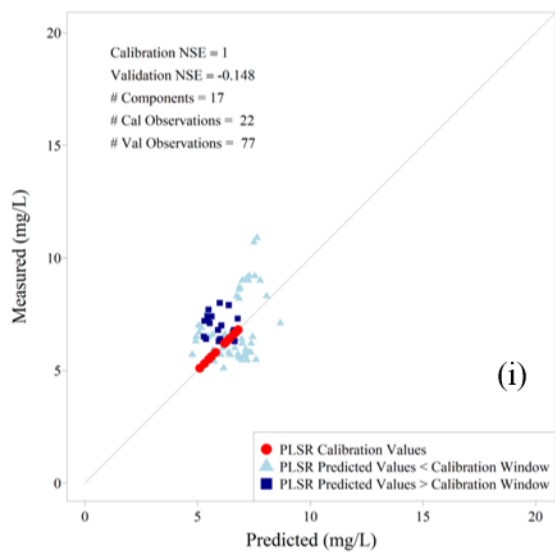
Samples 92 and 93, the only samples with a concentration >10 mg/L and those corresponding with the peak of the February event, were both under-predicted when any calibration was used that did not include these points, therefore suggesting the models may better fit the more extreme ends of the concentration range if the full range of concentrations is available (Figure B.1). In contrast, Window 3 particularly showed that when higher concentrations associated with the December and February events were not contributing to a fuller concentration range, most

validation concentrations were still over-predicted. Similar to trends observed in the 60-day moving window calibrations, Windows 1 – 8 all predicted a wide range of concentrations for samples with similar measured concentrations in the low to mid-range, producing the relatively flat slope for prediction data proceeding the calibration window. In the lower range of observed concentrations, the predicted concentration range of values became wider resulting in larger over-predictions when the February event was included in the calibration window and the cluster of samples with the highest magnitudes of over-prediction was still present.

Figure B.1. Measured vs. predicted concentrations for model calibrations built $ncomp_{rmsep}$ for Windows (a) 1, (b) 3, (c) 8, (d) 9, (e) 10, (f) 11, (g) 12, (h) 13, (i) 14 and (j) 18 showing the progression in general over-prediction to under-prediction of concentrations. Triangles represent all samples that preceded the calibration window and the squares represent all samples that fell after the calibration window.





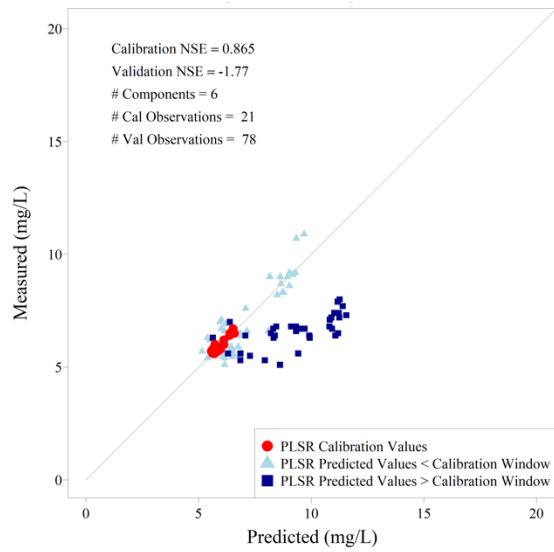


The shift from Window 8 to Window 9 signified a shift to calibration windows moving beyond the February event, signifying the range of concentrations would never be full again (Figure B.1). The range of prediction concentrations narrowed along with the concentration range used for calibration in Window 9 which was similarly observed in the 60-day moving window sequence results. Windows 10 and 11 demonstrated a shift to over-prediction of concentrations falling after the calibration window, however. There was a shift to mostly under-prediction in Window 12 and back to over-prediction of data falling after the calibration window in Window 13. Window 12 showed the quickest changing unexpected results, which made us question if the placement of this window differed from Windows 10, 11 and 13 because the calibration concentration range remained similar.

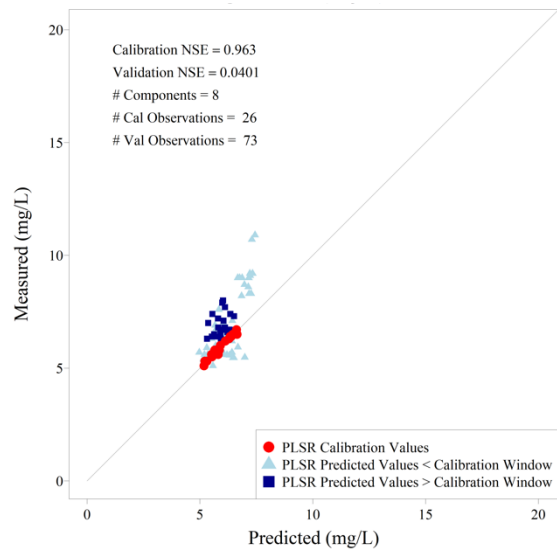
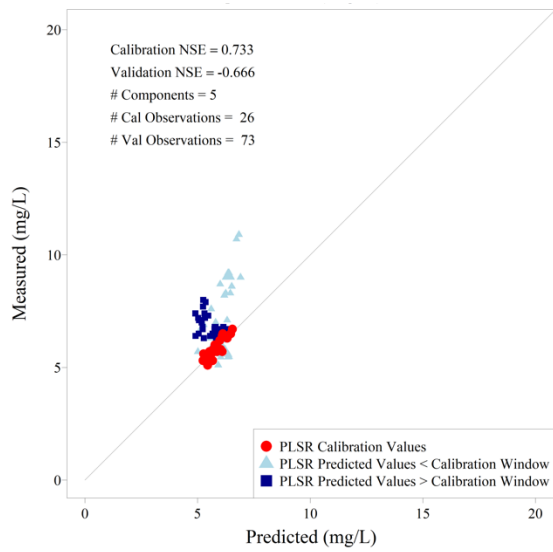
We inspected if number of components used to model these data played a role in this quick shift. Figure B.2 demonstrates that the trend in over-prediction following the calibration window for Window 13 using the $ncomp_{rmsep}$ number of components actually shifted to under-prediction when the $ncomp_{nse65}$ number of components was used. This showed that this part of the time series data was more sensitive to the number of components included in the model. Even though some general trends were still observed when the full range was and was not available, the trends seemed to be more variable for calibration windows following the February event using the 30-day window moving calibration. This indicated further that perhaps placement of calibration window among service intervals in addition to calibration concentration range and sample concentration distribution plays a role in prediction trends.

Figure B.2. Side by side comparison of measured DOC concentrations as a function of predicted DOC concentrations produced from a model with $ncomp_{nse65}$ number of components (left) and $ncomp_{rmsep}$ number of components (right) for 30-day calibration analysis for Windows (a) 11, (b) 12, (c) 13 & (d) 14. The $ncomp_{rmsep}$ number of components produced an unacceptable model for the Window 11 calibration, therefore only the results from a calibration model with $ncomp_{nse65}$ number of components is shown here.

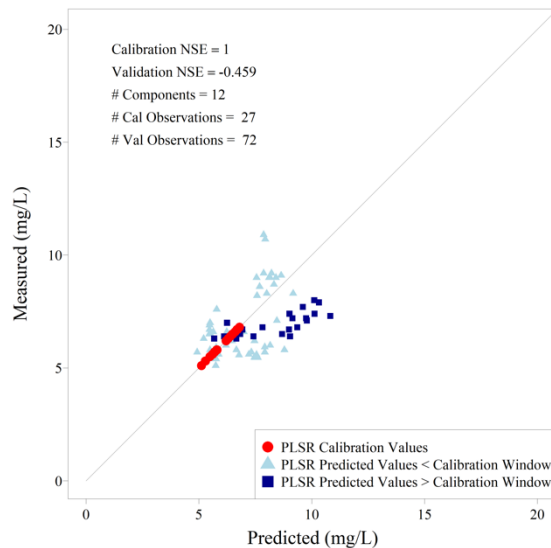
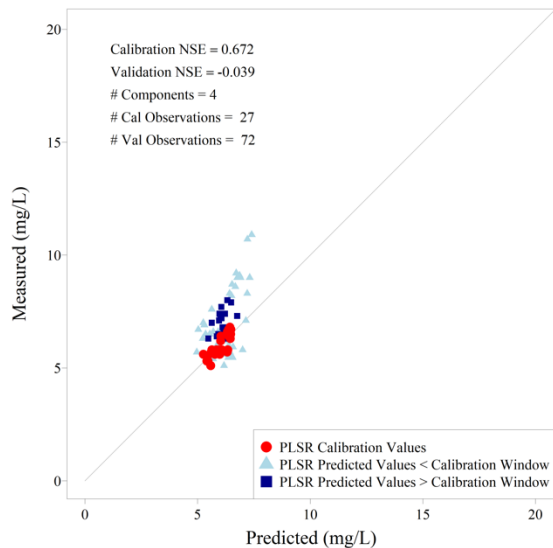
(a) 30-Day Window 11



(b) 30-Day Window 12



(c) 30-Day Window 13



(d) 30-Day Window 14

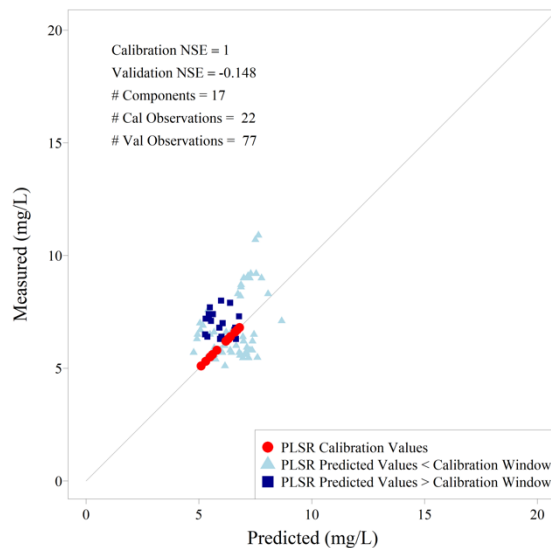
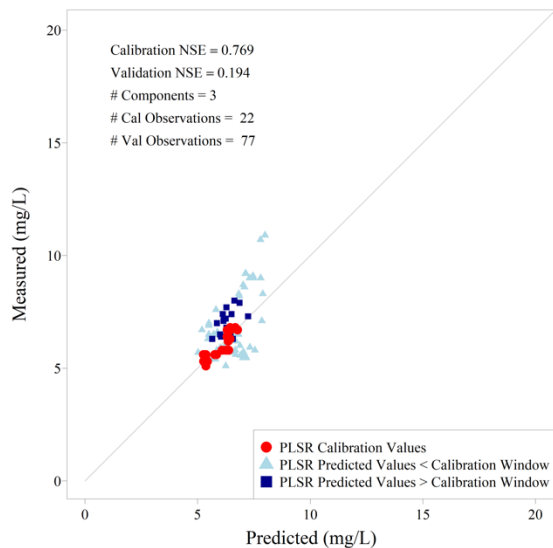
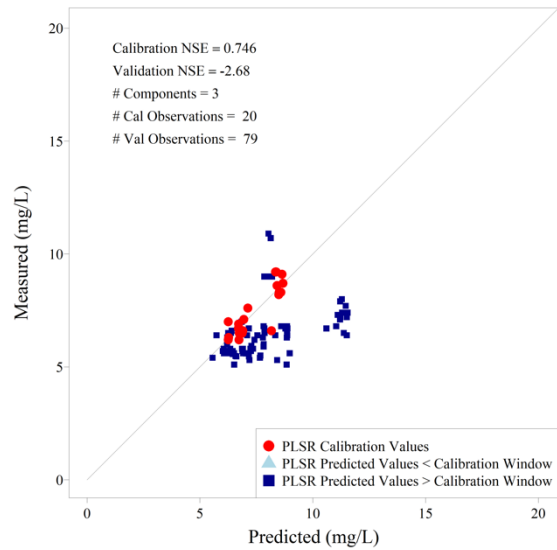
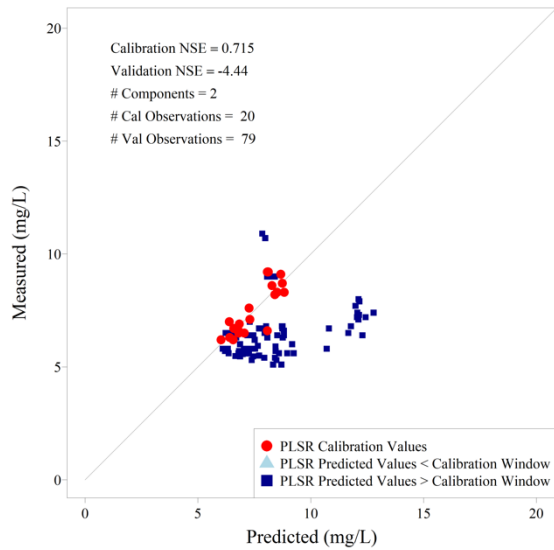


Figure B.3 demonstrates that in the 30-day moving window predictions, number of components also affects the range of residuals. Windows 1 and 2 both exhibited the cluster of samples over-predicted for the $ncomp_{nse65}$ and $ncomp_{rmsep}$ number of component models. Window 3, on the other hand, showed that a model using only 3 components did not isolate the cluster of over-predicted values, yet the model with 5 components did. This local calibration window only had 12 samples available for calibration, which could have made predicted data even more sensitive to additional components.

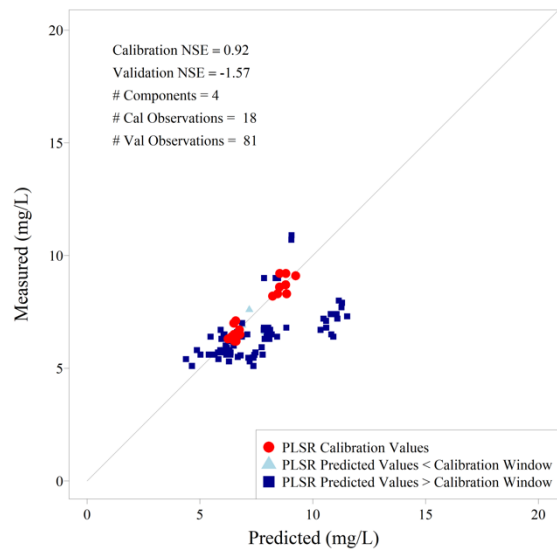
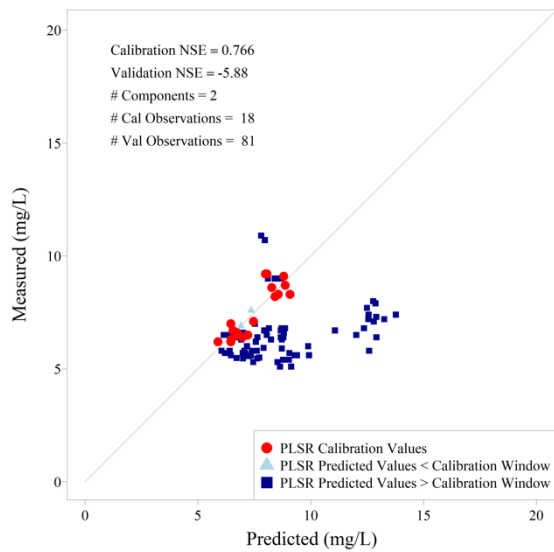
These findings suggest that the 30-day moving window calibration approach revealed some overall similar trends to the 60-day moving window calibrations, most importantly the identification of some type of clear transitional point from Window 8 to Window 9. The shorter windows for local calibration seemed to expose more sensitivity of predicted data to where the calibrated model fell within the time series.

Figure B.3. Side by side comparison of measured DOC concentrations as a function of predicted DOC concentrations produced from a model with $ncomp_{nse65}$ number of components (left) and $ncomp_{rmsep}$ number of components (right) for 30-day calibration Windows (a) 1, (b) 2 & (c) 3.

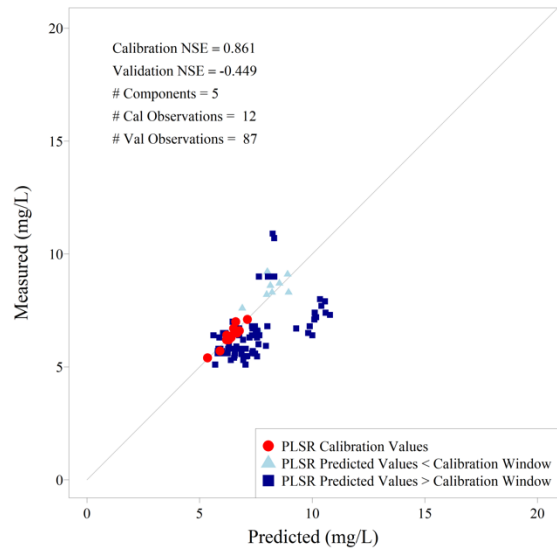
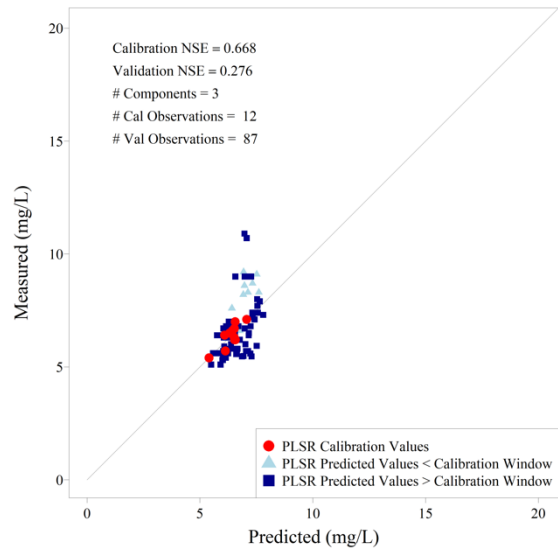
(a) 30-Day Window 1



(b) 30-Day Window 2



(c) 30-Day Window 3



APPENDIX C: A1 Single Water Quality Parameter Flow and Flux Duration Curves

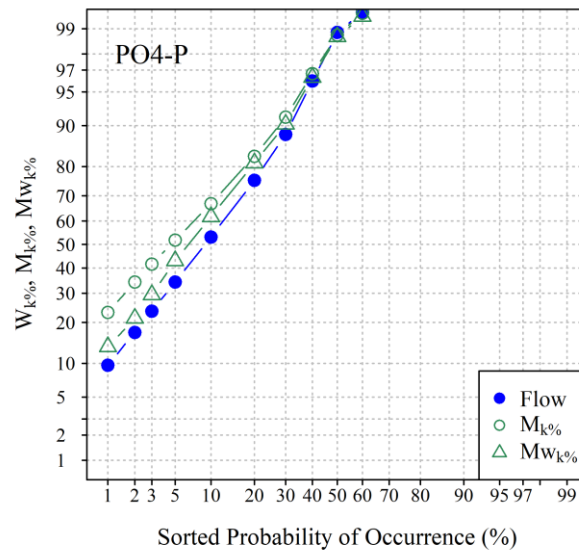


Figure C.1. Flow and flux duration curves for phosphate (PO4-P).

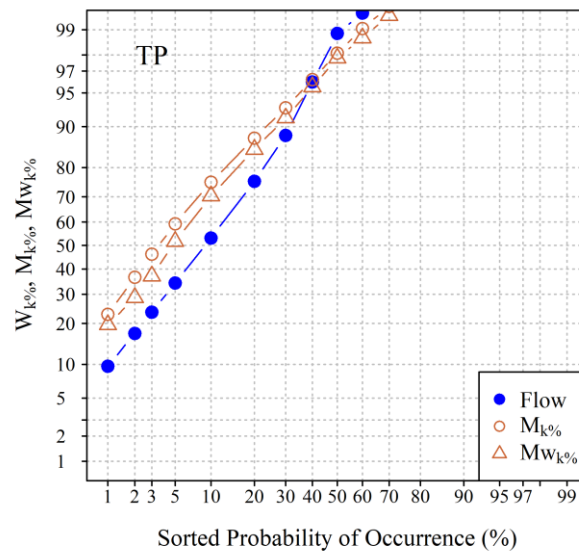


Figure C.2. Flow and flux duration curves for total phosphorus (TP).

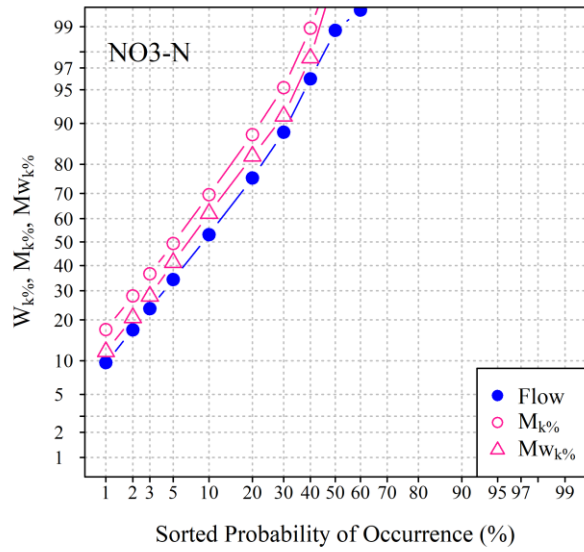


Figure C.3. Flow and flux duration curves for nitrate (NO₃-N).

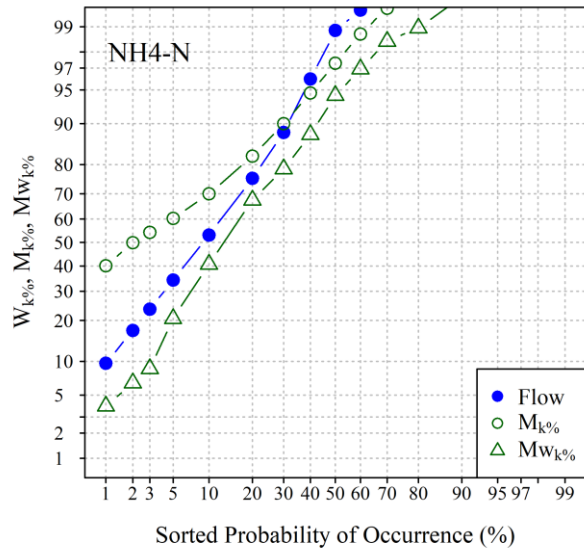


Figure C.4. Flow and flux duration curves for ammonium (NH₄-N).

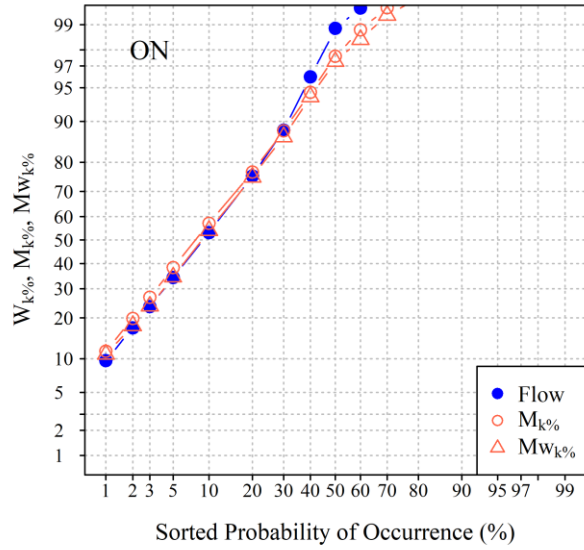


Figure C.5. Flow and flux duration curves for organic nitrogen (ON).

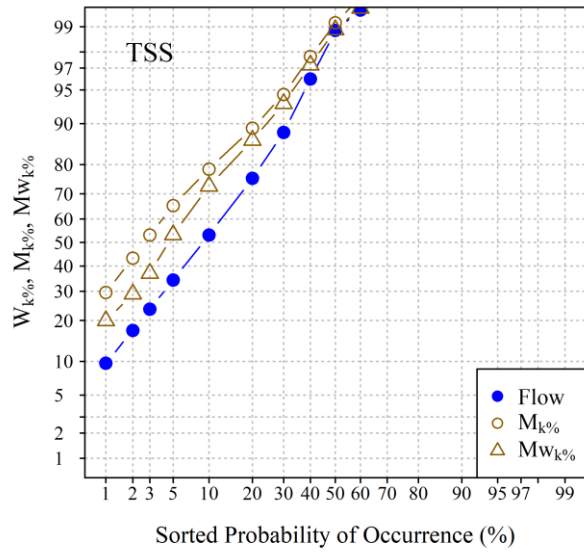


Figure C.6. Flow and flux duration curves for total suspended solids (TSS).

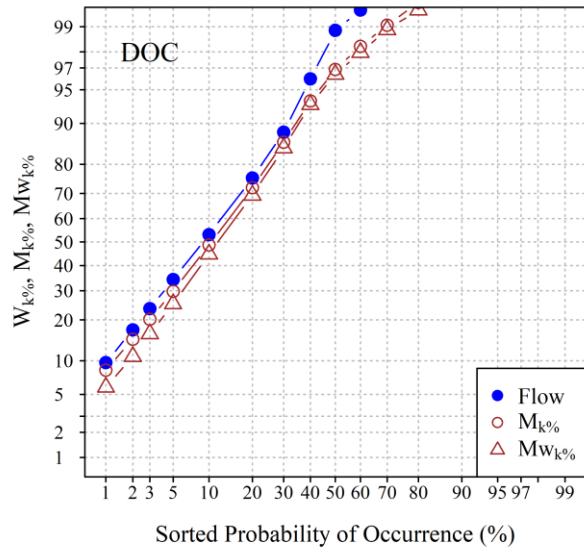


Figure C.7. Flow and flux duration curves for dissolved organic carbon (DOC).

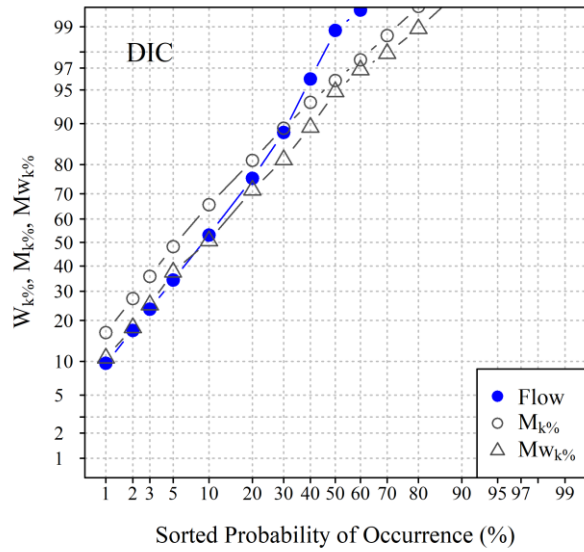


Figure C.8. Flow and flux duration curves for dissolved inorganic carbon (DIC).

APPENDIX D: A1 Hysteresis Plots

Normalized flow (Q_{norm}) and concentration (C_{norm}) time-series data were used to plot the hydrographs, chemographs and hysteresis loops for each rainfall triggered event. For each event, 10 water quality parameters were plotted: NO₃-N, NH₄-N, ON, PO₄-P, TP, DOC, DIC, TSS, Cl and pH. There were 32 rainfall triggered events available for hysteresis analysis, 12 of which occurred during multi-peak events. Multi-peak events were plotted and analyzed in two ways: 1) as one continuous event represented by one hysteresis loop and 2) as separate single-peak events represented by one hysteresis loop each. Event labels including the word “Multi” indicate that the first method was used and are numbered according to the number of the first single-peak event in the multi-peak series of events. Events produced by release of water from beaver dams and controlled drainage that occurred on the falling limbs of rainfall triggered events were included in multi-peak events described by the first method but were not analyzed as separate single-peak events. Hysteresis Index (HI) and Flushing Index (FI) values were calculated for all available events and water quality parameters. HI and FI indices could not be calculated for Event 49 (included in Event 49 Multi) because of the absence of a falling limb. Each single- and multi-peak event presented in this Appendix was evaluated on an individual basis, and details regarding the final events selected for HI and FI analysis discussed in Chapter 3 are in Appendix E.

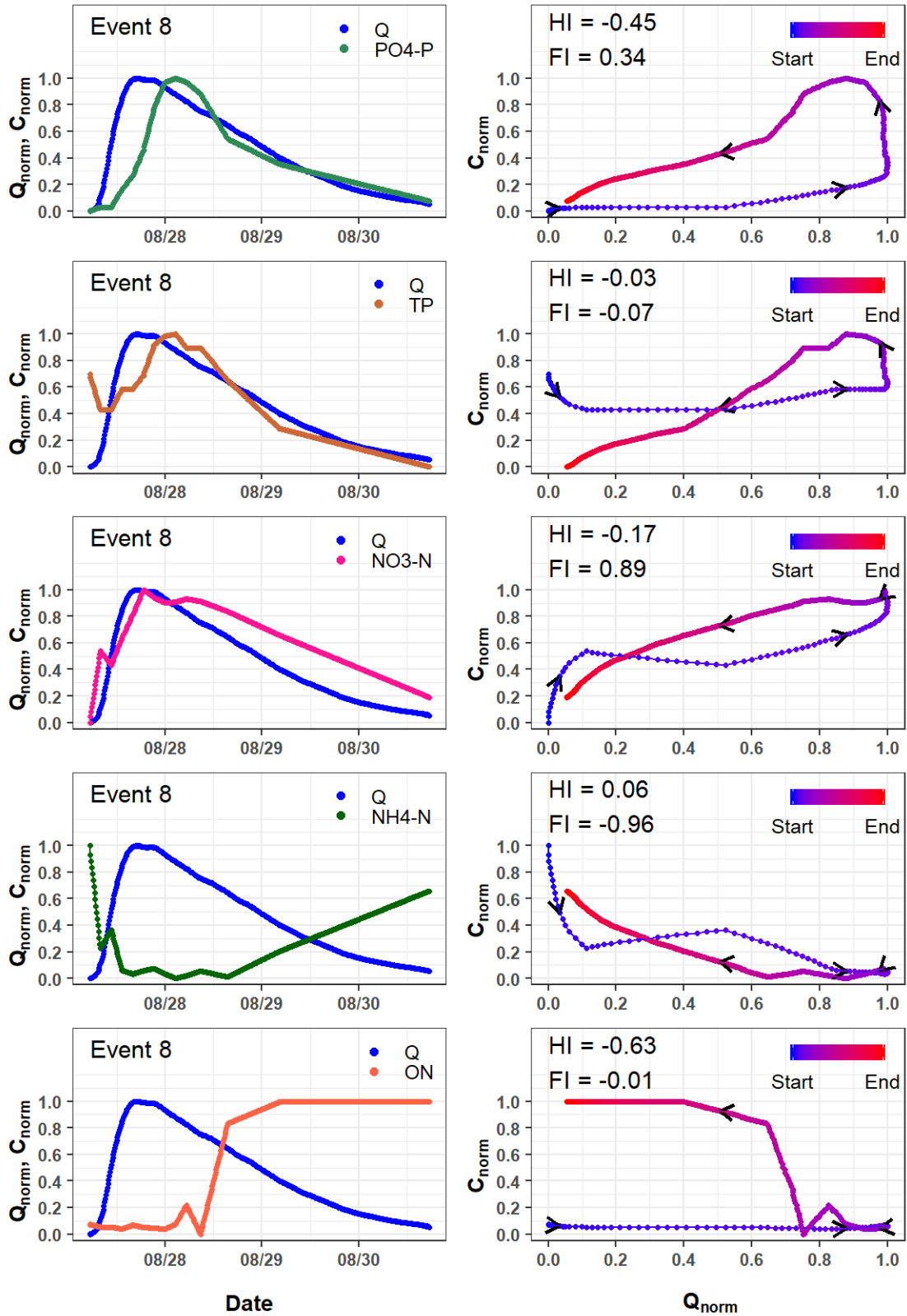


Figure D.1. Event 8 hydrographs, chemographs, and hysteresis loops for nitrogen and phosphorous species.

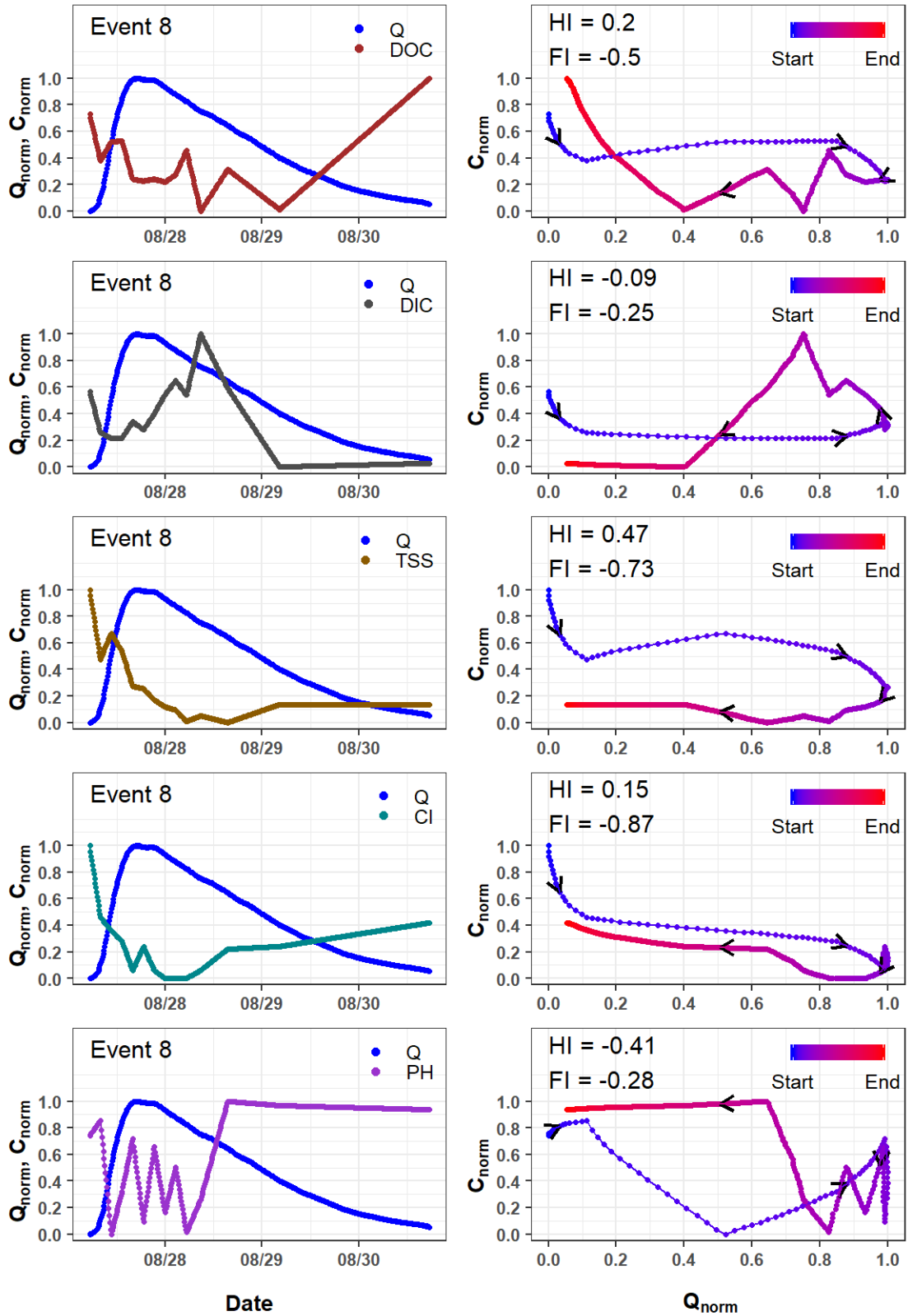


Figure D.2. Event 8 hydrographs, chemographs, and hysteresis loops for carbon species, suspended solids, chloride and pH.

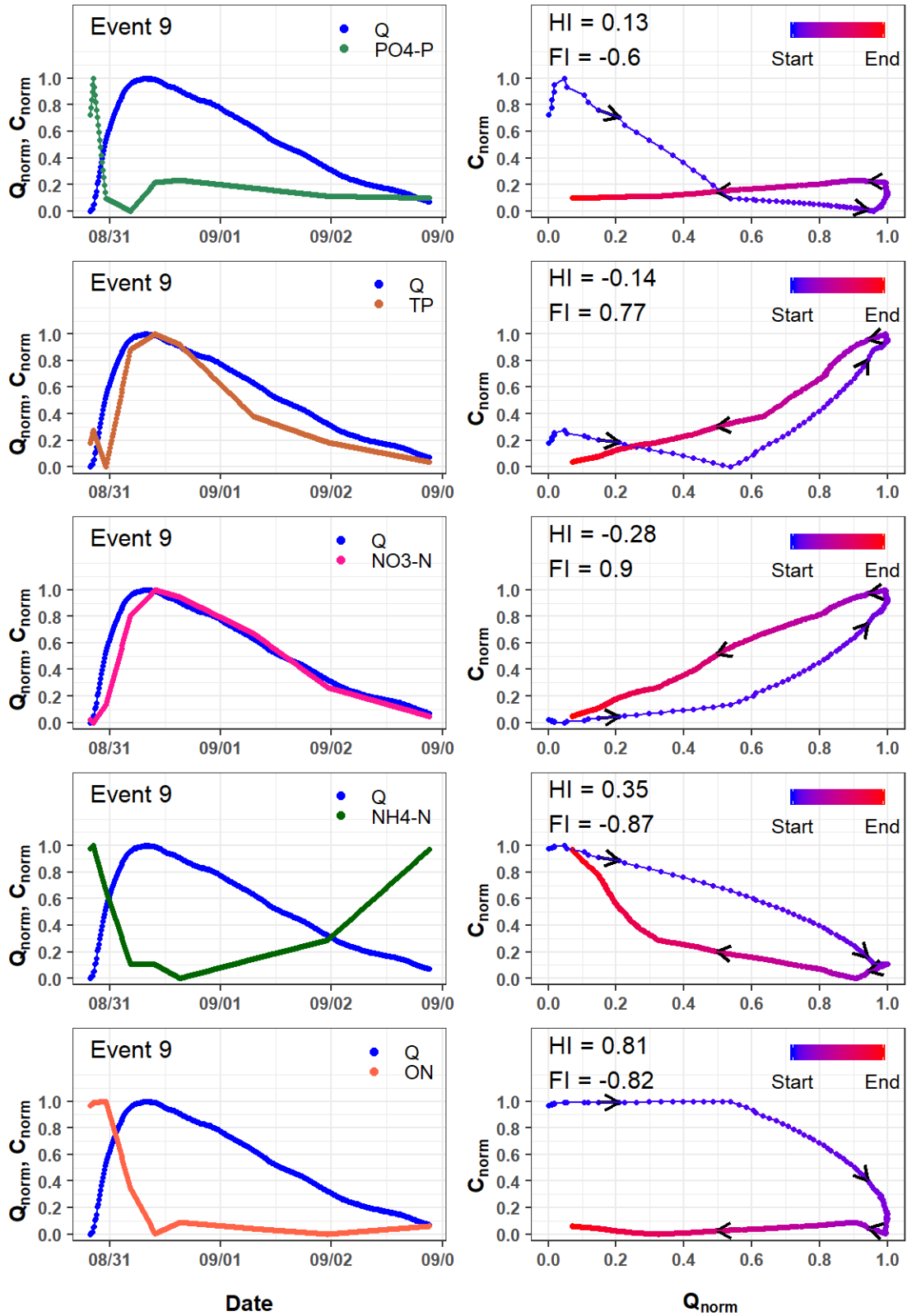


Figure D.3. Event 9 hydrographs, chemographs, and hysteresis loops for nitrogen and phosphorous species.

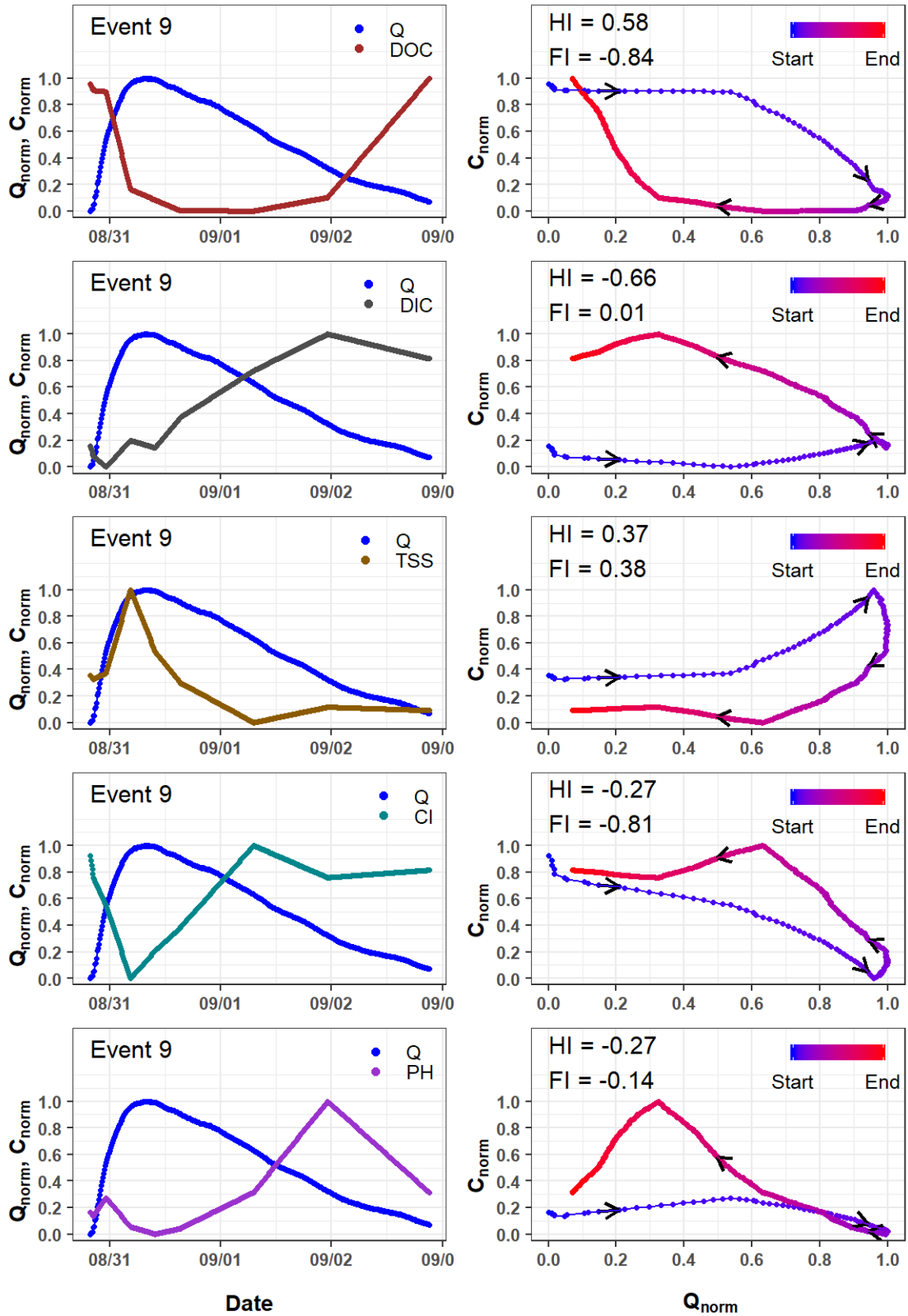


Figure D.4. Event 9 hydrographs, chemographs, and hysteresis loops for carbon species, suspended solids, chloride and pH.

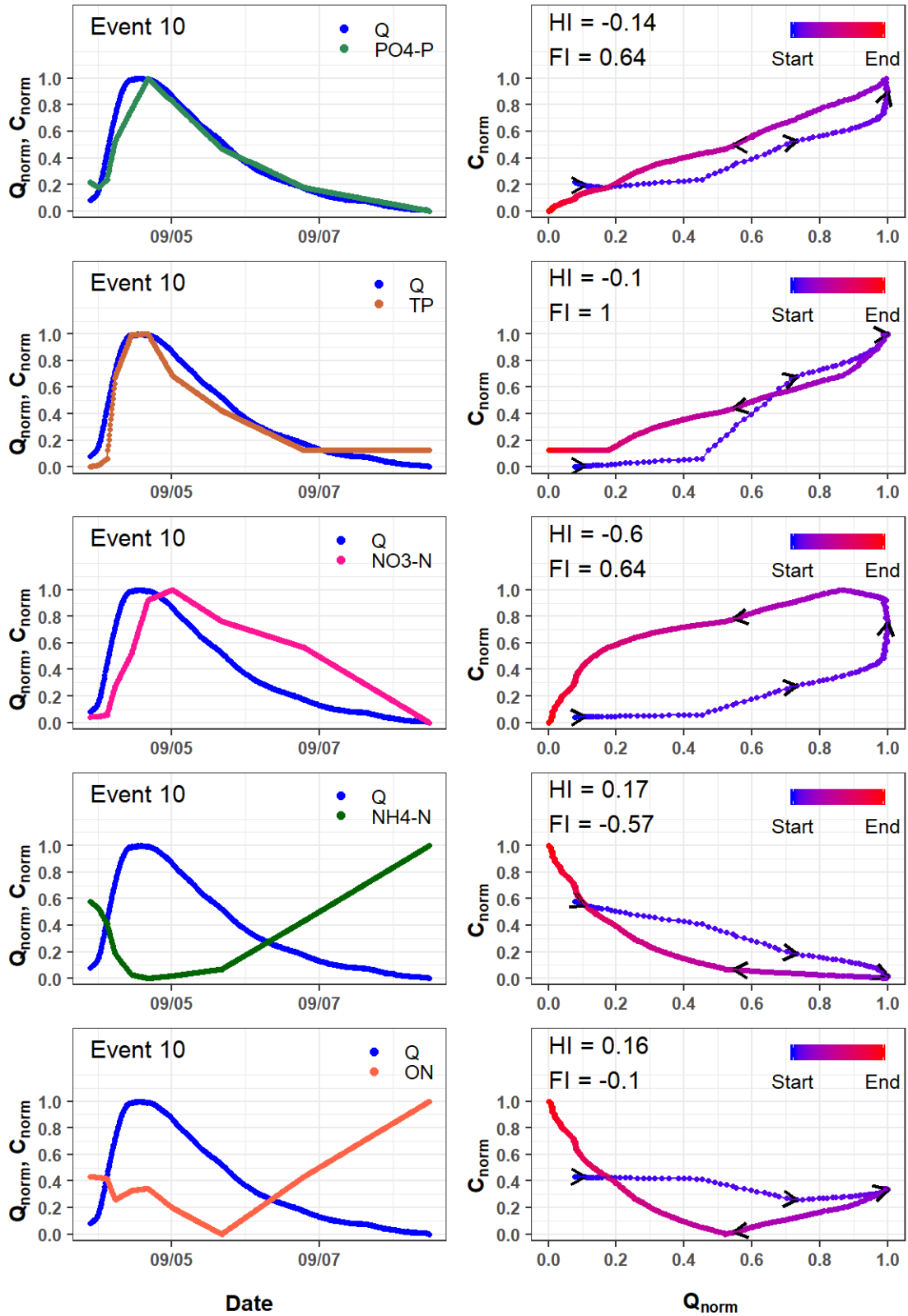


Figure D.5. Event 10 hydrographs, chemographs, and hysteresis loops for nitrogen and phosphorous species.

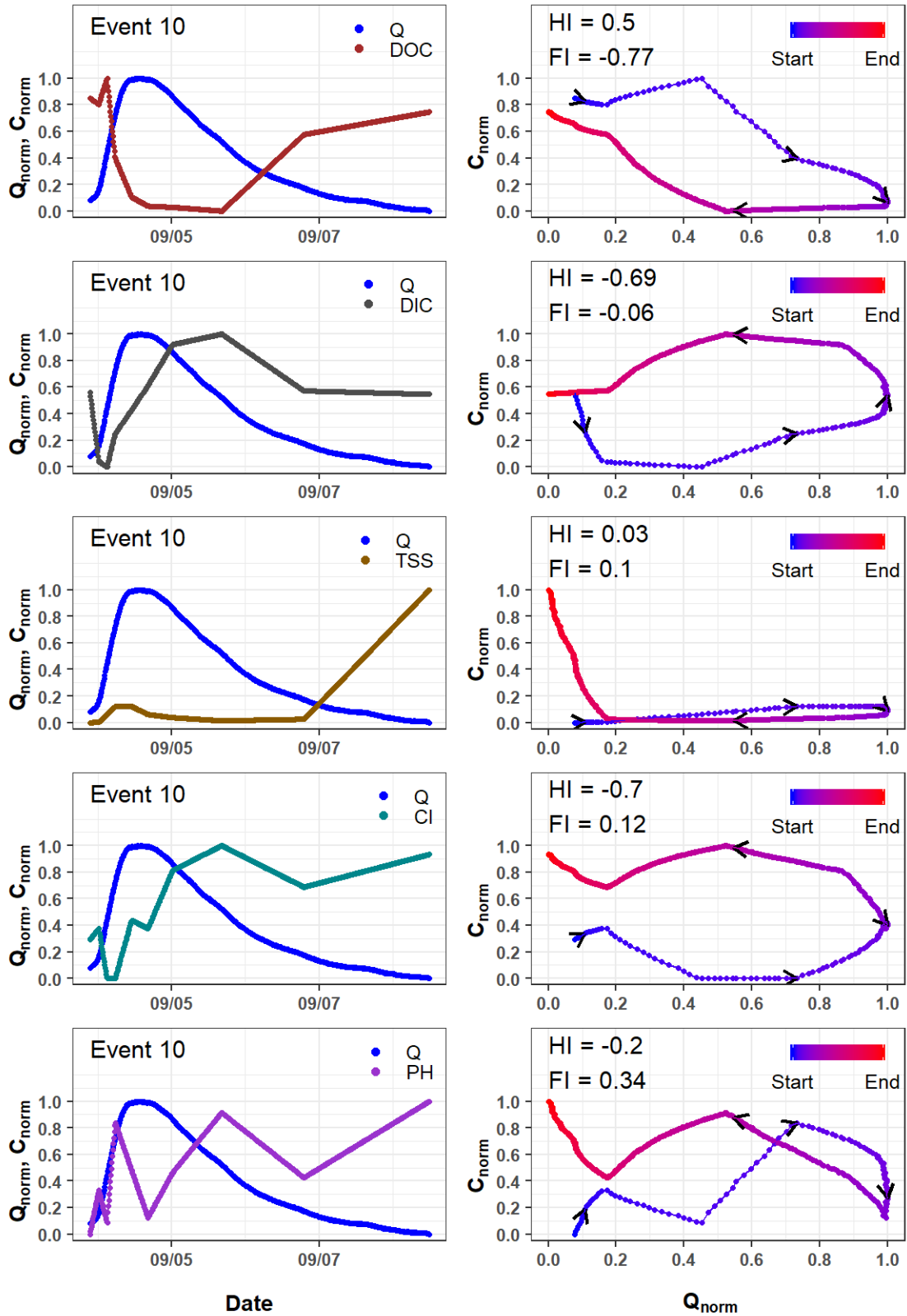


Figure D.6. Event 10 hydrographs, chemographs, and hysteresis loops for carbon species, suspended solids, chloride, and pH.

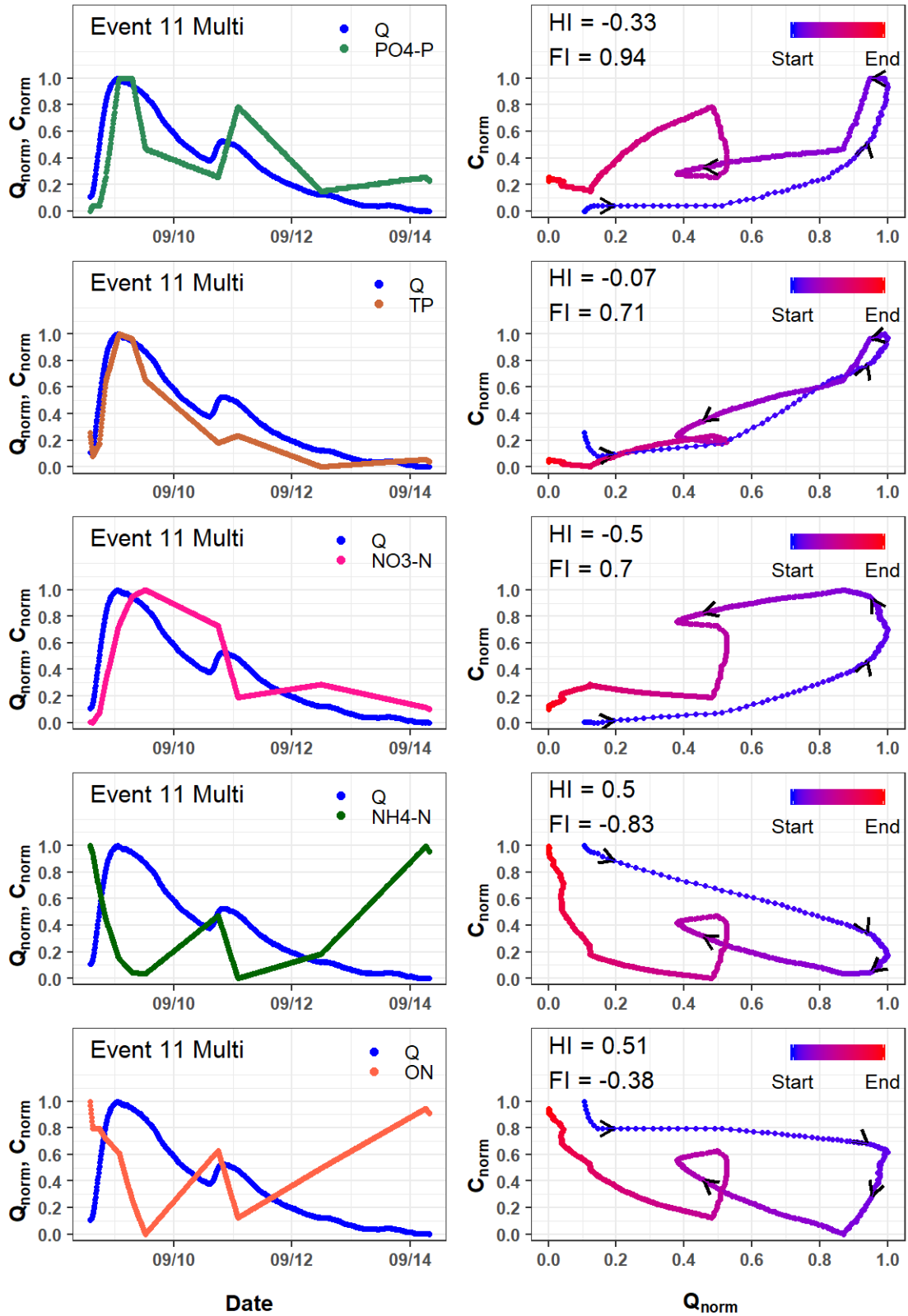


Figure D.7. Event 11 Multi (Events 11 & 12) hydrographs, chemographs, and hysteresis loops for nitrogen and phosphorous species.

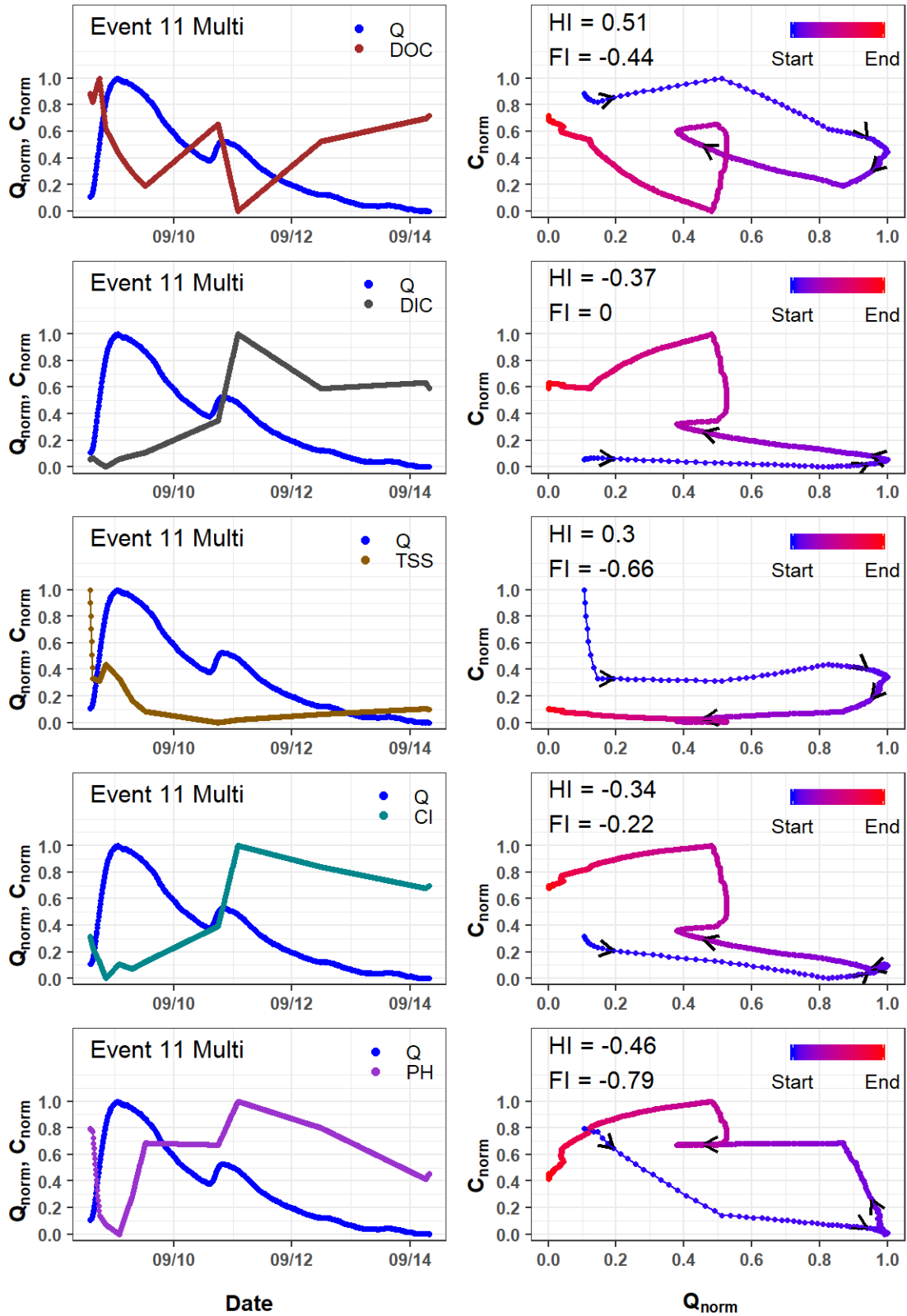


Figure D.8. Event 11 Multi (Events 11 & 12) hydrographs, chemographs, and hysteresis loops for carbon species, suspended solids, chloride, and pH.

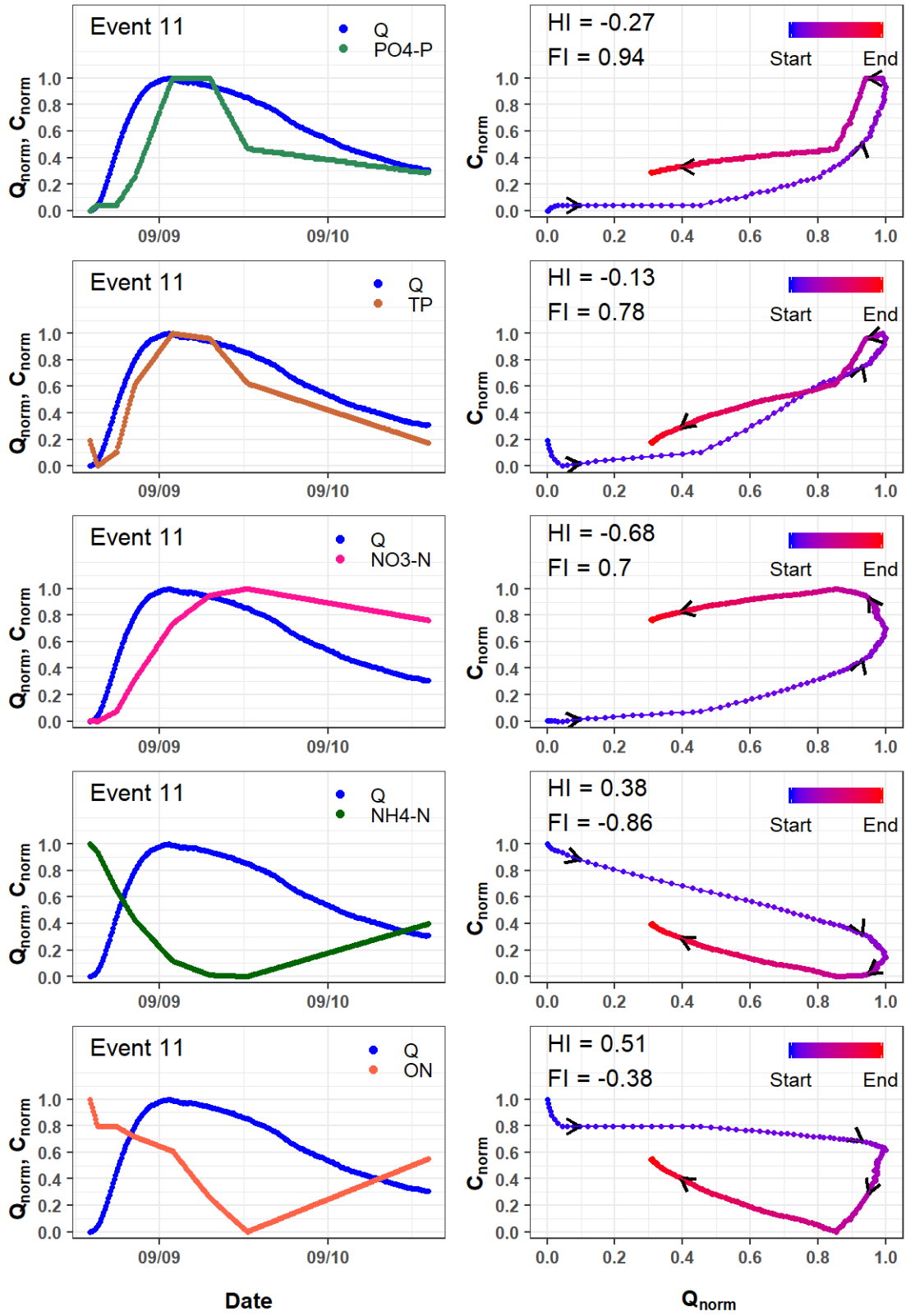


Figure D.9. Event 11 hydrographs, chemographs, and hysteresis loops for nitrogen and phosphorous species.

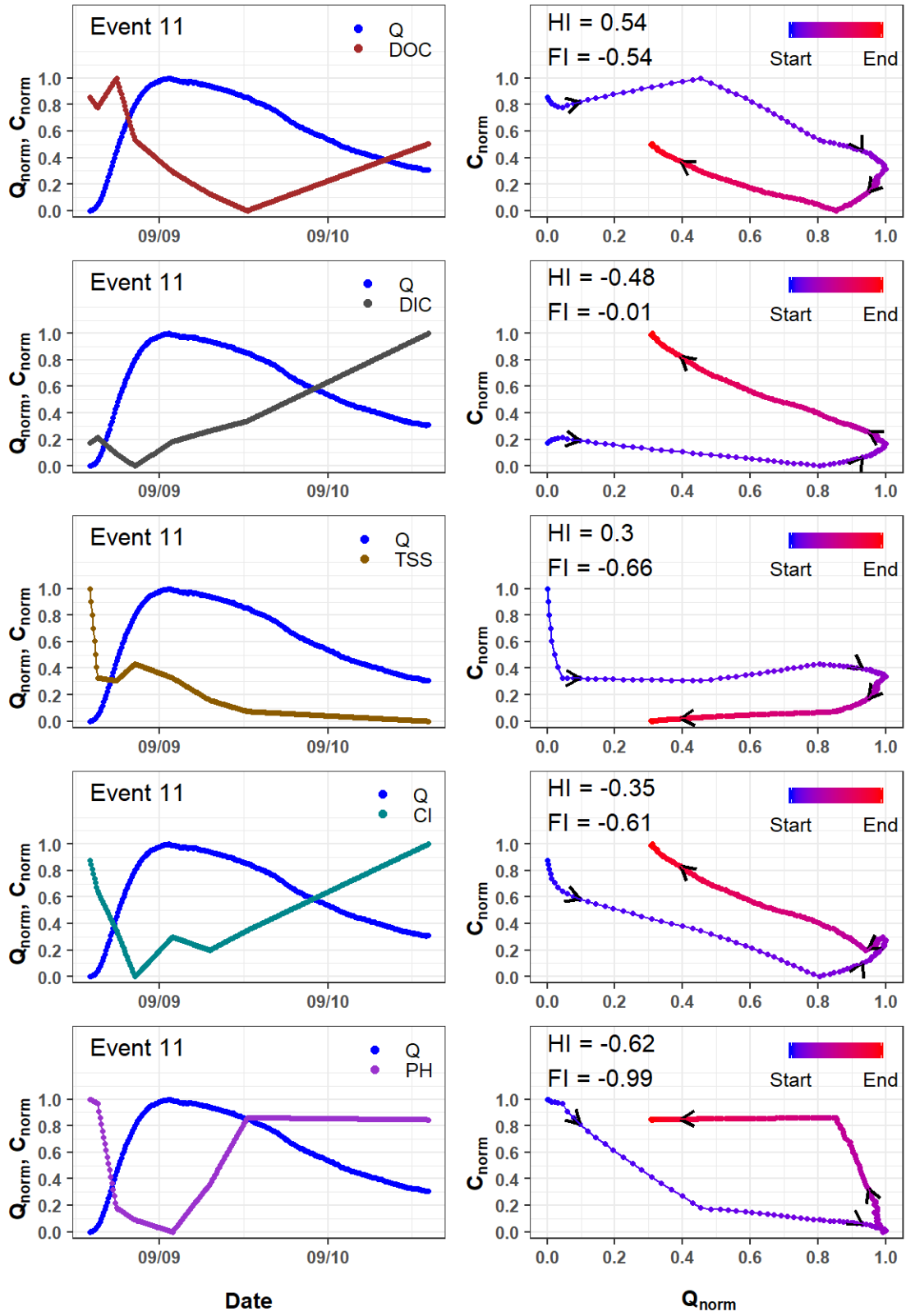


Figure D.10. Event 11 hydrographs, chemographs, and hysteresis loops for carbon species, suspended solids, chloride, and pH.

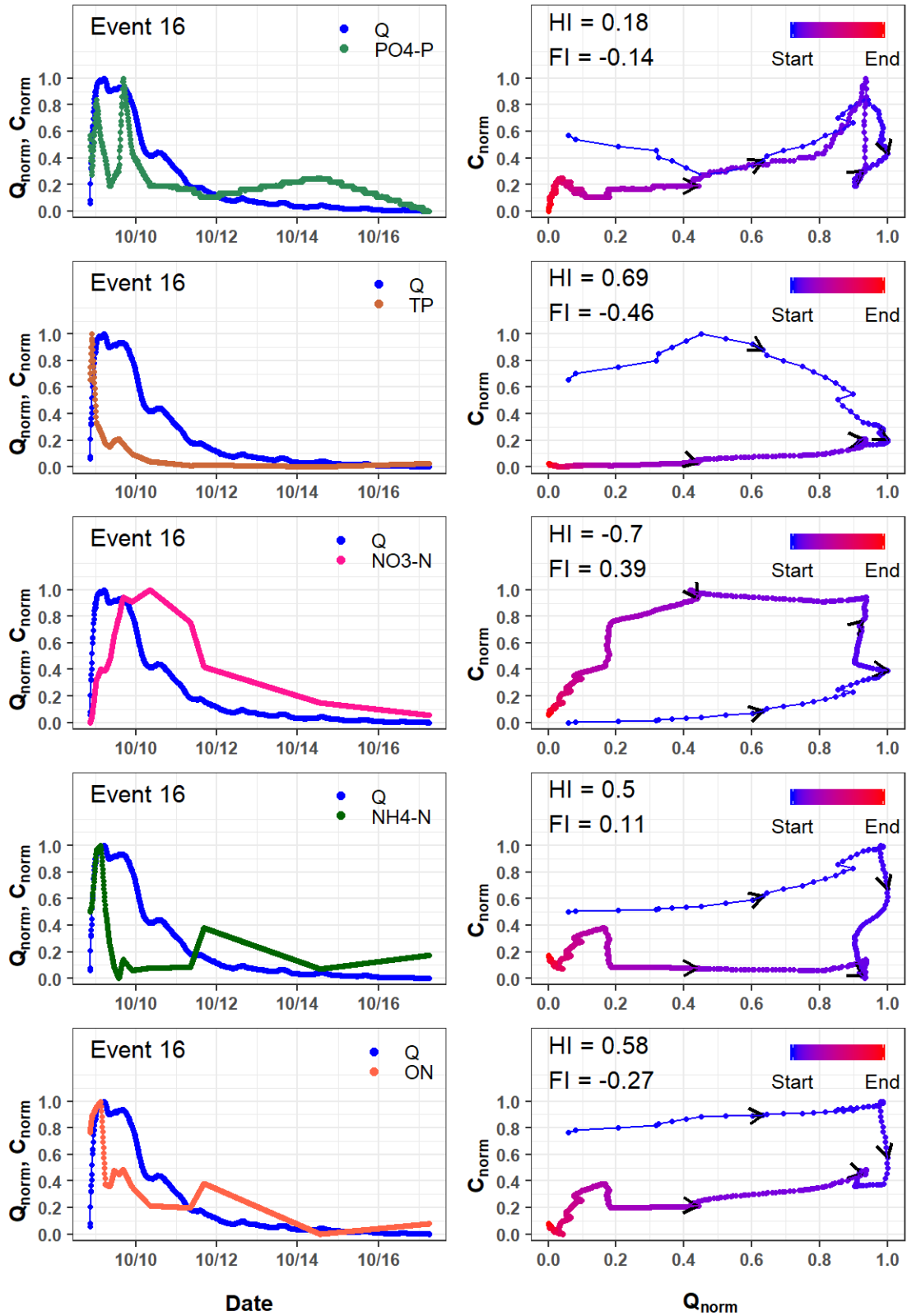


Figure D.11. Event 16 hydrographs, chemographs, and hysteresis loops for nitrogen and phosphorous species.

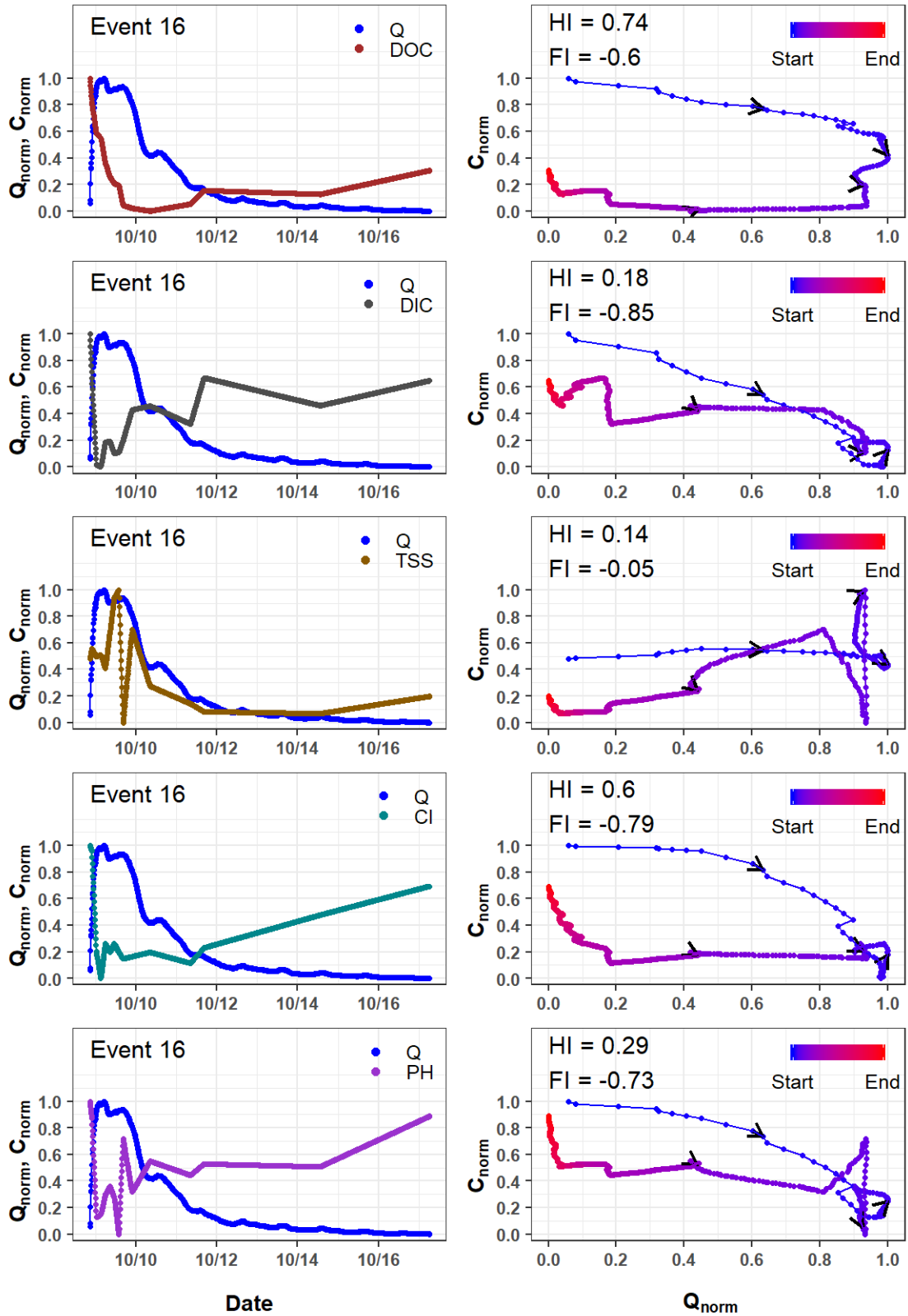


Figure D.12. Event 16 hydrographs, chemographs, and hysteresis loops for carbon species, suspended solids, chloride, and pH.

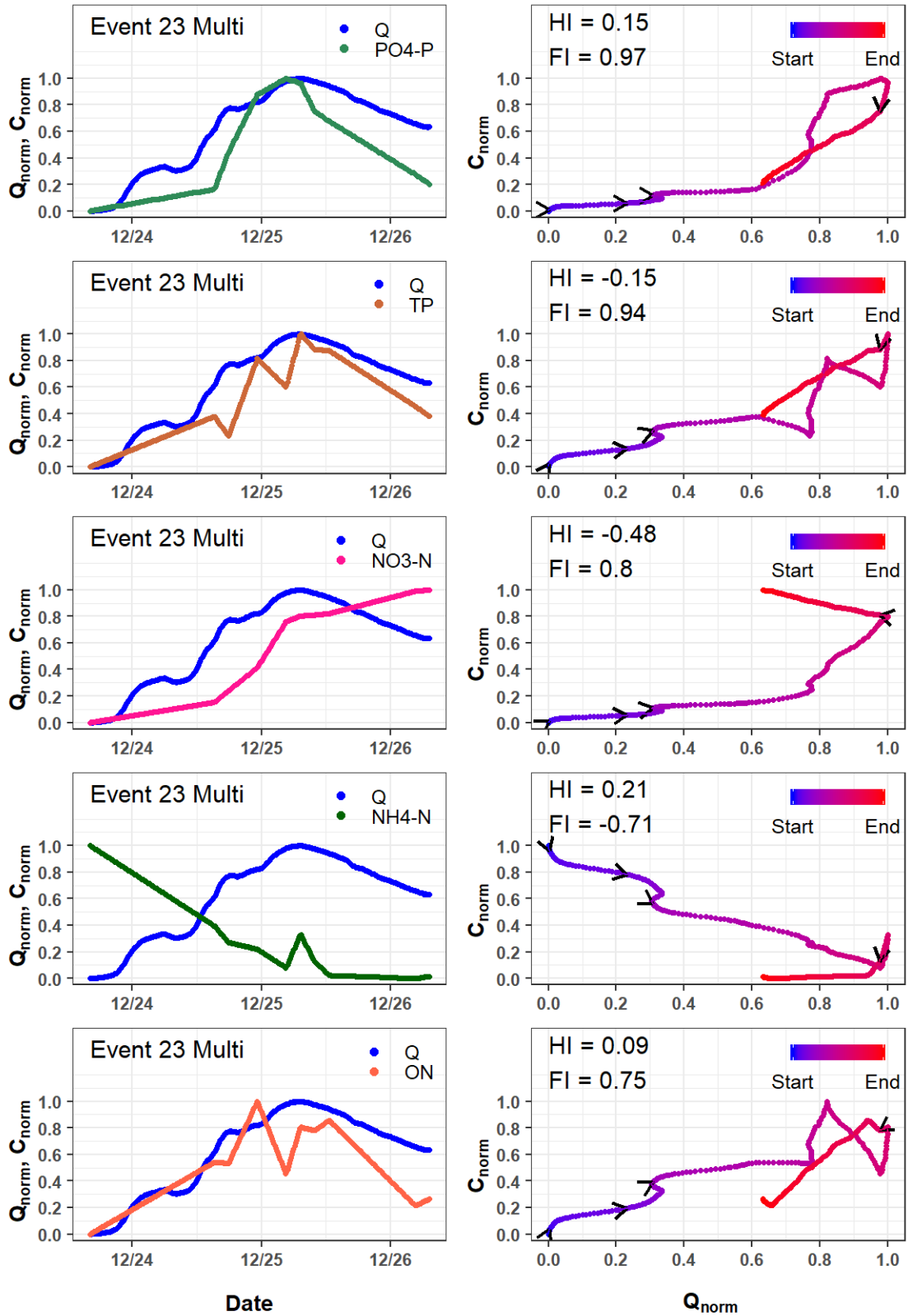


Figure D.13. Event 23 Multi (Events 23 & 24) hydrographs, chemographs, and hysteresis loops for nitrogen and phosphorous species

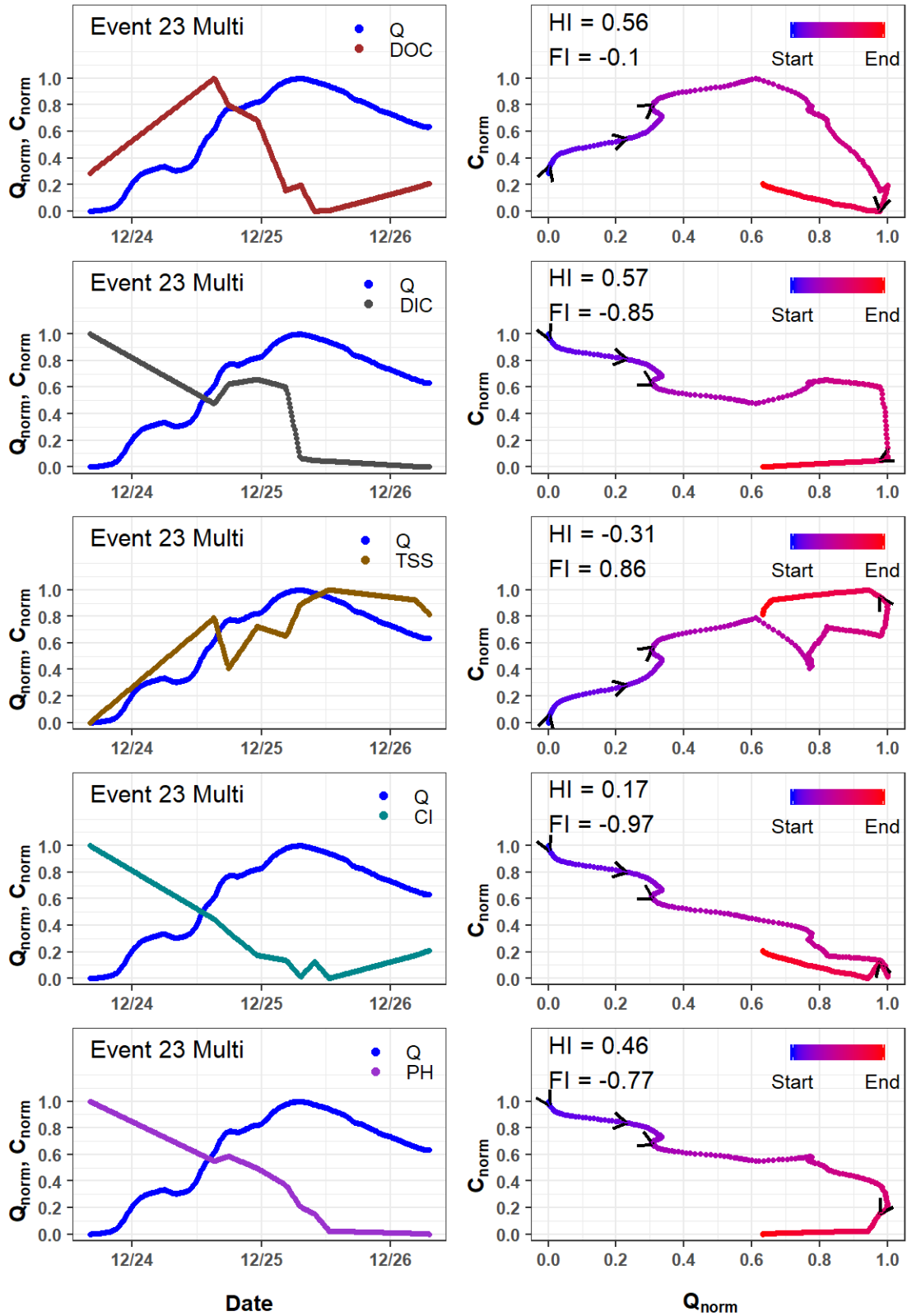


Figure D.14. Event 23 Multi (Events 23 & 24) hydrographs, chemographs, and hysteresis loops for carbon species, suspended solids, chloride, and pH.

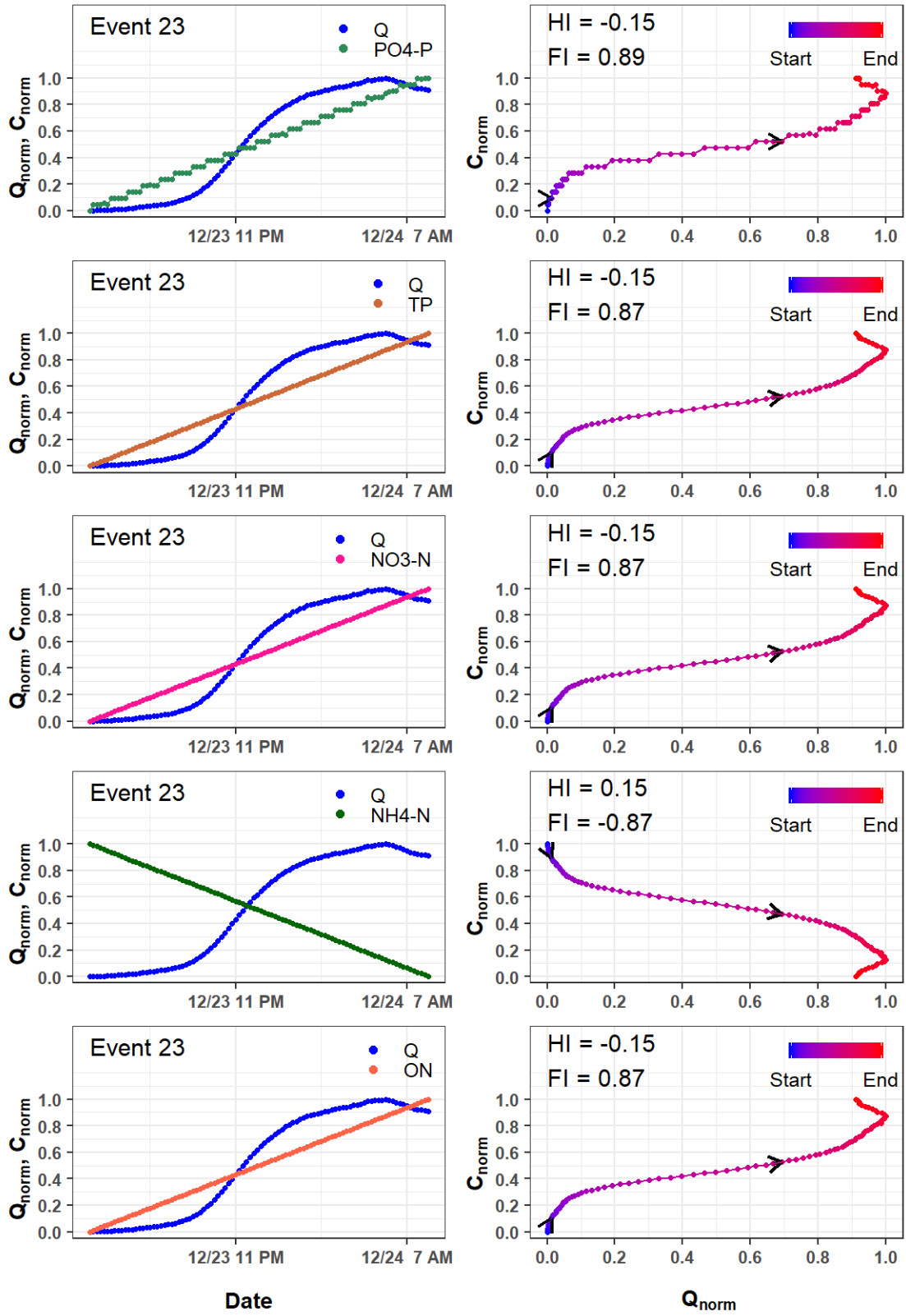


Figure D.15. Event 23 hydrographs, chemographs, and hysteresis loops for nitrogen and phosphorous species.

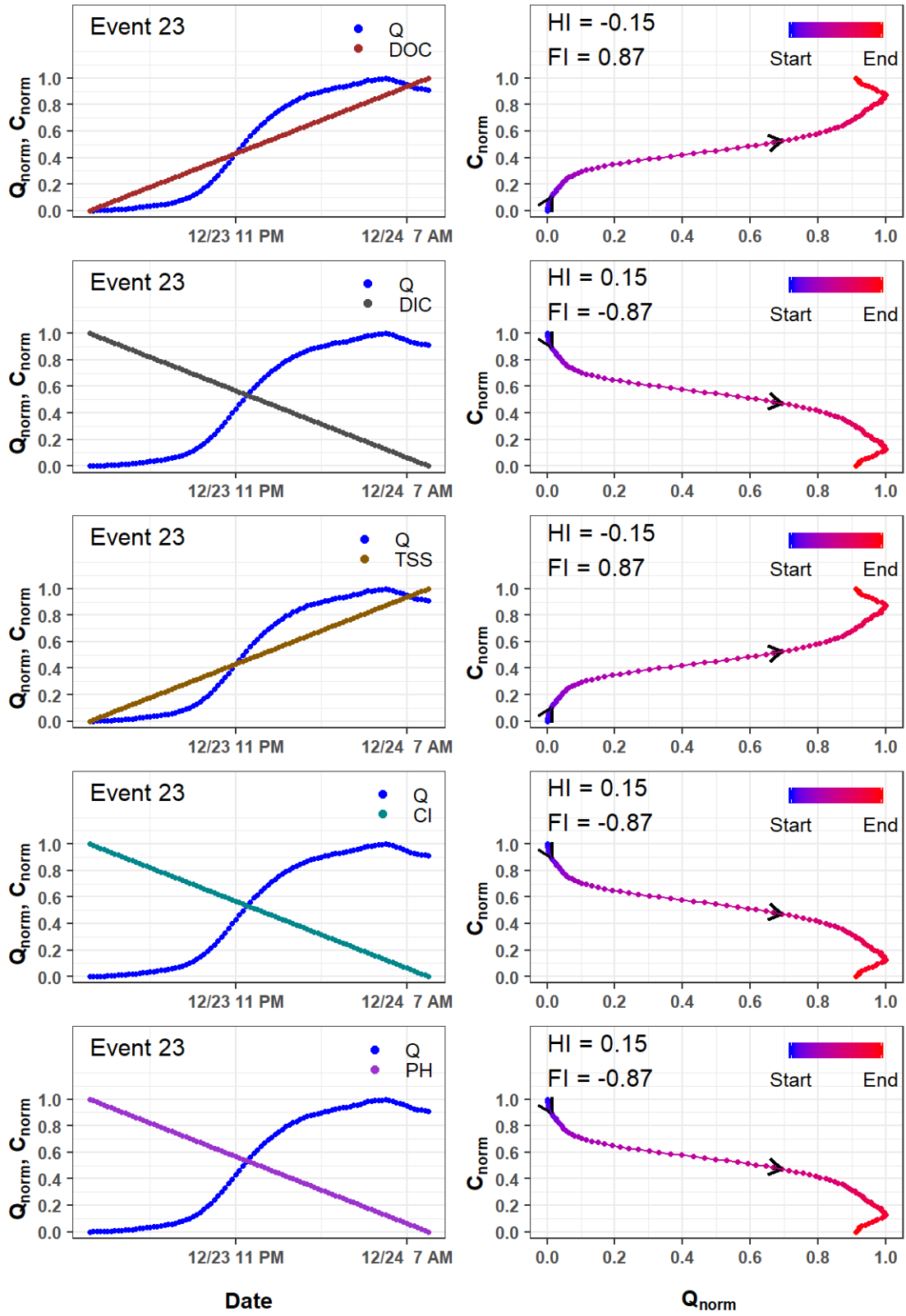


Figure D.16. Event 23 hydrographs, chemographs, and hysteresis loops for carbon species, suspended solids, chloride, and pH.

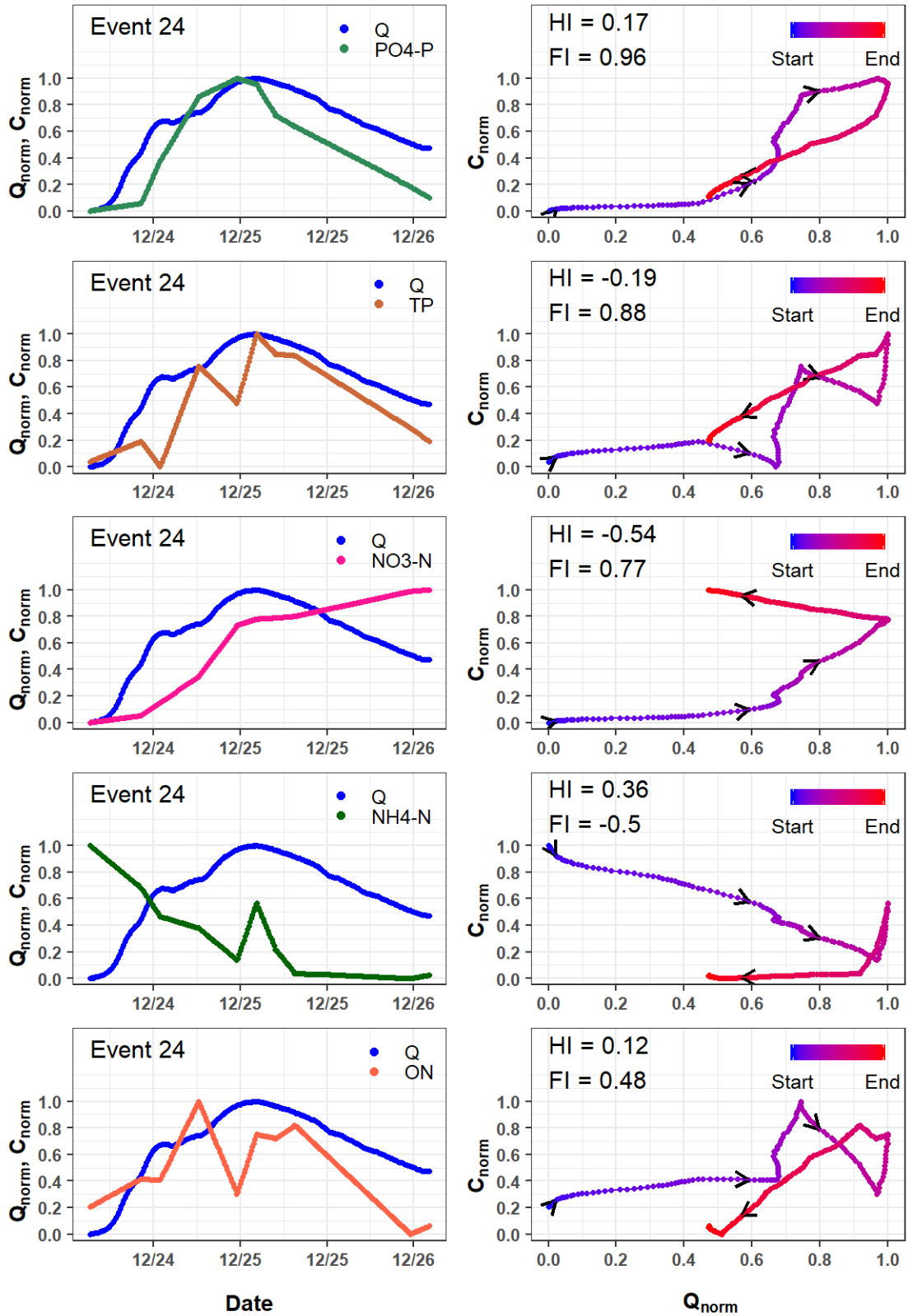


Figure D.17. Event 24 hydrographs, chemographs, and hysteresis loops for nitrogen and phosphorous species.

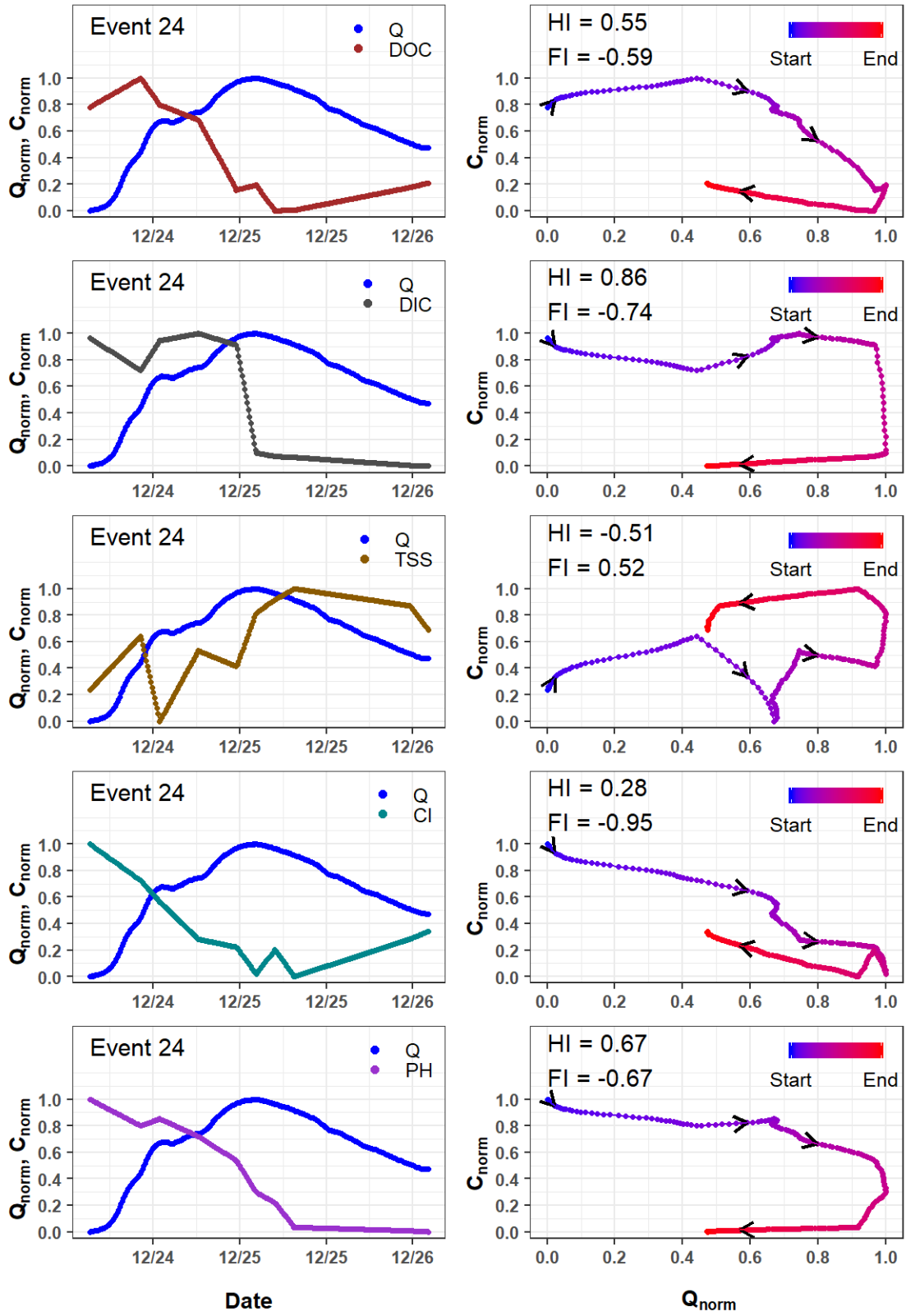


Figure D.18. Event 24 hydrographs, chemographs, and hysteresis loops for carbon species, suspended solids, chloride, and pH.

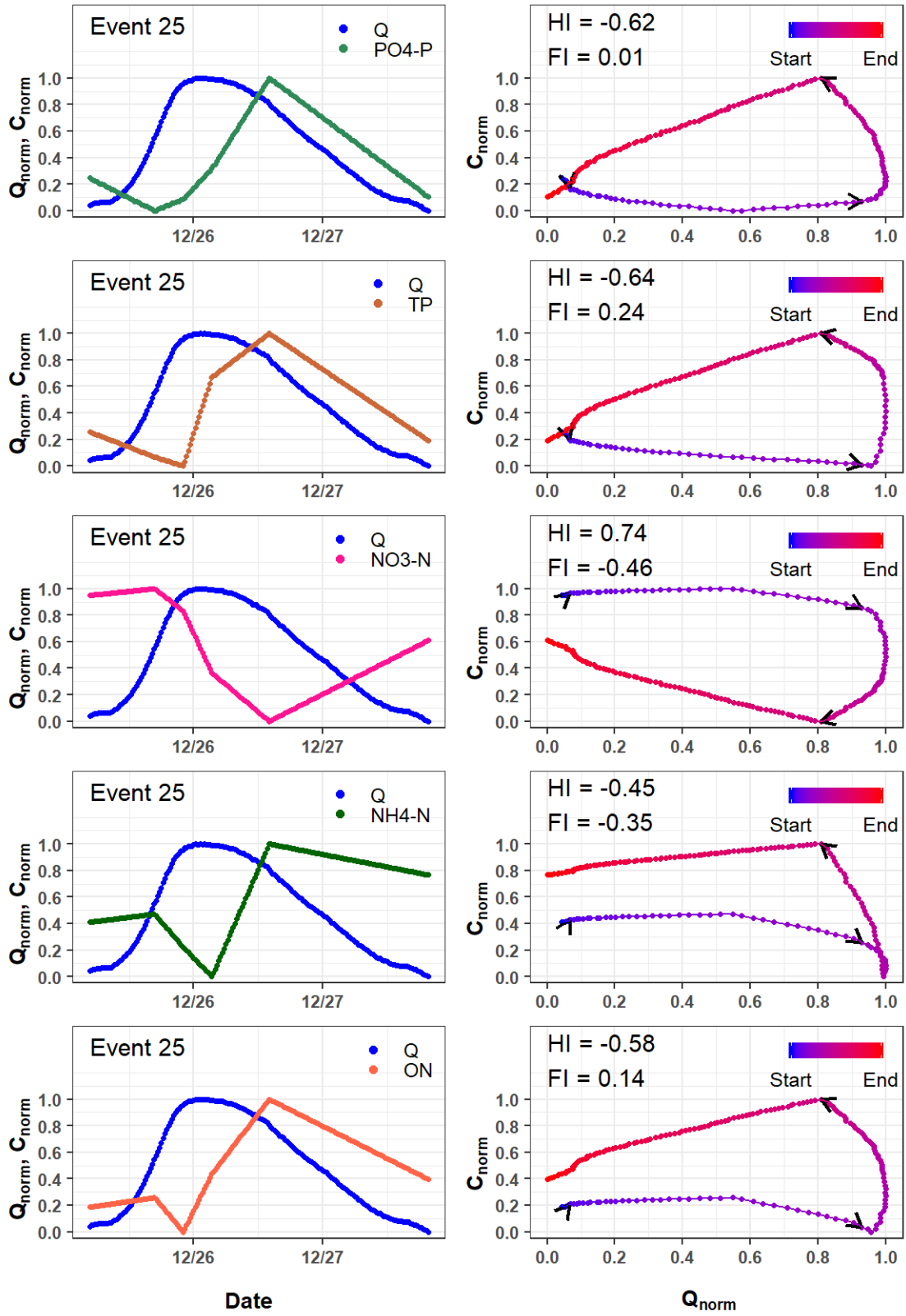


Figure D.19. Event 25 hydrographs, chemographs, and hysteresis loops for nitrogen and phosphorous species.

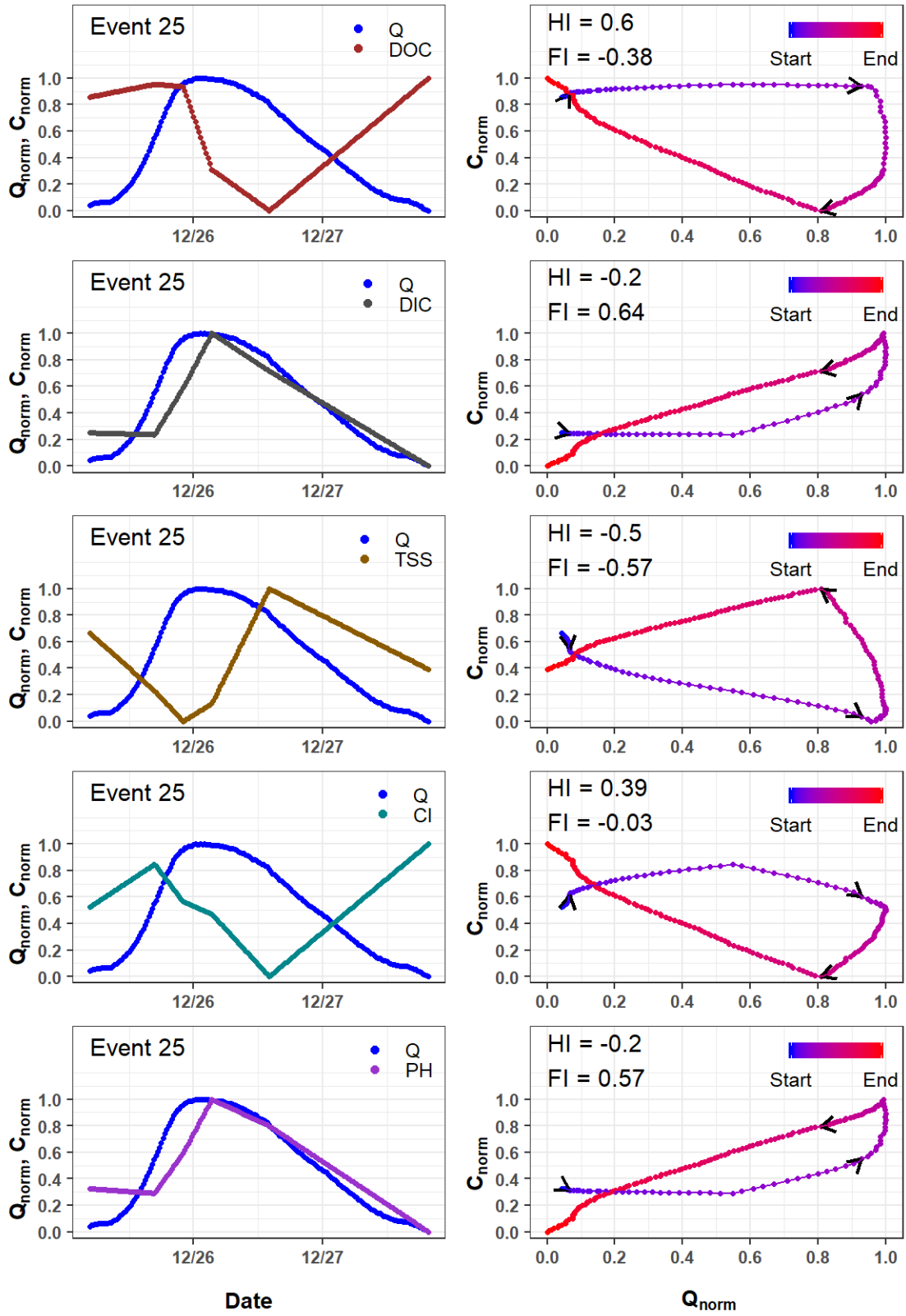


Figure D.20. Event 25 hydrographs, chemographs, and hysteresis loops for carbon species, suspended solids, chloride, and pH.

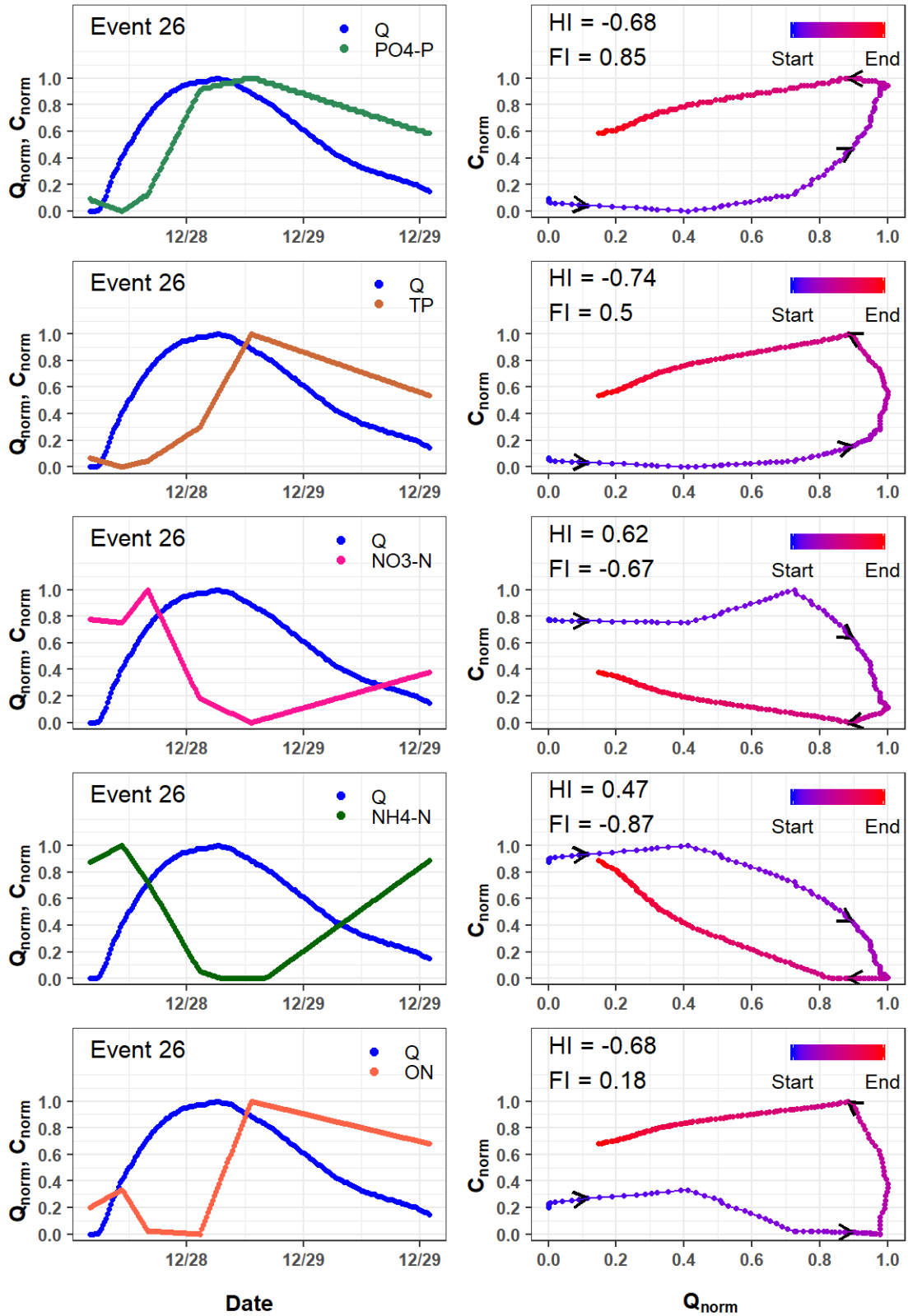


Figure D.21. Event 26 hydrographs, chemographs, and hysteresis loops for nitrogen and phosphorous species.

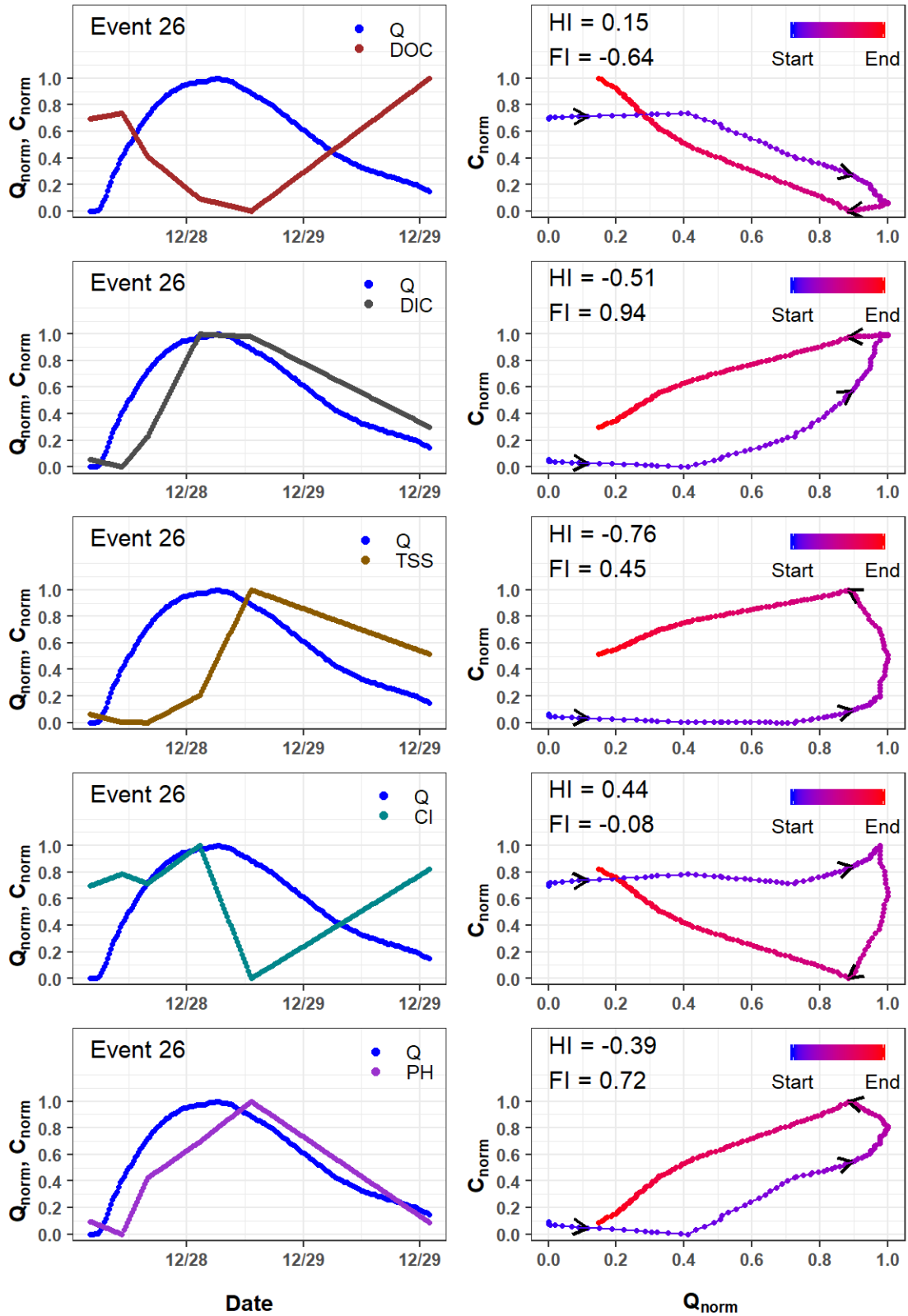


Figure D.22. Event 26 hydrographs, chemographs, and hysteresis loops for carbon species, suspended solids, chloride, and pH.

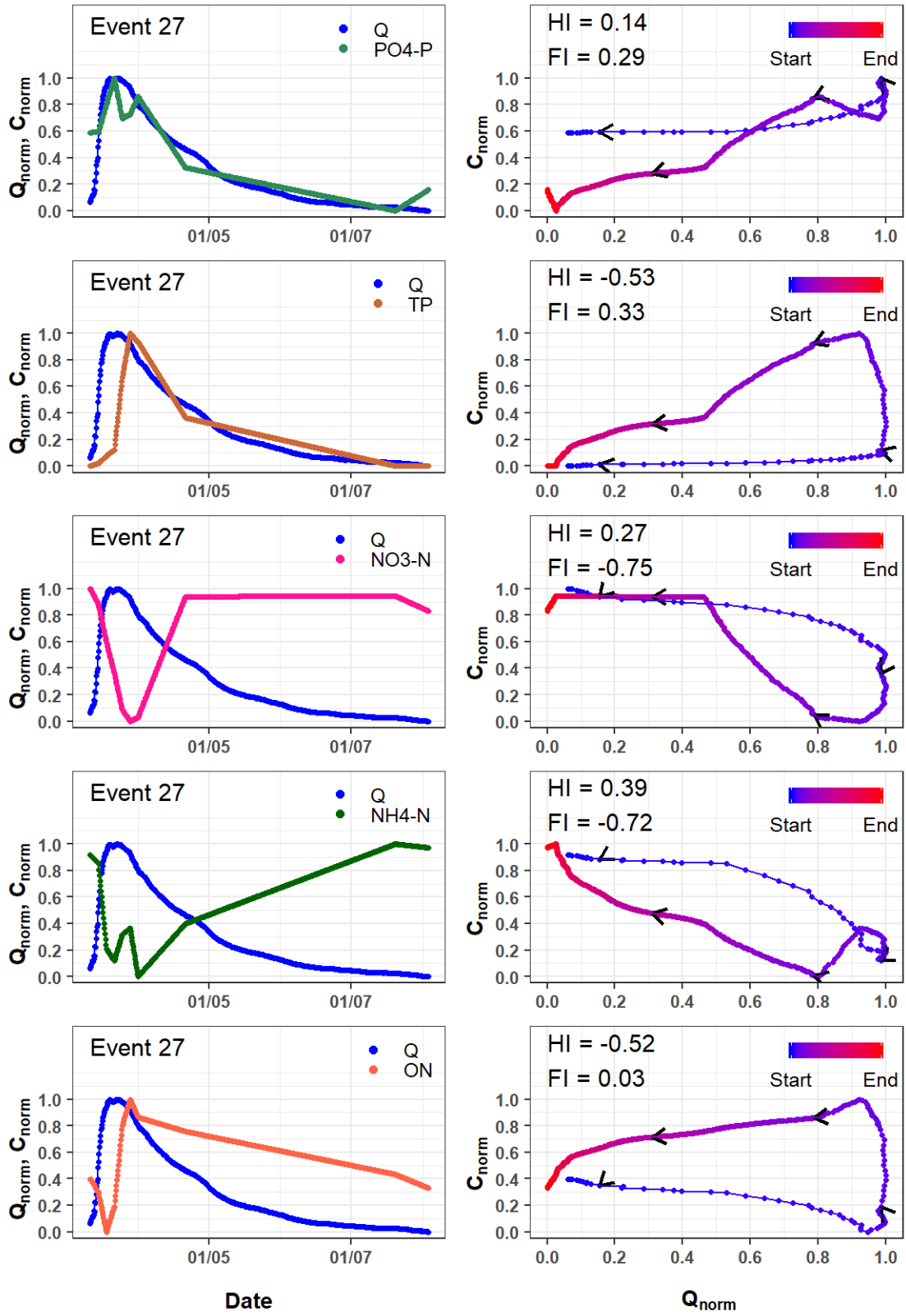


Figure D.23. Event 27 hydrographs, chemographs, and hysteresis loops for nitrogen and phosphorous species.

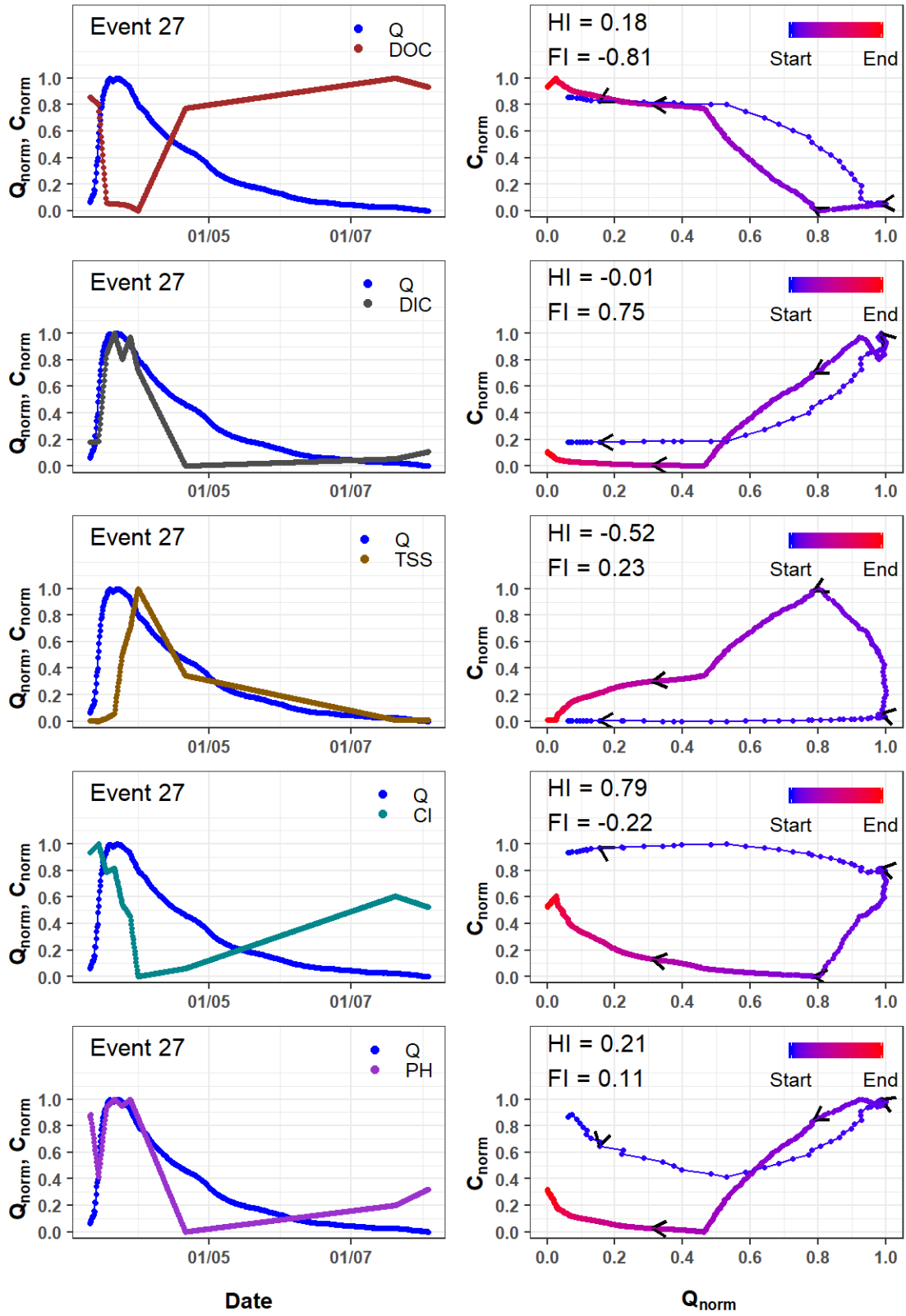


Figure D.24. Event 27 hydrographs, chemographs, and hysteresis loops for carbon species, suspended solids, chloride, and pH.

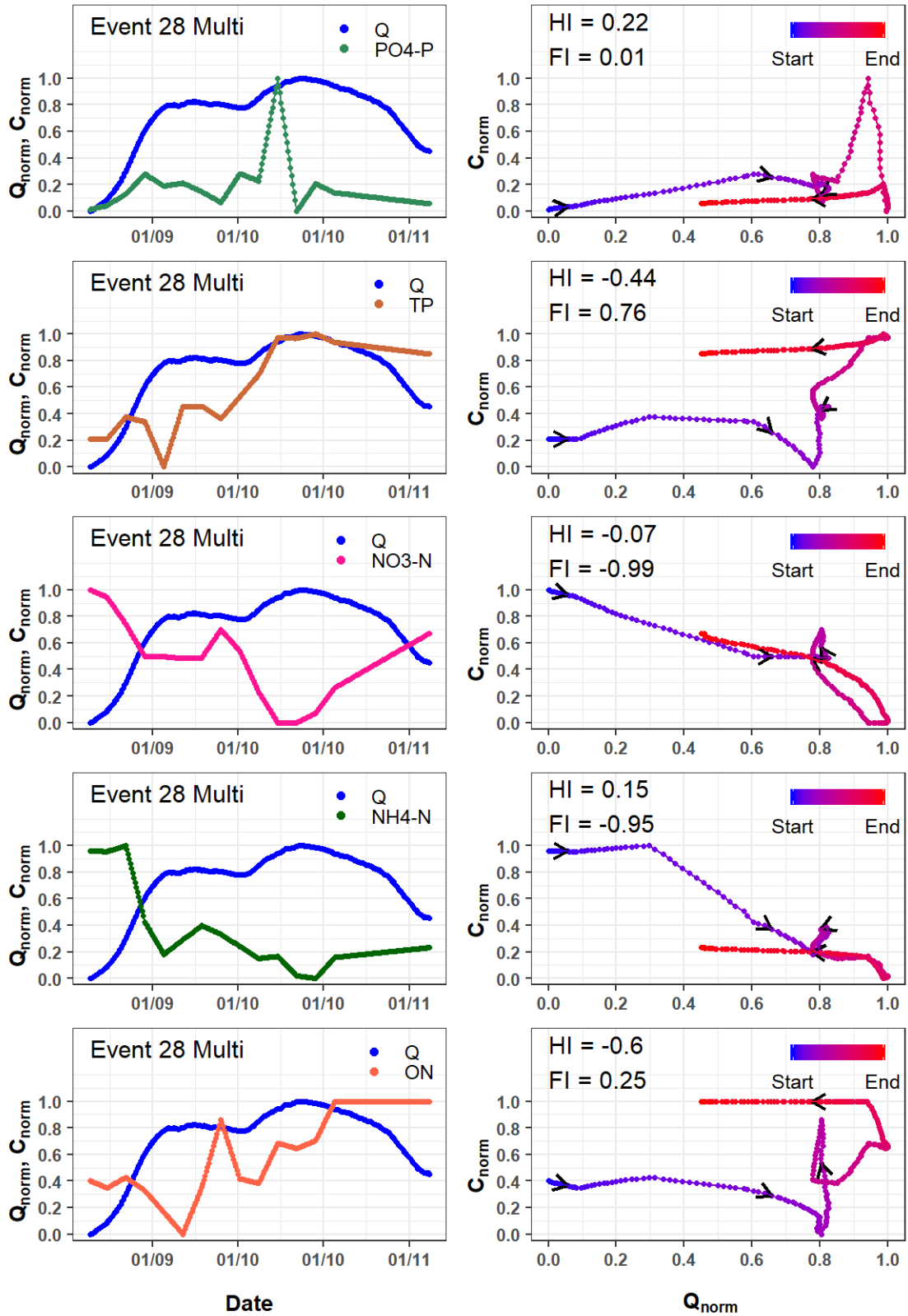


Figure D.25. Event 28 Multi (Events 28 & 29) hydrographs, chemographs, and hysteresis loops for nitrogen and phosphorous species.

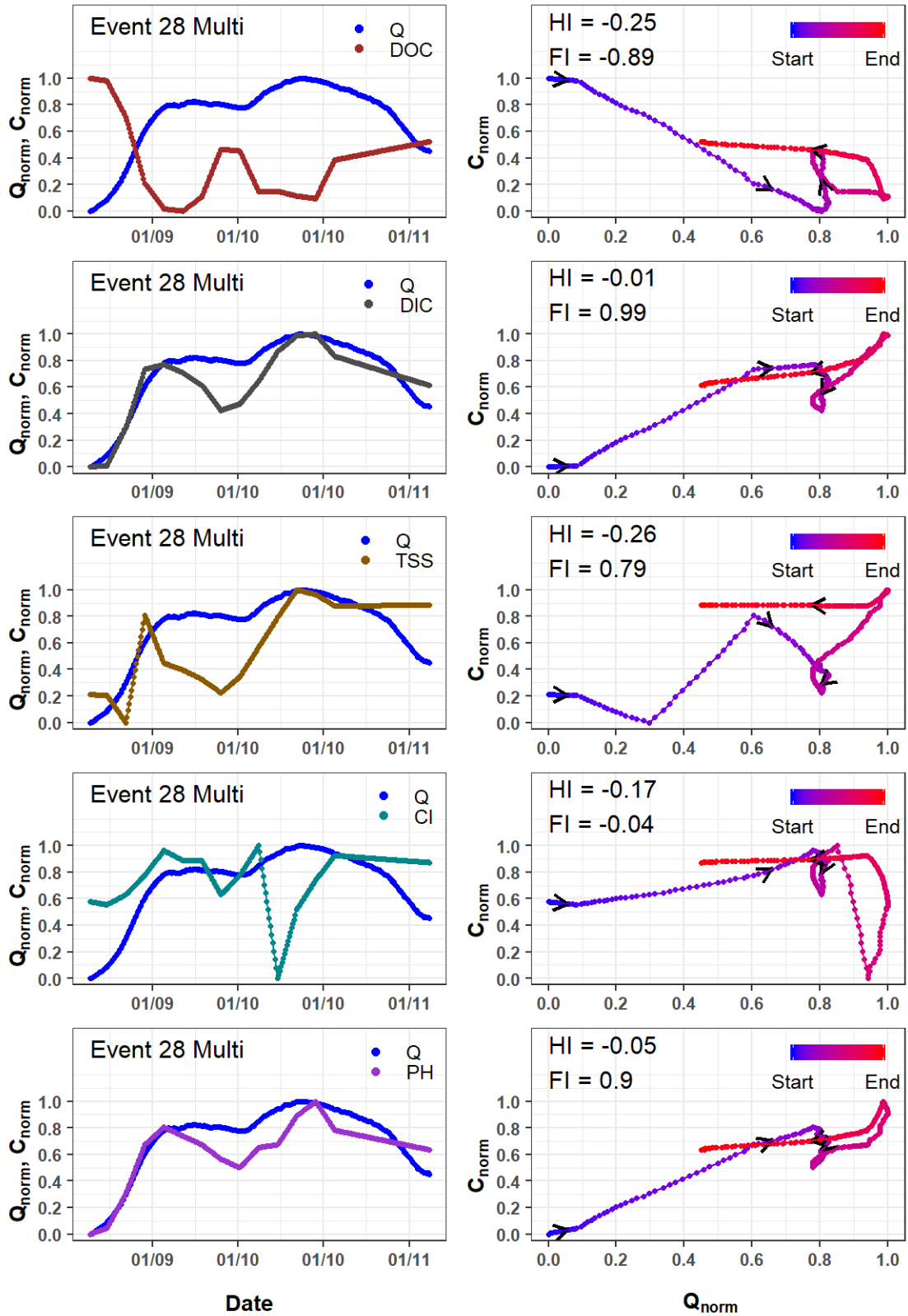


Figure D.26. Event 28 Multi (Events 28 & 29) hydrographs, chemographs, and hysteresis loops for carbon species, suspended solids, chloride, and pH.

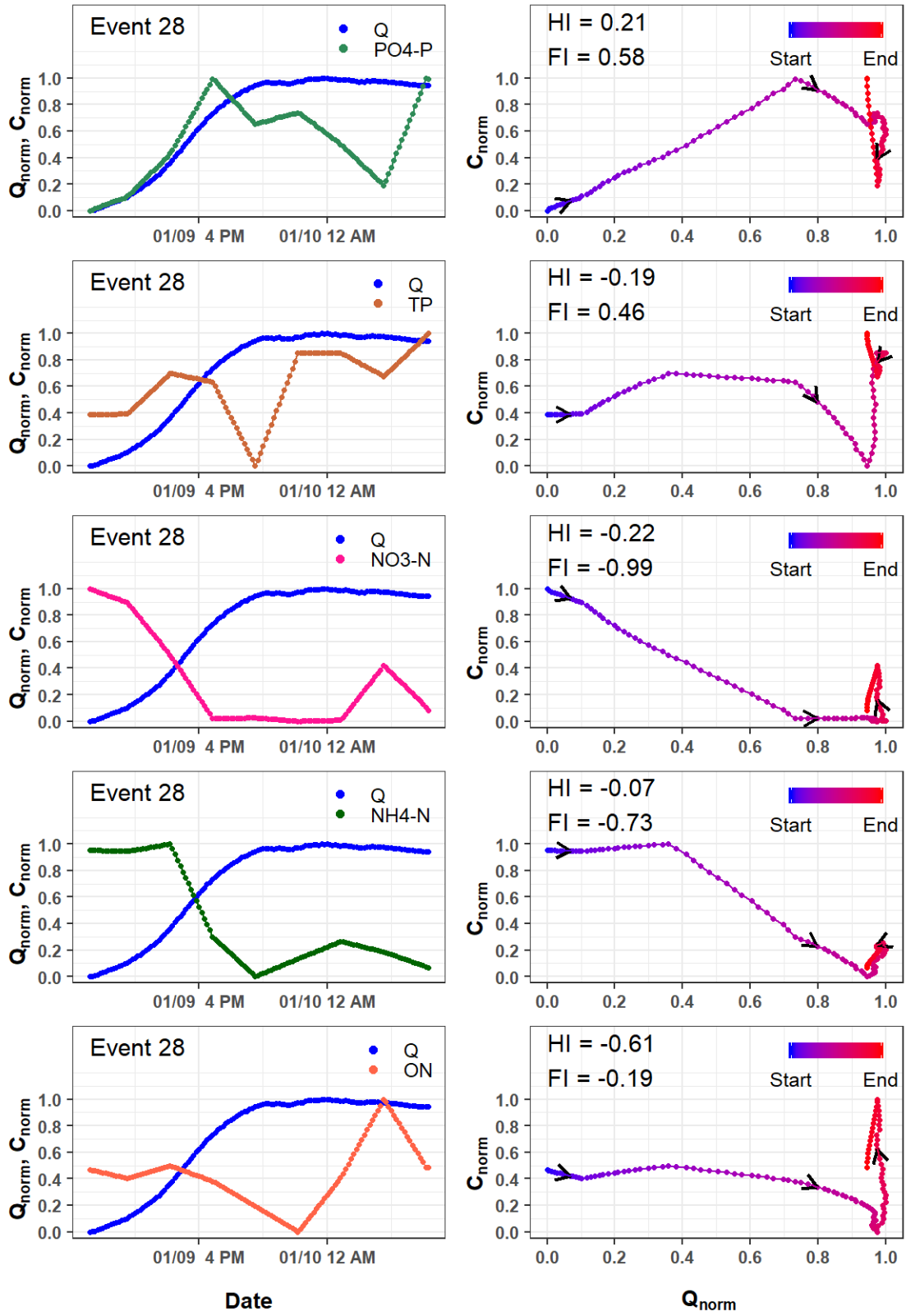


Figure D.27. Event 28 hydrographs, chemographs, and hysteresis loops for nitrogen and phosphorous species.

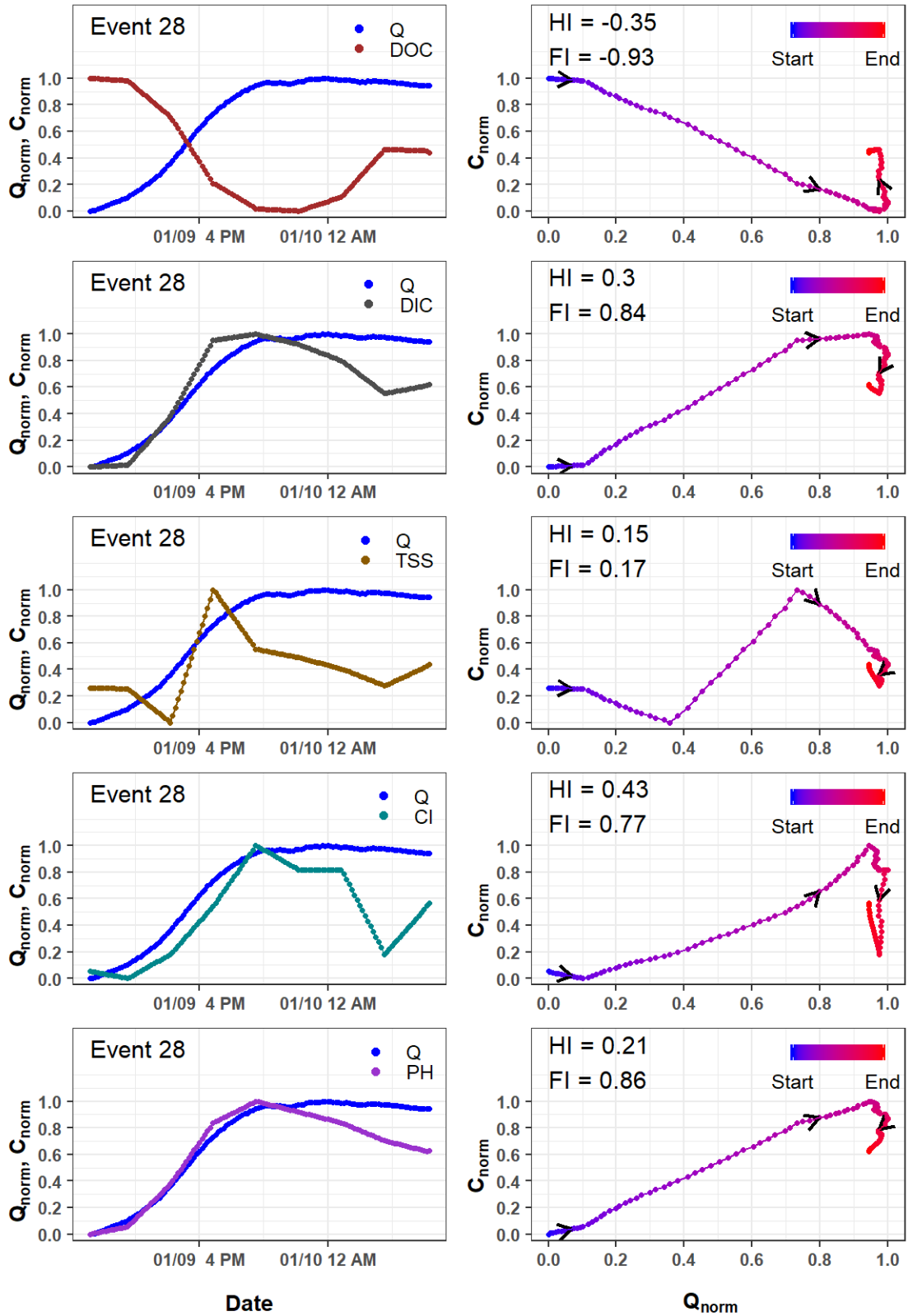


Figure D.28. Event 28 hydrographs, chemographs, and hysteresis loops for carbon species, suspended solids, chloride, and pH.

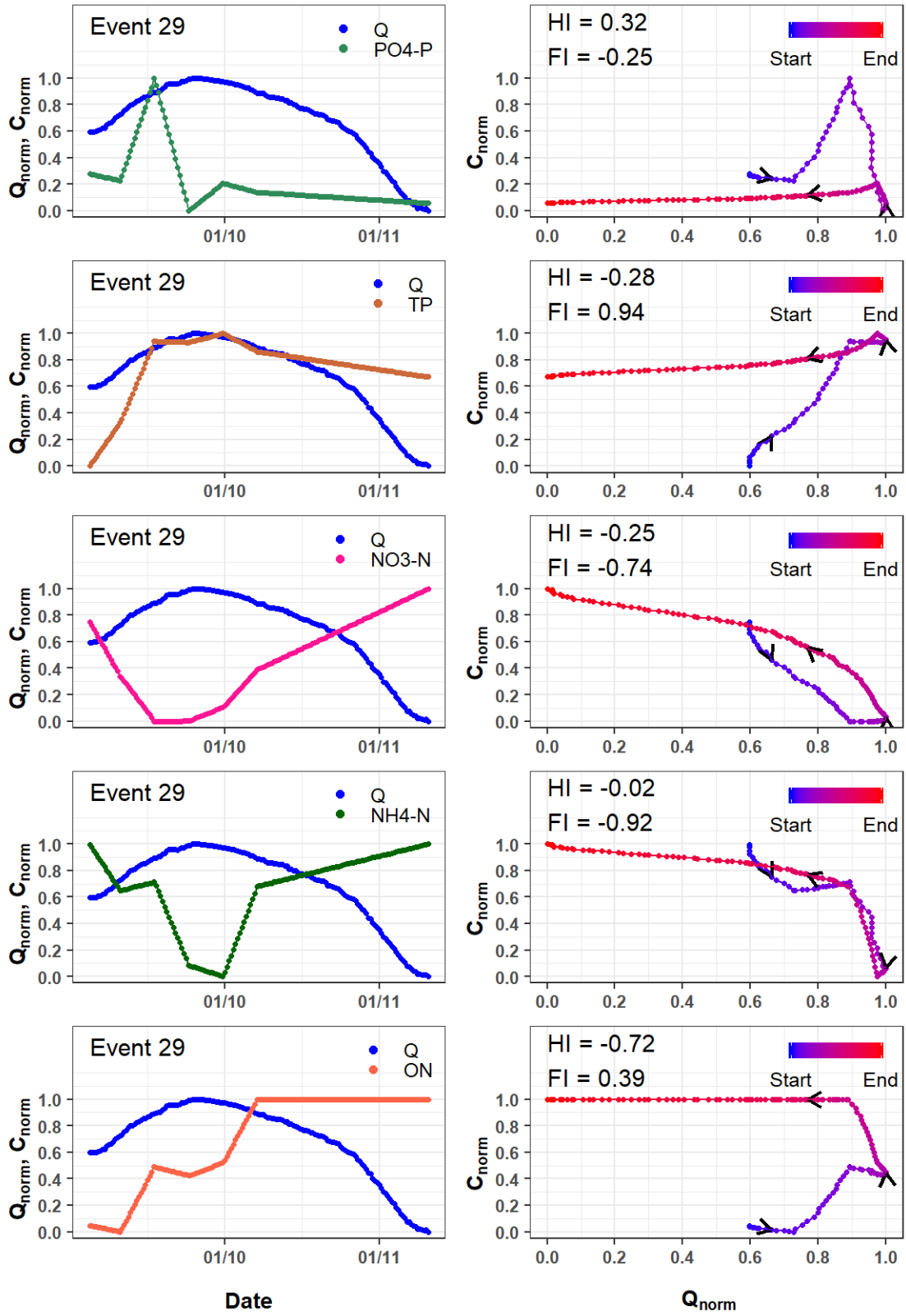


Figure D.29. Event 29 hydrographs, chemographs, and hysteresis loops for nitrogen and phosphorous species.

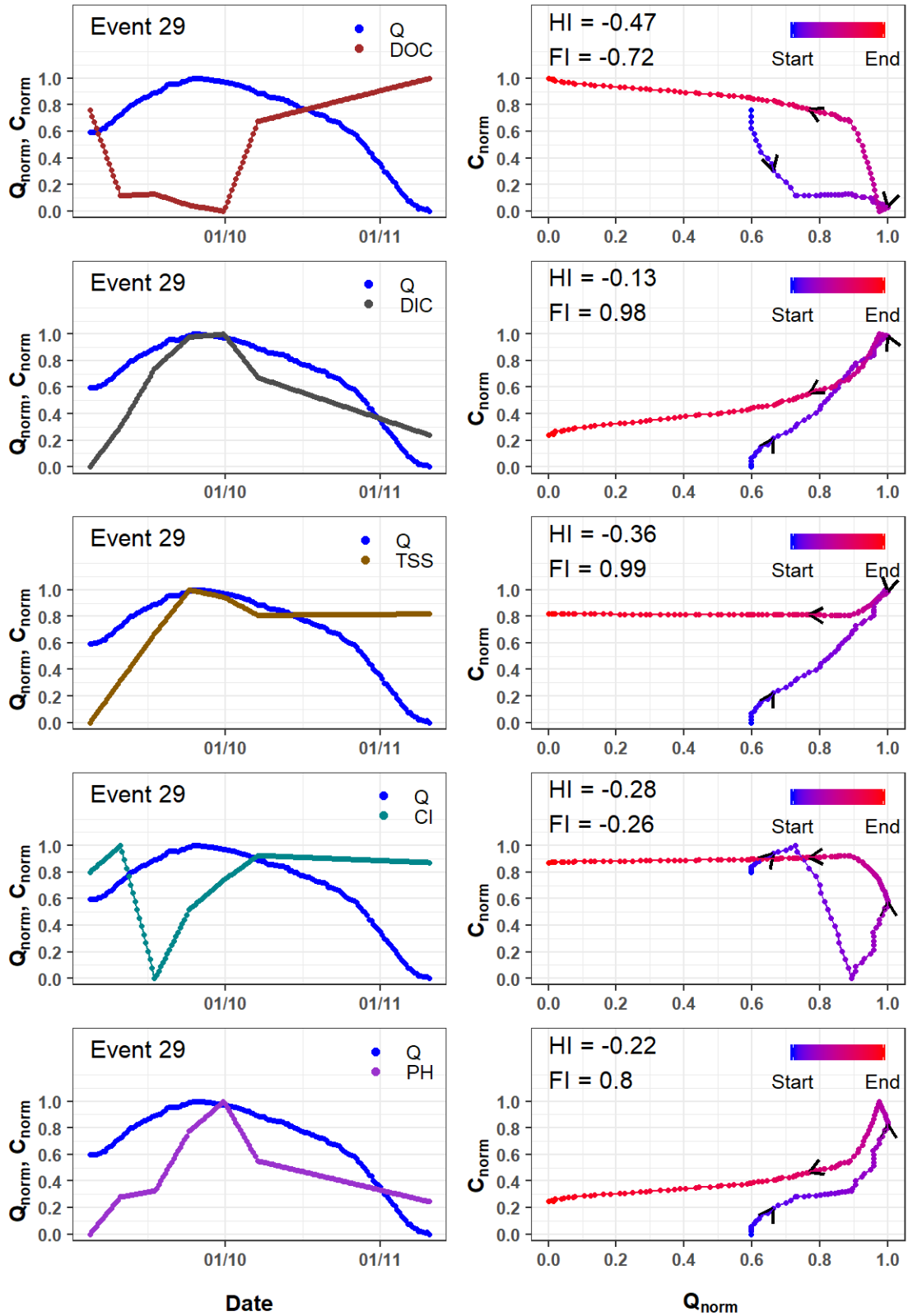


Figure D.30. Event 29 hydrographs, chemographs, and hysteresis loops for carbon species, suspended solids, chloride, and pH.

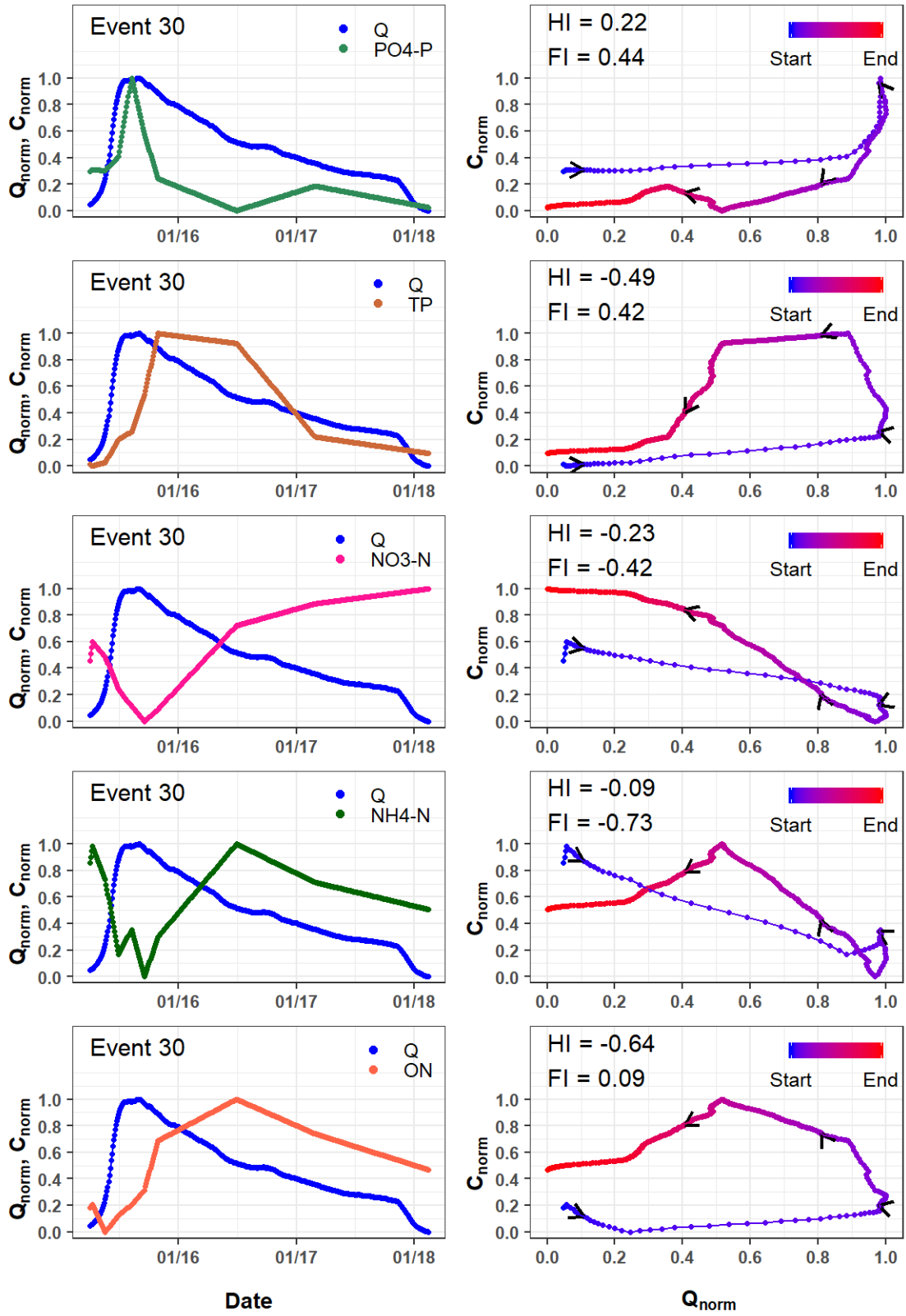


Figure D.31. Event 30 hydrographs, chemographs, and hysteresis loops for nitrogen and phosphorous species.

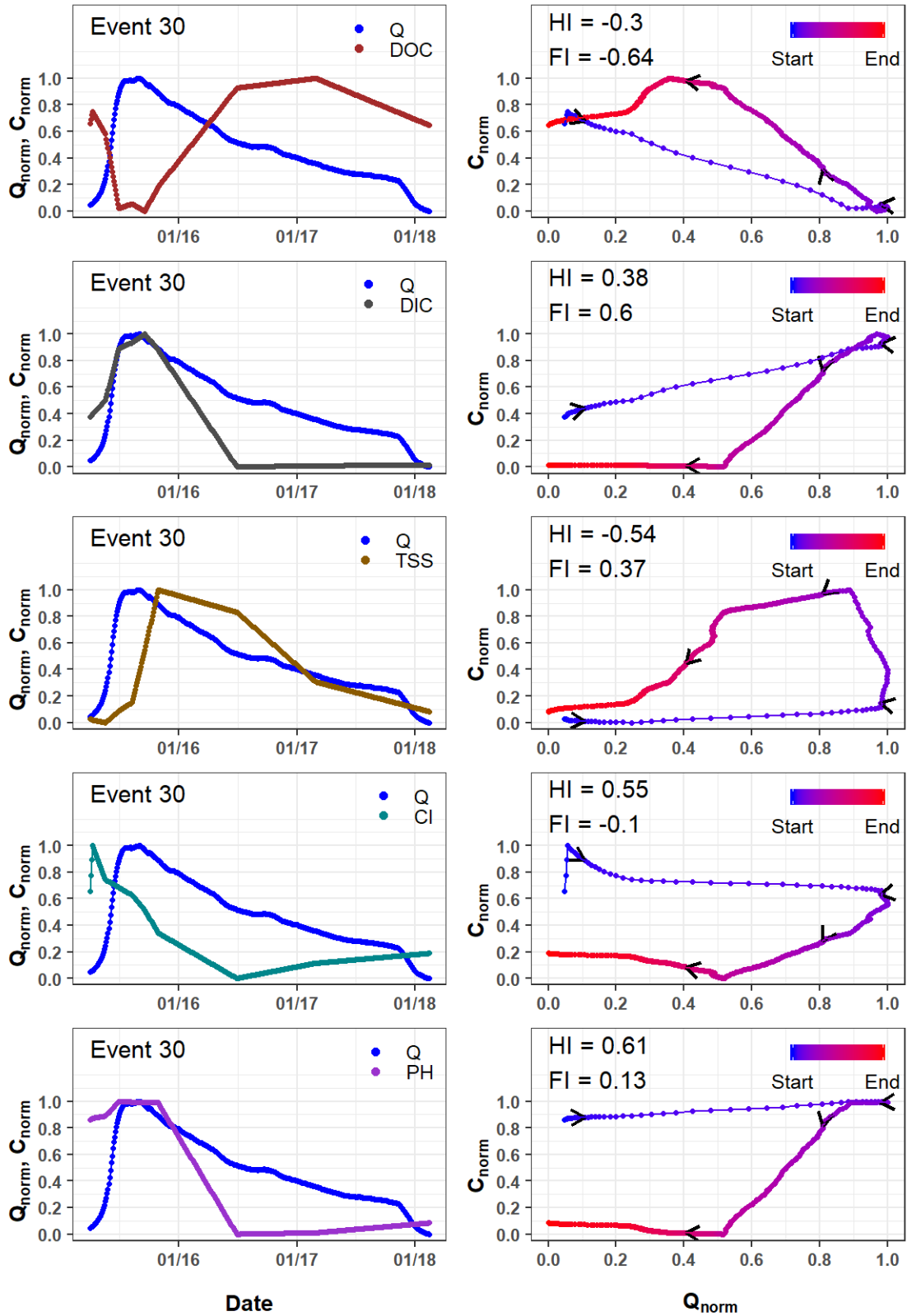


Figure D.32. Event 30 hydrographs, chemographs, and hysteresis loops for carbon species, suspended solids, chloride, and pH.

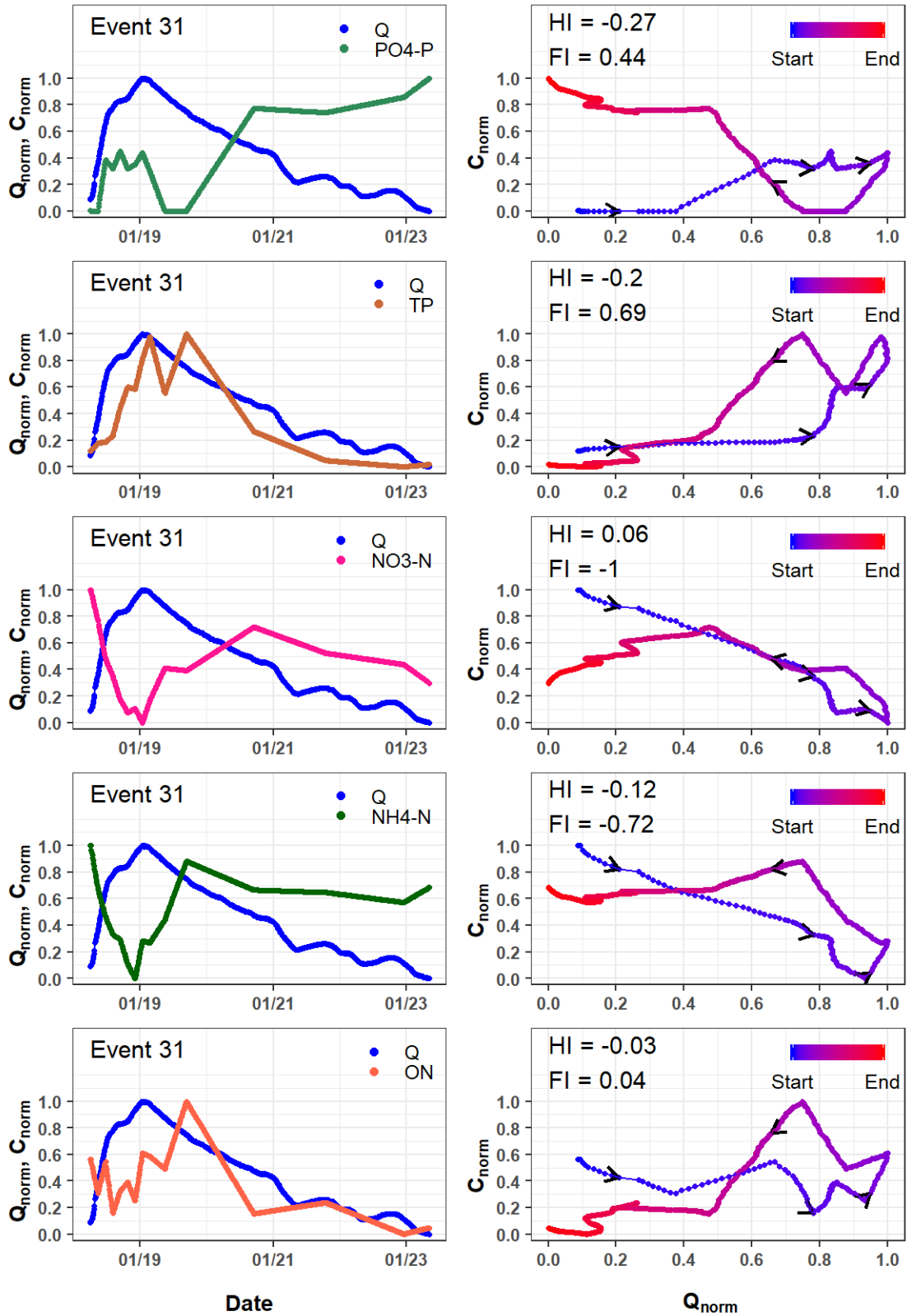


Figure D.33. Event 31 hydrographs, chemographs, and hysteresis loops for nitrogen and phosphorous species.

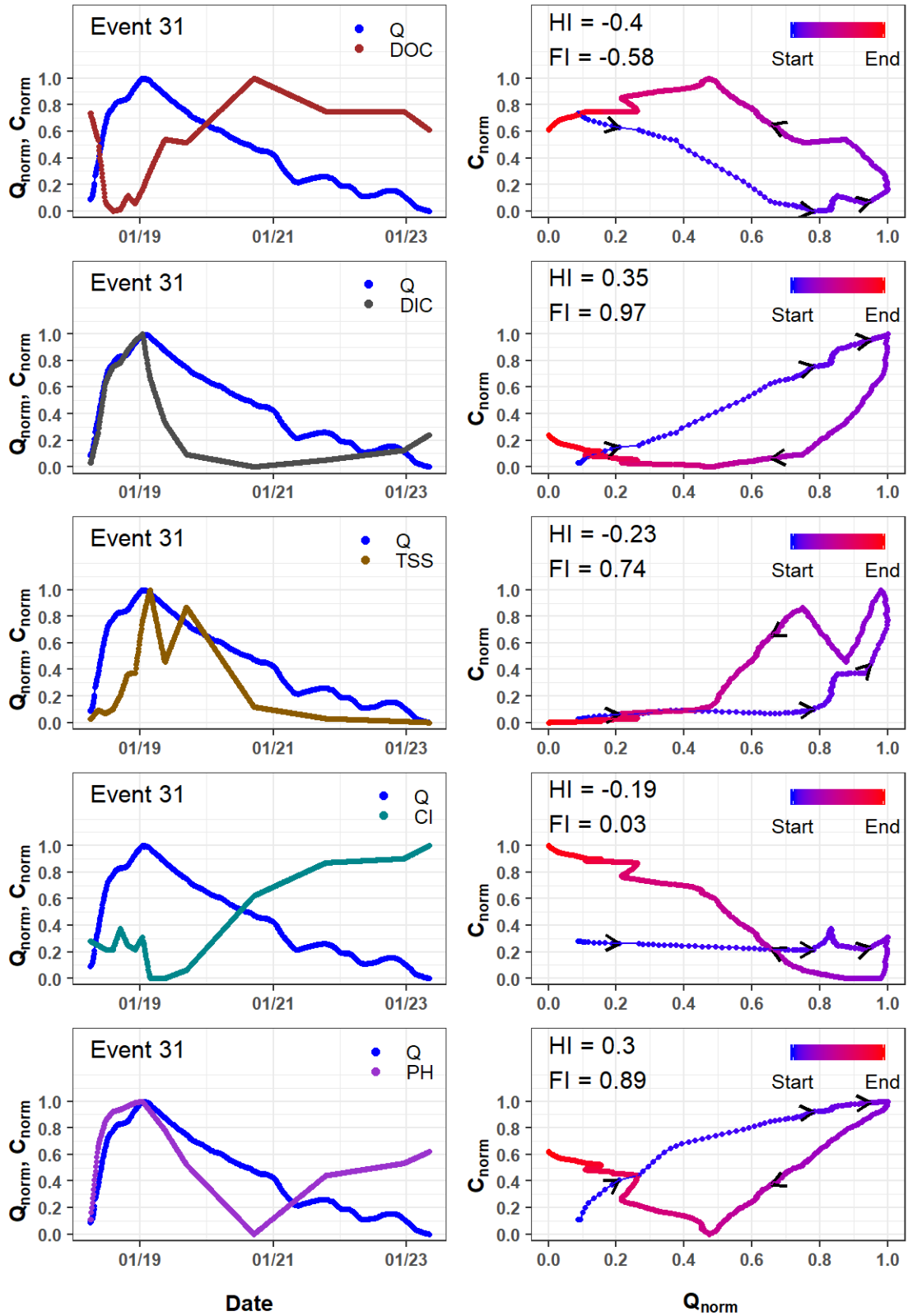


Figure D.34. Event 31 hydrographs, chemographs, and hysteresis loops for carbon species, suspended solids, chloride, and pH.

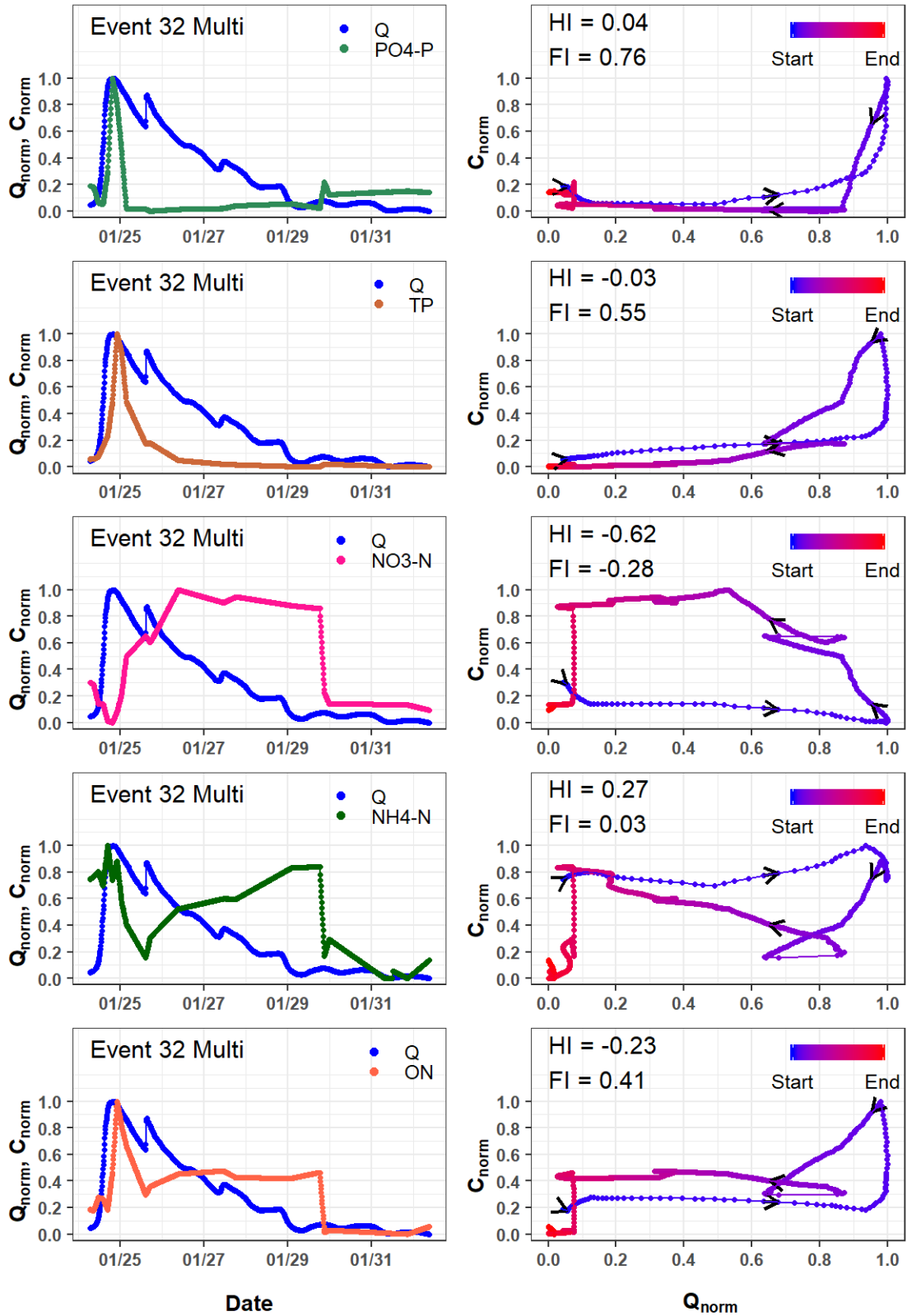


Figure D.35. Event 32 Multi (Events 32, 33 & 34) hydrographs, chemographs, and hysteresis loops for nitrogen and phosphorous species.

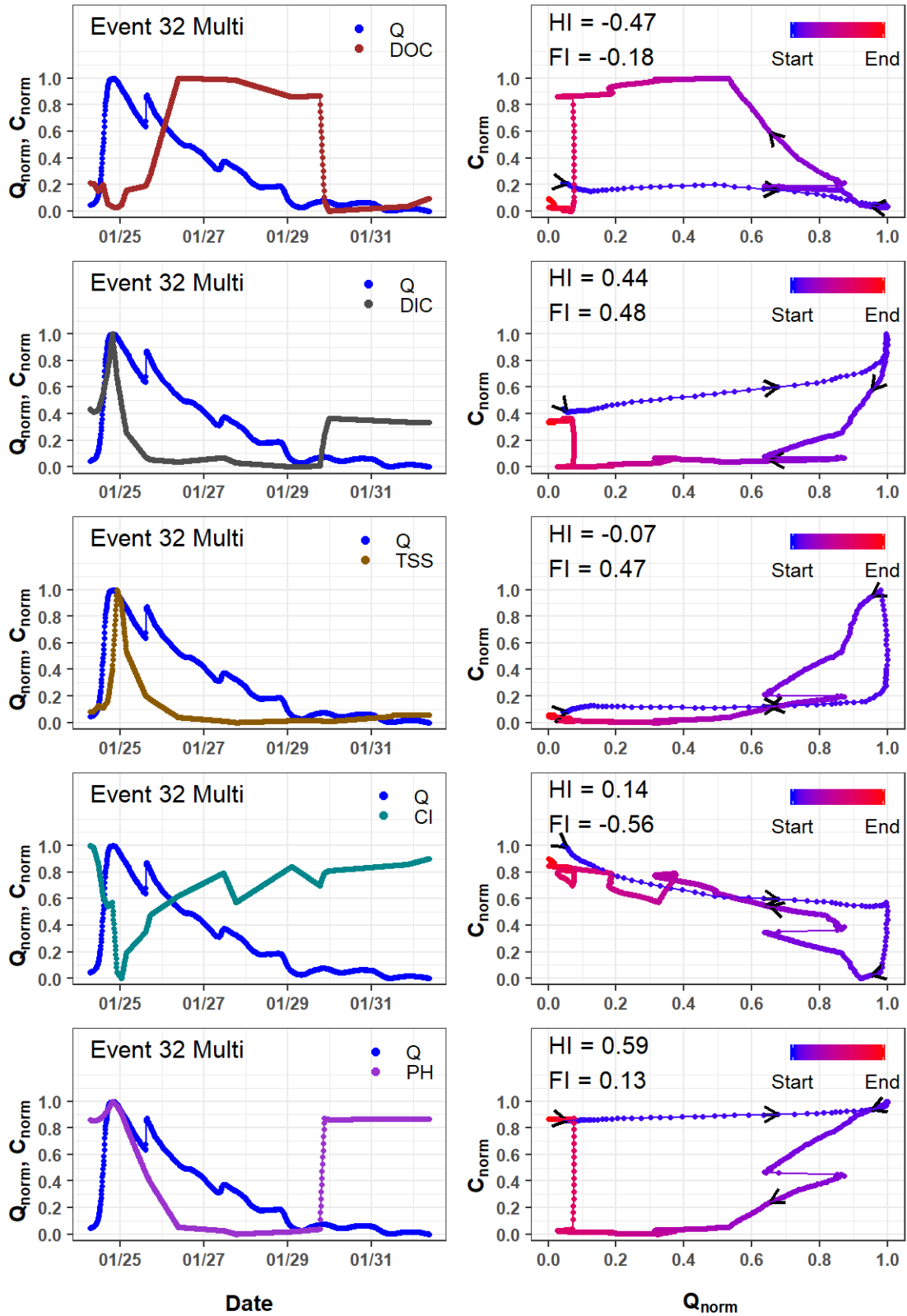


Figure D.36. Event 32 Multi (Events 32, 33 & 34) hydrographs, chemographs, and hysteresis loops for carbon species, suspended solids, chloride, and pH.

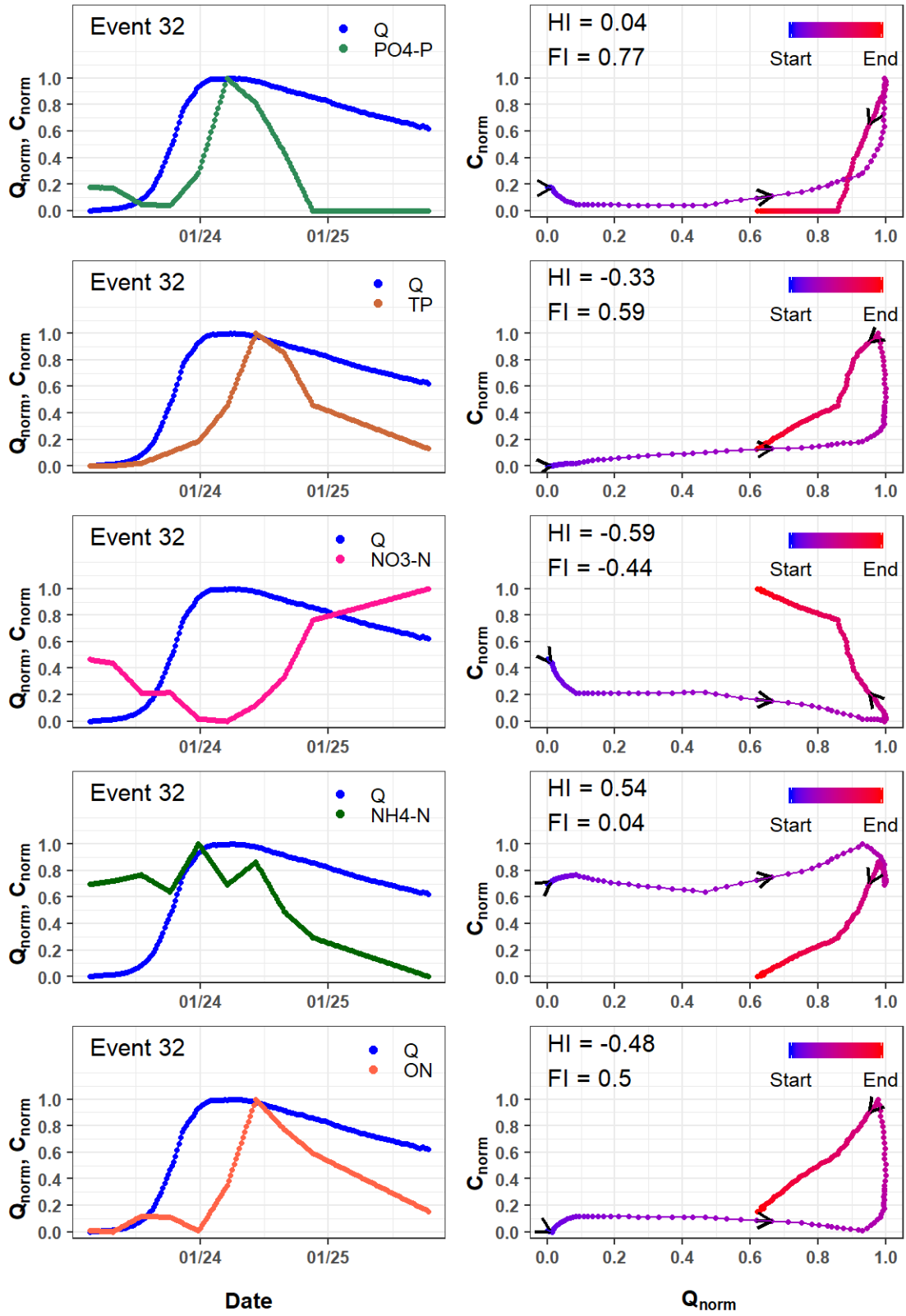


Figure D.37. Event 32 hydrographs, chemographs, and hysteresis loops for nitrogen and phosphorous species.

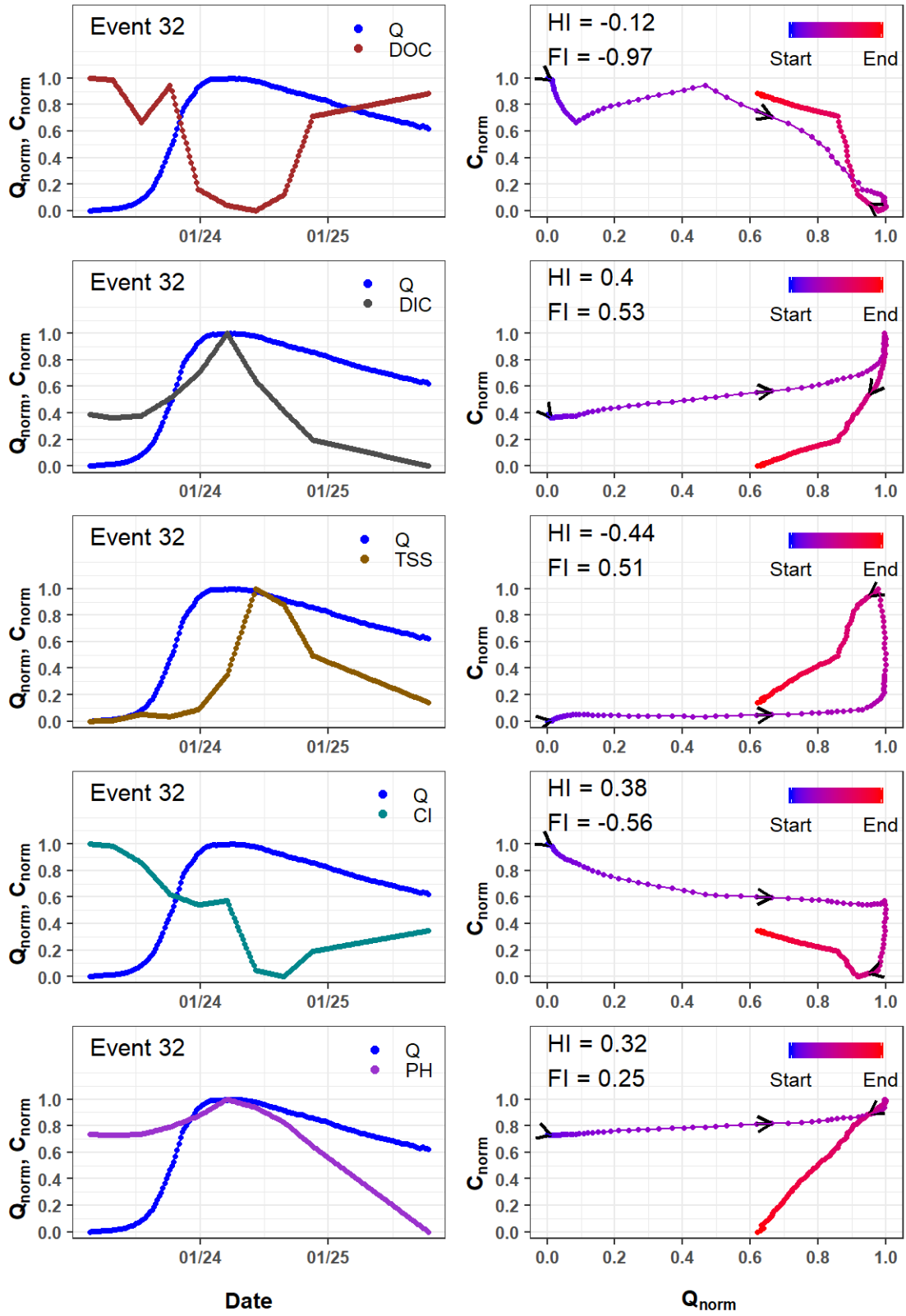


Figure D.38. Event 32 hydrographs, chemographs, and hysteresis loops for carbon species, suspended solids, chloride, and pH.

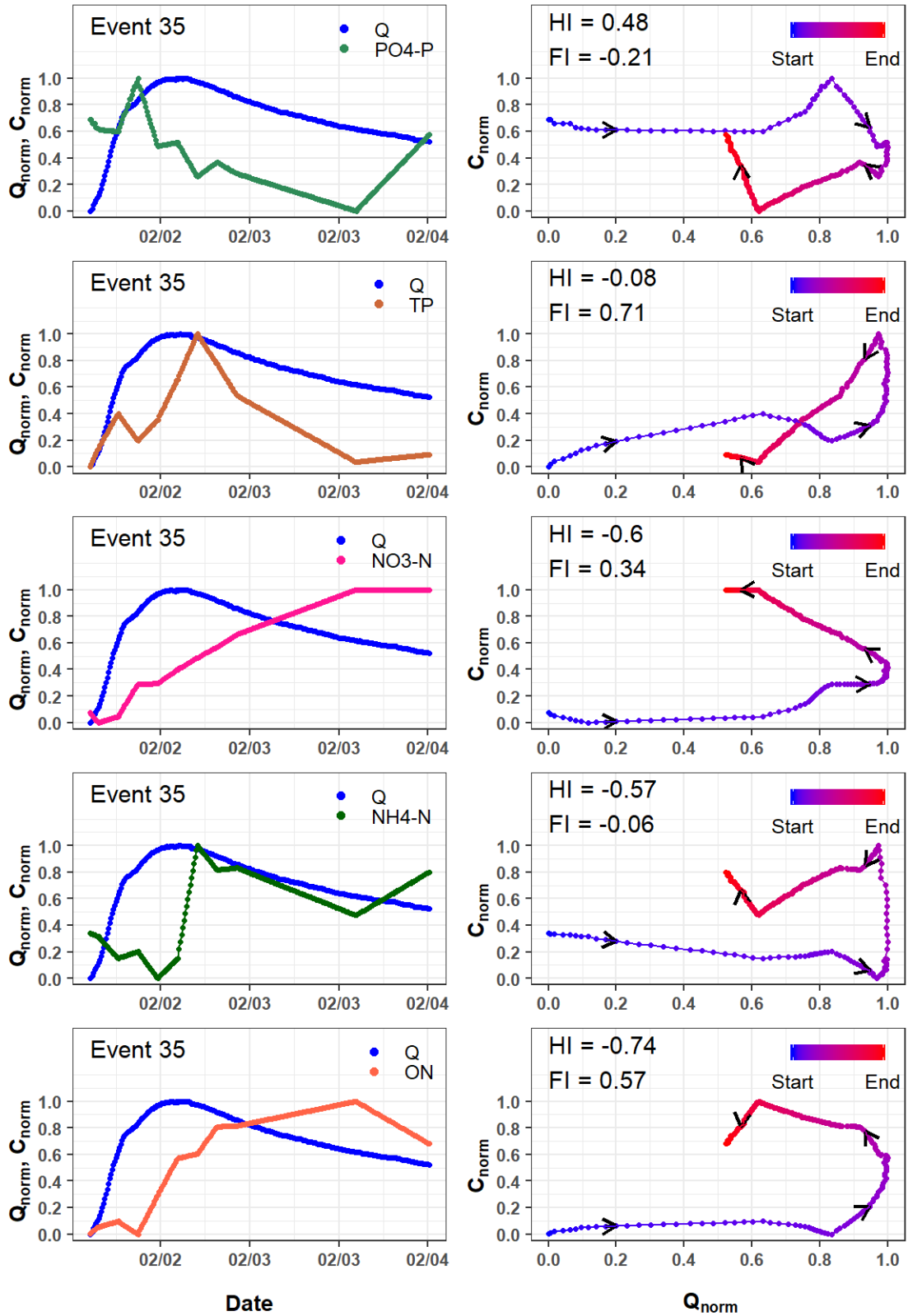


Figure D.39. Event 35 hydrographs, chemographs, and hysteresis loops for nitrogen and phosphorous species.

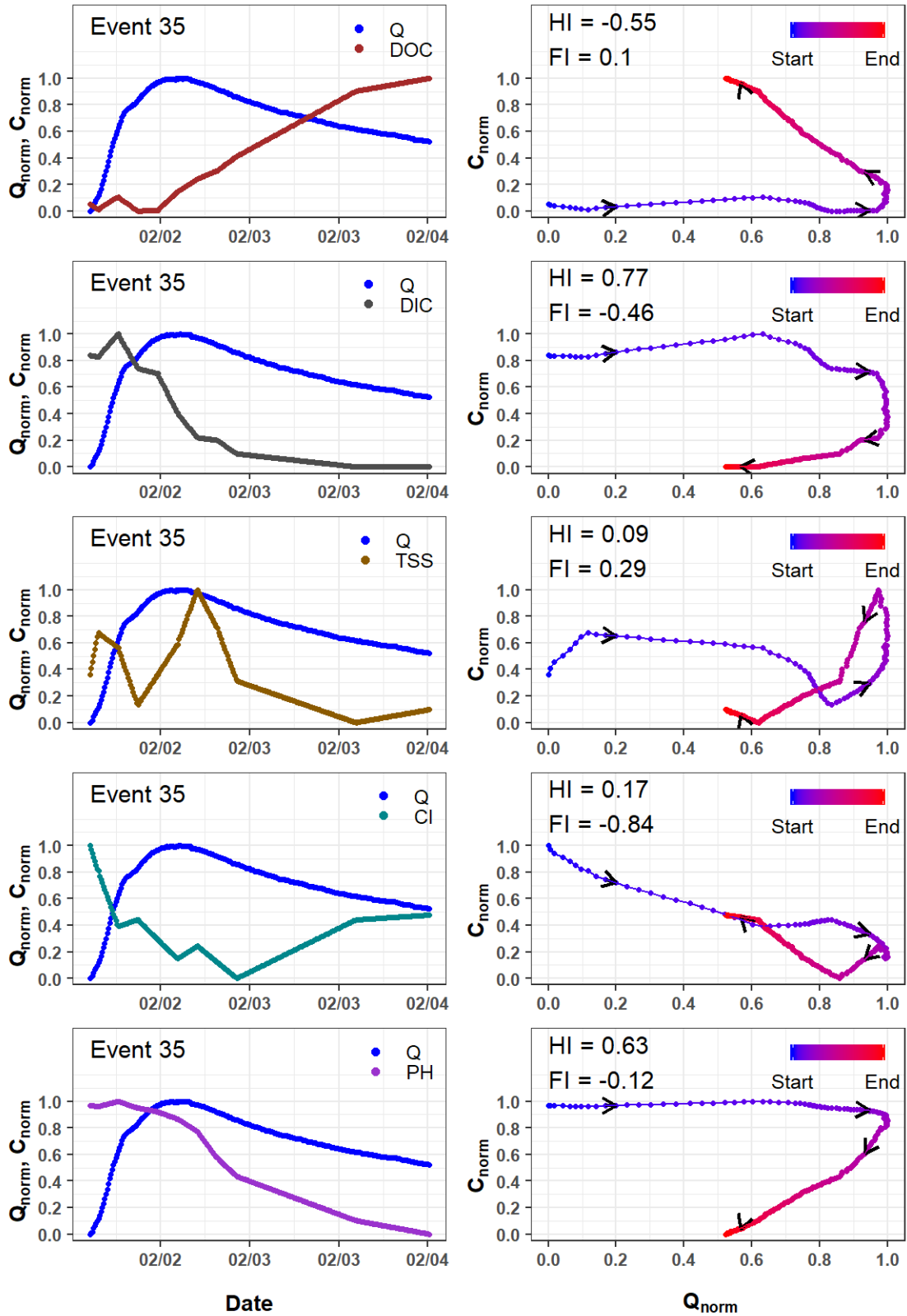


Figure D.40. Event 35 hydrographs, chemographs, and hysteresis loops for carbon species, suspended solids, chloride, and pH.

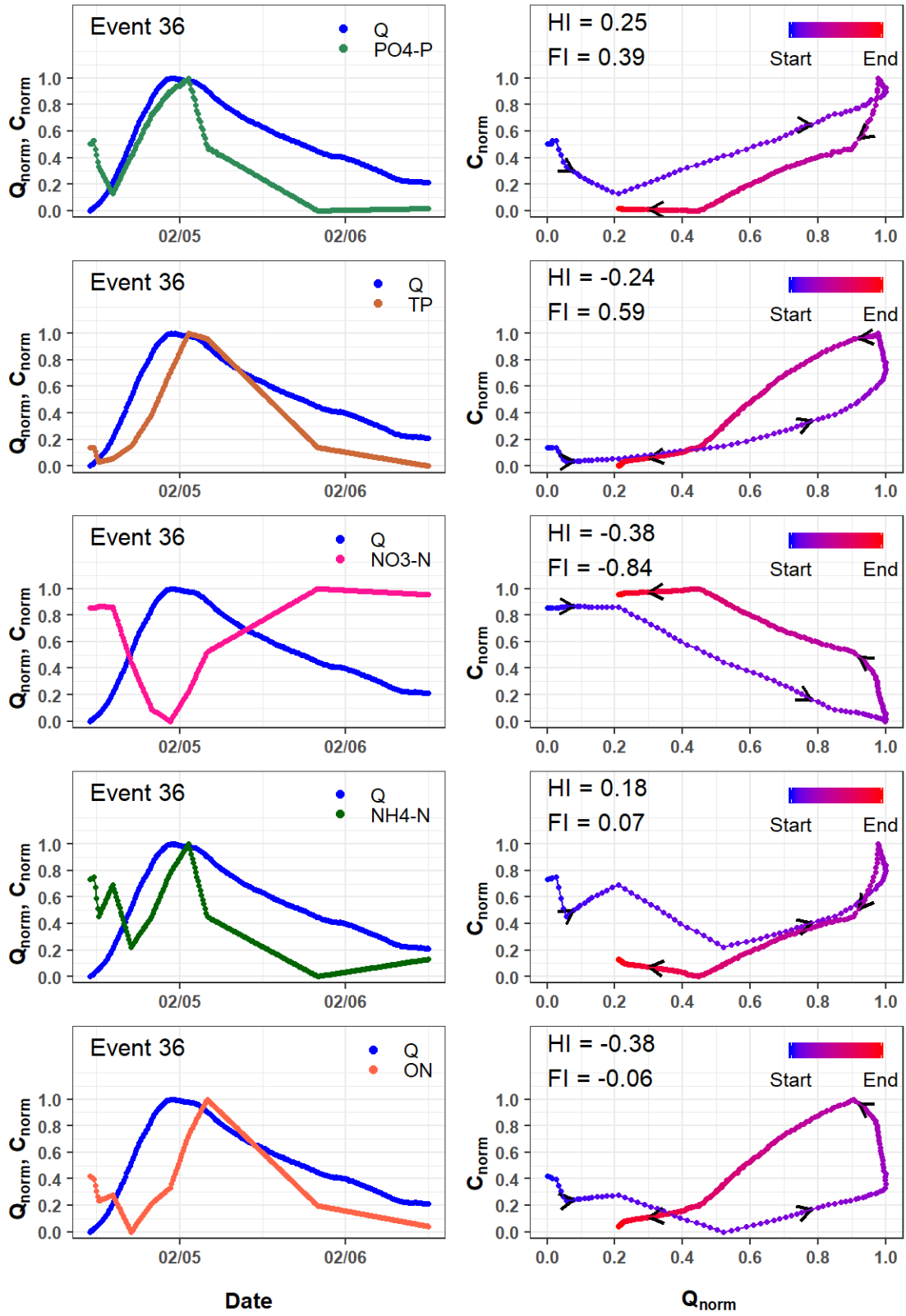


Figure D.41. Event 36 hydrographs, chemographs, and hysteresis loops for nitrogen and phosphorous species.

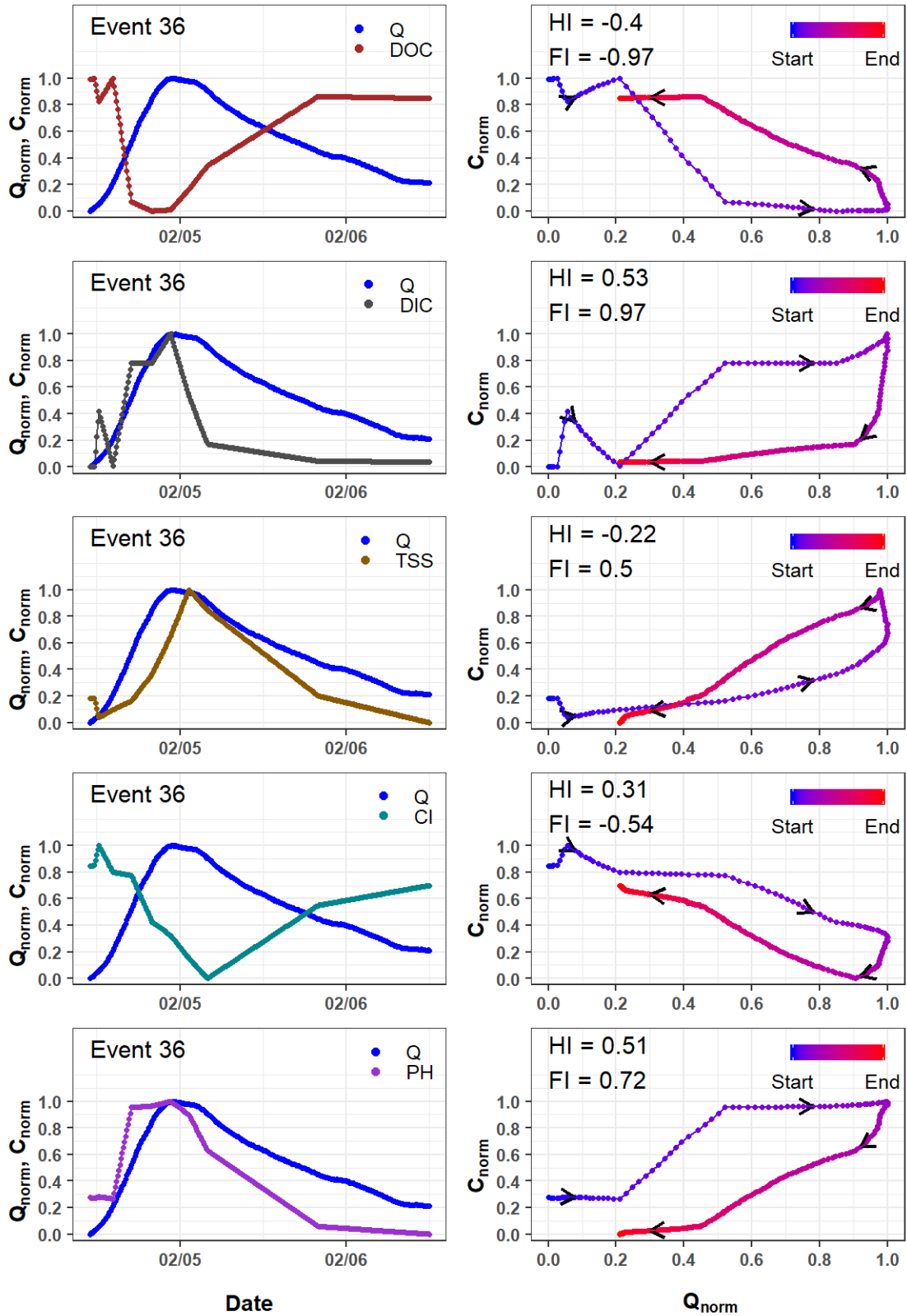


Figure D.42. Event 36 hydrographs, chemographs, and hysteresis loops for carbon species, suspended solids, chloride, and pH.

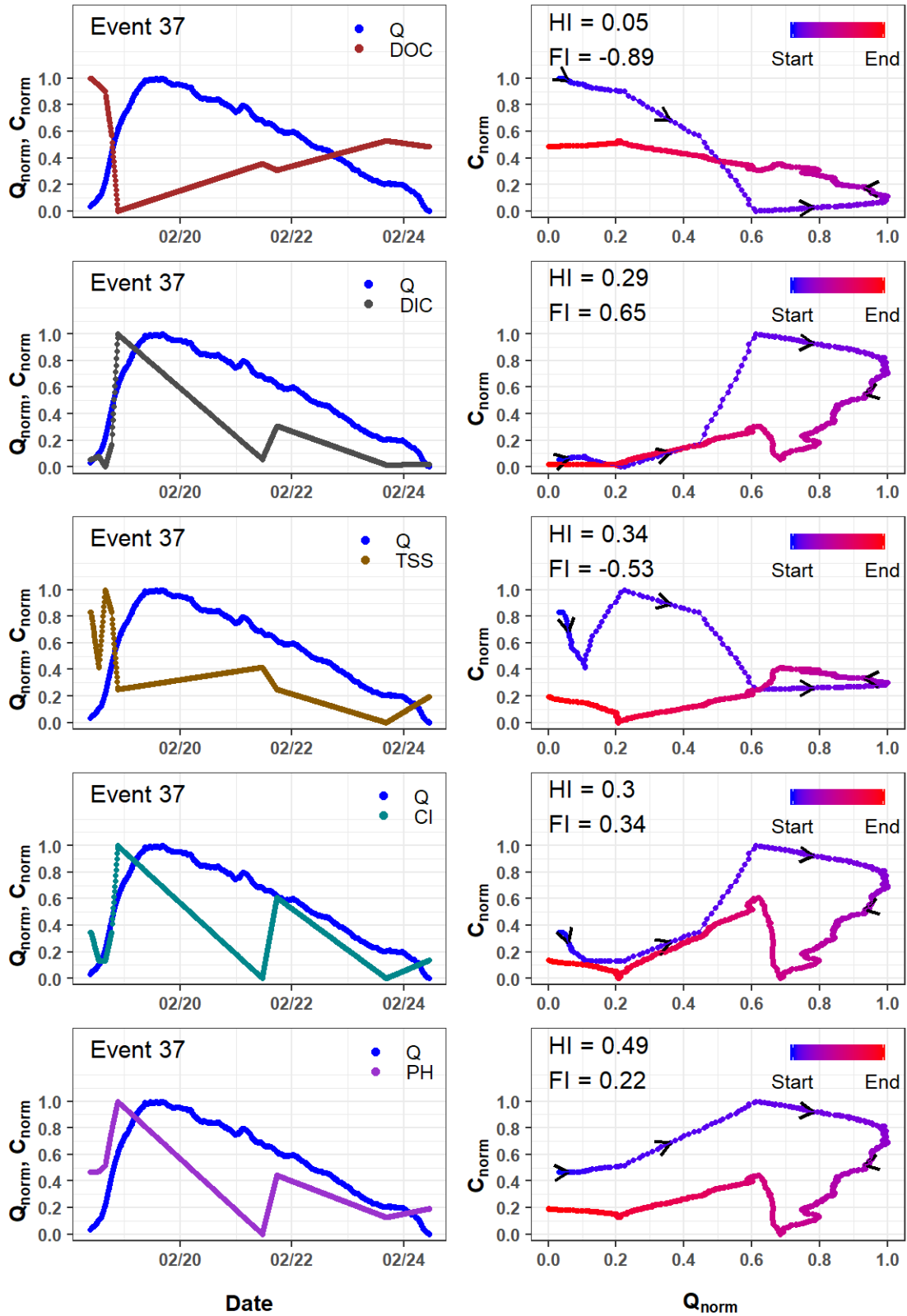


Figure D.43. Event 37 hydrographs, chemographs, and hysteresis loops for nitrogen and phosphorous species.

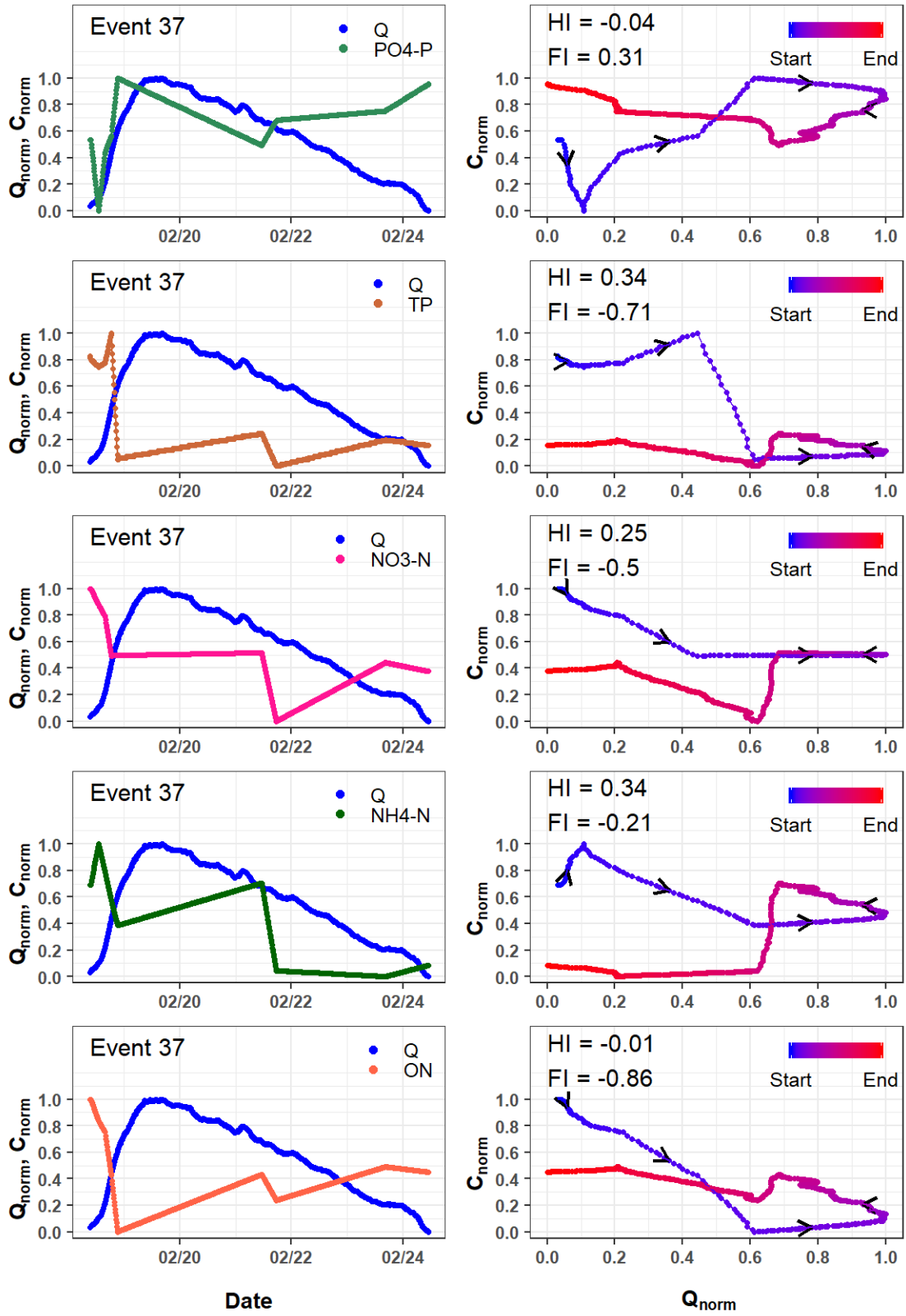


Figure D.44. Event 37 hydrographs, chemographs, and hysteresis loops for carbon species, suspended solids, chloride, and pH.

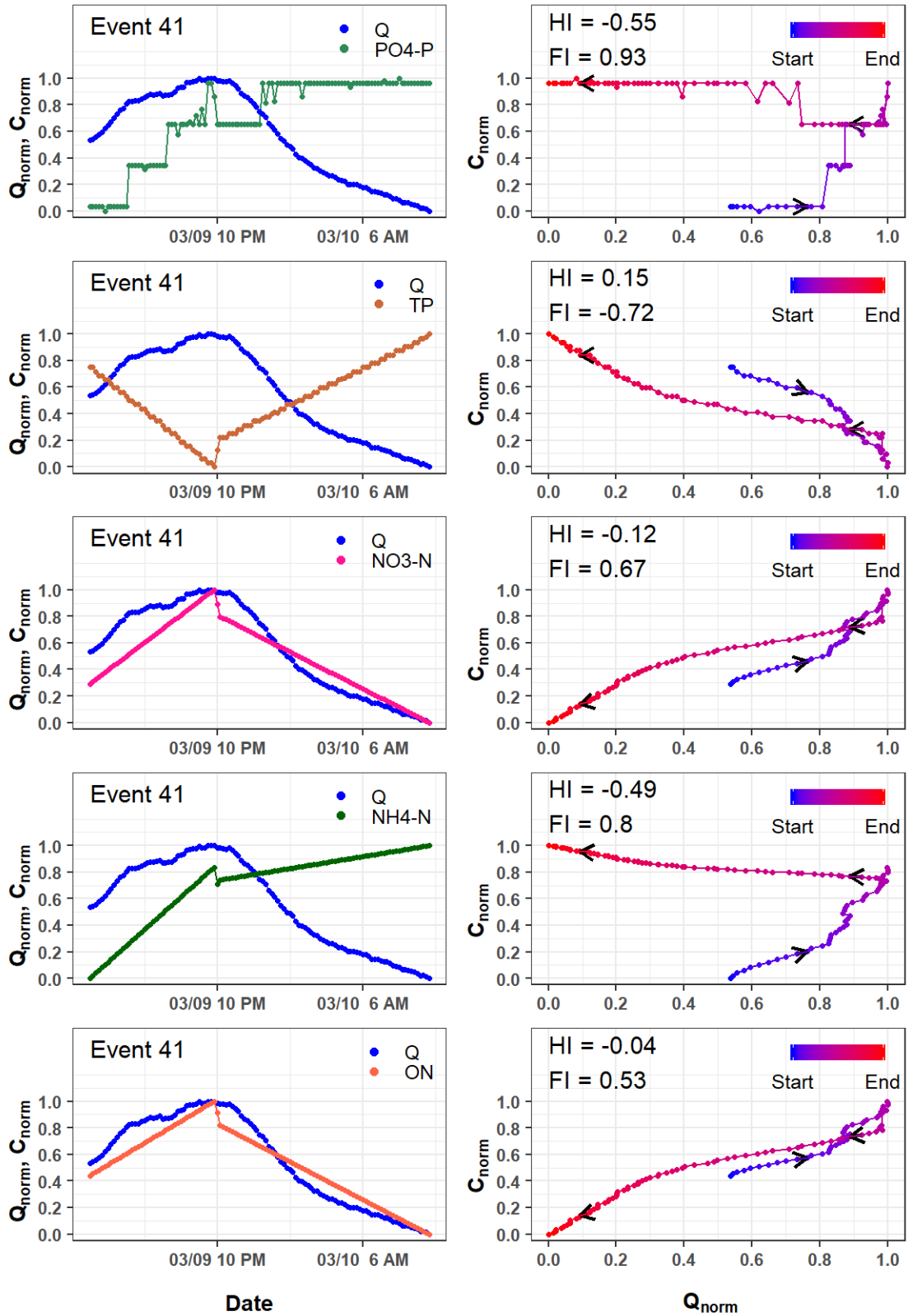


Figure D.45. Event 41 hydrographs, chemographs, and hysteresis loops for nitrogen and phosphorous species.

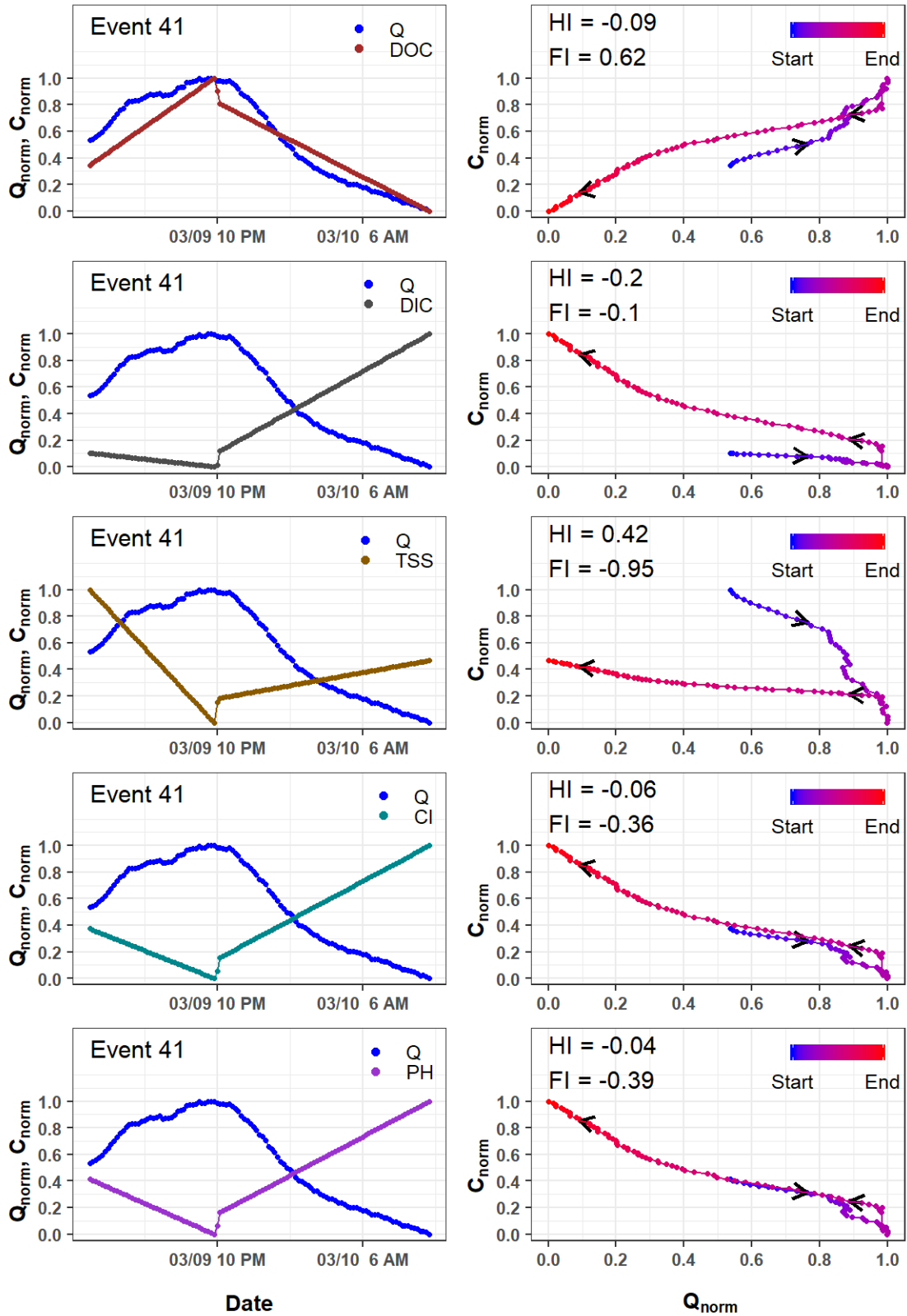


Figure D.46. Event 41 hydrographs, chemographs, and hysteresis loops for carbon species, suspended solids, chloride, and pH.

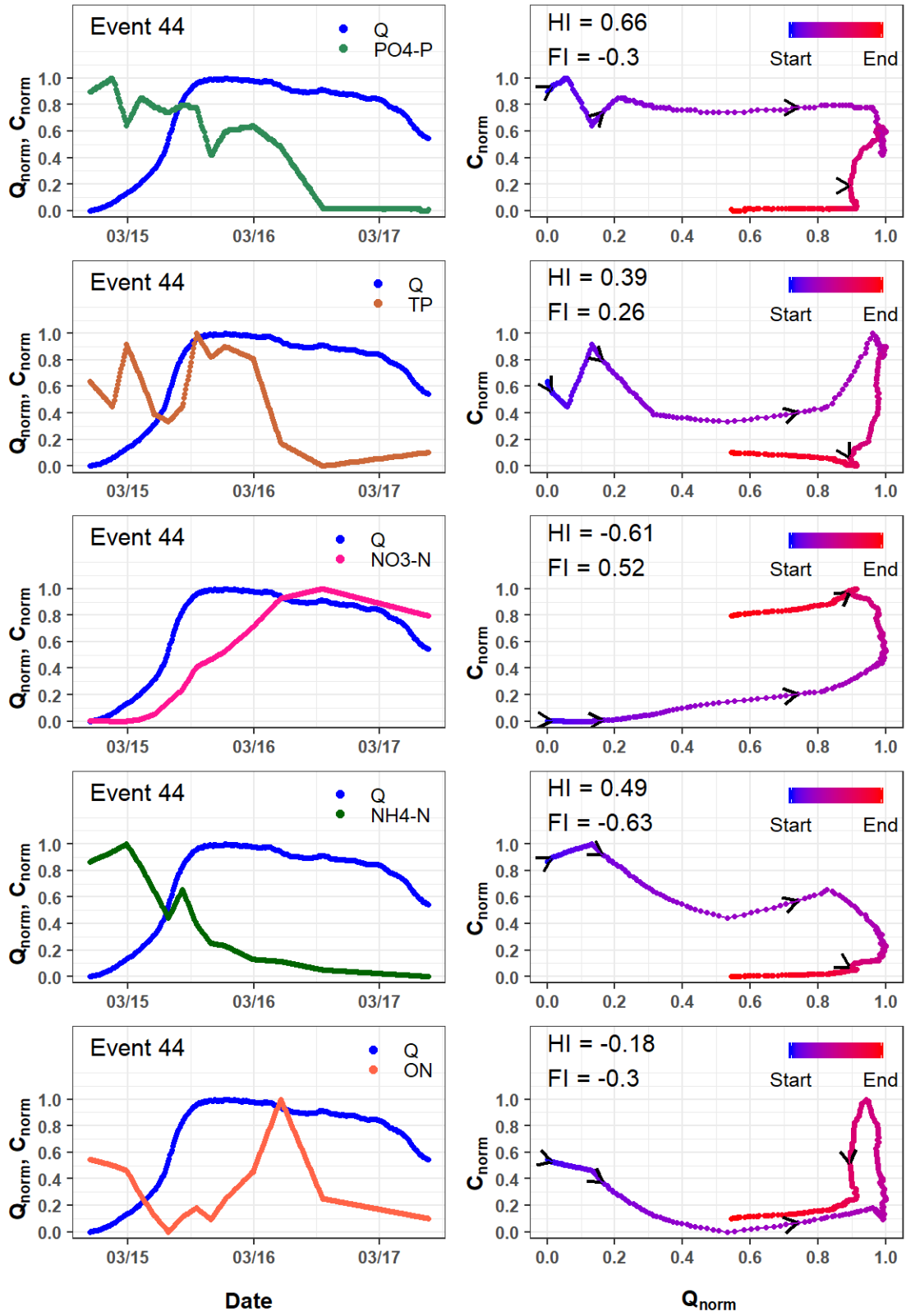


Figure D.47. Event 44 hydrographs, chemographs, and hysteresis loops for nitrogen and phosphorous species.

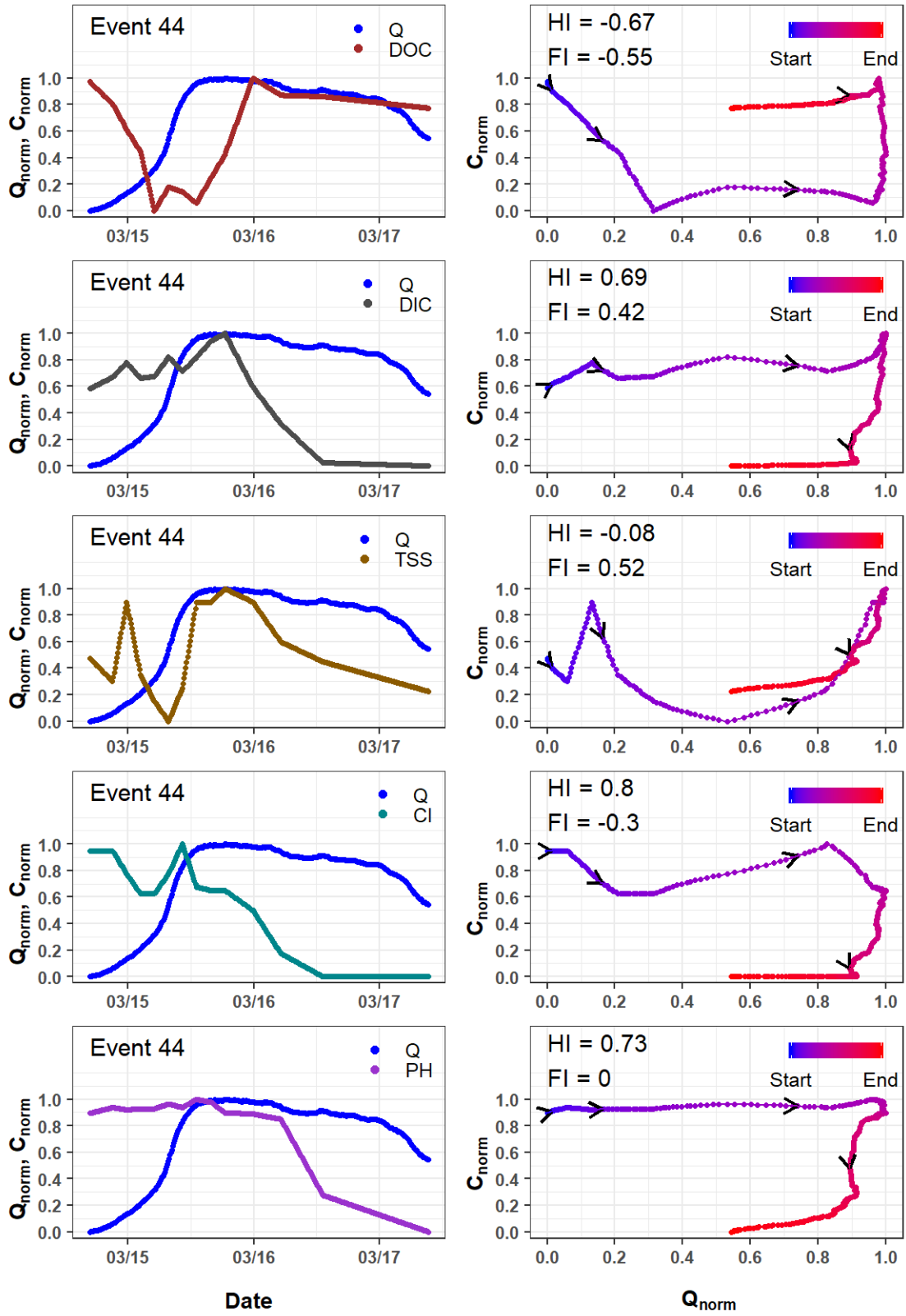


Figure D.48. Event 44 hydrographs, chemographs, and hysteresis loops for carbon species, suspended solids, chloride, and pH.

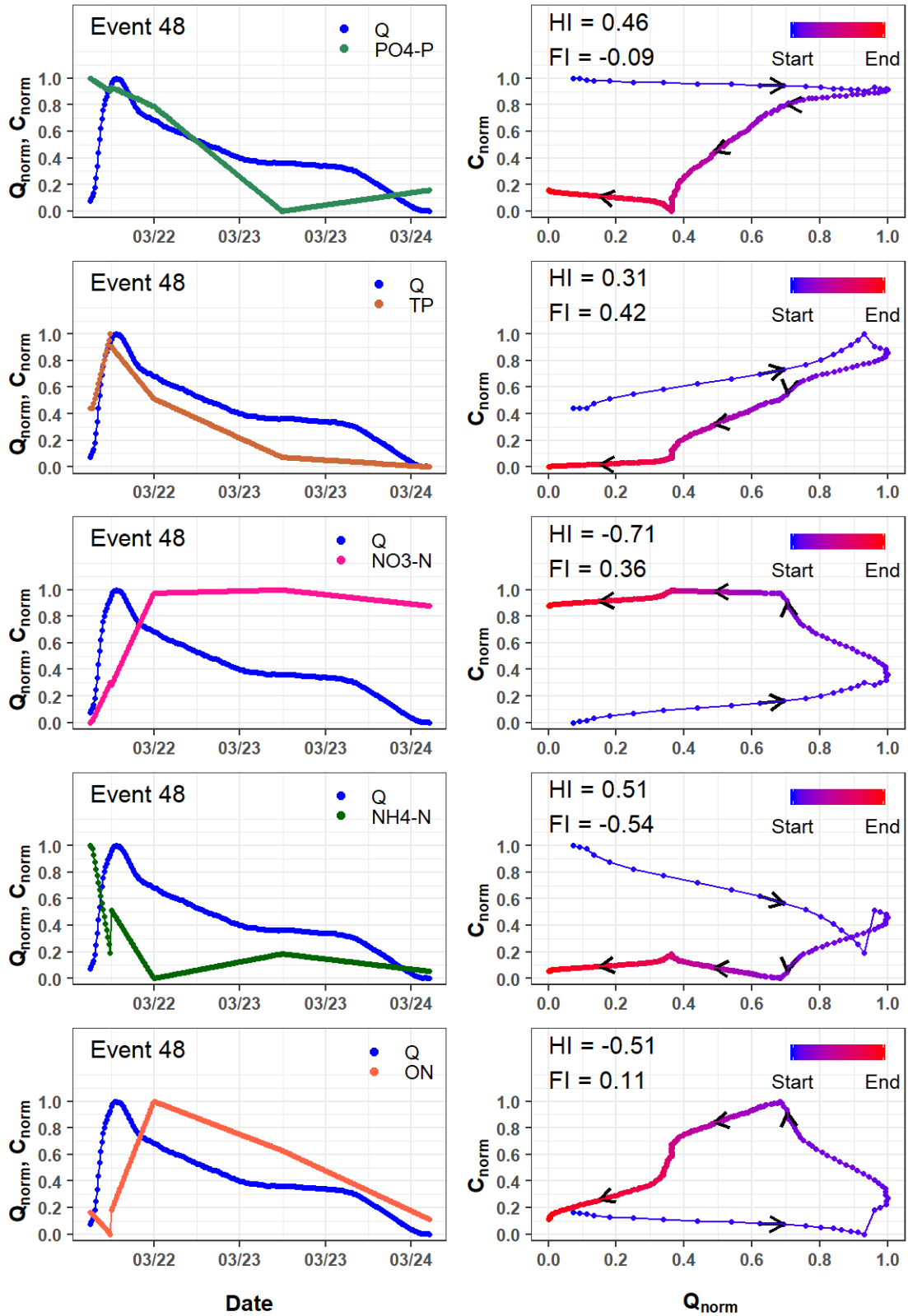


Figure D.49. Event 48 hydrographs, chemographs, and hysteresis loops for nitrogen and phosphorous species.

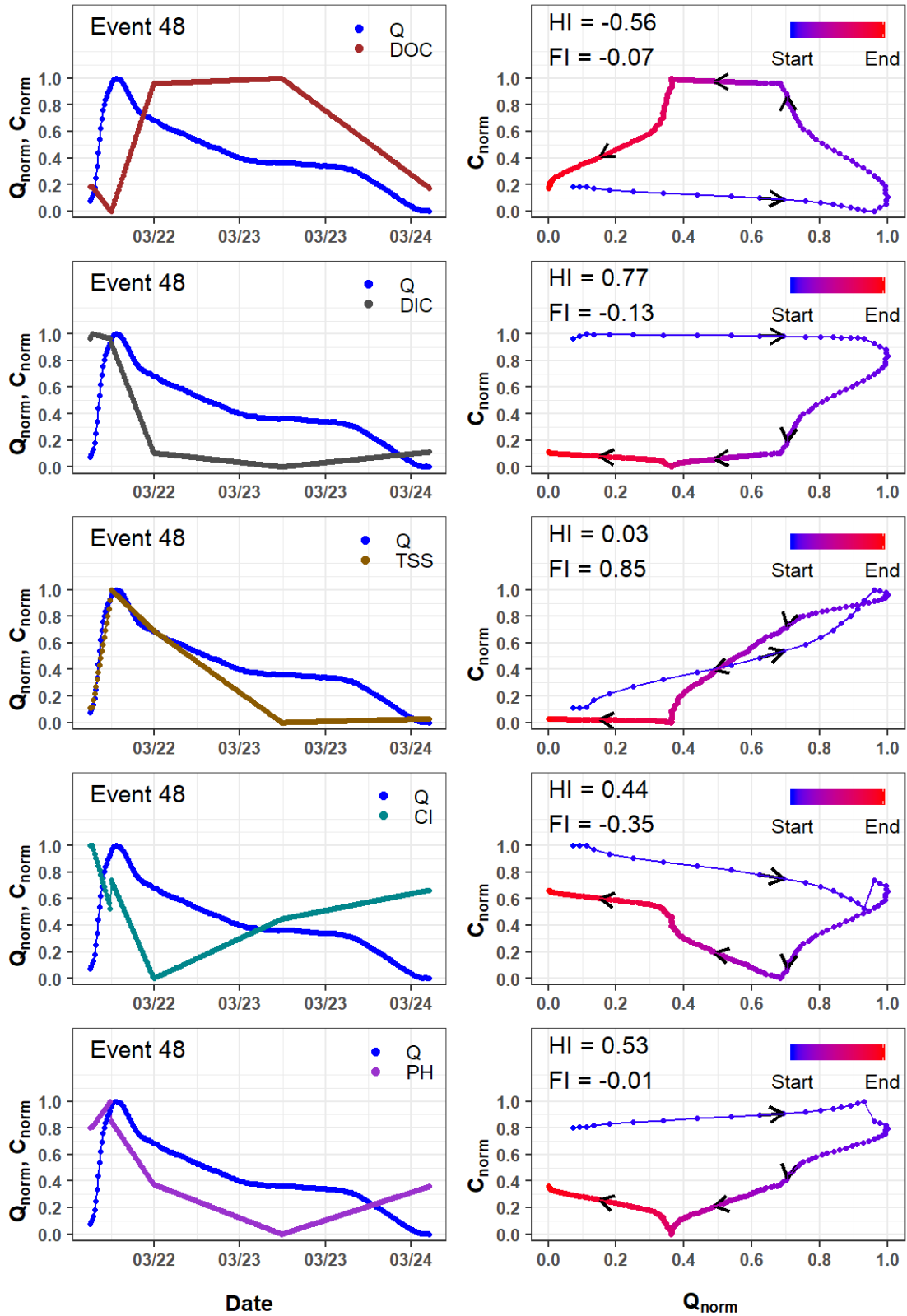


Figure D.50. Event 48 hydrographs, chemographs, and hysteresis loops for carbon species, suspended solids, chloride, and pH.

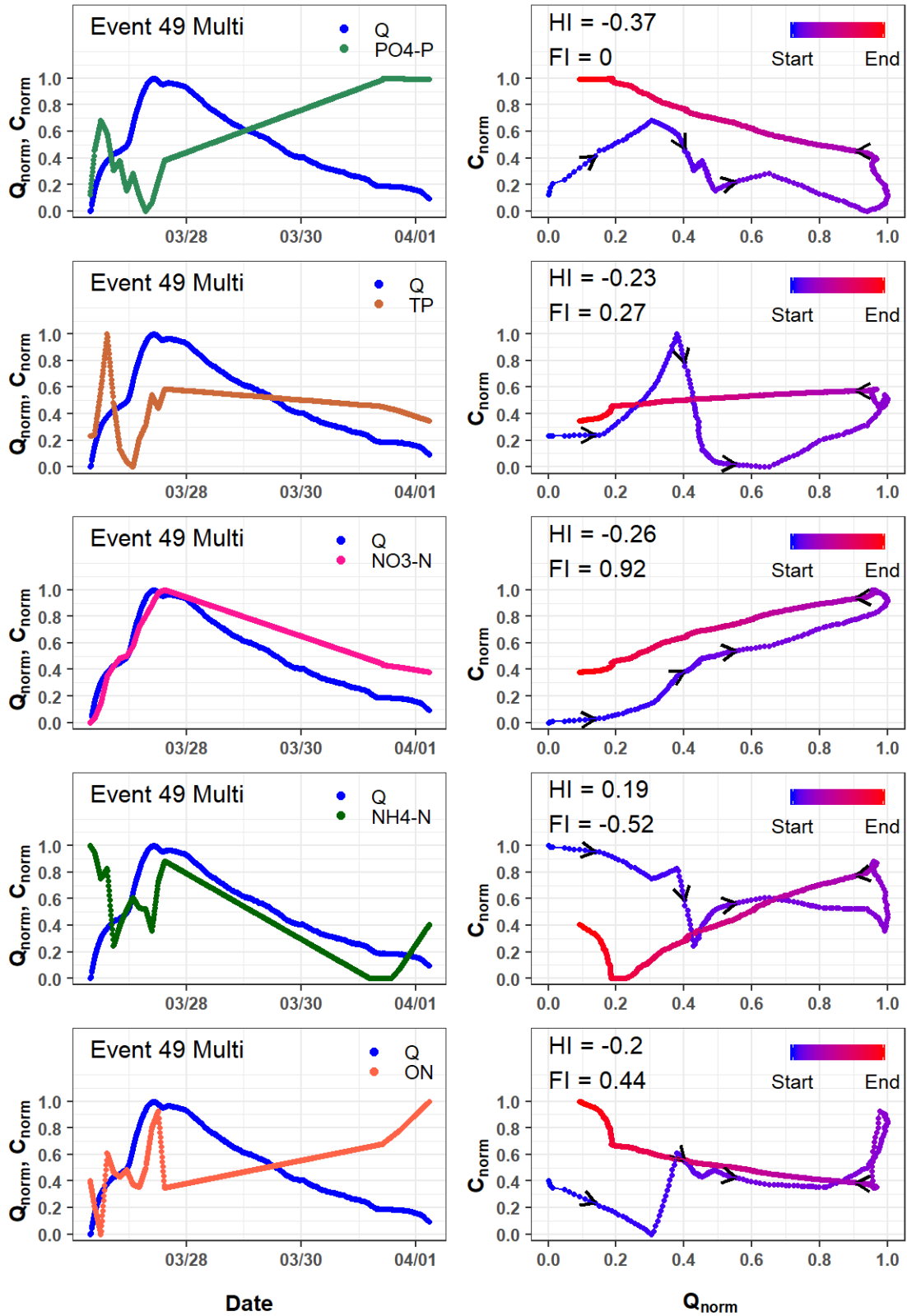


Figure D.51. Event 49 Multi (Events 49 & 50) hydrographs, chemographs, and hysteresis loops for nitrogen and phosphorous species.

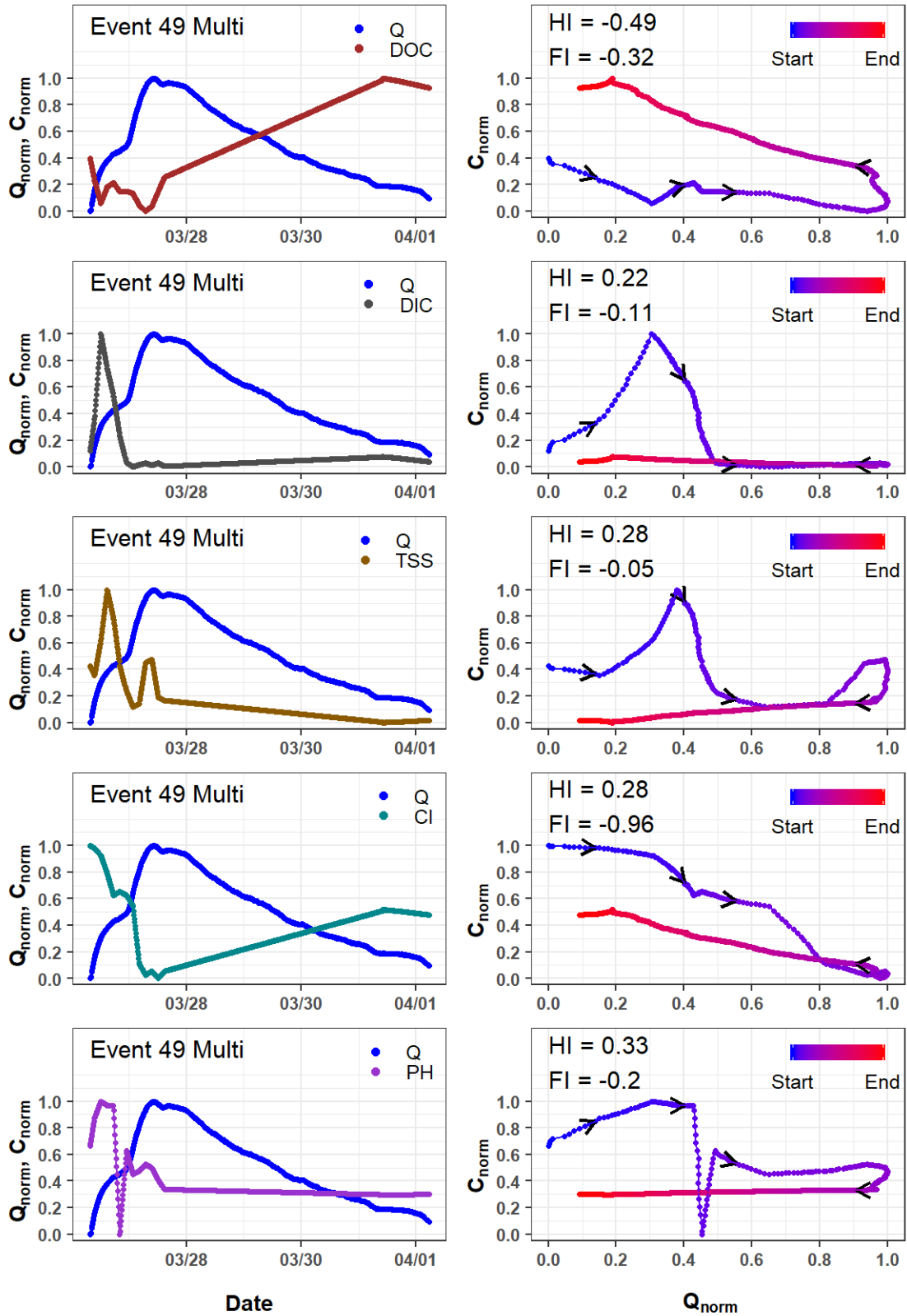


Figure D.52. Event 49 Multi (Events 49 & 50) hydrographs, chemographs, and hysteresis loops for carbon species, suspended solids, chloride, and pH.

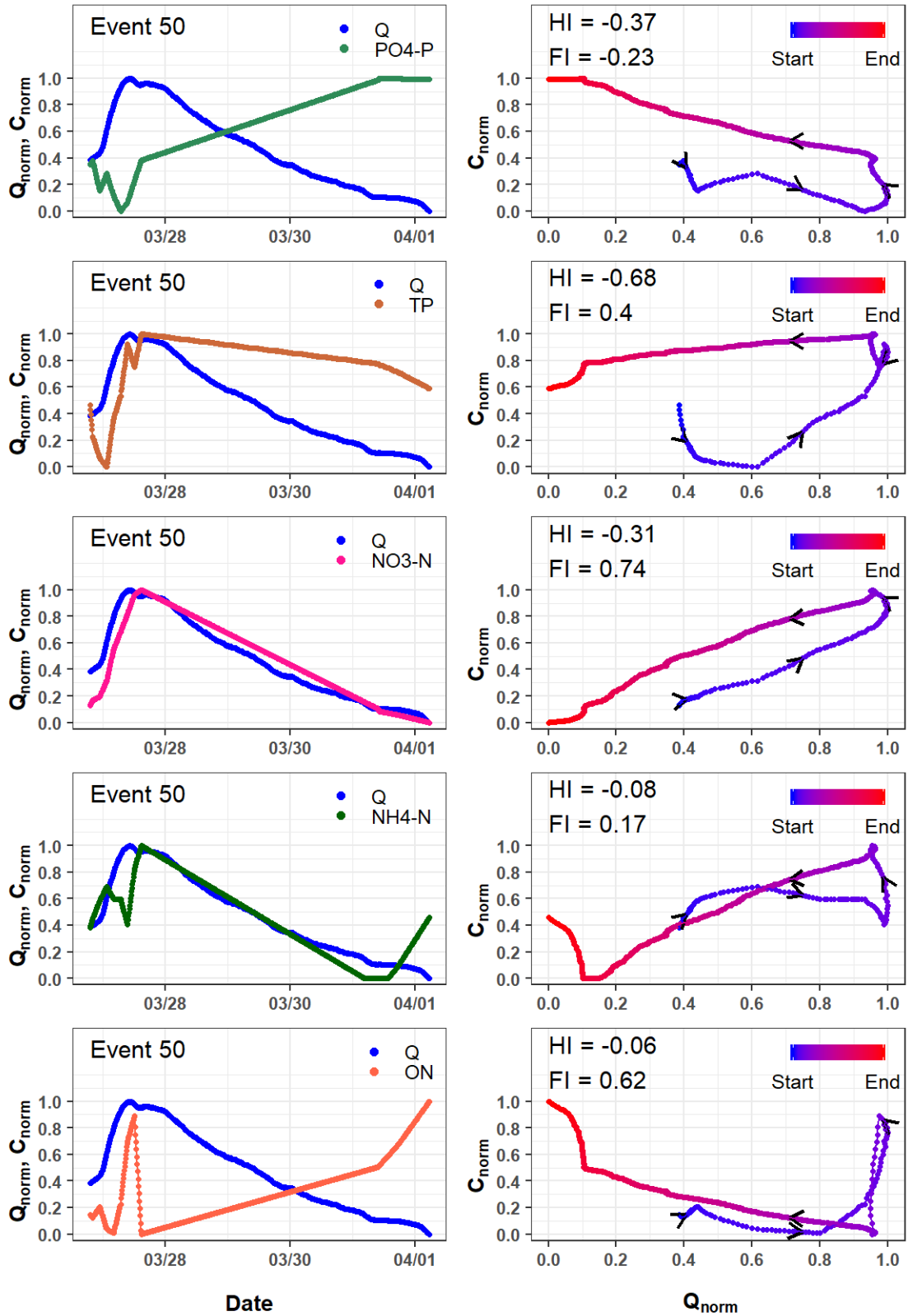


Figure D.53. Event 50 hydrographs, chemographs, and hysteresis loops for nitrogen and phosphorous species.

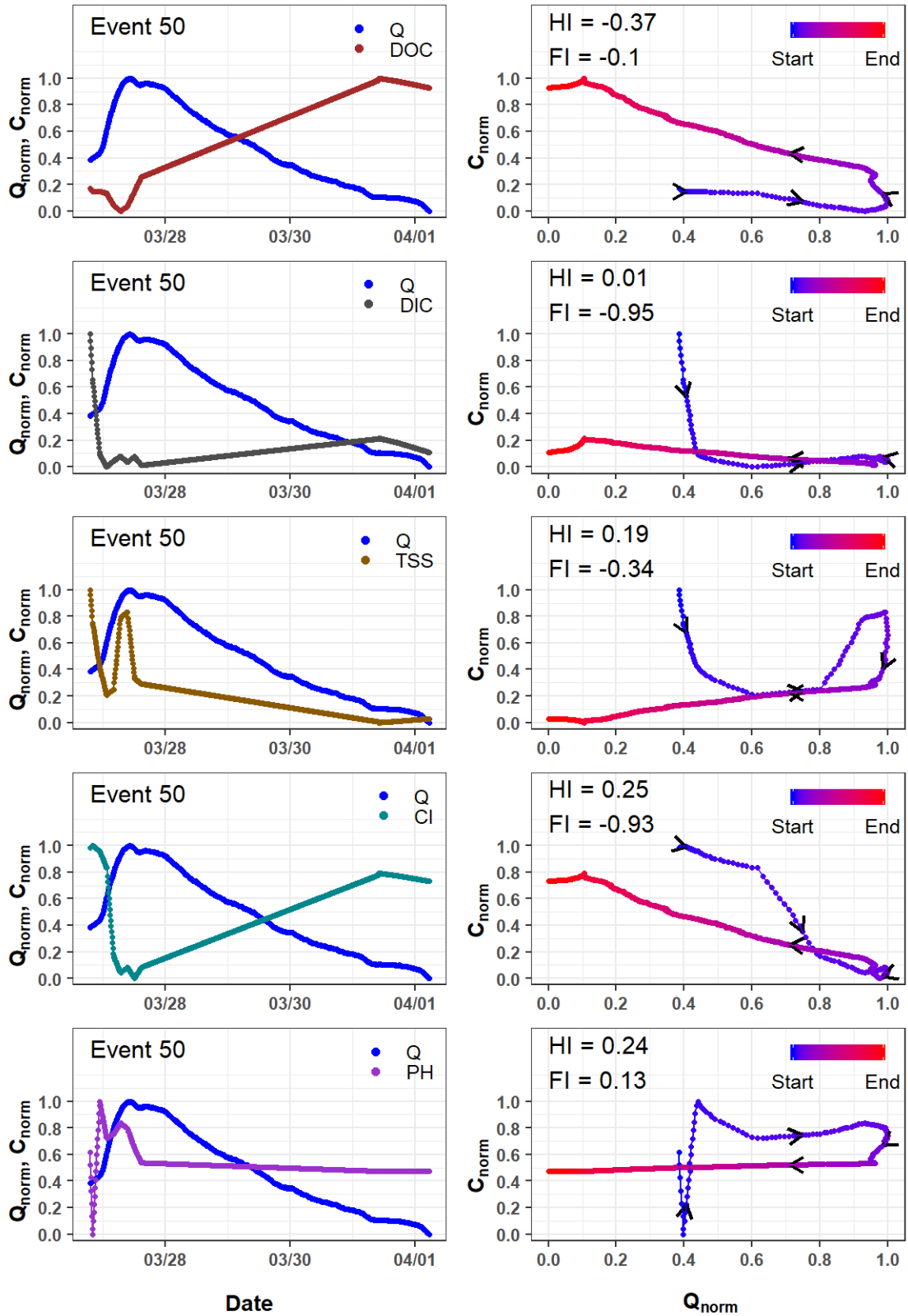


Figure D.54. Event 50 hydrographs, chemographs, and hysteresis loops for carbon species, suspended solids, chloride, and pH.

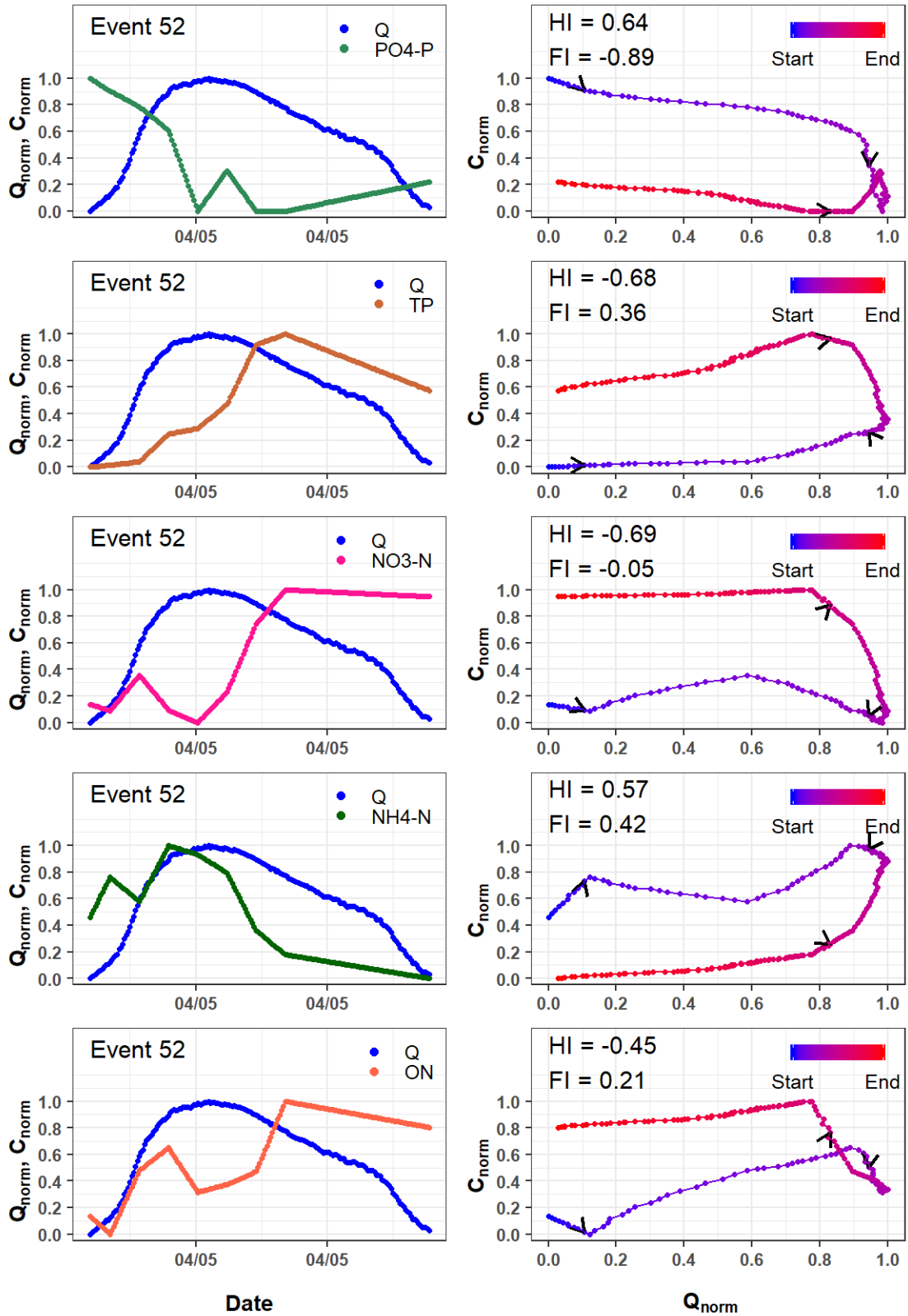


Figure D.55. Event 52 hydrographs, chemographs, and hysteresis loops for nitrogen and phosphorous species.

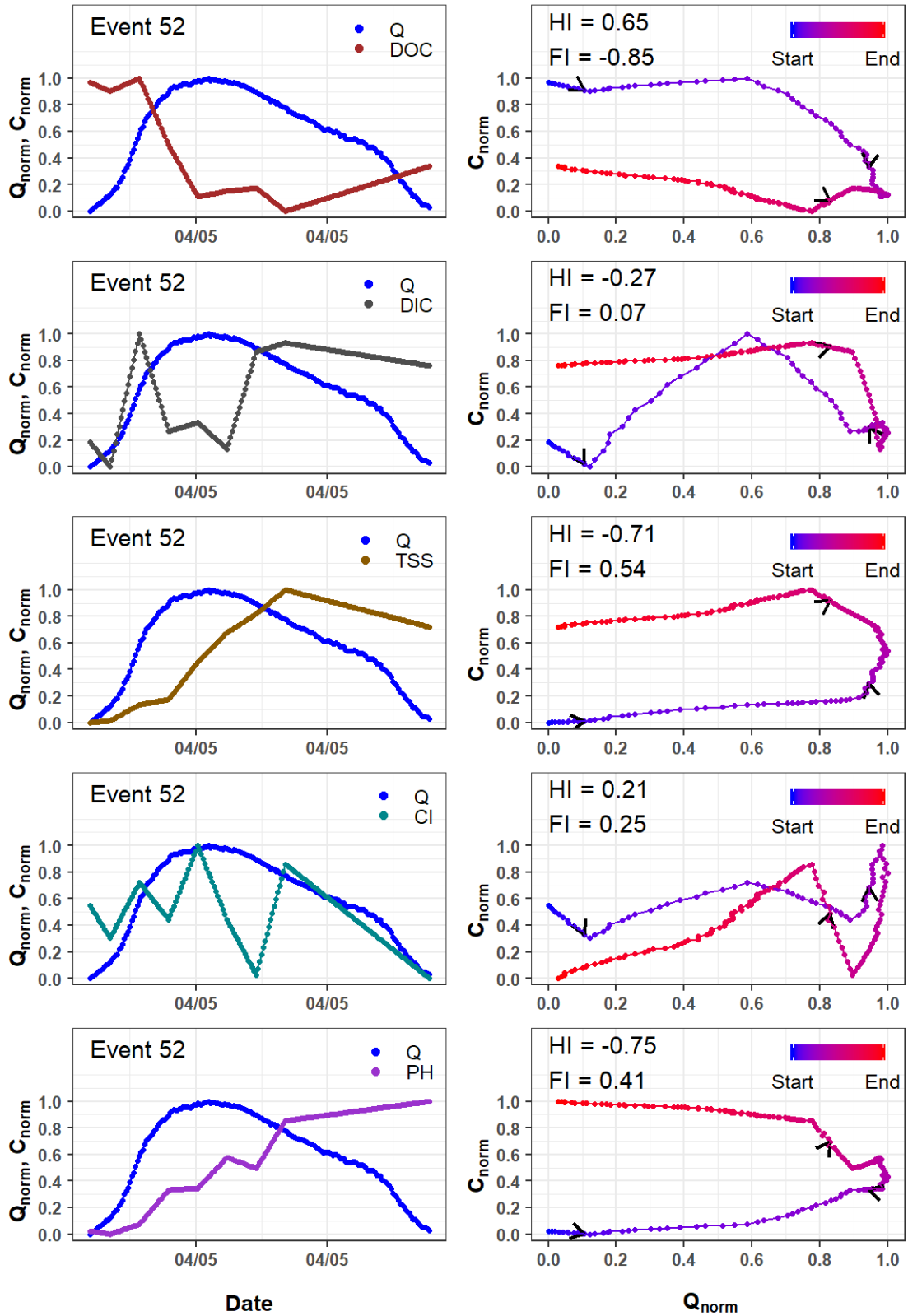


Figure D.56. Event 52 hydrographs, chemographs, and hysteresis loops for carbon species, suspended solids, chloride, and pH.

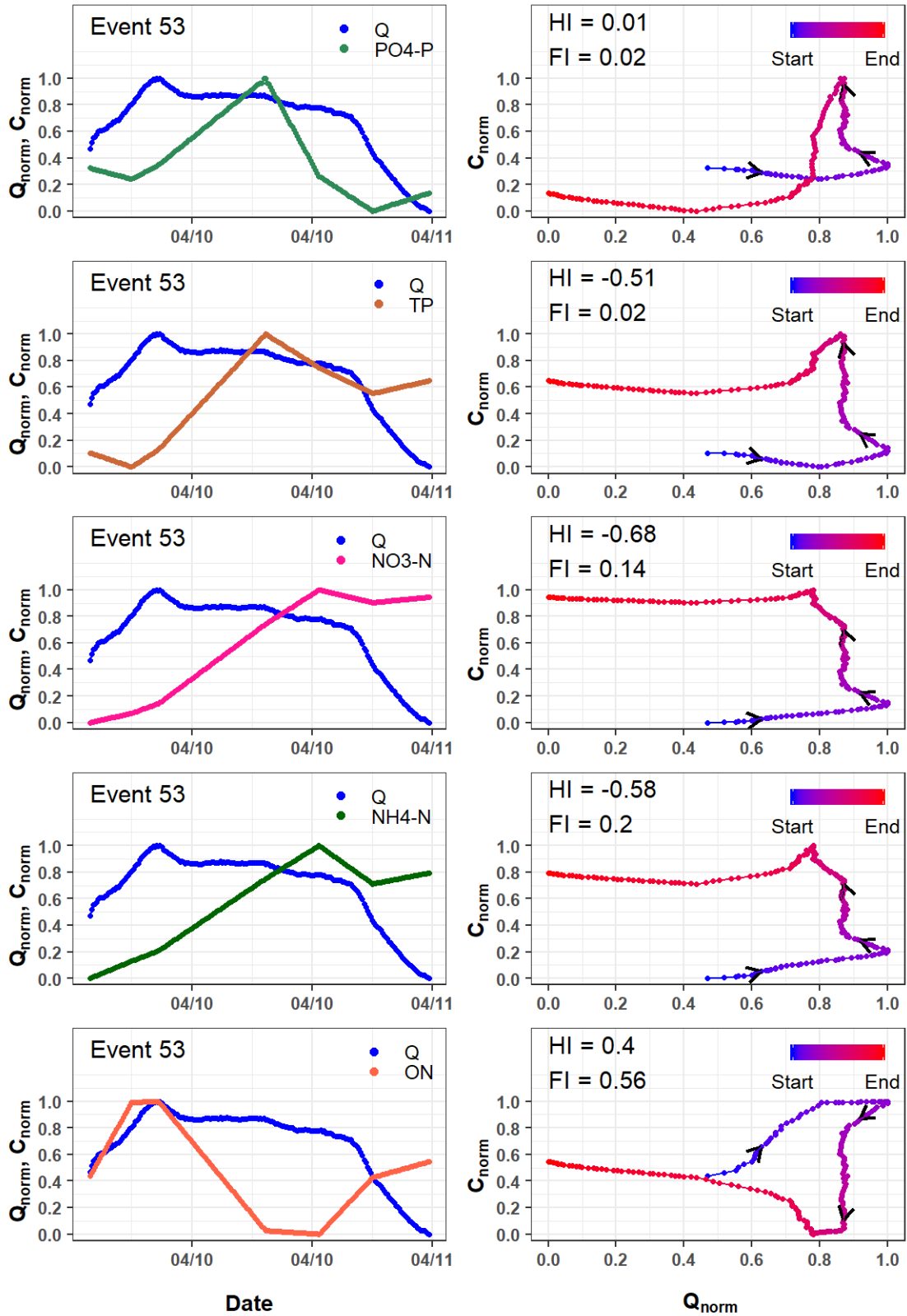


Figure D.57. Event 53 hydrographs, chemographs, and hysteresis loops for nitrogen and phosphorous species.

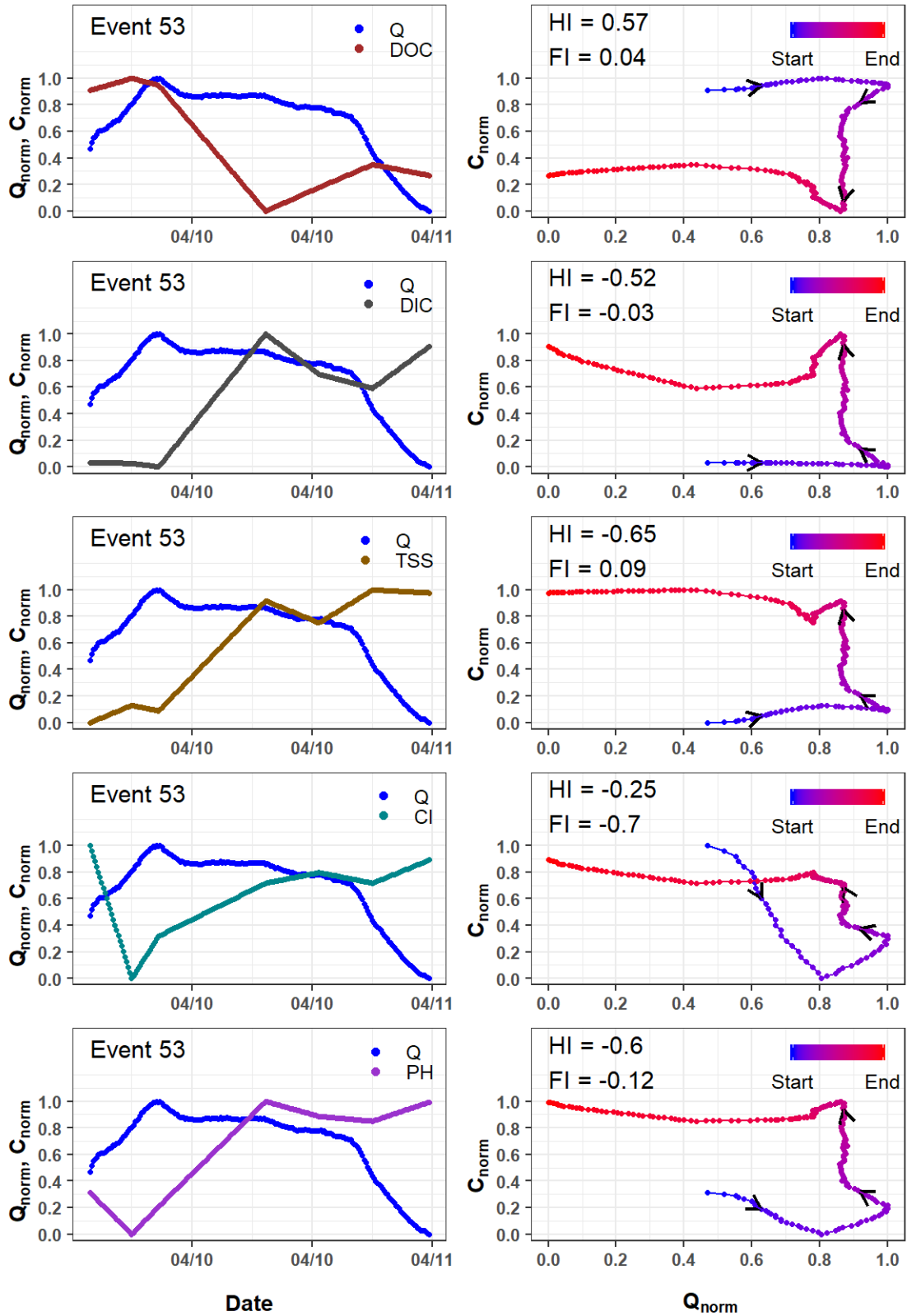


Figure D.58. Event 53 hydrographs, chemographs, and hysteresis loops for carbon species, suspended solids, chloride, and pH.

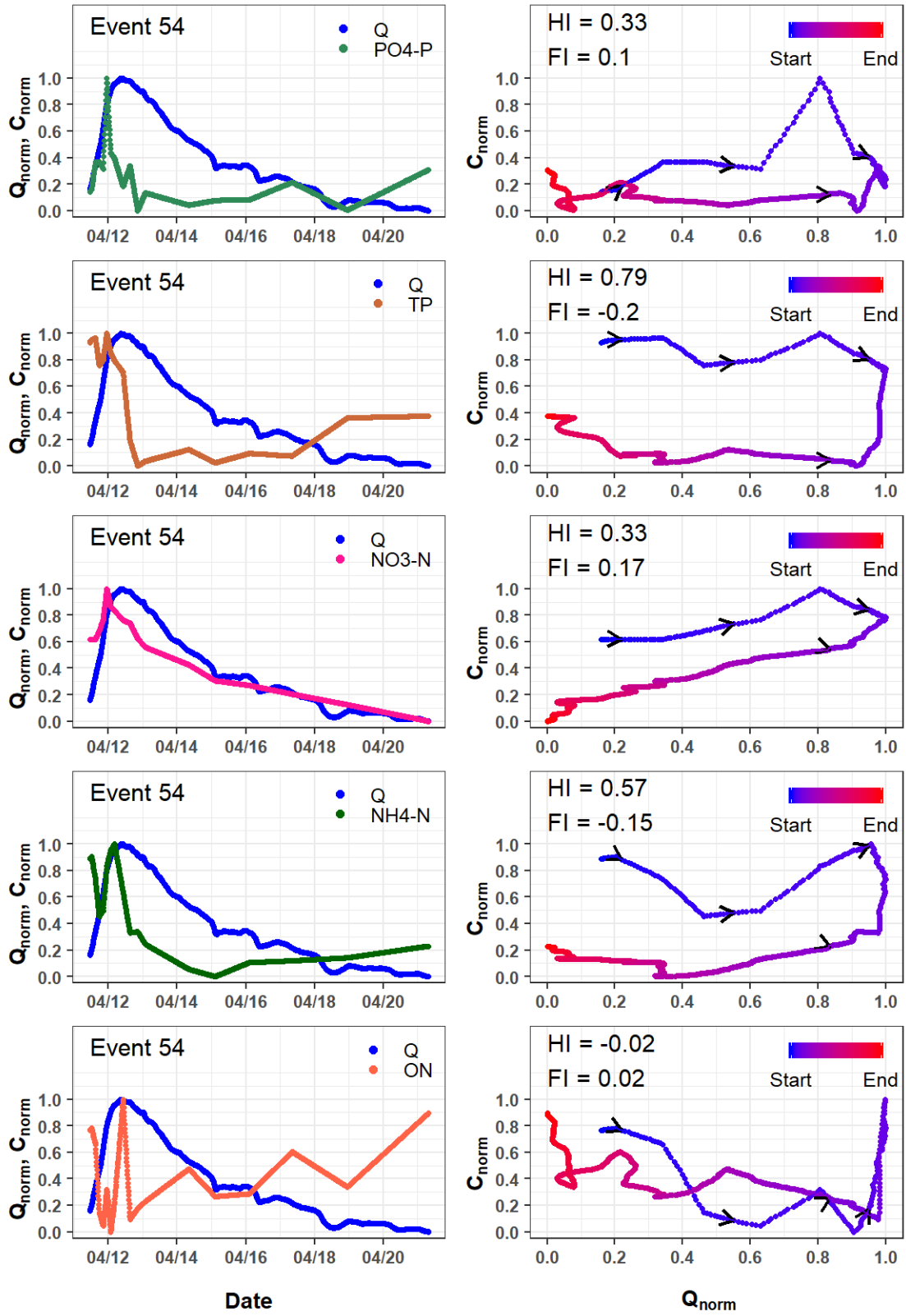


Figure D.59. Event 54 hydrographs, chemographs, and hysteresis loops for nitrogen and phosphorous species.

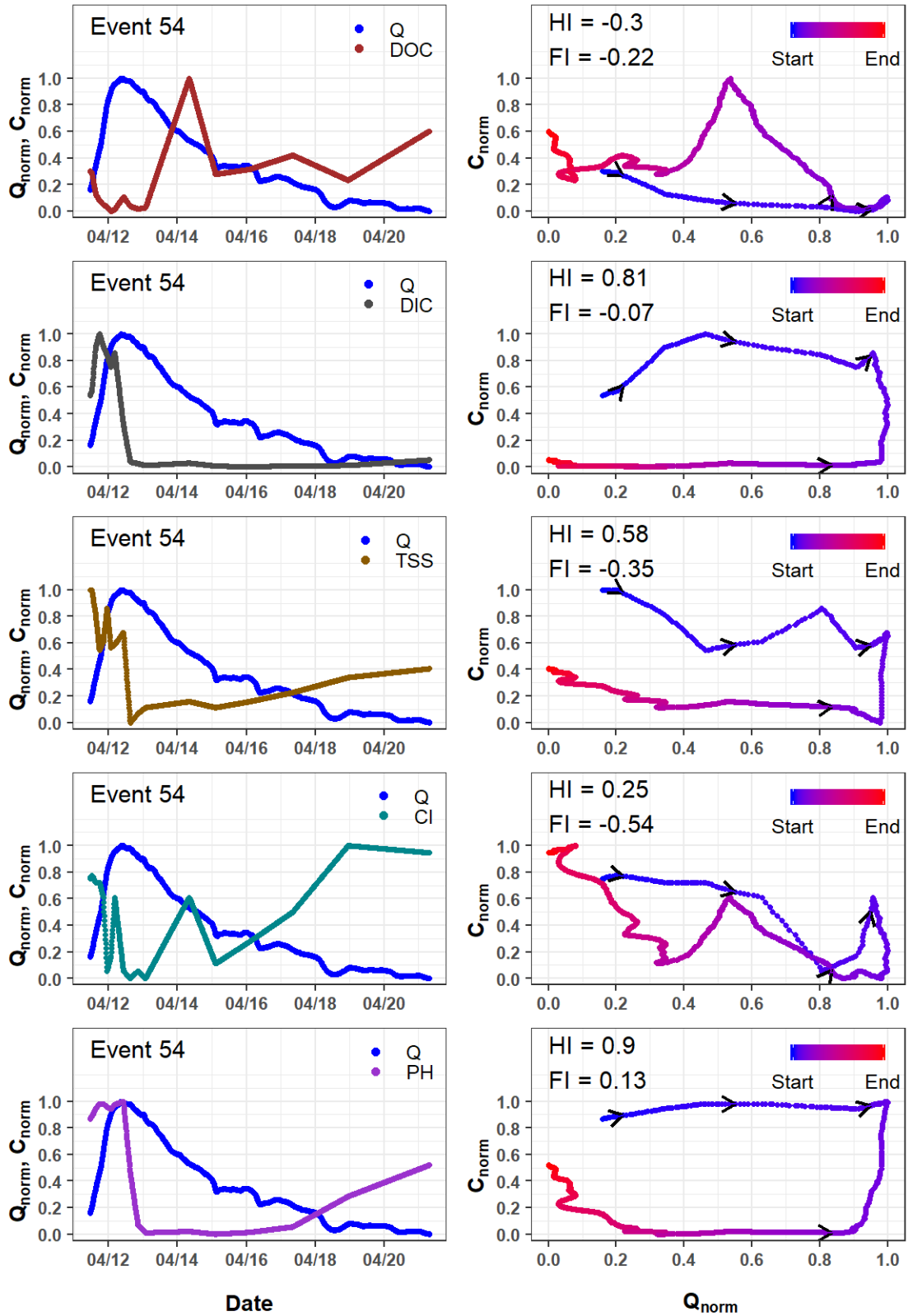


Figure D.60. Event 54 hydrographs, chemographs, and hysteresis loops for carbon species, suspended solids, chloride, and pH.

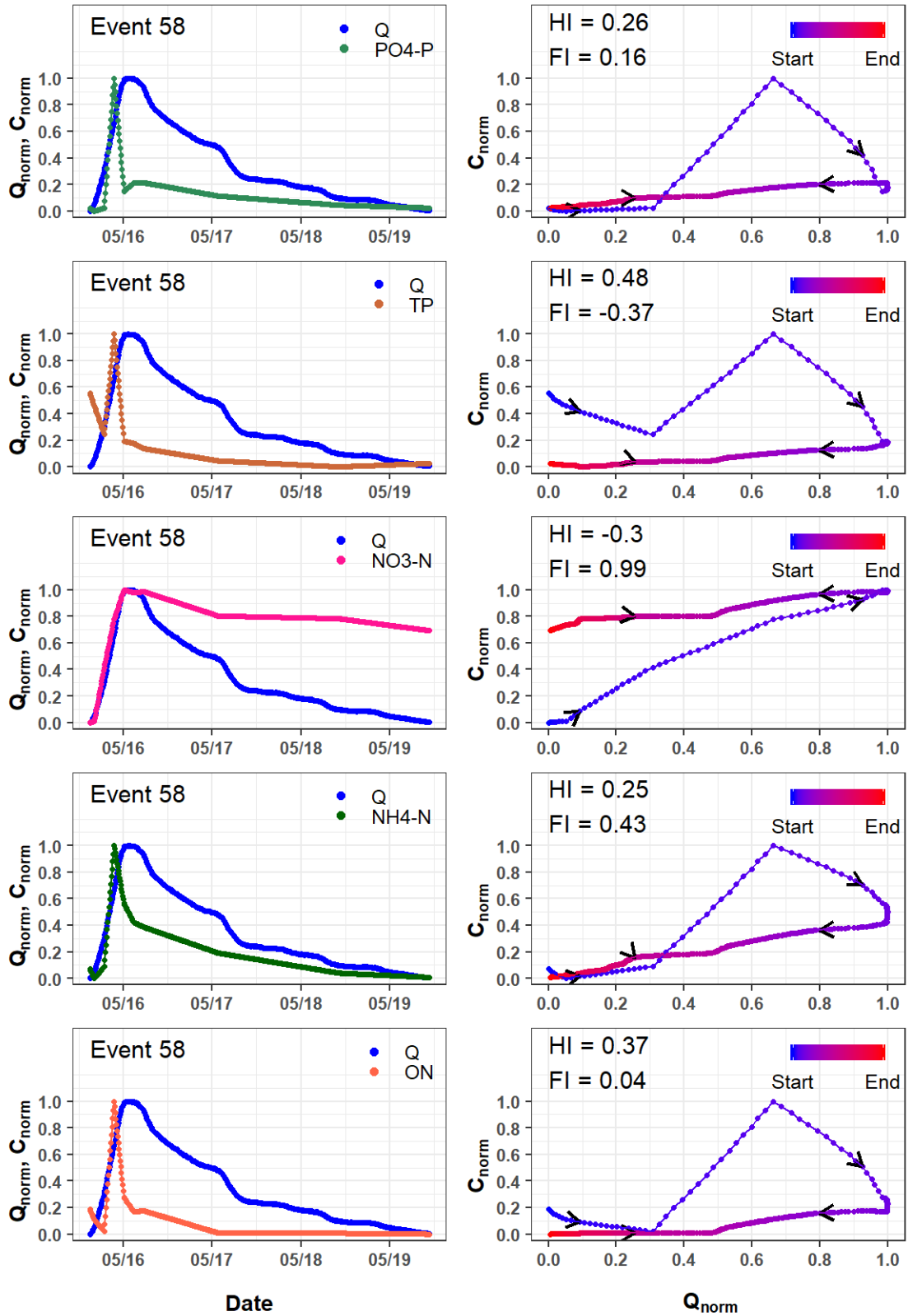


Figure D.61. Event 58 hydrographs, chemographs, and hysteresis loops for nitrogen and phosphorous species.

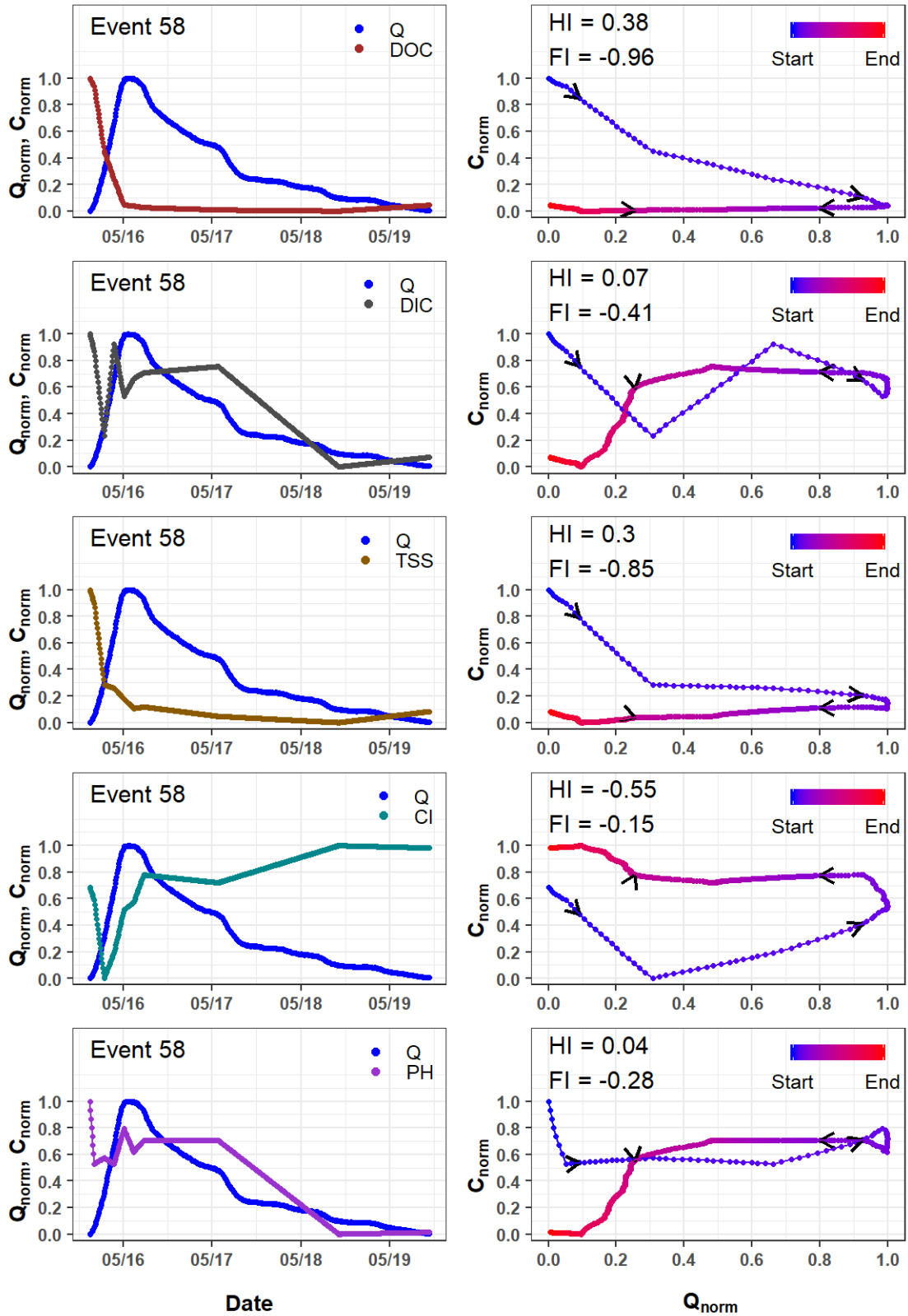


Figure D.62. Event 58 hydrographs, chemographs, and hysteresis loops for carbon species, suspended solids, chloride, and pH.

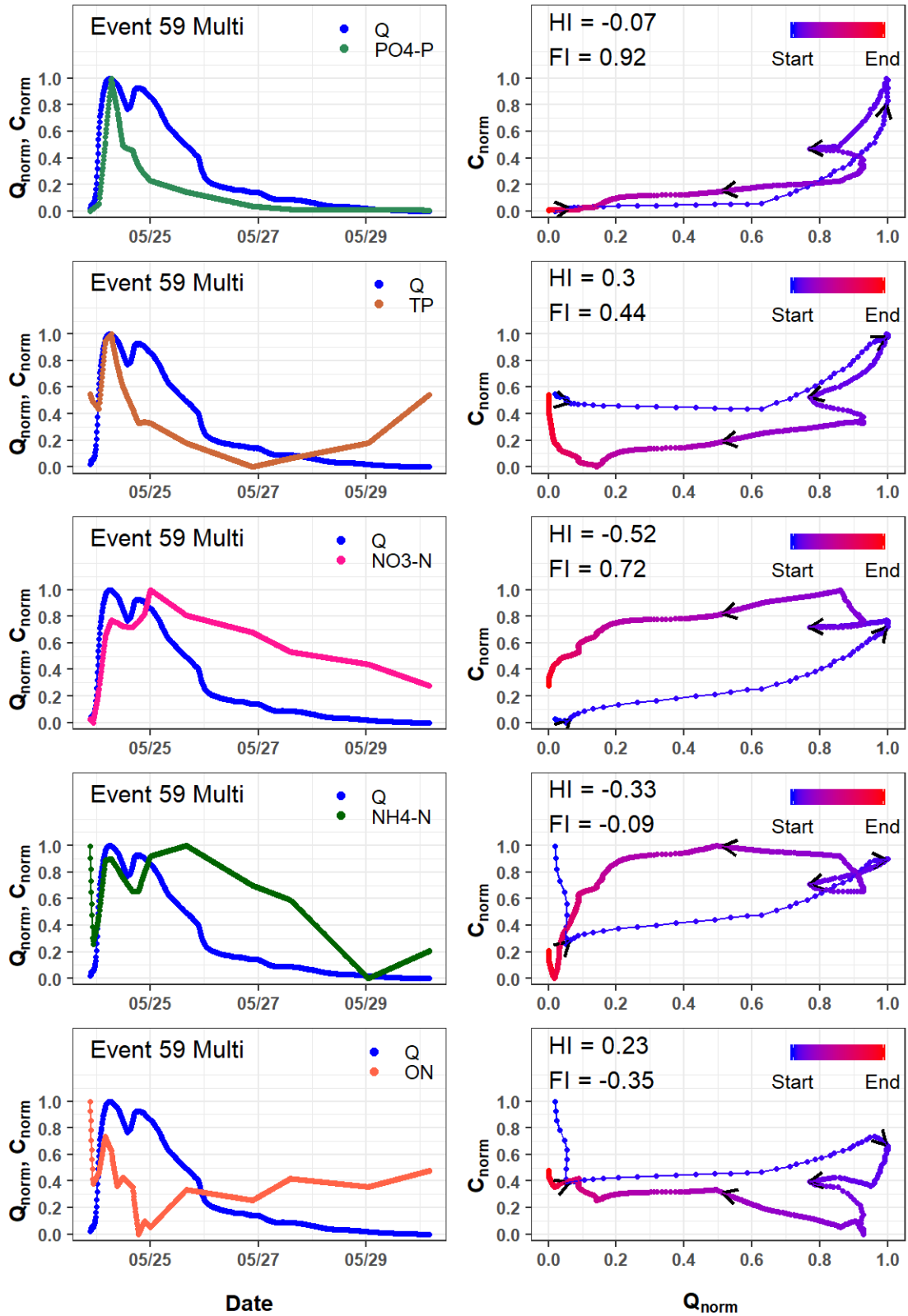


Figure D.63. Event 59 Multi (Events 59 & 60) hydrographs, chemographs, and hysteresis loops for nitrogen and phosphorous species.

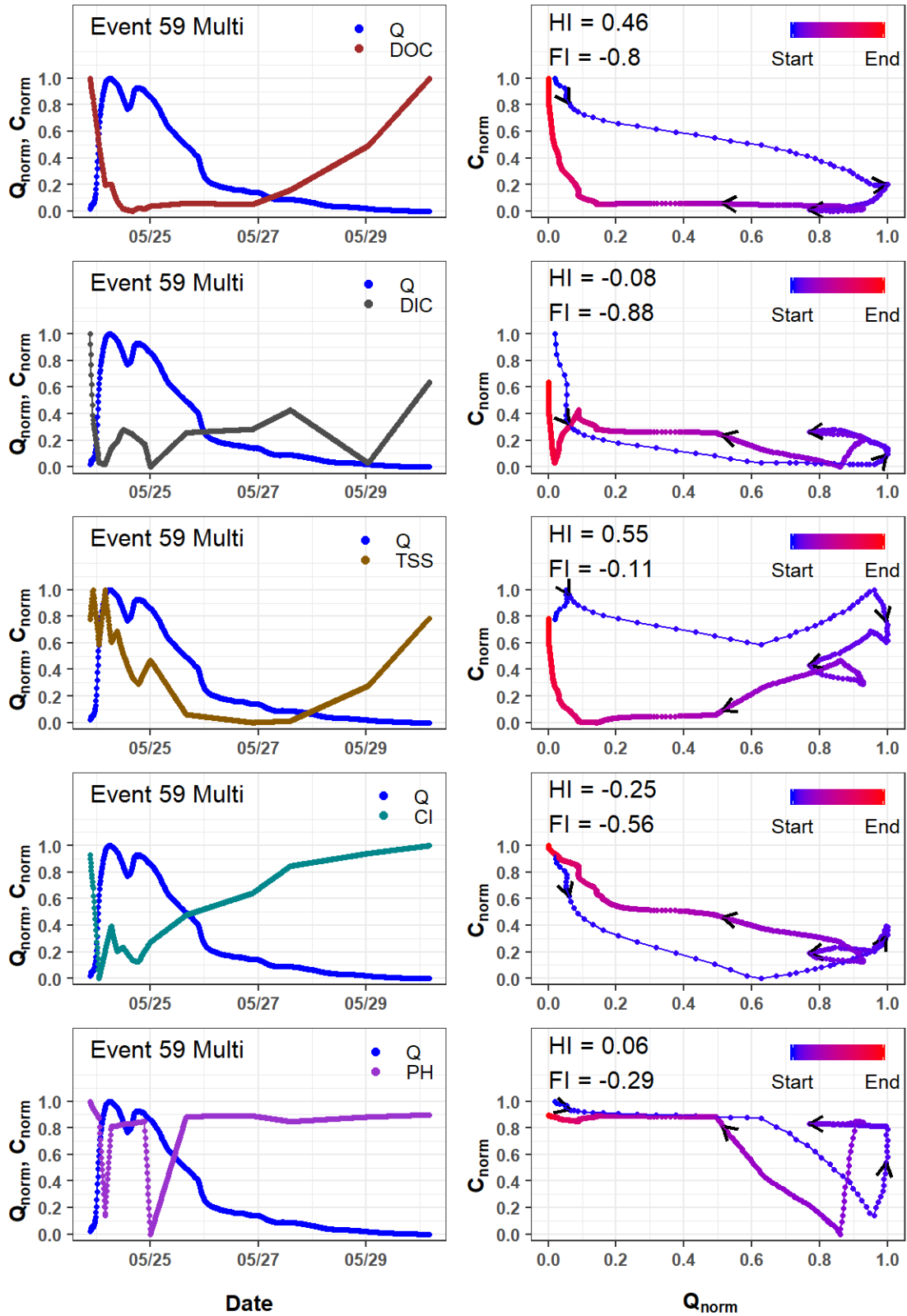


Figure D.64. Event 59 Multi (Events 59 & 60) hydrographs, chemographs, and hysteresis loops for carbon species, suspended solids, chloride, and pH.

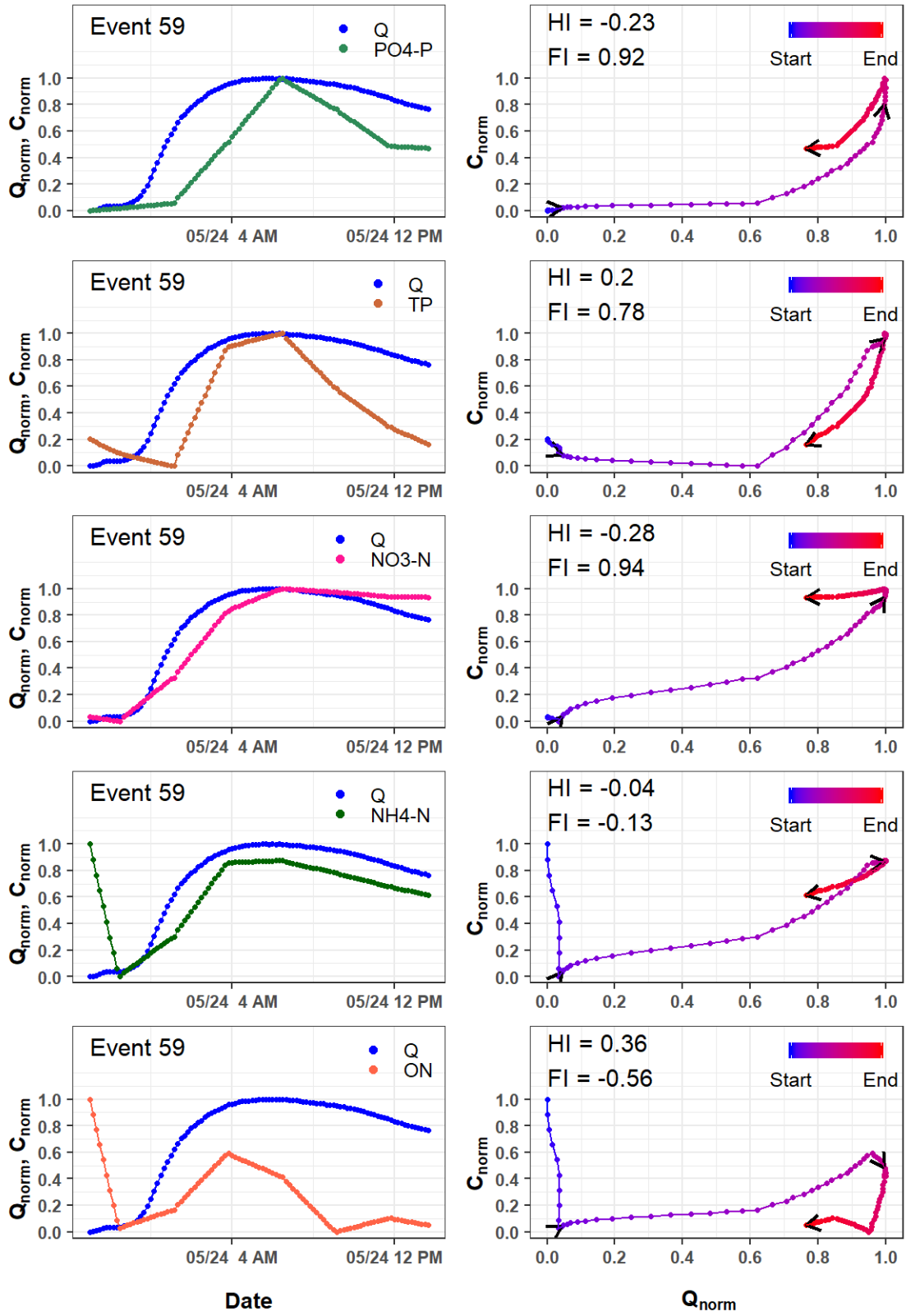


Figure D.65. Event 59 hydrographs, chemographs, and hysteresis loops for nitrogen and phosphorous species.

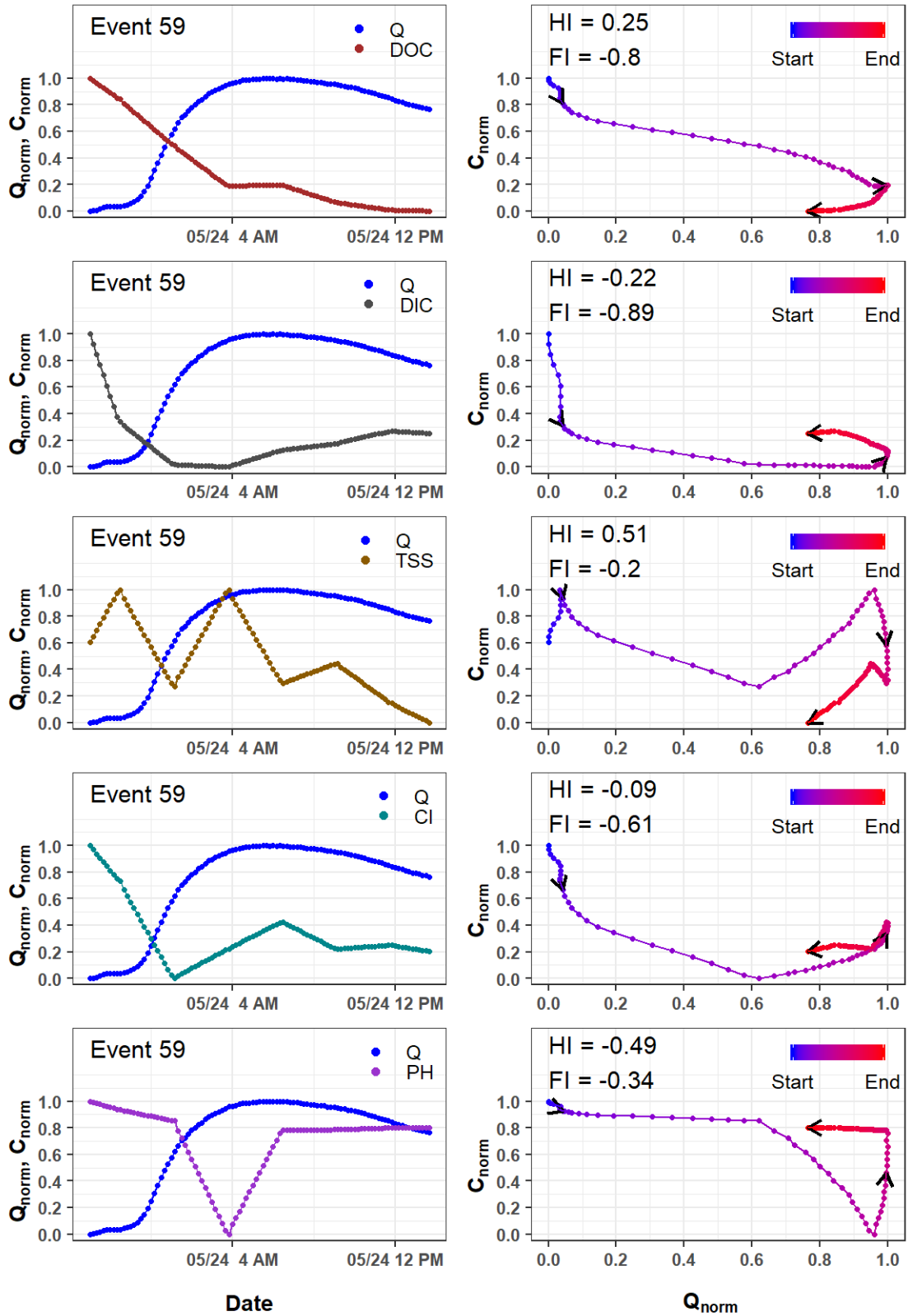


Figure D.66. Event 59 hydrographs, chemographs, and hysteresis loops for carbon species, suspended solids, chloride, and pH.

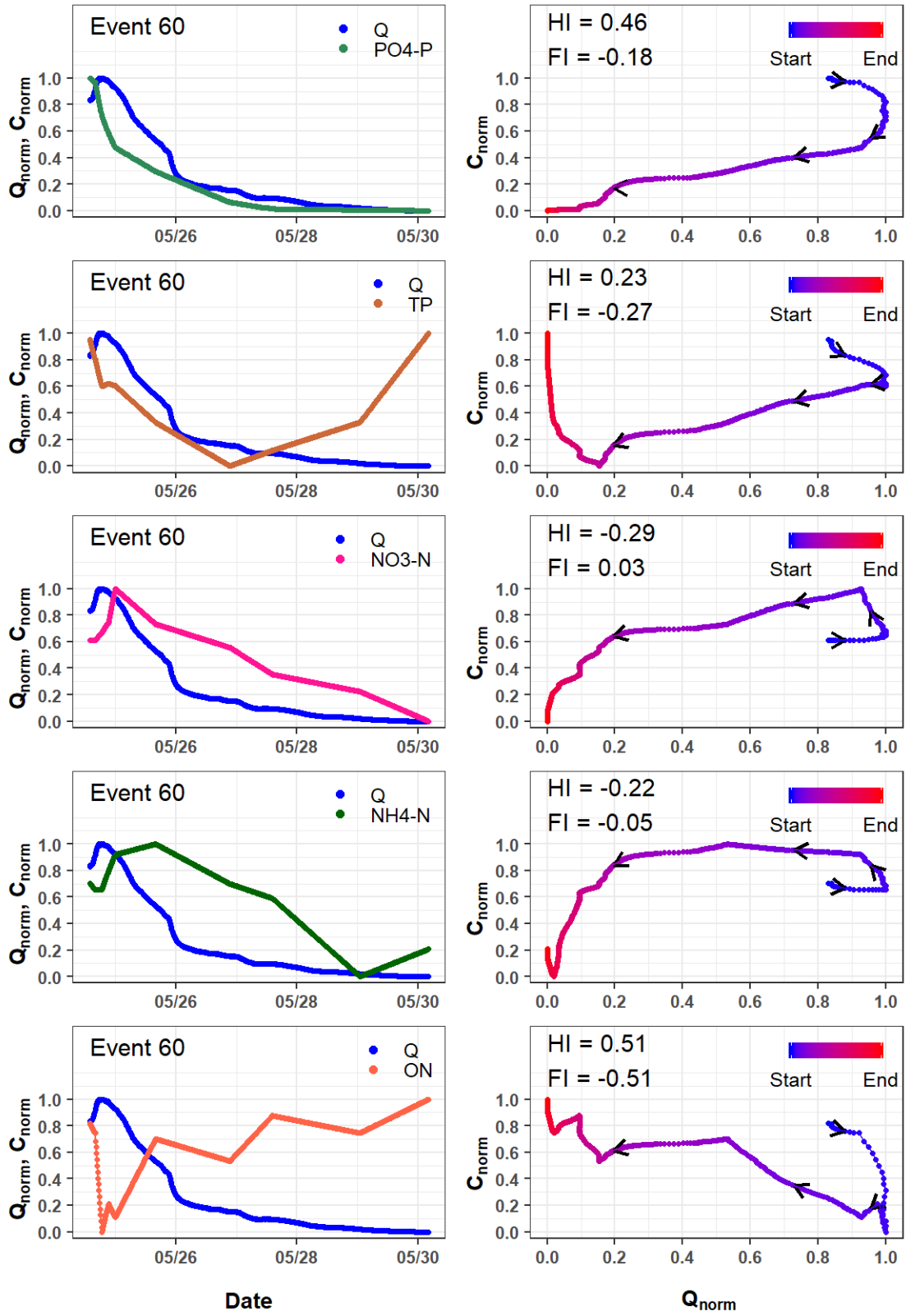


Figure D.67. Event 60 hydrographs, chemographs, and hysteresis loops for nitrogen and phosphorous species.

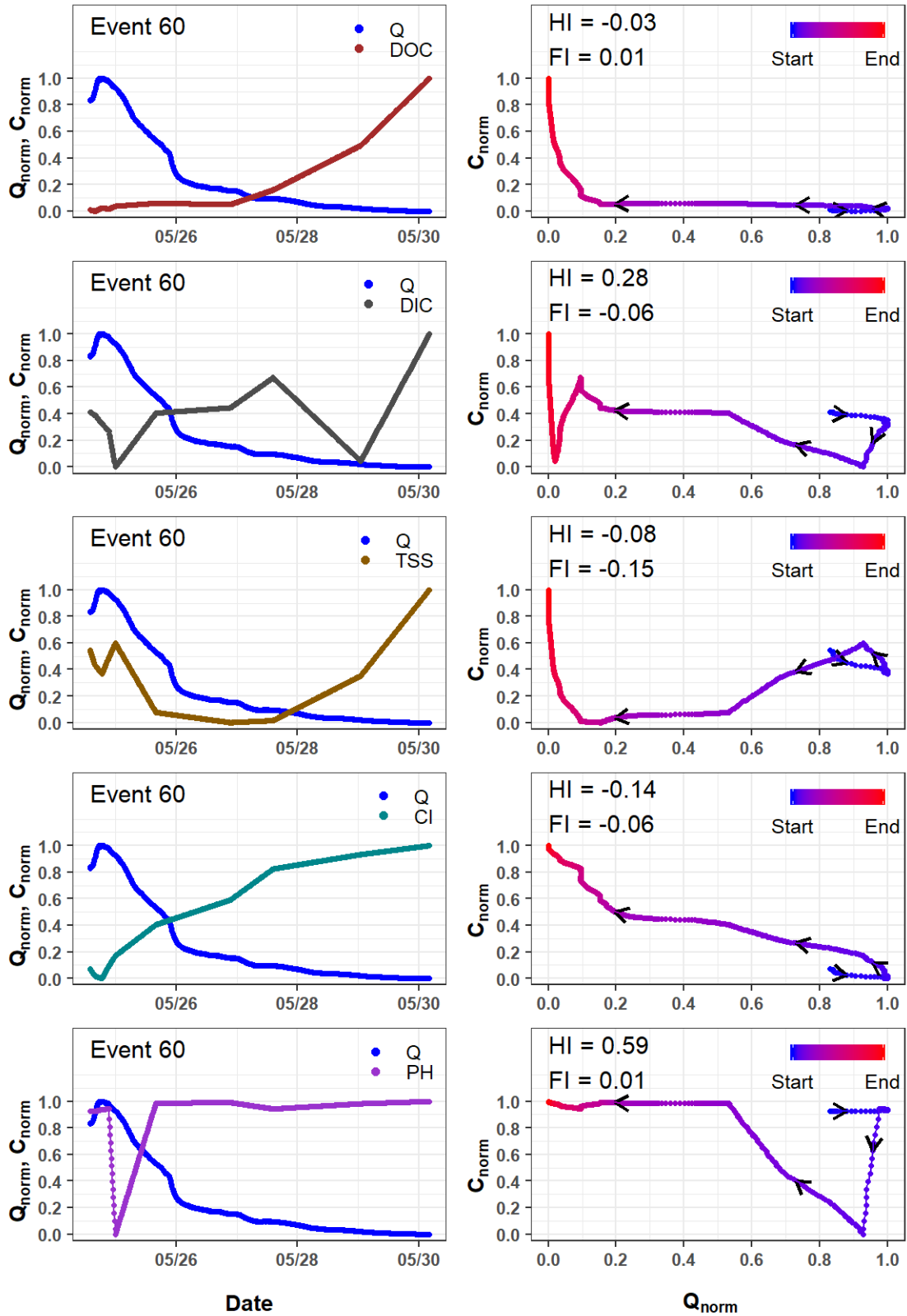


Figure D.68. Event 60 hydrographs, chemographs, and hysteresis loops for carbon species, suspended solids, chloride, and pH.

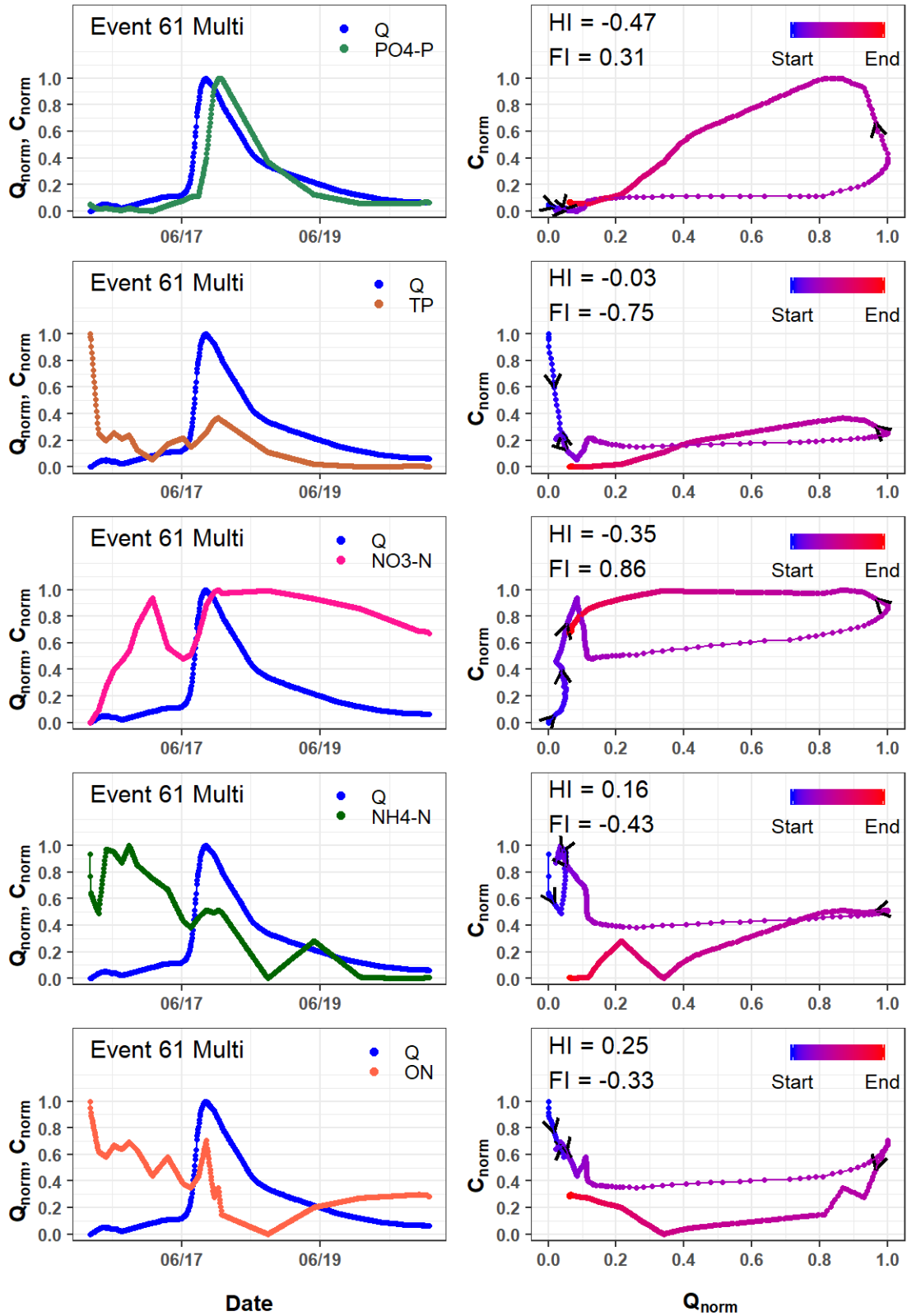


Figure D.69. Event 61 Multi (Events 61 & 62) hydrographs, chemographs, and hysteresis loops for nitrogen and phosphorous species.

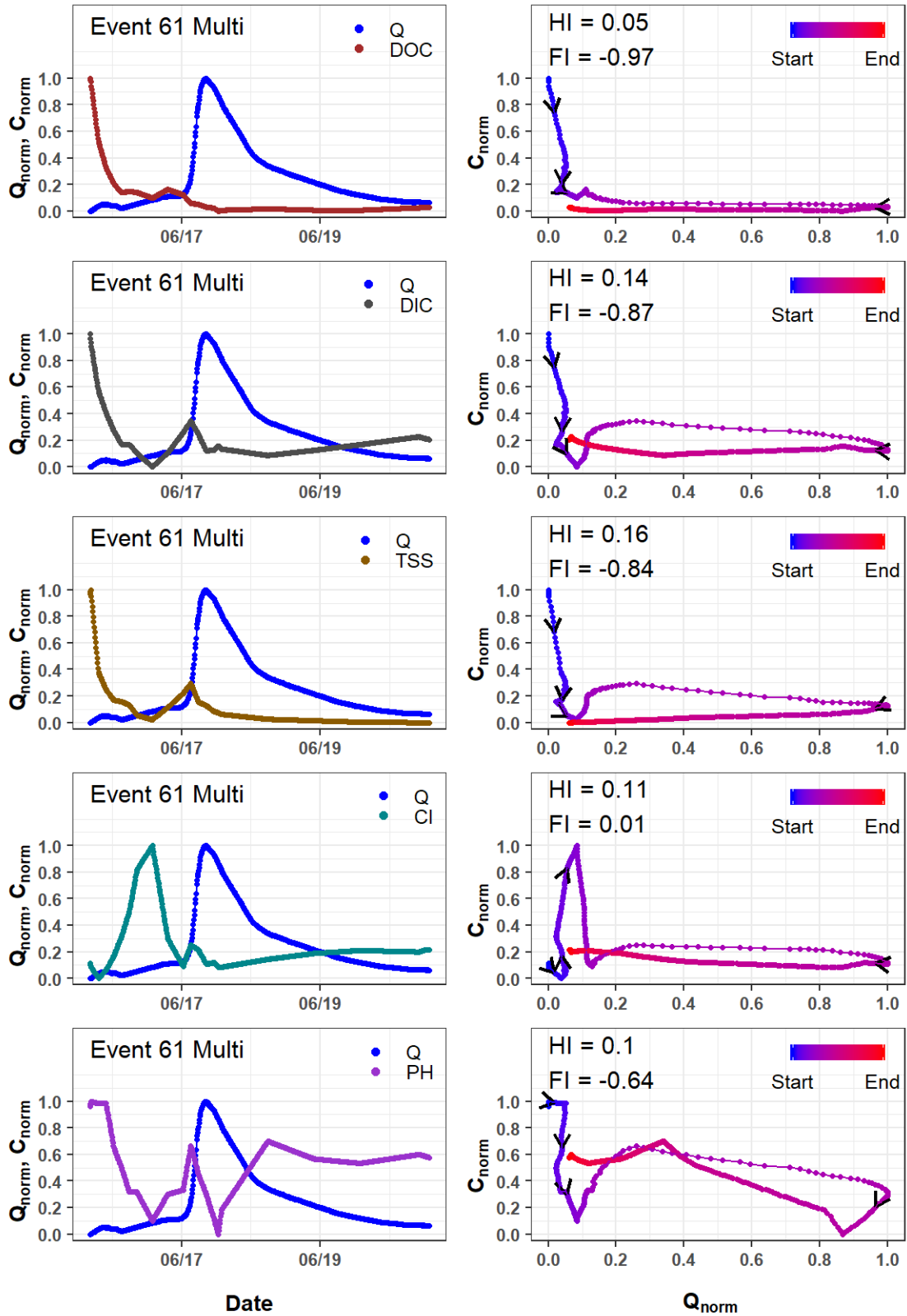


Figure D.70. Event 61 (Events 61 & 62) hydrographs, chemographs, and hysteresis loops for carbon species, suspended solids, chloride, and pH.

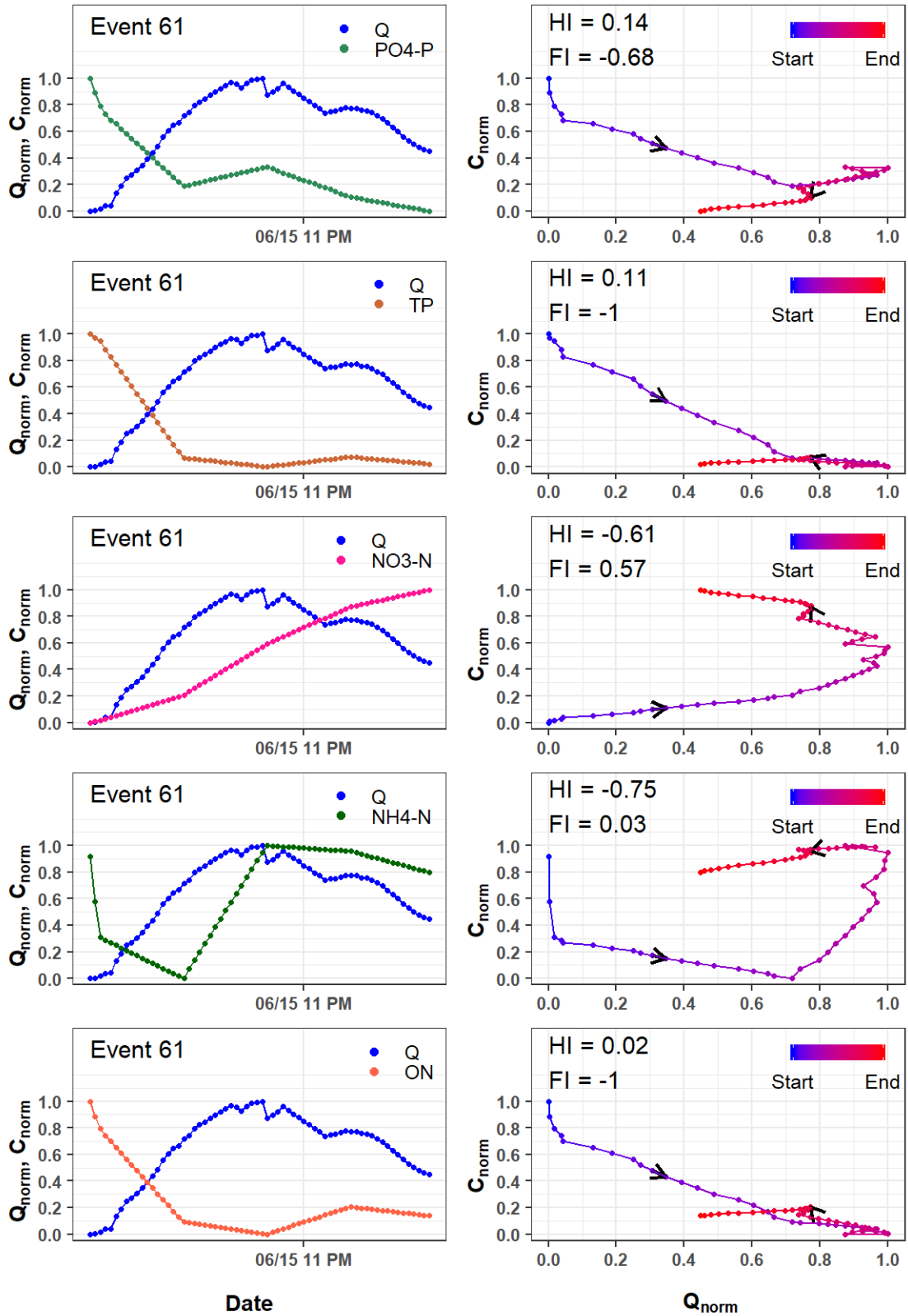


Figure D.71. Event 61 hydrographs, chemographs, and hysteresis loops for nitrogen and phosphorous species.

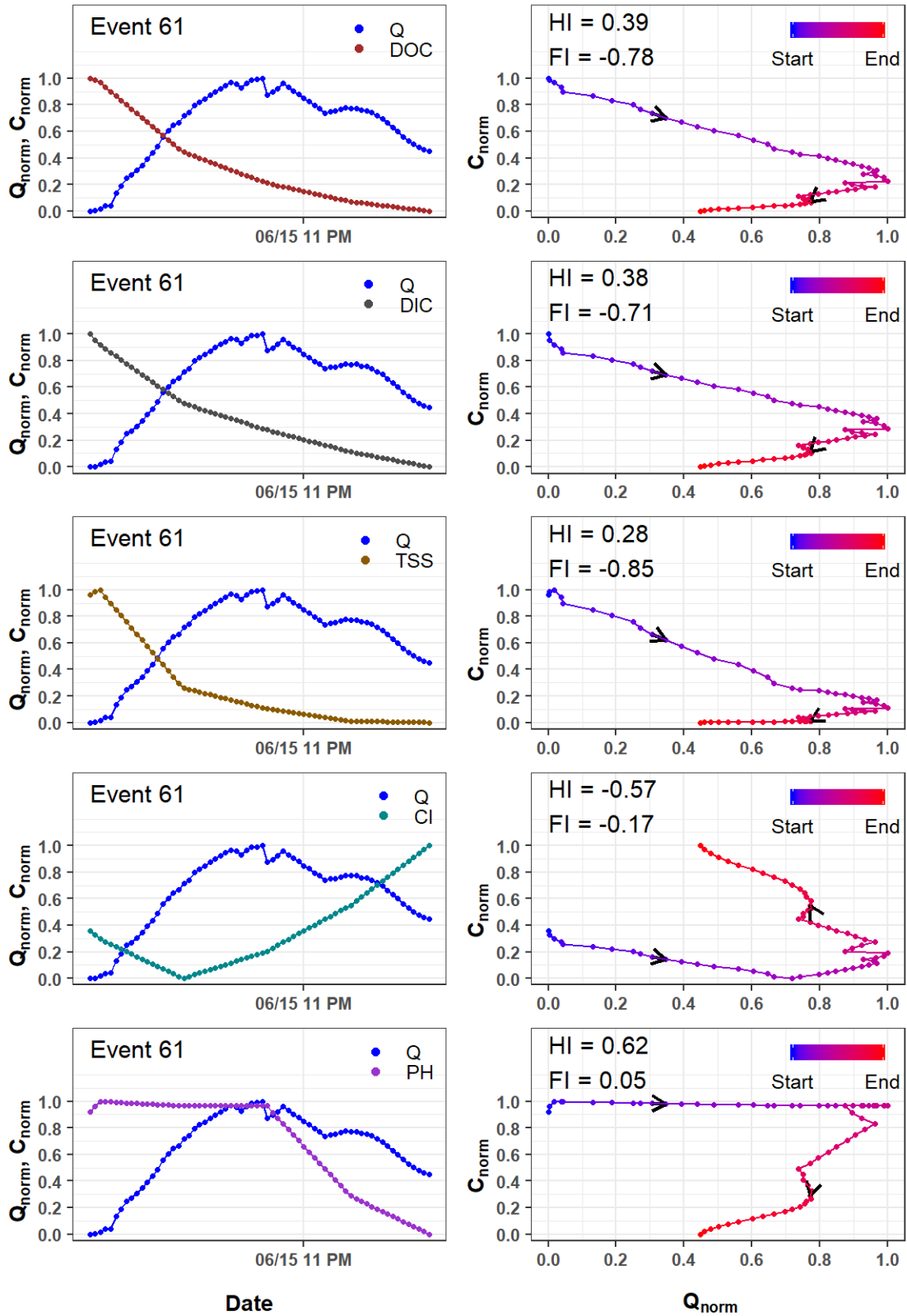


Figure D.72. Event 61 hydrographs, chemographs, and hysteresis loops for carbon species, suspended solids, chloride, and pH.

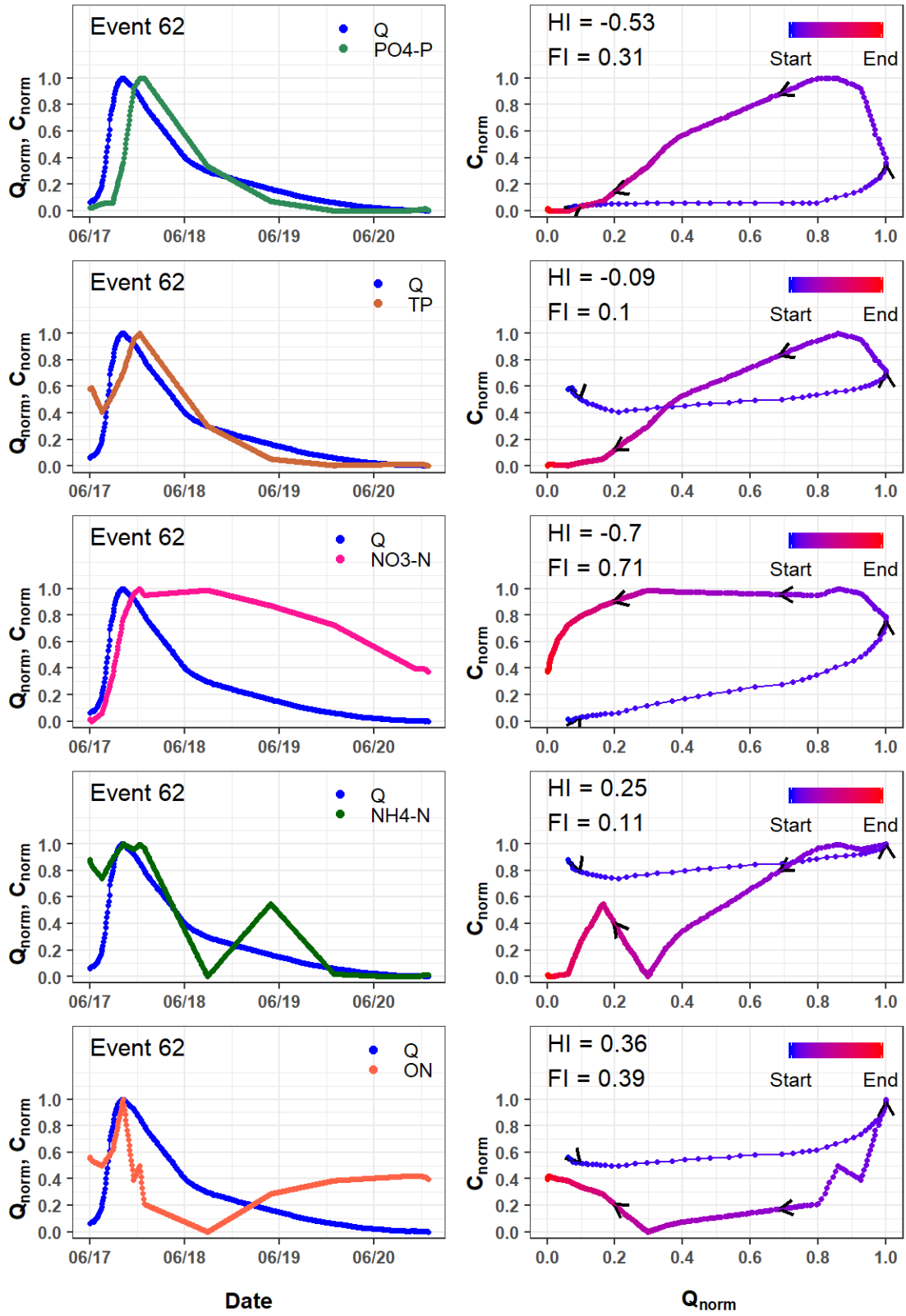


Figure D.73. Event 62 hydrographs, chemographs, and hysteresis loops for nitrogen and phosphorous species.

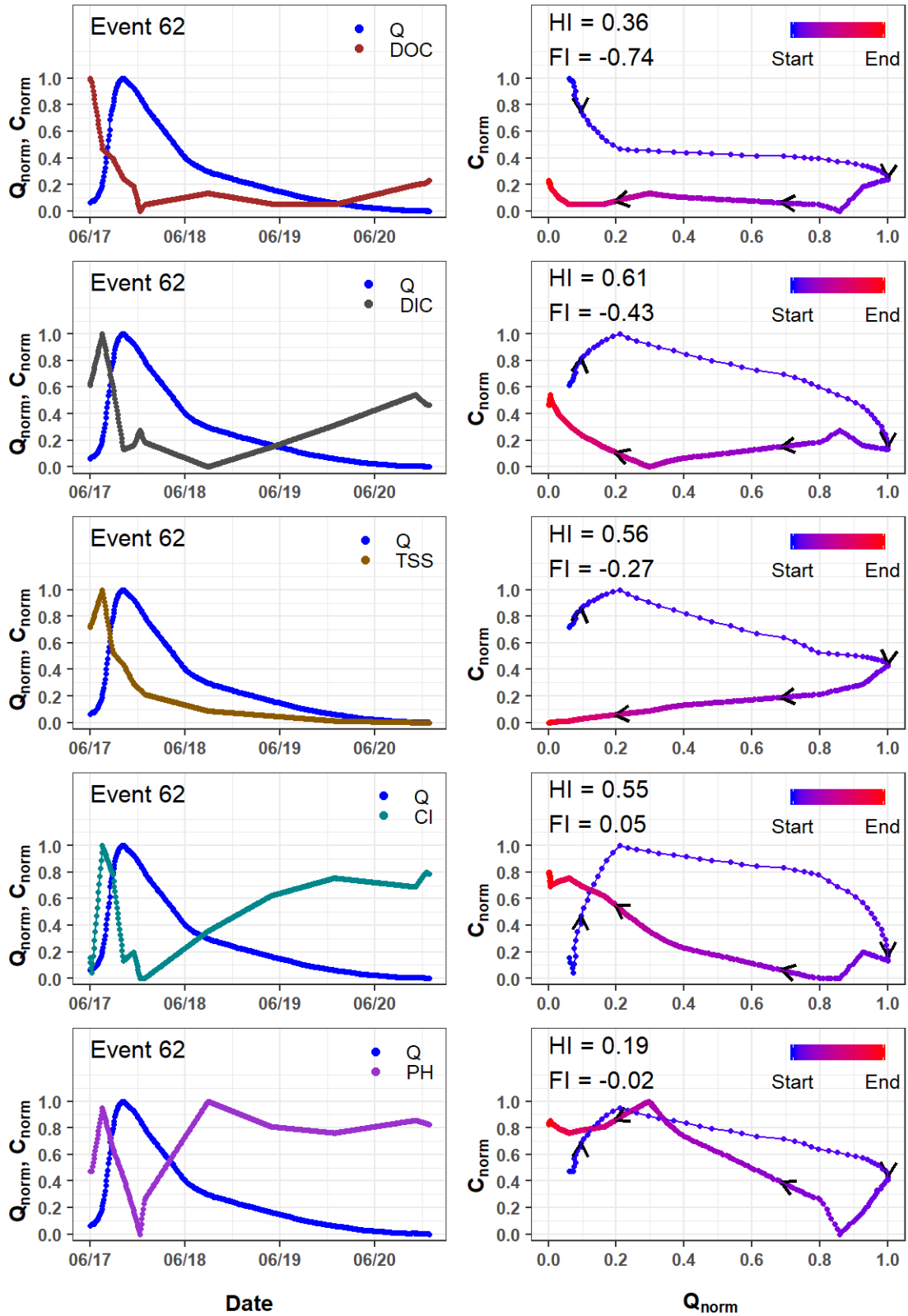


Figure D.74. Event 62 hydrographs, chemographs, and hysteresis loops for carbon species, suspended solids, chloride, and pH.

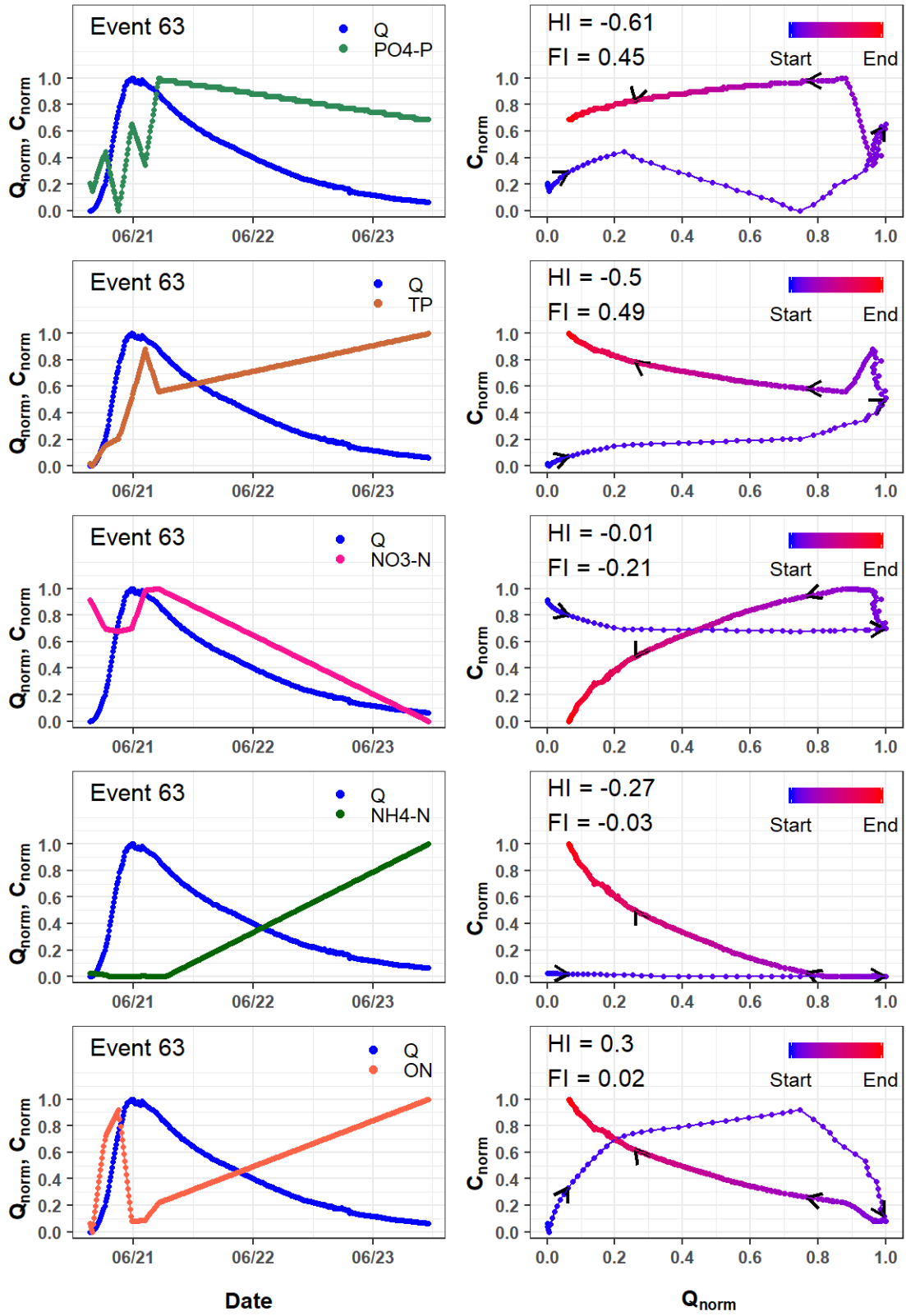


Figure D.75. Event 63 hydrographs, chemographs, and hysteresis loops for nitrogen and phosphorous species.

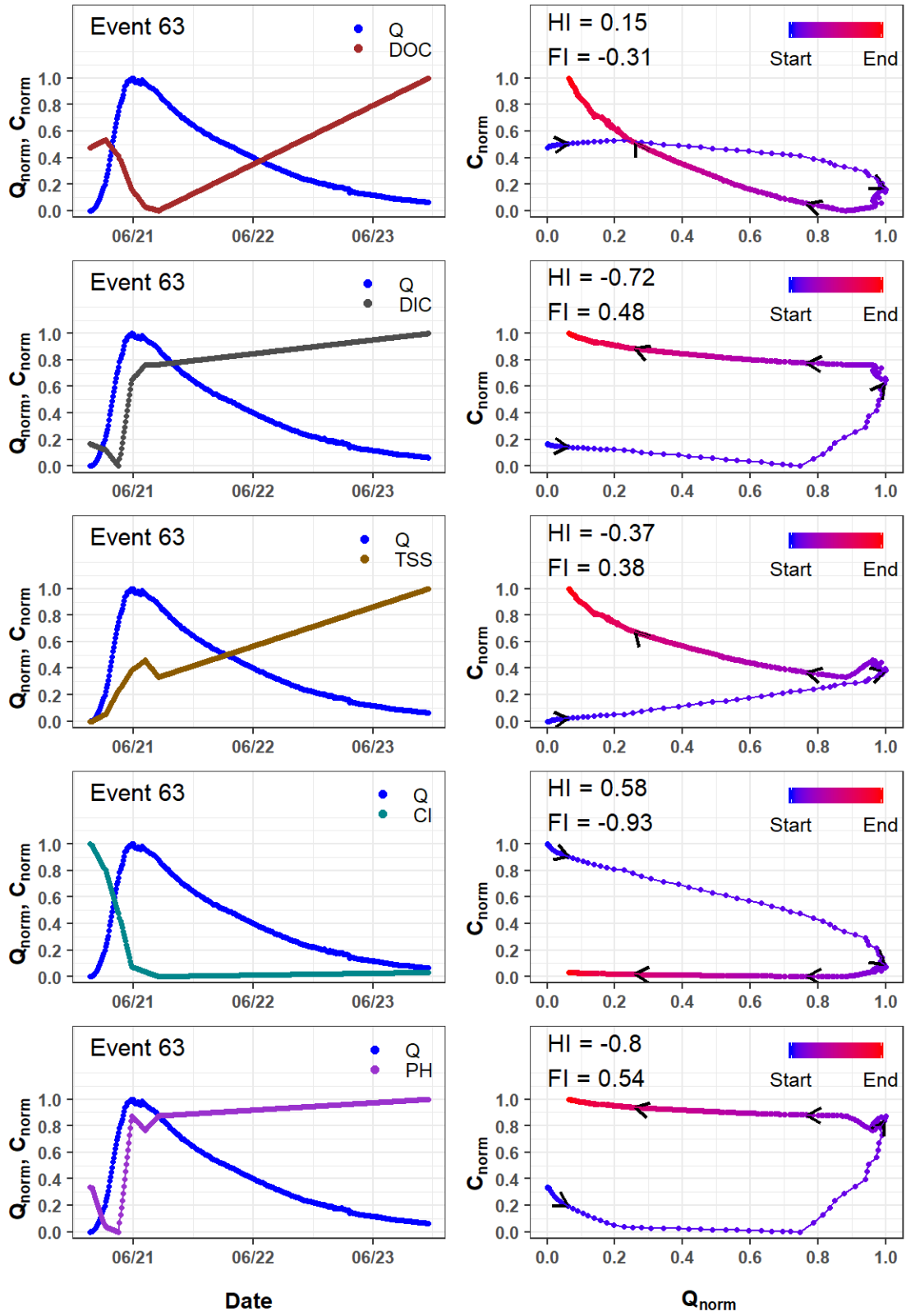


Figure D.76. Event 63 hydrographs, chemographs, and hysteresis loops for carbon species, suspended solids, chloride, and pH.

APPENDIX E: A1 Event Selection for Hysteresis Analysis

Hysteresis plots and C-Q dynamics were examined to determine which events were included in the final hysteresis analysis presented in Chapter 3. The flushing index (FI) and hysteresis index (HI) values and the interpretation of the values, flushing type, and hysteresis type respectively, are provided for each event and parameter provided in Appendix D. The interpretations correspond to those described in Chapter 3 and are listed in Table E.1. Events included in the analysis in Chapter 3 are identified and notes provide reasoning for elimination or when analysis of a “Multi” event was used instead of separate single peaks. Chloride and DIC hysteresis analyses were not provided in Chapter 3, but results are provided in this Appendix.

Table E.1. Summary of hysteresis index and flushing index value interpretations relating to C-Q dynamics.

HI (Loop Direction)	FI	HI Type	FI Type	C-Q Dynamics Interpretation
HI > 0 (Clockwise)	FI > 0	Lead	Concentration	Concentration effect, chemograph peak occurring before the hydrograph storm hydrograph peak
HI < 0 (Anti-Clockwise)	FI > 0	Lag	Concentration	Concentration effect, chemograph peak occurring after the hydrograph storm hydrograph peak
HI > 0 (Clockwise)	FI < 0	Lag	Dilution	Dilution effect, chemograph trough occurring after the hydrograph storm hydrograph peak
HI < 0 (Ani-Clockwise)	FI < 0	Lead	Dilution	Dilution effect, chemograph trough occurring before the hydrograph storm hydrograph peak

Due to the sluggish nature of flow in the subcatchment and time between rainfall events, the falling limb of a storm could last for days, thus flow could begin to increase for the next event

before flow rates returned to start values. In contrast, an event beginning at or near the falling limb of a larger event could start at a higher flow rate and end on a much lower flow rate. This caused an imbalance in the number of Q_{int} values that could be calculated on the rising and falling limbs for some events which led to lower numbers of matching Q_{int} pairs from which HI_{int} values could be calculated. This was especially true when multi-peak events were separated and examined as single-peak events. For example, Q_{int} values below 0.95 ($Q_{95\%}$) did not exist on the falling limb of Event 28 because Event 29 began shortly after flow began to recede. Combining Events 28 and 29 increased the number of matching Q_{int} rising and falling limb pairs by combining these events into one continuous multi-peak event. The smallest interval (int= 1%, 2%, 3%, ..., 97%, 98%, 99%) at which pairs of normalized flow values (Q_{int}) existed on the rising and falling limbs, such that HI_{int} values could be calculated, are summarized for each event in Table E.2. These values sometimes guided which events were used in the final analysis, but not always.

Table E.2. Minimum interval (int) at which there were matching Q_{int} values on the rising and falling limb for each event initially analyzed. HI_{int} values were calculated at 1% intervals. Single-peak events that occurred as parts of a multi-peak event listed following the “Multi” event with which they were associated and indicated by superscript letters A, B & C (i.e. Event 11 Multi was composed of single-peak events 11 & 12).

Event	Minimum Interval (int) with Matching $Q_{int,RL}$ & $Q_{int,FL}$ Pair
8	0.06
9	0.08
10	0.08
11 Multi	0.11
11 ^A	0.31
12 ^B	-

Table E.2. (continued)

16	0.06
23 Multi	0.64
23 ^A	0.92
24 ^B	0.48
25	0.05
26	0.15
27	0.07
28 Multi	0.46
28 ^A	0.95
29 ^B	0.6
30	0.05
31	0.09
32 Multi	0.05
32 ^A	0.63
33 ^B	-
34 ^C	-
35	0.53
36	0.22
37	0.04
41	0.54
44	0.55
48	0.08
49 Multi	0.1
49 ^A	-
50 ^B	0.39
52	0.03
53	0.47
54	0.16
58	0.01
59 Multi	0.02
59 ^A	0.77
60 ^B	0.83
61 Multi	0.07
61 ^A	0.45
62 ^B	0.07
63	0.07

Table E.3. Event hysteresis results for PO4-P. An x in the Final Analysis column indicates the event was included in final HI and FI results presented in Chapter 3. Single-peak events that occurred as parts of a multi-peak event are listed following the “Multi” event with which they were associated and indicated by superscript letters A, B & C (e.g., Event 11 Multi was composed of single-peak events 11 & 12).

PO4-P Event Hysteresis Results						
Event	HI	FI	HI Type	FI Type	Final Analysis	Notes
8	-0.45	0.34	Lag	Concentration	x	
9	0.13	-0.60	Lag	Dilution	x	
10	-0.14	0.64	Lag	Concentration	x	
11 Multi	-0.33	0.94	Lag	Concentration		Distinct single-peak dynamics needed to be separated
11 ^A	-0.27	0.94	Lag	Concentration	x	
12 ^B	-	-	-	-		Release of water for controlled drainage purposes
16	0.18	-0.14	Lag	Dilution	x	
23 Multi	0.15	0.97	Lead	Concentration		Not enough samples for Event 23 single-peak dynamics, combining Events 23 & 24 only extended the rising limb reducing the number of matching Q _{int} pairs, Event 24 displayed distinct single-peak dynamics
23 ^A	-0.15	0.89	Lag	Concentration		Not enough samples, low number of falling limb Q _{int} values
24 ^B	0.17	0.96	Lead	Concentration	x	
25	-0.62	0.01	Lag	Concentration	x	
26	-0.68	0.85	Lag	Concentration	x	
27	0.14	0.29	Lead	Concentration	x	
28 Multi	0.22	0.01	Lead	Concentration	x	Complex loop but still captured overall dynamics with longer rising and falling limb
28 ^A	0.21	0.58	Lead	Concentration		Low number of falling limb Q _{int} values
29 ^B	0.32	-0.25	Lag	Dilution		
30	0.22	0.44	Lead	Concentration	x	
31	-0.27	0.44	Lag	Concentration	x	

Table E.3. (continued)

32 Multi	0.04	0.76	Lead	Concentration		Dynamics for Event 32 were the clearest and including Events 33 and 34 made a complex loop
32 ^A	0.04	0.77	Lead	Concentration	x	
33 ^B	-	-	-	-		Release of water from beaver dam
34 ^C	-	-	-	-		Release of water from beaver dam
35	0.48	-0.21	Lag	Dilution	x	
36	0.25	0.39	Lead	Concentration	x	
37	-0.04	0.31	Lag	Concentration	x	
41	-0.55	0.93	Lag	Concentration		Concentrations too low
44	0.66	-0.30	Lag	Dilution	x	
48	0.46	-0.09	Lag	Dilution	x	
49 Multi	-0.37	0.00	Lead	Dilution		Event 49 added distinct single-peak dynamic different from Event 50 creating a complex loop
49 ^A	-	-	-	-		No falling limb
50 ^B	-0.37	-0.23	Lead	Dilution	x	
52	0.64	-0.89	Lag	Dilution	x	
53	0.01	0.02	Lead	Concentration	x	
54	0.33	0.10	Lead	Concentration	x	
58	0.26	0.16	Lead	Concentration	x	
59 Multi	-0.07	0.92	Lag	Concentration	x	
59 ^A	-0.23	0.92	Lag	Concentration		Low number of falling limb Q_{int} values
60 ^B	0.46	-0.18	Lag	Dilution		Low number of rising limb Q_{int} values
61 Multi	-0.47	0.31	Lag	Concentration		Distinct single-peak dynamic for Event 62, Event 61 only extended rising limb trend
61 ^A	0.14	-0.68	Lag	Dilution		
62 ^B	-0.53	0.31	Lag	Concentration	x	
63	-0.61	0.45	Lag	Concentration	x	

Table E.4. Event hysteresis results for TP. An x in the Final Analysis column indicates the event was included in final HI and FI results presented in Chapter 3. Single-peak events that occurred as parts of a multi-peak event are listed following the “Multi” event with which they were associated and indicated by superscript letters A, B & C (e.g., Event 11 Multi was composed of single-peak events 11 & 12).

TP Event Hysteresis Results						
Event	HI	FI	HI Type	FI Type	Final Analysis	Notes
8	-0.03	-0.07	Lead	Dilution	x	
9	-0.14	0.77	Lag	Concentration	x	
10	-0.10	1.00	Lag	Concentration	x	
11 Multi	-0.07	0.71	Lag	Concentration		Distinct single-peak dynamics needed to be separated, complex loop
11 ^A	-0.13	0.78	Lag	Concentration	x	
12 ^B	-	-	-	-		Release of water for controlled drainage purposes
16	0.69	-0.46	Lag	Dilution	x	
23 Multi	-0.15	0.94	Lag	Concentration		Not enough samples for Event 23 single-peak dynamics, combining Events 23 & 24 only extended the rising limb reducing the number of matching Q_{int} pairs, Event 24 displayed distinct single-peak dynamics
23 ^A	-0.15	0.87	Lag	Concentration		Not enough samples, low number of falling limb Q_{int} values
24 ^B	-0.19	0.88	Lag	Concentration	x	
25	-0.64	0.24	Lag	Concentration	x	
26	-0.74	0.50	Lag	Concentration	x	
27	-0.53	0.33	Lag	Concentration	x	
28 Multi	-0.44	0.76	Lag	Concentration	x	Complex loop but still captured overall dynamics with longer rising and falling limb
28 ^A	-0.19	0.46	Lag	Concentration		Low number of falling limb Q_{int} values
29 ^B	-0.28	0.94	Lag	Concentration		
30	-0.49	0.42	Lag	Concentration	x	
31	-0.20	0.69	Lag	Concentration	x	

Table E.4. (continued)

32 Multi	-0.03	0.55	Lag	Concentration		Dynamics for Event 32 were the clearest and including Events 33 and 34 made a complex loop
32 ^A	-0.33	0.59	Lag	Concentration	x	
33 ^B	-	-	-	-		Release of water from beaver dam
34 ^C	-	-	-	-		Release of water from beaver dam
35	-0.08	0.71	Lag	Concentration	x	
36	-0.24	0.59	Lag	Concentration	x	
37	0.34	-0.71	Lag	Dilution	x	
41	0.15	-0.72	Lag	Dilution	x	
44	0.39	0.26	Lead	Concentration	x	
48	0.31	0.42	Lead	Concentration	x	
49 Multi	-0.23	0.27	Lag	Concentration		Event 49 added distinct single-peak dynamic different from Event 50 creating a complex loop
49 ^A	-	-	-	-		No falling limb
50 ^B	-0.68	0.40	Lag	Concentration	x	
52	-0.68	0.36	Lag	Concentration	x	
53	-0.51	0.02	Lag	Concentration	x	
54	0.79	-0.20	Lag	Dilution	x	
58	0.48	-0.37	Lag	Dilution	x	
59 Multi	0.30	0.44	Lead	Concentration	x	
59 ^A	0.20	0.78	Lead	Concentration		Low number of falling limb Quint values
60 ^B	0.23	-0.27	Lag	Dilution		Low number of rising limb Quint values
61 Multi	-0.03	-0.75	Lead	Dilution		Most distinct single-peak dynamic for Event 62, Event 61 included change in concentration due to flow beginning following a dry period
61 ^A	0.11	-1.00	Lag	Dilution		
62 ^B	-0.09	0.10	Lag	Concentration	x	
63	-0.50	0.49	Lag	Concentration	x	

Table E.5. Event hysteresis results for NO₃-N. An x in the Final Analysis column indicates the event was included in final HI and FI results presented in Chapter 3. Single-peak events that occurred as parts of a multi-peak event are listed following the “Multi” event with which they were associated and indicated by superscript letters A, B & C (e.g., Event 11 Multi was composed of single-peak events 11 & 12).

NO ₃ -N Event Hysteresis Results						
Event	HI	FI	HI Type	FI Type	Final Analysis	Notes
8	-0.17	0.89	Lag	Concentration	x	
9	-0.28	0.90	Lag	Concentration	x	
10	-0.60	0.64	Lag	Concentration	x	
11 Multi	-0.50	0.70	Lag	Concentration		Distinct single-peak dynamics needed to be separated
11 ^A	-0.68	0.70	Lag	Concentration	x	
12 ^B	-	-	-	-		Release of water for controlled drainage purposes
16	-0.70	0.39	Lag	Concentration	x	
23 Multi	-0.48	0.80	Lag	Concentration		Not enough samples for Event 23 single-peak dynamics, combining Events 23 & 24 only extended the rising limb reducing the number of matching Q _{int} pairs, Event 24 displayed distinct single-peak dynamics
23 ^A	-0.15	0.87	Lag	Concentration		Not enough samples, low number of falling limb Q _{int} values
24 ^B	-0.54	0.77	Lag	Concentration	x	
25	0.74	-0.46	Lag	Dilution	x	
26	0.62	-0.67	Lag	Dilution	x	
27	0.27	-0.75	Lag	Dilution	x	
28 Multi	-0.07	-0.99	Lead	Dilution	x	Complex loop but still captured overall dynamics with longer rising and falling limb
28 ^A	-0.22	-0.99	Lead	Dilution		Low number of falling limb Q _{int} values
29 ^B	-0.25	-0.74	Lead	Dilution		
30	-0.23	-0.42	Lead	Dilution	x	
31	0.06	-1.00	Lag	Dilution	x	

Table E.5. (continued)

32 Multi	-0.62	-0.28	Lead	Dilution		Dynamics for Event 32 were the clearest and including Events 33 and 34 made a complex loop, dynamics specific to the lower end of the falling limb for N and C species as well as pH added to loop complexity
32 ^A	-	-	-	-	x	
33 ^B	-	-	-	-		Release of water from beaver dam
34 ^C	-0.03	-0.01	Lead	Dilution		Release of water from beaver dam
35	-0.60	0.34	Lag	Concentration	x	
36	-0.38	-0.84	Lead	Dilution	x	
37	0.25	-0.50	Lag	Dilution		Flat portion of the chemograph thought to be wrong, an artifact of too few samples
41	-0.12	0.67	Lag	Concentration	x	
44	-0.61	0.52	Lag	Concentration	x	
48	-0.71	0.36	Lag	Concentration	x	
49 Multi	-0.26	0.92	Lag	Concentration	x	
49 ^A	-	-	-	-		No falling limb
50 ^B	-0.31	0.74	Lag	Concentration		Multi-peak event captured the overall dynamics without creating a complex loop
52	-0.69	-0.05	Lead	Dilution	x	
53	-0.68	0.14	Lag	Concentration	x	
54	0.33	0.17	Lead	Concentration	x	
58	-0.30	0.99	Lag	Concentration	x	
59 Multi	-0.52	0.72	Lag	Concentration	x	
59 ^A	-0.28	0.94	Lag	Concentration		Low number of falling limb Quint values
60 ^B	-0.29	0.03	Lag	Concentration		Low number of rising limb Quint values
61 Multi	-0.35	0.86	Lag	Concentration		Event 62 had distinct single-peak dynamics
61 ^A	-0.61	0.57	Lag	Concentration		
62 ^B	-0.70	0.71	Lag	Concentration	x	
63	-0.01	-0.21	Lead	Dilution	x	

Table E.6. Event hysteresis results for NH4-N. An x in the Final Analysis column indicates the event was included in final HI and FI results presented in Chapter 3. Single-peak events that occurred as parts of a multi-peak event are listed following the “Multi” event with which they were associated and indicated by superscript letters A, B & C (e.g., Event 11 Multi was composed of single-peak events 11 & 12).

NH4-N Event Hysteresis Results						
Event	HI	FI	HI Type	FI Type	Final Analysis	Notes
8	0.06	-0.96	Lag	Dilution	x	
9	0.35	-0.87	Lag	Dilution	x	
10	0.17	-0.57	Lag	Dilution	x	
11 Multi	0.50	-0.83	Lag	Dilution		Distinct single-peak dynamics needed to be separated
11 ^A	0.38	-0.86	Lag	Dilution	x	
12 ^B	-	-	-	-		Release of water for controlled drainage purposes
16	0.50	0.11	Lead	Concentration	x	
23 Multi	0.21	-0.71	Lag	Dilution		Not enough samples for Event 23 single-peak dynamics, combining Events 23 & 24 only extended the rising limb reducing the number of matching Q _{int} pairs, Event 24 displayed distinct single-peak dynamics
23 ^A	0.15	-0.87	Lag	Dilution		Not enough samples, low number of falling limb Q _{int} values
24 ^B	0.36	-0.50	Lag	Dilution	x	
25	-0.45	-0.35	Lead	Dilution	x	
26	0.47	-0.87	Lag	Dilution	x	
27	0.39	-0.72	Lag	Dilution	x	
28 Multi	0.15	-0.95	Lag	Dilution	x	Complex loop but still captured overall dynamics with longer rising and falling limb
28 ^A	-0.07	-0.73	Lead	Dilution		Low number of falling limb Q _{int} values
29 ^B	-0.02	-0.92	Lead	Dilution		
30	-0.09	-0.73	Lead	Dilution	x	
31	-0.12	-0.72	Lead	Dilution	x	

Table E.6. (continued)

32 Multi	0.27	0.03	Lead	Concentration		Dynamics for Event 32 were the clearest and including Events 33 and 34 made a complex loop, dynamics specific to the lower end of the falling limb for N and C species as well as pH added to loop complexity
32 ^A	0.54	0.04	Lead	Concentration	x	
33 ^B	-	-	-	-		Release of water from beaver dam
34 ^C	-	-	-	-		Release of water from beaver dam
35	-0.57	-0.06	Lead	Dilution	x	
36	0.18	0.07	Lead	Concentration	x	
37	0.34	-0.21	Lag	Dilution	x	
41	-0.49	0.80	Lag	Concentration	x	
44	0.49	-0.63	Lag	Dilution	x	
48	0.51	-0.54	Lag	Dilution	x	
49 Multi	0.19	-0.52	Lag	Dilution	x	
49 ^A	-	-	-	-		No falling limb
50 ^B	-0.08	0.17	Lag	Concentration		
52	0.57	0.42	Lead	Concentration	x	
53	-0.58	0.20	Lag	Concentration	x	
54	0.57	-0.15	Lag	Dilution	x	
58	0.25	0.43	Lead	Concentration	x	
59 Multi	-0.33	-0.09	Lead	Dilution	x	
59 ^A	-0.04	-0.13	Lead	Dilution		Low number of falling limb Quint values
60 ^B	-0.22	-0.05	Lead	Dilution		Low number of rising limb Quint values
61 Multi	0.16	-0.43	Lag	Dilution		Event 62 had distinct single-peak dynamics
61 ^A	-0.75	0.03	Lag	Concentration	x	
62 ^B	0.25	0.11	Lead	Concentration	x	
63	-0.27	-0.03	Lead	Dilution	x	

Table E.7. Event hysteresis results for ON. An x in the Final Analysis column indicates the event was included in final HI and FI results presented in Chapter 3. Single-peak events that occurred as parts of a multi-peak event are listed following the “Multi” event with which they were associated and indicated by superscript letters A, B & C (e.g., Event 11 Multi was composed of single-peak events 11 & 12).

ON Event Hysteresis Results						
Event	HI	FI	HI Type	FI Type	Final Analysis	Notes
8	-0.63	-0.01	Lead	Dilution	x	
9	0.81	-0.82	Lag	Dilution	x	
10	0.16	-0.10	Lag	Dilution	x	
11 Multi	0.51	-0.38	Lag	Dilution		Distinct single-peak dynamics needed to be separated
11 ^A	0.51	-0.38	Lag	Dilution	x	
12 ^B	-	-	-	-		Release of water for controlled drainage purposes
16	0.58	-0.27	Lag	Dilution	x	
23 Multi	0.09	0.75	Lead	Concentration		Not enough samples for Event 23 single-peak dynamics, combining Events 23 & 24 only extended the rising limb reducing the number of matching Q_{int} pairs, Event 24 displayed distinct single-peak dynamics
24 ^A	-0.15	0.87	Lag	Concentration		Not enough samples, low number of falling limb Q_{int} values
23 ^B	0.12	0.48	Lead	Concentration	x	
25	-0.58	0.14	Lag	Concentration	x	
26	-0.68	0.18	Lag	Concentration	x	
27	-0.52	0.03	Lag	Concentration	x	
28 Multi	-0.60	0.25	Lag	Concentration	x	Complex loop but still captured overall dynamics with longer rising and falling limb
28 ^A	-0.61	-0.19	Lead	Dilution		Low number of falling limb Q_{int} values
29 ^B	-0.72	0.39	Lag	Concentration		
30	-0.64	0.09	Lag	Concentration	x	
31	-0.03	0.04	Lag	Concentration	x	

Table E.7. (continued)

32 Multi	-0.23	0.41	Lag	Concentration		Dynamics for Event 32 were the clearest and including Events 33 and 34 made a complex loop, dynamics specific to the lower end of the falling limb for N and C species as well as pH added to loop complexity
32 ^A	-0.48	0.50	Lag	Concentration	x	
33 ^B	-	-	-	-		Release of water from beaver dam
34 ^C	-	-	-	-		Release of water from beaver dam
35	-0.74	0.57	Lag	Concentration	x	
36	-0.38	-0.06	Lead	Dilution	x	
37	-0.01	-0.86	Lead	Dilution	x	
41	-0.04	0.53	Lag	Concentration	x	
44	-0.18	-0.30	Lead	Dilution	x	
48	-0.51	0.11	Lag	Concentration	x	
49 Multi	-0.20	0.44	Lag	Concentration	x	
49 ^A	-	-	-	-		No falling limb
50 ^B	-0.06	0.62	Lag	Concentration		
52	-0.45	0.21	Lag	Concentration	x	
53	0.40	0.56	Lead	Concentration	x	
54	-0.02	0.02	Lag	Concentration	x	
58	0.37	0.04	Lead	Concentration	x	
59 Multi	0.23	-0.35	Lag	Dilution	x	
59 ^A	0.36	-0.56	Lag	Dilution		Low number of falling limb Quint values
60 ^B	0.51	-0.51	Lag	Dilution		Low number of rising limb Quint values
61 Multi	0.25	-0.33	Lag	Dilution		Event 62 had distinct single-peak dynamics
61 ^A	0.02	-1.00	Lag	Dilution	x	
62 ^B	0.36	0.39	Lead	Concentration	x	
63	0.30	0.02	Lead	Concentration	x	

Table E.8. Event hysteresis results for DOC. An x in the Final Analysis column indicates the event was included in final HI and FI results presented in Chapter 3. Single-peak events that occurred as parts of a multi-peak event are listed following the “Multi” event with which they were associated and indicated by superscript letters A, B & C (e.g., Event 11 Multi was composed of single-peak events 11 & 12).

DOC Event Hysteresis Results						
Event	HI	FI	HI Type	FI Type	Final Analysis	Notes
8	0.20	-0.50	Lag	Dilution	x	
9	0.58	-0.84	Lag	Dilution	x	
10	0.50	-0.77	Lag	Dilution	x	
11 Multi	0.51	-0.44	Lag	Dilution		Distinct single-peak dynamics needed to be separated
11 ^A	0.54	-0.54	Lag	Dilution	x	
12 ^B	-	-	-	-		Release of water for controlled drainage purposes
16	0.74	-0.60	Lag	Dilution	x	
23 Multi	0.56	-0.10	Lag	Dilution		Not enough samples for Event 23 single-peak dynamics, combining Events 23 & 24 only extended the rising limb reducing the number of matching Q_{int} pairs, Event 24 displayed distinct single-peak dynamics
23 ^A	-0.15	0.87	Lag	Concentration		Not enough samples, low number of falling limb Q_{int} values
24 ^B	0.55	-0.59	Lag	Dilution	x	
25	0.60	-0.38	Lag	Dilution	x	
26	0.15	-0.64	Lag	Dilution	x	
27	0.18	-0.81	Lag	Dilution	x	
28 Multi	-0.25	-0.89	Lead	Dilution	x	Complex loop but still captured overall dynamics with longer rising and falling limb
28 ^A	-0.35	-0.93	Lead	Dilution		Low number of falling limb Q_{int} values
29 ^B	-0.47	-0.72	Lead	Dilution		
30	-0.30	-0.64	Lead	Dilution	x	
31	-0.40	-0.58	Lead	Dilution	x	

Table E.8. (continued)

32 Multi	-0.47	-0.18	Lead	Dilution		Dynamics for Event 32 were the clearest and including Events 33 and 34 made a complex loop, dynamics specific to the lower end of the falling limb for N and C species as well as pH added to loop complexity
32 ^A	-0.12	-0.97	Lead	Dilution	x	
33 ^B	-	-	-	-		Release of water from beaver dam
34 ^C	-	-	-	-		Release of water from beaver dam
35	-0.55	0.10	Lag	Concentration	x	
36	-0.40	-0.97	Lead	Dilution	x	
37	0.05	-0.89	Lag	Dilution	x	
41	-0.09	0.62	Lag	Concentration	x	
44	-0.67	-0.55	Lead	Dilution	x	
48	-0.56	-0.07	Lead	Dilution	x	
49 Multi	-0.49	-0.32	Lead	Dilution	x	
49 ^A	-	-	-	-		No falling limb
50 ^B	-0.37	-0.10	Lead	Dilution		
52	0.65	-0.85	Lag	Dilution	x	
53	0.57	0.04	Lead	Concentration	x	
54	-0.30	-0.22	Lead	Dilution	x	
58	0.38	-0.96	Lag	Dilution	x	
59 Multi	0.46	-0.80	Lag	Dilution	x	
59 ^A	0.25	-0.80	Lag	Dilution		Low number of falling limb Quint values
60 ^B	-0.03	0.01	Lag	Concentration		Low number of rising limb Quint values
61 Multi	0.05	-0.97	Lag	Dilution		Event 62 had distinct single-peak dynamics
61 ^A	0.39	-0.78	Lag	Dilution		
62 ^B	0.36	-0.74	Lag	Dilution	x	
63	0.15	-0.31	Lag	Dilution	x	

Table E.9. Event hysteresis results for TSS. An x in the Final Analysis column indicates the event was included in final HI and FI results presented in Chapter 3. Single-peak events that occurred as parts of a multi-peak event are listed following the “Multi” event with which they were associated and indicated by superscript letters A, B & C (e.g., Event 11 Multi was composed of single-peak events 11 & 12).

TSS Event Hysteresis Results						
Event	HI	FI	HI Type	FI Type	Final Analysis	Notes
8	0.47	-0.73	Lag	Dilution	x	
9	0.37	0.38	Lead	Concentration	x	
10	0.03	0.10	Lead	Concentration	x	
11 Multi	0.30	-0.66	Lag	Dilution		The falling limb of the chemograph had already been captured by the separated Event 11 dynamics, thus combining Events 11 & 12 did not add any value analysis
11 ^A	0.30	-0.66	Lag	Dilution	x	
12 ^B	-	-	-	-		Release of water for controlled drainage purposes
16	0.14	-0.05	Lag	Dilution	x	
23 Multi	-0.31	0.86	Lag	Concentration		Not enough samples for Event 23 single-peak dynamics, combining Events 23 & 24 only extended the rising limb reducing the number of matching Q_{int} pairs, Event 24 displayed distinct single-peak dynamics
23 ^A	-0.15	0.87	Lag	Concentration		Not enough samples, low number of falling limb Q_{int} values
24 ^B	-0.51	0.52	Lag	Concentration	x	
25	-0.50	-0.57	Lead	Dilution	x	
26	-0.76	0.45	Lag	Concentration	x	
27	-0.52	0.23	Lag	Concentration	x	
28 Multi	-0.26	0.79	Lag	Concentration	x	Complex loop but still captured overall dynamics with longer rising and falling limb
28 ^A	0.15	0.17	Lead	Concentration		Low number of falling limb Q_{int} values
29 ^B	-0.36	0.99	Lag	Concentration		

Table E.9. (continued)

30	-0.54	0.37	Lag	Concentration	x	
31	-0.23	0.74	Lag	Concentration	x	
32 Multi	-0.07	0.47	Lag	Concentration		Dynamics for Event 32 were the clearest and including Events 33 and 34 made a complex loop
32 ^A	-0.44	0.51	Lag	Concentration	x	
33 ^B	-	-	-	-		Release of water from beaver dam
34 ^C	-	-	-	-		Release of water from beaver dam
35	0.09	0.29	Lead	Concentration	x	
36	-0.22	0.50	Lag	Concentration	x	
37	0.34	-0.53	Lag	Dilution	x	
41	0.42	-0.95	Lag	Dilution	x	
44	-0.08	0.52	Lag	Concentration	x	
48	0.03	0.85	Lead	Concentration	x	
49 Multi	0.28	-0.05	Lag	Dilution	x	
49 ^A	-	-	-	-		No falling limb
50 ^B	0.19	-0.34	Lag	Dilution		
52	-0.71	0.54	Lag	Concentration	x	
53	-0.65	0.09	Lag	Concentration	x	
54	0.58	-0.35	Lag	Dilution	x	
58	0.30	-0.85	Lag	Dilution	x	
59 Multi	0.55	-0.11	Lag	Dilution	x	
59 ^A	0.51	-0.20	Lag	Dilution		Low number of falling limb Quint values
60 ^B	-0.08	-0.15	Lead	Dilution		Low number of rising limb Quint values
61 Multi	0.16	-0.84	Lag	Dilution		Event 62 had distinct single-peak dynamics
61 ^A	0.28	-0.85	Lag	Dilution		
62 ^B	0.56	-0.27	Lag	Dilution	x	
63	-0.37	0.38	Lag	Concentration	x	

Table E.10. Event hysteresis results for pH. An x in the Final Analysis column indicates the event was included in final HI and FI results presented in Chapter 3. Single-peak events that occurred as parts of a multi-peak event are listed following the “Multi” event with which they were associated and indicated by superscript letters A, B & C (e.g., Event 11 Multi was composed of single-peak events 11 & 12).

pH Event Hysteresis Results						
Event	HI	FI	HI Type	FI Type	Final Analysis	Notes
8	-0.41	-0.28	Lead	Dilution		Noisy data that caused loop to cross multiple times
9	-0.27	-0.14	Lead	Dilution	x	
10	-0.20	0.34	Lag	Concentration		Noisy dynamics
11 Multi	-0.46	-0.79	Lead	Dilution		Distinct single-peak dynamics needed to be separated
11 ^A	-0.62	-0.99	Lead	Dilution	x	
12 ^B	-	-	-	-		Release of water for controlled drainage purposes
16	0.29	-0.73	Lag	Dilution	x	
23 Multi	0.46	-0.77	Lag	Dilution		Not enough samples for Event 23 single-peak dynamics, combining Events 23 & 24 only extended the rising limb reducing the number of matching Q _{int} pairs, Event 24 displayed distinct single-peak dynamics
23 ^A	0.15	-0.87	Lag	Dilution		Not enough samples, low number of falling limb Q _{int} values
24 ^B	0.67	-0.67	Lag	Dilution	x	
25	-0.20	0.57	Lag	Concentration	x	
26	-0.39	0.72	Lag	Concentration	x	
27	0.21	0.11	Lead	Concentration	x	
28 Multi	-0.05	0.90	Lag	Concentration	x	Complex loop but still captured overall dynamics with longer rising and falling limb
28 ^A	0.21	0.86	Lead	Concentration		Low number of falling limb Q _{int} values
29 ^B	-0.22	0.80	Lag	Concentration		
30	0.61	0.13	Lead	Concentration	x	
31	0.30	0.89	Lead	Concentration	x	

Table E.10. (continued)

32 Multi	0.59	0.13	Lead	Concentration		Dynamics for Event 32 were the clearest and including Events 33 and 34 made a complex loop, dynamics specific to the lower end of the falling limb for N and C species as well as pH added to loop complexity
32 ^A	0.32	0.25	Lead	Concentration	x	
33 ^B	-	-	-	-		Release of water from beaver dam
34 ^C	-	-	-	-		Release of water from beaver dam
35	0.63	-0.12	Lag	Dilution	x	
36	0.51	0.72	Lead	Concentration	x	
37	0.49	0.22	Lead	Concentration	x	
41	-0.04	-0.39	Lead	Dilution	x	
44	0.73	0.00	Lead	Concentration	x	
48	0.53	-0.01	Lag	Dilution	x	
49 Multi	0.33	-0.20	Lag	Dilution		
49 ^A	-	-	-	-		No falling limb
50 ^B	0.24	0.13	Lead	Concentration	x	
52	-0.75	0.41	Lag	Concentration	x	
53	-0.60	-0.12	Lead	Dilution	x	
54	0.90	0.13	Lead	Concentration	x	
58	0.04	-0.28	Lag	Dilution	x	
59 Multi	0.06	-0.29	Lag	Dilution		Separating peaks caused a very low number of matching Quint values but pH dynamics were so quick changing and distinct they were split
59 ^A	-0.49	-0.34	Lead	Dilution	x	
60 ^B	0.59	0.01	Lead	Concentration	x	
61 Multi	0.10	-0.64	Lag	Dilution		Event 62 had distinct single-peak dynamics
61 ^A	0.62	0.05	Lead	Concentration		
62 ^B	0.19	-0.02	Lag	Dilution	x	
63	-0.80	0.54	Lag	Concentration	x	

Table E.11. Event hysteresis results for CI. Single-peak events that occurred as parts of a multi-peak event are listed following the “Multi” event with which they were associated and indicated by superscript letters A, B & C (e.g. Event 11 Multi was composed of single-peak events 11 & 12).

CI Event Hysteresis Results				
Event	HI	FI	HI Type	FI Type
8	0.15	-0.87	Lag	Dilution
9	-0.27	-0.81	Lead	Dilution
10	-0.70	0.12	Lag	Concentration
11 Multi	-0.34	-0.22	Lead	Dilution
11 ^A	-0.35	-0.61	Lead	Dilution
12 ^B	-	-	-	-
16	0.60	-0.79	Lag	Dilution
23 Multi	0.17	-0.97	Lag	Dilution
23 ^A	0.15	-0.87	Lag	Dilution
24 ^B	0.28	-0.95	Lag	Dilution
25	0.39	-0.03	Lag	Dilution
26	0.44	-0.08	Lag	Dilution
27	0.79	-0.22	Lag	Dilution
28 Multi	-0.17	-0.04	Lead	Dilution
28 ^A	0.43	0.77	Lead	Concentration
29 ^B	-0.28	-0.26	Lead	Dilution
30	0.55	-0.10	Lag	Dilution
31	-0.19	0.03	Lag	Concentration
32 Multi	0.14	-0.56	Lag	Dilution
32 ^A	0.38	-0.56	Lag	Dilution
33 ^B	-	-	-	-
34 ^C	-	-	-	-
35	0.17	-0.84	Lag	Dilution
36	0.31	-0.54	Lag	Dilution
37	0.30	0.34	Lead	Concentration
41	-0.06	-0.36	Lead	Dilution
44	0.80	-0.30	Lag	Dilution
48	0.44	-0.35	Lag	Dilution
49 Multi	0.28	-0.96	Lag	Dilution
49 ^A	-	-	-	-
50 ^B	0.25	-0.93	Lag	Dilution
52	0.21	0.25	Lead	Concentration
53	-0.25	-0.70	Lead	Dilution
54	0.25	-0.54	Lag	Dilution
58	-0.55	-0.15	Lead	Dilution
59 Multi	-0.25	-0.56	Lead	Dilution

Table E.11. (continued)

59A	-0.09	-0.61	Lead	Dilution
60 ^B	-0.14	-0.06	Lead	Dilution
61 Multi	0.11	0.01	Lead	Concentration
61 ^A	-0.57	-0.17	Lead	Dilution
62 ^B	0.55	0.05	Lead	Concentration
63	0.58	-0.93	Lag	Dilution

Table E.12. Event hysteresis results for DIC. Single-peak events that occurred as parts of a multi-peak event are listed following the “Multi” event with which they were associated and indicated by superscript letters A, B & C (e.g. Event 11 Multi was composed of single-peak events 11 & 12).

DIC Event Hysteresis Results				
Event	HI	FI	HI Type	FI Type
8	-0.09	-0.25	Lead	Dilution
9	-0.66	0.01	Lag	Concentration
10	-0.69	-0.06	Lead	Dilution
11 Multi	-0.37	0.00	Lead	Dilution
11 ^A	-0.48	-0.01	Lead	Dilution
12 ^B	-	-	-	-
16	0.18	-0.85	Lag	Dilution
23 Multi	0.57	-0.85	Lag	Dilution
23 ^A	0.15	-0.87	Lag	Dilution
24 ^B	0.86	-0.74	Lag	Dilution
25	-0.20	0.64	Lag	Concentration
26	-0.51	0.94	Lag	Concentration
27	-0.01	0.75	Lag	Concentration
28 Multi	-0.01	0.99	Lag	Concentration
28 ^A	0.30	0.84	Lead	Concentration
29 ^B	-0.13	0.98	Lag	Concentration
30	0.38	0.60	Lead	Concentration
31	0.35	0.97	Lead	Concentration
32 Multi	0.44	0.48	Lead	Concentration
32 ^A	0.40	0.53	Lead	Concentration
33 ^B	-	-	-	-
34 ^C	-	-	-	-
35	0.77	-0.46	Lag	Dilution
36	0.53	0.97	Lead	Concentration
37	0.29	0.65	Lead	Concentration
41	-0.20	-0.10	Lead	Dilution
44	0.69	0.42	Lead	Concentration
48	0.77	-0.13	Lag	Dilution
49 Multi	0.22	-0.11	Lag	Dilution
49 ^A	-	-	-	-
50 ^B	0.01	-0.95	Lag	Dilution
52	-0.27	0.07	Lag	Concentration
53	-0.52	-0.03	Lead	Dilution
54	0.81	-0.07	Lag	Dilution
58	0.07	-0.41	Lag	Dilution
59 Multi	-0.08	-0.88	Lead	Dilution

Table E.12. (continued)

59 ^A	-0.22	-0.89	Lead	Dilution
60 ^B	0.28	-0.06	Lag	Dilution
61 Multi	0.14	-0.87	Lag	Dilution
61 ^A	0.38	-0.71	Lag	Dilution
62 ^B	0.61	-0.43	Lag	Dilution
63	-0.72	0.48	Lag	Concentration

APPENDIX F: A1 Hysteresis Index vs. Flushing Index Plots for Original Event Data

Hysteresis index (HI) and flushing index (FI) results for all rainfall triggered single-peak and multi-peak events originally available for analysis are presented in the plots in this appendix.

This includes HI and FI results for multi-peak events treated as a single event and as separated single-peak events (rainfall triggered only). The quadrant in which each result falls reflects the results interpretations summarized in Table E.1. Color and shape refer to the identified phase in the double mass curve in which the event occurred. Sizes of the points are scaled to represent the percentage of annual flow each event contributed. Event numbers are labeled beside values and a letter “M” indicates a multipeak event.

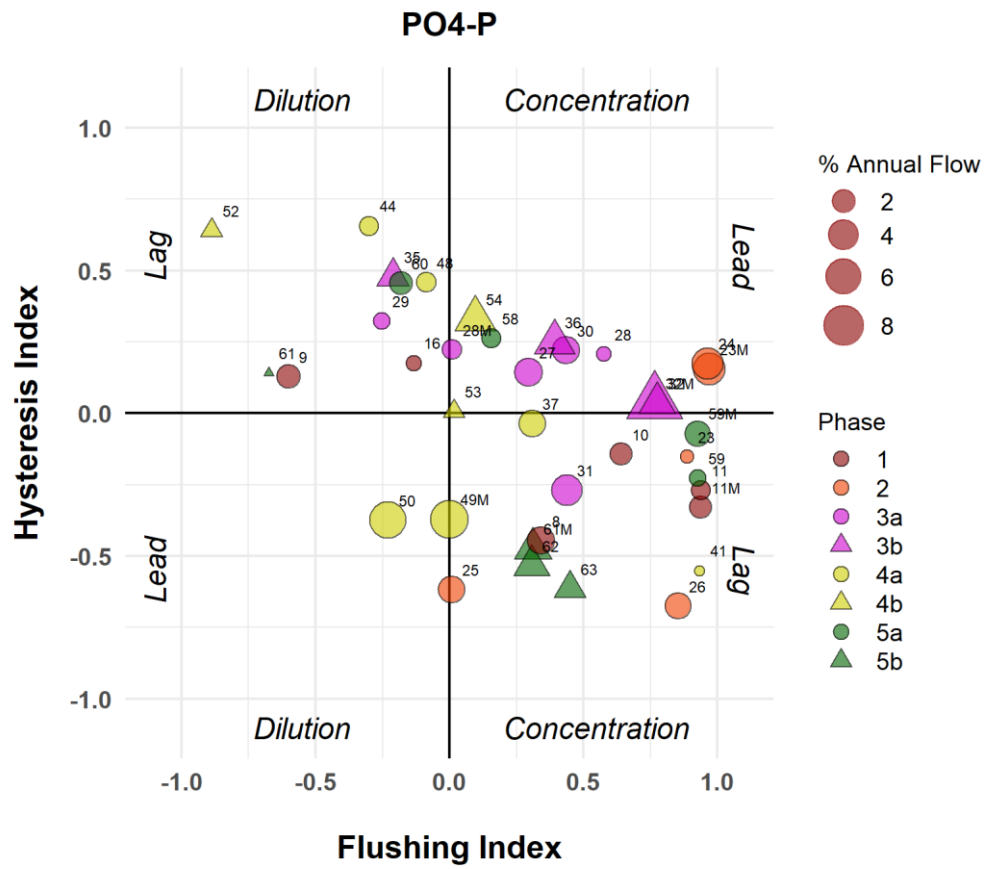


Figure F.1. Hysteresis index plotted as a function of flushing index for phosphate (PO4-P) including all rainfall triggered events originally available for analysis.

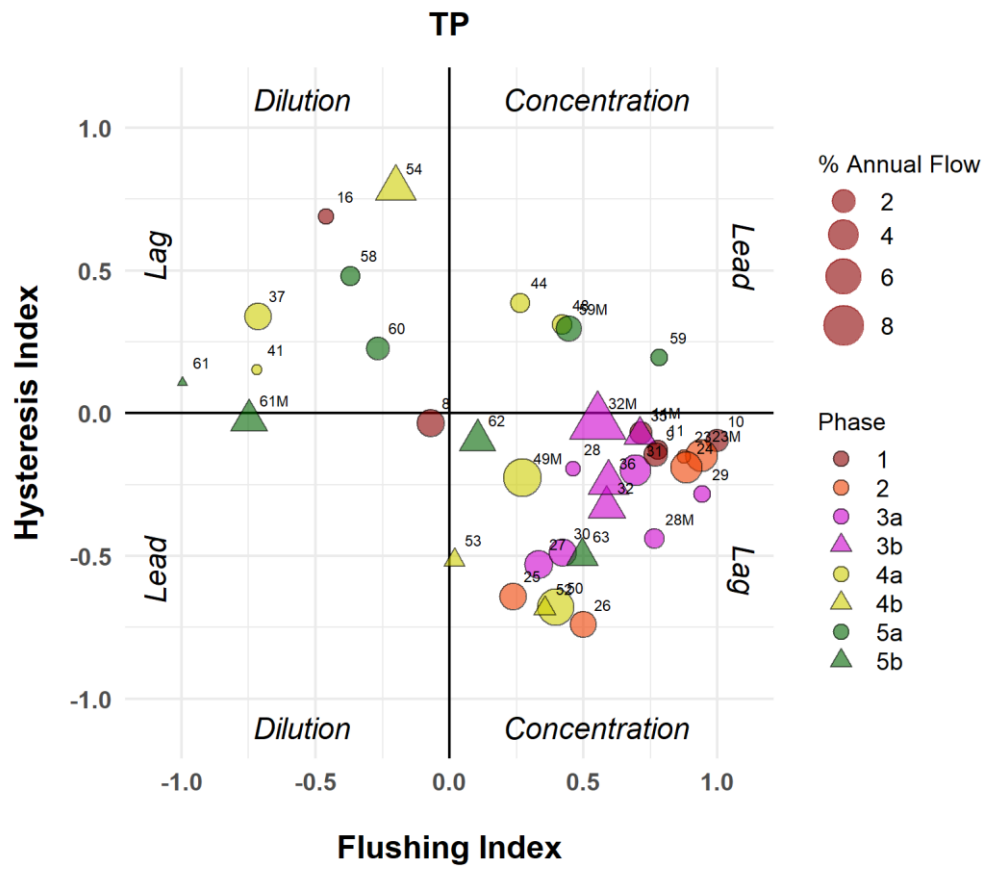


Figure F.2. Hysteresis index plotted as a function of flushing index for total phosphorus (TP) including all rainfall triggered events originally available for analysis.

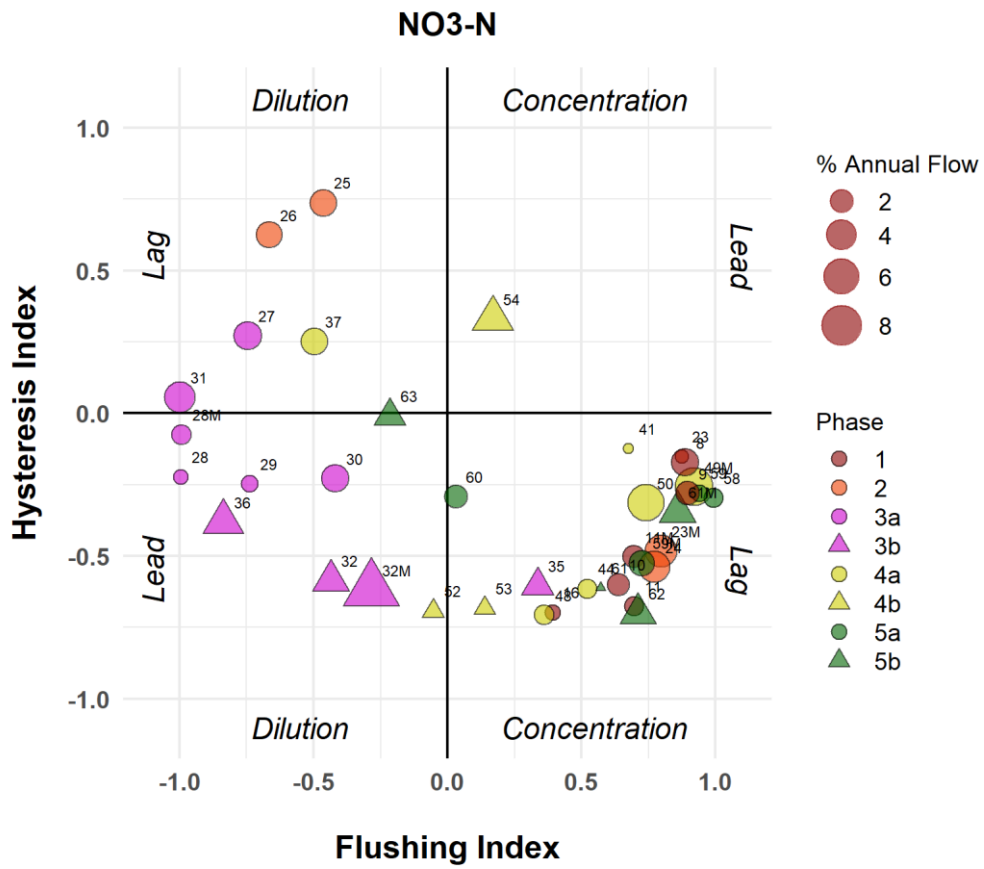


Figure F.3. Hysteresis index plotted as a function of flushing index for nitrate (NO₃-N) including all rainfall triggered events originally available for analysis.

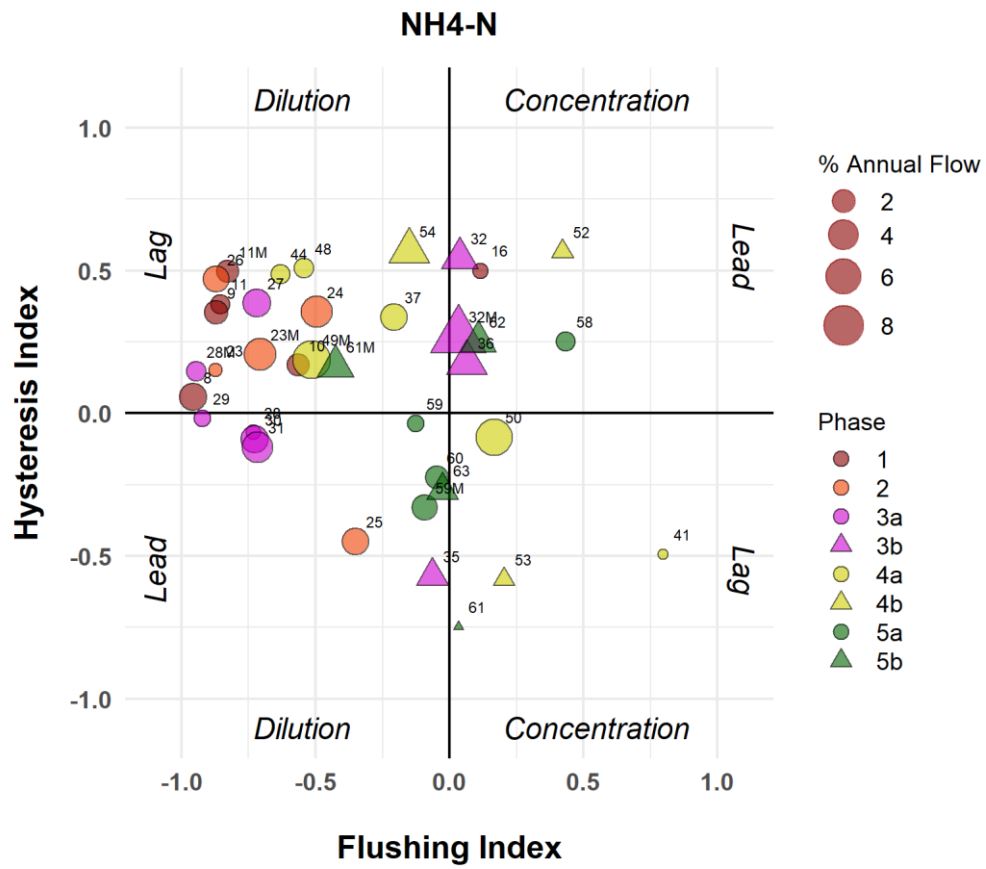


Figure F.4. Hysteresis index plotted as a function of flushing index for ammonium (NH₄-N) including all rainfall triggered events originally available for analysis.

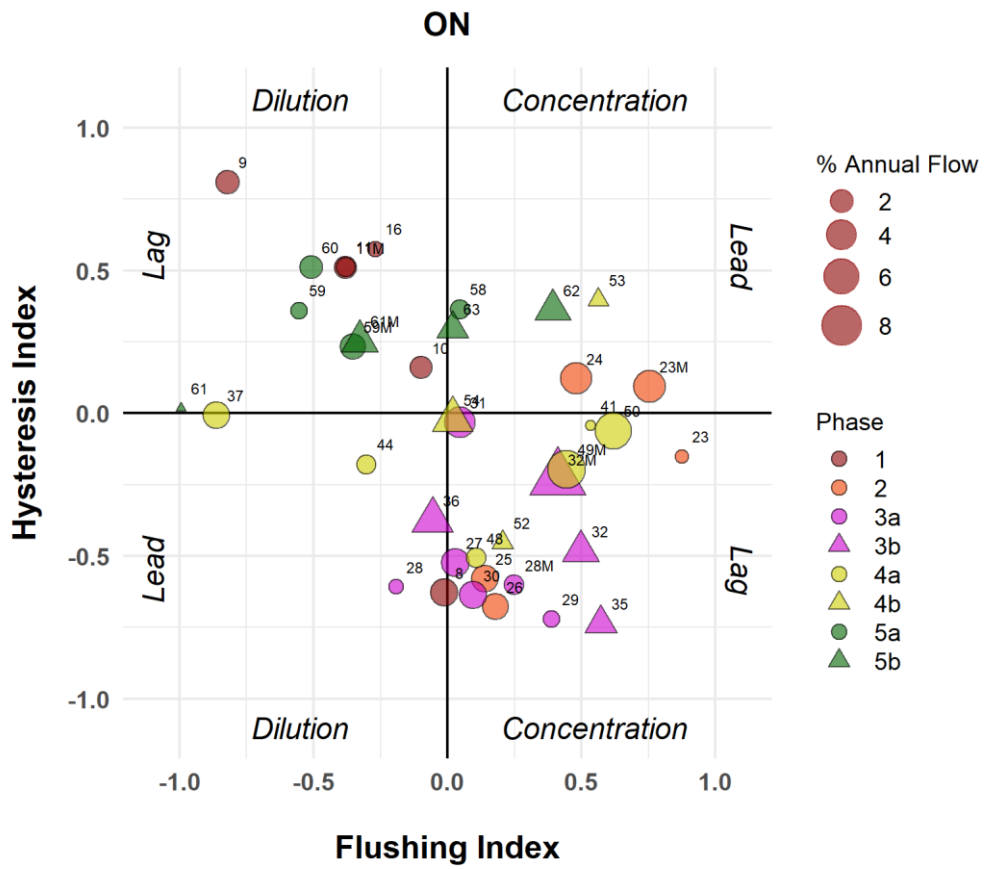


Figure F.5. Hysteresis index plotted as a function of flushing index for organic nitrogen (ON) including all rainfall triggered events originally available for analysis.

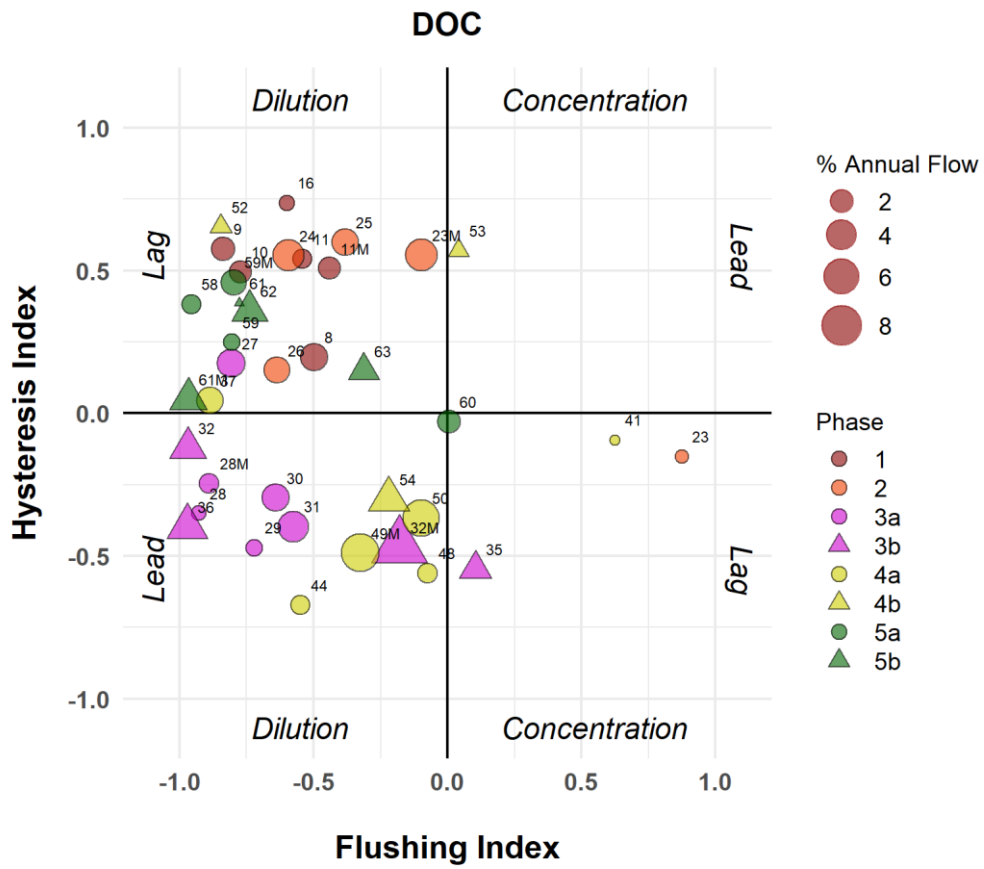


Figure F.6. Hysteresis index plotted as a function of flushing index for dissolve organic carbon (DOC) including all rainfall triggered events originally available for analysis.

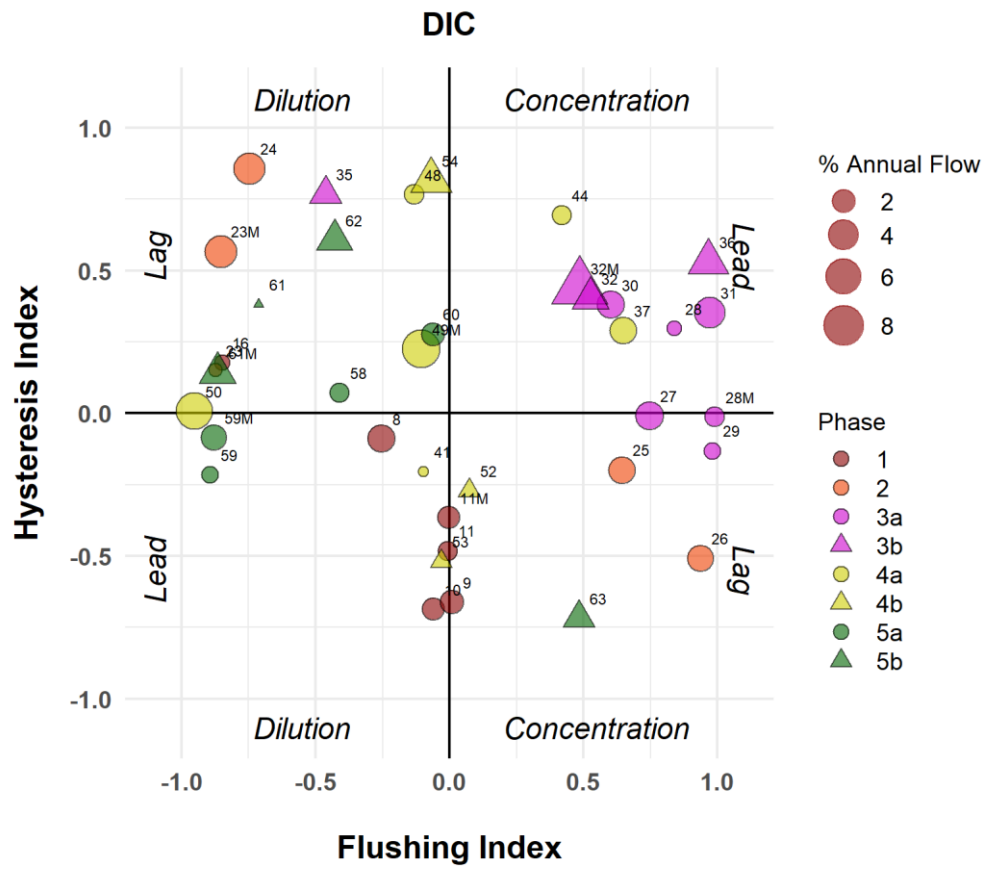


Figure F.7. Hysteresis index plotted as a function of flushing index for dissolved inorganic carbon (DIC) including all rainfall triggered events originally available for analysis.

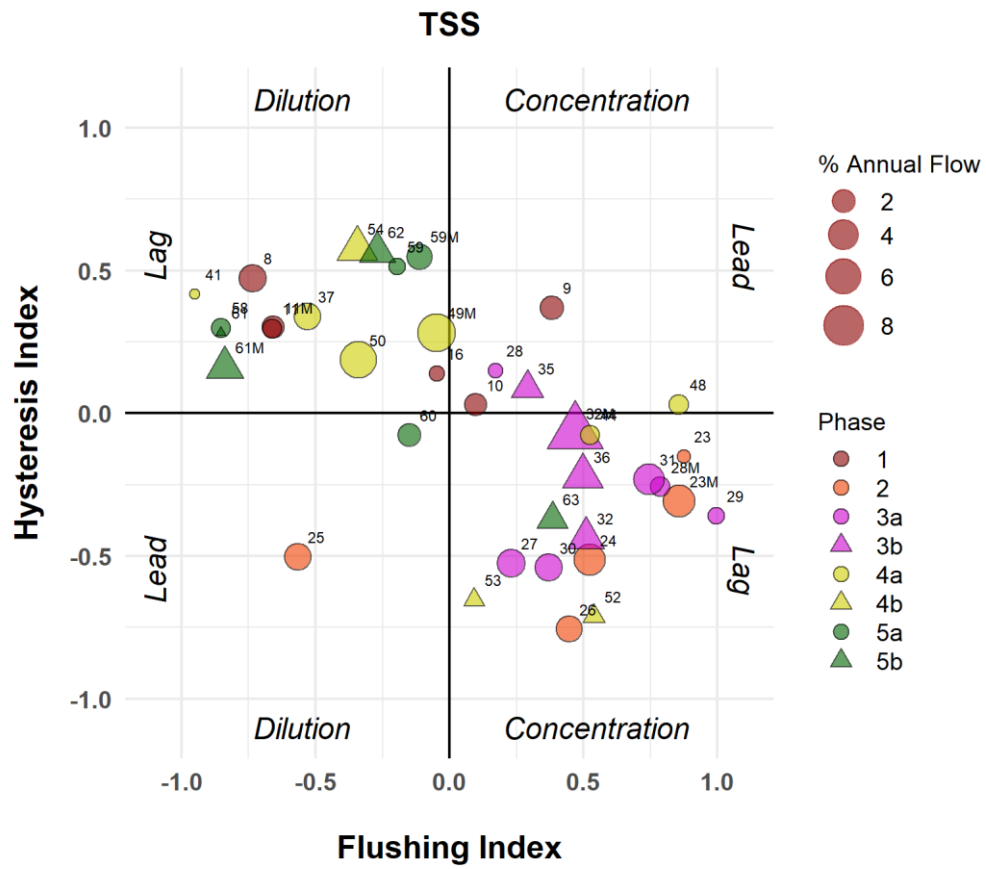


Figure F.8. Hysteresis index plotted as a function of flushing index for total suspended solids (TSS) including all rainfall triggered events originally available for analysis.

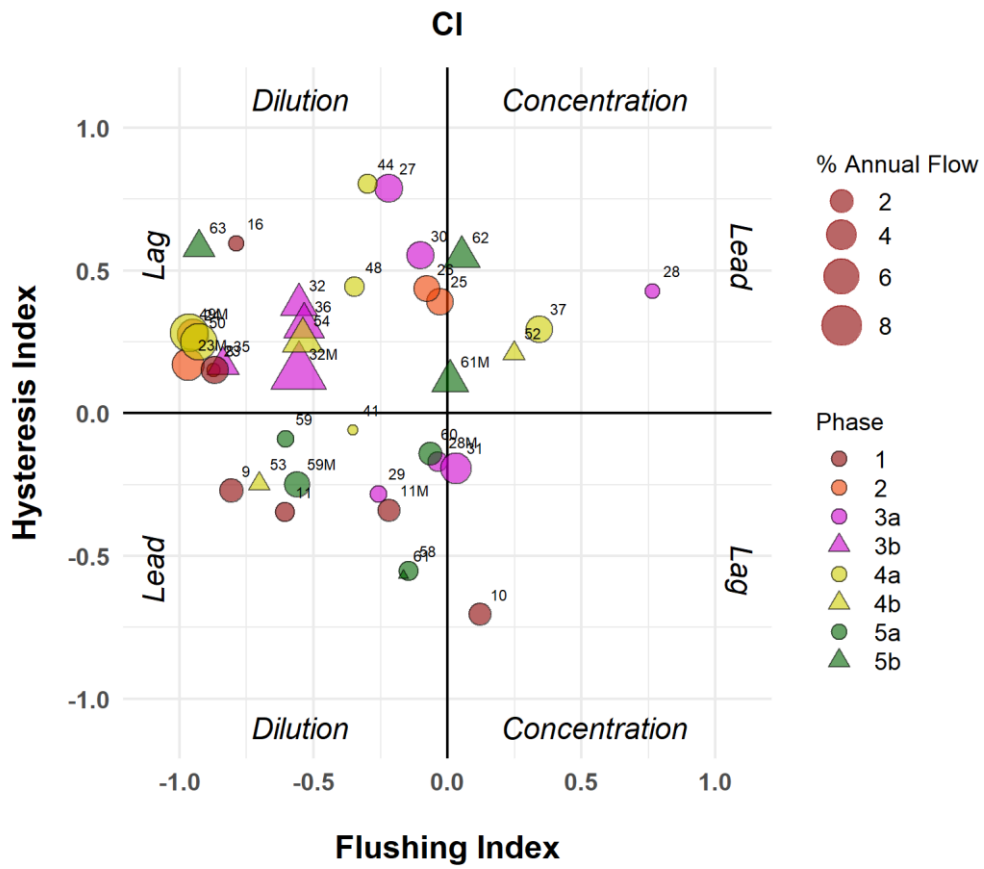


Figure F.9. Hysteresis index plotted as a function of flushing index for chloride (Cl) including all rainfall triggered events originally available for analysis.

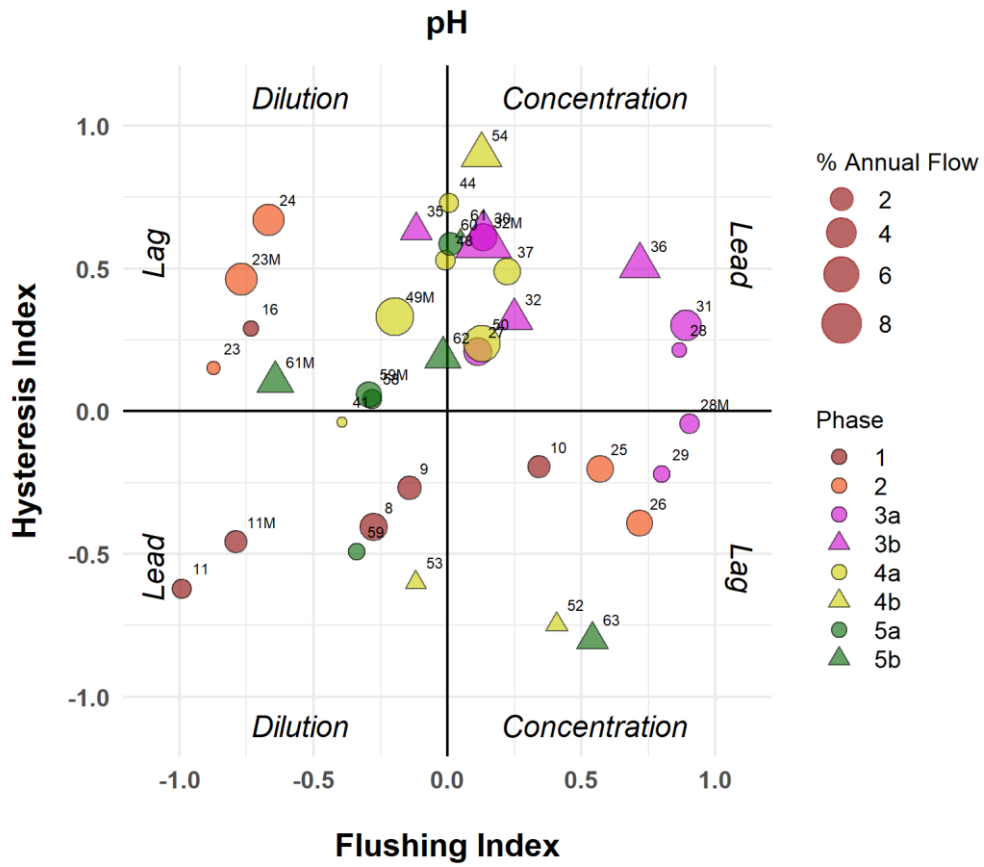


Figure F.10. Hysteresis index plotted as a function of flushing index for pH including all rainfall triggered events originally available for analysis.